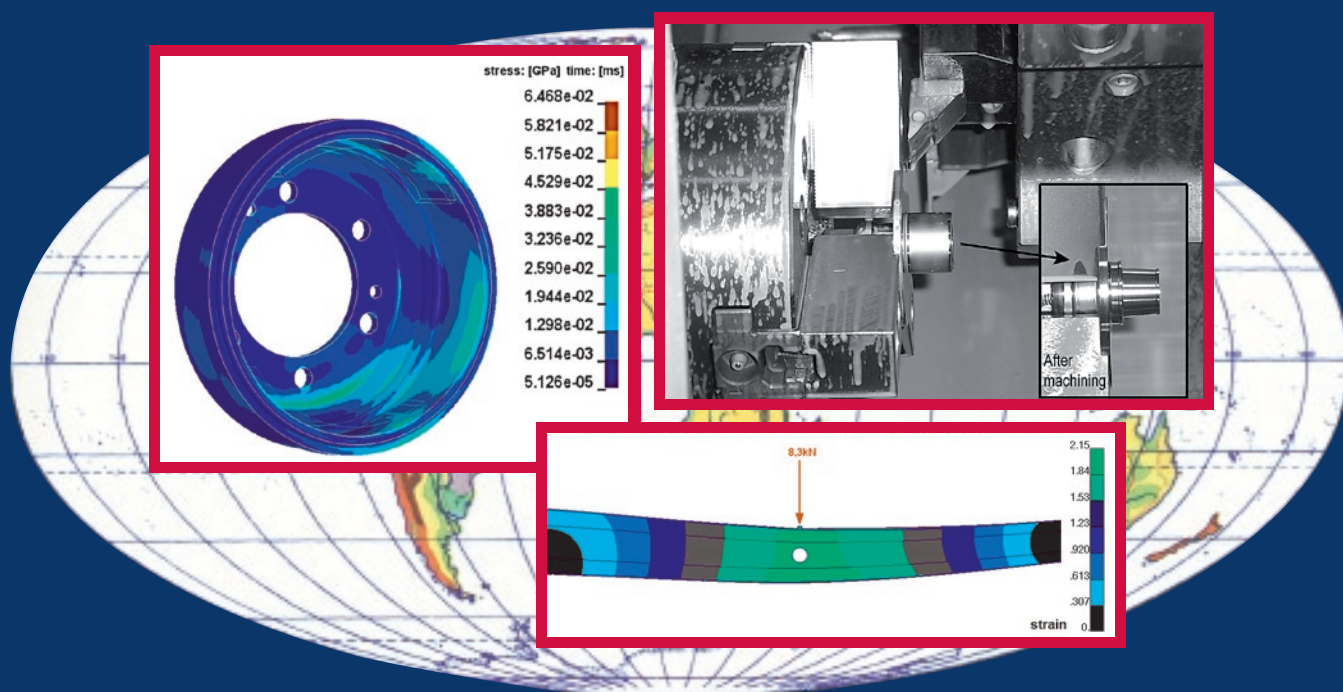


Vol. 15. No 4, 2013

ISSN 1507-2711
Cena: 25 zł (w tym 5% VAT)

EKSPLOATACJA I NIEZAWODNOŚĆ

MAINTENANCE AND RELIABILITY



Polskie Naukowo Techniczne Towarzystwo Eksploatacyjne
Warszawa

Polish Maintenance Society
Warsaw

Professor Andrzej Niewczas, PhD, DSc (Eng)

*Chair of Scientific Board
President of the Board of the Polish Maintenance Society*

Professor Holm Altenbach, PhD, DSc (Eng)
Martin Luther Universität, Halle-Wittenberg, Germany

Professor Zdzisław Chłopek, PhD, DSc (Eng)
Warsaw University of Technology, Warsaw

Professor Jan Dąbrowski, PhD, DSc (Eng)
Białystok Technical University, Białystok

Professor Sławczo Denczew, PhD, DSc (Eng)
The Main School of Fire Service, Warsaw

Dr Ilia Frenkel
Shamoon College of Engineering, Beer Sheva, Israel

Professor Olgierd Hryniewicz, PhD, DSc (Eng)
Systems Research Institute of the Polish Academy of Science, Warsaw

Professor Hong-Zhong Huang, PhD, DSc
University of Electronic Science and Technology of China, Chengdu, Sichuan, China

Professor Krzysztof Kolowrocki, PhD, DSc
Gdynia Maritime University

Professor Štefan Liščák
Žilinská univerzita, Žilina, Slovak Republic

Professor Vaclav Legat
Czech University of Agriculture, Prague, Czech Republic

Professor Leonas Povilas Lingaitis
Vilnius Gediminas Technical University, Vilnius, Lithuania

Professor Jerzy Merkiś, PhD, DSc (Eng)
Poznań University of Technology, Poznań

Professor Gilbert De Mey
University of Ghent, Belgium

Professor Tomasz Nowakowski, PhD, DSc (Eng)
Wrocław University of Technology, Wrocław

Professor Marek Orkisz, PhD, DSc (Eng)
Rzeszów University of Technology, Rzeszów

Professor Stanisław Piasecki, PhD, DSc (Eng)
*Systems Research Institute
of the Polish Academy of Sciences, Warsaw*

Professor Leszek Piaseczny, PhD, DSc (Eng)
Polish Naval Academy, Gdynia

Professor Stanisław Radkowski, PhD, DSc (Eng)
Warsaw University of Technology, Warsaw

Professor Andrzej Seweryn, PhD, DSc (Eng)
Białystok Technical University, Białystok

Professor Zbigniew Smalko, PhD, DSc (Eng)
Air Force Institute of Technology, Warsaw

Professor Marian Szczerek, PhD, DSc (Eng)
Institute for Sustainable Technologies, Radom

Professor Jan Szybka, PhD, DSc (Eng)
AGH University of Science and Technology, Cracow

Professor Katsumi Tanaka
Kyoto University, Kyoto, Japan

Professor David Vališ, PhD, DSc (Eng)
University of Defence, Brno, Czech Republic

Professor Irina Yatskiv
Riga Transport and Telecommunication Institute, Latvia

Co-financed by the Minister of Science and Higher Education

The Journal is indexed and abstracted in the Journal Citation Reports (JCR Science Edition), Scopus, Science Citation Index Expanded (SciSearch®) and Index Copernicus International.

The Quarterly appears on the list of journals credited with a high impact factor by the Polish Ministry of Science and Higher Education and is indexed in the Polish Technical Journal Contents database – BAZTECH and the database of the Digital Library Federation.

All the scientific articles have received two positive reviews from independent reviewers.

Our IF is 0.293

Editorial staff:	Dariusz Mazurkiewicz, PhD, DSc (Eng), Associate Professor (Editor-in-Chief, Secretary of the Scientific Board) Tomasz Klepka, PhD, DSc (Eng) (Deputy Editor-in-Chief) Teresa Błachnio-Krolopp, MSc (Eng) (Editorial secretary) Andrzej Koma (Typesetting and text makeup) Krzysztof Olszewski, PhD (Eng) (Webmaster)
Publisher:	Polish Maintenance Society, Warsaw
Scientific patronage:	Polish Academy of Sciences Branch in Lublin
Address for correspondence:	“Eksploracja i Niezawodność” – Editorial Office 20-618 Lublin, ul. Nadbystrzycka 36, Poland e-mail: office@ein.org.pl http://www.ein.org.pl/
Circulation:	550 copies

Prof. Leonas Povilas LINGAITIS – Obituary	III
Science and Technology	
Abstracts	IV
Henryk TOMASZEK, Michał JASZTAŁ, Mariusz ZIEJA	
Application of the Paris formula with $m=2$ and the variable load spectrum to a simplified method for evaluation of reliability and fatigue life demonstrated by aircraft components	
Uproszczona metodaszacowania niezawodności i trwałości zmęczeniowej elementów konstrukcji statku powietrznego z wykorzystaniem wzoru Parisa dla $m=2$ i zmiennego widma obciążenia	297
Jarosław SUGIER, George J. ANDERS	
Modelling and evaluation of deterioration process with maintenance activities	
Modelowanie i analiza procesu starzenia maszyn i urządzeń poddanych okresowym remontom	305
Vidas ŽURAILIS, Edgar SOKOLOVSKIJ, Jonas MATIJOŠIUS	
The opportunities for establishing the critical speed of the vehicle on research in its lateral dynamics	
Możliwości określenia prędkości krytycznej pojazdu na podstawie badań jego dynamiki poprzecznej	312
Marek KALBARCZYK, Remigiusz MICHALCZEWSKI, Witold PIEKOSZEWSKI, Marian SZCZEREK	
The influence of oils on the scuffing of concentrated friction joints with low-friction coated elements	
Wpływ olejów na zacieranie elementów z powłokami niskotarciowymi skojarzonymi w styku skoncentrowanym	319
Yi-Heng YANG, Kuo-Shong WANG	
Study of the characteristics about insulation damage based on the accelerated life tests	
Badanie charakterystyk uszkodzeń izolacji w oparciu o testy przyspieszonego starzenia	325
Marcin MICHALAK, Marek SIKORA, Jurand SOBCZYK	
Analysis of the longwall conveyor chain based on a harmonic analysis	
Analiza pracy łańcucha przenośnika ścianowego w oparciu o analizę harmoniczną	332
Paweł BARANOWSKI, Krzysztof DAMAZIAK, Jerzy MAŁACHOWSKI	
Brake system studies using numerical methods	
Badania układów hamulcowych metodami numerycznymi	337
Sławomir DUDA	
Numerical modeling and simulating the dynamic interactions within the drive system of electric rail vehicles	
Modelowanie i symulacja numeryczna oddziaływań dynamicznych w układzie napędowym elektrycznych pojazdów szynowych	343
Marek ROŚKOWICZ, Tomasz SMAL	
Research on durability of composite materials used in repairing aircraft components	
Badanie materiałów kompozytowych wykorzystanych do naprawy konstrukcji lotniczych	349
Wei LUO, Chunhua ZHANG, Xun CHEN, Yashun WANG	
System reliability demonstration with equivalent data from component accelerated testing based on reliability target transformation	
Stwierdzanie niezawodności systemu na podstawie równoważnych danych z przyspieszonych badań elementów składowych w oparciu o transformację celu niezawodnościowego	356
Jerzy MERKISZ, Piotr LIJEWSKI, Paweł FUĆ, Sylwester WEYMANN	
Exhaust emission tests from non-road vehicles conducted with the use of PEMS analyzers	
Badania emisji związków toksycznych spalin z pojazdów o zastosowaniach pozadrogowych z wykorzystaniem analizatorów PEMS	364
Bolesław KARWAT, Dariusz GŁOWIŃSKI, Emil STAŃCZYK	
Analysis of the influence of factors on the photometry of the optical light system of chmsl car lamps	
Analiza czynników wpływających na fotometrię systemu optyczno-światelnego lampy samochodowej typu chmsl	369
Gintautas BUREIKA, Giedrius BEKINTIS, Lionginas LIUDVINAVIČIUS, Gediminas VAIČIŪNAS	
Applying analytic hierarchy process to assess traffic safety risk of railway infrastructure	
Zastosowanie procesu hierarchii analitycznej do oceny zagrożenia bezpieczeństwa ruchu w odniesieniu do infrastruktury kolejowej	376

Artūras KERŠYS, Dalius KALISINSKAS, Saugirdas PUKALSKAS, Andrius VILKAUSKAS, Robertas KERŠYS, Rolandas MAKARAS

Investigation of the influence of hydrogen used in internal combustion engines on exhaust emission Badanie wpływu wodoru stosowanego w silnikach spalinowych na emisję spalin	384
--	------------

Wojciech CZUBA, Kazimierz FURMANIK

Analysis of a grain motion in the transfer area of the belt conveyor Analiza ruchu ziarna w przestrzeni przesypowej przenośnika taśmowego.....	390
---	------------

Chao ZHANG, Shaoping WANG

Solid lubricated bearings performance degradation assessment: A fuzzy self-organizing map method Ocena obniżenia charakterystyk łożysk ze smarem stałym: metoda rozmytych samoorganizujących się map	397
---	------------

Yan-Feng LI, Jinhua MI, Hong-Zhong HUANG, Shun-Peng ZHU, Ningcong XIAO

Fault tree analysis of train rear-end collision accident considering common cause failure Analiza drzewa uszkodzeń dla kolizji tylnej części składu pociągu z uwzględnieniem uszkodzenia spowodowanego wspólną przyczyną	403
---	------------

Adam ROSINSKI, Tadeusz DABROWSKI

Modelling reliability of uninterruptible power supply units Modelowanie niezawodności zasilaczy buforowych	409
---	------------

Krzysztof PARCZEWSKI, Henryk WNEK

Using mobile scaled vehicle to investigate the truck lateral stability Wykorzystanie mobilnego modelu pojazdu do analizy stateczności poprzecznej samochodu ciężarowego	414
--	------------

Wojciech ZĘBALA, Bogdan SŁODKI, Grzegorz STRUZIKIEWICZ

Productivity and reliability improvement in turning Inconel 718 alloy – case study Poprawa produktywności i niezawodności toczenia stopu Inconel 718 – studium przypadku	421
---	------------

Sylvia WERBIŃSKA-WOJCIECHOWSKA

Time resource problem in logistics systems dependability modelling Problem rezerwowania czasowego w modelowaniu niezawodności systemów logistycznych	427
---	------------

František GREŠKOVIČ, Ľudmila DULEBOVÁ, Branislav DULEBA, Aneta KRZYŽAK

Criteria of maintenance for assessing the suitability of aluminum alloys for the production of interchangeable parts injection mold Eksploatacyjne kryteria oceny przydatności stopów aluminium do produkcji wymiennych części form wtryskowych.....	434
---	------------

Dong ZHOU, Xu JIA, Chuan LV, Yongxiang LI

Maintainability allocation method based on time characteristics for complex equipment Metoda alokacji obsługiwalności złożonych urządzeń oparta na charakterystykach czasowych	441
---	------------

Tong YIFEI, Tang ZHAOHUI, Ye WEI, Yang ZHEN

Research on energy-saving optimization design of bridge crane Badania dotyczące optymalizacji energooszczędności konstrukcji suwnicy pomostowej	449
--	------------

Anna ŻYCZYŃSKA

The primary energy factor for the urban heating system with the heat source working in association Współczynnik nakładu nieodnawialnej energii pierwotnej dla miejskiego systemu ciepłowniczego ze źródłem ciepła pracującym w skojarzeniu ..	458
--	------------



PROF. LEONAS POVILAS LINGAITIS

OBITUARY

Vilnius Gediminas Technical University (VGTU) lost a long-term academic staff member, Head of Department of Railway Transport at the Faculty of Transport Engineering, Prof. Leonas Povilas Lingaitis. The professor passed away on 19 July 2013 after his illness at the age of 75.

The graduate of Kaunas Polytechnic Institute gained the mechanical engineering diploma in 1964 with the road construction machinery being his major. He worked in the construction bureau at the Radio Factory in Kaunas for 4 years before entering the Leningrad Polytechnic Institute in 1968. In 1971 Leonas P. Lingaitis was awarded the Doctor's degree in technical sciences and came back to Lithuania to develop his career as an associate professor at Vilnius Gediminas Technical University (at that time – Vilnius Civil Engineering Institute). In 1972 he worked at the Department of Automobiles and in 1985 he started working in the Department of Technologic Equipment. In 1988 Dr L. P. Lingaitis defended his thesis for Doctor Habilitus degree at Moscow Civil Engineering Institute and in 1990 was awarded the Professor's title at his home institution.

In 1994 Prof. L.P. Lingaitis was appointed the Head of the newly established Department of Railway Transport at the Faculty of Transport Engineering, and worked there till his last days. The Professor was the Dean of the Faculty of Transport Engineering in the period of 1998–2007.

Prof. Leonas Povilas Lingaitis was the coordinator of a variety of contracts for the research and expert analysis ordered by companies. He was the initiator, the leader, the author and co-author of more than 250 scientific articles, the author of a monograph and the co-author of two monographs. The Professor's mission in education resulted in his authorship of several manuals and 8 textbooks published for the university students. In 2002 the Ministry of Education and Sciences of the Republic of Lithuania granted L.P. Lingaitis with the state outstanding researcher's award. In the period of 2003–2006 the Professor won awards for his manuals "Railway Coach Maintenance", "Diagnostic Analysis of Rail Coaches", "Maintenance and Reliability of Railway Coaches". In 2006 on the occasion of VGTU 50th anniversary L. P. Lingaitis was awarded the University golden medal for the professor's fruitful academic activity and devotion to the academic community. In 2013 the Senate of Vilnius Gediminas Technical University conferred Leonas Povilas Lingaitis the title of Professor Emeritus.

Professor initiated and actively promoted the cooperation between the Department of Railway Transport and "Lithuanian Railways" Plc. Leonas Povilas Lingaitis was elected the member of Railway transport committee in the Lithuanian Confederation of Industrialists (LPK), a member of Technical Council in "Lithuanian Railways" Plc., a member of the Engineering Industries Association in Lithuania, and a member of Research and Information Technology Council in the Ministry of Transport and Communications. In 2004 the professor was awarded the name of a "Distinguished Railman" for his active scientific support and influence to the company "Lithuanian Railways", he was also selected the Chairman of the Union of the Narrow Gauge Railway in Lithuania. Prof. Leonas P. Lingaitis actively participated in international research projects, made over 40 scientific presentations in international conferences. He was involved in partnership activities with the colleagues of the relevant institutions and companies in Latvia, Belorussia, Poland and Ukraine. The professor was the member of editorial boards of two international scientific journals and the member of scientific committee of 5 international scientific conferences.

The colleagues will remember Leonas Povilas Lingaitis as a competent, and demanding leader, and at the same time hardworking, open to suggestions and a kind person.

Everyone who knew the Professor will always keep a bright memory of him. God bless Prof. Leonas Povilas Lingaitis.

prof. Gintautas Bureika

TOMASZEK H, JASZTAŁ M, ZIEJA M. **Application of the Paris formula with $m=2$ and the variable load spectrum to a simplified method for evaluation of reliability and fatigue life demonstrated by aircraft components.** Eksploatacja i Niezawodność – Maintenance and Reliability 2013; 15 (4): 297–304.

The presented paper is the follow-up to the study, where the method for assessment of the fatigue life of a structural component was outlined with consideration of the variable spectrum of loads and with use of the Paris formula for $m \neq 2$. Due to the different nature inherent to analytic forms of solutions for the Paris equations with their exponential parameter $m = 2$, that special case is the subject of a separate analysis. This paper also uses the transformation of a real spectrum with variable values of fatigue cycles into a homogenous spectrum with weighted cycles. The method was developed that uses the transformed spectrum to evaluate fatigue life for a selected component of the aircraft structure when the component suffers from an initial crack. The method for modeling of the crack length expansion uses a differential equation that is then subjected to transformations to obtain a partial differential equation of the Fokker-Planck type, which has a particular solution, explicitly the length density function for the crack of the component in question. That length density function served subsequently to determine reliability and fatigue life of a structural component where the crack length expanded from the permissible value l_d to the critical threshold l_{kr} .

SUGIER J, ANDERS GJ. **Modelling and evaluation of deterioration process with maintenance activities.** Eksploatacja i Niezawodność – Maintenance and Reliability 2013; 15 (4): 305–311.

In this paper, we present an approach which allows evaluation of various possible maintenance scenarios with respect to both reliability and economic criteria. The method is based on the concept of a life curve and discounted cost used to study the effect of equipment aging under different maintenance strategies. The deterioration process is first described by a Markov model and then its various characteristics are used to develop the equipment life curve and to quantify other reliability parameters. Based on these data, effects of various “what-if” maintenance scenarios can be examined and their efficiency compared. Simple life curves are combined to model equipment deterioration undergoing diverse maintenance actions, while computing other parameters of the model allows evaluation of additional critical factors, such as the probability of equipment failure. Additionally, the paper deals with the problem of the model adjustment so that the computed repair frequencies are close to the historical values, which is very important in practical applications of the method. Moreover, we discuss the problems which may arise if automatic adjustment is used in cases when the hypothetical maintenance policies go beyond the conditions upon which the original model was built.

ŽURAULIS V, SOKOLOVSKIJ E, MATIJOŠIUS J. **The opportunities for establishing the critical speed of the vehicle on research in its lateral dynamics.** Eksploatacja i Niezawodność – Maintenance and Reliability 2013; 15 (4): 312–318.

In this paper, the parameters important for lateral dynamics of vehicles are analyzed in order to establish the values of its critical speed on the moment of losing the stability. The values of the vehicle's speed yaw rate, the steering wheel angle, the lateral acceleration, and the roll angle obtained from experimental tests are filtered according to the set conditions and only the general values that mean the beginning of the vehicle slipping are selected. For more precise assessment of the selected values, a statistical analysis is carried out. The Normal distribution law describes scattering of the selected values in the most relevant way and concretizes the critical speed being established. In the end of the paper, the obtained values of the speed are compared to the results of the theoretical calculations. Conclusions assessing the developed technique of selection of the parameters are provided.

KALBARCZYK M, MICHALCZEWSKI R, PIEKOSZEWSKI W, SZCZEREK M. **The influence of oils on the scuffing of concentrated friction joints with low-friction coated elements.** Eksploatacja i Niezawodność – Maintenance and Reliability 2013; 15 (4): 319–324.

The paper presents the results of four-ball scuffing tests for the following oils: poly-alphaolefine oil (PAO 8), refined rapeseed oil (RzR), as well as mineral and synthetic oils of GL5 API performance level. Three material combinations of friction joints were investigated, with the upper ball material as a variable. In the research, 100Cr6 bearing steel balls were used. The tests were carried out for uncoated and low-friction coated balls. Two PVD coatings were used: a-C:H/W and MoS₂/Ti. The research results were compared with the outcome from the tests of the reference mineral oil (RL 219). The influence of oils on friction joint scuffing characteristics were determined using the scuffing load P_t and limiting pressure of seizure p_{oz} , obtained by means of the four-ball method with continuously increasing load. The obtained results indicate that, in case of concentrated friction joints with low-friction coated elements, the influence of selected oils on scuffing depends on the type of PVD coating used. The research findings also show the significant practical effect of aforementioned PVD

TOMASZEK H, JASZTAŁ M, ZIEJA M. **Uproszczona metoda szacowania niezawodności i trwałości zmęczeniowej elementów konstrukcji statku powietrznego z wykorzystaniem wzoru Parisa dla $m=2$ i zmiennego widma obciążenia.** Eksploatacja i Niezawodność – Maintenance and Reliability 2013; 15 (4): 297–304.

Prezentowany artykuł jest uzupełnieniem pracy, w której przedstawiono metodę oceny trwałości zmęczeniowej elementu konstrukcji dla zmiennego widma obciążenia z wykorzystaniem wzoru Parisa dla $m \neq 2$. Ze względu na odmienną postać analitycznych rozwiązań dla wykładnika równania Parisa $m=2$, ten szczególnie przypadek rozwiązań został przedstawiony w niniejszym opracowaniu. Pokazany został sposób przekształcenia widma rzeczywistego o zmiennych wartościach cykli w widmo jednorodne o cyklach ważonych. Wykorzystując widmo przekształcone opracowano metodę oceny trwałości zmęczeniowej wybranego elementu konstrukcji statku powietrznego z początkowym pęknięciem. Do modelowania przyrostu długości pęknięcia wykorzystano równanie różnicowe, z którego po przekształceniu otrzymano równanie różniczkowe cząstkowe typu Fokkera-Plancka. Rozwiązaniem szczególnym tego równania jest funkcja gęstości długości pęknięcia elementu. Wykorzystując następnie funkcję gęstości długości pęknięcia określono niezawodność i trwałość zmęczeniową elementu konstrukcji dla pęknięcia narastającego do wartości dopuszczalnej l_d mniejszej od wartości krytycznej l_{kr} .

SUGIER J, ANDERS GJ. **Modelowanie i analiza procesu starzenia maszyn i urządzeń poddanych okresowym remontom.** Eksploatacja i Niezawodność – Maintenance and Reliability 2013; 15 (4): 305–311.

Przedmiotem artykułu jest modelowanie różnych możliwych scenariuszy eksploatacyjnych maszyn i urządzeń, które uwzględnia kryteria zarówno niezawodnościowe, jak i ekonomiczne. Metoda opiera się na zastosowaniu krzywych życia (ang. life curves) oraz kosztów zdyskontowanych (ang. discounted costs) do analizy wpływu, jaki różne strategie eksploatacyjne wywierają na starzenie się sprzętu. Punktem wyjścia jest opisanie procesu starzenia przez model Markowa, którego charakterystyki umożliwiają następnie wyznaczenie kształtu krzywej życia oraz obliczenie innych parametrów niezawodnościowych badanego sprzętu. W oparciu o uzyskane dane możliwa jest ocena różnych hipotetycznych scenariuszy eksploatacyjnych oraz porównanie ich efektywności. Proste krzywe życia mogą być łączone ze sobą w celu wizualizacji starzenia sprzętu poddawanego różnorodnym możliwym czynnościom naprawczym, natomiast obliczenie innych charakterystyk modelu pozwala wyznaczyć dodatkowe ważne parametry, takie jak prawdopodobieństwo uszkodzenia. Dodatkowo artykuł opisuje zagadnienie korygowania parametrów modelu, tak aby obliczane w nim częstości napraw sprzętu były bliskie wartościom znanym z jego historii eksploatacji, co jest bardzo ważne w praktycznych zastosowaniach metody. Omawiamy także problemy mogące pojawić się, gdy algorytm automatycznego korygowania modelu jest stosowany w analizach hipotetycznych strategii eksploatacyjnych wykraczających poza warunki, dla których model oryginalny został opracowany.

ŽURAULIS V, SOKOLOVSKIJ E, MATIJOŠIUS J. **Możliwości określenia prędkości krytycznej pojazdu na podstawie badań jego dynamiki poprzecznej.** Eksploatacja i Niezawodność – Maintenance and Reliability 2013; 15 (4): 312–318.

Niniejsza praca analizuje parametry istotne dla dynamiki poprzecznej pojazdów w celu ustalenia wartości prędkości krytycznej w momencie utraty przez nie stabilności. Wartości szybkości zbieżności przez pojazd z kursu, kąta skrętu kierownicy, przyspieszenia poprzecznego oraz kąta odchylenia się pojazdu, uzyskane w badaniach doświadczalnych, dobrano pod kątem założonych warunków i tylko ogólne wartości oznaczające początek poślizgu pojazdu zostały wybrane. W celu dokładniejszej oceny wybranych wartości przeprowadzono analizę statystyczną. Prawo rozkładu normalnego opisuje odpowiednie rozproszenie wybranych wartości i konkretyzują ustalony prędkość krytyczną. W końcowej części pracy porównano uzyskane wartości prędkości z wynikami obliczeń teoretycznych. Wnioski służą ocenie opracowanej techniki doboru parametrów.

KALBARCZYK M, MICHALCZEWSKI R, PIEKOSZEWSKI W, SZCZEREK M. **Wpływ olejów na zacieranie elementów z powłokami niskotarciowymi skojarzonymi w styku skoncentrowanym.** Eksploatacja i Niezawodność – Maintenance and Reliability 2013; 15 (4): 319–324.

W artykule przedstawiono wyniki badań zacierania modelowego, czterokulowego wężła tarcia, smarowanego olejami bez dodatków smarnościowych: mineralnym olejem wzorcowym (RL 219), syntetycznym (PAO 8), rafinowanym olejem rzepakowym (RzR), oraz dwoma olejami handlowymi z dodatkami klasy GL5 na bazie mineralnej i syntetycznej. Przebadano trzy skojarzenia materiałowe, w których zmienną stanowił materiał kulki górnej. Zastosowano kulki ze stali łożyskowej (100Cr6) bez powłoki oraz z niskotarciowymi powłokami: a-C:H/W (WC/C) oraz MoS₂/Ti, osadzonymi metodą PVD. Rezultaty badań porównano z wynikami otrzymanymi dla mineralnego oleju wzorcowego (RL 219). Dokonano oceny wpływu oleju na zacieranie wężła tarcia, wykorzystując wskaźniki obciążenia zacierającego P_t oraz granicznego nacisku zatarcia p_{oz} , otrzymane przy zastosowaniu metody narastającym obciążeniem. Stwierdzono, że wpływ rodzaju oleju na zatarcie elementów stalowych pokrytych powłokami PVD jest zależny od rodzaju powłoki. Ważnym efektem praktycznym jest też wskazanie, że powłoki PVD nanoszone

coatings deposition on steel elements of friction joints, which is the interception of the anti-suffing function of the classical extreme pressure (EP) oil additives by the coating. Due to that fact, the usage of such coatings makes it possible to reduce the concentration of EP additives, resulting in more environmental friendly oils.

YANG Y-H, WANG K-S. Study of the characteristics about insulation damage based on the accelerated life tests. Eksploatacja i Niezawodność – Maintenance and Reliability 2013; 15 (4): 325–331.

In this study the Maximum Likelihood Estimator is taken to identify the characteristics of insulation failure about the class-H motors by considering the accelerated life testing data under censored situation from Nelson. Based on the Weibull survival modeling the failure is expressed as the series connection of three modes, namely the turn, phase, and ground, respectively, the so-called competing failure. The main concern in present investigation is about the variation of shape parameters, β with the temperature. The Gompertz-type relation of $\beta_i(T)$ is suggested with the reference temperature, T_{ri} for the i -th failure mode. It is found that the T_{ri} 's not only distinguish the characteristics of cumulative damage process about the insulation, but also involve the estimation of mean-time-to-failure (MTTF). Physically T_{ri} denotes the turning point of varied β_i as the i -th failure mode becomes moderate in a sense of less capability about the accumulation of insulation damage at higher temperature where corresponds the thermal degradation process. The numerical results indicate that the insulation technique used is acceptable as the operation temperature kept in the use condition 363K. According to the predicted lifetime as the temperature rises up to 440K, which still within the allowed range in application, the turn structure needs to be rearranged primarily, then the phase next. The ground mode has only influence on the failure at much higher temperature.

MICHALAK M, SIKORA M, SOBCZYK J. Analysis of the longwall conveyor chain based on a harmonic analysis. Eksploatacja i Niezawodność – Maintenance and Reliability 2013; 15 (4): 332–336.

This paper describes the use of harmonic analysis in the analysis of a longwall conveyor chain. Correct and stable operation of the chain is connected both with the safety of the work and the economic performance of the transportation process. The aim of the study was to show the ability to detect changes in conveyor work related to damage or improperly conducted procedure of chain length changing. Observation of the conveyor chain work was to monitor the power consumption of the three motors driving the conveyor. The analysis included nearly 26 000 startups have been reported within 20 months of the conveyor work. This paper describes the initial stage of raw measurement data analysis, and analysis of data transformed by the Fourier transform. As a result of the data analysis, diagnostic procedures allowing to signal deviations from the conveyor normal conditions were proposed.

BARANOWSKI P, DAMAZIAK K, MAŁACHOWSKI J. Brake system studies using numerical methods. Eksploatacja i Niezawodność – Maintenance and Reliability 2013; 15 (4): 337–342.

The paper presents the examples of numerical simulations of braking systems performed in order to determine the parameters of their work. Using a typical finite element and meshless numerical methods, dynamic analyses of the brake were performed paying particular attention on the phenomenon of thermo-mechanical coupling occurring in the process of braking, as well as wear processes occurring on the surface of the linings. The article presents sequence of research steps, including hybrid modelling of braking system.

DUDA S. Numerical modeling and simulating the dynamic interactions within the drive system of electric rail vehicles. Eksploatacja i Niezawodność – Maintenance and Reliability 2013; 15 (4): 343–348.

This paper shows the methodology that can be used to study the dynamic phenomena occurring in rail vehicle drive systems by taking into account its actual seating. The studies are performed by providing a detailed description of electromagnetic phenomena found in drive motors and contact phenomena at the interface between the wheel and rail. Forces determined based on the models below constitute the load of a rail vehicle drive system. The mathematical model of the motor has been implemented in Matlab/Simulink software and coupled with the vehicle model developed in the Simmechanics application. These models make it possible to determine the load of drive system for various vehicle dynamic states (startup, steady-state operation) depending on the locomotive load.

ROŚKOWICZ M, SMAL T. Research on durability of composite materials used in repairing aircraft components. Eksploatacja i Niezawodność – Maintenance and Reliability 2013; 15 (4): 349–355.

The paper presents methodology and results of research on durability of composite materials, which were applied to expedient repair of damaged aircraft components. Numerical calculation and experimental tests were conducted during research. The obtained results proved that failure of aircraft components is connected with local loss of stability in case of aircraft's skin

na elementy stalowych systemów tribologicznych, przejmując funkcje klasycznych, nieekologicznych na ogół, dodatków smarowościowych (EP), pozwalając na redukcję ich zawartości w środkach smarowych.

YANG Y-H, WANG K-S. Badanie charakterystyk uszkodzeń izolacji w oparciu o testy przyspieszonego starzenia. Eksploatacja i Niezawodność – Maintenance and Reliability 2013; 15 (4): 325–331.

W prezentowanej pracy zastosowano estymator największej wiarygodności do określenia charakterystyk uszkodzenia izolacji silników klasy H z wykorzystaniem danych z badań przyspieszonego starzenia w sytuacji cenzurowanej wg. Nelsona. Na podstawie Weibullowskiego modelu prawdopodobieństwa przetrwania, uszkodzenie określono jako szereg trzech przyczyn dotyczących, odpowiednio, zwoju, fazy i ziemi, czyli jako tzw. uszkodzenie konkurujące. Głównym zagadnieniem przedstawionych badań jest zmienność parametrów kształtu β wraz z temperaturą. Zaproponowano zależność Gomperta $\beta_i(T)$, z temperaturą odniesienia T_{ri} , dla n -tego trybu awaryjnego. Stwierdzono, że temperatury T_{ri} nie tylko wyróżniają charakterystykałościowego procesu uszkodzenia izolacji, ale również służą ocenie średniego czasu do awarii (MTTF). W kategoriach fizycznych T_{ri} oznacza punkt zwrotny o zróżnicowanym β_i gdy n -ta przyczyna uszkodzenia staje się umiarkowana w sensie mniejszej zdolności akumulacji uszkodzeń izolacji w wyższej temperaturze, odpowiadającej procesowi termicznej degradacji. Wyniki liczbowe wskazują, że stosowana technologia izolacji jest akceptowalna, ponieważ temperatura pracy wynosi 363K. Zgodnie z prognozowanym czasem pracy, wraz ze wzrostem temperatury do 440K, co nadal mieści się w dozwolonym zakresie temperatur użytkowania, zachodzi konieczność zmiany najpierw struktury zwoju a w dalszej kolejności struktury fazy. Przyczyny dotyczące gruntu mają wpływ na uszkodzenie jedynie przy wyższych temperaturach.

MICHALAK M, SIKORA M, SOBCZYK J. Analiza pracy łańcucha przenośnika ścianowego w oparciu o analizę harmoniczną. Eksploatacja i Niezawodność – Maintenance and Reliability 2013; 15 (4): 332–336.

Artykuł opisuje zastosowanie analizy harmonicznego do analizy stanu łańcucha przenośnika ścianowego. Poprawna i stabilna praca łańcucha wiąże się zarówno z bezpieczeństwem prowadzenia prac jak i ekonomiczną wydajnością procesu. Celem przeprowadzonych badań było wskazanie możliwości wykrywania zmian pracy przenośnika związanych z uszkodzeniem bądź przeprowadzoną w sposób nieprawidłowy procedurą zmiany długości łańcucha. Obserwacja pracy łańcucha przenośnika polegała na monitorowaniu poboru prądu przez trzy silniki napędzające przenośnik. Analizie poddano blisko 26 000 uruchomień, jakie odnotowano w okresie 20 miesięcy pracy przenośnika. W pracy opisano etap wstępnej analizy surowych danych pomiarowych, a także analizy danych przekształcony transformacją Fouriera. W rezultacie analizy danych zaproponowano procedury diagnostyczne pozwalające sygnalizować odstępstwa od normalnych warunków pracy przenośnika.

BARANOWSKI P, DAMAZIAK K, MAŁACHOWSKI J. Badania układów hamulcowych metodami numerycznymi. Eksploatacja i Niezawodność – Maintenance and Reliability 2013; 15 (4): 337–342.

W pracy przedstawiono przykłady symulacji numerycznych układów hamulcowych wykonanych w celu wyznaczenia parametrów ich pracy. Stosując siatkowe i bezsiatkowe metody numeryczne przeprowadzono dynamiczne analizy pracy hamulca ze zwróceniem szczególnej uwagi na zjawiska sprzężone (ciepłno – mechaniczne) występujące w procesie hamowania oraz procesy zużycia zachodzące na powierzchni okładziny cierniej. W artykule przedstawiono kolejne kroki badań obejmujące modelowanie hybrydowe układu hamulcowego.

DUDA S. Modelowanie i symulacja numeryczna oddziaływań dynamicznych w układzie napędowym elektrycznych pojazdów szynowych. Eksploatacja i Niezawodność – Maintenance and Reliability 2013; 15 (4): 343–348.

W niniejszej pracy przedstawiono metodologię, która może być zastosowana do badania zjawisk dynamicznych w układach napędowych pojazdów szynowych z uwzględnieniem rzeczywistego ich osadzenia. Badania są realizowane przy szczegółowym opisie zjawisk elektromagnetycznych w silnikach napędowych oraz zjawisk kontaktowych na styku współpracy koła z szyną. Wyznaczone z powyższych modeli siły stanowią obciążenie układu napędowego pojazdu szynowego. Sformułowany model matematyczny silnika zaimplementowano w programie Matlab/Simulink i sprzężono go z modelem pojazdu opracowanym w programie Simmechanics. Modele te umożliwiają na wyznaczenie obciążenia układu napędowego, dla różnych stanów dynamicznych pojazdu (rozruch, praca ustalona) w zależności od obciążenia lokomotywy.

ROŚKOWICZ M, SMAL T. Badanie materiałów kompozytowych wykorzystanych do naprawy konstrukcji lotniczych. Eksploatacja i Niezawodność – Maintenance and Reliability 2013; 15 (4): 349–355.

W artykule zaprezentowano metodologię i wyniki badań wytrzymałościowych materiałów kompozytowych, które zostały zastosowane do naprawy doraźnej elementów konstrukcji lotniczych. Podczas badania wykorzystano obliczenia numeryczne i badania eksperymentalne. Otrzymane rezultaty dowodzą, że uszkodzenie elementów konstrukcji lotniczych związane jest z lokalną utratą stateczności, w przypadku poszycia samolotów, oraz utratą

and stiffness in case of girders and beams. The damaged components were repaired with the use of a metal insert and a composite patch. The use of a metal insert, which had the same stiffness as repaired elements, was a solution which allowed to restore local stiffness of repaired components. Composite patches which were formed with glass, carbon or aramid fabrics impregnated with epoxy resins, also created an adhesive bonds and joined all elements of repaired zone. The experimental tests proved that the executed repairs whose time was limited to 120 minutes improved stability, stiffness and fatigue life of the repaired components.

LUO W, ZHANG C, CHEN X, WANG Y. **System reliability demonstration with equivalent data from component accelerated testing based on reliability target transformation.** Eksploatacja i Niezawodność – Maintenance and Reliability 2013; 15 (4): 356–363.

The reliability demonstration test (RDT) programs in general proceed at various levels, including component, subsystem, and system in the verification and validation phase of the product life cycle. The system reliability demonstration within feasible duration becomes a considerable issue because of the marketplace demands for decreased development time and cost. A method based on reliability target transformation is proposed to accomplish the system reliability demonstration with the data from the RDT of the components. In order to shorten the test time, the RDT plan for component under the accelerated condition is first designed. Then, the reliability target of the system with different lifetimes required by the producer and the consumer is transferred to the target with the same specified mission time, which should meet the time constraint of the system level test. Next, the lower limit confidence of component reliability at the system mission time are estimated and converted to the equivalent binomial component data by the curve fitting method, then they are synthesized to the equivalent binomial system data by the Bayesian method. Finally, the system reliability demonstration is considered. The system classical attribute acceptance sampling plan at the mission time is used to make decisions using the equivalent binomial system data. If the decision cannot be made, the system Bayesian attribute acceptance sampling plan will be designed with the equivalent data as the prior parameters and the complementary system test will be conducted.

MERKISZ J, LIJEWSKI P, FUĆ P, WEYMANN S. **Exhaust emission tests from non-road vehicles conducted with the use of PEMS analyzers.** Eksploatacja i Niezawodność – Maintenance and Reliability 2013; 15 (4): 364–368.

The paper discusses the issue of exhaust emissions from non-road vehicle engines. In the first part of the paper American regulations on the procedures of engine testing in operation were briefly characterized. The said regulations are a novel solution and were introduced as one of the first of this type worldwide. In the next part of the paper the authors presented the results of the exhaust emission tests from a farm tractor performed under actual operating conditions during fieldwork. For this purpose PEMS (Portable Emissions Measurement System) was used. The tests were carried out for different test procedures such as the NTE (Not-To-Exceed) procedure. The analysis of the test results was performed chiefly in the aspect of the NTE test applicable in the U.S. The analysis pertains chiefly to the engine operating conditions and exhaust emissions. European legislation currently does not require such tests and that is why the presented tests are related to the American procedures. The performed tests and their analysis led to a formulation of conclusions related to the engine operating conditions and its exhaust emissions.

KARWAT B, GŁOWIŃSKI D, STAŃCZYK E. **Analysis of the influence of factors on the photometry of the optical light system of CHMSL car lamps.** Eksploatacja i Niezawodność – Maintenance and Reliability 2013; 15 (4): 369–375.

The article presents an analysis of the construction of CHMSL (Centre High-Mounted Stop Lamp) car lamps and a study of the influence of individual components on the photometric parameters (light intensity). The authors have conducted a detailed study of the various design elements and the impact of their settings on each photometric parameter of the tested lamp. There is also a presentation of research results on the impact of plastic injection technologies used to manufacture the lamp, such as holding pressure, holding time and injection speed, on the photometric parameters of the CHMSL lamp's optical system.

BUREIKA G, BEKINTIS G, LIUDVINAVIČIUS L, VAIČIŪNAS G. **Applying analytic hierarchy process to assess traffic safety risk of railway infrastructure.** Eksploatacja i Niezawodność – Maintenance and Reliability 2013; 15 (4): 376–383.

The Analytic Hierarchy Process is described in recent research works as an emerging multicriteria decision-making approach to solving large, dynamic, and complex

sztywności, w przypadku belek i żebier. Uszkodzone elementy zostały naprawione z użyciem metalowej wkładki usztywniającej i łąty kompozytowej. Użycie wkładki o tej samej sztywności co naprawiany materiał pozwoliło odzyskać sztywność w trefie uszkodzenia. Łaty kompozytowe, które zostały uformowane z wielu warstw tkaniny (szklanej, węglowej i aramidowej) i nasączone żywicą epoksydową, pozwoliły na utworzenie złącza klejowego, w ramach którego scalono wszystkie elementy węzła naprawczego. Badania eksperymentalne dowiodły, że przeprowadzone naprawy, których czas był ograniczony do 120 minut, poprawiły stateczność, sztywność i trwałość zmęczeniową naprawionych komponentów.

LUO W, ZHANG C, CHEN X, WANG Y. **Stwierdzanie niezawodności systemu na podstawie równoważnych danych z przyspieszonych badań elementów składowych w oparciu o transformację celu niezawodnościowego.** Eksploatacja i Niezawodność – Maintenance and Reliability 2013; 15 (4): 356–363.

Ogólnie, oprogramowanie do badań stwierdzających niezawodność (RDT) można stosować na różnych poziomach, w tym na poziomie elementu składowego, podsystemu i systemu, w fazie weryfikacji i walidacji cyklu życia produktu. Stwierdzenie niezawodności systemu w realnym terminie staje się ważkim problemem ze względu na wymogi rynku co do zmniejszenia czasu i kosztów rozwoju. W prezentowanej pracy zaproponowano metodę opartą na transformacji celu niezawodnościowego, wedle której niezawodność systemu stwierdza się na podstawie danych z RDT części składowych. Aby skrócić czas testowania, w pierwszej kolejności tworzy się plan RDT dla części składowej w warunkach przyspieszonych. Następnie cel niezawodnościowy systemu przy różnych czasach pracy wymaganych przez producenta, jak i konsumenta, zostaje przetransponowany na cel o tym samym określonym czasie użytkowania, który powinien spełniać ograniczenie czasowe dla badań na poziomie systemu. Następnie szacuje się dolne granice przedziałów ufności dla niezawodności komponentów w określonym czasie eksploatacji systemu oraz przekształca się je na równoważne dane dwumienne dla części składowych z wykorzystaniem metody dopasowywania krzywych; dalej, są one syntetyzowane do równoważnych dwumiennych danych dotyczących systemu z zastosowaniem metody Bayesa. Pozwala to na stwierdzenie niezawodności systemu. Decyzje podejmuje się na podstawie równoważnych danych dwumiennych dotyczących systemu z wykorzystaniem klasycznego planu wyrzykowej kontroli odbiorczej systemu według zadanych charakterystyk dla określonego czasu użytkowania. Jeżeli decyzja nie może zostać podjęta w ten sposób, konstruuje się bayesowski plan wyrzykowej kontroli odbiorczej systemu wg. zadanych charakterystyk, gdzie dane równoważne stanowią parametry a priori, oraz przeprowadza się uzupełniające badania systemu.

MERKISZ J, LIJEWSKI P, FUĆ P, WEYMANN S. **Badania emisji związków toksycznych spalin z pojazdów o zastosowaniach pozadrogowych z wykorzystaniem analizatorów PEMS.** Eksploatacja i Niezawodność – Maintenance and Reliability 2013; 15 (4): 364–368.

Artykuł dotyczy problemu badań emisji związków toksycznych spalin z silników pojazdów o zastosowaniach pozadrogowych (non-road). W pierwszej części artykułu krótko scharakteryzowano przepisy amerykańskie nt. procedur badań silników w eksploatacji. Przepisy te są nowatorskim rozwiązaniem i zostały wprowadzone jako jedno z pierwszych tego typu rozwiązań na świecie. W dalszej części artykułu przedstawiono wyniki badań emisji związków toksycznych spalin silnika ciągnika rolniczego, wykonane w rzeczywistych warunkach eksploatacji, podczas wykonywania prac polowych. Do tego celu wykorzystano aparaturę PEMS (Portable Emissions Measurement System). Badania te wykonano dla różnych procedur badawczych, m.in. w teście NTE (Not-To-Exceed). Analizę wyników badań przeprowadzono głównie w aspekcie testu NTE, obowiązującego w Stanach Zjednoczonych. Analiza ta dotyczy przede wszystkim warunków pracy silników oraz emisji związków szkodliwych. Europejskie regulacje prawne w chwili obecnej nie nakładają obowiązku wykonywania takich badań, dlatego w zaprezentowane badania odnoszą się do procedur amerykańskich. Wykonane badania i ich analiza pozwoliły na sformułowanie wniosków dotyczących warunków pracy i emisji z silnika.

KARWAT B, GŁOWIŃSKI D, STAŃCZYK E. **Analiza czynników wpływających na fotometrię systemu optyczno-świetlnego lampy samochodowej typu CHMSL.** Eksploatacja i Niezawodność – Maintenance and Reliability 2013; 15 (4): 369–375.

Artykuł zawiera analizę budowy lampy samochodowej typu CHMSL (ang. Centre High-Mounted Stop Lamp), oraz badania wpływu poszczególnych jej elementów konstrukcyjnych na parametry fotometryczne (natężenie światła). Autorzy przeprowadzili szczegółowe badania w zakresie wpływu konstrukcji poszczególnych elementów i ich ustawienia względem siebie na parametry fotometryczne badanej lampy. Przedstawiono również wyniki badań w zakresie wpływu wykonania elementów lampy w technologii wtrysku tworzyw sztucznych takich jak: ciśnienie docisku, czas docisku i prędkość wtrysku na parametry fotometryczne całego systemu optyczno-świetlnego lampy typu CHMSL.

BUREIKA G, BEKINTIS G, LIUDVINAVIČIUS L, VAIČIŪNAS G. **Zastosowanie procesu hierarchii analitycznej do oceny zagrożenia bezpieczeństwa ruchu w odniesieniu do infrastruktury kolejowej.** Eksploatacja i Niezawodność – Maintenance and Reliability 2013; 15 (4): 376–383.

Najnowsze prace badawcze opisują proces hierarchii analitycznej jako nowy wielokryterialny model podejmowania decyzji służący rozwiązywaniu dużych, dynamicznych i

problems, which reflect real situations, such as strategic planning of management or resources, justification of introducing new technologies or determining the effectiveness of systems' operation. The paper presents an application of the Analytic Hierarchy Process to performance evaluation through a case study of Lithuanian railway traffic safety risk. The results of the performed study show that the application of the Analytic Hierarchy Process method can help railway traffic control managers effectively evaluate the railway infrastructure objects from the perspective of traffic safety risk and make long-term strategic plans for preventing the accidents on railway lines even under difficult economic and transportation conditions. A model for assessing railway infrastructure objects from the perspective of traffic safety risk, developed and realized by the authors for Lithuanian Railways two real lines, is presented. Finally, basic conclusions and recommendations are given.

KERŠYS A, KALISINSKAS D, PUKALSKAS S, VILKAUSKAS A, KERŠYS R, MAKARAS R. **Investigation of the influence of hydrogen used in internal combustion engines on exhaust emission.** Eksploatacja i Niezawodność – Maintenance and Reliability 2013; 15 (4): 384–389.

This article deals with the possibility to use hydrogen in gasoline and diesel engines. Hydrogen production in a vehicle and hydrogen generators mounted in a vehicle are overviewed. Under operation of the hydrogen generator electrical current changes with temperature, to stabilize current the current pulse generator is used. Modifications of an intake manifold were made in order to supply hydrogen to an engine. For this purpose a special universal plate to evenly mix the hydrogen with fuel mix was made designed. The experimental and rig tests were performed. The rig tests were carried out at constant 2200 rpm. It was found that smokiness, in both cases decreases with an additional deployment of hydrogen. Other indicators of the exhaust gas using the hydrogen in case of the rig tests are worse. A possible cause of negative influence is an excessive amount of hydrogen, which releases at 25 A current.

CZUBA W, FURMANIK K. **Analysis of a grain motion in the transfer area of the belt conveyor.** Eksploatacja i Niezawodność – Maintenance and Reliability 2013; 15 (4): 390–396.

Transfer chutes are critical areas within conveyor transfer systems in terms of maintenance and high levels of energy consumption. Appropriate chute design allows material stream to be uniformly fed on the receiving conveyor with a desired stable tangential speed. This reduces the motion resistances and belt wear. Any construction work associated with a transfer chute should be preceded by a thorough analysis of the stream trajectory. The simplest case is to consider the motion of a single grain. The article presents an analysis of grain motion in a parallel chute and a methodology of calculating the impact angle and tangential speed of the grain at the point of contact with the receiving conveyor belt. Based on calculations made on developed model it was determined which of the basic input parameters have the most significant impact on the changes of observed output parameters.

ZHANG C, WANG S. **Solid lubricated bearings performance degradation assessment: A fuzzy self-organizing map method.** Eksploatacja i Niezawodność – Maintenance and Reliability 2013; 15 (4): 397–402.

Solid lubricated bearings are common components in space mechanisms, and their reliability and performance degradation assessment are very crucial. In this study, a fuzzy self-organizing map method is used to perform performance degradation assessment. Feature vectors are constructed by indices of vibration as well as friction torque signal. Self-organizing map is then used to perform performance degradation assessment and the subjection of each feature vector to normal cluster on output layer is used as degradation indicator. Accelerated life test results show that this method can make effective performance degradation assessment and describe degradation degree in the whole life time.

LI Y-F, MI J, HUANG H-Z, ZHU S-P, XIAO N. **Fault tree analysis of train rear-end collision accident considering common cause failure.** Eksploatacja i Niezawodność – Maintenance and Reliability 2013; 15 (4): 403–408.

Along with the development of modern design technology and the increasing complication of modern engineering systems, component dependency has become a universal phenomenon during the failure analysis of systems. Ignoring the dependency among the failure behaviors of system components may lead to a huge error or even yield faulty results. In this paper, three types of models and two kinds of modeling methods are introduced for solving the common cause failure issues. The fault tree model of the train rear-end collision accident has been proposed based on the explicit modeling method. The probability of occurrence of the train rear-end collision accident is calculated using the square root model. The result shows that common cause failure has significant influences on the system reliability.

złożonych problemów, które odzwierciedlają rzeczywiste sytuacje, takie jak strategiczne planowanie zarządzania lub zasobów, uzasadnianie wprowadzenia nowych technologii lub określanie efektywności działania systemów. W pracy opisano zastosowanie procesu hierarchii analitycznej do oceny działania, przedstawiając studium przypadku dotyczące bezpieczeństwa ruchu kolejowego na Litwie. Wyniki przeprowadzonego badania wskazują, że stosowanie metody procesu hierarchii analitycznej może pomóc menedżerom ds. sterowania ruchem kolejowym skutecznie oceniać obiekty infrastruktury kolejowej z punktu widzenia zagrożenia bezpieczeństwa ruchu oraz konstruować długoterminowe plany strategiczne mające na celu zapobieganie wypadkom na liniach kolejowych, nawet w trudnych warunkach gospodarczych i transportowych. Przedstawiono model oceny obiektów infrastruktury kolejowej z punktu widzenia zagrożenia bezpieczeństwa ruchu drogowego, opracowany i zrealizowany przez autorów dla dwóch linii Kolei Litewskich. Na zakończenie, podano podstawowe wnioski i zalecenia.

KERŠYS A, KALISINSKAS D, PUKALSKAS S, VILKAUSKAS A, KERŠYS R, MAKARAS R. **Badanie wpływu wodoru stosowanego w silnikach spalinowych na emisję spalin.** Eksploatacja i Niezawodność – Maintenance and Reliability 2013; 15 (4): 384–389.

Przedstawiony artykuł dotyczy możliwości wykorzystania wodoru w silnikach benzynowych i wysokoprężnych. Omówiono wytwarzanie wodoru w pojeździe oraz w generatorach wodoru zamontowanych w pojeździe. W trakcie funkcjonowania generatora wodoru prąd elektryczny zmienia się wraz z temperaturą; w celu stabilizacji prądu stosuje się generator impulsów prądowych. Aby dostarczyć wodoru do silnika dokonano modyfikacji kolektora dolotowego. Do tego celu zaprojektowano specjalną uniwersalną płytę do równomiernego mieszania wodoru z mieszaną paliwową. Przeprowadzono próby eksperymentalne i próby na stanowisku badawczym. Próby na stanowisku badawczym prowadzono przy stałej prędkości obrotowej 2200 rpm. Stwierdzono, że zadymienie w obu przypadkach zmniejsza się wraz z dodatkowym wykorzystaniem wodoru. Inne wskaźniki spalin przy wykorzystaniu wodoru w przypadku badań na stanowisku badawczym wypadają mniej korzystnie. Możliwą przyczyną tego negatywnego oddziaływania jest nadmierna ilość wodoru, który uwalnia się w obecności prądu o wartości 25 A.

CZUBA W, FURMANIK K. **Analiza ruchu ziarna w przestrzeni przesyłowej przenośnika taśmowego.** Eksploatacja i Niezawodność – Maintenance and Reliability 2013; 15 (4): 390–396.

Przenośnikowe węzły przesyłowe są miejscami newralgicznymi z punktu widzenia eksploatacji jak również energochłonności systemów transportowych. Odpowiednie ukształtowanie konstrukcji przesyłu, pozwala na podawanie strugi transportowanego urobku na przenośnik odbierający w sposób równomierny, stabilny i z pożądaną prędkością styczną. Dzięki temu zmniejszane są opory ruchu w przesyłach, jak również zużycie taśmy. Prace konstrukcyjne związane z zabudową przesyłu, powinny być poprzedzone gruntowną analizą trajektorii ruchu strugi. Najprostszym przypadkiem do rozpatrzenia jest ruch pojedynczego ziarna. W artykule przedstawiono analizę ruchu ziarna w przesyłach równoległych oraz metodykę obliczeń kątów padania jak również prędkości stycznych ziarna w miejscu jego upadku na taśmę przenośnika odbierającego. Na podstawie obliczeń modelowych określono, które z podstawowych parametrów przesyłu mają najistotniejszy wpływ na zmiany obserwowanych wielkości.

ZHANG C, WANG S. **Ocena obniżenia charakterystyk łożysk ze smarem stałym: metoda rozmytych samoorganizujących się map.** Eksploatacja i Niezawodność – Maintenance and Reliability 2013; 15 (4): 397–402.

Łożyska ze smarem stałym to powszechnie stosowane elementy urządzeń, a ich niezawodność i ocena degradacji charakterystyk są bardzo istotne. W przedstawionej pracy wykorzystano metodę rozmytych samoorganizujących się map do oceny obniżenia charakterystyk. Wektory cech skonstruowano za pomocą wskaźników wibracji, jak również sygnału momentu tarcia. Następnie dokonano oceny obniżenia charakterystyk z wykorzystaniem samoorganizującej się mapy, a za wskaźnik degradacji przyjęto przynależność każdego wektora cech do normalnej grupy w warstwie wyjściowej. Wyniki badań przyspieszonych pokazują, że przy użyciu omawianej metody można dokonywać skutecznej oceny obniżenia charakterystyk a także opisywać stopień degradacji w całym okresie eksploatacji.

LI Y-F, MI J, HUANG H-Z, ZHU S-P, XIAO N. **Analiza drzewa uszkodzeń dla kolizji tylnej części składu pociągu z uwzględnieniem uszkodzenia spowodowanego wspólną przyczyną.** Eksploatacja i Niezawodność – Maintenance and Reliability 2013; 15 (4): 403–408.

Wraz z rozwojem nowoczesnych technologii projektowania i rosnącej komplikacji nowoczesnych systemów inżynierskich, zależność między komponentami stała się zjawiskiem powszechnym w analizie uszkodzeń systemów. Ignorowanie zależności między zachowaniami uszkodzeniowymi komponentów systemu może doprowadzić do ogromnego błędu, a nawet dać całkowicie błędne wyniki. W niniejszej pracy, przedstawiono trzy typy modeli i dwa rodzaje metod modelowania służących do rozwiązywania typowych problemów związanych z uszkodzeniami spowodowanymi wspólną przyczyną. Zaproponowano model drzewa uszkodzeń dla kolizji tylnej części składu pociągu w oparciu o metodę modelowania bezpośredniego. Prawdopodobieństwo wystąpienia kolizji tylnej części składu pociągu obliczono przy użyciu modelu pierwiastka kwadratowego. Wynik pokazuje, że uszkodzenie spowodowane wspólną przyczyną ma znaczący wpływ na niezawodność systemu.

ROSINSKI A, DABROWSKI T. **Modelling reliability of uninterruptible power supply units.** Eksploatacja i Niezawodność – Maintenance and Reliability 2013; 15 (4): 409–413.

This paper discusses issues related to reliability of uninterruptible power supplies equipped with automatic protection mechanisms (short circuit protection – SCP, overload protection – OLP, overvoltage protection – OVP). Relationships for determining probability of system states: full operational capability, partial capability and failure were derived. The impact of time taken to restore the state of full operational capability on probability of different system states was also analysed.

PARCZEWSKI K, WNEK H. **Using mobile scaled vehicle to investigate the truck lateral stability.** Eksploatacja i Niezawodność – Maintenance and Reliability 2013; 15 (4): 414–420.

This paper presents the results of an attempt to transfer resistance to the side overturning of the vehicle to the mobile vehicle in the scale of ~ 1:5 on the real vehicle. Due to the substantial cost of testing and the danger of rollover real vehicle attempt was made to reproduce the behaviour of the vehicle, using the conditions of similarity. The paper presents methods of risk detection and control algorithms in stability systems equipped with a safety feature to prevent rollover. The analysis was based on the tests carried out at research training ground. Shows the results of tests on a real and a mobile smaller scale vehicles, and the values of obtained rollover risk indicators.

ZĘBALA W, SŁODKI B, STRUZIIEWICZ G. **Productivity and reliability improvement in turning Inconel 718 alloy – case study.** Eksploatacja i Niezawodność – Maintenance and Reliability 2013; 15 (4): 421–426.

The paper presents an investigation of Inconel 718 alloy finishing turning, using a procedure that allows the optimal cutting data to be found with a maximization of the metal removal rate as the optimization criterion. The optimization procedure does not allow the required values of the chosen surface roughness indicator, cutting force and cutting tool wedge temperature to be exceeded at the same time. The optimization procedure includes the preliminary cutting tests for establishing the range of cutting data (feed and depth of cut) for the correct chip breaking as well as research concerning micro-hardness measurements which enables the cold work zone to be determined and the minimal value of the feed to be defined. The functionality of the algorithm was verified by using the improvement in machining productivity and reliability of an aircraft engine element as an example.

WERBIŃSKA-WOJCIECHOWSKA S. **Time resource problem in logistics systems dependability modelling.** Eksploatacja i Niezawodność – Maintenance and Reliability 2013; 15 (4): 427–433.

Article presents an overview of some recent developments in the area of mathematical modelling of technical systems' maintenance decisions with the use of delay-time concept. Thus, the literature overview from 1984–2012 in the analysed research area is given. The problem of time relations occurred in logistic systems performance processes is investigated. Later, the example of DT model implementation in the area of logistic system of sixteen forklifts performance analysis is investigated.

GREŠKOVIČ F, DULEBOVÁ L, DULEBA B, KRZYŻAK A. **Criteria of maintenance for assessing the suitability of aluminum alloys for the production of interchangeable parts injection mold.** Eksploatacja i Niezawodność – Maintenance and Reliability 2013; 15 (4): 434–440.

With increasing production of plastics crop up also the need to improve their processing abilities. New methods and materials in the construction of forms are examined. Low weight and easy machinability predestines aluminium alloys for use as a material for the production of injection moulds for manufacturing of small series production. The paper deals with the verification of the suitability for selected aluminium alloys for the production of mould inserts based on problem, which occurred at real injection mould used for small series production. Massive wear of material at contact of ejector pin made from 1.1203 and insert made of Al-alloy caused deformations at final moulding. At next experiments were four types of Al alloys used. At following materials hardness and wear of materials was evaluated. To simulate the adhesive wear of friction pairs 1.1203 – Al alloy with and without greasing was adhesive wear test machine AMSLER used with simulation of surface contact. Wear intensity was evaluated by the coefficient of friction.

ZHOU D, JIA X, LV C, LI Y. **Maintainability allocation method based on time characteristics for complex equipment.** Eksploatacja i Niezawodność – Maintenance and Reliability 2013; 15 (4): 441–448.

Maintainability allocation is an important step in product quality design. Traditional allocation methods are limited such that the allocated mean time to repair for each

ROSINSKI A, DABROWSKI T. **Modelowanie niezawodności zasilaczy buforowych.** Eksploatacja i Niezawodność – Maintenance and Reliability 2013; 15 (4): 409–413.

W artykule przedstawiono zagadnienia związane z niezawodnością zasilaczy buforowych wyposażonych w automatyczne zabezpieczenia (przeciwzwarceniowe – SCP, przeciążeniowe – OLP, nad napięciowe – OVP). Wyznaczono zależności pozwalające określić prawdopodobieństwa przebywania systemu w stanach: pełnej zdatności, niepełnej zdatności i niezdatności. Dokonano również analizy wpływu czasu przywrócenia stanu pełnej zdatności na wartości prawdopodobieństw przebywania zasilacza w wyróżnionych stanach technicznych.

PARCZEWSKI K, WNEK H. **Wykorzystanie mobilnego modelu pojazdu do analizy stateczności poprzecznej samochodu ciężarowego.** Eksploatacja i Niezawodność – Maintenance and Reliability 2013; 15 (4): 414–420.

Praca przedstawia próbę przeniesienia wyników badań odporności na przewrócenie pojazdu na bok z mobilnego modelu pojazdu w skali ~1:5 na pojazd rzeczywisty. Z uwagi na znaczny koszt badań i niebezpieczeństwo przewrócenia pojazdu rzeczywistego starano się odwzorować zachowanie się pojazdu, wykorzystując warunki podobieństwa. W pracy przedstawiono sposoby detekcji zagrożenia oraz algorytmy sterowania układów stabilizacji toru jazdy wyposażonych w funkcję zabezpieczającą przed przewróceniem. Analizę przeprowadzono w oparciu o próby poligonowe. Przedstawiono wyniki badań pojazdu rzeczywistego i mobilnego modelu w mniejszej skali oraz uzyskane wartości wskaźników zagrożenia przewróceniem pojazdu.

ZĘBALA W, SŁODKI B, STRUZIIEWICZ G. **Poprawa produktywności i niezawodności toczenia stopu Inconel 718 – studium przypadku.** Eksploatacja i Niezawodność – Maintenance and Reliability 2013; 15 (4): 421–426.

Artykuł opisuje badania obróbki wykończeniowej toczeniem stopu Inconel 718, mające na celu optymalizację parametrów skrawania z uwzględnieniem maksymalizacji objętościowej wydajności obróbki, jako kryterium optymalizacyjnego. Proponowana procedura uwzględnia wymagane w procesie ograniczenia dotyczące wartości parametru chropowatości obrabianej powierzchni, siły skrawania oraz maksymalnej temperatury w strefie skrawania. Procedura optymalizacyjna zawiera wstępne testy mające na celu ustalenie w lokalnych warunkach obróbki użytecznego zakresu parametrów skrawania (posuwu i głębokości skrawania) dla otrzymania korzystnej postaci wiórów. Wykonane pomiary mikrotwardości w strefie skrawania umożliwiły określenie wielkości strefy zgniotu warstwy wierzchniej, co z kolei pozwoliło na zdefiniowanie minimalnej wartości posuwu. Procedurę optymalizacyjną zweryfikowano na przykładzie obróbki wybranej powierzchni elementu silnika lotniczego. Osiągnięto znaczną poprawę produktywności i niezawodności procesu obróbki.

WERBIŃSKA-WOJCIECHOWSKA S. **Problem rezerwowania czasowego w modelowaniu niezawodności systemów logistycznych.** Eksploatacja i Niezawodność – Maintenance and Reliability 2013; 15 (4): 427–433.

W artykule przedstawiono zagadnienia związane z matematycznym modelowaniem utrzymania systemów technicznych w stanie zdatności z wykorzystaniem koncepcji opóźnień czasowych (DT). Przedstawiono przegląd literatury z badanego obszaru obejmujący okres 1984–2012. Następnie został omówiony problem relacji czasowych w systemach logistycznych. W ostatnim punkcie, został przedstawiony przykład zastosowania modelu DT do oceny niezawodności szesnastu wózków widłowych funkcjonujących w wybranym systemie.

GREŠKOVIČ F, DULEBOVÁ L, DULEBA B, KRZYŻAK A. **Eksploatacyjne kryteria oceny przydatności stopów aluminium do produkcji wymiennych części form wtryskowych.** Eksploatacja i Niezawodność – Maintenance and Reliability 2013; 15 (4): 434–440.

Z powodu zwiększenia produkcji różnorodnych elementów z tworzyw polimerowych zauważana jest konieczność poprawiania procesów przetwórczych, w tym konstrukcji maszyn i narzędzi do ich przetwórstwa. Dlatego badane są nowe metody i materiały w budowie form używanych w procesie wtryskowym. Niska waga i dobra obrabialność stopów aluminium sprawiają, że materiały te są chętnie stosowane do produkcji form wtryskowych w produkcji małoseryjnej. Artykuł dotyczy weryfikacji przydatności wybranych stopów aluminium do produkcji wymiennych części form wtryskowych pod kątem zapewnienia jak najdłuższej prawidłowej eksploatacji narzędzi. Zagadnienie przedstawione w artykule dotyczy rzeczywistych problemów, które wystąpiły w formach wtryskowych stosowanych do produkcji krótkich serii. Występujące znaczne zużycie materiału na styku wypychacza wykonanego ze stali 1.1203 i części formy wykonanej ze stopów aluminium oraz deformacje stopu aluminium wpływają na jakość przedmiotów produkowanych z tworzyw polimerowych. W kolejnych eksperymentach przetestowano cztery rodzaje stopów Al. Wyznaczono twardość materiałów i zużycie ściernie. Aby symulować współpracę węzłów tarcia 1.1203 – Al przeprowadzono testy z i bez użycia środka smarowego za pomocą urządzenia AMSLER.

ZHOU D, JIA X, LV C, LI Y. **Metoda alokacji obsługiwalności złożonych urządzeń oparta na charakterystykach czasowych.** Eksploatacja i Niezawodność – Maintenance and Reliability 2013; 15 (4): 441–448.

Alokacja obsługiwalności jest ważnym krokiem w projektowaniu jakości produktów. Tradycyjne metody alokacji są ograniczone w takim sensie, że alokowany średni czas do

unit design apartment cannot be totally controlled by the corresponding design apartment. This paper proposes a new time characteristics-based maintainability allocation method to solve the aforementioned problem. The relationship between design content and repair time is considered in this method, and repair time is divided into common and individual repair time. Common repair time, which is determined by the overall system design, is deducted from the total repair time. Individual repair time is allocated to the specific unit through proper traditional allocation method. A case study is performed, and results demonstrate that the new method is more suitable and effective than original methods in terms of maintainability allocation.

YIFEI T, ZHAOHUI T, WEI Y, ZHEN Y. **Research on energy-saving optimization design of bridge crane.** Eksploatacja i Niezawodność – Maintenance and Reliability 2013; 15 (4): 449–457.

Bridge crane is one of the most widely used cranes in our country, which is indispensable equipment for material conveying in the modern production. The security of bridge crane is always focused on when being used. The important indicators of crane performances include strength, stiffness, and crane weight, which mainly depend on the structure design of the bridge crane. So it is of importance to research on energy-saving optimization design by means of finite element analysis, ADMAS and Matlab. In this paper, the framework of energy-saving optimization is proposed. Secondly, taking 50 t – 31.5 m bridge crane as research object, its structure is described and the FE model of the bridge cranes is developed for the finite element analysis. Thirdly, shape optimal mathematical model of the crane is proposed for shape optimization as well as size optimal mathematical model for size optimization and topology optimal mathematical model for topology optimization. Besides, further comprehensive energy-saving optimizations are carried out as well as cross-section optimization. Finally, system-level energy-saving optimization design of bridge crane is further carried out with energy-saving transmission design results feedback to energy-saving optimization design of metal structure. The optimization results show that structural optimization design can reduce total mass of crane greatly by using the finite element analysis and optimization technology premised on the design requirements of cranes such as stiffness, strength and so on, thus energy-saving design can be achieved.

ŻYCZYŃSKA A. **The primary energy factor for the urban heating system with the heat source working in association.** Eksploatacja i Niezawodność – Maintenance and Reliability 2013; 15 (4): 458–462.

The paper explores the methodology for determining primary energy factor based on EU directives and domestic regulations. The estimation of the above mentioned coefficient for a selected urban heating system was performed on the basis of real measurements obtained during the operation of a system and conveyed by the producers as well as heating distributor. The analysis was conducted for the several variants and extended over four years, that is from 2008 to 2011. The results achieved in the operating conditions were compared to the values obligatory to apply in calculations.

naprawy dla każdego działu projektowania jednostki produktu nie może być całkowicie kontrolowany przez odpowiedni dział projektowania. W niniejszej pracy zaproponowano rozwiązanie tego problemu wykorzystujące nową metodę alokacji obsługiwalności opartą na charakterystykach czasowych. W proponowanej metodzie bierze się pod uwagę związek między zawartością projektu a czasem naprawy, czas naprawy zaś dzieli się na wspólny i indywidualny. Wspólny czas naprawy, który zależy od ogólnej konstrukcji systemu, odejmuje się od całkowitego czasu naprawy. Indywidualny czas naprawy alokuje się do konkretnej jednostki za pomocą odpowiedniej tradycyjnej metody alokacji. W pracy przeprowadzono studium przypadku, którego wyniki pokazują, że nowa metoda jest bardziej odpowiednia i skuteczna jeśli chodzi o alokację obsługiwalności niż metody stosowane pierwotnie.

YIFEI T, ZHAOHUI T, WEI Y, ZHEN Y. **Badania dotyczące optymalizacji energooszczędności konstrukcji suwnicy pomostowej.** Eksploatacja i Niezawodność – Maintenance and Reliability 2013; 15 (4): 449–457.

Suwnica pomostowa jest jednym z najczęściej używanych typów suwnic w Chinach i stanowi niezbędne wyposażenie do transportu materiałów w nowoczesnej produkcji. Kluczową kwestią dotyczącą obsługi suwnicy pomostowej jest zawsze bezpieczeństwo. Ważnymi wskaźnikami wydajności suwnicy są m.in. wytrzymałość, sztywność oraz ciężar suwnicy, które zależą głównie od konstrukcji suwnicy. Konieczne są zatem badania nad optymalizacją energooszczędności konstrukcji za pomocą analizy elementów skończonych, ADMAS oraz Matlab. W niniejszej pracy zaproponowano koncepcję optymalizacji energooszczędności. Po drugie, opisano budowę suwnicy pomostowej (50 t – 31.5 m) oraz opracowano model MES suwnicy do analizy metodą elementów skończonych. Po trzecie, przyjmując minimalną pojemność jako funkcję celu, wysokość i szerokość suwnicy jako zmienne projektowe, a naprężenie, energię odkształcenia, modalnych jako ograniczenia, ustalono optymalny model matematyczny kształtu żurawia dla celów optymalizacyjnego projektowania kształtu. Po czwarte, przyjmując minimalny udział objętościowy jako funkcję celu, a grubość płyt jako zmienne projektowe, ustalono optymalny model matematyczny rozmiarów do celów optymalizacyjnego projektowania rozmiarów. Po piąte, przyjmując minimalny udział objętościowy jako funkcję celu, a gęstości materiału każdego z elementów jako zmienne projektowe, ustalono optymalny model matematyczny topologii do celów optymalizacyjnego projektowania topologii. Wreszcie, wykonano multidyscyplinarny energooszczędny projekt optymalizacyjny systemu suwnicy pomostowej, a wyniki energooszczędnego projektowania układu napędu zostały wykorzystane jako informacja zwrotna przy energooszczędnym projektowaniu optymalizacyjnym konstrukcji metalowej. Wyniki optymalizacji pokazują, że optymalizacyjne projektowanie konstrukcji z wykorzystaniem analizy MES oraz technologii optymalizacji opartej na wymogach projektowych dla suwnic, takich jak sztywność, wytrzymałość itd., może znacznie obniżyć całkowitą masę dźwigu, a co za tym idzie zwiększyć jego energooszczędność.

ŻYCZYŃSKA A. **Współczynnik nakładu nieodnawialnej energii pierwotnej dla miejskiego systemu ciepłowniczego ze źródłem ciepła pracującym w skojarzeniu.** Eksploatacja i Niezawodność – Maintenance and Reliability 2013; 15 (4): 458–462.

W artykule przedstawiono metodykę określania współczynnika nakładu nieodnawialnej energii pierwotnej w oparciu o dyrektywy UE oraz przepisy krajowe. Na podstawie rzeczywistych pomiarów uzyskanych podczas eksploatacji układu i przekazanych przez producentów i dystrybutora ciepła, przeprowadzono obliczenia w/w współczynnika dla wybranego miejskiego systemu ciepłowniczego. Analizę wykonano dla kilku wariantów i objętość okres czterech lat tj. od 2008 r. do 2011 r. Wyniki otrzymane w warunkach eksploatacyjnych zostały porównane z wartościami obowiązującymi do stosowania w obliczeniach.

Article citation info:

TOMASZEK H, JASZTAL M, ZIEJA M. Application of the Paris formula with $m=2$ and the variable load spectrum to a simplified method for evaluation of reliability and fatigue life demonstrated by aircraft components. *Eksplotacja i Niezawodność – Maintenance and Reliability* 2013; 15 (4): 297–304.

Henryk TOMASZEK
Michał JASZTAL
Mariusz ZIEJA

APPLICATION OF THE PARIS FORMULA WITH $M=2$ AND THE VARIABLE LOAD SPECTRUM TO A SIMPLIFIED METHOD FOR EVALUATION OF RELIABILITY AND FATIGUE LIFE DEMONSTRATED BY AIRCRAFT COMPONENTS

UPROSZCZONA METODA SZACOWANIA NIEZAWODNOŚCI I TRWAŁOŚCI ZMĘCZENIOWEJ ELEMENTÓW KONSTRUKCJI STATKU POWIETRZNEGO Z WYKORZYSTANIEM WZORU PARISA DLA $M=2$ I ZMIENNEGO WIDMA OBCIĄŻENIA*

The presented paper is the follow-up to the study, where the method for assessment of the fatigue life of a structural component was outlined with consideration of the variable spectrum of loads and with use of the Paris formula for $m \neq 2$. Due to the different nature inherent to analytic forms of solutions for the Paris equations with their exponential parameter $m = 2$, that special case is the subject of a separate analysis. This paper also uses the transformation of a real spectrum with variable values of fatigue cycles into a homogenous spectrum with weighted cycles. The method was developed that uses the transformed spectrum to evaluate fatigue life for a selected component of the aircraft structure when the component suffers from an initial crack. The method for modeling of the crack length expansion uses a differential equation that is then subjected to transformations to obtain a partial differential equation of the Fokker-Planck type, which has a particular solution, explicitly the length density function for the crack of the component in question. That length density function served subsequently to determine reliability and fatigue life of a structural component where the crack length expanded from the permissible value l_d to the critical threshold l_{kr} .

Keywords: fatigue of structures, reliability, fatigue life, random spectrum of loads.

Prezentowany artykuł jest uzupełnieniem pracy, w której przedstawiono metodę oceny trwałości zmęczeniowej elementu konstrukcji dla zmiennego widma obciążenia z wykorzystaniem wzoru Parisa dla $m \neq 2$. Ze względu na odmienną postać analitycznych rozwiązań dla wykładnika równania Parisa $m=2$, ten szczególny przypadek rozwiązań został przedstawiony w niniejszym opracowaniu. Pokazany został sposób przekształcenia widma rzeczywistego o zmiennych wartościach cykli w widmo jednorodne o cyklach ważonych. Wykorzystując widmo przekształcone opracowano metodę oceny trwałości zmęczeniowej wybranego elementu konstrukcji statku powietrznego z początkowym pęknięciem. Do modelowania przyrostu długości pęknięcia wykorzystano równanie różnicowe, z którego po przekształceniu otrzymano równanie różniczkowe cząstkowe typu Fokkera-Plancka. Rozwiązaniem szczególnym tego równania jest funkcja gęstości długości pęknięcia elementu. Wykorzystując następnie funkcję gęstości długości pęknięcia określono niezawodność i trwałość zmęczeniową elementu konstrukcji dla pęknięcia narastającego do wartości dopuszczalnej l_d mniejszej od wartości krytycznej l_{kr} .

Słowa kluczowe: zmęczenie konstrukcji, niezawodność, trwałość zmęczeniowa, losowe widmo obciążenia.

1. Introduction

Assessment of the fatigue life for components that are ‘operated’ under variable load spectrum is really troublesome to formulate analytical relationships. Thus, it is a main subject of world-wide scientific research [1–6, 16, 18]. However, the assessment of the fatigue life for components that are ‘operated’ under variable load spectrum is

crucial to manage flight safety for civilian and military aircraft. Therefore, there is a necessity to find simplified methods, that could be practically applied in aviation transport [7, 9, 13–15, 18]. In this paper the simplified method is used that has already been disclosed in [17]. The applied simplification consists in transformation of the variable spectrum of loads to a homogenous one with weighted cycles.

(*) Tekst artykułu w polskiej wersji językowej dostępny w elektronicznym wydaniu kwartalnika na stronie www.ein.org.pl

This paper is the follow-up to the previous study [17] where the simplified method for assessment of the fatigue life of an aircraft structural component was outlined with consideration for the variable spectrum of loads and with use of the Paris formula for $m \neq 2$. The forms of analytic solutions for this problem differ from each other depending on the exponent parameter for the Paris formula, i.e. whether $m \neq 2$ or $m = 2$. It is why this study is dedicated to the case when the exponent in the Paris formula $m = 2$.

It is assumed that the length of the initial crack within a structural component is l_0 and then the crack expands due to the effect of a load with a variable spectrum up to the length of that is still permissible and safe as being less than the critical length of l_{kr} . It is also assumed that the expansion rate of the crack is subject to a deterministic rule defined by the Paris equation [8]:

$$\frac{dl}{dN} = C(\Delta K)^m, \quad (1)$$

where:

ΔK – variation range for the coefficient of stress intensity factor,

C, m – material-dependent constants,

N – the variable that represents the number of load cycles of a structural component.

For the case in question, i.e. when $m = 2$, the formula(1) adopts the following form:

$$\frac{dl}{dN} = C(\Delta K)^2. \quad (2)$$

2. Determination of the crack expansion rate for $m = 2$ and for transformed spectrum of loads applied to a structural component

Transformation of a real load spectrum with variable load values into a homogenous spectrum with weighted cycles is based on the following assumptions:

- 1) Each component of an aircraft is operated under variable loads during the aircraft missions;
- 2) The spectrum of loads affecting the aircraft component during a standard mission is available. The load is a multiplication of a standard cycle;
- 3) It is assumed that the available standard load makes it possible to calculate:
 - the total number of load cycles during a single flight,
 - the spectrum comprises L thresholds with the maximum values of stresses $\sigma_1^{\max}, \sigma_2^{\max}, \dots, \sigma_L^{\max}$;
- 4) For the analyzed spectrum the repetition numbers of the maximum stress threshold is the following:
 σ_1^{\max} occurs n_1 times, σ_2^{\max} occurs times, ..., σ_L^{\max} occurs n_L times; Therefore, for the entire flight the repetition numbers of the predefined stress threshold amounts to $N_c = \sum_{i=1}^L n_i$;
- 5) The minimum values for the predefined stress thresholds is calculated with the use of the following formula:

$$\sigma_{i, sr}^{\min} = \frac{\sigma_{i,1}^{\min} + \sigma_{i,2}^{\min} + \dots + \sigma_{i,n_i}^{\min}}{n_i}, \text{ where } i = 1, 2, \dots, L;$$

- 6) The values of maximum σ_i^{\max} and minimum $\sigma_{i, sr}^{\min}$ stress values for operation cycles with frequencies P_i of their occurrences are summarized in Table 1;

Table 1. Maximum σ_i^{\max} and minimum $\sigma_{i, sr}^{\min}$ stress values for operation cycles with frequencies P_i of their occurrences

σ_i^{\max}	σ_1^{\max}	σ_2^{\max}	...	σ_i^{\max}	...	σ_L^{\max}
$\sigma_{i, sr}^{\min}$	$\sigma_{1, sr}^{\min}$	$\sigma_{2, sr}^{\min}$...	$\sigma_{i, sr}^{\min}$...	$\sigma_{L, sr}^{\min}$
P_i	$P_1 = \frac{n_1}{N_c}$	$P_2 = \frac{n_2}{N_c}$...	$P_i = \frac{n_i}{N_c}$...	$P_L = \frac{n_L}{N_c}$

- 7) The asymmetry coefficients for operation cycles are summarized in Table 2.

Table 2. Asymmetry coefficients \hat{R}_i for operation cycles with U_i factors that take into account the impact of these coefficients on the cracking rates

i^{th} cycle	1	2	...	i	...	L
\hat{R}_i	\hat{R}_1	\hat{R}_2	...	\hat{R}_i		\hat{R}_L
U_i	U_1	U_1	...	U_i	...	U_L

where:

$$\hat{R}_i = \frac{\sigma_{i, sr}^{\min}}{\sigma_i^{\max}}, \quad U_i = \alpha_1 + \alpha_2 \hat{R}_i + \alpha_3 \hat{R}_i^2, \quad \alpha_1, \alpha_2, \alpha_3 - \text{empirical coefficients [11, 12].}$$

- 8) Ranges for stress variations are calculated by the formula:

$$\Delta\sigma_i = \sigma_i^{\max} - \sigma_{i, sr}^{\min}$$

and summarized in Table 3.

Table 3. Ranges for stress variations $\Delta\sigma_i$ with frequencies P_i of their occurrences

cycle types	1	2	...	i	...	L
$\Delta\sigma_i$	$\Delta\sigma_1$	$\Delta\sigma_2$...	$\Delta\sigma_i$		$\Delta\sigma_L$
P_i	P_1	P_2	...	P_i	...	P_L

- 9) Considering the effect exercised by overload cycles onto expansion of cracks (Table 4)

$$\Delta\sigma_{i, ef} = C_i^P \Delta\sigma_i$$

where:

C_i^P – coefficients that represents retardation of the crack expansion after occurrence of overload cycles [10].

Table 4. Variation ranges $\Delta\sigma_{i, ef}$ for effective stress with consideration of overload cycles

cycle types	1	2	...	i	...	L
coefficients	C_1^P	C_2^P	...	C_i^P		C_L^P
$\Delta\sigma_{i, ef}$	$\Delta\sigma_{1, ef}$	$\Delta\sigma_{2, ef}$...	$\Delta\sigma_{i, ef}$...	$\Delta\sigma_{L, ef}$

For the foregoing assumptions the relationship (1) with regard to the rate of crack development assumes the following form:

$$\frac{dl}{dN} = C\pi^{\frac{m}{2}} \left(\sum_{i=1}^L P_i U_i (\Delta\sigma_{i,ef})^m \right) M_k^m l^{\frac{m}{2}}, \quad (3)$$

where:

M_k – the parameter that indicates the location of the crack within the structural component and its dimensions with respect to dimensions of the overall component [8].

Having considered all the possible load cycles the relationship (3) adopts the form:

$$\frac{dl}{dN} = C\pi M_k^2 \left(\sum_{i=1}^L P_i U_i (\Delta\sigma_{i,ef})^2 \right) l, \quad (4)$$

Where: $i=1,2,\dots,L$

The relationship (4) can be expressed as a function of time or, more precisely, the function of an aircraft flying time. For this purpose it is assumed that:

$$N = \lambda t, \quad (5)$$

where:

λ – intensity (frequency) of occurrence of load cycles in a structural component;
 N – number of load cycles;
 t – overall flying time of an aircraft.

For the case in question $\lambda = 1/\Delta t$, where Δt stands for duration of the fatigue cycle for the specific component. The easiest way to determine the Δt parameter is the use the following equation:

$$\Delta t = \frac{T}{N_c}, \quad (6)$$

where:

T – average duration of a standard flight of an aircraft and assumed for determination of a load cycle,
 N_c – number of load cycles within a standard load spectrum.

After the foregoing substitutions and transformations the formula (4) adopts the following form:

$$\frac{dl}{dt} = \lambda C\pi M_k^2 \left(\sum_{i=1}^L P_i U_i (\Delta\sigma_{i,ef})^2 \right) l. \quad (7)$$

The formula (7) makes it possible to calculate the rate of crack expansions for the homogenous spectrum with weighted cycles of a single type.

3. Determination of the density function for a crack length as a function of time (flying time)

Let $U_{l,t}$ stand for the probability that the crack length of a component is l for the overall flying time t of an aircraft. The difference equation for the foregoing assumptions adopts the following form [7, 18]:

$$U_{l,t+\Delta t} = (1 - \lambda\Delta t)U_{l,t} + \lambda\Delta t U_{l-\Delta l,t}, \quad (8)$$

where:

Δl – expansion of the crack length during a single equivalent cycle.

The value of the crack length expansion, calculated on the basis of the equation (7) amounts to:

$$\Delta l = \lambda C\pi M_k^2 \left(\sum_{i=1}^L P_i U_i (\Delta\sigma_{i,ef})^2 \right) l \Delta t. \quad (9)$$

The equation (8) can be rewritten in the functional form:

$$U(l, t + \Delta t) = (1 - \lambda\Delta t)U(l, t) + \lambda\Delta t U(l - \Delta l, t). \quad (10)$$

where:

$U(l, t)$ – the density function for the crack length after expiring of the t total flying time expressed in flying hours;
 $(1 - \lambda\Delta t)$ – probability that no equivalent load cycle occurs during the time interval with the length of Δt ;

$\lambda\Delta t$ – probability that an equivalent load cycle occurs during the time interval with the length of Δt .

The equation (10) can be converted into a partial differential equation. For that purpose the following approximations are made:

$$\left. \begin{aligned} U(l, t + \Delta t) &\cong U(l, t) + \frac{\partial U(l, t)}{\partial t} \Delta t \\ U(l - \Delta l, t) &\cong U(l, t) - \frac{\partial U(l, t)}{\partial l} \Delta l + \frac{1}{2} \frac{\partial^2 U(l, t)}{\partial l^2} (\Delta l)^2 \end{aligned} \right\}. \quad (11)$$

After substitution of (11) for (10) the following formula is obtained:

$$\frac{\partial U(l, t)}{\partial t} = -\lambda \frac{\partial U(l, t)}{\partial l} \Delta l + \frac{1}{2} \lambda (\Delta l)^2 \frac{\partial^2 U(l, t)}{\partial l^2} \quad (12)$$

where:

$$\Delta l = \lambda C\pi \left(\sum_{i=1}^L P_i U_i (\Delta\sigma_{i,ef})^2 \right) M_k^2 l \Delta t.$$

Since, $\lambda\Delta t = 1$, then:

$$\Delta l = C\pi \left(\sum_{i=1}^L P_i U_i (\Delta\sigma_{i,ef})^2 \right) M_k^2 l. \quad (13)$$

Let:

$$C\pi M_k^2 = C_2, \quad (14)$$

$$\Delta l = C_2 \left(\sum_{i=1}^L P_i U_i (\Delta\sigma_{i,ef})^2 \right) l. \quad (15)$$

Substitution of (15) for (12) leads to the following equation:

$$\frac{\partial U(l, t)}{\partial t} = -\lambda \frac{\partial U(l, t)}{\partial l} C_2 \left(\sum_{i=1}^L P_i U_i (\Delta\sigma_{i,ef})^2 \right) l + \frac{1}{2} \lambda C_2 \left(\sum_{i=1}^L P_i U_i (\Delta\sigma_{i,ef})^2 \right) l^2 \frac{\partial^2 U(l, t)}{\partial l^2}. \quad (16)$$

The solution of the equation (7) should be substituted for the crack length in the equation (16):

$$\begin{aligned} \frac{dl}{dt} &= \lambda C_2 \left(\sum_{i=1}^L P_i U_i (\Delta\sigma_{i,ef})^2 \right) l, \\ \int_{l_0}^l \frac{dx}{x} &= \int_0^t C_2 \left(\sum_{i=1}^L P_i U_i (\Delta\sigma_{i,ef})^2 \right) dt, \\ l &= l_0 e^{\lambda C_2 \left(\sum_{i=1}^L P_i U_i (\Delta\sigma_{i,ef})^2 \right) t}. \end{aligned} \quad (17)$$

Where, according to the formula (14),

$$C_2 = C\pi M_k^2.$$

With consideration of (17), coefficients of the equation (16) can be expressed in the following way:

$$\alpha(t) = \lambda C_2 \left(\sum_{i=1}^L P_i U_i (\Delta \sigma_{i,ef})^2 \right) l_0 e^{\lambda C_2 \left(\sum_{i=1}^L P_i U_i (\Delta \sigma_{i,ef})^2 \right) t} \quad (18)$$

$$\begin{aligned} \beta(t) &= \lambda \left[C_2 \left(\sum_{i=1}^L P_i U_i (\Delta \sigma_{i,ef})^2 \right) l_0 e^{\lambda C_2 \left(\sum_{i=1}^L P_i U_i (\Delta \sigma_{i,ef})^2 \right) t} \right]^2 = \\ &= \lambda C_2^2 \left(\sum_{i=1}^L P_i U_i (\Delta \sigma_{i,ef})^2 \right)^2 l_0^2 e^{2\lambda C_2 \left(\sum_{i=1}^L P_i U_i (\Delta \sigma_{i,ef})^2 \right) t}. \end{aligned} \quad (19)$$

For $m=2$, the equation (16) with coefficients in the form of the relationships (18) and (19) is as follows:

$$\frac{\partial U(l, t)}{\partial t} = -\alpha(t) \frac{\partial U(l, t)}{\partial l} + \frac{1}{2} \beta(t) \frac{\partial^2 U(l, t)}{\partial l^2}. \quad (20)$$

The particular solution for the equation (20) is as follows [7, 18]:

$$U(l, t) = \frac{1}{\sqrt{2\pi A(t)}} e^{-\frac{(l-B(t))^2}{2A(t)}} \quad (21)$$

where:

$B(t)$ – the average increment in the crack length for the overall flying time t calculated as:

$$B(t) = \int_0^t \alpha(t) dt \quad (22)$$

$A(t)$ – variance for the average increment in the crack length for the overall flying time t calculated as:

$$A(t) = \int_0^t \beta(t) dt \quad (23)$$

Computation of the integral (22):

$$\begin{aligned} B(t) &= \int_0^t \alpha(t) dt = \lambda C_2 \left(\sum_{i=1}^L P_i U_i (\Delta \sigma_{i,ef})^2 \right) l_0 \int_0^t e^{\lambda C_2 \left(\sum_{i=1}^L P_i U_i (\Delta \sigma_{i,ef})^2 \right) t} dt = \\ &= \lambda C_2 \left(\sum_{i=1}^L P_i U_i (\Delta \sigma_{i,ef})^2 \right) l_0 \frac{1}{\lambda C_2 \left(\sum_{i=1}^L P_i U_i (\Delta \sigma_{i,ef})^2 \right)} \left[e^{\lambda C_2 \left(\sum_{i=1}^L P_i U_i (\Delta \sigma_{i,ef})^2 \right) t} \right]_0^t = \\ &= l_0 (e^{\lambda C_2 \left(\sum_{i=1}^L P_i U_i (\Delta \sigma_{i,ef})^2 \right) t} - 1). \end{aligned} \quad (24)$$

Computation of the integral (23):

$$\begin{aligned} A(t) &= \int_0^t \beta(t) dt = \lambda C_2^2 \left(\sum_{i=1}^L P_i U_i (\Delta \sigma_{i,ef})^2 \right)^2 l_0^2 \int_0^t e^{2\lambda C_2 \left(\sum_{i=1}^L P_i U_i (\Delta \sigma_{i,ef})^2 \right) t} dt = \\ &= \frac{\lambda C_2^2 \left(\sum_{i=1}^L P_i U_i (\Delta \sigma_{i,ef})^2 \right)^2 l_0^2}{2\lambda C_2 \left(\sum_{i=1}^L P_i U_i (\Delta \sigma_{i,ef})^2 \right)} \left[e^{2\lambda C_2 \left(\sum_{i=1}^L P_i U_i (\Delta \sigma_{i,ef})^2 \right) t} \right]_0^t = \\ &= \frac{1}{2} C_2 l_0^2 \left(\sum_{i=1}^L P_i U_i (\Delta \sigma_{i,ef})^2 \right) (e^{2\lambda C_2 \left(\sum_{i=1}^L P_i U_i (\Delta \sigma_{i,ef})^2 \right) t} - 1). \end{aligned} \quad (25)$$

Where, according to the formula (14),

$$C_2 = C\pi M_k^2.$$

4. Determination of reliability and fatigue life for a selected structural component of an aircraft

The diagram of a growing risk of a catastrophic hazard due to the crack of a structural component is shown in Fig. 1.

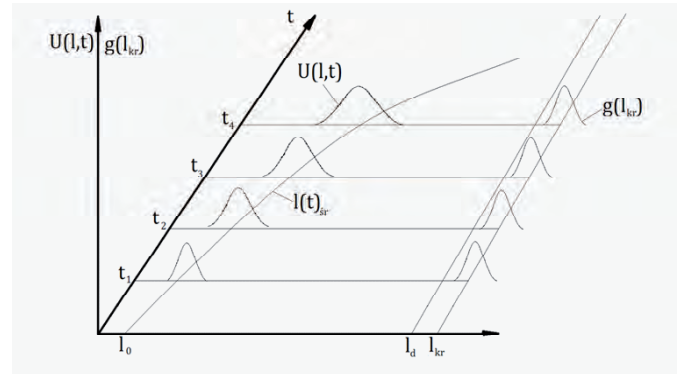


Fig. 1. The diagram of a growing risk of a catastrophic hazard due to the crack of a structural component [18]

The component is deemed damaged when the current length of a crack l exceeds the value of a critical threshold l_{kr} or is equal thereto. Thus

$$l - l_{kr} \geq 0.$$

Where both l and l_{kr} are exemplifications of random variables \hat{L}_t and L_{kr} . Therefore,

$$\varkappa = \hat{L}_t - L_{kr}. \quad (26)$$

The function of a random variable density \varkappa is calculated from the relationship:

$$f(\varkappa)_t = \int_0^\infty g(l - \varkappa) U(l, t) dl. \quad (27)$$

Therefore, the probability of the damage of a structural component is expressed by the relationship:

$$Q_t = P\{L_t - \hat{L}_{kr} \geq 0\} = \int_0^\infty f(\varkappa)_t d\varkappa. \quad (28)$$

Finally, the reliability of a component can be calculated by means of the function:

$$R(t) = 1 - \int_0^\infty f(\varkappa)_t d\varkappa. \quad (29)$$

Reliability of structural components can be also calculated in another manner. The critical length of cracks is to be determined by means of a stress intensity coefficient in the following form:

$$K = M_k \sigma \sqrt{\pi l}. \quad (30)$$

The coefficient that is determined by the relationship (30) becomes the critical parameter K_c when critical length l_{kr} and critical stress σ_{kr} are reached. This critical parameter is referred to as the cracking resistance of a material:

$$K_c = M_k \sigma_{kr} \sqrt{\pi l_{kr}}. \quad (31)$$

Hence, after a simple transformation:

$$l_{kr} = \frac{K_c^2}{M_k^2 \sigma_{kr}^2 \pi}.$$

By substitution of (31) and incorporation of a safety factor, one can calculate the maximum permissible (safe) length of a crack:

$$\bar{l}_d = \frac{K_c^2}{k M_k^2 \sigma_{kr}^2 \pi}, \quad (32)$$

where:

k – safety factor.

With consideration of the initial length l_0 of a crack one can calculate the maximum permissible increment of the crack length l_d with use of the following formula:

$$l_d = \bar{l}_d - l_0. \quad (33)$$

Next, the formula (33) is used to find out the reliability of a structural component:

$$R(t)_{l_d} = \int_{-\infty}^{l_d} U(l, t) dl \quad (34)$$

Normalization of the integrand in the equation (34) leads to the following expression:

$$R(t)_{l_d} = \int_{-\infty}^{\frac{l_d - B(t)}{\sqrt{A(t)}}} U(z, t) dz, \quad (35)$$

where:

$$z = \frac{l - B(t)}{\sqrt{A(t)}},$$

whilst $B(t)$, $A(t)$ are expressed by the relationships (24) and (25).

For the assumed reliability level, the upper limit for the integral (35) can be looked up in the tables for normal distribution. It enables to establish the relationship:

$$Q_{l_d} = \frac{l_d - B(t)}{\sqrt{A(t)}} \quad (36)$$

where:

Q_{l_d} – the upper limit for the integral (35), for that limit the integral value is equal to $R(t)_{l_d}$.

Resolving of the equation (36) enables to calculate the value of the overall flying time (the desired lifetime of a structural component) that guarantees that the assumed reliability level is achieved.

5. Final remarks with a numerical example

To illustrate the newly developed method the following example shows the way to calculate expansion rates for the average length of a crack in a component made of steel with specific material properties and exposed to the effect of a real load spectrum. The calculations were carried out for the spectrum of loads with variable amplitudes after having the load spectrum transformed in the manner that is explained in Section 2. The original load spectrum corresponds to real load affecting the component [7]. The characteristic parameters of the transformed load used for further investigations as summarized in the Table 5 below. Table 5 shows boundary ranges $\Delta\sigma_i$ for stress variations in the cycle within the presumed load thresholds i together with the frequencies P_i of their occurrence as well as coefficients that take into account the impact of the cycle asymmetry on crack expansion.

For the defined model material the following values of coefficients related to materials were assumed for calculations:

$$m = 2,$$

$$C = 5 \cdot 10^{-9}.$$

The presented example assumes that the initial length of the crack within the component is $l_0 = 10$ mm, whilst the maximum permissible length of the crack was calculated with the use of the equation (32) and it equals to $\bar{l}_d = 25$ mm. It was also assumed for calculations that the coefficient that reflects retardation of the crack expansion after occurrence of overload cycles $C_1^P = 1$, whereas the coefficient that takes into account the impact of the cycle asymmetry on crack expansion is defined by the empirical formula $U_i = 0,55 + 0,33\hat{R}_i + 0,12\hat{R}_i^2$. Alteration of the M_k coefficient in pace with expansion of the crack has been considered in the process of numerical computations according to the formula:

Table 5. Characteristic parameters for the transformed spectrum of loads

Load threshold i	1	2	3	4	5	6	7
Number of cycles	1	5	4	10	30	50	140
σ_i^{max} [MPa]	186	159	141	129	112	93	72
$\sigma_{i,ef}^{min}$ [MPa]	-28	-13	8	17	23	27	27
\hat{R}_i coefficient	-0,1505	-0,0818	0,0567	0,1317	0,2053	0,2903	0,375
Stress range $\Delta\sigma_{i,ef}$ [MPa]	214	172	133	112	89	66	45
U_i factor	0,5030	0,5238	0,5691	0,5955	0,6228	0,6559	0,6906
Share of the threshold in the spectrum (frequency of occurrence) P_i	0,0042	0,0208	0,0167	0,0417	0,125	0,2083	0,5833

$$M_k = 1 + 0,128 \left(\frac{l}{b} \right) - 0,288 \left(\frac{l}{b} \right)^2 + 1,525 \left(\frac{l}{b} \right)^3, \quad (37)$$

where:

l – current length of the crack;

b – width of the component towards the direction where the crack expands.

Then, the transformed equation (24) that expresses the average crack length was used to establish, based on the equation (5), the relationship between that crack length and the number of the load cycles N :

$$B(N) = l_0 \cdot (e^{C \cdot \pi \cdot M_k^2 \cdot \left(\sum_{i=1}^L P_i \cdot U_i \cdot (\Delta \sigma_{i,ef})^2 \right) \cdot N} - 1). \quad (38)$$

The foregoing equation made it possible to calculate an increase in the average crack length from the initial value of $l_0 = 10$ mm to the maximum permissible limit $\bar{l}_d = 25$ mm, where the relationship was sought between the crack length and the N number load cycles. The variation of the average crack length as the function of load cycle numbers is shown in Fig. 2.

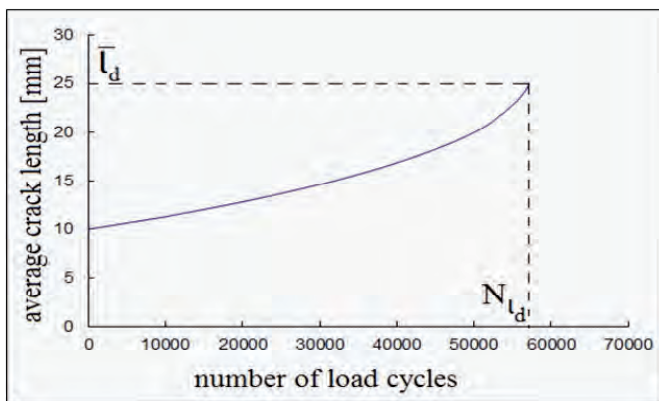


Fig. 2. Increase in the average crack length as the function of the number of load cycles

On the exclusive basis of calculations related to the growth of the average length of fatigue cracks $B(N)$ it is easy to find out that the maximum permissible crack length $\bar{l}_d = 25$ mm is achieved after $N_{l_d} = 57115$ of load cycles. However, the comprehensive calculations of the fatigue life for a specific component take also into account the probabilistic factors, therefore the variance $A(N)$ of the crack length as described by the formula (25) must be additionally included. For that purpose the equation (36) is used and it depends on the number of load cycles N established on the basis of the equation (5):

$$Q_{l_d} = \frac{l_d - B(N)}{\sqrt{A(N)}}. \quad (39)$$

For the assumed reliability level $R(N)_{l_d}^* = 0,99958$ the upper limit $Q_{l_d} = 3,34$ for the integral (35) can be looked up in tables of normal standard distribution. Having resolved the above equation the number of load cycles $N_{l_d} = 56750$ is obtained, which is the fatigue life of the examined component with consideration of probability factors.

The advantage of the foregoing method lies in the fact that the method takes account of physical phenomena that are associated with the variable spectrum of loads. It must be kept in mind that this study reveals the method that is suitable solely in the case when the material of the structural component exhibits appropriate features. These properties are conventionally reflected as the material constant that occurs as the exponent $m=2$ in the Paris formula. The values of material constants that are involved in the method (except for the presumed $m=2$ parameter) can be either found out from experiments or estimated on the basis of operational data for expansion of cracks, where the method of moments or the trustworthiness function (e.g. the C coefficient of the Paris equation) are applied to calculations. When the fatigue life is to be determined for such a structural component where assumption of the exponent $m \neq 2$ for the Paris equation is justified, the method already disclosed in [17] should be applied.

References

1. Bolotin V, Belousov I. Early fatigue crack growth as the damage accumulation process. *J Probabilist Eng Mech* 2001; 16: 279–87.
2. Castiglioni C. A stochastic model for estimating the fatigue life of structural steel details. *J Construct Steel Res* 1991; 18: 111–38.
3. Castillo E, Fernández-Canteli A, Castillo C, Mozos C. A new probabilistic model for crack propagation under fatigue loads and its connection with Wöhler fields. *Int J Fatigue* 2010; 32(4): 744–53.
4. Ghonem H, Provan W. Micromechanics theory of fatigue crack initiation and propagation. *Eng Fract Mech* 1988; 13: 963–977.
5. Kim Jung-Kyu, Shim Dong Suk. Probabilistic analysis on variability of fatigue crack growth using the Markov chain. *J Mech Sci Technol* 1998; 12(6): 1135–1142.
6. Kocańda D, Kocańda S, Tomaszek H. Probabilistic description of fatigue crack growth in a titanium alloy under complex stress state. In: Blom AF, editor. *Proc. Eighth Int. Fatigue Congress, EMAS, Sweden; 2002: 1299–306.*
7. Kocańda D, Tomaszek H, Jasztal M. Predicting fatigue crack growth and fatigue life under variable amplitude loading, *Fatigue of Aircraft Structures - Monographic Series Issue 2010*, Institute of Aviation Scientific Publications, Warsaw 2010: 37–51.
8. Kocańda S, Szala J. *Podstawy obliczeń zmęczenia*, PWN, Warszawa 1985.
9. Liu Y, Mahadevan S. Stochastic fatigue damage modeling under variable amplitude loading. *Int J Fatigue* 2007; 29: 1149–61.
10. Rama Chandra Murthy A., Palani, Nagesh R. Iyer G.S., An improved Wheeler model for remaining life prediction of cracked plate panels under tensile-compressive overloading, *SID*, 1 No 3 (2005): 203–213.
11. Schijve J, The significance of fractography for investigations of fatigue crack growth under variable-amplitude loading, *Fatigue Fract Eng Mater Struct* 22 (1999): 87–99.
12. Schijve J, Skorupa M, Skorupa A, Machniewicz T, Gruszczyński P. Fatigue crack growth in aluminium alloy D16 under constant and variable amplitude loading, *Int. J. Fatigue*, 26 (2004): 1–15.
13. Skorupa M. Load interaction effects during fatigue crack growth under variable amplitude loading – a literature review. Part I. Empirical trends. *Fatigue Fract Eng Mater Struct* 1998; 21:987–1006.
14. Skorupa M. Load interaction effects during fatigue crack growth under variable amplitude loading – a literature review. Part II. Qualitative interpretation. *Fatigue Fract Eng Mater Struct* 1999; 22: 905–926.

15. Sobczyk K, Trębicki J. Cumulative jump-correlated model for random fatigue. J Eng Fract Mech 1991; 40: 201–210.
16. Tang J, Spencer BF. Reliability solution for the stochastic fatigue crack growth problem. J Eng Fract Mech 1989; 12(2): 419–433.
17. Tomaszek H, Jasztal M, Zieja M. A simplified method to assess fatigue life of selected structural components of an aircraft for a variable load spectrum. Eksploatacja i Niezawodność – Maintenance and Reliability 2011; 4: 29–34.
18. Tomaszek H., Żurek J., Jasztal M. Prognozowanie uszkodzeń zagrażających bezpieczeństwu lotów statków powietrznych, Wydawnictwo Naukowe ITE-PIB, Radom 2008.

Prof. Henryk TOMASZEK, Ph.D., D.Sc. (Eng.)

Air Force Institute of Technology
ul. Księcia Bolesława 6, 01-494 Warsaw, Poland
E-mail: henryk.tomaszek@itwl.pl

Michał JASZTAL, Ph.D. (Eng.)

Military University of Technology
ul. Kaliskiego 2, 00-908 Warsaw, Poland
E-mail: mjasztal@wat.edu.pl

Mariusz ZIEJA, Ph.D. (Eng.)

Air Force Institute of Technology
ul. Księcia Bolesława 6, 01-494 Warsaw, Poland
E-mail: mariusz.zieja@itwl.pl

Jarosław SUGIER
George J. ANDERS

MODELLING AND EVALUATION OF DETERIORATION PROCESS WITH MAINTENANCE ACTIVITIES

MODELOWANIE I ANALIZA PROCESU STARZENIA MASZYN I URZĄDZEŃ PODDANYCH OKRESOWYM REMONTOM*

In this paper, we present an approach which allows evaluation of various possible maintenance scenarios with respect to both reliability and economic criteria. The method is based on the concept of a life curve and discounted cost used to study the effect of equipment aging under different maintenance strategies. The deterioration process is first described by a Markov model and then its various characteristics are used to develop the equipment life curve and to quantify other reliability parameters. Based on these data, effects of various “what-if” maintenance scenarios can be examined and their efficiency compared. Simple life curves are combined to model equipment deterioration undergoing diverse maintenance actions, while computing other parameters of the model allows evaluation of additional critical factors, such as the probability of equipment failure. Additionally, the paper deals with the problem of the model adjustment so that the computed repair frequencies are close to the historical values, which is very important in practical applications of the method. Moreover, we discuss the problems which may arise if automatic adjustment is used in cases when the hypothetical maintenance policies go beyond the conditions upon which the original model was built.

Keywords: Deterioration modelling, probabilistic methods, maintenance policy, risk assessment.

Przedmiotem artykułu jest modelowanie różnych możliwych scenariuszy eksploatacyjnych maszyn i urządzeń, które uwzględnia kryteria zarówno niezawodnościowe, jak i ekonomiczne. Metoda opiera się na zastosowaniu krzywych życia (ang. life curves) oraz kosztów zdyskontowanych (ang. discounted costs) do analizy wpływu, jaki różne strategie eksploatacyjne wywierają na starzenie się sprzętu. Punktem wyjścia jest opisanie procesu starzenia przez model Markowa, którego charakterystyki umożliwiają następnie wyznaczenie kształtu krzywej życia oraz obliczenie innych parametrów niezawodnościowych badanego sprzętu. W oparciu o uzyskane dane możliwa jest ocena różnych hipotetycznych scenariuszy eksploatacyjnych oraz porównanie ich efektywności. Proste krzywe życia mogą być łączone ze sobą w celu wizualizacji starzenia sprzętu poddawanego różnorodnym możliwym czynnościom naprawczym, natomiast obliczenie innych charakterystyk modelu pozwala wyznaczyć dodatkowe ważne parametry, takie jak prawdopodobieństwo uszkodzenia. Dodatkowo artykuł opisuje zagadnienie korygowania parametrów modelu, tak aby obliczane w nim częstości napraw sprzętu były bliskie wartościom znanym z jego historii eksploatacji, co jest bardzo ważne w praktycznych zastosowaniach metody. Omawiamy także problemy mogące pojawić się, gdy algorytm automatycznego korygowania modelu jest stosowany w analizach hipotetycznych strategii eksploatacyjnych wykraczających poza warunki, dla których model oryginalny został opracowany.

Słowa kluczowe: modelowanie procesu starzenia, metoda probabilistyczna, polityka remontowa, ocena ryzyka.

1. Introduction

Selection of an efficient maintenance strategy plays a very important role in the management of today's complex systems. When searching for an optimal strategy, numerous issues must be taken into account and, among them, reliability and economic factors are often equally important. On the one hand, for obvious reasons, in successful system operation failures should be avoided and this opts for extensive and frequent maintenance activities. On the other, superfluous maintenance may result in large and unnecessary costs. Finding a reasonable balance between these two factors is the key point in efficient maintenance management and to facilitate finding such a balance some measures should be available that allow for quantitative evaluation of the deterioration process of a system which is subjected to various maintenance actions (inspections, repairs, replacements, etc.).

The purpose of the development described in this work is to provide a computer tool for evaluating both the risks and the costs associated with the selection of various possible maintenance strategies. Rather than searching for a solution to a problem: “what maintenance

strategy would lead to the best reliability and dependability parameters of the system operation”, in this approach different maintenance scenarios can be examined in the “what-if” type of studies and then, using the tool, their reliability and economic effects can be automatically estimated so that the persons managing the maintenance is assisted in making informed decisions ([13, 34]). The mathematical approach that form the basis of this tool uses semi-Markov model first introduced in 1990 [4] and then improved and extended in [1 – 3, 5 – 6, 10 – 18, 22 – 32].

The method of maintenance evaluation which is the subject of this work has been presented initially in [8] and its specific extensions were further described in [26 – 28]. In this paper, after summarizing the current state of the development in Sections 2 and 3, we discuss one particular problem of automatic adjustment of the model which is required for representation of the deterioration process with modified repair frequencies (Section 4) and, finally, we include an original study of practical application that illustrates potential of this method in real-world situations (Section 5).

(*) Tekst artykułu w polskiej wersji językowej dostępny w elektronicznym wydaniu kwartalnika na stronie www.ein.org.pl

2. Modelling deterioration and maintenance

Probabilistic maintenance models [1 – 8, 11 – 12, 14, 21 – 25, 31] are the preferred tools for quantifying the effect of inspection and maintenance on reliability and costs. Their important advantage, apart from relative simplicity even when applied for complex technical systems or elements, is the ability to incorporate uncertainties associated with the deterioration of equipment and the outcomes of inspection and maintenance. The impact which maintenance makes on performance of the system – on both its reliability parameters and operational effectiveness – can be analysed with various performance measures, including: cost of performing inspection, maintenance and repair [8, 11 – 12, 15, 18, 22 – 23, 25, 31], unavailability (or availability) [2, 11, 25, 31], frequency of failure [15], first passage time (FPT) [18, 21], cost of interruption or cost of lost revenue [15]. As investigated in [32], additional care must be paid when analysing maintenance with non-periodic inspections because classic models may be unable to provide accurate results in such situations. To handle them appropriately new probabilistic models have been proposed in [1, 3].

In the typical approach, maximizing the performance measures becomes the objective of maintenance optimization like, for example in [12, 23], when single objective optimization is aimed at minimization of the operation and maintenance cost. In the more comprehensive solutions, the optimization has two objectives, e.g., to maximize the availability and to minimize the cost [11, 31] or to maximize the FPT while minimizing life cycle cost and unavailability [25]. In the latter solution, the objective function is formulated by assigning different weight factors for FPT, unavailability and life cycle cost.

In general, tuning parameters of the maintenance policy in the search of the optimal configuration can be realized using sensitivity analyses or optimization techniques. For example, modification of the inspection rates is used in [2, 18, 22] where sensitivity analyses were applied to investigate the behaviour of reliability and cost measures. In [11, 25, 31] the task is solved using optimization methods based on simulated annealing algorithm and Markov decision process.

At the heart of the methodology proposed in this paper is the probabilistic model that assumes that the equipment will deteriorate in time and, if not maintained, will eventually fail. If the deterioration process is discovered, preventive maintenance is performed which can restore the condition of the equipment. Such a maintenance activity will return the system to a specific state of deterioration, whereas repair after failure will restore to “as new” condition [5, 17]. The maintenance policy components that must be recognized are: monitoring or inspection (how the equipment state is determined), the decision process (which determines the outcome of the decision), and finally, the maintenance actions (or possible decision outcomes).

2.1. Construction of the model

All the necessary assumptions about the aging process and maintenance activities can be incorporated in an appropriate state-space (Markov) model [11, 14, 16, 19, 24, 33]. It consists of the states the equipment can assume in the process, and the possible transitions between them. In a Markov model, the rates associated with the transitions are assumed to be constant in time.

The method described in this work uses a model of the Asset Maintenance Planner (AMP) [6–7]. The AMP model is designed for equipment exposed to deterioration but undergoing maintenance at prescribed times. It computes the probabilities, frequencies and mean durations of the states of such equipment. The basic ideas in the AMP model are the probabilistic representation of the deterioration process through discrete stages, and the provision of a link between deterioration and maintenance. For a structure of a typical AMP model see Fig. 1.

In the model, the deterioration progress is represented by a chain of deterioration states $D1 \dots DK$ which leads to the state F symbolizing

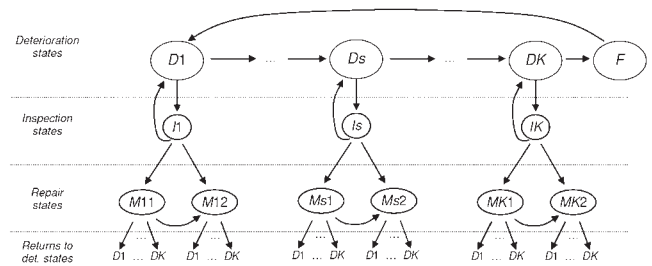


Fig. 1. Structure of the state-transition model which represents the deterioration process together with the inspection and repair events (an example with two types of repairs is shown).

occurrence of a failure. In most situations, it is sufficient to represent deterioration by three stages: an initial ($D1$), a minor ($D2$), and a major ($D3$) stage ($K = 3$). This last is followed, in due time, by equipment failure (F) which requires extensive repair or replacement.

In order to slow deterioration and thereby extend equipment life-time, the operator will carry out maintenance according to some pre-defined policy. In the model of Fig. 1, regular inspections (I_s) are performed which result in decisions to continue with minor ($Ms1$) or major ($Ms2$) maintenance or do nothing (more than two types of repairs can also be included). The expected result of all maintenance activities is a single-step improvement in the deterioration chain; however, allowances are made for cases where no improvement is achieved or even where some damage is done through human error in carrying out the maintenance, which results in returning to the stage of more advanced deterioration.

The choice probabilities (at transitions from inspection) and the probabilities associated with the various possible outcomes are based on user input and can be estimated, e.g., from historical records or operator expertise.

Mathematically, the model in Fig. 1 can be represented by a semi-Markov process, and solved by the well-known procedures. The solution will yield all the state probabilities, frequencies and mean durations. Moreover, the model can be further analysed using Monte Carlo methods: starting from any given state Dk , transitions of the system are simulated until the failure state F is reached and the corresponding time moments are recorded as the values of the first passage times (FPT) to failure. These times are subsequently taken as the estimates of the mean remaining lifetimes in each deterioration state. Specific issues arising in numerical implementation of this idea are discussed in [20].

2.2. Using the model to estimate the life curve and the probability of failure

A convenient way to represent the deterioration process is by the *life curve* of the equipment [5]. Such a curve shows the relationship between asset condition, expressed in either engineering or financial terms, and time. For examples please refer to Fig. 3 in Section 5 where life curves will be used in a case study presenting various types of analysis carried out for evaluation of the maintenance scenarios.

As pointed out above, computing the average first passage time (FPT) from the first deterioration state ($D1$) to the failure state (F) yields an average lifetime of the equipment, i.e., the length of its life curve. On the other hand, solving the model for the state probabilities makes possible computing the expected state durations, which are used to determine the shape of the curve (some additional decisions are required as to how the deterioration states are mapped to the ranges of the asset condition values, which is discussed in [8] and [29]). Simple life curves obtained for different maintenance policies can be later combined if constructing composite life curves which de-

scribe various maintenance scenarios are required (as an example see Fig. 4 in Section 5).

Having the model and the life curve, one can compute the probability of failure (*PoF*) within given time period T for the equipment which is in some specific asset condition. The procedure is as follows:

- 1° For the current asset condition (an input parameter), find from the life curve the corresponding deterioration state D_s and then compute a state progress SP (%), i.e., estimate how long the equipment has already been in the D_s state (this is calculated with the assumption that the value of asset condition decreases with constant rate when the system remains in D_s , hence simple proportionality rule can be used).
- 2° Running FPT analysis on the model, find the distributions $D_s(t)$ and $D_{s+1}(t)$ of the first passage time from the current state D_s and the subsequent deterioration state $D(s+1)$, to the failure state F .
- 3° Interpreting the state progress as a weight which balances the current equipment condition between D_s and $D(s+1)$, estimate the final value of the probability as:

$$PoF = D_s(T) \cdot (1 - SP) + D_{s+1}(T) \cdot SP \quad (1)$$

3. Automatic adjustment of the model

Preparing the Markov model for some specific equipment is not an easy task and requires expert intervention. The goal is to create the model representing closely the real-life deterioration process known from the records that usually describe equipment operation under a regular maintenance policy with some specific frequencies of inspections and repairs. The model itself permits calculation of the repair frequencies and compliance of the computed and recorded frequencies is a very desirable feature that verifies the trustworthiness of the model.

At this point, we will describe briefly a method of model adjustment proposed in [26] and [29] that aims at reaching such a compliance. It can be used also for a different task: fully automatic generation of a model for a new maintenance policy with modified frequencies of repairs which is very often required during the evaluation of various hypothetical maintenance options.

3.1. The method

Let K represents the number of deterioration states and R the number of repairs in the model under consideration. Also, let P^{sr} = probability of selecting maintenance r in state s (assigned to decision after state I_s) and P^{s0} = probability of returning to state D_s from inspection I_s (situation when no maintenance is scheduled as a result of the inspection). Then, for all states $s = 1 \dots K$:

$$P^{s0} + \sum_r P^{sr} = 1 \quad (2)$$

Let F^r represents the frequency of repair r acquired through solving the model. The problem of model tuning can be formulated as follows:

Given an initial Markov model M_0 , constructed as above and producing the frequencies of repairs $F_0 = [F_0^1, F_0^2, \dots, F_0^R]$, adjust the probabilities P^{sr} so that some goal frequencies F_G are achieved.

Since the model presented in Fig. 1 has many parameters, one could devise different approaches manipulating their values to achieve the desired effect. We have selected to vary the probability values

since these are usually guessed by an expert whereas the repair rates and their durations are largely based on historical records.

The vector F_G usually corresponds to the observed historical values of the frequencies of various repairs but can also represent new hypothetical repair frequencies of some possible maintenance policy. In the proposed solution, a sequence of tuned models $M_0, M_1, M_2, \dots, M_N$ is evaluated with each consecutive model approximating desired goal with a better accuracy. Starting with $i = 0$ the procedure consists of the following steps:

- 1° For model M_i compute the vector of repair frequencies F_i .
- 2° Evaluate an error of M_i as a distance between vectors F_G and F_i .
- 3° If the error is within the user-defined limit, consider M_i as the final model and stop the procedure ($N = i$); otherwise proceed to the next step.
- 4° Create a new model M_{i+1} through tuning values of P_i^{sr} , then correct P_i^{s0} according to (2).
- 5° Proceed to step 1° with the next iteration.

3.2. Approximating model probabilities

Of all the steps outlined in the previous section, it is clear that tuning the probabilities P_i^{sr} in step 4° is the heart of the whole procedure.

In general, the probabilities represent $K \cdot R$ free parameters and their uncontrolled modification could lead to a serious deformation of the model. To avoid this, a restrictive assumption is made: if the probability of some particular maintenance must be modified, it is modified proportionally in all deterioration states, so that at all times

$$P_0^{1r} : P_0^{2r} : \dots : P_0^{Kr} \sim P_i^{1r} : P_i^{2r} : \dots : P_i^{Kr} \quad (3)$$

for all repairs ($r = 1 \dots R$).

This assumption also significantly reduces dimensionality of the problem, as now only R scaling factors $X_{i+1} = [X_{i+1}^1, X_{i+1}^2, \dots, X_{i+1}^R]$ must be found to get all new probabilities for the model M_{i+1} :

$$P_{i+1}^{sr} = X_{i+1}^r \cdot P_0^{sr}, \quad r = 1 \dots R, \quad s = 1 \dots K \quad (4)$$

Moreover, although the frequency of a repair r depends on the probabilities of all repairs (modifying probability of one repair changes, among others, state durations in the whole model; thus, it changes the frequency of all states) it can be assumed that, in a case of a single-step small adjustment, its dependence on repairs other than r can be considered negligible and

$$F_i^r = F_i^r(X_i^1, X_i^2, \dots, X_i^R) \approx F_i^r(X_i^r) \quad (5)$$

With these assumptions, generation of a new model is reduced to the problem of solving R non-linear equations in the form of

$F_i^r(X_i^r) = F_G^r$. This can be accomplished with one of the standard root-finding algorithms.

One point of the procedure requires additional attention, though: applying equation (4) with $X_{i+1} > 1$ may violate the condition

$$\sum_{r=1}^R P_{i+1}^{sr} \leq 1 \quad (6)$$

in some deterioration state s . This situation needs special tests that would detect such illegal probability values and reduce them proportionally so that their sum does not exceed 1: a so called *scale-down transformation* needs to be applied. As practical studies show, such conditions do occur during model tuning towards repair frequencies that are remarkably higher than F_0^r from the initial model M_0 . In its simplest form, the scale-down operation consists in dividing each probability P^{sr} in the offending state s by the sum of all repair probabilities in this state:

$$P^{sr} = P^{sr} / S_{Ds}, \quad S_{Ds} = \sum_{r=1}^R P^{sr} \quad (7)$$

This will also imply that $P^{s0} = 0$ which means that every inspection ends with some repair and there are no direct returns from I_s state to D_s . Moreover, this obligatory correction mechanism can result in a violation of the proportionality rule (3), as an inevitable side effect.

3.3. Numerical implementation

The following three approximation algorithms were implemented in the task of solving equation (5): Newton method working on a linear approximation of F^r functions (the NOLA method), the secant method and the false position (*falsi*) method. For their detailed presentation please refer to [26] and [29].

Generally, if the scale-down operation (7) does not disturb the iteration flow, any of the approximation algorithms can arrive at the requested goal frequencies with just a few steps, even if imposed precision margins are very narrow. The iterative scheme is very efficient with regard to this aspect. Moreover, practical tests have shown that although simplifications of the NOLA solution may seem critical, it is reasonably efficient and stable in the real-world cases because it has one advantage over its more sophisticated rivals: since it does not depend on previous approximations, selection of the starting point is not so important and the accuracy during the first iterations is often better than in the secant or *falsi* methods. Superiority of the latter methods, especially of the *falsi* algorithm, manifests itself in the later stages of the approximation when the potential problems with initial selection of the starting point have been diminished.

4. Correction of the adjustment procedure for saturated models

Adjusting the model to the repair frequencies that are substantially higher than the original ones may lead to the *model saturation* – a condition in which repair probabilities reach the limit (6) in every state D_s and there is no room for further increase if the adjustment procedure is limited only to the simple probability scaling as expressed in equation (4). In this situation, bringing together the two requirements: tuning the model towards high repair frequencies and, at the same time, keeping the modifications of the internal structure within a safe range that does not break proper relation with the original, is a challenge and is discussed in this section.

4.1. The problem

For practical illustration of the problem we will use two real-world Markov models, A and B that are especially prone to probability saturation. Both models have the same general structure with $K = R = 3$, i.e., they include three deterioration states ($D1 \div D3$) and three repairs: minor (index = 1), medium (2) and major (3). The main difference between them lies in the distributions of the repair probabilities P^{sr} in the deterioration states (or, strictly speaking, in inspection states $I1 \div I3$ associated with the deterioration states, as in Fig. 1).

The model A has been created with an assumption that although there are no repairs in the first state $D1$, when the equipment is in subsequent states $D2$ and $D3$ every inspection leads to some sort of repair and the totals $S_{D2} = S_{D3} = 1$ ($P^{20} = P^{30} = 0$). Actual probability distribution in each state is chosen so that in the medium deterioration state $D2$ the minor repair is the most common ($P^{21} = 0.80$) while in the major deterioration $D3$ the distribution is more balanced with medium repair taking half of the chances ($P^{32} = 0.50$).

The model B is a sibling of A with just one difference: repair probabilities in $D2$ and $D3$ are lowered by, respectively, 20% and 10%, which means that after inspections $I2$ and $I3$ it is possible to return to D_s without undertaking any repair ($P^{20} = 0.2$ and $P^{30} = 0.1$). From the point of view of the current discussion, model B, as opposite to model A, has more potential for the probability growth.

In the following analysis, a series of models for the goal frequencies will be generated in cases A and B

$$F_G = [\alpha \cdot F_0^1, F_0^2, F_0^3]$$

with factor α increasing from 0.5 (frequency of the minor repair reduced by half) to 2.0 (minor repair performed twice as often) in steps of 0.1. Values of α will be expressed as %. Frequency of the minor repair (no. 1) was selected as the varying parameter in F_G just as an example with frequencies of the other repairs remaining constant, but equivalent results could be demonstrated with changing the frequencies of medium or major repairs.

As it was discussed with greater detail in [30], both models can be successfully adjusted only up to the point of saturation which is reached for $\alpha = 100\%$ for model A (i.e., the initial model is already saturated) and 130% for model B. As it turns out, in this particular case the values $P^{20} = 0.2$ and $P^{30} = 0.1$ in model B leave enough room for approximately 30% increase of F^1 . In both saturation situations probabilities in the states $D2$ and $D3$ sum up to unity and cannot be further increased, while in $D1$ the P^{11} is zero and applying the scaling factor as in equation (4) cannot produce any increase. On the other hand, the procedure has no problems with an adjustment towards frequencies lower than the saturated ones and, in such cases, the probabilities are scaled accordingly.

4.2. Modification of the adjustment procedure

The above examples of unsuccessful tuning can be used for illustration of the proposed extension to the algorithm: if the model gets saturated after some adjustment iteration but there is still a state with null repair probability, the process can be continued in the same iterative way after some non-zero probability is added in this state. Such modification, though, goes beyond the restrictive assumption expressed by equation (3) and, being a more serious invasion into the model structure, must be applied in a cautious and thoughtful manner.

In particular, the following two issues must be taken into account: (1) forcing non-zero probability in some state before it is not absolutely necessary, i.e., prior to the model saturation, instantly changes reaction to the adjustment iterations; hence, may change the final result of the tuning also in cases when the standard procedure would be able to produce the correct result; (2) replacing the null value of P^{sr} , even if delayed up to the moment of saturation, but with probability which is too high for the actual needs, also may affect the final result in a way that is against the general idea of conservative tuning which should try to preserve the structure of the original model with minimal possible modifications. Consequences of the improper modifications that violate the above rules were presented in [30].

After analyses of numerous case studies like the above two examples, the following modification of the adjustment procedure has been found to be the most flexible and efficient solution that gives optimal results in a broad range of practical cases. Its main idea is not only

to delay the increase of null probability until the moment of model saturation, but also to scale its value adequately.

The modification does not amend the general iterative scheme defined in point 3.1 in steps $1^\circ \div 5^\circ$; the changes are limited only to the internal details of step 4° , which computes new probability values for the next model M_{i+1} . The modified implementation of this operation detects and deals differently with the following two cases:

- If the model is not saturated, i.e., there is a state with $0 < S_{D_s} < 1$, the standard approach is applied: in all states the values of P^{sr} are multiplied by the scaling factors X^r (equation (4)) and then, if required, they are scaled down as in equation (7).
- If the model is saturated but there is a state with $P^{sr} = 0$ (a chance for probability increase), this particular null probability is replaced with a predicted average increase of P^{sr} in other states computed by the regular method as described above; after this the model is no longer saturated and the iterative scaling of this probability can be continued with the standard algorithm.

It should be noted that in case (b) the new value that replaces the null probability is computed as an average of the predicted *actual* increases of probabilities for a given repair in other states: these increases will be scaled down with equation (7) because these states, by virtue of the method, will be saturated. As a result, the applied value of the increase will be proportional to the needs of particular situation but, at the same time, it will be additionally constrained.

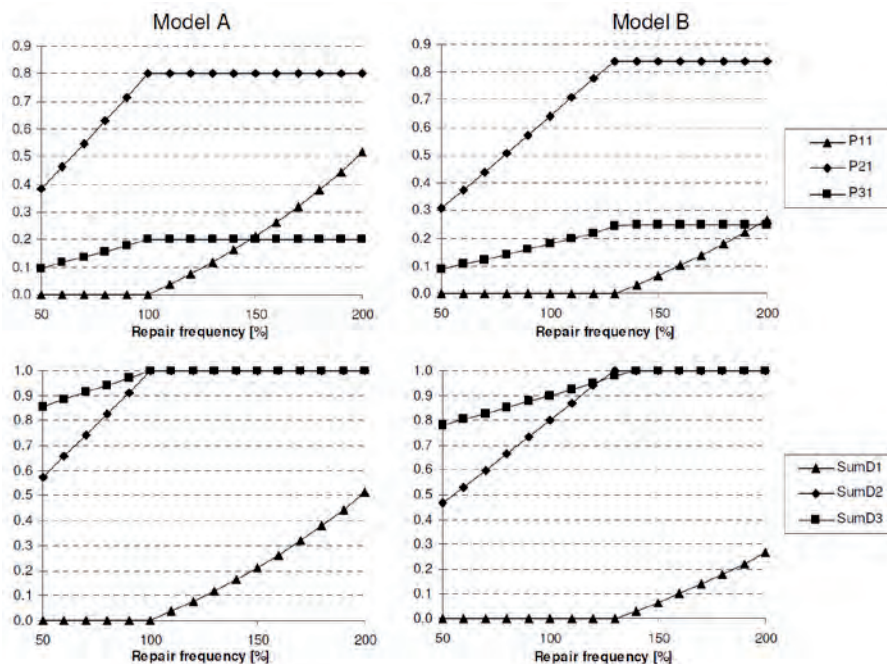


Fig. 2. Successful tuning of the models A (left) and B (right) beyond the point of model saturation by the proposed extension of the adjustment procedure.

Figure 2 presents the results obtained after application of this extended procedure to the models A and B: the upper graphs shows probabilities of the minor repair in all three deterioration states (P^{11}) and the lower graphs – sum of all repair probabilities in every state (S_{D_s}). For both models, the adjustment can be successfully completed beyond the point of saturation, i.e., up to the doubled frequency of the minor repair, while for goal frequencies without model saturation ($\alpha < 100\%$ for model A and $\alpha < 130\%$ for model B) the results are identical to the outcomes of the standard (unmodified) procedure.

Moreover, the graphs unveil the actual mechanism of model adjustment. Before saturation $P^{11} = S_{D1} = 0$ and scaling only P^{21} and P^{31} is enough for reaching the goal frequencies. At the point when this becomes insufficient ($\alpha = 110\%$ and $\alpha = 140\%$) the null values of P^{11}

are increased and further growth is limited to the $D1$ state with the other two remaining saturated.

5. Evaluating reliability and cost for different maintenance strategies

The methodology presented in the two previous sections will be now illustrated by a practical example of maintenance evaluation. The example is based on a real-world piece of equipment with a model created and fine-tuned so that it represents the actual reliability and maintenance parameters found in the historical records. According to them, the average equipment life has been found to reach 18.7 years of operation before failure. The model includes three deterioration states and represents the default maintenance policy with three possible repair types corresponding to, respectively, minor, medium and major repairs.

5.1. Life curves

Fig. 3 presents life curves computed for this equipment with various repair policies. The rightmost one represents the standard (historical) policy with all three repairs implemented with their typical frequencies, while the leftmost one – corresponding to the average equipment life of approx. 10 years – has been created from the model with all repairs removed (so called “do nothing” policy). As it is shown, in this specific case, turning off all the maintenance actions results in shortening of the equipment life by 46% and this fact can be compared to expected economic savings. The other three curves represent the following mid-range scenarios which were selected in this work as typical examples of the solutions that may be considered in the real-world applications:

- turning off the major repair without changing the frequencies of the remaining two ones (minor and medium), which has been evaluated to reduce the average equipment life to 14.7 years (i.e. by 21%),
- keeping only the medium repair with minor and major ones removed (equipment life reduced by 28% to 13.4 years),
- reducing by half the frequencies of all three repairs (equipment life reduced by 40% to 11.3 years).

It should be stressed that in the three mid-range cases the curves have been computed using models that were tuned to required repair frequencies with the numerical procedure described earlier in this paper.

Having such models not only the shape and length of the curves can be evaluated, but also other significant reliability characteristics, with the probability of failure within the specific time horizon being one of the most important in further analysis.

5.2. Maintenance scenarios

The models and the life curves for different repair policies can be used for evaluation of various maintenance scenarios. As examples, we will consider a situation when, with an initial equipment deterioration estimated as 80% of “as new” condition, some specific actions – a repair or just a change in maintenance policy – will take place after a 3 year delay while the effects will be evaluated for a 10 year time period. The actions in the scenarios will be as follows:

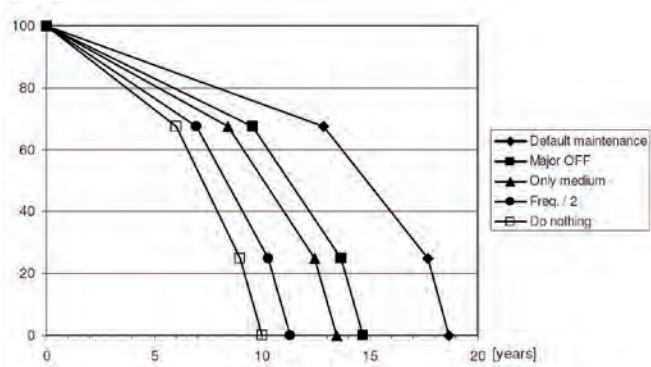


Fig. 3. Life curves for equipment with different repair policies

- adopting “do nothing” policy, which means just stopping all inspections and repairs; in case of failure the equipment will be refurbished and its condition restored to 85%,
- replacing the equipment with “as new” one and then switching to the “do nothing” policy,
- performing a major refurbishment of the equipment which restores its condition to 85% and then continuing with a medium repair only.

Fig. 4 shows the composite life curves created over a period of 10 years for the above scenarios and compares them to the “continue as before” policy. The composite curves were constructed with the appropriate segments of the basic curves from Fig. 3. Starting from the initial asset condition of 80% of the initial asset value, which corresponds to the equipment ca. 8 year old, the curves run down to 72% during the first three years and then split at the moment of the action. For the “do nothing” action deterioration rate speeds up, while for the two other actions the asset condition is first increased as a result of the replacement or refurbishment and, then, a new reduced repair policy is applied, which again causes a higher rate of deterioration. The shapes of the curves make possible a quantitative comparison of these processes and allow evaluation of their effects.

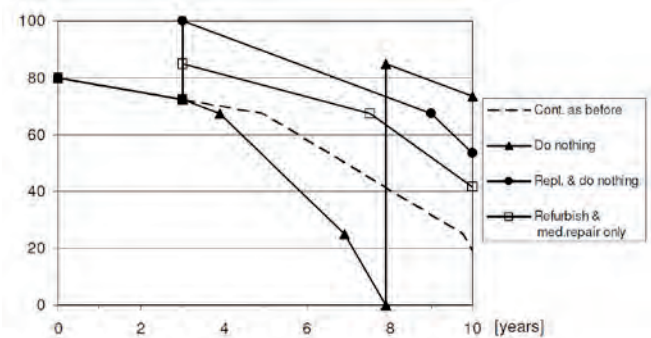


Fig. 4. Life curves for different maintenance scenarios over a time horizon of 10 years

It can be noted that, in the case of “do nothing” action, it is predicted that the equipment will fail within the time horizon under consideration. While in such a case, different actions (repairs or replacements) may take place, in this specific scenario it is assumed that the equipment will be repaired with its condition restored to 85%, but other courses of action can also be modelled.

5.3. Probability of failure

Probability of failure within the time horizon computed for the strategies under consideration is shown in Fig. 5. Values on the graphs are presented as functions of the action delay time (100% = 3 years)

and they are compared against the probability of failure for the unmodified standard maintenance (“continue as before”). The value of this probability has been computed to be 42%.

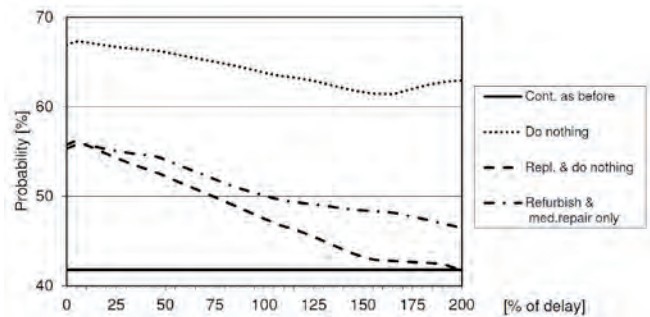


Fig. 5. Probability of equipment failure within a period of 10 years as a function of action delay

It can be seen in case of all three scenarios that, since the new maintenance policy after the action is more or less reduced, the more the action is delayed, the less probable equipment failure becomes. For evident reasons adopting “do nothing” policy leads to the highest values of the failure probability, while replacing the equipment and “doing nothing” afterwards turned out to be a less dangerous strategy (in terms of failure probability) than refurbishing and then keeping only the medium repair. Whether the differences in the economic expenses of these two possible strategies justify this discrepancy in the reliability parameter or not – remains an open question and generally depends on the costs associated with the equipment failures.

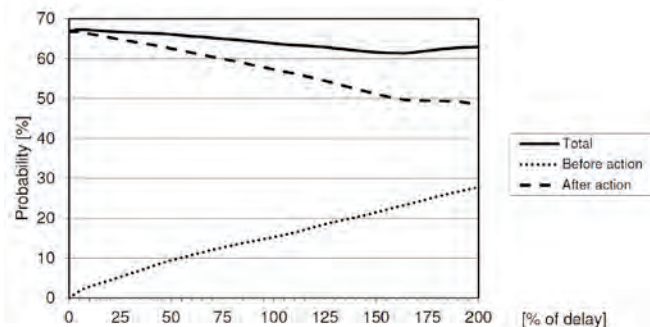


Fig. 6. Probability of equipment failure before and after the action for “do nothing” scenario

One interesting observation can be made about the curve for “do nothing” strategy: its decrease is not strictly monotonic and there is a local minimum at the level of 61% for the delay equal to 164% (4.9 years) after which the probability begins to rise slowly. To explain this rise, the two components: the probability of failure before and after the action should be investigated and they are shown in Fig. 6. In general, these two components behave as expected: the later the action takes place, the higher the probability of failure before and the lower probability of failure after the action but the rates of these two flows – increasing and decreasing – are not constant and do not sum up into a monotonic decrease. In this case, the probability of failure after the action falls down to some extent slower after the point of 164% and this causes the local minimum in the total probability of failure.

5.4. Cost analysis

In financial evaluations, the costs are expressed as the present value (PV) quantities and this approach should also be used in this kind of studies because maintenance decisions on aging equipment include

timing, and the time value of money is an important consideration in any decision analysis. The cost difference is often referred to as the Net Present Value (NPV). In the case of maintenance, the NPV can be obtained for several re-investment options which are compared with the "Continue as before" policy.

Cost evaluation for any maintenance scenario involves calculation of the following three fundamental classes of components:

1. cost of the maintenance activities,
2. cost of the selected action (i.e., refurbishment or replacement),
3. cost associated with failures (cost of repairs, system cost, penalties).

To compute the PV, inflation and discount rates are required for the specified time horizon. The cost of maintenance over the time horizon is the sum of the maintenance costs incurred by the original maintenance policy for the duration of the delay period (up to the action), and the costs incurred by the new policy for the remainder of the time horizon (after the action). The costs associated with the equipment failure over the time horizon can be computed similarly except that the failure costs before and after the action should be multiplied by the respective probabilities of failures, and the two products added.

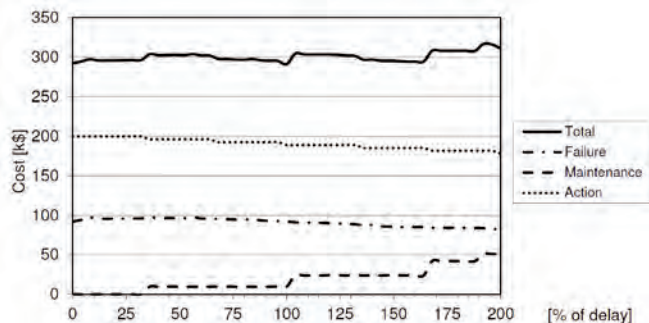


Fig. 7. Estimated cost of "replace & do nothing" scenario (the total value and the three components)

Fig. 7 presents the plots showing the cost analysis for the exemplary scenario "replace and then do nothing". Again (as it was in the case of the probability of failure) the values are visualized as functions of the action delay varying in the range $0 \div 200\%$ of the user-specified reference value. In this particular case, this value was 3 years and the

costs correspond to the estimated expenses over the period of 10 years (i.e., for 150% delay one can read the costs incurred over the period of 10 years evaluated for situation when the replacement was delayed for 4.5 years).

The "Maintenance" component that can be seen in this figure includes inspection and repair costs that were incorporated in the model and, since in this scenario there is no maintenance after the replacement, for 0% delay (the action done immediately) all the maintenance activities are suspended from the start of the time horizon and the value of this component falls to zero. Only after delaying the action by 35% the first repair is expected to be performed (incurring some non-zero cost) while the further increase of this delay causes more and more repairs to take place – hence several noticeable jumps appear in the flow of this curve. As for the cost of the replacement itself ("Action"), although it does not depend on the delay, is not constant due to the PV calculations. Also cost of the failure (loss of equipment, penalties, loss of revenue, repair cost, etc.) although assumed to be constant for each specific scenario, in this analysis fluctuates due to changes in probabilities of failure (estimated separately for the periods before and after the action) and, to a lesser extent, also due to the PV calculations.

6. Conclusions

The purpose of the method presented in this paper is to help the maintenance supervisor in choosing an effective yet cost-efficient maintenance policy. Based on the Markov models representing deterioration process, the equipment life curve and other reliability parameters can be evaluated. Once a database of equipment models is prepared, the end-user can perform various studies with different maintenance strategies and compare expected outcomes. As the results are visualized through the relatively simple concept of a life curve, no detailed expert knowledge about internal reliability parameters or configuration is required.

Additionally, we have presented a method for automatic adjustment of a given deterioration model to the requested new repair frequencies. Such a task arises often either in fine-tuning of the model to historical records of equipment operation or during analyses of the possible hypothetical maintenance options. The proposed adjustment method strives to be as conservative as possible with regard to the amount of alterations introduced to the existing model in order to avoid its deformation and, consequently, corruption of the produced results.

References

1. Abeygunawardane SK, Jirutitijaroen P. A Realistic Maintenance Model Based on a New State Diagram. Proc. Int. Conf. Probabilistic Methods Applied to Power Systems 2010.
2. Abeygunawardane SK, Jirutitijaroen P. Effects of maintenance on reliability of probabilistic maintenance models. Proc. Int. Conf. Probabilistic Methods Applied to Power Systems 2012.
3. Abeygunawardane SK, Jirutitijaroen P. New State Diagrams for Probabilistic Maintenance Models. IEEE Transaction on Power Systems 2011; 26: 2207–2213.
4. Anders GJ, Endrenyi J, Stone GC, Ford GL. A Probabilistic Model for Evaluation of Remaining Life of Electrical Insulation in Rotating Machines. IEEE Transactions on Energy Conversion 1990; 5: 761–767.
5. Anders GJ, Endrenyi J. Using Life Curves in the Management of Equipment Maintenance. Proc. Int. Conf. Probabilistic Methods Applied to Power Systems 2004.
6. Anders GJ, Leite da Silva A. M. Cost Related Reliability Measures for Power System Equipment. IEEE Transactions On Power Systems 2000; 15: 654–660.
7. Anders GJ, Maciejewski H. Estimation of impact of maintenance policies on equipment risk of failure. Proc. Int. Conf. Dependability of Computer Systems DepCoS – RELCOMEX 2006; 351–357.
8. Anders GJ, Sugier J. Risk assessment tool for maintenance selection. Proc. Int. Conf. Dependability of Computer Systems DepCoS – RELCOMEX 2006; 306–313.
9. Billinton R, Allan R N. Reliability Evaluation of Engineering Systems: Concepts and Techniques. Berlin Heidelberg: Springer Verlag, 1992.
10. Chan GK, Asgarpour S. Optimum maintenance policy with Markov processes. Electric Power Systems Research 2006; 76: 452–456.
11. Chan GK, Asgarpour S. Preventive Maintenance with Markov Processes. Proc. North American Power Symposium 2001; 510–515.

12. Chiang JH, Yuan J. Optimal maintenance policy for a Markovian system under periodic inspection. *Reliability Engineering & System Safety* 2001; 71: 165–172.
13. Endrenyi J, Aboresheid S, Allan RN, Anders GJ, Asgarpoor S, Billinton R, Chowdhury N, Dialynas E N, Fipper M, Fletcher R H, Grigg C, McCalley J, Meliopoulos S, Mielnik TC, Nitu P, Rau N, Reppen ND, Salvaderi L, Schneider A, Singh Ch. The Present Status of Maintenance Strategies and the Impact of Maintenance on Reliability. *IEEE Transactions on Power Systems* 2001; 16: 638–646.
14. Endrenyi J, Anders GJ, Leite da Silva A M. Probabilistic Evaluation of the Effect of Maintenance on Reliability – An Application. *IEEE Transactions on Power Systems* 1998; 13: 567–583.
15. Ge H, Asgarpoor S. Parallel Monte Carlo simulation for reliability and cost evaluation of equipment and systems. *Electric Power Systems Research* 2011; 81: 347–356.
16. Hosseini MM, Kerr R M, Randall RB. An inspection model with minimal and major maintenance for a system with deterioration and Poisson failures. *IEEE Transactions on Reliability* 2000; 49: 88–98.
17. Hughes DT, Russell DS. Condition Based Risk Management (CBRM), a Vital Step in Investment Planning for Asset Replacement. *Proc. 3rd IEE International Conference on Reliability of Transmission and Distribution Networks* 2005; 261–265.
18. Jirutitijaroen P, Singh C. The effect of transformer maintenance parameters on reliability and cost: A probabilistic model. *Electric Power Systems Research* 2004; 72: 213–224.
19. Limnios N, Oprisan G. *Semi-Markov Processes and Reliability*. Boston: Birkhauser, 2001.
20. Maciejewski H. Estimation of Impact of Maintenance Policies on Equipment Risk of Failure. *Proc. Int. Conf. Dependability of Computer Systems DepCoS – RELCOMEX* 2006; 351–357.
21. Maciejewski H. Reliability Centered Maintenance of Repairable Equipment. *Proc. Int. Conf. Dependability of Computer Systems DepCoS – RELCOMEX* 2009; 332–339.
22. Natti S, Kezunovic M, Singh C. Sensitivity analysis on the probabilistic maintenance model of circuit breaker. *Proc. Int. Conf. Probabilistic Methods Applied to Power Systems* 2006.
23. Park DH, Jung GM, Yum JK. Cost minimization for periodic maintenance policy of a system subject to slow degradation. *Reliability Engineering & System Safety* 2000; 68: 105–112.
24. Perman M, Senegacnik A, Tuma M. Semi-Markov Models with an Application to Power-Plant Reliability Analysis. *IEEE Transactions on Reliability* 1997; 46: 526–532.
25. Stopczyk M, Sakowicz B, Anders GJ. Application of a semi-Markov model and a simulated annealing algorithm for the selection of an optimal maintenance policy for power equipment. *International Journal on Reliability and Safety* 2008; 2: 129–145.
26. Sugier J, Anders GJ. Modeling changes in maintenance activities through fine-tuning Markov models of ageing equipment. *Proc. Int. Conf. Dependability of Computer Systems DepCoS – RELCOMEX* 2007; 336–343.
27. Sugier J, Anders GJ. Modifying Markov models of ageing equipment for modeling changes in maintenance policies. *Proc. Int. Conf. Dependability of Computer Systems DepCoS – RELCOMEX* 2009; 348–355.
28. Sugier J, Anders GJ. Probabilistic evaluation of deterioration processes with maintenance activities. *Summer Safety and Reliability Seminars SSARS* 2011; 1: 177–184.
29. Sugier J, Anders GJ. Verification of Markov models of ageing power equipment. *Proc. Int. Conf. Probabilistic Methods Applied to Power Systems* 2008; 1–6.
30. Sugier J. Avoiding probability saturation during adjustment of Markov models of ageing equipment. *Advances in Intelligent and Soft Computing: Dependable computer systems*. Springer 2011; 97: 205–217.
31. Tomasevich CL, Asgarpoor S. Optimum maintenance policy using semi-Markov decision processes. *Electric Power Systems Research* 2009; 79: 1286–1291.
32. Welte T M. Using state diagrams for modeling maintenance of deteriorating systems. *IEEE Transaction on Power Systems* 2009; 24: 53–66.
33. Yin L, Fricks R M, Trivedi K S. Application of Semi-Markov Process and CTMC to Evaluation of UPS System Availability. *Proc. Annual Reliability and Maintainability Symposium* 2002, 584–591.
34. Zhang T, Nakamura M, Hatazaki H. A decision methodology for maintenance interval of equipment by ordering based on element repair-replacement rate. *IEEE Power Engineering Society Summer Meeting* 2002; 2: 969–974.

Jarosław SUGIER, Ph.D.

Institute of Computer Engineering,
Control and Robotics
Wrocław University of Technology
ul. Janiszewskiego 11/17
50-372 Wrocław, Poland
E-mail: jaroslaw.sugier@pwr.wroc.pl

Prof. George J. ANDERS

Department of Microelectronics and Computer Science
Technical University of Łódź
ul. Wólczańska 221/223
90-924 Łódź, Poland
E-mail: george.anders@bell.net

Vidas ŽURAULIS
Edgar SOKOLOVSKIJ
Jonas MATIJOŠIUS

THE OPPORTUNITIES FOR ESTABLISHING THE CRITICAL SPEED OF THE VEHICLE ON RESEARCH IN ITS LATERAL DYNAMICS

MOŽLIVOŠČI OKREŠLENIA PRĘDKOŚCI KRYTYCZNEJ POJAZDU NA PODSTAWIE BADAŃ JEGO DYNAMIKI POPRZECZNEJ

In this paper, the parameters important for lateral dynamics of vehicles are analyzed in order to establish the values of its critical speed on the moment of losing the stability. The values of the vehicle's speed yaw rate, the steering wheel angle, the lateral acceleration, and the roll angle obtained from experimental tests are filtered according to the set conditions and only the general values that mean the beginning of the vehicle slipping are selected. For more precise assessment of the selected values, a statistical analysis is carried out. The Normal distribution law describes scattering of the selected values in the most relevant way and concretizes the critical speed being established. In the end of the paper, the obtained values of the speed are compared to the results of the theoretical calculations. Conclusions assessing the developed technique of selection of the parameters are provided.

Keywords: critical speed, lateral dynamics, vehicle sideslip, stability, circular motion.

Niniejsza praca analizuje parametry istotne dla dynamiki poprzecznej pojazdów w celu ustalenia wartości prędkości krytycznej w momencie utraty przez nie stabilności. Wartości szybkości zbieżności przez pojazd z kursu, kąta skrętu kierownicy, przyspieszenia poprzecznego oraz kąta odchylenia się pojazdu, uzyskane w badaniach doświadczalnych, dobrano pod kątem założonych warunków i tylko ogólne wartości oznaczające początek poślizgu pojazdu zostały wybrane. W celu dokładniejszej oceny wybranych wartości przeprowadzono analizę statystyczną. Prawo rozkładu normalnego opisuje odpowiednie rozproszenie wybranych wartości i konkretyzuje ustaloną prędkość krytyczną. W końcowej części pracy porównano uzyskane wartości prędkości z wynikami obliczeń teoretycznych. Wnioski służą ocenie opracowanej techniki doboru parametrów.

Słowa kluczowe: prędkość krytyczna, dynamika poprzeczna, poślizg pojazdu, stabilność, ruch obrotowy.

1. Introduction

Assessment of parameters of vehicles became a topical and permanently disputable object for persons involved in creation and improvement of vehicles and, of course, all traffic participants as early as since their appearance on roads. Each of the above-mentioned categories has its own goals, namely: striving for technological progress; ensuring safe and reliable exploitation; adaptability to various situations of the daily life to the maximum possible extent. Modernity of today vehicle systems and the possibilities of their diagnostics enable to carry out a detailed exploration of various parameters of movement that become important in improving the safety systems, in investigation of traffic events or upon striving to clear up (upon the maximum accuracy) the regularities of movement of a vehicle, as a totality of aggregates with different properties. A moment of losing control of a vehicle may be identified as a critical value of speed that may be found upon applying various methods. If all the systems are precisely assessed and mathematically described, an application of the numerical method for estimating the parameters is possible; however, it requires a particularly detailed technique for application of fundamental knowledge and often is too complicated for many cases of establishment. So, experimental tests are used for estimation of certain regularities upon real conditions.

On investigation of the parameters of lateral dynamics of a vehicle, a model of a vehicle with four degrees of freedom is most frequently used. Such a model assesses the key parameters and does not charge the calculations with data of low importance. The calculation

technique based on the said model takes into account the loads onto the wheels and the nonlinearity of the tires and it enables to calculate the lateral forces acting the tires and the sideslip angles [1] and [5]. Longitudinal and lateral speed estimation is often used from vehicle cornering stiffness, friction parameters in various driving maneuvers [20]. Chinese scientists apply methods of analysis to data collected from sensors in order to introduce the earlier developed algorithms in active safety systems of vehicles. The interaction between the tire and the road dependently on the speed and character of driving is analyzed. For the research, experiments, mathematical models and computer programs, are used [8].

Lateral stability of a vehicle depends not only on the acting lateral forces, but on the longitudinal dynamics as well. Sideslip in vehicle usable in auto racing is formed artificially by the parking brake or by considerable increasing the tractive force of driving wheels. The performance parameters of such movement and the algorithms usable for their processing were explored by scientists of Switzerland and USA in 2010 [18]. The surface of the road where the vehicle is moving distinguishes itself for the type of the pavement, unevenness and geometrical parameters, thus the road parameters considerably impact the general dynamics of the vehicle [16].

At Heudiasyc laboratory (France), the investigations on the sideslip angle of a vehicle dependently on the acting lateral forces in case of a sudden turn were carried out [15]. On double lane change and slalom maneuvers upon the lateral acceleration up to 4 g, the results of experiments and mathematical simulation differed inconsiderably; however, when lateral acceleration exceeded 0.6 g, the results became

markedly different because of nonlinearity of tires that's assessment required special investigation in each case.

On expert's examinations of traffic events, various cases of traffic events, such as collisions of vehicles [12], hitting a pedestrian [19], turning turtle [13], collisions with obstacles [14] and so on, are examined. If sideslip of wheels takes place on a traffic event, it is very important to estimate precisely the lateral dynamics parameters of adherence of the wheels with the pavement and to establish the initial moments of losing the stability and critical speed [3] and [13].

Operation of electronic stability systems (ESP) is based on control of the intensity of the rotational speed of the body, angular rotational speeds of wheels and the acting accelerations. According to the data from the sensors, the established processing algorithm assesses a stability of the vehicle and, when required (when the limit of stability provided by the manufacturer is overstepped), sends signals to the control systems [7] and [10]. In critical stability cases, operation of the traction system and the vehicle braking system is very important, so activation of the said systems on the proper moment is a matter of a great relevance [21].

2. Vehicle model

Analysis of the dynamics of a vehicle moving along a circular trajectory is convenient upon using a model with four degrees of freedom (DOF) (Fig. 1). This mathematical model provides a possibility of vehicle body longitudinal and lateral movement, yaw (ψ) and roll (φ) movement. In Fig. 1, v_x and v_y are the longitudinal and lateral components of the speed vector, respectively, in the point A that is the center of mass of the vehicle plane's projection. On the vehicle standing or uniform rectilinear movement, the center of mass is leant at the angle θ in respect of the point B. This leaning is caused by the position of the axis of inclination that, in its turn, is impacted by the structure of the vehicle's suspension. On turning, the lateral force acting upon the vehicle causes a rotation of the sprung masses (m_s) at the angle φ around the said axis. In the presented model, the steering angles $\delta_{1,2}$ and sideslip angles $\alpha_{1,2,3,4}$ of all wheels are shown as well. C is the center of mass on low-speed turning of the vehicle at the radius R' without sideslip, and C' is the momentary center of mass on turning at a larger angle R' with a higher speed. In such a case, the tire planes differ from the directions of the speed vector $v_{1,2,3,4}$ by angles $\alpha_{1,2,3,4}$.

According to Lagrange's equation, the equations of motion for 4-DOF vehicle model are derived:

$$\begin{aligned} m(\ddot{v}_x - \dot{\psi}v_y) + m_s(h'\dot{\varphi}\dot{\psi} + 2h'\dot{\psi}\dot{\varphi}) &= F_{1x}\cos\delta_1 + F_{2x}\cos\delta_2 - F_{1y}\sin\delta_1 - F_{2y}\sin\delta_2 - F_{xd}; \\ m(\ddot{v}_y + \dot{\psi}v_x) - m_s(h'\dot{\varphi}\dot{\psi} - h'\dot{\psi}^2\varphi) &= F_{1x}\sin\delta_1 + F_{2x}\sin\delta_2 + F_{1y}\cos\delta_1 - F_{2y}\cos\delta_2 + F_{3y} + F_{4y}; \\ I_z\ddot{\psi} + \dot{\varphi}(I_z\dot{\theta} - I_{xz}) - m_s h' \varphi(\dot{v}_x - \dot{\psi}v_y) &= F_{1x}\sin\delta_1 a + F_{2x}\sin\delta_2 a + F_{1y}\cos\delta_1 a - F_{2y}\cos\delta_2 a + \\ + M_{1z} + M_{2z} - F_{3y}b - F_{4y}b + M_{3z} + M_{4z} + F_{1x}\cos\delta_1 s_1 - F_{2x}\cos\delta_2 s_1 - F_{1y}\sin\delta_1 s_1 - F_{2y}\sin\delta_2 s_1; \\ \dot{\varphi}(I_x + m_s h'^2) + m_s h'(\dot{v}_y^2 + \dot{\psi}v_x) + \dot{\psi}(I_z\dot{\theta} - I_{xz}) - \varphi\dot{\psi}^2(m_s h'^2 + I_y - I_z) + \\ + \dot{\varphi}(k_{\varphi 1} + k_{\varphi 2}) + \varphi(c_{\varphi 1} + c_{\varphi 2}) - \varphi m_s g h' &= 0. \end{aligned} \quad (1)$$

where: m – total mass of the vehicle, m_s – sprung mass, F_x – tractive forces, F_y – lateral forces, F_{xd} – aerodynamics and rolling resistance forces, I_x, I_y, I_z – moments of inertia around x, y and z axes, I_{xz} – inertia product of the sprung mass, M_{iz} – self-aligning moment generated by wheel i , R and R' – radius of the cornering vehicle, moving without sideslip and with sideslip, s_1 and s_2 – distances from the center of gravity to the front and rear wheel, a and b – distances from the center of gravity to the front and rear axle, h' – arm length of roll moment, $c_{\varphi 1,2}$ – roll stiffnesses of front and rear exes, $k_{\varphi 1,2}$ – damping coefficient of front and rear exes.

3. Experimental procedure

On a natural test, the vehicle is involved in circular movement at the agreed diameter upon gradual increasing the speed up to the limit when following the trajectory becomes impossible because of sideslip. Such a test is not classified as steady-state circular test, because the speed is changed. In addition, the driver is provided a freedom in correction of the steering wheel angle for maintaining the agreed circular trajectory of movement. A test of such a type was described in the international standard ISO 4138 [9]. In addition to circular movement of the constant radius, the standard also provides research techniques for cases when constant steering wheel angle and constant speed are kept.

On the tests, the ability rating of the vehicle Toyota Avensis is fixed by the equipment mounted on its sprung masses, namely: a tri-axial $\pm 3g$ accelerometer and a ± 150 deg/s gyroscope mounted on the windscreen of the vehicle; a noncontact optical speed sensor Correvit S-350 Aqua in front of the vehicle (Fig. 2a); three laser sensors HF-500C for measuring the pitch and roll angles of the body; and a wire potentiometric steering wheel angle sensor Kuebler D8 for steering wheel angle measurement. For the tests, a closed 80 m long and 60 m wide site with asphalt concrete pavement was used.

Drives are carried out along a circular trajectory with the radii of 10, 15 and 20 metres, respectively; each test is repeated at least for four times. In such a way, it is tried to avoid possible gross errors of measurement.

During the experiment, information from the sensors is fixed by the data collection equipment Corrsys-Datron DAS-3 (Fig. 2b.) and later is processed in the general time scale by software *TurboLab 6.0*. Data collection and graphical presentation during the tests is provided in Fig. 3.

4. Analysis of experimental data

For a detailed analysis, the most varying parameters on curved trajectory were selected: the vehicle speed, the yaw rate, the steering wheel angle, the lateral acceleration, and the roll angle. Although all above-listed parameters are measured directly during the tests, the target value, i.e. critical speed, is a complex result of

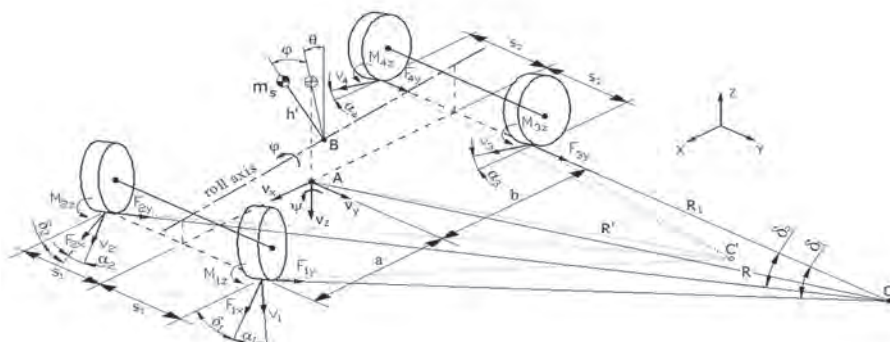


Fig. 1. 4-DOF vehicle model

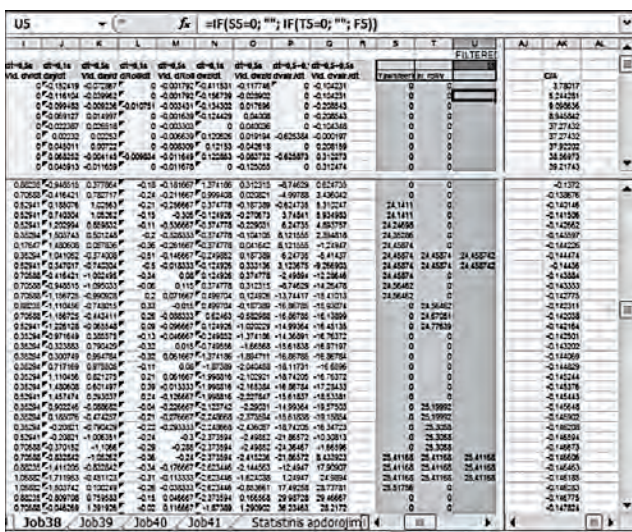


a)

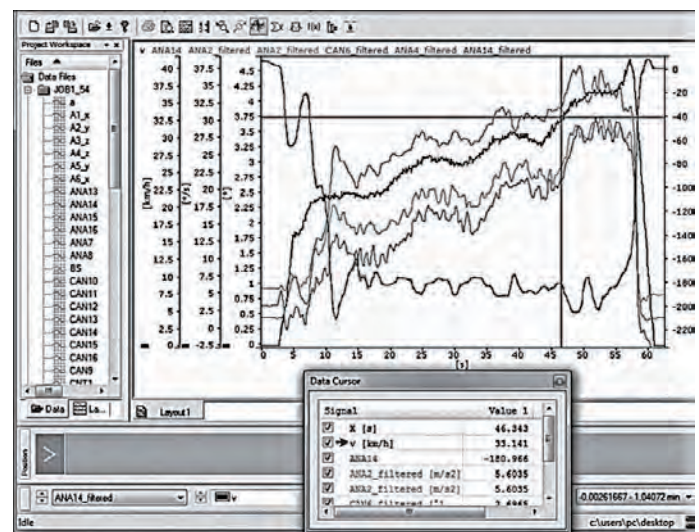


b)

Fig. 2. Equipped vehicle during experimental procedure



a)



b)

Fig. 3. Data selection during experimental procedure: a) data window of numerical form, b) window of signal analysis in TuboLab 6.0 software

the measurement that is obtained upon applying additional methods of analysis. A complex measurement is considered establishing the values of parameters of the same character by measuring various indirect parameters or their dependences. Therefore, obtaining the optimal result it is necessary to evaluate the overall parameter changes over time combining them as much as possible.

In order to establish the critical speed according to the parameters fixed during the tests, a special filter is formed. Generated selection model separates moments corresponding to moving in critical speed: 1) the conditions of sideslip of the vehicle according to the intensity of the yaw and the steering wheel angle change:

$$\begin{cases} \frac{d\psi}{dt} > 0; \\ \frac{d\delta_v}{dt'} \leq 0; \end{cases} \quad (2)$$

$$\begin{cases} \frac{d\psi}{dt} < 0; \\ \frac{d\delta_v}{dt'} \geq 0. \end{cases} \quad (3)$$

Here the first part of the condition (2) selects preliminary moments of slipping when the intensity of the yaw rate of the vehicle upon no change of the steering wheel angle or its reducing. To such cases of slipping, oversteering is attributed. The second part of the condition (3) selects expectable moments of slipping when the steering wheel angle is not changed or increased and the vehicle turns less and less. It is considered that understeering takes place;

2) the condition of sideslip of the vehicle according to the lateral acceleration that affects the vehicle and the roll angle intensity dependently on the longitudinal acceleration:

$$\begin{cases} \frac{da_y}{dt} < 0; \\ \frac{d\phi}{dt} < 0; \\ \frac{dv}{dt} \geq 0. \end{cases} \quad (4)$$

where: $dt \in [t_i; t_{i+5})$, $dt' \in [t_{vr}; t_{i+5} + t_{vr})$.

In this group of conditions (4), the moments when upon maintaining a constant speed of circular movement or its increasing, the limit of

Table 1. The statistical series of the selected values of speed according to the data on circular movement*

Range, v , km/h	15–20	20–25	25–30	30–35	35–40	40–45	45–50
Frequency, m_i	1	22	77	53	28	3	0
Statistical probability, p_i	0,005	0,120	0,418	0,288	0,152	0,016	0,000
$\sum p_i$	0,005	0,125	0,543	0,832	0,984	1,000	1,000

* at the radius of 15 meters

adhesion of the wheels with the road surface is overstepped and the acting lateral acceleration and lateral angle of inclination of sprung masses becomes less.

The specified dependence dt covers the interval with five measurement points. In the specific case, it means 0.5 s, because the frequency of general registration of parameters is 10 Hz. So, a 0.5 s interval is accepted for examination of variation of a relevant parameter and within such an interval, a remarkable character of variation of a certain parameter may be assessed. The interval dt' provided at the parameter of steering wheel angle δ_v covers five measurement points as well; however, this parameter is shifted by the value of t_{vr} that means the driver's reaction time to turn steering wheel. According to psychophysiological properties of a driver, the reaction time to turn steering wheel is 1.2–1.4 times longer than the usual reaction time [11]. Taking into account that during the tests, the driver was ready for possible turns of the steering wheel, the said time t_{vr} is not increased on application of selection of critical speed and accepted to be 0.5 s.

After establishing that the parameters satisfy the set conditions, the speed of the vehicle in the beginning of the interval is presented as the result of the selection. It is considered that the conditions are satisfied when the processed parameters satisfy one inequality from the first condition and the inequality of the second condition. Only a measuring line that satisfies the both conditions may be selected.

A variant when $d\psi/dt' = 0$ is not included in the conditions of sideslip, because in such a case, slipping is impossible while maintaining a trajectory of constant radius. The case when is not assessed as well, because, in accordance with the preset conditions of the test,

on increasing the vehicle speed, the values of a_y and ϕ will naturally grow (in absence of sideslip) because of centrifugal acceleration.

The moments according to the condition 1 or the condition 2 of sideslip provided in the formulas (2, 3) and (4) are selected in respect of zero, i.e. it is established whether the intensity of the parameter variation was positive or negative. However, striving for more precise identification of the critical speed, optimization of the said values would be convenient. For this purpose, the precise data on the performance of the specified vehicle, including its inertness, lateral stiffness of the tires and stiffness, stiffness and damping of the suspension, are required. However, such a precise assessment would not allow applying the established trend. If a less number of parameters is used for data filtration and a typical scattering of the values of the critical speed is obtained, statistical data processing methods are applied for a further analysis.

5. Statistical processing of the results

After selection of the measurement data according to the formed conditions, scattering of preliminary critical speeds upon certain regularity is obtained. For more precise establishing the target value of speed, the said regularity is assessed upon applying statistical data analysis. In course of establishing the distribution of the selected values of speed, the series of the values is formed first of all and divided into ranges (Table 1). Frequency m_i shows the number of values (selected speeds) included in the relevant range and p_i shows the statisti-

cal probability of appearance of the values in the said range. $\sum p_i$ is integral statistical probability. Statistical processing will make it easier to identify the most commonly recurrent filtered value of critical speed and assess the accuracy of adapted statistical law of distribution.

If the frequency in each interval is known, the average value of the selected speeds is calculated as follows:

$$\bar{T}_{vid} = \sum_{i=1}^n T_{Vi} \cdot \frac{m_i}{N} \quad (5)$$

where: T_{Vi} – the average value of speed in the i -th interval, m_i – frequency of access to the range, N – the number of selected values of speed. The extent of deviation of the selected values of speed from the average value is calculated as follows:

$$\sigma = \sqrt{\sum_{i=1}^n (T_{Vi} - \bar{T}_{vid})^2 \cdot \frac{m_i}{N}} \quad (6)$$

For applying the theoretical distribution law, the relative deflection of the values of speed should be assessed. It is described by the coefficient of variation:

$$v = \frac{\sigma}{\bar{T}_{vid}} \quad (7)$$

In all analyzed cases (driving along different circles), according to the formed statistical series and calculated performance curves, it was found that $v \leq 0.33$ [17]; it means that the selected values of speed are distributed according to the Normal distribution (the Gaussian law) and the shapes of drawn histograms of the distributed values and differential curves $f(T)$ (Fig. 4) preliminary support the statement.

A proper substantiation of the chosen distribution law may be provided upon using the criteria. For reasoning a feasibility of the chosen mathematical model according to all values of the sample, the so called Pearson compatibility criterion χ^2 [4] is most frequently applied. Pearson criterion is based on a comparison of the number of events obtained in empirical way m_i with the expected events of the theoretical distribution in the same interval n_{pi} . Upon applying the compatibility criterion χ^2 for verifying the zero hypothesis, the probabilities p_i of finding the random variable H in the intervals are calculated on the base of a hypothetical function as follows:

$$p_i = P(h_{i-1} \leq H \leq h_i) = \int_{h_{i-1}}^{h_i} f(h)dh = F(h_i) - F(h_{i-1}) \quad (8)$$

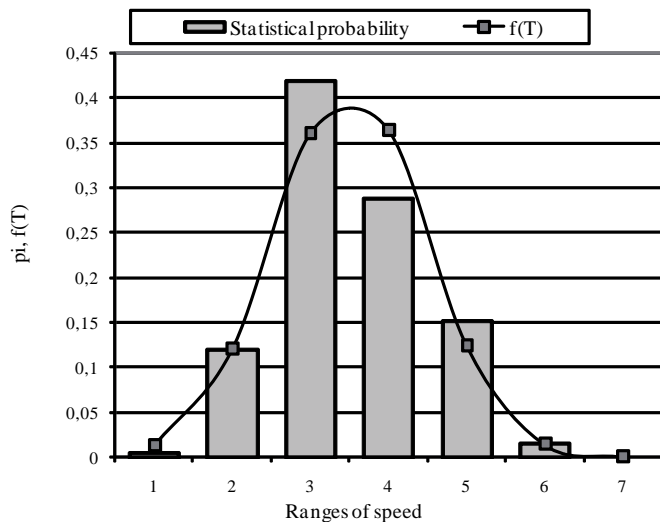


Fig. 4. Histogram and graph of theoretical differential function, $R=15$ m

where: $i = 1, 2, \dots, k$ – the numbers of intervals.

On multiplying the calculated probabilities by the sample n , the theoretical frequencies np_i of the intervals, i.e. the frequencies expected if the zero hypothesis is veridical, are found. On the base of the available values, the compatibility criterion χ^2 is calculated as follows:

$$\chi^2 = \sum_{i=1}^k \frac{(m_i - np_i)^2}{np_i} \quad (9)$$

The number of the model's degrees of freedom is calculated as follows:

$$\nu = k - r - 1 \quad (10)$$

where: $k = 7$ – the number of intervals in the formed statistical series, $r = 2$ – the number of parameters of the distribution law under verification: the sample average and dispersion.

According to the level of importance 0.05 and the degree of freedom from χ^2 distribution quantile tables [4], it is found that the critical value $\chi_{0.05;4}^2 = 9.488$. The value $\chi^2 = 6.257$ calculated according to

the formula (9) is less than $\chi_{\alpha;\nu}^2$, so the hypothesis that the chosen distribution law duly describes the selected results of the experiment is confirmed. This condition is satisfied for the data on driving along the trajectories of the radius 10 and 20 meters.

On formation of the differential curve $f(T)$, the theoretical probabilities of the applied distribution law are calculated for each interval:

$$f(T) = \frac{A}{\sigma} \varphi_0 \left(\frac{T_{Vi} - \bar{T}_{vid}}{\sigma} \right) \quad (11)$$

where: A – the difference between values of the interval, $A = 5$ km/h, φ_0 – the value to be taken from statistical references.

For finding the probability of critical stability on circular movement of the vehicle with a certain speed, diagrams of the empirical and theoretical functions are drawn (Fig. 5). For a calculation of the integral curve, the following formula is used:

$$F(t) = F_0 \left(\frac{T_g - \bar{T}_{vid}}{\sigma} \right) \quad (12)$$

where: T_g – the value of the end of the statistical series interval, F_0 – the value to be taken from statistical references.

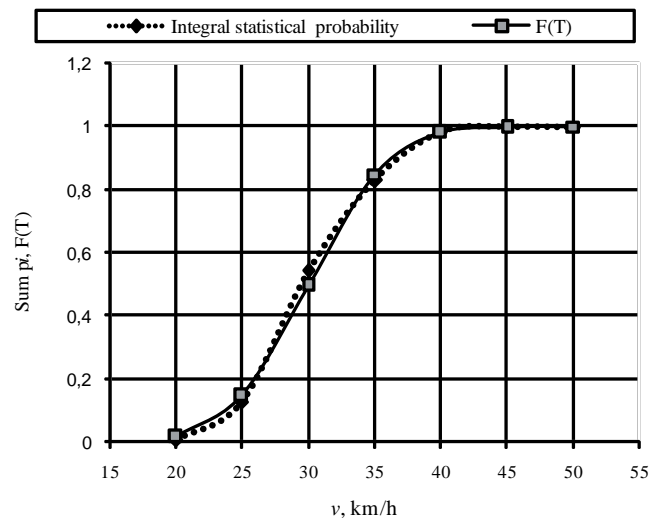


Fig. 5. Graphs of empirical and theoretical function, $R=15$ m

It may be seen from the diagrams provided in Fig. 5 that starting from approximately 35 km/h, the vehicle moving at the radius of 15 m is prone to sideslip in 90 % of cases. On further increasing the speed, the probability of slipping grows up to almost 100 %.

6. The assessment of the data selection technique

Statistical analysis of the selected experimental values of speed enables a comparison of its results to the results obtained upon applying the methods used in calculations of lateral dynamics of vehicles. In a general case, the lateral force acting in the vehicle center of mass is found as follows:

$$F_y = m \frac{v^2}{R} \quad (13)$$

Then the following equation may be written:

$$m \frac{v^2}{R} = m \dot{v}_y \quad (14)$$

The adhesion coefficient for sideslip, like for longitudinal slip, dependently on the vertical load or as a combined slip effect [6] according to the theory of the circle of adhesive forces:

$$\mu_y = \frac{F_y}{F_z} = \frac{m \dot{v}_y}{mg} = \frac{\dot{v}_y}{g} \quad (15)$$

$$\left(\frac{\mu_x}{\mu_{x,\max}} \right)^2 + \left(\frac{\mu_y}{\mu_{y,\max}} \right)^2 = 1 \quad (16)$$

The value of the speed at the slip that exceeds the limits of friction according to the equation (11):

$$v = \sqrt{\dot{v}_y \cdot R} = \sqrt{\mu_y g R} \quad (17)$$

where: \dot{v}_y – lateral acceleration; μ_y – lateral adhesion coefficient; g – gravitational acceleration.

On comparing the values found according to the formula (17) with the experimental values after their statistical analysis, typical inadequacies are observed. When the normal distribution law was applied in analyzing the movement along the trajectory of the radius of 15 meters, the found average value of critical speed was 30.05 km/h with relative scattering equal to 0.16. If the values of lateral acceleration are selected for a moment of the experiment when the vehicle has lost its stability (the values of speed exceed the established critical value and the trajectory of movement is kept by correction of the steering wheel only), the average value of the critical speed according to the formula (17) is 35.74 km/h. The comparison of the statistically assessed experimental values with theoretically calculated values of critical speed on movement along circular trajectories with the radius of 10, 15 and 20 meters is provided in Table 2.

Table 2. The experimental and theoretically calculated values of critical speed

Radius of the trajectory of movement R , m	10	15	20
The critical speed established by experiments and statistical analysis v_{cr} , km/h	27.86	30.05	35.13
The theoretical critical speed v_{cr}^* , km/h	30.57	35.74	42.12
The coefficient for assessing the inadequacies of the established values of critical speed	0.911	0.841	0.834

So, on comparison of the theoretically calculated values of the critical speed with the results of the experiment after their selection and statistical analysis, it was found that the inadequacies of the values for all trajectories involved in the experiment varies between 8.87 % ($R = 10$ m) and 16.60 % ($R = 20$ m). For assessing the said inadequacies, the correction coefficients provided in the table 3 may be used.

7. Conclusions

1. The established inadequacies between the theoretically calculated values of the critical speed and the processed experimental values point out that in the activities related to analysis of dynamics of vehicles where fixing of the initial moment of losing a stability by the vehicle is important, an application of the data selection technique developed for the conditions (2), (3) and (4) is purposeful. For simplified calculations, the values of correction coefficients provided in the table 3 may be used. The found inadequacies do not negate the fundamental calculation methods; they only provide an alternative algorithm for assessing the parameters when fixing of the initial moment of losing stability by the vehicle is important.
2. On the established moments of losing stability, it is still possible to stop the slip and to return the vehicle to the desired trajectory by actions of the driver or by active safety systems, so the technique may be useful in the activities related to expert's examination of traffic events, where, in addition to the speed of the vehicle after irreversible losing its control, it is important to identify it's speed when the driver still has technical possibilities to regain its control.
3. The said technique may be used in improving vehicle stability, its active braking and other active safety systems, because sensors installed in electronic systems of modern vehicles may establish the values of parameters that cause increasing efficiency of the systems after processing the values according to the set algorithm.

References

1. Baffet G, Charara A, Lechner D. Estimation of Vehicle Sideslip, Tire Force and wheel Cornering Stiffness. Control Engineering Practice 2009; vol. 17: 1255–1264.
2. Bonett DG. Confidence Interval for a Coefficient of Quartile Variation. Computational Statistics & Data Analysis 2006; 50: 2953–2957.
3. Brach RM. An Analytical Assessment of the Critical Speed Formula. Society of Automotive Engineers 1997; 9.
4. Braghin F, Cheli F, Melzi S, Sabbioni E. Race Driver Model. Computers and Structures 2008; 86: 1503–1516.
5. Chu L, Zhang Y, Shi Y, Xu M. Vehicle Lateral and Longitudinal Velocity Estimation Based on Unscented Kalman Filter. 2nd International Conference on Education Technology and Computer 2012; 427–432.
6. Grip HF, Imsland L, Johansen T A, Fossen T I, Kalkkuhl J C, Suissa A. Nonlinear vehicle side-slip estimation with friction adaptation. Automatica 2008; 44: 611–622.
7. Guoye W, Juanli Z, Yanli F, Yanru Z. Study on ESP Control Principle of Light Off-road Vehicle Based on Brake / Drive Integrated Control. Physics Proceda 2012; 25: 834–841.
8. Hu D, Zong Ch, Na H. Research on Information Fusion Algorithm for Vehicle Speed Information and Road Adhesion Property Estimation. Proceedings of the IEEE International Conference on Mechatronics and Automation, Changchun, China 2009; 3229–3234.
9. ISO 4138:2004(E). Passenger Cars – Steady-state Circular driving behavior – Open-loop Test Methods. International Organization for Standardization. Geneva; 19 p.
10. Lauffenburger J Ph, Basset M, Coffin F, Gissinger GL. Driver-aid System Using Path-planning for Lateral Vehicle Control. Control Engineering Practice 2003; 11: 217–231.
11. Martinėnas B. Experimental Data Statistical Analysis. 2004, Vilnius: Technics; 101 p.
12. Prentkovskis O, Sokolovskij E, Bartulis V. Investigating Traffic Accidents: a Collision of Two Motor Vehicles. Transport 2010; 25 (2): 105–115.
13. Sokolovskij E. Automobile Braking and Traction Characteristics on the Different Road Surfaces. Transport 2007; 22 (4): 275–278.
14. Sokolovskij E, Prentkovskis O, Pečeliūnas R, Kinderytė-Poškienė J. Investigation of Automobile Wheel Impact on the Road Border. The Baltic Journal of Road and Bridge Engineering 2007; 2 (3): 119–123.
15. Stephant J, Charara A, Meizel D. Evaluation of a Sliding Mode Observer for Vehicle Side Slip Angle. Control Engineering Practice 2007; 15: 803–812.
16. Vansauskas V, Bogdevičius M. Investigation into the Stability of Driving an Automobile on the Road Pavement with Ruts. Transport. Vilnius: Technika. 2009; 24 (2): 170–179.
17. Villagra J, d'Andrea-Novell B, Fliess M, Mounier H. A Diagnosis-Based Approach for Tire-Road Forces and Maximum Friction Estimation.

- Control Engineering Practice 2011; 19: 174–184.
18. Voser Ch, Hindiyeh RY, Garde JCh. Analysis and Control of High Sideslip Manoeuvres. *Vehicle System Dynamics* 2010; 48: 317–336.
 19. Weng Y, Jin X, Zhao Z, Zhang X. Car-to-pedestrian Collision Reconstruction With Injury as an Evaluation Index. *Accident Analysis and Prevention* 2010; 42: 1320–1325.
 20. Wesemeier D, Isermann R. Identification of Vehicle Parameters Using Stationary Driving Maneuvers. *Control Engineering Practice* 2009; 17: 1426–1431.
 21. Yoon J, Cho W, Kang J, Koo B, Yi K. Design and Evaluation of a Unified Chassis Control System for Rollover Prevention and Vehicle Stability Improvement on a Virtual Test Track. *Control Engineering Practice* 2010; 18: 585–597.
 22. Zaranka J. The Impact of Motor Vehicle Driver Behavior Factors on Traffic Safety. Doctoral Disertation. 2012, Vilnius, Technics; 116 p.

Vidas ŽURAULIS, M.Sc.

Edgar SOKOLOVSKIJ, Ph.D., D.Sc., Assoc. Prof.

Jonas MATIJOŠIUS, Ph.D.

Department of Automobile Transport

Vilnius Gediminas Technical University

Basanavičiaus str., 28 LT-03224 Vilnius, Lithuania

E-mails: vidas.zuraulis@vgtu.lt, edgar.sokolovskij@vgtu.lt, jonas.matijosius@vgtu.lt

Marek KALBARCZYK
Remigiusz MICHALCZEWSKI
Witold PIEKOSZEWSKI
Marian SZCZEREK

THE INFLUENCE OF OILS ON THE SCUFFING OF CONCENTRATED FRICTION JOINTS WITH LOW-FRICTION COATED ELEMENTS

WPŁYW OLEJÓW NA ZACIERANIE ELEMENTÓW Z POWŁOKAMI NISKOTARCIOWYMI SKOJARZONYMI W STYKU SKONCENTROWANYM*

The paper presents the results of four-ball scuffing tests for the following oils: polyalphaolefine oil (PAO 8), refined rapeseed oil (RzR), as well as mineral and synthetic oils of GL5 API performance level. Three material combinations of friction joints were investigated, with the upper ball material as a variable. In the research, 100Cr6 bearing steel balls were used. The tests were carried out for uncoated and low-friction coated balls. Two PVD coatings were used: a-C:H:W and MoS₂/Ti. The research results were compared with the outcome from the tests of the reference mineral oil (RL 219). The influence of oils on friction joint scuffing characteristics were determined using the scuffing load P_s and limiting pressure of seizure p_{sz} , obtained by means of the four-ball method with continuously increasing load. The obtained results indicate that, in case of concentrated friction joints with low-friction coated elements, the influence of selected oils on scuffing depends on the type of PVD coating used. The research findings also show the significant practical effect of aforementioned PVD coatings deposition on steel elements of friction joints, which is the interception of the anti-scuffing function of the classical extreme pressure (EP) oil additives by the coating. Due to that fact, the usage of such coatings makes it possible to reduce the concentration of EP additives, resulting in more environmental friendly oils.

Keywords: scuffing, seizure, oils, coatings, four-ball tester.

W artykule przedstawiono wyniki badań zacierania modelowego, czterokulowego węzła tarcia, smarowanego olejami bez dodatków smarnościowych: mineralnym olejem wzorcowym (RL 219), syntetycznym (PAO 8), rafinowanym olejem rzepakowym (RzR), oraz dwoma olejami handlowymi z dodatkami klasy GL5 na bazie mineralnej i syntetycznej. Przebadano trzy skojarzenia materiałowe, w których zmienną stanowił materiał kulki górnej. Zastosowano kulki ze stali łożyskowej (100Cr6) bez powłoki oraz z niskotarciowymi powłokami: a-C:H:W (WC/C) oraz MoS₂/Ti, osadzonymi metodą PVD. Rezultaty badań porównano z wynikami otrzymanymi dla mineralnego oleju wzorcowego (RL 219). Dokonano oceny wpływu oleju na zacieranie węzła tarcia, wykorzystując wskaźniki obciążenia zacierającego P_s oraz granicznego nacisku zatarcia p_{sz} , otrzymane przy zastosowaniu metody z narastającym obciążeniem. Stwierdzono, że wpływ rodzaju oleju na zatarcie elementów stalowych pokrytych powłokami PVD jest zależny od rodzaju powłoki. Ważnym efektem praktycznym jest też wskazanie, że powłoki PVD nanoszone na elementy stalowych systemów tribologicznych, przejmują funkcje klasycznych, nieekologicznych na ogół, dodatków smarnościowych (EP), pozwalając na redukcję ich zawartości w środkach smarowych.

Słowa kluczowe: zacieranie, zatarcie, oleje, powłoki, aparat czterokulowy.

1. Introduction

Heavily loaded friction joints, such as gears, rolling bearings, and cam-follower units are neuralgic parts of engines and transmissions, and millions of these parts are produced each year. In recent years, there has been a considerable development in the area of the construction of machine parts in the direction of size and energy-consumption reduction. Unfortunately, the size reduction is followed by an increase in the contact stresses, which results in higher risk of scuffing and may lead to machine failure.

The introduction of new technological solutions is inevitable, because the producers of heavily loaded machine parts predict that further increase in the durability by means of conventional technologies, like those connected with modelling of the mechanical strength of the base material of gears (mainly steel), is practically impossible [6]. A similar problem can also be observed in the field of lubricant

modification, especially in the case of an increase in the concentration of active anti-scuffing (EP) additives, which lead to a significant decrease in the resistance to pitting of the friction joints [27]. The research carried out by the authors [17, 29] indicate that the deposition of thin antiwear PVD/CVD (physical vapour deposition/chemical vapour deposition) coatings on machine elements by means of vacuum methods represent a promising direction in the aspect of machine life extension. In recent years, the antiwear PVD/CVD coatings have revolutionised the market of cutting and forming tools. It is estimated that approx. 80% of the currently used cutting tools are coated in order to increase their durability.

The typical coatings that are used for the tools cannot be deposited on the friction joints elements, due to the insufficient resistance to fatigue wear (pitting) [23]. Only in the case of low-friction thin hard coatings, such as WC/C and MoS₂/Ti, the resistance to pitting can be

(*) Tekst artykułu w polskiej wersji językowej dostępny w elektronicznym wydaniu kwartalnika na stronie www.ein.org.pl

obtained on a similar level as in the case of steel material, even under lubrication with oils without additives.

The application of coating, even on only one of the friction joint elements, results in the change in the chemical composition of the contacting materials, in the level of residual stresses, and in surface physical structure, leading to a change in the relation between the machine elements and the lubricant. The range of PVD/CVD coatings application is limited by the lack of knowledge about the interaction between coatings and components of lubricants. Unfortunately, most research on the characteristics of wear mechanisms for coatings have been performed under conditions of dry friction. Therefore, the obtained results cannot be referred to heavily loaded, lubricated friction joints [2, 11, 12, 15, 26]. The problem of coating applications on machine parts is a relatively new, so the research findings available in literature, related to the physical and chemical interactions between the lubricants and the coated elements, are incomplete and ambiguous [16, 22]. The processes that occur in the contact zone between the coating and the lubricant components are insufficiently identified, especially when the friction joint working under extreme conditions is considered [3, 8, 16, 28]. Some of these interactions might be modified by the proper selection of lubricant additives; however, the selection requirements developed for steel friction joints do not apply to tribosystems in which at least one element is coated.

The application of coatings on machine parts is in the focus of interest of many leading research institutes worldwide [10, 20, 21]. In Europe, investigation on coating deposition on gears for the increase of scuffing resistance was realized in the COST 532 Action EU framework [1] and other projects. In the USA, similar works were part of NASA's research field [7].

In the literature, there are many references to the application of diamond-like coatings (DLC) on the gear teeth, the units of the camshafts (pivots), pushers and piston rings [4, 5, 9]. The coatings are mainly used on parts working with uncoated elements and subjected to scuffing [Fig.1].

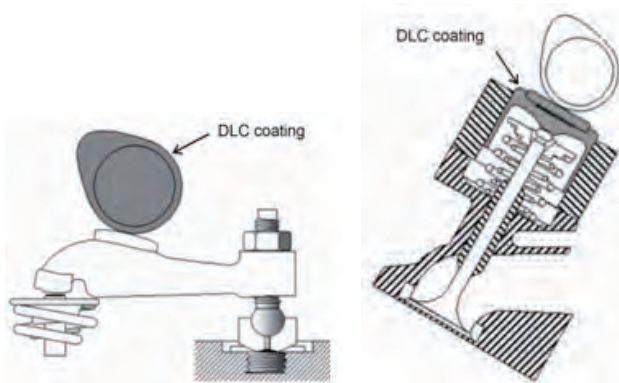


Fig. 1. The images of machine units with coated elements

2. Test method

For evaluation of scuffing resistance, a four-ball tribosystem was employed [11-13]. Test balls were made of 100Cr6 bearing steel with a diameter of 12.7 mm (0.5 in.) with R_a surface roughness of 0.032 and 60 ± 2 HRC hardness. The four-ball tribosystem is presented in Fig. 2.

The three stationary bottom balls (2) are fixed in the ball pot (4) and pressed against the top ball (1) under the continuously increasing load P . The top ball is fixed in the ball chuck (3) and rotates at the constant speed n . The tribosystem is immersed in the tested lubricant.

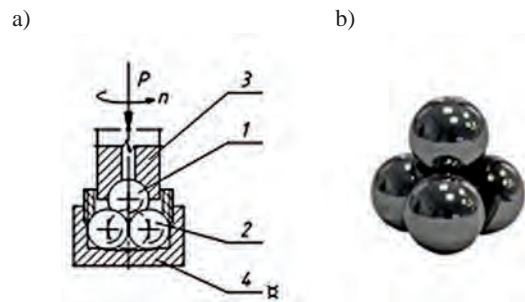


Fig. 2. Model four-ball tribosystem for testing scuffing: a) tribosystem: 1 - top ball, 2 - lower balls, 3 - ball chuck, 4 - ball pot, b) photograph

During the run, the curve of friction torque is recorded until seizure occurs or a load of 7200 N is achieved.

The investigation was performed under following conditions:

- Shaft rotational speed [rpm]: 500
- Sliding speed [m/s]: 0.19
- Speed of load growth [N/s]: 409
- Maximum load [N]: 7200 ± 100
- Initial load [N]: 0
- Starting temperature [°C]: approx. 20
- Min. number of tests: 3 per each tested friction joint.

An example of friction torque course (M_t) obtained at the continuously increasing load (P) is shown in Fig. 3.

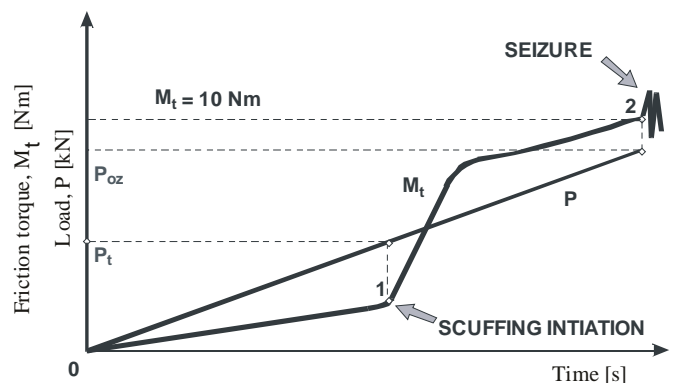


Fig. 3. An example of simplified friction torque curve (M_t) obtained under continuously increasing load (P): 1 - scuffing initiation, 1-2 - scuffing propagation, 2 - seizure

Scuffing initiation occurs at the time of a sudden increase in the friction torque - Point 1. The load at this moment is called the scuffing load and is denoted as P_t (according to the standard [18]). In accordance with the test method, the load still increases (over the value of P_t) until seizure occurs (i.e. friction torque exceeds 10 Nm - Point 2). The load at this moment is called the seizure load and is denoted as P_{oz} . If 10 Nm is not reached, the maximum load (c.a. 7200 N) is considered to be the seizure load (even though there is no seizure) [17].

The p_{oz} - limiting pressure of seizure is calculated from the following equation (1):

$$p_{oz} = 0,52 \frac{P_{oz}}{d^2} \quad (1)$$

Where:

P_{oz} - the load P under which the seizure occurs,
 d - the average diameter of wear scar on the lower balls.

3. The aim and the subjects of the study

The aim of the study was to determine the influence of oils on the scuffing characteristics of steel friction joints and friction pairs with elements with deposited low-friction coatings. The tested friction joints were lubricated with the following oils: RL 219 mineral reference oil, PAO 8 synthetic polyalphaolephin oil, RzR rapeseed refined oil, and two API GL5 class commercial oils containing EP additives (GL5m mineral and GL5s synthetic). The physiochemical properties of these oils are presented in the Table 1.

Table 1. The physiochemical characteristic of investigated oils

Property	Unit	Oil				
		RL 219	PAO 8	RzR	GL5m	GL5s
Viscosity at 40 °C	mm ² /s	49.31	47.04	25.68	40.00	81.00
Viscosity index	-	99	140	213	106	194
Density at 15 °C	g/ml	0.874	0.832	0.921	0.880	0.879
Flash point	°C	225	260	332	220	205

The tests were done for uncoated and low-friction coated balls. Two PVD coatings were used - WC/C and MoST. The WC/C coating is a DLC type representing a-C:H:Me group. The coating consisted of an elemental Cr adhesion layer adjacent to the steel substrate, followed by an intermediate transition region consisting of alternating lamellae of Cr and WC, and an outermost W containing a hydrocarbon (a-C:H:W) layer. The composition of the outermost a-C:H:W layer, in atomic percentage, is approximately 12% W, 70% C, 15% H, and 3% Ni. The a-C:H:W coating was deposited using PVD (Physical Vapour Deposition) by reactive sputtering. MoST is the commercial name of a low-friction composite coating MoS₂/Ti. The MoS₂/Ti coating is deposited by DC Magnetron Sputtering using a CFUBMSIP process (closed field unbalanced magnetron sputter ion plating). The coating procedure starts with ion cleaning, followed by a 70 nm Ti layer, a 200 nm MoS₂/Ti multilayer, a 900 nm MoS₂/Ti (non-multilayer) and a last step of a 50 nm layer of MoS₂ giving the characteristic surface colour.

4. The results of scuffing tests

The resistance to scuffing was determined by calculating: P_t scuffing load and p_{oz} limiting pressure of seizure. The p_{oz} indirectly characterizes the resistance to wear in sliding motion. The higher the P_t and p_{oz} indicators are, the higher the resistance to scuffing and seizure is. The P_t and p_{oz} , shown in the diagrams were calculated on the bases of at least three test runs for each investigated friction joint; whereas, the diagrams showing the characteristics of friction torque present only one of selected results from each tested friction joint.

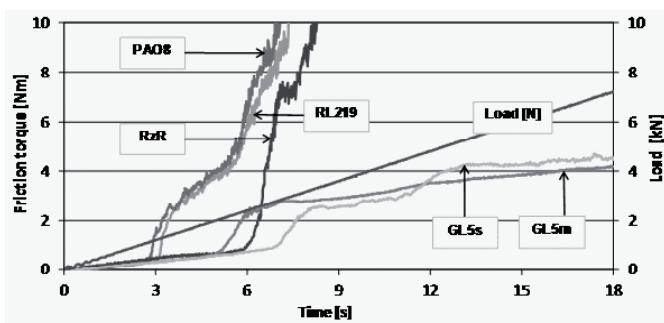


Fig. 4. Graphs of friction torque for steel-steel couples lubricated with tested oils

The friction torque lines obtained for the steel-steel friction joint lubricated with tested oils are shown in Fig. 4.

As it is shown in the graph, in the case of steel-steel (100Cr6-100-Cr6) friction pair, only the commercial GL5 quality class oils prevent the friction joint from seizure. It is because these oils contain EP (Extreme Pressure) anti-scuffing additives and are designed to lubricate the heavily loaded steel pairs.

The other base oils (without additives) do not prevent seizure; however, the vegetable oil demonstrates a level of resistant to scuffing initiation as high as the commercial synthetic oil, significantly exceeding the P_t obtained for GL5m mineral oil. It is important to remark that the rapeseed oil has the lowest viscosity at 40°C among all tested lubricants.

The average values of P_t scuffing load obtained for steel friction joints, under conditions of lubrication with investigated oils, are presented in Fig 5.

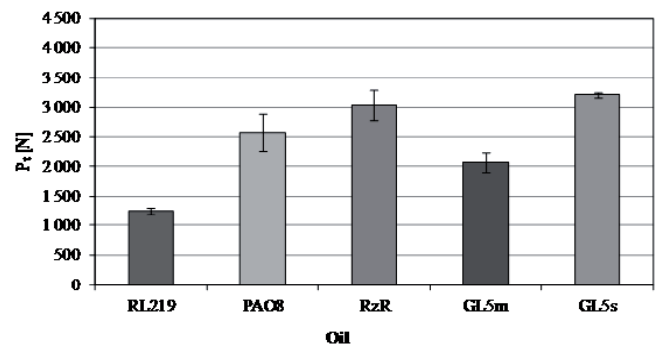


Fig. 5. The P_t scuffing load for steel-steel friction joints lubricated with tested oils

It should be emphasized that, although the steel-steel friction joint lubricated with RzR oil has a higher value of P_t in comparison with friction joint lubricated with mineral commercial GL5 oil, the rapeseed oil do not provide full protection against scuffing.

The average values of p_{oz} limiting pressure of seizure, obtained for steel friction joints under conditions of lubrication with investigated oils are presented in Fig 6.

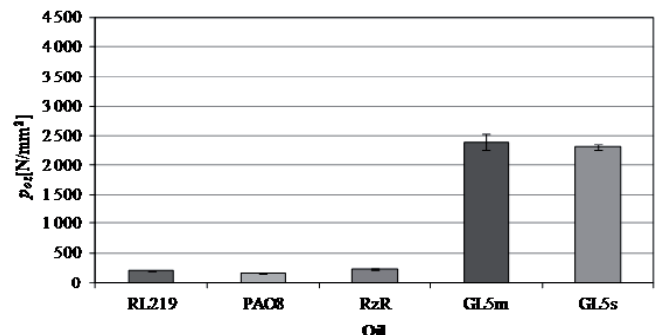


Fig. 6. The p_{oz} limiting pressure of seizure for steel-steel friction joints lubricated with tested oils

As it is shown in the Figures 4 and 6, the average values of p_{oz} limiting pressure of seizure are nearly similar for all three base oils. Due to the fact that there was no seizure observed for both GL5 oils, the maximum P_{oz} value was taken to account for p_{oz} calculating, giving approximate information about the wear, which is slightly lower for the friction joint lubricated with synthetic GL5s oil.

The four-ball tests were also performed for all investigated oils, lubricating the friction joint with three lower balls of steel and the upper ball coated with WC/C thin, hard, low-friction coating. The fric-

tion torque lines obtained for the WC/C-steel friction joint lubricated with tested oils are shown in Fig. 7.

As the friction torque graphs indicate, the WC/C-steel pairs lubricated with GL5 oils and the synthetic base oil did not undergo seizure. The introduction of a WC/C coated upper ball to the tribosystem results in a significant increase in the resistance to scuffing of all couples lubricated with tested oils. As it is shown in Fig. 6, the friction torque lines for both synthetic oils, are almost overlapped, which can be interpreted as taking over of the EP additives action by the WC/C coating. This feature of WC/C confirms the results from the earlier, low-friction coating research [14, 29].

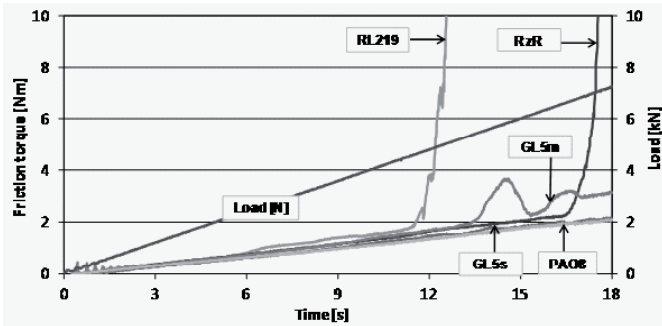


Fig. 7. Graphs of friction torque for WC/C-steel couples lubricated with tested oils

The average values of P_t scuffing load obtained for WC/C-steel friction joints under conditions of lubrication with investigated oils are presented in Fig. 8.

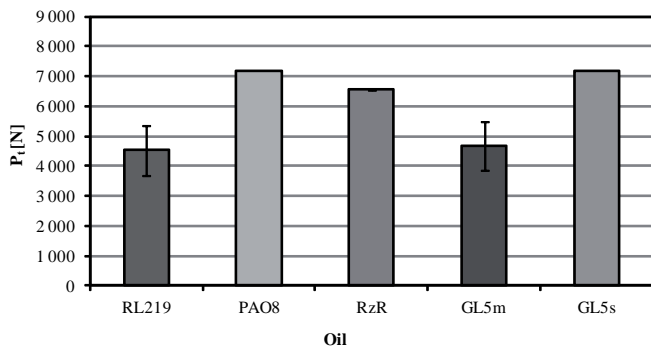


Fig. 8. The P_t scuffing load for WC/C-steel friction joints lubricated with tested oils

The P_t scuffing load for WC/C-steel for the mineral oil is four times higher than for the steel tribosystem. In case of rapeseed oil, the increase is twofold. The highest P_t value was obtained for the both synthetic oils – base and commercial. Considering the scuffing load value for the WC/C-steel couple lubricated with base and commercial mineral oils, the high spread of results as compared to the remaining oils can be observed. Interestingly, despite the increase in scuffing load, the friction joint lubricated with mineral oil did not achieve anti-seizure protection. In contrast to the synthetic oils, the effect of the action of EP additives is very clear in case of mineral oils. The case of vegetable oil is also interesting, because, for WC/C- steel friction joint, a difference in P_t of 1.5 times can be observed as compared to the reference oil lubricated joint, even in spite of the kinematic viscosity of rapeseed oil, which is substantially lower.

The average values of p_{oz} limiting pressure of seizure, obtained for WC/C-steel friction joints, under conditions of lubrication with investigated oils, are presented in Fig. 9.

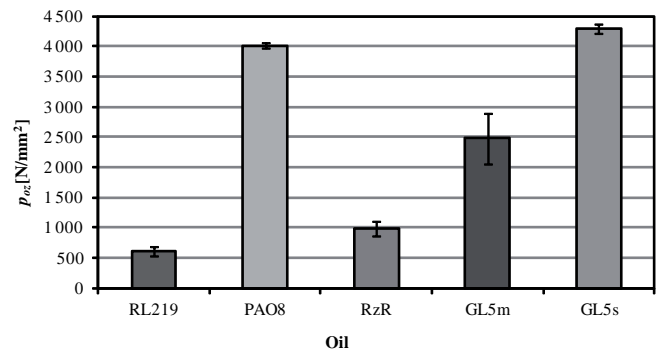


Fig. 9. The p_{oz} limiting pressure of seizure for WC/C-steel friction joints lubricated with tested oils

The results indicate that both synthetic oils represent the highest resistance to wear with a slight advantage for commercial GL5s oil.

Apart from steel-steel and steel-WC/C friction joints, the four-ball tests were also performed for all investigated oils, lubricating the friction joint with three lower balls of steel and the upper ball coated with MoS₂/Ti coating. The friction torque graphs obtained for the MoS₂/Ti-steel friction joint lubricated with tested oils are shown in Fig. 10.

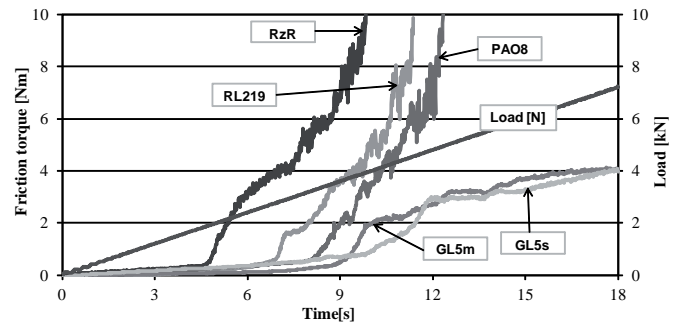


Fig. 10. Graphs of friction torque for MoS₂/Ti-steel couples lubricated with tested oils

The lines of friction torque for MoS₂/Ti-steel couples indicate that, in comparison with the steel reference friction joint, there is an observable improvement in the resistance to scuffing in almost all tested cases. The only exception is the friction joint lubricated with rapeseed oil.

The average values of P_t scuffing load and p_{oz} limiting pressure of seizure obtained for MoS₂/Ti-steel friction joints under conditions of lubrication with the investigated oils are presented respectively in Figs. 11 and 12.

The differences in P_t values in all tested cases do not exceed 50%. Considering p_{oz} limiting pressure of seizure, there is a certain improvement in protection against seizure; however, it is much lower

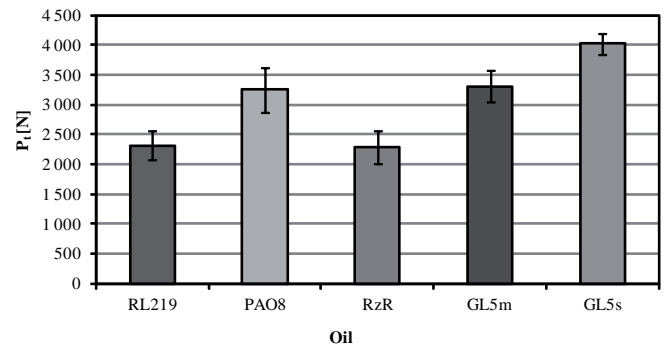


Fig. 11. The P_t scuffing load for MoS₂/Ti-steel friction joints lubricated with tested oils

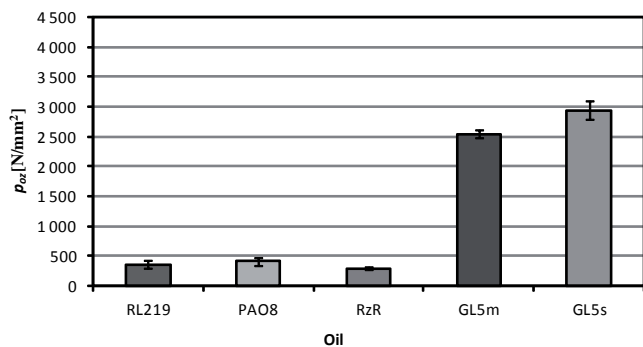


Fig. 12. The p_{02} limiting pressure of seizure for MoS_2/Ti -steel friction joints lubricated with tested oils

than in the case of WCC-steel friction joint, especially lubricated with synthetic base oil.

For MoS_2/Ti -steel friction joint, the best anti-scuffing and anti-seizure protection is provided by lubricating the tested friction joint with the GL5 commercial oils.

5. Conclusions

The obtained results indicate that, in the case of the tested concentrated friction joints, the role of selected oils on scuffing is crucial. The influence of the oil on the scuffing wear of friction joints with PVD coated steel elements depends on the type of deposited coating. The introduction of a friction joint element with a low-friction coating favourably affects most of the obtained scuffing characteristics, which is confirmed by following observations:

1. In the case of steel-steel friction joint, only the commercial oils provide the friction joint with an effective protection against sei-

zure. The vegetable oil ensures a longer time before scuffing initiation in comparison to mineral-based commercial oil; however, in the consequence of the lack of extreme pressure additives, seizure of the friction joint lubricated with RzR takes place under only a slightly higher load than in the case of the mineral-based reference oil and PAO 8 oil. The characteristics of scuffing for the friction joint lubricated with PAO 8 and RL 219 overlap, demonstrating the lowest scuffing protection among tested lubricants.

2. The use of a-C:H:W coating improves scuffing resistance in all tested cases. For the vegetable oil and mineral commercial oil, the scuffing load is nearly two times higher; however, the protection from seizure is not provided. The most significant change is observed for the friction joint lubricated with PAO 8, where the scuffing characteristic overlaps with the one obtained for the synthetic commercial oil containing the EP additives. **It follows that the coating takes the role of the additives**, which is convergent with the results obtained by the authors in their previous works.
3. The application of MoS_2/Ti coating has a negative result in the form of scuffing initiation acceleration for the friction joint lubricated with vegetable oil. On the other hand, the friction joints lubricated with PAO 8 demonstrates approximately a twofold increase in both the scuffing load and in limiting the load of seizure, in comparison with uncoated friction joint. The MoS_2/Ti coating also improves a level of the protection from seizure for the friction joints lubricated with the tested commercial oils.
4. The highly important demonstrated and practical effects of this research are that the PVD coatings deposited on steel elements of tribosystems intercept the function of most commonly used EP additives and that the usage of such coatings makes it possible to reduce the oil additive concentrations, resulting in more environmental friendly oils.

Scientific work executed within the Strategic Programme "Innovative Systems of Technical Support for Sustainable Development of Economy" within Innovative Economy Operational Programme, No. POIG.01.01.02-14-034/09-00

References

1. Vercammen K, Van Acker K, Meneve J. Current trends in tribology. Belgium: VITO, 2004.
2. Totten GE, Liang H. Mechanical Tribology. Materials, characterization, and applications. New York-Bazylea: Marcel Dekker, Inc., 2004.
3. Equey S, Roos S, Mueller U, Hauert R, Spencer N D, Crockett R. Reactions of zinc-free anti-wear additives in DLC/DLC and steel/steel contacts. Tribology International 2008; 41: 1090–1096.
4. Gählin R, Larsson M, Hedenqvist P. ME-C:H coatings in motor vehicles. Wear 2001; 249: 302–309.
5. Hauert R. An overview on the tribological behavior of diamond-like carbon in technical and medical applications. Tribology International 2004; 37: 991–1003.
6. Joachim F. Influence of coatings and surface improvements on the lifetime of gears. Proc. COST 532 "Triboscience and Tribotechnology". Ghent, Belgium 2004: 138–147.
7. Krantz TL, Cooper CV, Townsend DP, Hansen BD. Increased Surface Fatigue Lives of Spur Gears by Application of a Coating. 2003; Raport NASA/TM-2003-212463.
8. Łuksa A ed. Ekologia płynów eksploatacyjnych. Radom: MCNEMT, 1990.
9. Makoto Kano. DLC Coating Technology Applied to Sliding Parts of Automotive Engine. New Diamond and Frontier Carbon Technology 2006; 16: 201–210.
10. Martins R, Amaro R, Seabra J. Influence of low friction coatings on the scuffing load capacity and efficiency of gears. Tribology International 2008; 41: 234–242.
11. Michalczewski R. Charakterystyki tribologiczne cienkich powłok niskotarciowych typu DLC i MoS_2 w warunkach tarcia suchego. ZEM 2006;146: 117–131.
12. Michalczewski R, Piekoszewski W. Wear and friction of low friction coatings in dry conditions. Tribologia, Finish Journal of Tribology 2007; 26: 9–21.
13. Michalczewski R, Piekoszewski W, Szczerek M, Tuszyński W. Chemomechanical synergy of PVD/CVD coatings and environmentally friendly lubricants in rolling and sliding contacts. Proc. COST 532 "Triboscience and Tribotechnology". Ghent, Belgium 2004: 181–190.
14. Michalczewski R, Piekoszewski W, Szczerek M, Tuszyński W. The lubricant-coating interaction in rolling and sliding contacts. Tribology International 2009; 42: 554–560.
15. Michalczewski R, Piekoszewski W, Szczerek M, Tuszyński W. A method for tribological testing of thin hard coatings. Tribotest Journal 2002; 9: 117–130.
16. Neville A, Morina A, Haque T, Voong M. Compatibility between tribological surfaces and lubricant additives. How friction and wear

- reduction can be controlled by surface/lube synergies. *Tribology International* 2007; 40: 1680–1695.
17. Patent Nr 179123 - B1 – G01N 33/30 Sposób oceny przeciwzatarciowych własności środków smarowych na aparacie 4-kulowym.
 18. PN-76/C04147 Przetwory naftowe. Badanie własności smarnych olejów i smarów.
 19. Piekoszewski W, Szczerek M, Tuszyński W. A method for testing lubricants under conditions of scuffing. Part II. The anti-seizure action of lubricating oils. *Tribotest Journal* 2002; 9: 35–48.
 20. Podgornik B, Jacobson S, Hogmark S. Influence of EP and AW additives on the tribological behaviour of hard low friction coatings. *Surface and Coatings Technology* 2003; 165: 168–175.
 21. Shimizu S. Fatigue Limit Concept and Life Prediction Model for Rolling Contact Machine Elements. *Tribology Transaction* 2002; 45: 39–46.
 22. Stallard J, Teer D G. A study of tribological behaviour of CrN, Graphit-iC and Dymon-iC coatings under oil lubrication. *Surface and Coatings Technology* 2004; 188–189: 525–529.
 23. Szczerek M, Michalczewski R, Piekoszewski W. The problems of application of PVD/CVD thin hard coatings for heavy-loaded machine components. San Diego: Proceedings of the ASME/STLE International Joint Tribology Conference 2007; ASME Part A: 35–37.
 24. Szczerek M, Tuszyński W. A method for testing lubricants under conditions of scuffing. Part I. Presentation of the method. *Tribotest Journal* 2002; 8/4: 273–284.
 25. Szczerek M, Tuszyński W. A method for assessing performance of automotive gear oils. New horizons for tribology and lubricants. *Handbuch der Tribologie und Schmierungstechnik* 2002; 10: 108–115.
 26. Tuszyński W, Szczerek M, Michalczewski R. Investigation of antiwear coatings deposited by the PVD process. *Tribotest Journal* 2003; 10: 3–18.
 27. Tuszyński W, Piekoszewski W. Effect of the type and concentration of lubricating additives on the antiwear and extreme pressure properties and rolling fatigue life of a four-ball tribosystem. *Lubrication Science* 2006; 18/4: 309–328.
 28. Vercammen K, Van Acker K A, Vanhulsel A, Barriga J, Arnsek A, Kalin M, Meneve J. Tribological behaviour of DLC coatings in combination with biodegradable lubricants. *Tribology International* 2004; 37: 983–989.
 29. Vlad M, Szczerek M, Michalczewski R, Kajdas C, Tomastik C, Osuch-Słomka E. The influence of antiwear additive concentration on the tribological behaviour of a-C:H/W/steel tribosystem. *Proc. IMechE Part J: Journal Engineering Tribology* 2010; 224/10: 1079–1089.

Marek KALBARCZYK, M.Sc. (Eng.)

Remigiusz MICHALCZEWSKI, Ph.D., D.Sc. (Eng.)

Witold PIEKOSZEWSKI, Ph.D., D.Sc. (Eng.)

Tribology Department

Institute for Sustainable Technologies (ITeE-PIB)

ul. Pułaskiego 6/10, 26-600 Radom, Poland

e-mails: marek.kalbarczyk@itee.radom.pl,

witold.piekoszewski@itee.radom.pl, remigiusz.michalczewski@itee.radom.pl

Prof. Marian SZCZEREK, Ph.D., D.Sc. (Eng.)

Tribology Department

Institute for Sustainable Technologies (ITeE-PIB)

ul. Pułaskiego 6/10, 26-600 Radom, Poland

University of Technology and Humanities

Faculty of Mechanical Engineering

ul. Krasickiego 54, 26-600 Radom

e-mail: marian.szczerek@itee.radom.pl

Yi-Heng YANG
Kuo-Shong WANG

STUDY OF THE CHARACTERISTICS ABOUT INSULATION DAMAGE BASED ON THE ACCELERATED LIFE TESTS

BADANIE CHARAKTERYSTYK USZKODZEŃ IZOLACJI W OPARCIU O TESTY PRZYSPIESZONEGO STARZENIA

In this study the Maximum Likelihood Estimator is taken to identify the characteristics of insulation failure about the class-H motors by considering the accelerated life testing data under censored situation from Nelson. Based on the Weibull survival modeling the failure is expressed as the series connection of three modes, namely the turn, phase, and ground, respectively, the so-called competing failure. The main concern in present investigation is about the variation of shape parameters, β with the temperature. The Gompertz-type relation of $\beta_i(T)$ is suggested with the reference temperature, T_{ri} for the i -th failure mode. It is found that the T_{ri} 's not only distinguish the characteristics of cumulative damage process about the insulation, but also involve the estimation of mean-time-to-failure (MTTF). Physically T_{ri} denotes the turning point of varied β_i as the i -th failure mode becomes moderate in a sense of less capability about the accumulation of insulation damage at higher temperature where corresponds the thermal degradation process. The numerical results indicate that the insulation technique used is acceptable as the operation temperature kept in the use condition 363K. According to the predicted lifetime as the temperature rises up to 440K, which still within the allowed range in application, the turn structure needs to be rearranged primarily, then the phase next. The ground mode has only influence on the failure at much higher temperature.

Keywords: accelerated life testing, competing failure mode, insulation degradation, Gompertz-type relation of shape parameter.

W prezentowanej pracy zastosowano estymator największej wiarygodności do określenia charakterystyk uszkodzenia izolacji silników klasy H z wykorzystaniem danych z badań przyspieszonego starzenia w sytuacji cenzurowanej wg. Nelsona. Na podstawie Weibullowskiego modelu prawdopodobieństwa przetrwania, uszkodzenie określono jako szereg trzech przyczyn dotyczących, odpowiednio, zwoju, fazy i ziemi, czyli jako tzw. uszkodzenie konkurujące. Głównym zagadnieniem przedstawionych badań jest zmienność parametrów kształtu β wraz z temperaturą. Zaproponowano zależność Gompertza $\beta_i(T)$, z temperaturą odniesienia T_{ri} , dla n -tego trybu awaryjnego. Stwierdzono, że temperatury T_{ri} nie tylko wyróżniają charakterystykąłosciowego procesu uszkodzenia izolacji, ale również służą ocenie średniego czasu do awarii (MTTF). W kategoriach fizycznych T_{ri} oznacza punkt zwrotny o zróżnicowanym β_i gdy n -ta przyczyna uszkodzenia staje się umiarkowana w sensie mniejszej zdolności akumulacji uszkodzeń izolacji w wyższej temperaturze, odpowiadającej procesowi termicznej degradacji. Wyniki liczbowe wskazują, że stosowana technologia izolacji jest akceptowalna, ponieważ temperatura pracy wynosi 363K. Zgodnie z prognozowanym czasem pracy, wraz ze wzrostem temperatury do 440K, co nadal mieści się w dozwolonym zakresie temperatur użytkowania, zachodzi konieczność zmiany najpierw struktury zwoju a w dalszej kolejności struktury fazy. Przyczyny dotyczące gruntu mają wpływ na uszkodzenie jedynie przy wyższych temperaturach.

Słowa kluczowe: badania przyspieszonego starzenia, konkurujące przyczyny uszkodzeń, degradacja izolacji, funkcja Gompertza dla parametru kształtu.

Abbreviations

ALT	-	accelerated life test,
CFMA	-	competing failure mode analysis,
fpdd	-	failure probability density distribution,
MLE	-	maximum likelihood estimation,
MTTF	-	mean-time-to-failure,

Symbols

β_i, θ_i	-	shape and scale parameter of each failure mode,
τ	-	observed lifetime,
X_i	-	random failure lifetime of the failure mode,
m	-	number of failure modes,
L	-	likelihood function,

r	-	number of failures among test samples,
n	-	total sample size,
δ_{ij}	-	decision factor of the likelihood function,
p	-	number of test levels,
$f_{S,i}$	-	failure probability density distribution for the i -th mode failure,
r^*	-	rate constant of the reaction,
A^*	-	characteristic parameter for the chemical process,
E_a	-	activation energy of the reaction,
K	-	Boltzmann constant,
T	-	temperature in Kelvin,
L_T	-	estimation of the lifetime,
T_{ri}	-	reference temperature.

1. Introduction

Accelerated life tests (ALT) are usually carried out by stressing specimens at overstress conditions to explore the defects and estimate the mean-time-to-failure (MTTF) at normal use. The basic assumption in conducting ALT is that the tests should be followed the same failure mechanism as the product failed at normal condition. The failure mechanism is related to the degradation of the material due to the stress from certain physical phenomena. Due to the complexity of the product geometry, failure may occur at different locations, each with its own particular features, e.g. the notch shape which is in common to induce the fatigue failure of structure etc. These are the so-called the failure modes. There is a specific probability for failure at each different position. The lifetime estimation becomes obviously optimistic if only the most frequently occurred failure mode considered. The competing failure mode analysis (CFMA) takes all potential failure modes into account at the same time. The other mission of CFMA is to predict the proportion of each mode in the apparent failure which is observed under the same mechanism without the location details. Such information helps in the product development. In early study, Nelson [11] took the concept of competing risk in the analysis of ALT. Sometimes to simplify the tests, the failure is periodically checked as the system function qualified with the particular mode or not, i.e. the recorded time may not be the exact time as the system failed at those modes considered. To shorten the total time of ALT the process is in usual terminated with a certain amount of survivals, the so-called censored situation [13]. In this case the estimation becomes much more sophisticated. It should be not only conformed in some degree with the data but also explained well with physical sense. Therefore, a deep understanding of the material degradation with stress has to be addressed. In the present study the motor failure due to the deterioration of insulation, which is caused by the thermogravimetric phenomenon of insulation materials, is investigated about the censored data as multiple failure modes involved. At higher temperature the mass loss rate becomes larger, thus it leads to weaken the insulation more seriously and results in a shorter lifetime of the product. The Maximum Likelihood Estimation (MLE) [5] is a typical approach adopted for the prediction in such case.

The Weibull distribution is widely used in the reliability expression due to its flexibility in describing different behavior of the hazard rate. Klein and Basu [8] investigated the ALT data with the Weibull distribution as several failure modes considered. Miller and Nelson [10] applied the MLE in the analysis of a set of step-stress ALT data as the lifetime decreased exponentially with the temperature. Later Bai et al [1] studied how to arrange a failure-censored ALT sampling plan with equal recorded test time at different thermal environment.

All of these studies worked on that the scale parameter, η , varies based on Arrhenius assumption [4] and the shape parameter β remains fixed in the analysis. The Arrhenius assumption describes the deterioration of oxidation which introduces acid groups into the insulation to increase the conductivity and power factor of the insulation. However the shape parameter characterizes the process of the insulation damage due to the material degradation as well as the increasing stress from continuous changing of the local geometry i.e. β should be considered varying with the temperature also. It is also known that these parameters are related to a number of load cycles and other factors in fatigue [7]. From experience as the thermal environment kept at lower temperature the damage process continues in a submerged manner. At higher temperature, another type of deterioration, thermal decomposition [2], becomes an important factor. The polymer chains break into shorter units occurs in all polymers including cellulose at elevated temperatures even in the absence of oxygen. In terms of reliability the insulation vanishes more or less suddenly, i.e. the corresponding shape parameter should be much larger than one. On the contrary, as the temperature at higher level the material degradation is more serious,

the reliability decays in a some degree of constant failure rate situation. Such point of view has already been mentioned by Nelson [12]. Seo and Kim [14] designed an accelerated life test sampling plan in the consideration of the Weibull distribution with both shape and scale parameter taken in the power-law forms of temperature. On the other hand, [3] made an estimation followed Bayesian framework for the ALT data about all possible failure modes by constant failure assumption, each hazard rate with different proportion to the temperature.

A mature technology should be robustness against the operation condition within an acceptable range during its service. In other word it needs be reliable and predictable. Generally to the electrical insulation material, the dielectric strength is degraded with rising temperature. The density of material is losing and becomes non-uniform, this causes the specimens not only have shorten life but also the failures become more unpredictable. Based on the thermogravimetric analysis, it requires that the characteristic of cumulative damage of insulation changes little as the operation condition around the normal temperature, thus the motor quality can be assured. Meanwhile at much higher temperature environment, say beyond an assumed reference point, the characteristic of damage process is basically changed with less capability of accumulation and then the insulation failure tends to be in a constant hazard rate situation. This means that the failures are induced mainly by some unpredictable fluctuations of circumstance, e.g. the moisture, etc. It is worth to denote that such change differs from the estimation about lifetime, which is related primarily to the scale parameter by Arrhenius assumption, decreasing with increasing the temperature. Therefore the shape parameter should slip down from its saturation value to one, as the constant failure rate situation, when the thermal environment at much higher temperature. Gompertz-type variation [17] can be chosen as one of the candidate to show such tendency. It is

$$y(x) = z \times \exp[-b \times \exp[-cx]] \quad (1)$$

where z is the upper asymptote and c is the change rate. $(\ln \frac{1}{b}) / (-c)$ denotes the inflection point of Eq. (1). The effects of varying z , b and c for y are depicted in Fig. 1.

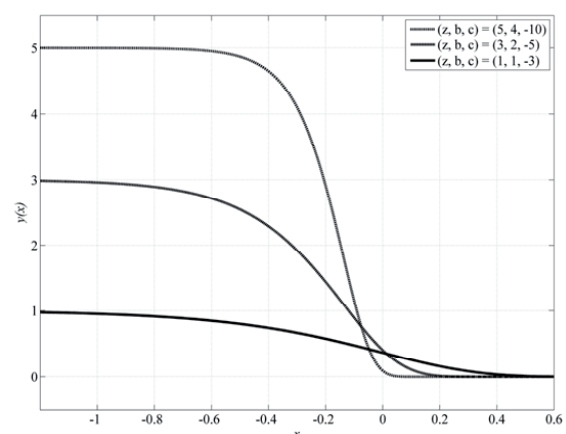


Fig. 1. Typical Gompertz variation curves

2. Model assumptions and likelihood function for competing failure analysis

Consider in the presence of m failure causes, the observed lifetime τ of a set of tests is the minimum among X_1, X_2, \dots, X_m ; X_i the random failure lifetime of mode i , i.e.

$$\tau = \min(X_1, X_2, \dots, X_m) \quad (2)$$

Let the failure modes be independent to each other, thus a series connection of these modes represents the apparent failure in the tests. Now we have the reliability $R_{cf}(t)$ as

$$\begin{aligned} R_{cf}(t) &= P(\tau > t) = P(X_1 > t, X_2 > t, \dots, X_m > t) \\ &= \prod_{i=1}^m P(X_i > t) = \prod_{i=1}^m R(t) \end{aligned} \quad (3)$$

with probability density function $f_{cf}(t)$ as

$$f_{cf}(t) = -\frac{dR(t)}{dt} = -\sum_{i=1}^m \left[\frac{dR_i(t)}{dt} \left(\prod_{j=1, j \neq i}^m R_j(t) \right) \right]. \quad (4)$$

Suppose that the Weibull survival model for the i -th failure mode in the ALT data exists as the scale and shape parameter both varied with the thermal environment condition. The corresponding reliability decays with the time t as

$$R_i(t) = \exp \left[- \left(\frac{t}{\theta_i(T)} \right)^{\beta_i(T)} \right], \quad (5)$$

where $\theta_i(T)$ and $\beta_i(T)$ are the scale and shape parameter, respectively, of the Weibull expression, T the temperature. The probability density function $f_i(t)$ becomes

$$f_i(t) = \frac{\beta_i(T)}{\theta_i(T)} \left(\frac{t}{\theta_i(T)} \right)^{\beta_i(T)-1} \exp \left[- \left(\frac{t}{\theta_i(T)} \right)^{\beta_i(T)} \right]. \quad (6)$$

Let the r -th among n causes lead to n specimens failed, and each failure comes only from a single cause. The corresponding likelihood function L is defined as

$$L = \prod_{j=1}^r \prod_{i=1}^m \left(f_i^{\delta_{ij}}(t_j) \times R_i^{1-\delta_{ij}}(t_j) \right) \times \prod_{j=r+1}^n R_{cf}(t_j), \quad (7)$$

where δ_{ij} is the decision factor, i.e. $\delta_{ij}=1$ as the specimen failed in test time point t_j with the i -th failure mode; otherwise $\delta_{ij}=0$. For censored testing the effect of j -th survival on the likelihood function is accounted in the term $\prod_{j=r+1}^n R_{cf}(t_j)$. For a p -constant temperature levels ALT, the likelihood function becomes

$$L = \prod_{k=1}^p \prod_{j=1}^r \prod_{i=1}^m \left(f_i^{\delta_{ijk}}(t_{jk}) \times R_i^{1-\delta_{ijk}}(t_{jk}) \right) \times \prod_{k=1}^p \prod_{j=r+1}^n R_{cf}(t_{jk}). \quad (8)$$

The probability density function for the i -th mode failure is expressed as

$$f_{S,i}(t) = \frac{dR_i(t)}{dt} \times \prod_{j=1, j \neq i}^m R_j(t) = f_i(t) \times \prod_{j=1, j \neq i}^m R_j(t). \quad (9)$$

The integral value of $f_{S,i}(t)$ is the proportion of i -th mode failure on the total. It points out which modes should be paid attention and improved in the product developing.

3. Temperature dependence of the Weibull parameters

A rough examining about the data shown in Table 1 reveals three facts, as the temperature kept at lower level,

- (1) the average failure time \bar{X}_g about the ground mode, is overall the largest one,
- (2) for all modes \bar{X}_i decreases as the temperature increasing, and
- (3) the failure times are much more concentrated, respectively, for each mode.

The third point requires that the smaller shape parameter is the higher temperature is.

3.1. Arrhenius relationship for the scale parameter

Arrhenius relation presents the chemical reaction rate among the material components under a specific thermal environment. It is expressed as

$$r^* = A^* \times \exp \left[- \frac{E_a}{KT} \right],$$

where r is the rate constant of reaction, A^* the characteristic parameter about the chemical process, K the Boltzmann constant, E_a the activation energy of the reaction and T the temperature in Kelvin scale. Since higher reaction rate yields less lifetime of the insulation, a straightforward assumption can be made as $r \cdot L_T \sim \text{constant}$, while L_T is the estimation of lifetime. Therefore we have

$$L_T = \exp \left[A + \frac{B}{T} \right]. \quad (10)$$

For the Weibull description of reliability the expected lifetime varies primarily with the scale parameter (a proportional factor related to a gamma function of both parameters), thus for the i -th mode scale parameter θ_i can be assumed in the form as

$$\theta_i(T) = \exp \left[A_i + \frac{B_i}{T} \right], \quad (11)$$

where A_i and B_i are decided by maximizing the likelihood estimator shown in the previous section.

3.2. Gompertz relationship for the shape parameter

The ASTM standard D3850 [15] provides the measurement of thermal stability about the content of volatile components of the in-

sulation material involved. As the specimen operated under a harsh thermal environment, the effect of material decomposition [9] [16] will lead to the loss of insulation property early. The sustainability is much lower as the mass loss rate is small because of less normal material existed. Thus, any disturbance can destroy the insulation. To modeling of the thermal decomposition process, the Gompertz model and its modified forms have been successfully applied [6] [18]. According to the observed fact mentioned in the beginning of this section, in this study, the shape parameter varying with temperature is suggested in the form

$$\beta_i(T) = 1 + z_i \times \exp \left[-\exp \left[-c_i \left(\frac{1}{T} - \frac{1}{T_{ri}} \right) \right] \right], \quad (12)$$

T_{ri} is the reference temperature which plays the role of b , see Eq. 1 in the combination $b = \exp \left(\frac{c_i}{T_{ri}} \right)$. When the testing temperature beyond

the reference much higher the failure occurrence is considered rather unpredicted, thus the corresponding β reduces to one. Since at such circumstance a significant change of the characteristic of insulation decay has taken place, the process of damage accumulation becomes mild; the failure tends to be a constant failure rate condition.

4. Case study

Consider a set of data by Nelson [10], see Table 1, which collected from a thermal-accelerated life tests of Class-H motor insulation. The material of Class-H motor insulation consists of silicone elastomeric and the combination of others such as mica, glass fiber, asbestos etc. Insulation failed according to three failure modes, namely turn, phase and ground, each occurring at different parts of the system. The life of the motor is the first occurrence of these failures. In atypical test of motor insulation the turn insulation is the winding coils, the phase is a sheet of insulation laid between the phases and the ground insulation

Table 1. Class-H motor insulation data under competing failure mode (hours) [11]

463K				513K			
M	Turn	Phase	Ground	M	Turn	Phase	Ground
1	7228	10511	10511+	1	1175	1175+	1175
2	7228	11855	11855+	2	1881+	1881+	1175
3	7228	11855	11855+	3	1521	1881+	1881+
4	8448	11855	11855+	4	1569	1761	1761+
5	9167	12191+	12191+	5	1617	1881+	1881+
6	9167	12191+	12191+	6	1665	1881+	1881+
7	9167	12191+	12191+	7	1665	1881+	1881+
8	9167	12191+	12191+	8	1713	1881+	1881+
9	10511	12191+	12191+	9	1761	1881+	1881+
10	10511	12191+	12191+	10	1953	1953+	1953+
493K				533K			
M	Turn	Phase	Ground	M	Turn	Phase	Ground
1	1764	2436	2436	1	1632+	1632+	600
2	2436	2436	2490	2	1632+	1632+	744
3	2436	2436	2436	3	1632+	1632+	744
4	2436	2772+	2772	4	1632+	1632+	744
5	2436	2436+	2436	5	1632+	1632+	912
6	2436	4116+	4116+	6	1128	1128+	1128
7	3108	4116+	4116+	7	1512	1512+	1320
8	3108	4116+	4116+	8	1464	1632+	1632+
9	3108	3108	3108+	9	1608	1608+	1608
10	3108	4116+	4116+	10	1896	1896	1896

M: mode, S: sequence

is the slot cell. In thermal-accelerated life test, specimens go into an oven which is then raised to test temperature.

There is no voltage applied to the insulation in the oven. After a specified time at temperature, the specimens are removed from the oven and cooled to room temperature then a specified voltage is applied to the insulation, which failure (breaks down) or survives. Survivors go back into the oven for the next cycle at temperature. A median life over 20,000 hours is expected with temperature below 453K. In the table it presents the recorded failure times for each mode (turn, phase and ground, respectively) under different thermal environment, as the temperature held at 463K, 493K, 513K and 533K, respectively.

During the testing the motors were kept going on run till the rest failure modes appeared after the first shown. The failure is assumed as the voltage drops below the threshold defined for the particular mode. The recorded time in Table 1 is the midway between periodical inspections for the failure. It is quite different in real application; the first appearance of the defined failure may not cause the end of motor life at once but lead to less efficiency. For details, the motors appeared as in the sequence 1, 2 and 3 in the table at temperature 463K, of which the insulation decays did not reach the thresholds of the defined failure modes till at 7228 hours all of these three motors were disqualified on the turn mode and then the motor 1 failed at 10511 hours, motor 2 and 3 at 11855 hours all on the mode phase afterward quitted the tests with mode ground still qualified by marked plus to denote the censoring time. The other tests in Table 1 were also carried out in the same manner.

The LE, Eq. (8), is maximizing with the parameters shown in the relation of θ 's and β 's, see Eq. (11) and (12), as the data in Table 1 taken. The identified parameters for each failure mode are given in Table 2. In this study, the shape parameter β is assumed either with Gompertz-type variation or fixed. The results in Table 2 for β fixed assumption present the characteristics of insulation damage of the mode turn and phase are quite similar to each other but the mode ground with less cumulative tendency due to its small value of β . This also can be found for β followed Gompertz-type variation assumption, see Fig. 2a. Comparing these two assumptions the shape parameter of both are similar to each other for the mode ground and phase, respectively. But the corresponding for turn is quite different with larger in the Gompertz-type variation case. Such difference leads to the life estimation with remarkable change, see Table 3. The identified numerical value of reference temperature for each mode nears to the inflection point of the corresponding Gompertz curve, this reflects that the characteristics of damage process about the insulation change as mentioned in the introduction. The variations of scale parameter with the temperature for these modes are given in Fig. 2b.

Table 2. The fitted parameters for the ALT data in Table 1, θ expressed in Eq. (11)

β with Gompertz-type-relation in Eq. (12)		β fixed
Mode		
Turn	$\beta(z, g, T_r)$	(6.69, 5789, 516)
	$\theta(A, B)$	(−5.16, 6644)
Phase	$\beta(z, g, T_r)$	(3.31, 5983, 839)
	$\theta(A, B)$	(−4.25, 6381)
Ground	$\beta(z, g, T_r)$	(1.54, 69112, 614)
	$\theta(A, B)$	(−12.63, 10753)

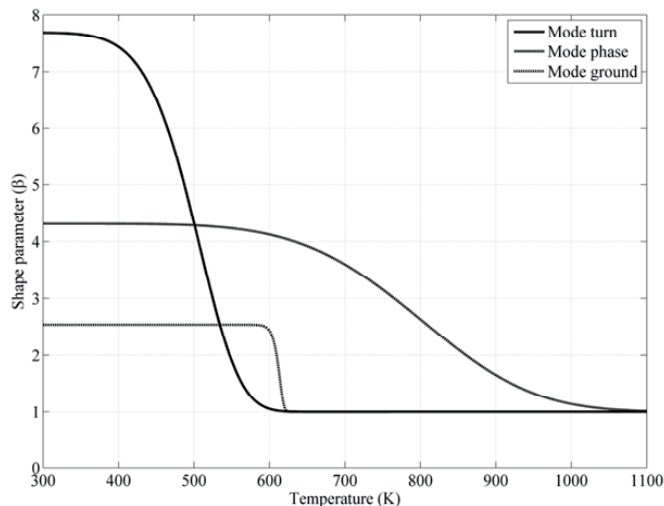
The plots show that all have similar trend. The important information of scale parameter relates to the lifetime estimation. From CFMA the mode with the lowest scale parameter dominates the apparent failure, i.e. the actual lifetime is somewhat below that of dominant mode. At lower temperature, say below 450K, the failure due to the ground

Table 3. The comparison of the MTTF in hours for each failure mode and the apparent failure at maximum allowed temperature (453K) and use condition (363K)

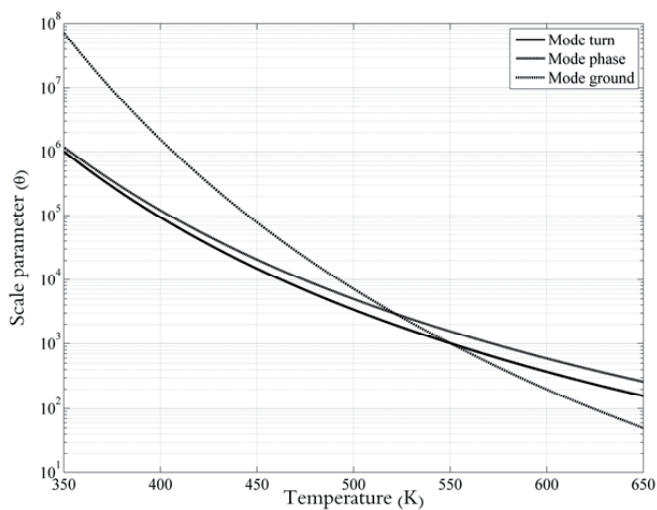
Mode	β fixed		β with Gompertz-relation Eq. (12) for T_r			Nelson (1990)	
	453K	363K	453K	400K	363K	453K	363K
Turn	9.82E3	2.54E5	1.25E4	1.94E4	4.79E5	1.23E4	1.00E6
Phase	1.70E4	5.58E5	1.71E4	2.58E4	5.55E5	1.70E4	5.41E5
Ground	3.95E4	9.99E6	5.92E4	8.83E4	9.70E6	3.51E4	4.81E6
Apparent failure (failure in series connection)	9.52E3*	2.51E5	1.19E4*	1.85E4*	4.43E5	1.16e4*	5.22E5

* denotes not qualified with respect to the specification

mode can be ignored because its scale parameter is much larger than the other two; however as temperature higher than 550K the effect of ground mode failure becomes significant. The MTTF at maximum allowed temperature (453K) and use condition (363K) for these failure modes and the corresponding apparent failure are shown in Table 3. The predictions based on β -fixed assumption are quite different with the other two especially about the MTTF of the apparent failure which is dominated by the mode turn primarily and then the mode phase secondly while the mode ground has little influence.



a)



b)

Fig. 2. The variations of (a) shape parameter and (b) scale parameter with the temperature for each failure mode

The MTTF prediction by Nelson [11] follows the reliability with a log-normal distribution under constant deviation with the data in Table 1 except those of mode turn at 533K. In the present study all information in Table 1 is taken into account. For comparison of the models Fig. 3 shows the predicted reliability variations with the data at 463K. It shows that present study with β varied with temperature fits the data even better among the models. The approach from Bunea [13] is taken in a different way, the reliability drops in a constant failure rate manner, i.e. $\beta = 1$, which deviates from the data obviously, but with acceptable MTTF prediction.

The comparisons of models based on the two assumptions about β in this study are made in Fig. 4 for the temperature at 463K and 533K, respectively. Although the fitting based on β -fixed assumption is well at higher temperature but not for the lower one, such limits its application in the life estimation. This also coincides with the results shown in Table 3. At lower temperature the mode turn dominates the failure; however as the temperature getting high, the mode ground becomes meaningful. It seems that the influence of the mode phase maintains the same level about the apparent failure in the mentioned temperature range. The sum of failure probability density distributions (fpdd) of the three modes from Eq. (9) denotes the actual failure distribution. The area beneath the fpdd of some particular mode represents the percentage of that mode failure on the total. Table 4 provides such information which can be double checked with Fig. 2b about the scale parameter variation vs. temperature.

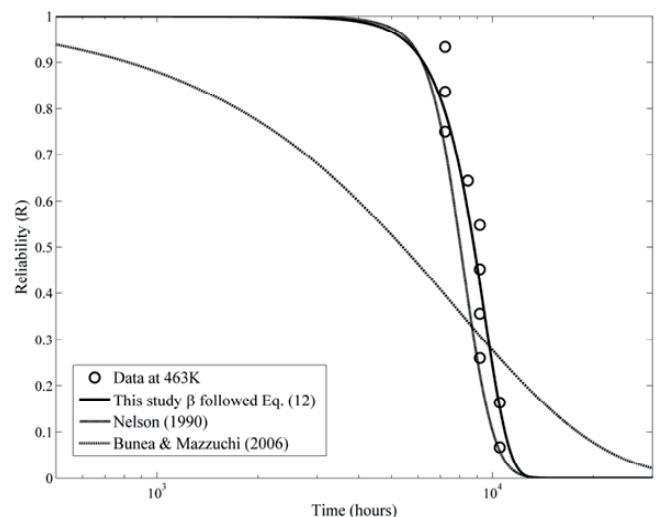


Fig. 3. The comparison of reliability fittings for data at temperature 463K

Finally the predicted reliabilities of the test motors are given in Fig. 5 for the temperature at the allowable range the lower 363K, 400K and upper 453K, respectively. It is interest that decay trend of

Table 4. The corresponding percentage of occurrence for each failure mode in the series connection at 4 test temperature and maximum allowed temperature (453K), use condition (363K)

Mode \ Temperature	363K	453K	463K	493K	513K	533K
Turn	68.7%	80.0%	79.2%	75.8%	68.8%	57.9%
Phase	31.2%	18.6%	18.6%	15.8%	13.6%	10.4%
Ground	0.1%	1.4%	2.2%	8.4%	17.6%	31.7%

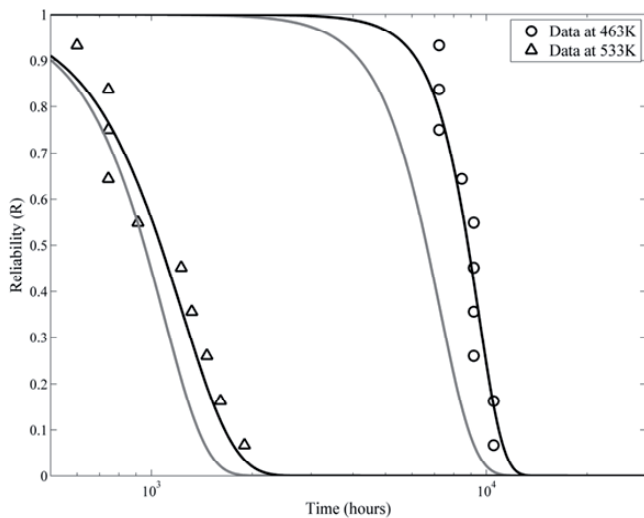


Fig. 4. The reliability fittings based on the MLE with β -temperature depended in black and β -fixed in grey at 463K (—) and 533K (—), respectively

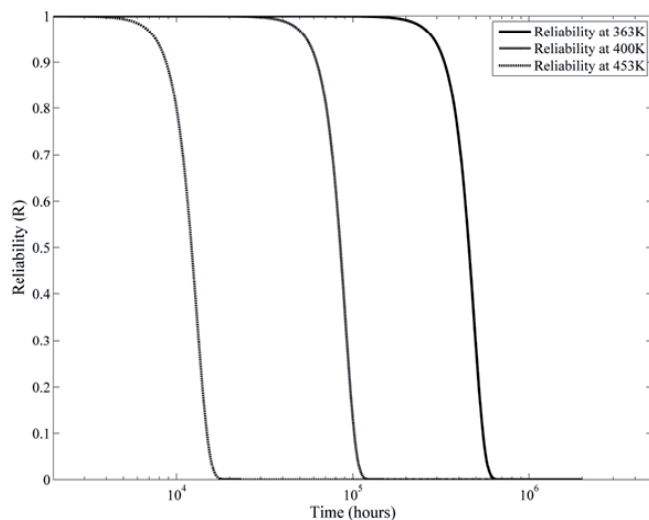


Fig. 5. The predicted variations of reliability at the allowable temperature lower 363K, 400K and upper 453K, respectively

these two curves are very similar to each other. This is because that the shape parameter, mainly decided by the mode turn, tends to its saturation value $\beta=7.69$, i.e. the characteristic of damage process about

insulation changes little as the temperature within the allowable operation range. In other words the insulation technology of the test motors is suitable. The geometry about the mode turn and phase structure need to be improved for longer MTTF to meet the standard requirement as the operation temperature up to 440K and higher within the allowed range, see Table 3.

5. Conclusions

In the present study the Maximum Likelihood Estimator is taken to investigate the characteristics of the insulation failure about class-H motors with accelerated life tests data under censored situation. Three failure modes namely the turn, phase, and ground, respectively, are considered in the estimation, the so-called competing failure analysis. Several remarks can be summarized as follows:

a. About the model:

1. Weibull representation of the reliability for each failure mode is suitable as taking the shape parameter varied with the temperature, this is necessary due to its influence on the estimation of the scale parameters which closely related to the MTTF prediction;
2. Gompertz-type variation of the shape parameter is likely appropriated to depict the characteristics of cumulative damage process about the insulation; instead of Gompertz-type relation, other curves with both ends saturated can be considered, e.g. arctangent, logistic-like, etc. to show the variation of β with the temperature;
3. The existence of reference temperature distinguishes the behavior of damage accumulation and correspond the thermal decomposition process.

b. About the motor in the testing:

1. The insulation technique used is acceptable as the operation temperature kept in the use condition used 363K;
2. As the temperature rises up to 440K, which still within the allowed range in application, the turn structure needs to be rearranged primarily, then the phase next;
3. The mode ground has only influence on the failure at much higher temperature.
4. Based on T_r , the maximum test temperature should below 516K because the behavior of failure is quite different to normal use condition. This is also referring to Nelson's result [11].

Acknowledgement: This work was supported by grant NSC 97-2221-E-008-043-MY3 from the National Science Council, Taiwan.

References

1. Bai DS, Chun YR, Kim JG. Failure-censored Accelerated Life Tests Sampling Plans for Weibull Distribution under Expected Test Time Constraint. Reliability Engineering and System Safety 1995; 50: 61–68.
2. Beyler CL, Hirschler MM. Thermal Decomposition of Polymers. The SFPE Handbook of fire protection engineering (Section 1, Chapter 7). NFPA, Quincy, MA, 1988.
3. Bunea C, Mazzuchi TA. Competing Failure Modes in Accelerated Life Testing. Journal of Statistical Planning and Inference 2006; 136: 1608–1620.

4. Dakin TW. Electrical Insulation Deterioration Treated as a Chemical Rate Phenomenon. Transactions of the American Institute of Electrical Engineers 1948; 67: 113–122.
5. Dempster AP, Laird NM, Rubin DB. Maximum Likelihood from Incomplete Data via the EM Algorithm. Journal of the Royal Statistical Society 1977; 39: 1, 1–38.
6. Tai HS, Hsu CH. Kinetic Analysis of Thermal Degradation of Polypropylene Using a Modified Gompertz Model. Journal of Hazardous, Toxic, and Radioactive Waste Management 2012; 15: No. 1, 39–50.
7. Karolczuk A. The probabilistic model of fatigue life estimation for structural elements with heterogeneous stress distribution. The Archive of Mechanical Engineering 2008; LV, 3: 209–221.
8. Klein JP, Basu AP. Accelerated Life Test under Competing Weibull Causes of Failure, J. Commun. Statist. Theor. Meth. 1982; 11: 2271–2286.
9. Kuwahara H, Sudo S, Iijima M. and Ohya S. Dielectric Properties of Thermally Degraded Chloroprene Rubber. Polymer Degradation and Stability 2010; 95: 2461–2466.
10. Miller R, Nelson W. Optimum Simple Step-Stress Plans for Accelerated Life Testing. IEEE Transactions on Reliability 1983; 32: 59–65.
11. Nelson W. Graphical Analysis of Accelerated Life Test Data with a Mix of Failure Modes, IEEE Transactions on Reliability 1975; R-24: 230–237.
12. Nelson W. Accelerated Testing, Statistical Model, Test Plans, and Data Analyses. John Wiley & Sons, Inc., N.Y., 1990.
13. Nelson W. Theory and Applications of Hazard Plotting for Censored Failure Data. Technometrics 2000; Special 40th Anniversary Issue, 42: 1, 12–25.
14. Seo JH, Jung M, Kim CM. Design of Accelerated Life Test Sampling Plans with a Nonconstant Shape Parameter. European Journal of Operational Research 2006; 197: 659–666.
15. Standard Test Method for Rapid Thermal Degradation of Solid Electrical insulating Materials By Thermogravimetric Method. ASTM D3850-94, reapproved in 2000.
16. Tanaka T, Montanari GC. Polymer Nanocomposites as Dielectrics and Electrical Insulation-Perspectives for Processing Technologies. Material Characterization and Future Application, IEEE Transactions on Dielectrics and Electrical Insulation 2004; 11: 5, 763–784.
17. Winsor CP. The Gompertz Curve as a Growth Curve. Proceedings of the National Academy of Sciences 1932; 18: 1–8.
18. Zwietering MH, Jongenburger I, Rombouts FM. and VantRietK. Modelling of the bacterial growth curve. Applied and Environmental Microbiology 1990; 56(6): 1875–1881.

Yi-Heng YANG, Ph.D. candidate

Prof. Kuo-Shong WANG, Ph.D.

Department of Mechanical Engineering

National Central University

Taoyuan 32001, Taiwan

E-mails: 973403008@cc.ncu.edu.tw, kuoshongwang@gmail.com

Marcin MICHALAK

Marek SIKORA

Jurand SOBCZYK

ANALYSIS OF THE LONGWALL CONVEYOR CHAIN BASED ON A HARMONIC ANALYSIS

ANALIZA PRACY ŁAŃCUCHA PRZENOŚNIKA ŚCIANOWEGO W OPARCIU O ANALIZĘ HARMONICZNĄ*

This paper describes the use of harmonic analysis in the analysis of a longwall conveyor chain. Correct and stable operation of the chain is connected both with the safety of the work and the economic performance of the transportation process. The aim of the study was to show the ability to detect changes in conveyor work related to damage or improperly conducted procedure of chain length changing. Observation of the conveyor chain work was to monitor the power consumption of the three motors driving the conveyor. The analysis included nearly 26 000 startups have been reported within 20 months of the conveyor work. This paper describes the initial stage of raw measurement data analysis, and analysis of data transformed by the Fourier transform. As a result of the data analysis, diagnostic procedures allowing to signal deviations from the conveyor normal conditions were proposed.

Keywords: device diagnostics, harmonic analysis, longwall conveyor.

Artykuł opisuje zastosowanie analizy harmonicznej do analizy stanu łańcucha przenośnika ścianowego. Poprawna i stabilna praca łańcucha wiąże się zarówno z bezpieczeństwem prowadzenia prac jak i ekonomiczną wydajnością procesu. Celem przeprowadzonych badań było wskazanie możliwości wykrywania zmian pracy przenośnika związanych z uszkodzeniem bądź przeprowadzoną w sposób nieprawidłowy procedurą zmiany długości łańcucha. Obserwacja pracy łańcucha przenośnika polegała na monitorowaniu poboru prądu przez trzy silniki napędzające przenośnik. Analizie poddano blisko 26 000 uruchomień, jakie odnotowano w okresie 20 miesięcy pracy przenośnika. W pracy opisano etap wstępnej analizy surowych danych pomiarowych, a także analizy danych przekształcony transformacją Fouriera. W rezultacie analizy danych zaproponowano procedury diagnostyczne pozwalające sygnalizować odstępstwa od normalnych warunków pracy przenośnika.

Słowa kluczowe: diagnostyka urządzeń, analiza harmoniczna, przenośnik ścianowy

1. Introduction

In the industry, including coal mining, there is observed significant increase in the importance of information derived from the monitoring systems. The main task of the monitoring system is to visualize the current state of the devices (e.g. power consumption, temperature, fluid pressure and levels (cooling, hydraulic) etc.).

It can be assumed that at the present time functionality of monitoring systems provides full monitoring and visualization of any industrial process (production, machines and equipment work, natural hazards, etc.). The data collected by these systems are mainly used for the current visualization and reporting.

At the moment, more and more software developers and users of monitoring systems indicate the need for analysis of the data collected in their repositories. In particular, the purpose of this analysis may be defining the diagnostic models of monitored devices [2, 7, 15]. Identification of diagnostic model may be done through the planned experiments or analysis of data collected during device operation. In this paper we concentrate on the second approach. Based on data collected by SMOK [13], the longwall monitoring system, we present how the application of the Fourier transform can be used to detect changes in longwall conveyor chain (in particular by joining the chains with different parameters).

This paper is organized as follows: the next section provides a short overview of the work related to diagnostics of mining machines, in particular longwall conveyor. The following part describes the stages of initial data processing and a substantial processing of the

recorded signals. This is followed by diagnostic models, based on an analysis of the value described here in the paper as a *basic period*.

2. Analysis of longwall conveyor

The problem of monitoring and diagnosing the condition of machines used in the mining industry was raised in [2, 4, 5, 6, 10, 11, 15]. It has also been reviewed extensively in [2, 5, 15]. Papers [2, 15] also present new methods of extracting and processing of diagnostic features to discover diagnostic relations. In particular, a part of the work [2] was devoted to the diagnosis of belt conveyors, used as the main transport device in the mining industry. In [11] power consumption and temperature of a coal combine cutting heads were monitored. Therefore, three operating states of the coal combine were defined. Two of the identified states describe different but correct conditions of mining. This work has identified a parameter describing the efficiency of the coal combine cooling system.

Diagnosis of longwall conveyor was the subject of such works as [4, 6, 10]. The work [4] presents a method for detecting defects on a conveyor chute of the bottom side of the conveyor. Based on the analysis of power consumption of longwall conveyor driving motors during one repair shift, the damage was localized with an accuracy of one section. In [6] a comprehensive management system of the conveyor belt components was proposed. The system allows generating both summary statements and, operational and analytical reports. These reports allow for evaluation of the conveyors monitored in the system.

(*) Tekst artykułu w polskiej wersji językowej dostępny w elektronicznym wydaniu kwartalnika na stronie www.ein.org.pl

In [10] power consumption of motor driving the conveyor is analyzed. The result of the study is to propose summary reports of motor operation including the level of exceeded values of the rated current as well as the duration of the exceedances. In addition there was proposed rule-based description of the operating parameters of the motor, based on association rules [1].

3. Acquisition of measurement data

The results presented in the latter part of the paper were obtained due to the analysis of power consumption of each of the motors driving the conveyor transport system. We analyzed data from two periods of operation of the conveyor. Later in the paper, the time interval between the turning on and turning off the conveyor will be called *startups*. In the first period (called P) lasting more than 19 months, there were more than 24 500 *startups* of the conveyor, in the second period (called NP) more than 1 200 startups were reported. The most important, from the point of view of data analysis, was that in the second period a part of the chain was replaced with another one. Unfortunately, information about the difference in the construction of both chains was not available, therefore, it could not be assumed that replaced part of the chain was composed of links of different size or scrapers were placed in the other intervals.

Observation of work consisted in measuring the power consumption by each of the three motors of the conveyor within one second intervals. Motors identified as M1 and M2, served as a “pulling”, the task of the motor denoted as M3 was pulling the chain from under the conveyor (turning back). The analyzed conveyor was equipped with two-speed starter.

3.1. Initial processing of data

The aim of the analysis was to evaluate the work of conveyor in a steady state. In the measurement data concerning each startup the first two phases were omitted: work at low speed and switching the motor from low to high speed. Duration of speed shifting phase and consequent increase in the values of current was based on observations at 20 seconds from the moment of switching on high speed.

In the next step of data processing all startups were discarded from the analysis, the duration of which is less than 80 seconds, since assuming the conveyor moving speed is about 1.5 m/s in this time conveyor path was shorter than the length of the longwall (it was more than 110m).

The last stage of pre-processing was the data smoothing. The smoothing process consisted of averaging the value of power consumption based on n preceding and n subsequent values (moving average).

Taking as $x(i)$, unsmoothed value of current at the time i , the smoothed value at the moment i is given by formula (1):

$$x'(i) = \frac{\sum_{j=i-n}^{i+n} x(j)}{2n+1} \quad (1)$$

where: $x'(i)$ represents a new smoothed value, n is a smoothing parameter, whose value equaled 5 (which corresponds to averaging nine consecutive values). This value allows to compromise between filtering fast-changing current intensity components and keeping the nature of the course. This value was determined by observing smoothed courses of 30 randomly chosen long (more than 120 s) startups. For the first four and last four mea-

surements averaging were not performed. Sample comparison of the original and smoothed course is shown in Fig. 1.

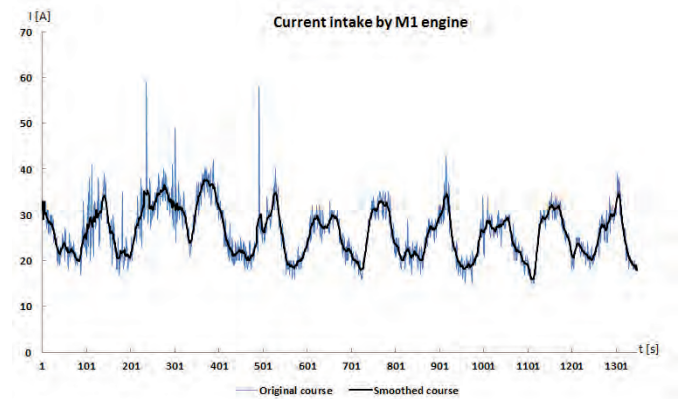


Fig. 1. Comparison of unsmoothed and smoothed courses describing the current consumption of one of the motors.

3.2. Data transformation into the frequency domain

Diagnosis of a chain in conveyor means studying periodicity of rolling the chain through the conveyor. The aim is to check whether during conveyor operation, periodicity of the conveyor work can be registered and whether changes of periodicity can be associated with damage or improperly conducted “repairs” of the chain.

It should be noted that it is impossible to diagnose individual links in the chain, this happens due to the sampling frequency of measurement data. Sampling time in the monitoring system is one second, the conveyor during its work moves at a speed of about 1.5 m/s ($\pm 10\%$). As a result, between two consecutive samples the conveyor travels generally longer than the length of a single link.

For the collected measurement data the Fourier transform was used. For each of the motors the changes frequency spectrum of current was obtained. After analyzing the spectra for many motors of many startups, it was observed that the initial values of the spectrum (corresponding to the lowest frequencies) obtain disproportionately high values (especially for the first argument, corresponding to the constant component of signal), thereby distorting the spectrum of motors work. Therefore, it was concluded that the domain of spectrum should be reduced of the initial arguments. Finally, it was found that the first two arguments obtained in the distribution will be excluded.

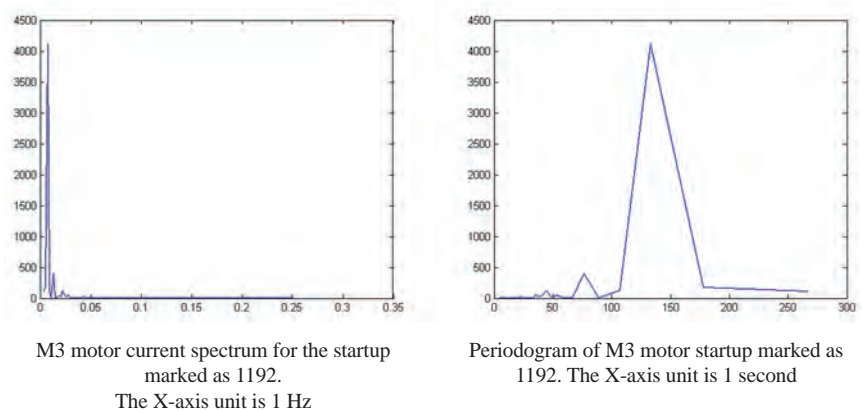


Fig. 2. Illustration of spectrum transform into periodogram

Due to the fact that distribution values showed the highest significance in the initial (the lowest) frequency domain (fractional hertz) it was decided to consider time domain instead of frequency domain. Fur-

ther analysis was based on the periodogram observation that showed how input course of current intensity change is distributed into sinusoidal changes in a specified period of time. Comparison of the spectrum and the periodogram for a selected startup is illustrated in Fig. 2.

In the example, for each single startup and at the same time for each of the three motors, were obtained graphs showing changes in the current intensity depending on the period of these changes. Further analysis of the data focused on local maxima in received periodograms. For each of the motors five periods with the greatest local maxima in periodogram were taken into account, sorting them from the most significant. These periods are marked: M11, M12, ..., M15 and analogically M21, M22, ..., M25 and M31, M32, ..., M35.

4. Analysis of longwall conveyor motors

After analyzing periodograms, in such a way as described in the previous section, each conveyor startup was characterized by a vector of 15 features. Analysis of the resulting data set has demonstrated that it is impossible to determine the relationship between the *basic period* (the *basic period* T means the time in which the chain travels equal to twice the length of the conveyor), and one (for example, the largest) value in periodogram.

The first attempt to identify the basic period was based on the calculation of arithmetic mean values of M11, M21 and M31, separately for startups recognized as correct (startups of period P) and incorrect startups (startups of period NP). Mean values of M11, M21, M31 for correct startups marked γ_i , $i \in \{1,2,3\}$. Mean values of M11, M21, M31 for incorrect startups were marked β_i , $i \in \{1,2,3\}$. Then, for each startup there was calculated distance between γ_i and M11, M21 and M31, as well as for β_i and M11, M21 and M31. On this basis startups were being classified as correct or incorrect. The highest accuracy was achieved for means γ_3 and β_3 . However, the results were not satisfactory, because the variance of the variable M31 for correct and incorrect startups was very high. As a result, algorithm reflecting presented way of classification was characterized by low sensitivity and specificity (i.e. a large number of correct startups was recognized as incorrect and vice versa).

It was necessary to take actions leading to a situation in which the variance of the strongest period, derived from the analysis of periodograms of motors M3, M2, M1 would be as small as possible. Therefore such a filter is defined to minimize the variance for correct startups, ignoring the incorrect, with assumption that in case of incorrect starts the basic period should change.

Therefore the following actions were taken:

- 1) Startups of less than 4 minutes were removed. For startups shorter than 4 minutes in most cases the strongest period was less than 70 seconds, it was then considered that the length of the chain is longer than 110 meters, so these periods were found to be incorrect;
- 2) In order to determine the basic period that allows distinguishing between correct and incorrect start the following logic rule was fixed (RL):

```
IF M31=M21=M11 THEN T=M31
ELSE
IF ((M31=M22=M12) OR (M31=M23=M13) OR (M31=M24=M14) OR
(M31=M25=M15)) THEN T=M31
ELSE
IF ((M31<M22) AND (M22=M12) AND (Time>300)) THEN T=M22
ELSE T=M31
```

In the formula above it can be observed that it was necessary to extend the duration of the startup to 5 minutes (300 seconds), the remaining part of the formula is somehow responsible for negotiating the length of the basic period, which can be identified in periodogram.

Using the methodology outlined above, there was obtained the mean value for the basic period for the correct startups equal to $\gamma = 117$ s,

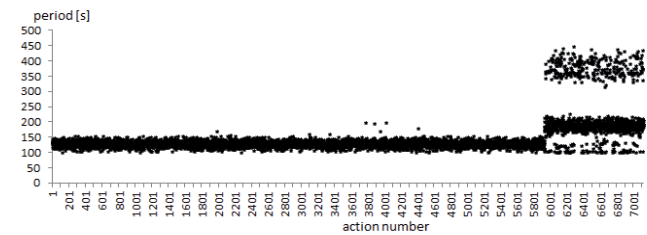


Fig. 3. The chart of the basic period of each startup after the final data filtration.

with a standard deviation $\sigma = 36.28$ s. For incorrect startups these values were $\beta = 158.43$ s, $\sigma = 105.66$ s. In order to further reduce the variance of the basic period for correct startups, all startups of which the basic period $T < 100$ s were removed. Finally, there were achieved 7125 startups, among which for correct startups the mean of the basic period was $\gamma = 128.45$ s, and the standard deviation $\sigma = 8.63$ s (Fig. 3).

Presented way of filtration and identification of the basic period does not allow for the diagnostics of the conveyor after each startup, as these shorter than 5 minutes will not be the subject of evaluation, however, we obtain the possibility of diagnosing on average of every second startup. Average daily number of startups was 25, while the average daily number of startups, for which performing the diagnostic procedure is possible, is 12.

Now it is possible to perform diagnostic procedure using the parameters γ and β . However, this will be a diagnostic procedure for a specific type of change in working conditions of conveyor (lengthening the chain by combining different chains). In order to diagnose unknown types of error it is necessary to monitor whether the basic period and its standard deviation change.

Distribution of the basic period for correct startups was a normal distribution (Shapiro-Wilk W test was performed), ninety-five percent of startups should therefore lie in the interval $[\gamma - 1.95996\sigma, \gamma + 1.95996\sigma]$. It appears that it can be assumed that the distribution of the basic period is a normal distribution, with various values of the mean (γ) and the standard deviation σ . If, however, it turned out differently, it is always under the Chebyshev inequality holds. It says that for any $k > 1$ probability that a randomly selected feature value differs from the expected value by more than $\pm k\sigma$ is at most $1/k^2$, which is outside the range $[\gamma - 2\sigma, \gamma + 2\sigma]$ is at most 25% of the feature value.

This information can be used in the following way: as an incorrect startup (or rather: different from the pattern found to be diagnostically correct) will be considered such a startup, the basic period of which will

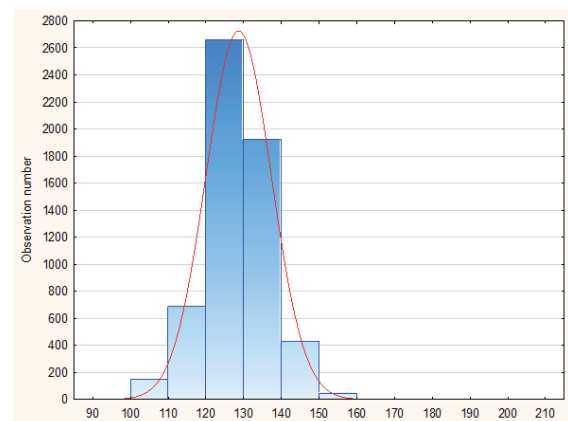


Fig. 4. Distribution of the basic period for correct startups.

not lie in the mentioned intervals. In such a case, the user would have the ability to view courses of current on all three motors and browse periodograms. As a result, one would qualify startups as actually incorrect, or could change the value of the basic period, when it would clearly result from the periodogram, thus, from the actual reconstruction of the conveyor. The second option would include the phase of updating parameters used in diagnostic procedures. Information about the reconstruction of the structure of the monitored device or its location is often registered into diagnostic or monitoring systems with a delay.

To further reduce the number of the user interventions, incorrect startups may be only these for which the basic period will be an outlier. For the filtered the basic periods, median M and the first and third quartiles ($Q1$ and $Q3$, respectively) can be calculated, then the interquartile range IQR is expressed by the formula (2)

$$IQR = Q_3 - Q_1 \quad (2)$$

Values lying in the ranges $(Q_3 + 1.5IQR, Q_3 + 3IQR]$ and $[Q_1 - 3IQR, Q_1 - 1.5IQR)$ are considered outliers. Values greater than $Q_3 + 3IQR$ and less than $Q_1 - 3IQR$ are considered extreme outliers. In the case of diagnosis referred to in this paper, the user would observe all startups for which outliers in the basic period were registered.

Information about specificity and sensitivity of diagnostic procedure described above is presented in Table 1. Diagnostic procedures verification was performed on the data set used for defining the Table.

Table 1. Information about the number of true positives (TP), true negatives (TN), false positives (FP) and false negatives (FN) for different diagnostic methods.

Method	TP	FP	TN	FN
Normal distribution (2σ)	5713	212	123	1077
Normal distribution (1σ)	5119	806	316	884
Outliers	5718	207	1146	54
Distance from the means γ, β	5921	4	923	277

Taking all the analyses into consideration, the following diagnostics scheme can be proposed:

1. Select a group of startups reflecting correct operation of the conveyor.
2. Select a group of startups reflecting incorrect operation of the motor (if there are startups describing different types of failure, for each failure type create a separate group). Point 2 can be omitted if you have examples only of correct startups.

(the following points concern of all three motors, these actions apply only to startups selected in step 2)

3. For all the startups perform the processes of deleting low speed and switching into high speed.
4. For all startups perform data smoothing process.
5. For all startups perform the process of determining the Fourier transform, skip the first two components and determine the reciprocal of arguments in frequency domain.
6. For all startups find the first five maximum values in periodogram and determine their equivalent arguments.
7. For each startup specify a value of the basic period according to the rule RL (section 3.3).
8. Determine the arithmetic means and standard deviations, as well as quartiles and interquartile range for correct startups group.

9. Determine the arithmetic means and standard deviations for all identified groups of incorrect startups.
 10. Determine limits for outliers (formula (2)).
 11. For each new startup begin the diagnostic procedure, checking whether startup parameters qualify it as correct or incorrect.
- Block diagram of the procedure is shown in Fig. 5.

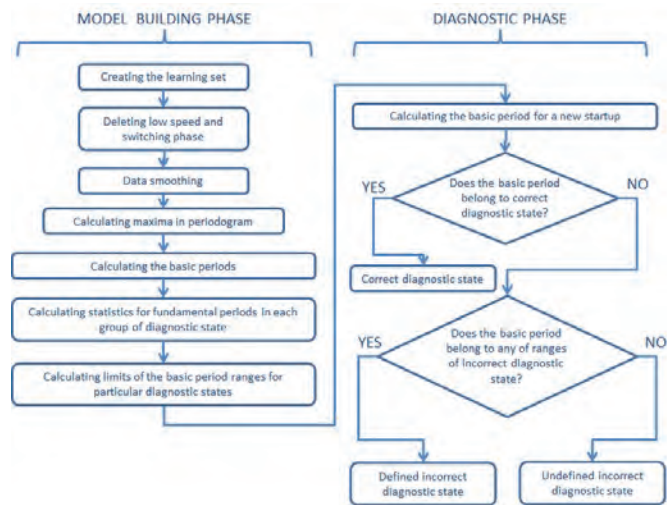


Fig. 5. Block diagram of the diagnostic procedure.

The diagnostic procedure presented above includes some inconvenience. The most important one is the need to define the rule (RL) identifying the basic period. Such methodology is not appropriate if the ultimate goal is automation of the diagnosis process. As it is known, in order to define the diagnostic model of the device, machine learning also can be applied [7, 15]. As sets of correct (Period A) and incorrect (Period B) startups of conveyor were available, rule induction algorithm PART was used [3, 14]. Calculations were carried out in Weka environment [14]. Detailed description of PART algorithm can be found in [3].

In the data set submitted to the algorithm, each startup was characterized by already mentioned in section 3.2 vector of 15 features (local maxima in periodograms), also used to identify the rule RL . The results are presented in Table 2. The first line of Table 2 presents the results obtained by using 10-fold cross validation. The second line presents the result of the analysis of whole available set of examples (i.e. without isolating a test set).

Table 2. Information about the number of true positives (TP), true negatives (TN), false positives (FP) and false negatives (FN) for the basic period identification based on rule induction

Metod	TP	FP	TN	FN
PART (10CV)	5875	51	1138	60
PART	5896	30	1173	25

As it can be observed, the results obtained by PART and the diagnostic method based on the distance from the means γ, β (the last line of Table 1) are satisfactory. The best sensitivity and specificity lies in the method applying the PART algorithm to recognize correct and incorrect startups. Therefore, in the diagnostic scheme (points 1-11), points 8 and 9 can be replaced by training the classifier and including it into the diagnostic process.

The fact is, that presented methods of identification the correct values of the basic period (including the method based on rule induction) need a set of positive examples (correct startups) and negative

examples (incorrect startups). This diagnostic method can be used only after a certain period of conveyor work. In the initial period of operation, we may assume that the conveyor is working properly, and the Fourier analysis (in particular analysis of the values classified as outliers in terms of the basic period) allows for identification of potentially incorrect startups. After collecting sufficient number of negative examples based on the Fourier analysis (based on the characteristics resulting from the analysis), the classifier is determined and then it is used for fully automatic diagnostics.

Note also that the set of negative examples can be created based on startups considered as incorrect for various reasons (reflecting various types of damage). In this situation we may deal with so-called *concept drift*, resulting in the need to re-train classifier on the extended set of negative examples, in order to improve its sensitivity and specificity. However, this process can be automated.

The procedure suggested here including: acquisition of a set of positive and negative examples, monitoring the classifier quality and (if necessary) re-training it, has successfully been applied to predict the total energy of seismic events that were recorded in a given period of time in coal mines [8] and to predict the concentration of methane [9].

Certainly, acquisition of diagnostic knowledge (correct and incorrect startups) can be carried out also by the planned experiment [7].

However, it is definitely more complicated in underground conditions of conveyor work.

5. Summary

This paper presents the diagnostic procedure, which allows monitoring work of a longwall conveyor, with particular emphasis on the diagnostics of “transporting” chain. Diagnostic procedure is based on harmonic analysis, power analysis, monitoring of outliers, as well as the induction of classification rules. The work presents all the necessary steps to allow the implementation of the presented diagnostic procedure. The results are satisfactory, developed diagnostic procedure can with high precision indicate correct and incorrect startups. The procedure generates a small number of so-called false alarms which is especially important for the dispatcher monitoring more devices working. It is planned to implement presented diagnostic procedure into the monitoring system DEMKop [12] (the successor of the SMOk system).

The work was financed by the European Union through the European Social Fund (contract number: UDA-POKL.04.01.01-00-106/09 – first author) and the Rector of the Silesian University of Technology (grant RGH-2/RAU0/2012 – second author). The authors also wish to thank the anonymous reviewers, who served a valuable remarks and comments.

References

1. Agrawal R, Shrikant R. Fast algorithms for mining association rules. Proc. of the 20th Int. Conf. Very Large Databases (VLDB), 1994.
2. Bartelmus W. Condition Monitoring of Open Cast Mining Machinery. Oficyna Wydawnicza Politechniki Wrocławskiej, Wrocław 2006.
3. Frank E, Witten IH. Generating Accurate Rule Sets Without Global Optimization. In: Proc. of the 15th Int. Conf. on Mach. Learn., 1998: 144–151.
4. Gąsior S. Diagnosis of longwall chain conveyor, Przegląd Górniczy, 2001; 57 (7–8): 33–36.
5. Jurdziak L, Zimroz R. Dlaczego diagnostyka maszyn się opłaca i ile można na tym zaoszczędzić? Prace Naukowe Instytutu Górnictwa Politechniki Wrocławskiej; 106: 139–150, 2004.
6. Kacprzak M, Kulinowski P, Wędrychowicz D. Computerized information system used for management of mining belt conveyors operation. Eksploatacja i Niezawodność – Maintenance and Reliability 2011; 13 (2): 81–93.
7. Korbicz J, Kościelny JM, Kowalczyk Z, Cholewa W. Fault Diagnosis: Models, Artificial Intelligence, Applications, Springer 2004.
8. Sikora M. Induction and pruning of classification rules for prediction of microseismic hazards in coal mines. Expert Systems with Applications 38(6), 2011, 6748–6758.
9. Sikora M, Krzystanek Z, Bojko B, Śpiechowicz K. Application of hybrid machine learning method for description and on-line assessment of methane hazards in a mine excavation: Journal of Mining Sciences 2011; 47 (4), 493–505.
10. Sikora M, Michalak M. Analiza pracy silników przenośników ścianowych – propozycje raportów i wizualizacji, Mechanizacja i Automatyzacja Górnictwa, No 5/436 2007, Wydawnictwo Centrum EMAG, Katowice 2007, s. 17–26
11. Sikora M, Michalak M. Eksploracja baz danych systemów monitorowania na przykładzie obserwacji pracy kombajnu chodnikowego, Bazy Danych: Rozwój metod i technologii, (Tom 1: Architektura, metody formalne i zaawansowana analiza danych), WKŁ, Warszawa 2008: 429–437.
12. System SMOK: <http://www.somar.com.pl/products/smok,18,2,48>
13. System DEMKop: <http://www.somar.com.pl/katalog-wyrobow/demkop,18,2,71>
14. Witten IH, Frank E. Data mining: practical machine learning tools and techniques. Morgan Kaufmann, 2005.
15. Zimroz R. Metody adaptacyjne w diagnostyce układów napędowych maszyn górniczych. Oficyna Wydawnicza Politechniki Wrocławskiej, Wrocław 2010.

Marcin MICHALAK, Ph.D. (Eng.)

Marek SIKORA, Ph.D.

Institute of Computer Science

Silesian University of Technology

ul. Akademicka 16, 44-100 Gliwice, Poland

E-mails: Marek.Sikora@polsl.pl, Marcin.Michalak@polsl.pl

Jurand SOBCZYK, Ph.D. (Eng.)

Somar SA

ul. Karoliny 4, 40-186 Katowice, Poland

E-mail: J.Sobczyk@somar.com.pl

Paweł BARANOWSKI
Krzysztof DAMAZIAK
Jerzy MAŁACHOWSKI

BRAKE SYSTEM STUDIES USING NUMERICAL METHODS

BADANIA UKŁADÓW HAMULCOWYCH METODAMI NUMERYCZNYMI*

The paper presents the examples of numerical simulations of braking systems performed in order to determine the parameters of their work. Using a typical finite element and meshless numerical methods, dynamic analyses of the brake were performed paying particular attention on the phenomenon of thermo-mechanical coupling occurring in the process of braking, as well as wear processes occurring on the surface of the linings. The article presents sequence of research steps, including hybrid modelling of braking system.

Keywords: brakes, FEM modelling, SPH modelling, thermomechanics, friction.

W pracy przedstawiono przykłady symulacji numerycznych układów hamulcowych wykonanych w celu wyznaczenia parametrów ich pracy. Stosując siatkowe i bezsiatkowe metody numeryczne przeprowadzono dynamiczne analizy pracy hamulca ze zwróceniem szczególnej uwagi na zjawiska sprzężone (cieplno – mechaniczne) występujące w procesie hamowania oraz procesy zużycia zachodzące na powierzchni okładziny ciernej. W artykule przedstawiono kolejne kroki badań obejmujące modelowanie hybrydowe układu hamulcowego.

Słowa kluczowe: hamulce, modelowanie MES, modelowanie SPH, termomechanika, tarcie.

1. Introduction

This paper discusses the issues associated with the operation of the braking system, which is one of the most important safety systems in a car [23]. As a result of braking friction surfaces of the lining are heated to the temperature up to 500°C [14, 15, 19]. Such thermal conditions and other phenomena accompanying the process of braking cause a constant grow of requirements for the properties of materials used for brake linings.

On the other hand, increasing availability of appropriate tools causes that, as in many other areas, numerical analyses become increasingly important in the brakes design process. Nevertheless, the nature of the physical processes associated with braking makes their correct modelling (using the most popular analytical tools based on the finite element method) virtually impossible [20] at the moment. The above statement seems to be surprising, but only to the point where we will realize what should be included in a numerical modelling of the brake process, such as:

- nonlinearities associated with large rotation,
- nonlinearities of boundary conditions (contact, friction),
- non-stationary nature of the process,
- thermo-mechanical coupling,
- wear of linings required to model change in geometry of friction pair.

For this reason, in the numerical studies of braking systems, various simplifications are usually used. For example, the geometry of brake is simplified to axisymmetric representation [24] or system is analysed in the plain strain [16].

In the case of temperature field analysis, many authors define stationary or non-stationary heat sources and ignore the fact that heat is generated by friction [2, 4, 8, 21]. In other words: thermo-mechanical coupling is omitted in investigations.

Wear of the friction pair is most commonly investigated using tools developed by tribology. From the point of view of this work

these methods can be divided into those that use semi-empirical equations describing surface wear [3, 12, 17], and those in which models describe some aspects of the phenomena occurring at the micro level, i.e. the level of the surface layer of components. Review of publications representing the latter approach can be found in [26].

An interesting attempt to implement a tribological approach to macro models is presented in [18], where a procedure for random generation of irregularities appearing on the working surface of the brake pad was described. In [25] attempts to assess the lining wear in the macroscopic model, however the problem was brought to the analysis of the sole brake pad running in stationary conditions. Popular linear Archard model was used to describe the wear process. A more accurate model of the whole brake is described in [1], although thermal effects were also omitted and geometry changes resulting from the wear were modelled based on experimental measurements by the arbitrary movement of nodes in the direction normal to the contact surface.

Above examples show the difficulties that arise when trying to take into account the microscopic processes accompanying wear in the macroscopic models of whole components. In the case of brake, this inconvenience manifests itself when we will try to include a sufficiently accurate description of the surface friction geometry in the assembly model [17, 20]. One way to solve this problem is the implementation of meshless methods. Here analysed object is represented by a set of points (particles) with a finite size which can form any shape [22]. Although known for about 30 years, these methods become popular in the analysis of tribological processes quite recently [11, 20]. Authors, as part of this trend, also applied this meshless approach to simulate wear of friction surface.

Presented paper discusses numerical simulations of braking process conducted using LS-Dyna explicit code. Obtained results for brake with two pistons and for modified set-up with additional third piston are compared. Due to the fact that a number of thermo-mechanical phenomena begin in micro scale, it was decided to carry out the analysis of contact surfaces in a microscopic scale including the wear

(*) Tekst artykułu w polskiej wersji językowej dostępny w elektronicznym wydaniu kwartalnika na stronie www.ein.org.pl

process using the aforementioned meshless method, more particular Smooth Particle Hydrodynamics (SPH) technique.

In the earlier work authors presented results of a drum brake analyses [10]. Numerical models presented there enabled the development of modelling procedure that allows to estimate the efficiency of brakes and to predict the most exposed areas to wear (Fig. 1)

Obtained results showed that algorithms of conversion of work done by friction forces into heat are working properly. This was one of the most important elements necessary for proper numerical description of brake. It should be pointed out, though, that the algorithms are very sensitive to the parameters describing thermal and mechanical properties of brake materials. Another important factor strongly affecting results is a discretisation of contact areas of interacting bodies. This translates into accurate values of contact forces, which is a key factor for the proper definition of heat flux generated by friction.

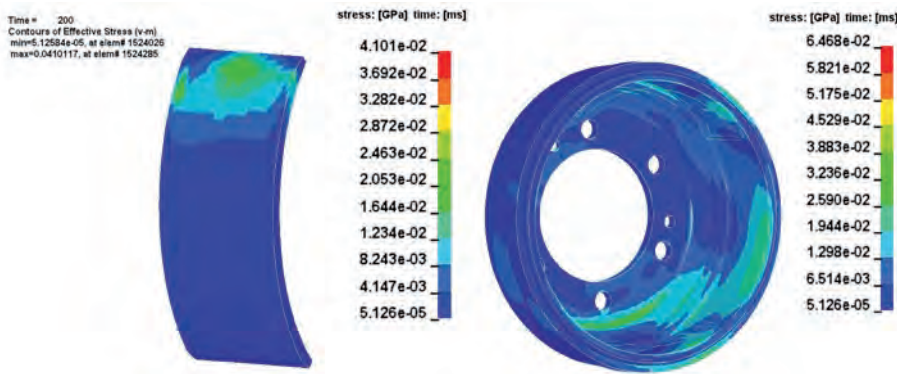


Fig. 1. Stress distribution in the brake lining and drum at the specific moment of time [10]

2. Description of numerical methods used in brakes studies

In order to model disc brakes mentioned earlier, commercial software LS-Dyna was used. This program utilizes method of direct integration of complete dynamic equation of motion using slightly modified central difference scheme. In this approach velocity and acceleration of a point are described as follows [13]:

$$\dot{x}_{n+\frac{1}{2}} = \frac{1}{\Delta t} \frac{1}{n+\frac{1}{2}} [x_{n+1} - x_n] \quad (1)$$

$$\ddot{x}_n = \frac{1}{\Delta t} \left[\dot{x}_{n+\frac{1}{2}} - \dot{x}_{n-\frac{1}{2}} \right] \quad (2)$$

Matrix equation of motion for nonlinear case is described as follows [13]:

$$M\ddot{x}_n = F_n^{ext} - F_n^{int} - C\dot{x}_n \quad (3)$$

where: M – global stiffness matrix, C – global damping matrix,

F_n^{ext} – external forces (vector) F_n^{int} – internal forces (vector).

As it was mentioned before, in each numerical model, contact conditions between lining and drum or disk were defined. It was assumed that friction coefficient in the lining-drum (disk) pair has constant value of $\mu = 0.4$ (chosen based on experimental data [14, 15]). Contact algorithm was based on penalty function approach [9,13]. Based on calculated friction forces, heat generation was computed using the following formula:

$$F_f \frac{dS}{dt} = mc_p \frac{dT}{dt} \quad (4)$$

where: F_f – friction force, S – distance of braking, t – time, m – mass, c_p – specific heat, T – temperature.

Due to the fact that braking time covered by analyses was short enough no convection and radiation were included in performed simulations.

3. Numerical model of disc brake

After studies on the brake drum, authors decided to conduct, in addition to the previous tests, analyses on disc brake setup. Obtained results gave a broader view of the phenomena occurring during the braking process and the possibility to support the design process of brakes by numerical analysis. Figure 2 shows the CAD model of discussed brake system.

At a later stage of investigation FE model was developed based on the CAD geometry.

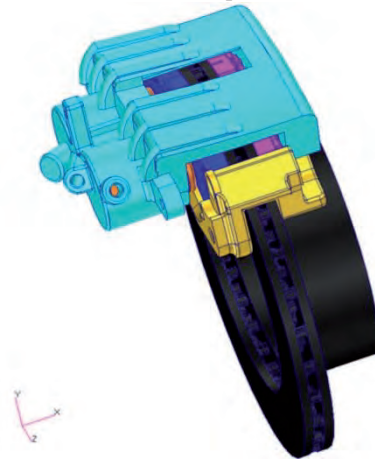


Fig. 2. CAD model of brake system with dual-piston clamping system [5]

Figure 3 shows the model of brake after discretization process. Due to the complex shape of the disc, it was modelled using tetragonal elements (TET4), while pads and lining were modelled using hexagonal solid elements (HEX8). Running belt test bench was modelled as a concentrated mass (with proper moments of inertia defined) connected to the disc via beam elements. The entire model consisted of approximately 150500 elements and 40300 nodes.

3.1. Initial and boundary conditions

Solution to the problem – involving solution of differential equations – requires initial and boundary conditions, i.e. adoption of appropriate loads (e.g. power, torque force, pressure) and constraints of FE model by taking back the degrees of freedom in the selected

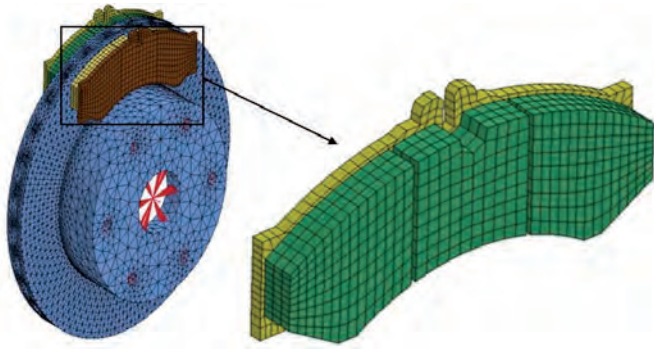


Fig. 3. Numerical model of the disc-brake system [5]

nodes. In addition, the solution must include constitutive equations with stress and displacement equilibrium conditions.

Each part of FE model was given the same material properties as in the drum brake model [10]. The disc was supported in the mounting holes (Fig. 4), which was an approximation of the actual conditions of restraint.

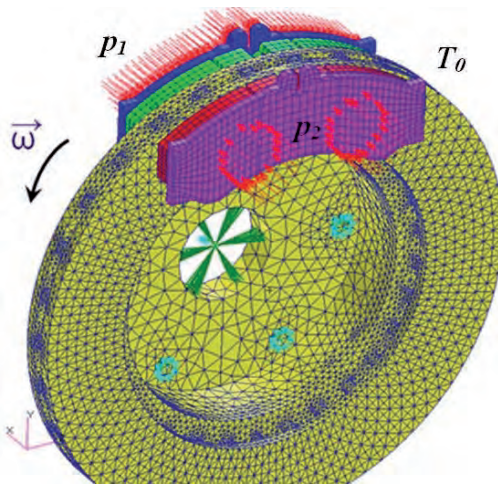


Fig. 4. Initial boundary conditions in the numerical model of disc brake system [5]

In areas of pistons and clamp interaction, pressure corresponding to this prevailing in the hydraulic system on the stand was applied to the pads ($p_1 = 6.238$ MPa at the calliper side and $p_2 = 25.858$ MPa at the pistons side). Also, the initial rotational velocity $\omega_0 = 42.0$ rad/s was applied to the disc and concentrated mass. Moreover, initial temperature $T_0 = 20^\circ$ (293 K) was prescribed to all nodes in the model.

3.2. Results of two-piston brake numerical analyses

The figures below shows the results of the two piston brake. Figure 5 shows distribution of the normal stress in lining: a) pushed against calliper, b) pushed against pistons, for a selected time $t = 0.4$ s.

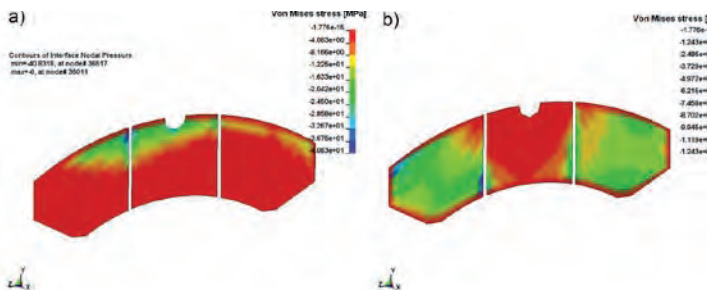


Fig. 5. Normal stresses on the brake pad surfaces at $t=0.4$ s, a) pressed using clamp, b) pressed using pistons

Above figures shows uneven work conditions of inner and outer lining. Based on this it can be concluded that this visible inequality can be resulted from the badly selected stiffness and geometry of the brake calliper. Thus, it was decided to modify the brake system.

3.3. Model of improved brake version

Based on the conducted research, it was decided that from the efficiency and economy point of view, the best direction of the brake design modification will be to apply additional pistons, keeping – if possible – outer dimensions of brake intact. The outcome was a three pistons brake, with altered calliper geometry, utilizing the same disc and the brake pads.

From the point of view of FEM modelling, the proposed design modifications were very small. The use of the same disc and pads allowed to use the same finite element mesh with initial conditions and constraints unchanged. The only change, compared to the original mode, was a different method of application of the pressure acting on the structure (Fig. 6). Applied pressure values were as follows: $p_1 = 55.954$ MPa outside of the calliper, $p_2 = 34.289$ MPa inside of the calliper, $p_3 = 22.408$ MPa external pistons and $p_4 = 21.279$ MPa middle piston.

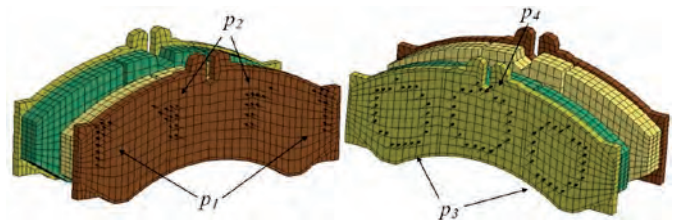


Fig. 6. Forces distribution in the triple-piston brake system

3.4. Comparative analysis

Applied modifications resulted in higher stresses on the surface of the pads. In order to compare working conditions of the structure before and after the modification, graphs of temperature versus time for both layouts (Fig. 7) and change of the rotational speed of the disc in time were prepared (Fig. 8). As expected, increasing the number of pistons resulted in increased pads downforce acting on disc. As a result, temperature raised and the brake disc deceleration increased.

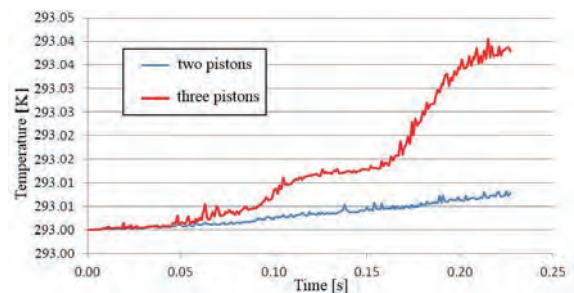


Fig. 7. Comparison graph of temperature versus time for the both cases

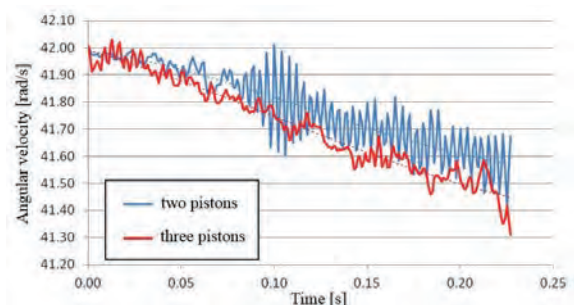


Fig. 8. Comparison graph of angular velocity versus time for the both cases

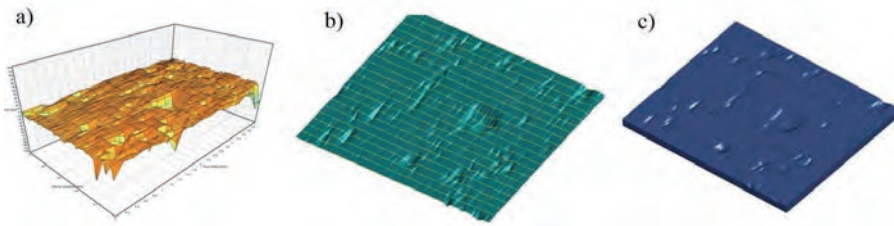


Fig. 9. Subsequent stages of the microscopic model development process; a) profilometer model, b) geometrical model, c) FE model

4. Microscopic model of pad lining

All the processes occurring on the surface lining, disc or drum, have their origin in micro areas of contacting bodies [7]. Therefore, authors decided to develop a numerical model of lining surface, in which surface roughness and the traces of destruction were mapped in the microscopic scale. This decision resulted also from the fact that such approach is difficult to implement in case of a global model of the braking system, where it is virtually impossible to introduce a fine mesh correctly reproducing roughness of a lining surface. The proposed microscopic scale modelling has enabled a more accurate numerical representation of the impact of surface roughness on the phenomena occurring on the surface of the friction lining. Figure 9 shows the successive stages of developin the numerical model of lining in microscopic scale. Whole process is described in more detail in [7].

Developed micro-sample had dimensions of 4 mm x 4 mm x 0.25 mm. It was modelled with 25600 solid hexagonal elements (HEX) with 32805 nodes. Both lining sample and counter sample were given material properties taken from literature. In order to simulate a braking process the linear velocity $v = 19.79$ m/s was applied to all lining sample nodes and pressure $p = 0.587$ MPa (Fig. 10) was applied on its upper surface. Initial and boundary conditions directly corresponded to conditions encountered during the experiment, which have been widely described in [6].

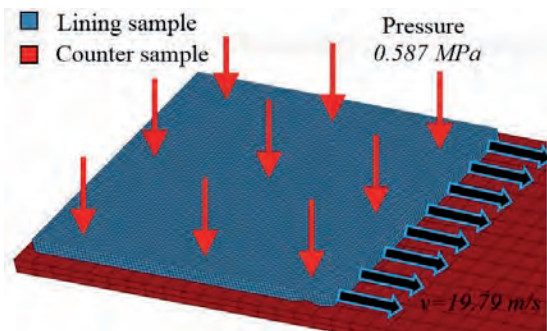


Fig. 10. Initial boundary conditions in the microscopic model [6]

4.1. Analysis results

From the carried out dynamic numerical analyses obtaining temperature distribution for sample as well as for counter-sample was ob-

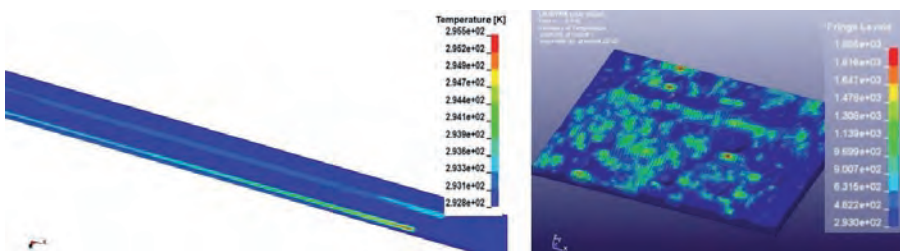


Fig. 11. Temperature distribution on the counter-surface and microscopic lining surface at the time $t=0.15$ s

tained. In Fig. 11 temperature result for a given time $t=0.15$ s is presented, while changes of temperature as a function of time for the highest peak and entire model of the sample is shown in Fig. 12.

Foregoing figures show that the maximum temperature is generated on the roughness peaks, which in combination with the conditions occurring during the braking process causes the grinding of these vertices, the propagation of wear and hot spots generation [7]. Taking all

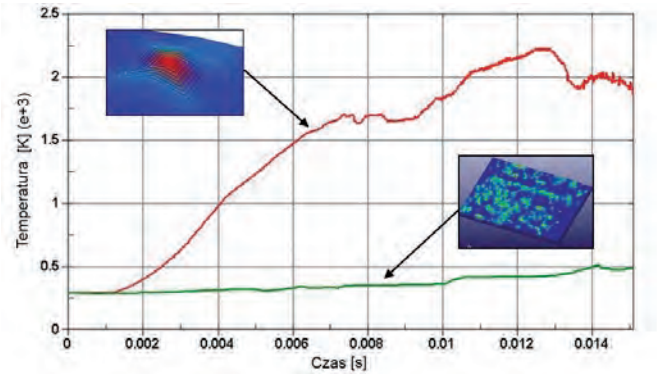


Fig. 12. Temperature versus time graph for the whole microscopic model and for the highest roughness peak

above into consideration, authors decided to reproduce the wear process of samples using SPH method in micro-scale.

4.2. Modelling of lining wear using SPH

Smooth Particle Hydrodynamics method (SPH) is a meshless method especially useful in simulation where large deformation of the material takes place, i.e., crash tests and fluid flow. It was developed in order to avoid significant reduction of accuracy generated by finite element mesh at large deformation. The main advantage of the SPH method is the lack of a mesh connecting the nodes.

The basis of this method is interpolation. Distributions of physical parameters replaced by the corresponding estimates at a given interpolation kernel [13] are given by:

$$\Pi^k f(x) = \int f(y)W(x-y, h)dy \quad (5)$$

where: W is approximation kernel.

Approximation kernel W has the following form:

$$W(x, h) = \frac{1}{h(x)^d} \theta(x) \quad (6)$$

where: d – number of space dimensions, h – smoothing length, defining distance at which particle can interact with other particles.

Finite elements of sample model were replaced by the hydrodynamics particles. Initial and boundary conditions were identical as for the FEM model in a microscopic scale. The one and a major difference between those two lied in the strain based eroding criterion allowing the pieces of material (SPH particles) to detach from the lining model. Figure 13 shows the results of

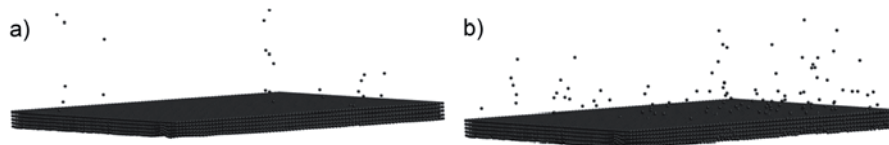


Fig. 13. SPH lining model erosion for the two chosen moment of time, a) $t = 0.08$ s, b) $t = 0.2$ s

the numerical analysis involving a process of failure of the sample for two specific moments of time.

Based on obtained results it can be seen, that the proposed implementation of algorithm of linings material failure works properly. It is difficult to clearly determine whether it fully reflect the real mechanics of material damage, but from numerical point of view, the procedure seems to work properly. To have a complete picture of the wear process nature used in the study, its exact characteristics and parameters should be measured and acquired. This would allow for more exact simulation of wear process. Despite the lack of such data, due to the promising effects of the application of meshless methods, authors decided to investigate and develop this approach much more thoroughly. At the moment researches on hybrid models involving a combination of FEM modelling techniques SPH are conducted. In Figures 14 and 15 an initial computational model is presented where

pads are modelled using SPH particles whereas the simplified brake disc is modelled using solid elements.

5. Conclusions

This paper presents the results of the investigations covering a broad phenomenon, which is certainly the braking process. After analysing the results it can be stated, that today, with the help of numerical methods, it is possible to perform detailed analysis of the brake during its operation. The main problems, however, are long calculation runtimes and hardware resources requirements. Also, the need for obtaining the full characteristics of the material as a function of temperature, which have a significant impact on the results, is an additional factor that hinders the use of numerical simulations in the brake design process. Another limitation is associated with FEM discretization, which should be detailed enough to include surface roughness and at the same time should give acceptable calculation time. Therefore, authors decided to conduct separate studies on macroscopic objects (drum brakes and disc) and microscopic (sample friction lining). The simulations results showed that the macroscopic approach allows for conclusions of the general nature of the brake (like the uniformity of pad work or comparative analyses), but is not enough detailed to predict the wear of pads, which – for example – prevents to predict life of the brakes.

The proposed concept of numerical description of the surface layer wear will be further modified and investigated, in order to find optimal parameters for modelling the process of wear. Authors hope that with combining the SPH method and FEM modelling it will be possible to simulate the braking process using numerical model of the whole brake and also to include such details as surface roughness in the calculations. At the moment, performing such analysis using the classical FEM and available hardware is practically impossible.

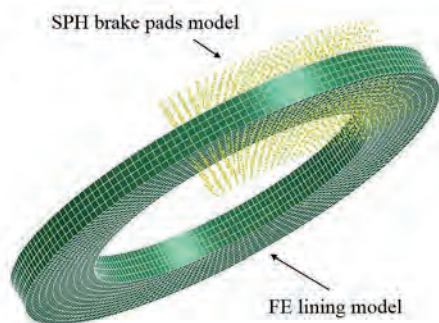


Fig. 14. Hybrid model (SPH+FEM) of the brake system

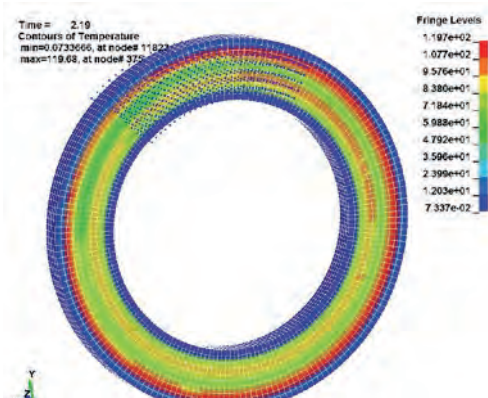


Fig. 15. Hybrid model of the brake system – temperature [K] distribution at the specific moment of time

References

1. Abu Bakar AR, Ouyangb H. Wear prediction of friction material and brake squeal using the finite element method, *Wear* 2008, 264: 1069-1076.
2. Adamowicz A, Grzes P. Influence of convective cooling on a disc brake temperature distribution during repetitive braking, *Applied Thermal Engineering* 2011, 31: 2177-2185.
3. Attanasio A, Ceretti E, Fiorentino A, Cappellina C, Giardinij C. Investigation and FEM-based simulation of tool wear in turning operations with uncoated carbide tools, *Wear* 2007, 263: 1175-1188.
4. Bagnoli F, Dolce F, Bernabei M. Thermal fatigue cracks of fire fighting vehicles gray iron brake discs, *Engineering Failure Analysis* 2009, 16: 152-163.

5. Baranowski P, Damaziak K, Jachimowicz J, Małachowski J, Niezgoda T. Badania numeryczne wybranego układu pojazdu specjalnego w aspekcie poprawy bezpieczeństwa, *Modelowanie Inżynierskie* 2011, 42: 19–26.
6. Baranowski P, Damaziak K, Małachowski J, Mazurkiewicz Ł, Kastek M, Polakowski H, Piątkowski T. Experimental and numerical tests of thermomechanical processes occurring on brake pad lining surface, *Surface Effects and Contact Mechanics* 2011, 10: 15–24.
7. Baranowski P, Małachowski J. Badania numeryczne zjawisk termomechanicznych występujących na powierzchni czarnej tarczy hamulcowej, *Wojskowa Akademia Techniczna*, 2010.
8. Belhocine A, Bouchetara M. Thermal analysis of a solid brake disc, *Applied Thermal Engineering* 2012, 32: 59–67.
9. Belytschko T, Liu WK, Moran B. *Nonlinear Finite Elements for continua and structures*, John Wiley & Sons, 2000.
10. Damaziak K, Małachowski J, Sybilski K, Jachimowicz J. Analiza numeryczna obszaru współpracy pomiędzy okładziną i bębnem hamulcowym, *Górnictwo Odkrywkowe* 2010, 4(51): 84–88.
11. Dmitriev AI, Osterle W. Modelling of brake pad-disc interface with emphasis to dynamics and deformation of structures, *Tribology Int.* 2010, 43: 719–727.
12. Fouvry S, Paulin C, Liskiewicz T. Application of an energy wear approach to quantify fretting contact durability: Introduction of a wear energy capacity concept, *Tribology Int.* 2007, 40: 1428–1440.
13. Hallquist JO. *LS-Dyna. Theory manual*, California Livermore Software Technology Corporation, 1998.
14. Kajka R, Harla R. Raport 26/LW/2009. Instytut Lotnictwa, Warszawa, 2009.
15. Kajka R, Harla R. Raport 27/LW/2009. Instytut Lotnictwa, Warszawa, 2009.
16. Lei W, Zefeng W, Wei L, Xuesong J. Thermo-elastic-plastic finite element analysis of wheel/rail sliding contact, *Wear* 2011, 271: 437–443.
17. Lodygowski A, Voyiadjis GZ, Deliktas B, Palazotto A. Non-local and numerical formulations for dry sliding friction and wear at high velocities, *Int. J. of Plasticity* 2011, 27: 1004–1024.
18. Müller M, Ostermeyer GP. A Cellular Automaton model to describe the three-dimensional friction and wear mechanism of brake systems, *Wear* 2007, 263: 1175–1188.
19. Nowicki B. *Chropowatość i falistość powierzchni*. WNT, Warszawa, 1991.
20. Popova VL, Psakhie SG. Numerical simulation methods in tribology, *Tribology Int.* 2007, 40: 916–923.
21. Qi HS, Day AJ. Investigation of disc/pad interface temperatures in friction braking, *Wear* 2007, 262: 505–513.
22. Rojek J. Modelowanie i symulacja komputerowa złożonych zagadnień mechaniki nieliniowej metodami elementów skończonych i dyskretnych, *Prace IPPT*, Warszawa, 2007.
23. Ścieszka S. F.: *Hamulce czarne*. Gliwice-Radom, WZP-ITE, 1998.
24. Shahzamanian MM, Sahari BB, Bayat M, Mustapha F, Ismarrubie ZN. Finite element analysis of thermoelastic contact problem in functionally graded axisymmetric brake disks, *Composite Structures* 2010, 92: 1591–1602.
25. Söderberg A, Andersson S. Simulation of wear and contact pressure distribution at the pad-to-rotor interface in a disc brake using general purpose finite element analysis software, *Wear* 2009, 267: 2243–2251.
26. Subutay SA. Modelling of subsurface deformation and damage in an aluminum-silicon alloy subjected to sliding contact, *Dissertation*, Windsor, Ontario, Canada, 2006.

Paweł BARANOWSKI, M.Sc. (Eng.)

Krzysztof DAMAZIAK, M.Sc. (Eng.)

Jerzy MAŁACHOWSKI, Ph.D., D.Sc. (Eng.), Assoc. Prof.

Department of Mechanics and Applied Computer Science

Faculty of Mechanical Engineering

Military University of Technology

Gen. S. Kaliskiego 2, 00-908 Warsaw, Poland

E-mails: pbaranowski@wat.edu.pl, kdamaziak@wat.edu.pl,

jerzy.malachowski@wat.edu.pl

Sławomir DUDA

NUMERICAL MODELING AND SIMULATING THE DYNAMIC INTERACTIONS WITHIN THE DRIVE SYSTEM OF ELECTRIC RAIL VEHICLES

MODELOWANIE I SYMULACJA NUMERYCZNA ODDZIAŁYWAŃ DYNAMICZNYCH W UKŁADZIE NAPĘDOWYM ELEKTRYCZNYCH POJAZDÓW SZYNOWYCH*

This paper shows the methodology that can be used to study the dynamic phenomena occurring in rail vehicle drive systems by taking into account its actual seating. The studies are performed by providing a detailed description of electromagnetic phenomena found in drive motors and contact phenomena at the interface between the wheel and rail. Forces determined based on the models below constitute the load of a rail vehicle drive system. The mathematical model of the motor has been implemented in Matlab/Simulink software and coupled with the vehicle model developed in the Simmechanics application. These models make it possible to determine the load of drive system for various vehicle dynamic states (startup, steady-state operation) depending on the locomotive load.

Keywords: rail vehicle, electromechanical drive system.

W niniejszej pracy przedstawiono metodologię, która może być zastosowana do badania zjawisk dynamicznych w układach napędowych pojazdów szynowych z uwzględnieniem rzeczywistego ich osadzenia. Badania są realizowane przy szczegółowym opisie zjawisk elektromagnetycznych w silnikach napędowych oraz zjawisk kontaktowych na styku współpracy koła z szyną. Wyznaczone z powyższych modeli siły stanowią obciążenie układu napędowego pojazdu szynowego. Sformułowany model matematyczny silnika zaimplementowano w programie Matlab/Simulink i sprzężono go z modelem pojazdu opracowanym w programie Simmechanics. Modele te umożliwiają na wyznaczenie obciążenia układu napędowego, dla różnych stanów dynamicznych pojazdu (rozruch, praca ustalona) w zależności od obciążenia lokomotywy.

Słowa kluczowe: pojazd szynowy, elektromechaniczny układ napędowy.

1. Introduction

In many contemporary mechanical systems the structural deformability plays a key role. The numerical approach to analyzing the kinematics and dynamics of deformable multi-member systems originates from classical methods described in literature [2, 3]. Their common feature is the assumption that the absolute motion of any mechanism component is decomposed into the basic motion of components superimposed by small elastic deformations. It signifies that in the case of elastic deformations the lack of their influence on the system motion is assumed, while internal forces, resulting from this motion, play a key role in creating the deformations of individual mechanism components. Therefore the analysis of multibody system of rigid bodies is used to examine the internal forces introduced as external forces to solve the problem of component deformation. The main limitation of this approach is the necessity to assume the linearity of deformations, which eliminates significant non-linear effects from analysis results.

In the past, many papers on modeling rail vehicle drive systems, were based on the assumption that the system consisted of rigid bodies or that the elastic deformations generated as a result of dynamic interactions had little importance or were just negligible.

Investigating the dynamic phenomena of rail vehicle drive systems when not including the very vehicle leads to oversimplification. The load of drive system is very complex. On the one hand, there are forces coming from the electric motor constituting the drive of the vehicle, and being also, in some locomotive models, electrically coupled with the drives of remaining axles; on the other hand, there are forces coming from the interaction between the wheel and the rail.

These forces are determined by the travel of the very vehicle, and this vehicle movement results from the application of these forces. It is undoubtedly the coupling between the drive system dynamics and the vehicle dynamics that makes it necessary to take into account the real seating of rail vehicle drive system in the body constituting the vehicle chassis.

2. Modeling the drive system of an electric locomotive

Modeling the dynamics of machine or vehicle drive systems is especially significant for receiving information on dynamic phenomena, such as start-up or braking. The model of drive system and power transmission from the driving motor to wheels should take into account the dynamic analysis performed. In high power systems, it is important to develop a model that would describe transverse-torsional vibrations. It allows us to include the transverse rigidity of drive system components, as well as the rigidity and slackness of bearings.

One of the methods for constructing a physical model used to study the dynamics of machine drive systems is the so-called hybrid method [9], constantly developed by the employees of the Department of Theoretical and Applied Mechanics of the Silesian University of Technology in Gliwice. It consists in representing a real system using rigid and finite elements. In this method components featuring a clear flexibility, including long shafts, are modeled by using a two-node beam element, and the disks of the toothed wheels or e.g. clutches as rigid elements. Individual drive system components, constituting subsystems, are connected by a proper kinematic pair modeling the

(*) Tekst artykułu w polskiej wersji językowej dostępny w elektronicznym wydaniu kwartalnika na stronie www.ein.org.pl

assumed relative motion of elements connected by this pair. In addition, individual subsystems can interact with each other by forces or torques resulting from the action of force generation components, e.g. a spring or a damper (a leaf spring or shock absorber), a force resulting from the deformations of flexible components (deflection of a toothed wheel in the toothed gear, deflection of bearing rolling components). Proper models for a toothed gear used to construct the physical model of the drive system of the rail vehicle under analysis have been described in papers [9].

A dynamic equation for the drive system motion in the matrix method can be expressed in the following form:

$$\mathbf{M}\ddot{\mathbf{q}}(t) + \mathbf{B}\dot{\mathbf{q}}(t) + \mathbf{K}\mathbf{q}(t) = \mathbf{f} \quad (1)$$

$$\mathbf{q} = [\dots, u_i, v_i, \psi_i, w_i, \theta_i, \varphi_i, \dots]^T \quad (2)$$

where: \mathbf{M} , \mathbf{B} , \mathbf{K} – are, respectively, the matrices of inertia, damping and rigidity, \mathbf{f} – column matrix for generalized forces.

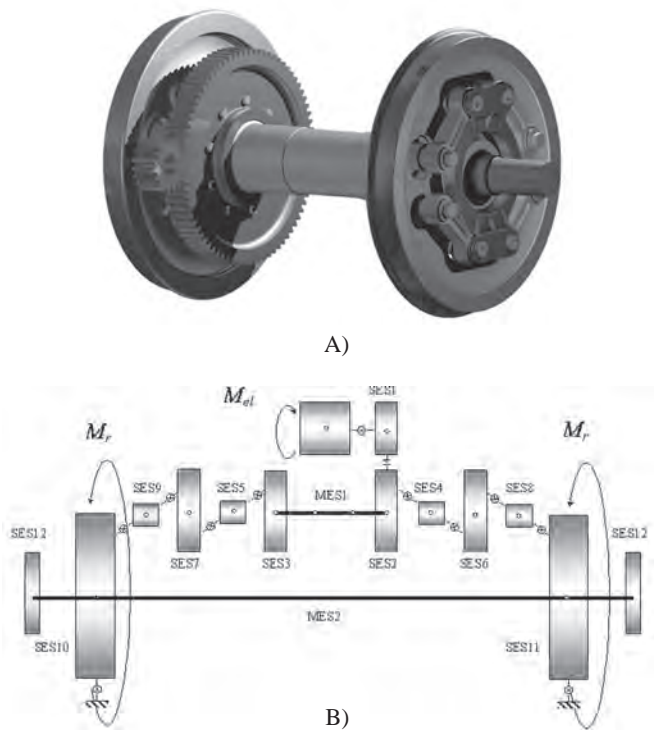


Fig. 1. A) CAD model of the driving system, B) Physical model of a railway vehicle with the use of hybrid method (Lumped-Parameter Method, Finite-Element Method)

The above-presented approach to modeling drive systems assumes system motion described in generalized coordinates with holonomic constraints. This model makes it possible to analyze the transverse-torsional vibrations of rail vehicle drive system forced by operating conditions. Active forces applied on the system result from driving torque and contact torques generated as a result of interactions between the wheel and rail. In this case numerical calculations for the drive system model are performed separately for the whole vehicle model, assuming that the elastic deformations of drive system do not affect the vehicle travel, while contact forces (wheel – rail interface), resulting from this travel play a key role in generating deformations in individual drive system components. This method can be especially useful for analyzing torsional vibrations.

Another solution for the analysis of drive system dynamics is to build a model based on the multibody system formalism. Then, the drive system model and the vehicle model constitute an integral whole. However, it results in creating a complex, multiple-free-of-freedom model, generating considerable calculation costs.

3. Modeling an electric rail vehicle

Studying the dynamic phenomena in complex electro-mechanical systems requires adopting a physical model of the real object under analysis, representing its most significant features and phenomena, required from the point of view of dynamics analysis performed. This model frequently constitutes a compromise between the accuracy in object representation and the complexity of describing phenomena occurring in this object, thus affecting the credibility of the solution obtained, duration of simulation, and in extreme cases, the opportunity to obtain any solution. In the case of electromechanical systems, the drive parts – both mechanical and electrical – are mutually coupled dynamic systems. To analyze dynamic phenomena, especially in unstable conditions, it is necessary to use the model allowing for implementing an electro-mechanical feedback [5].

The electromagnetic and mechanical systems of the electric rail vehicle powertrain couple mutually through electromagnetic torque (M_e) and angular rotor velocity (ω). Because of the rail vehicle system presented in Fig. 2, an analysis of dynamics in railway vehicles and the driving system coupled with it must take into account the analysis of electromagnetic and mechanical systems.

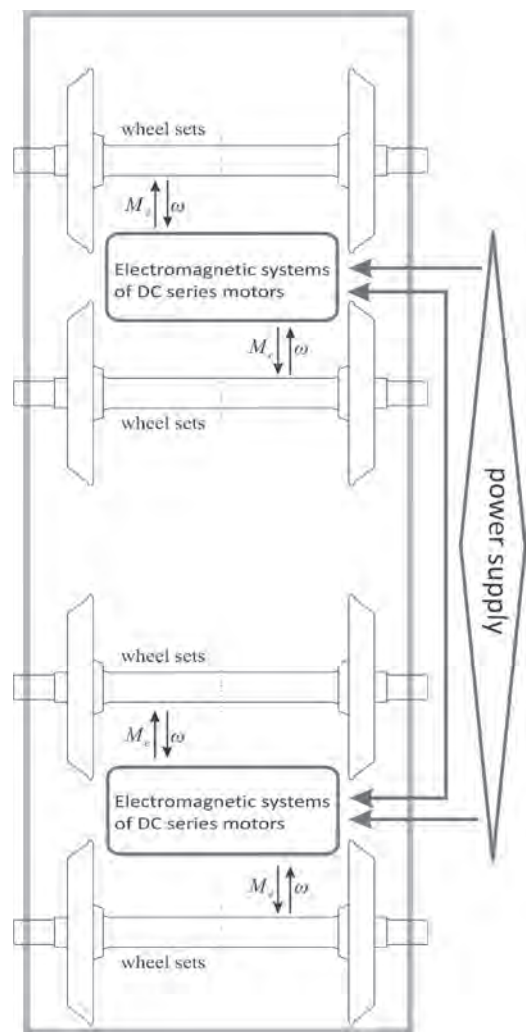


Fig. 2. Structure of a driving system

Taking into account the unique character of the solution for the electric locomotive driving system (type of its electric motor, number of motors and the configuration of their connections), further down the paper presents an electromagnetic model of the locomotive chosen for further analysis. For this purpose electric locomotive type EU07 has been chosen [1]. In spite of being aware that this is a bit obsolete locomotive, this one was chosen because of easy access to construction documentation making it possible to model this vehicle in a virtual space to determine the basic features of the vehicle, including its weight and moment of inertia, necessary to build a mechanical system model.

In their operation mode the traction motors of the EU07 locomotive operate in two configurations. During start-up four motors are connected in series; then, to increase the voltage the motors are switched over to a parallel circuit, two motors per branch. A serial locomotive motor connection was analyzed.

A substitute schematic diagram for motor circuits connected in series has been adopted for the need of modeling (Fig. 3).

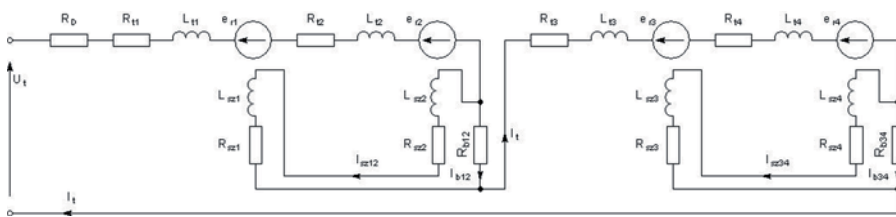


Fig. 3. Assumed substitute diagram of series connected electric motors for switching program of contactors 0÷27

For the above-adopted schematic diagram, voltage equations for circuits and physical connections were formulated [1]. Individual symbols presented in Fig. 3. have the following meaning: I_t – traction motor armature current, I_{sz12} , I_{sz34} – currents conducted by excitation windings in motors S1, S2 and S3, S4, k_{Ei} – machine constants, ϕ_{ni} – streams at normal excitation, $f(I_{sz})$ – relative non-linear magnetizing characteristics (Fig. 4), R_{ti} – armature resistances, R_{b12} , R_{b34} – shunt resistances for excitation winding, R_{sz} – serial circuit resistances, R_D – total of additional resistances, L_{sz} , L_t – inductance for excitation windings, ω_i – rotor angular velocities, e_{ri} – voltages induced in armature circuits.

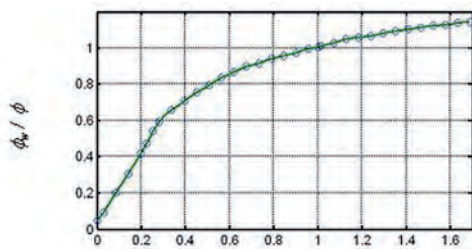


Fig. 4. Relative magnetizing characteristic

As a result of analyzing the construction form of a rail vehicle, a physical model of the vehicle has been created in the form of a multi-rigid-body (Fig. 5) system mutually coupled with proper kinematic pairs and elastic and damping components, and then its interpretation in SimMechanics application was obtained. The necessary parameters describing a model, including weights, moments of inertia and dimensions determining the position of kinematic pairs were obtained from a 3D model, created by using the Autodesk Inventor software. Remaining parameters, i.e. rigidity and suspension components damping for the first and second unsprung mass reduction, were obtained in the documentation submitted by the Zakłady Naprawcze Lokomotyw Elektrycznych (Electric Locomotive Repair Plant) in Gliwice, Poland.

Studying the dynamics of electric rail vehicles requires creating three intercoupled models: a vehicle model including drive system

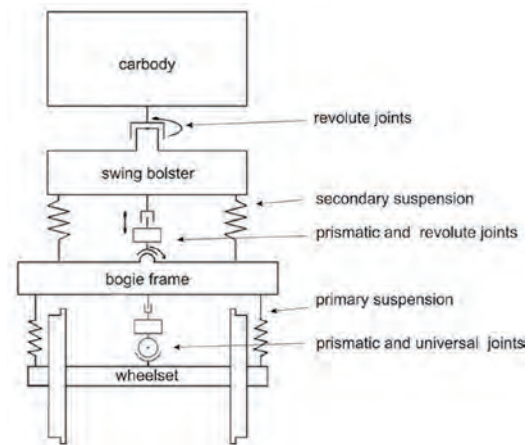


Fig. 5. Physical model of the vehicle under consideration

models, a rail model, and a model for the wheel – rail interface. At the first stage of rail vehicle modeling process, during its travel on the railway track the subsystem models are built separately. Then, the models are interconnected to make a complete system. This method was implemented in proprietary software created in the Matlab environment. The calculation algorithm used to analyze the rail vehicle travel on any railway track is presented in the form of a schematic diagram in Fig. 6.

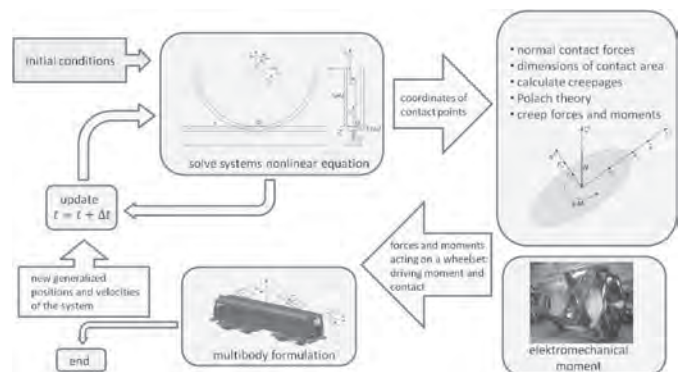


Fig. 6. Calculation algorithm used to analyze the rail vehicle travel dynamics on any railway track

The presented algorithm used to develop the computer program for analyzing the rail vehicle travel dynamics on any railway track can be expressed in a few steps [4, 6, 7, 8]:

- Assuming initial conditions for generalized coordinates $\mathbf{q}(t^0)$ and generalized velocities $\dot{\mathbf{q}}(t^0)$, as well as determining initial surface parameter values $s_r(t^0)$, $u_r(t^0)$, $s_w(t^0)$ and $u_w(t^0)$ related to a specific wheel-rail pair;
- Solving a non-linear equation system to obtain the surface parameters that determine the contact point coordinates related to a specific wheel - rail pair;
- Calculating normal forces during the contact that are generated as a result of the wheel-rail interaction and depend on the contact surface size;

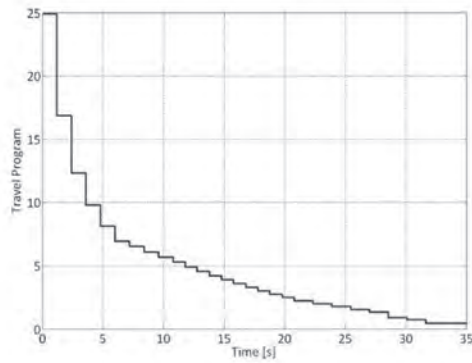


Fig. 7. Travel program

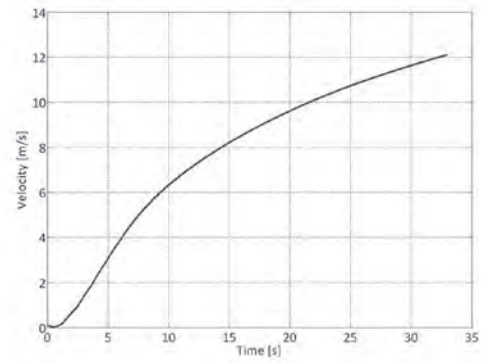


Fig. 8. Velocity of the first wheelset center of mass as a function of time

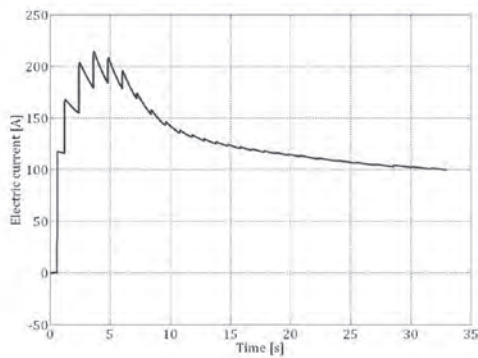


Fig. 9. Course of changes in the electric current of the stator in the auxiliary circuit of motor connections in a serial system as a function of time

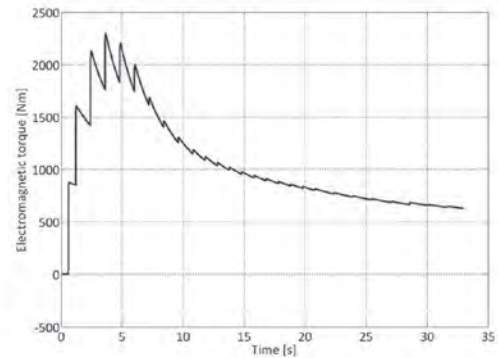


Fig. 10. Course of variations in an electromagnetic torque on the S1 motor as a function of time

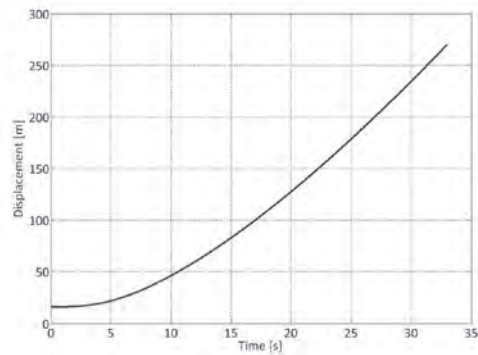


Fig. 11. Displacement of the first wheelset center of mass as a function of time

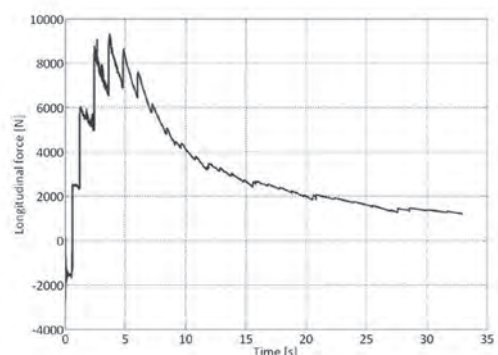


Fig. 12. Longitudinal force at the point of contact of the rail with the left wheel of the first wheelset as a function of time

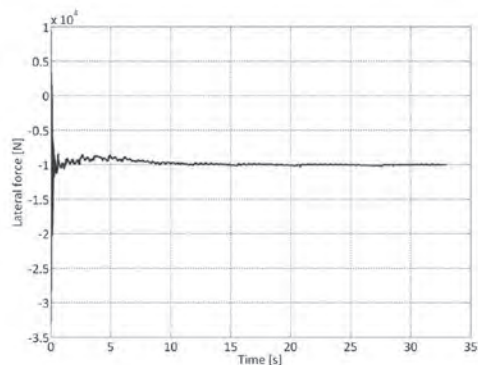


Fig. 13. Lateral force at the point of contact of the rail with the left wheel of the first wheelset as a function of time

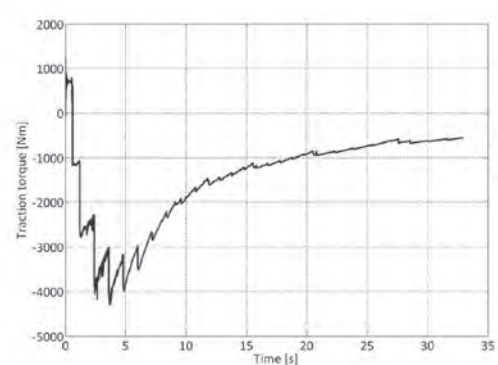


Fig. 14. Traction torque at the point of contact of the rail with the left wheel of the first wheelset as a function of time

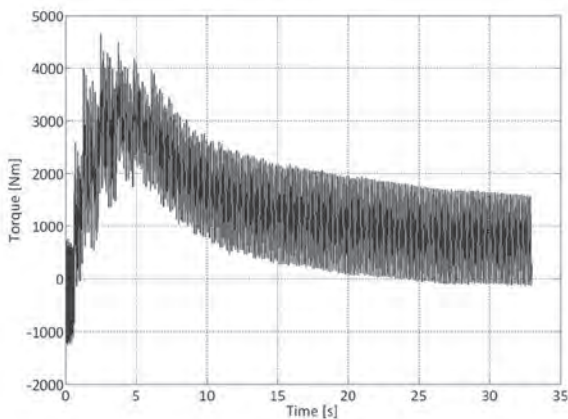


Fig. 15. Torque in the selected pair of the driving system

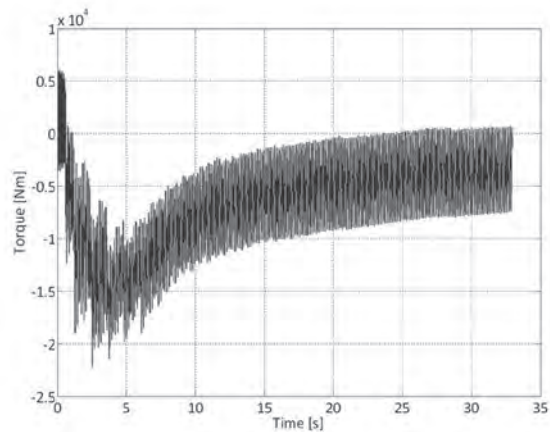


Fig. 16. Torque in the selected pair of the driving system

- Calculating micro slides, tangent micro slides and spin moments generated as a result of the wheel-rail interaction;
- Determining the drive torques for each axle of the wheelset separately,
- Adding the forces and torques occurring in the contact, related to each wheel, as well as adding drive torques to the vector of external forces acting on the system. Using the multi-member system formalism to obtain a solution, new generalized system positions and velocities for subsequent time step $t + \Delta t$;
- Updating the system for another moment by adopting initial data from the previous step to determine non-generalized surfaces related to each wheel-rail pair;
- Continuing the whole process for a new time step until final time for the analysis performed is obtained.

Studies have been performed using the adequate models of:

- The vehicle developed based on the multi-member system formalism in the Matlab/SimMechanics software,
- Discrete dynamic models for the electromechanical drive system, developed by using the Matlab/SimMechanics software and the Matlab application script,
- Electric motor connections constituting the rail vehicle drive system developed by using the Matlab/Simulink software,
- The wheel-rail contact, used to determine the support and guide forces developed by using the proprietary script package from the Matlab software.

4. Numerical simulation of a rail vehicle travel and dynamic interactions in drive system kinematic pairs

As a result of numerical calculations performed, the curves of changes in drive system parameters, displacements, vehicle velocities as well as contact forces and torques for the travel program presented in Fig. 7 (contact switch over for connecting motors in serial mode) are obtained.

For the case under analysis, in the case of the straight-line start-up of a rail vehicle, the examples of curves for the changes of torsional

torque in selected kinematic pairs, Fig. 15 – between the large and small toothed wheels (SES1 – SES2, Fig. 1), Fig. 16 – between the modeling element for the wheelset and the cross joint (SES8 – SES11, Fig. 1) are presented. As shown in Figures presented (Fig. 15 and 16), the external load has a significant impact on the vibration profile of the signal.

5. Final conclusions

Each mechanism has its operating life. Therefore, for economic reasons it is important to properly determine the dates of overhauls or just for routine periodic inspections. It can be obtained by having a thorough knowledge of dynamic phenomena occurring in the system under analysis, by applying numerical simulations performed on the adequate vehicle model. One of the most susceptible to wear and tear and important part of a rail vehicle is its drive system.

Using the methods of numerical modeling and simulation to provide dynamic analyses in the kinematic pairs of electric rail vehicle makes it possible to identify the state of loads for system components under different operating conditions and it can constitute a basis for forming vehicle traction characteristics effectively. Such studies can be successfully used both to modify the existing objects and to assist the design-construction process for the prototypes of new vehicles.

The developed vehicle model, in the form of an electro-mechanical system including dedicated programs used to determine vehicle support and guiding forces, makes it possible to obtain:

- the curves of kinematic parameter changes at selected model points (for displacements, velocity and acceleration values), mutual interaction forces in individual kinematic pairs and the wheel-rail interface;
- point of interface between the wheel and rail (separately for its rolling part and flange), the dimensions of contact ellipses on the rail and wheel surface, including the places where they occur.

The presented results for computer simulations allow us additionally to come to the conclusion that the algorithms developed are general in their character and can be successfully used to determine the constructional features of similarly constructed electro-mechanical systems.

Acknowledgement: This paper is realized within the framework of research project No. 6700/B/T07/2011/40 funded by National Science Centre in Poland.

References

1. Duda S. Electromechanical model of electric locomotive EU07 (in Polish). Modelowanie Inżynierskie; 2011 41 (3): 47–54.
2. Geradin M, Cardona A. Flexible Multibody Dynamics. A Finite Element Approach. John Wiley & Sons, LTD 2001.

3. Gonçalves J, Ambrósio J. Advanced Modeling of Flexible Multibody Systems using Virtual Bodies, NATO ARW on Computational Aspects of Nonlinear Structural Systems with Large Rigid Body Motion, (J. Ambrósio, M. Kleiber, Eds.), IOS Press, The Netherlands.
4. Lankarani HM, Nikravesh PEX. A Contact Force Model with Hysteresis Damping for Impact Analysis of Multibody Systems, AMSE Journal of Mechanical Design, 1990, 112, 369–376.
5. Mężyk A. Analiza i kształtowanie cech dynamicznych napędów elektromechanicznych. Monografia, Gliwice 2001.
6. Polach O. A Fast Wheel-Rail Forces Calculation Computer Code. Vehicle System Dynamics, 1999; Supplement 33: 728–739.
7. Pombo J, Ambrósio J. General Spatial Curve Joint for Rail Guided Vehicles: Kinematics and Dynamics, Multibody Systems Dynamics, 2003; 9: 237–264.
8. Shabana AA, Zaazaa KE, Sugiyama H. Railroad Vehicle. Dynamics. A Computational Approach. Taylor & Francis Group 2008.
9. Świtoński E. i in.: Modeling of mechatronic drive systems (in Polish). Wydawnictwo Politechniki Śląskiej, Gliwice 2004.

Sławomir DUDA, Ph.D. (Eng.)

Department of Theoretical and Applied Mechanics

Silesian University of Technology

ul. Konarskiego 18A, 44-100 Gliwice, Poland

E-mail: Sławomir.Duda@polsl.pl

Marek ROŚKOWICZ
Tomasz SMAL

RESEARCH ON DURABILITY OF COMPOSITE MATERIALS USED IN REPAIRING AIRCRAFT COMPONENTS

BADANIE MATERIAŁÓW KOMPOZYTOWYCH WYKORZYSTANYCH DO NAPRAWY KONSTRUKCJI LOTNICZYCH

The paper presents methodology and results of research on durability of composite materials, which were applied to expedient repair of damaged aircraft components. Numerical calculation and experimental tests were conducted during research. The obtained results proved that failure of aircraft components is connected with local loss of stability in case of aircraft's skin and stiffness in case of girders and beams. The damaged components were repaired with the use of a metal insert and a composite patch. The use of a metal insert, which had the same stiffness as repaired elements, was a solution which allowed to restore local stiffness of repaired components. Composite patches which were formed with glass, carbon or aramid fabrics impregnated with epoxy resins, also created an adhesive bonds and joined all elements of repaired zone. The experimental tests proved that the executed repairs whose time was limited to 120 minutes improved stability, stiffness and fatigue life of the repaired components.

Keywords: failures of aircraft, expedient repair, composite materials, composite patch, research on durability of composite materials.

W artykule zaprezentowano metodologię i wyniki badań wytrzymałościowych materiałów kompozytowych, które zostały zastosowane do naprawy doraźnej elementów konstrukcji lotniczych. Podczas badania wykorzystano obliczenia numeryczne i badania eksperymentalne. Otrzymane rezultaty dowodzą, że uszkodzenie elementów konstrukcji lotniczych związane jest z lokalną utratą stateczności, w przypadku poszycia samolotów, oraz utratą sztywności, w przypadku belek i żeber. Uszkodzone elementy zostały naprawione z użyciem metalowej wkładki usztywniającej iłaty kompozytowej. Użycie wkładki o tej samej sztywności co naprawiany materiał pozwoliło odzyskać sztywność w trefie uszkodzenia. Łaty kompozytowe, które zostały uformowane z wielu warstw tkaniny (szklanej, węglowej i aramidowej) i nasączone żywicą epoksydową, pozwoliły na utworzenie złącza klejowego, w ramach którego scalono wszystkie elementy węzła naprawczego. Badania eksperymentalne dowiodły, że przeprowadzone naprawy, których czas był ograniczony do 120 minut, poprawiły stateczność, sztywność i trwałość zmęczeniową naprawionych komponentów.

Słowa kluczowe: uszkodzenia samolotów wojskowych, naprawa doraźna, materiały kompozytowe, lata (nakładka) kompozytowa, badanie wytrzymałości materiałów kompozytowych.

1. Introduction

Composites are often used in airplane structures because of their specific strength [5]. Therefore, the repairs with use of composite materials are an effective method of damages removal in case of aircraft components. The composite materials are bonded to the damaged structure with adhesives. The repairs executed with the use of composites are particularly accepted in relation to thin skin elements, which are made of aluminum alloy [7]. The skins repairs include cracks of air components, dents and material losses of fuselage and wings skin [1, 3].

An assessment of repair feasibility is an important stage of preparation and execution of repair. There is a lack of standard guidelines which may be used to perform a repair. Individual airplanes manufacturers create their own repair procedures for certain products. The procedures present a scope and technology of repairs without specific criteria. The assessment of repair feasibility requires defining the scope of repair and effect of damage to adjacent structure elements [2]. The experiences of some companies providing repair of airplane components show that the general principle of repair designing and

its execution is reduction of a damaged component safety coefficient to a level not lower than 1.2. The assessment of safety coefficient changes can be provided with the use of modern numerical calculation systems [6, 9].

2. Methodology of research

The opportunities of repair of damaged components were assessed with use of chosen composite materials. The composite patches were shaped in order to substitute metal plates and riveted joints were replaced with adhesive joints. A repair of skin components was researched on the basis of "TS-8 Bies" aircraft and a repair of girders and beams was researched on the basis of "Su-22" aircraft.

The numerical calculations were used to assess the effect of defects in the research aircraft components. The numerical calculations were conducted with finite elements method (Nastran/Patran software environment). Hexagonal elements of HEX8 type were used to create numerical model. The loads were modeled with elements of RBE 3 type.

(*) Tekst artykułu w polskiej wersji językowej dostępny w elektronicznym wydaniu kwartalnika na stronie www.ein.org.pl

The experimental research studies on composite materials used in repairing of aircraft skin, were conducted with use of a research stand. The stand was constructed especially for planned tests, in order to verify the conclusions of numerical calculations and assess the repair feasibility of damaged component with use of composites (Fig. 1). The horizontal tail of "TS-8 Bies" aircraft was mounted in the frame, which was bolted to the forceful floor. The loads were generated with hydraulic actuator controlled by HNC 100 controller of Rexroth Bosh company. The actuator with tail was also mounted on the special frame.

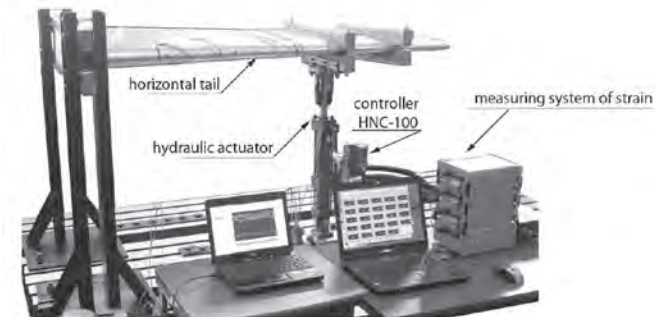


Fig. 1. The research stand with strain gauge bridge of National Instruments and ESAM Traveller Company

The strain gauges were used to measure strain in tail skin. The strain gauges were arranged on the surface of skin according to the scheme presented in the Fig. 2.

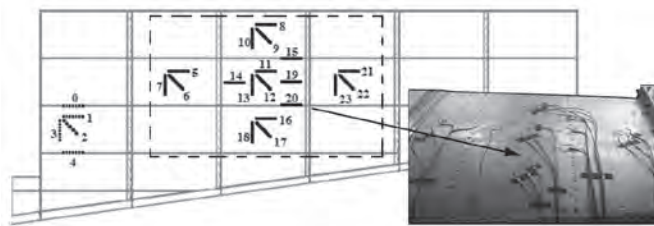


Fig. 2. The arrangement of strain gauges on the surface of tail skin

The effectiveness of girder repair was checked by a comparative analysis of stiffness of girder which was undamaged, damaged and repaired. The stiffness was determined during bending tests. The fixing method of the tested girder and the used research stand is presented in the Fig. 3. The distance between supports was 717 mm and the girder was loaded between supports with use of loading stanchion. A change in strain of the loaded girder was determined in function of the force. A strain sensor was mounted under flange of the girder. On the basis of the obtained results it was possible to assess an effectiveness of applied repairs.



Fig. 3. Method of a girder mounting in the research stand

3. Research on composite materials used in repairing aircraft skin

3.1. Numerical calculations of damaged skin structure

A model of "TS-8 Bies" aircraft horizontal tail was generated in order to execute numerical calculations. The horizontal tail was built with skin, stringers, ribs and two girders: front and rear. The geometric model of plane tail was generated (Fig. 4) with particular emphasis on accurate mapping of its individual components.

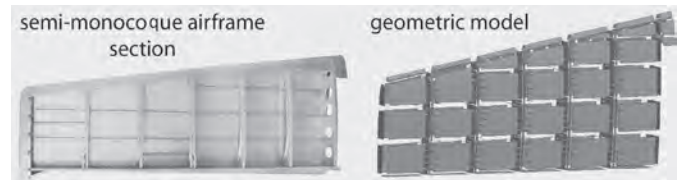


Fig. 4. The section of "TS-8 Bies" aircraft horizontal tail and its geometric model

On the basis of the geometric model, numerical model was generated which included elements of SHELL type (skin, beams, girders' skin) and elements of BAR type (stringers and girder's flange). There were boundary conditions (loads and mounts) assumed which correspond with the method of the tail mounting on the testing machine.

The numerical model was loaded in the same way as the real component in the experimental research. It was assumed that the external force would have value of 1000 N when loading the tail. The value was determined in the analysis, which described ultimate loads for this type of semi-monocoque airframe [7]. The same material features were assumed for all finite elements of model, i.e. duralumin 2024T4. The stress and strain distribution was analyzed in the undamaged and damaged tail during numerical calculations. The damage was modeled in the shape of a hole with a diameter of 100 mm, which was located in the middle of tail skin (Fig. 5).

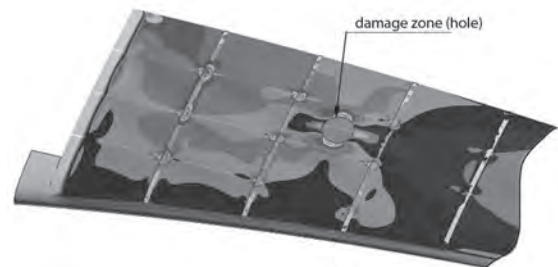


Fig. 5. The model of a tail with damage in the shape of a hole located in the middle of the skin between supporting girders of the generated airframe

The comparison of reduced stress distribution in the damaged and undamaged zone is presented in the Fig. 6. In the area of damage accumulation of stress was observed. More than twofold increase in stress was noticed in the direction parallel to the tail girder and decrease in stress was noticed in the direction parallel to the stringers. This kind of changes in the skin is specific in case of loss of local stability of the skin (in the zone between stringers and girders). On the basis of numerical calculations it was assumed that due to the damage, the changes in stress and strain are limited to skin zone bounded by ribs and stringers. The changes occur to the minimum extent outside these strengthening elements. Simultaneously, the numerical calculations prove that the damage caused a greater effort of supporting elements, i.e. ribs and stringers directly adjacent to the damaged zone. At the same time it was observed that the rivet joints between the supporting components and the skin carried greater loads.

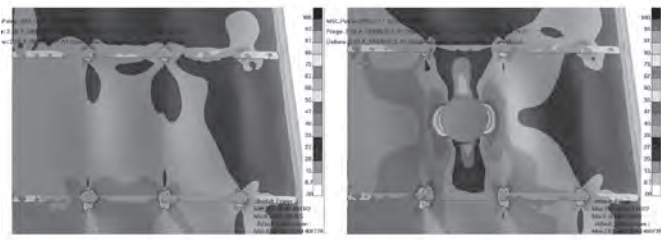


Fig. 6. The comparison of stress distribution in the tested tail: undamaged zone (on the left), damaged zone (on the right)

Taking into account the obtained results it seems that the main criteria of repair of a thin semi-monocoque airframe, which does not include supporting components, are stiffness reconstruction of skin in the damaged zone and sustaining stability of repaired element.

3.2. The experimental verification

The experimental tests were conducted in order to verify the obtained results of numerical calculations. The research on strain in the skin; in statically loaded structure was conducted before damage and after damage. The damage was in the shape of a hole with a diameter of 60 mm and was made by milling in the upper skin of tail according to the scheme presented in the Fig. 7.

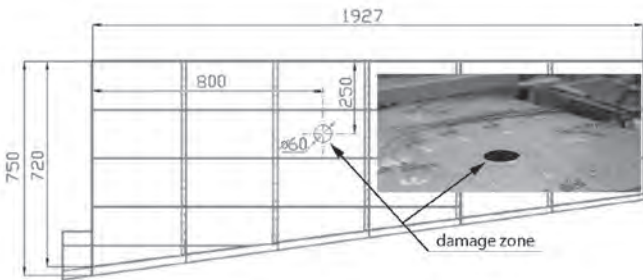


Fig. 7. The geometry of the damage and view of the hole made in the upper skin of tail

The horizontal tail was loaded with the force of 880 N that corresponded with a displacement of the actuator of 25 mm. The values of maximum main strain were determined on the basis of the strain gauges' rosettes placed in the subsequent construction zones. The values of strain were defined in chosen zones of undamaged and loaded construction (case no. 1) and in damaged and loaded construction (case no 2). The results are presented in the Fig. 8.

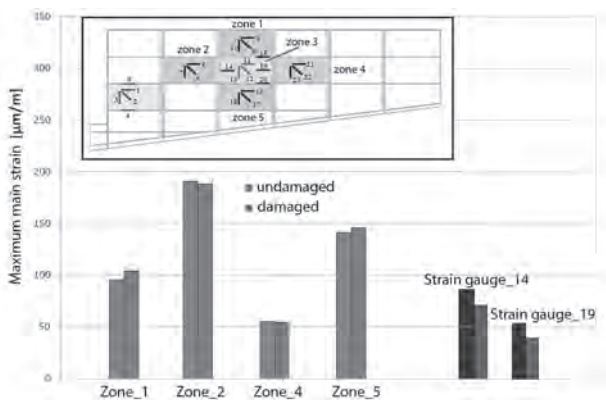


Fig. 8. Maximum main strain in the chosen zones of loaded construction

The results of performed tests showed that maximum main strain in the zones adjacent to damaged zone (outside the supporting elements) did not change significantly. A significant decrease in strain

was registered in strain gauges no. 14 and 19 which were located in the damaged zone. The obtained results confirmed conclusions of the numerical calculations.

3.3. Research on construction repaired with composite materials

On the basis of the numerical calculations and the experimental research it was claimed that the main aim of skin repair should be stiffness reconstruction of a part of skin in the damage zone (between supporting elements) and therefore, stability sustaining of the repaired element. With the use of results concerning repaired plates [8] which were loaded by shear, the method of tail skin repair was proposed. It included material loss supplemented by a disk-shaped insert of duralumin 2024T4 and formation of one-sided strengthening composite patch achieved by means of vacuum bag method. One of the essential conditions of the skin repair effectiveness is to ensure proper sensitivity of composite patch to deformation. Thus, the composite patch of 6 layers of glass fabric Synglass E81 weighing 101 g/m² was formed. The layers of fabric in a disk-shape were arranged according to the scheme (0/45/90)₂ and the successive layers had a diameter of 5 mm less than each previous one in order to obtain a stepped effect. The first layer had a diameter of 100 mm. The last layer with a diameter of 110 mm was made of aramid fabric with the weight of 61 g/m² in order to protect the composite patch against mechanical damage. The epoxy resin L418/H418 of German company MGS was used to join all elements of the patch. Because there was access to only one side of the tail skin, the problem of holding up of duralumin insert had to be solved during composite patch formation. In order to achieve it a special composite ring was formed on the inside of tail skin. The composite ring consisted of 3 layers of glass fabric and its outside layer had a diameter of 100 mm and its inside layer had a diameter of 40 mm. Sealing the gap between the repaired skin and the metal insert was possible due to the application of the inside ring. In the Fig. 9 there is presented the scheme of layers in the repaired zone and the view of repairing zone prepared to curing process.

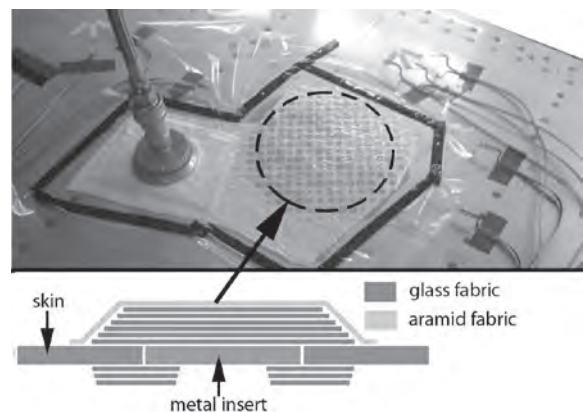


Fig. 9. The scheme of the composite patch application and the repaired area

The applied patch was cured at normal temperature for 24 hours and then heated up at temperature of 80°C within 15 hours with heating blanket. The strain gauges no. 11, 12 and 13 were bonded on the composite patch in order to monitor conditions of the repaired zone (metal insert and composite patch) during durability tests (compare Fig. 8). The repaired structure was research on durability. The cyclic load was applied by shifting a hydraulic actuator with the frequency of 0.5 Hz. The shift of the hydraulic actuator was equal to 25 mm as it was in static tests. 20 000 cycles were performed to analyze the strain changes in the repaired zoned, particularly in the composite patch (strain gauges no. 11, 12 and 13) and in the adjacent area to the repaired zone. The changes of maximum principle strain during

durability tests are presented in the Fig. 10. Strain changes after 2000, 5000 and 20 000 load cycles are presented.

On the basis of the research included in the paper [4], it can be assumed that re-damage of repair zone (including disbonding of metal insert) causes significant change of maximum principle strain in the composite patch and in the repaired skin. Since this kind of phenomenon did not occur during the conducted tests, it can be assumed that the repaired zone was not damaged again during presented durability research. An interesting phenomenon of strain decrease in the composite patch was noticed in relation to the number of load cycles. The strains of the composite patch measured directly after durability tests were higher than the strains measured a few hours after completion of tests.

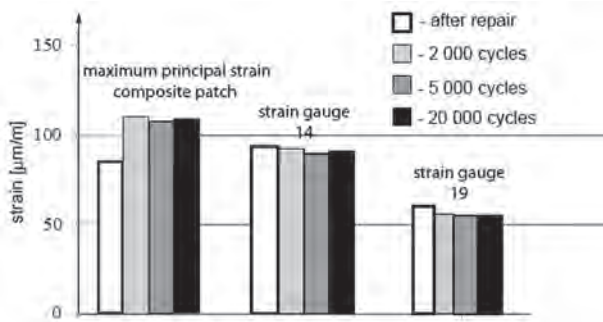


Fig. 10. Maximum principle strain in the composite patch and in the repaired zone

4. Research on composites materials used in repairing aircraft girder

4.1. Numerical calculation of a damaged girder

An important criterion of girder repair effectiveness is restoration of its initial stiffness before damage. Therefore, in the first step numerical calculations were executed in order to assess stiffness changes caused by damage. A numerical model of the girder was created on the basis of the girder geometry of tail-plane of the “Su-22” Aircraft. The created model is presented in the Fig. 11. The following features of materials (duralumin B93) were assumed during analysis: longitudinal modulus of elasticity – 72GPa, Poisson’s ratio – 0,3.

The load was modeled by applying force to the middle node of the group creating a stanchion (Fig. 12). The stiffness of elements which creating stanchion was increased due to defining their modulus of longitudinal elasticity two orders of magnitude greater. Additionally, the stanchion’s nodes were immobilized along the X and Y axis. The value of the loaded force was 8.3 kN and it was caused by assumption that maximum strain of girder in the loaded part is 2 mm.

The following damages during research were assumed:

- damage in the middle part of the girder partition in the shape of a hole of 29 mm diameter located in the axle of force loading;
- damage in the girder flange in the shape of a rectangle of 30 x 40 mm.

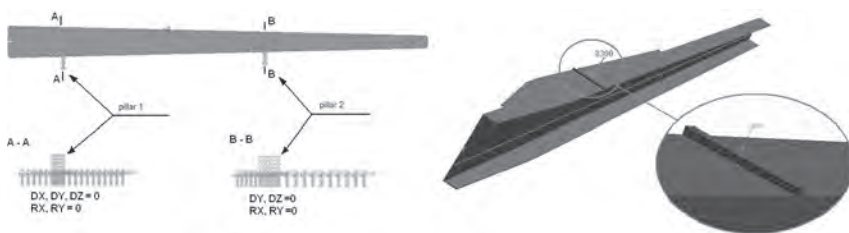


Fig. 11. Method of the girder anchoring and loading

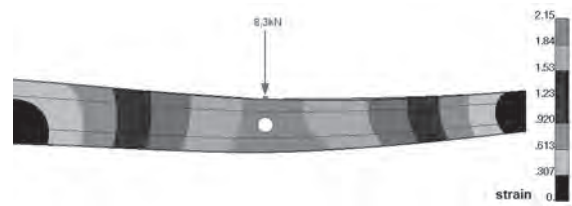


Fig. 12. Method of the girder loading and strain distribution for damage in shape of a hole

According to obtained results, it could be claimed that the damage in the shape of a hole did not influence significantly the stiffness of the girder – the value of strain changed slightly. It was also determined that the damage of the girder flange caused higher loss of stiffness than the damage of the girder partition. Taking into consideration the obtained results it seems that repair of a girder partition should be much easier to execute and more effective. The above conclusions were checked in experimental tests.

4.2. Experimental tests of the repaired girder

Effectiveness of the horizontal tail repair of the “Su-22” Aircraft’s girder (Fig. 13) was tested. The girder is produced with duralumin PA7 (partition) and PA30 (flanges). The girder was a type of convergent girder and consisted of a partition (wall) made with sheet metal of 2 mm thickness and riveted to it convergent flanges.



Fig. 13. The tested girder and the horizontal tail from where the girder was dismantled (left) and geometric dimensions of the girder (right)

In the first step the undamaged girder was tested. As a result of the bending tests a graph was determined which presents the girder’s strain in function of the force (Fig. 14). The maximum deflection of the undamaged girder was 1.74 mm at the force of 8.3 kN.

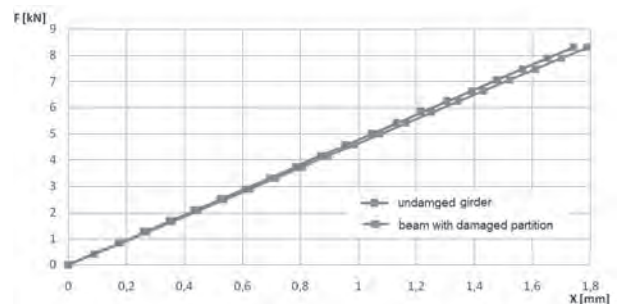


Fig. 14. Dependence of the girder’s strain in function of the force changes – $F=f(x)$

Then the damaged girder was tested. The damage had a shape of the hole of 29 mm diameter and was located in the axle of the load (Fig. 15). The value of the force did not change. As a result of the damage a change of girder’s stiffness was noticed. The maximum deflection of the researched part of girder was 1.79 mm (Fig. 14).

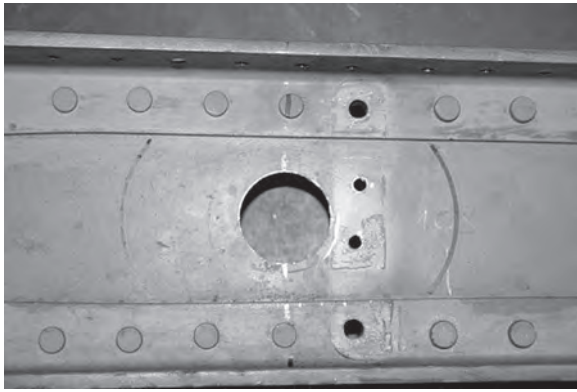


Fig. 15. The view of the girder's damaged partition

Subsequently, a repair of the damaged partition of the girder was executed. The repair was fixed with the use of composite materials and epoxy resin (Epidian 57/Z1). At the beginning, a metal insert (duralumin 2024) was set in the hole. Afterwards, a strengthening composite patch was formed with use of several layers of carbon and glass fabrics, which were laminated with the use of the mentioned epoxy resin (Fig. 16).

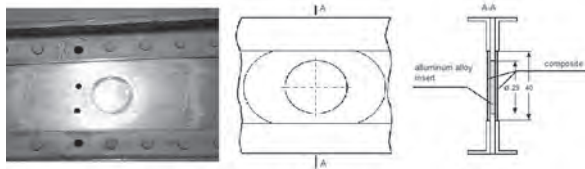


Fig. 16. Method of the girder's partition repair

The strengthening patch was formed in the elliptic shape with dimensions of 140×48 mm. Two sorts of plain wave fabrics were used to form the patch. The first one was glass fabric of Belgian company Synglass weighing 160g/m^2 and carbon fabric of KDL company weighing 160g/m^2 as well as. The strengthening patch was formed with five layers of 1.2 mm thickness. The first and last layers were formed with glass fabric and the middle layers were formed with carbon fabric (Fig. 17). The layers of fabric were laminated with epoxy resin. The surface for bonding was cleaned with extraction petrol. The repaired zone was cured in a thermal chamber at the temperature of 100°C within 30 minutes. The presented repair was completed within 120 minutes.

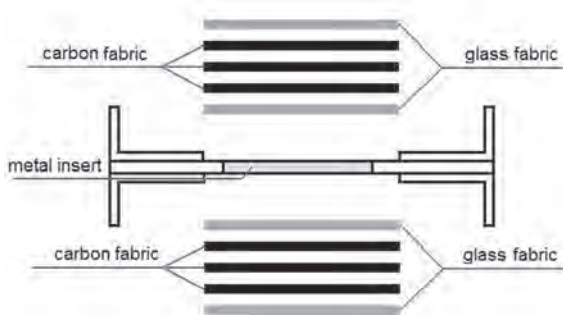


Fig. 17. Method of composite patch forming

Then stiffness was determined by means of bending test which was conducted in the same conditions as the undamaged girder. As a result, a curve $F=f(x)$ was determined (Fig. 18). It was noticed that the applied repair allowed us to restore the initial stiffness of the damaged girder.

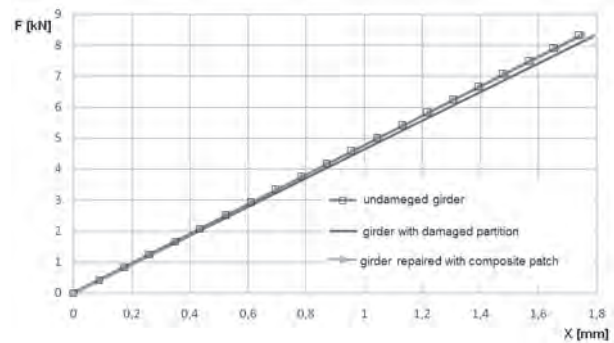


Fig. 18. Dependence of the girder's strain in function of the force changes – $F=f(x)$

Additionally, fatigue test of the repaired girder was executed. The girder was subjected to cyclical force in the range of $0 \dots 8.3$ kN. The load cycle was repeated 200 times and organoleptic assessment of the repaired zone was executed. No re-damages were detected. After that stiffness of the researched girder was determined again and no changes were observed.

The next step was to conduct research on the girder which had damage in the flange. The damage was designed in a few steps and after each step the dependence of $F = f(x)$ was determined. The damages were as follows (Fig. 19):

- case no. 1., a single cut in the middle of the flange which was located 120 mm from the axle of force loading;
- case no. 2, double cut in the middle of the flange which was located 80 and 120 mm from the axle of load;
- case no. 3, an extraction in the girder flange in the shape of rectangle of $30 \text{ mm} \times 40 \text{ mm}$.

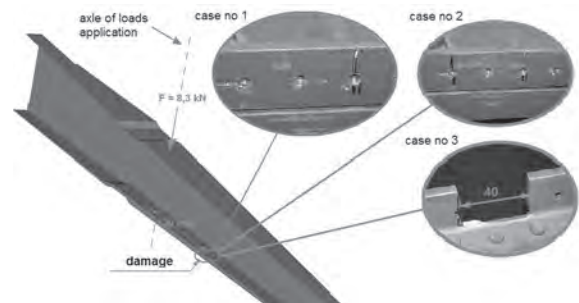


Fig. 19. A fragment of the girder with three damages in the flange

The obtained results of the dependence of $F = f(x)$ are presented in the Fig. 20.

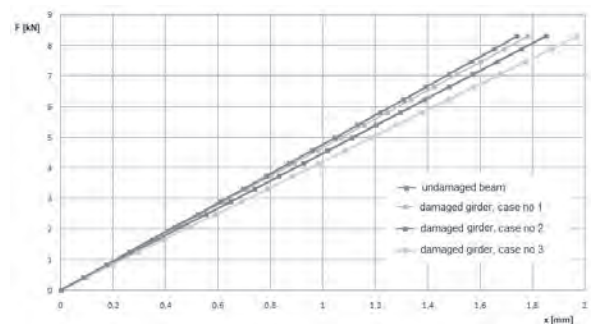


Fig. 20. Dependence of the girder's strain in function of the force changes – $F=f(x)$

Afterwards, the damaged flange of the girder was repaired with use of duralumin and a steel plate and rivets. The strengthening plate was riveted to the inside of the girder in the place of the damage. The

dimensions of the plate were $140 \times 25\text{mm}$ and thickness was 2.5mm . The thickness of the plate was selected taking into account the possibility of access to the rivets' heads during crimping. The strengthening plate was one-sided in order not to change external dimensions of the girder. The duralumin rivets were used in the repair, which had a diameter of 4mm and a shank length of 10mm . Furthermore, the metal insert which was made with the same material as the repaired girder was implemented in the place of damage (extraction). The view of the repaired zone is depicted in the Fig. 21.

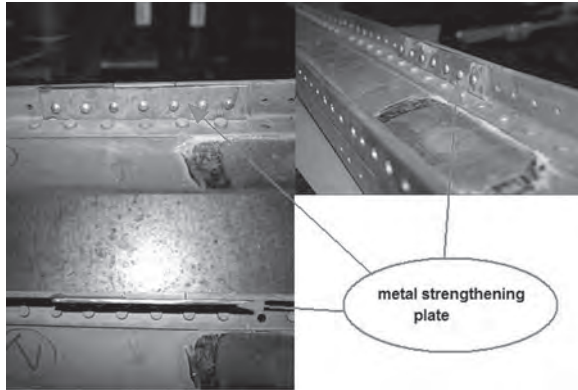


Fig. 21. The view of the repaired zone

The comparison analysis of the girder stiffness which was undamaged, damaged and repaired with riveted plates, is presented in the Fig. 22.

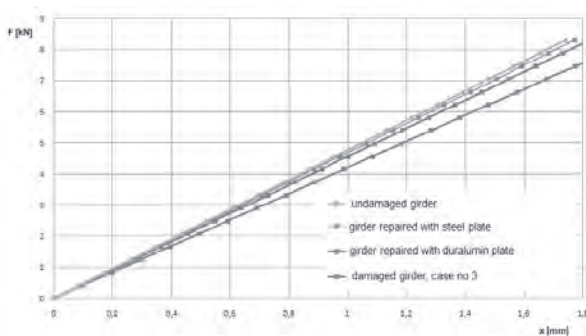


Fig. 22. The comparison analysis of the girder's stiffness which was undamaged, damaged and repaired with riveted metal plates – $F=f(x)$

As a result of the researched repairs it was not possible to restore initial stiffness of the girder. According to predictions the stiffness of the repaired girder was closest to the initial stiffness in case of using steel plate.

Furthermore, the repair was applied where a composite patch and adhesive joint were used. The damage (extraction) in the girder was implemented with a metal insert of the same material as the girder. Then, there were laminated subsequent layers of carbon, glass or aramid fabric to form a strengthening patch. The epoxy resin of Epidian 57/Z-1 was used to saturate and join layers of fabric. The strengthening patch was formed in the shape of a rectangle which had dimensions of $150 \times 25\text{mm}$ (joined to inside of the girder's flange) and $120 \times 40\text{mm}$ (glued to outside of the girder's flange). 10 layers of fabric were used from the inside and 3 layers were used from the outside of the girder's flange in order to form a composite patch. The number of outside layers was limited to keep the external dimensions of the girder (Fig. 23). The surface of repaired element was cleaned and degreased with extraction petrol and subsequent layers were laminated with epoxy resin, which was hardened in the temperature of 100°C within 45 minutes.

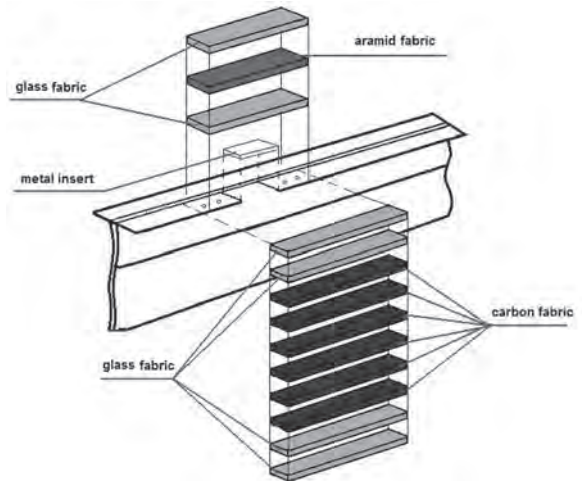


Fig. 23. Method of the strengthening composite patch forming

The view of the repaired zone is presented in the Fig. 24 and research on the girder's strain in function of the force changes ($F=f(x)$) is presented in the Fig. 25.

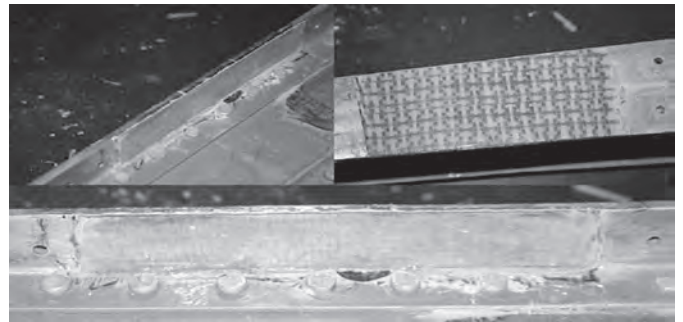


Fig. 24. The view of the repaired flange of the girder

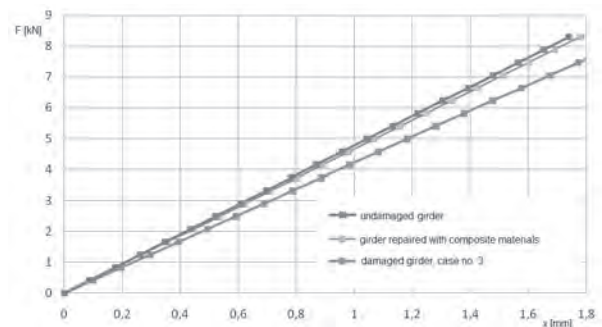


Fig. 25. The comparison analysis of the girder's stiffness which was undamaged, damaged and repaired with composite patch – $F=f(x)$

The initial stiffness of the girder was not restored as a result of the conducted repair. However, the obtained stiffness was close to the one which was determined for the girder that was repaired with steel riveted plate. Furthermore, fatigue tests of the repaired girder were executed. The girder was subjected to cyclical force in the range of $0 \dots 8.3\text{kN}$. The load cycle was repeated 50 and 100 times and organoleptic assessment of the repaired zone was executed. No re-damages were detected but the stiffness of the repaired girder changed little according to the curve presented in the Fig. 26.

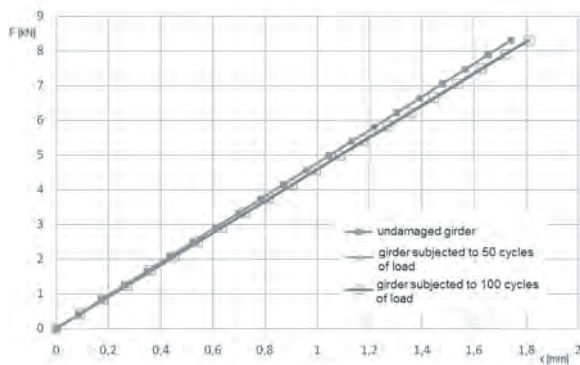


Fig. 26. The comparison analysis of the girder's stiffness which was undamaged, damaged and repaired and subjected to fatigue tests – $F=f(x)$

5. Conclusions

Taking into account the performed studies, the following conclusions can be drawn:

- The skin damage of a semi-monocoque structure causes a local change (increase) in strain mainly in the damage zone, which is limited to adjacent ribs and stringers.
- Stiffness reconstruction of the damaged elements should be main criterion in designing aircraft structure in order to protect them against local loss of stability.

References

1. Chester RJ, Walker KF, Chalkley PD. Adhesively bonded repairs to primary aircraft structure. *International Journal of Adhesion and Adhesives* 1999; 19.
2. Cichosz E. External load of aircraft (In polish). Warsaw: WAT, 1968.
3. Jones R, Chiu WK, Smith R. Airworthiness of composite repairs: Failure mechanisms. *Engineering Failure Analysis* 1995; 2: 117–128.
4. Kijewski P, Rośkowicz M. Diagnose of a composite patch (In polish). *Technology and Assembly Automation* 2011; 2: 49–55.
5. Komorek A, Przybyłek P. Examination of the influence of cross-impact load on bend strength properties of composite materials, used in aviation. *Eksplotacja i Niezawodność – Maintenance and Reliability* 2012; 14(4): 265–269.
6. Kuczmazewski J. Fundamentals of metal-metal adhesive joints design. Lublin: University of Technology and Polish Academy of Science, 2006, ISBN 83-89293-11-0.
7. Rośkowicz M, Smal T. The use of composite adhesives in repairing of aircraft semi-monocoque airframe. In electronic proceeding of the 15th European Conference on Composite Materials, Venice, 24–28.06.2012.
8. Rośkowicz M. Stability of composite repair plate (In polish). *Bulletin WAT* 2007; 4(648): 257–272.
9. Rudawska A, Dębski H. Experimental and numerical analysis of adhesively bonded aluminium alloy sheets joints. *Eksplotacja i Niezawodność – Maintenance and Reliability* 2011; 1(49): 4–10.

- The use of composite materials and metal inserts is an effective technology, which can be used to perform repair of the skin of the semi-monocoque airframe. The use of an insert which has the same stiffness as a repaired element is a solution that allows restoration of its local stiffness. The composite patch joins all elements of repaired zone and increases its fatigue life.
- Damage of a girder's partition (wall) can be effectively removed with a composite patch. The conducted repair allowed us to restore the initial stiffness of the repaired girder. Moreover, this kind of repair enables us to sustain fatigue life of the repaired component.
- Damage of the girder's flange causes more trouble. The repair is more time consuming and it is difficult to restore the initial stiffness of the damaged component. The mentioned damage has a greatest impact on the stiffness of considered element. Repairs were executed with 3 technologies in this case. The best results were obtained for repair with use of steel riveted plate and composite patch. The conducted experimental tests confirmed the usefulness of composite patching as an effective repair technology.
- Various methods of expedient repairs were researched. Some assumptions were made while executing repairs. First of all, It should be possible to perform the assumed repairs in the field conditions with the use of basic tools and materials. Secondly, time of repair was limited to 120 minutes.

Marek ROŚKOWICZ, Ph.D. (Eng.)

Institute of Aircraft Technology,
Military University of Technology
ul. Sylwestra Kaliskiego 2, 00-908 Warszawa 49, Poland
E-mail: marek.roskowicz@wat.edu.pl

Tomasz SMAL, Ph.D. (Eng.)

Institute of Command
The general Tadeusz Kosciuszko Military Academy of Land Forces
ul. Czajkowskiego 109, 51-150 Wrocław, Poland
E-mail: t.smal@wso.wroc.pl

Wei LUO
Chunhua ZHANG
Xun CHEN
Yashun WANG

SYSTEM RELIABILITY DEMONSTRATION WITH EQUIVALENT DATA FROM COMPONENT ACCELERATED TESTING BASED ON RELIABILITY TARGET TRANSFORMATION

STWIERDZANIE NIEZAWODNOŚCI SYSTEMU NA PODSTAWIE RÓWNOWAŻNYCH DANYCH Z PRZYSPIESZONYCH BADAŃ ELEMENTÓW SKŁADOWYCH W OPARCIU O TRANSFORMACJĘ CELU NIEZAWODNOŚCIOWEGO

The reliability demonstration test (RDT) programs in general proceed at various levels, including component, subsystem, and system in the verification and validation phase of the product life cycle. The system reliability demonstration within feasible duration becomes a considerable issue because of the marketplace demands for decreased development time and cost. A method based on reliability target transformation is proposed to accomplish the system reliability demonstration with the data from the RDT of the components. In order to shorten the test time, the RDT plan for component under the accelerated condition is first designed. Then, the reliability target of the system with different lifetimes required by the producer and the consumer is transferred to the target with the same specified mission time, which should meet the time constraint of the system level test. Next, the lower limit confidence of component reliability at the system mission time are estimated and converted to the equivalent binomial component data by the curve fitting method, then they are synthesized to the equivalent binomial system data by the Bayesian method. Finally, the system reliability demonstration is considered. The system classical attribute acceptance sampling plan at the mission time is used to make decisions using the equivalent binomial system data. If the decision cannot be made, the system Bayesian attribute acceptance sampling plan will be designed with the equivalent data as the prior parameters and the complementary system test will be conducted.

Keywords: reliability demonstration, accelerated testing, equivalent binomial component data; reliability target transformation, Bayesian attribute acceptance sampling plan.

Ogólnie, oprogramowanie do badań stwierdzających niezawodność (RDT) można stosować na różnych poziomach, w tym na poziomie elementu składowego, podsystemu i systemu, w fazie weryfikacji i walidacji cyklu życia produktu. Stwierdzenie niezawodności systemu w realnym terminie staje się ważkim problemem ze względu na wymogi rynku co do zmniejszenia czasu i kosztów rozwoju. W prezentowanej pracy zaproponowano metodę opartą na transformacji celu niezawodnościowego, wedle której niezawodność systemu stwierdza się na podstawie danych z RDT części składowych. Aby skrócić czas testowania, w pierwszej kolejności tworzy się plan RDT dla części składowej w warunkach przyspieszonych. Następnie cel niezawodnościowy systemu przy różnych czasach pracy wymaganych przez producenta, jak i konsumenta, zostaje przetransponowany na cel o tym samym określonym czasie użytkowania, który powinien spełniać ograniczenie czasowe dla badań na poziomie systemu. Następnie szacuje się dolne granice przedziałów ufności dla niezawodności komponentów w określonym czasie eksploatacji systemu oraz przekształca się je na równoważne dane dwumiennie dla części składowych z wykorzystaniem metody dopasowywania krzywych; dalej, są one syntetyzowane do równoważnych dwumiennych danych dotyczących systemu z zastosowaniem metody Bayesa. Pozwala to na stwierdzenie niezawodności systemu. Decyzje podejmuje się na podstawie równoważnych danych dwumiennych dotyczących systemu z wykorzystaniem klasycznego planu wyrzykowej kontroli odbiorczej systemu według zadanych charakterystyk dla określonego czasu użytkowania. Jeżeli decyzja nie może zostać podjęta w ten sposób, konstruuje się bayesowski plan wyrzykowej kontroli odbiorczej systemu wg. zadanych charakterystyk, gdzie dane równoważne stanowią parametry a priori, oraz przeprowadza się uzupełniające badania systemu.

Słowa kluczowe: stwierdzanie niezawodności; badania przyspieszone; równoważne dane dwumiennie dla części składowych; transformacja celu niezawodnościowego; bayesowski plan wyrzykowej kontroli odbiorczej systemu wg. zadanych charakterystyk.

1. Introduction

Before being disposed to the markets, the product is subjected to a number of phases, including product planning, design and development, verification and validation, production. In the planning phase, all the products are required to achieve a reliability target that need

to be demonstrated. In the design and development phase, the target of the product (also termed the system) is allocated to its subsystems and components, and according to these targets, the reliability is designed into the system proactively. In the verification and validation phase as well as the production phase, the reliability targets of

the components, the subsystems, and the system are demonstrated through the reliability demonstration test (RDT).

Because of the marketplace demands for decreased development time and cost, the RDT is required to be accomplished within feasible test duration. For the components, the accelerated life testing (ALT) can be adopted in RDT to shorten the test time [1, 4-5, 15, 18], which is termed the accelerated life reliability demonstration test (ALRDT). However, for the system reliability demonstration, the accelerated testing may not be applied due to the complexity of the system. The acceptance sampling plan is often employed for system reliability demonstration. And the literature on the acceptance sampling plan can be classified by the classical (commonly used) plan [3, 9, 12] and Bayesian plan [2, 7, 11, 16-17].

Further, the system reliability demonstration method utilizing the component data is generally considered. In the literature, there are two main approaches to demonstrate the system reliability target. One approach is that the system reliability target is demonstrated through the component test based on the derived relationship between the system reliability target and the component test plan. Mazumdar [10] proposed an optimum procedure for component testing with type-I censoring to demonstrate the series system reliability, and Rajgopal and Mazumdar [13] developed a system-based component test plan for a series system with type-II censoring. Yan and Mazumdar [20], and Rajgopal and Mazumdar [14] provided the component-testing procedure for a parallel system with type-II censoring, respectively. The time to failure for the components is assumed an exponentially distributed in the methods above, and the methods can only be applied to the series system or the parallel system, but be not suitable for the complex system that comprises of the components with other lifetime distributions. The other approach is that the system reliability target is demonstrated through designing the system test plan with component data. Li and Cai [7] designed the system attribute acceptance sampling plan through synthesizing the binomial subsystem data by the Bayesian method, which can reduce the sample size for the flight testing. Ten and Xie [17] also proposed a Bayesian reliability demonstration test plan for series-systems with binomial subsystem data, where the approximate lower limit confidence (ALLC) of system reliability was estimated using the binomial subsystem data and was utilized to calculate the system prior distribution parameters. However, the system prior distribution parameters cannot be derived directly utilizing the component data for the case that the components of the system undergo the accelerated testing (AT).

In some applications, the lifetime at the specified reliability is selected as the reliability measure for the target to be demonstrated, where the lifetimes required by the producer and the consumer are different. In this case, the system attribute acceptance sampling test plan at the specified mission time cannot be utilized directly. Additionally, the system attribute test plan is unfeasible when the mission time for the target is long.

In this paper, a system reliability demonstration test methodology with equivalent binomial data from component ALRDT based on reliability target transformation is developed. The ALRDT of the components is first conducted within feasible test duration. With the parameter estimates of the lifetime distribution for the components, the system reliability target with different lifetimes required by the producer and the consumer can be transferred to the target at the same specified mission time with different reliability required by the producer and the consumer, where the mission time meets the time constraint of the system level test. Next, the LLC of component reliability at the specified mission time is estimated and converted to the equivalent binomial component data, and they are synthesized to the equivalent binomial system data. Finally, the system reliability demonstration is considered. The system classical attribute acceptance sampling plan at the mission time is designed to make decisions using the equivalent binomial system data. If the decision cannot be made,

the system Bayesian attribute acceptance sampling plan at the mission time will be designed with the equivalent binomial system data as the prior parameters and the complementary system level test for the mission time will be conducted.

2. Assumptions

(1) Life distribution

Assume that the lifetime of the x th component follows the Weibull distribution, then the reliability at t is

$$R_x(t) = \exp\left(-(t/\eta_x)^{\delta_x}\right) \quad (1)$$

where η_x and δ_x are the scale and shape parameters for the x th component, $x=1,2,\dots,l$, and l is the number of components in the system. The time to failure of the components for the system is assumed to be statistically independent.

(2) Accelerated model

The accelerated model often indicate that the η_x is a log linear function of a (possibly transformed) stress S , given as

$$\ln \eta_x = \gamma_{0,x} + \gamma_{1,x} \cdot f(S) \quad (2)$$

where $\gamma_{0,x}$ and $\gamma_{1,x}$ are the parameters of the accelerated model for the x th component and $f(S)$ is the function of the stress S . Additionally, the acceleration factor a_x is equal to $\eta_{0,x}/\eta_{a,x}$, where $\eta_{0,x}$ and $\eta_{a,x}$ are the scale parameters when the stresses are the normal stress S_0 and the accelerated stress S_a , respectively. And the shape parameter δ_x is constant and independent of the stress.

(3) The reliability targets

Let $t_{0,x}(R_x)$ and $t_{1,x}(R_x)$ with the corresponding risks α_x and β_x denote the reliability target of the x th component required by the producer and the consumer, where $t_{0,x}(R_x)$ and $t_{1,x}(R_x)$ are the lifetimes at the specified reliability R_x for $x=1,2,\dots,l$. And let $t_{0,s}(R_s)$ and $t_{1,s}(R_s)$ with the corresponding risks α_s and β_s denote the reliability target of the system required by the producer and the consumer, where $t_{0,s}(R_s)$ and $t_{1,s}(R_s)$ are the lifetimes at the specified reliability R_s .

3. Test Methodology

A system reliability demonstration test methodology is developed here. The purpose of the proposed methodology is to demonstrate that the system reliability as well as the components reliability meets the reliability targets required by the producer and the consumer prior to the field deployment. The four generic steps are given as follows, and the flowchart of the test methodology is described in Fig 1.

- 1) The reliability targets of the components are first to be demonstrated. They are subjected to time-censored ALRDT to accomplish the demonstration within feasible test duration.
- 2) If all the components pass the test, the system reliability demonstration is considered. As $t_{0,s}(R_s)$ and $t_{1,s}(R_s)$ are different, the system acceptance attribute sampling plan at the mission time cannot be designed. So the reliability target of the system should be transferred. The transferred target is $R_{0,s}(t_{st})$ and $R_{1,s}(t_{st})$, which denote the reliability at the same mission time

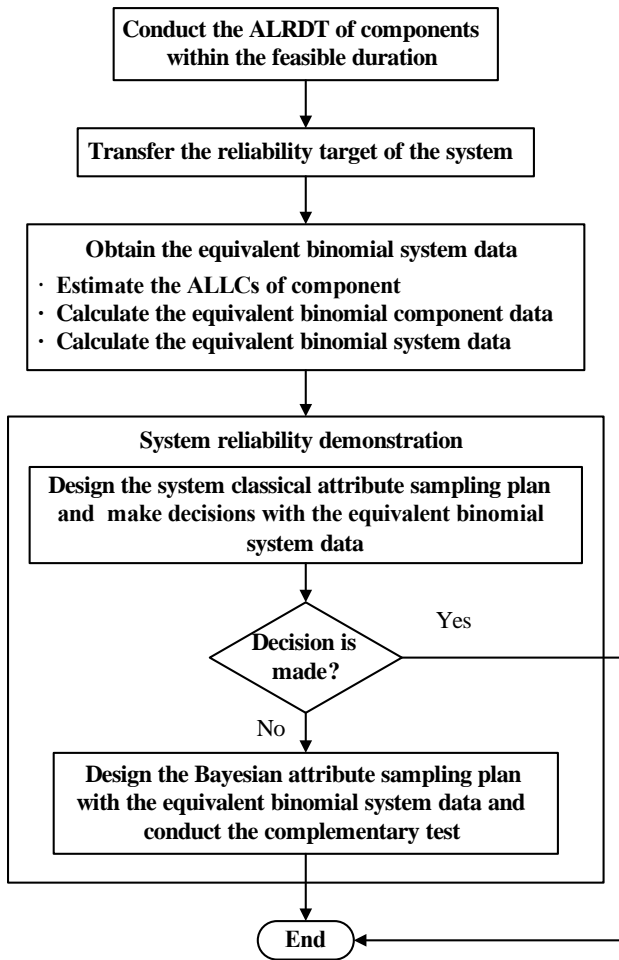


Fig.1 The flowchart of the proposed methodology

t_{st} required by the producer and the consumer, respectively. Note that the specified time t_{st} should meet the constraint of the system test duration.

- 3) In order to utilize the component data for system reliability demonstration, the LLCs of component at t_{st} under two confidence levels (CLs) are estimated and then converted to the equivalent binomial component data at t_{st} by the curve fitting method. And the system equivalent binomial data can be obtained through synthesizing the equivalent binomial component data by the Bayesian method.
- 4) According to the system transferred target, the system classical attribute acceptance sampling plan for the mission time t_{st} is designed. And if the decision can be made using the system equivalent binomial data, the system level test is not needed. Otherwise, the system Bayesian attribute acceptance sampling plan is designed, where the system prior distribution parameters are obtained from the equivalent binomial system data. Then, the complementary system level test will be conducted until the time reaches t_{st} and the decision is made in terms of the number of failures occurs during the test.

3.1. Time-censored ALRDT plan for components

For the x th component, assume that the n_x specimens are randomly sampled from a lot and then are tested simultaneously under the specified accelerated stress until the censoring time $t_{a0,x}$,

$x=1,2,\dots,l$. The producer's risk and the consumer's risk can be expressed through calculating the acceptance probability of operating characteristic (OC) curve when the reliability are set to $R_x(t_{0,x})$ and $R_x(t_{1,x})$, respectively [1]. Additionally, the cost of time-censored ALRDT for the x th component comprises of two parts:

- 1) the cost of conducting the test is $C_1 t_{a0,x}$;
- 2) the cost of samples is $C_2 n_x$.

The optimum plan $D_{cx} = (n_x, c_x, t_{a0,x})$ for the x th component can be solved by

$$\min_{D_{cx}} [C_1 t_{a0,x} + C_2 n_x] \quad (3)$$

subject to

$$\begin{cases} n_x \leq n_{\lim,x} \\ t_{a0,x} \leq t_{\lim,x} \\ \alpha'_x = 1 - \sum_{r=0}^{c_x} C_{n_x}^r \left(1 - \exp \left(\frac{\ln(R_x(t_{0,x}))}{t_{0,x}^{\delta_x}} \cdot (t_{a0,x} \cdot a_x)^{\delta_x} \right) \right)^r \left(1 - \exp \left(\frac{\ln(R_x(t_{0,x}))}{t_{0,x}^{\delta_x}} \cdot (t_{a0,x} \cdot a_x)^{\delta_x} \right) \right)^{n-r} \leq \alpha_x \\ \beta'_x = \sum_{r=0}^{c_x} C_{n_x}^r \left(1 - \exp \left(\frac{\ln(R_x(t_{1,x}))}{t_{1,x}^{\delta_x}} \cdot (t_{a0,x} \cdot a_x)^{\delta_x} \right) \right)^r \left(1 - \exp \left(\frac{\ln(R_x(t_{1,x}))}{t_{1,x}^{\delta_x}} \cdot (t_{a0,x} \cdot a_x)^{\delta_x} \right) \right)^{n-r} \leq \beta_x \end{cases} \quad (4)$$

where c_x is the acceptance number of failures; α'_x and β'_x are the actual values of risks; $n_{\lim,x}$ and $t_{\lim,x}$ are the limits of n_x and $t_{a0,x}$, respectively; and $x=1,2,\dots,l$. The D_{cx} can be calculated by the exhaustive method when $t_{a0,x}$ is discretized with a fixed step size.

For the x th component, the n_x specimens undergo the AT simultaneously until the time reaches $t_{a0,x}$, $x=1,2,\dots,l$. The reliability of the x th component is accepted if $f_x \leq c_x$ and is rejected otherwise, where f_x denotes the number of failures at $t_{a0,x}$, $x=1,2,\dots,l$. It should be noted that the test plans depend on the design parameters a_x and δ_x for $x=1,2,\dots,l$. Pre-estimates of unknown design parameters are needed in previous studies. Such prior pre-estimates may be from past experiences, similar data, testing data in the design and development phase, and the preliminary test.

3.2. System reliability target transformation

After the ALRDT of the components, the $\hat{\eta}_{a,x}$ for $x=1,2,\dots,l$ can be estimated using the censoring data and then $\hat{\eta}_{0,x} = \hat{\eta}_{a,x} \cdot a_x$. With the $\hat{\eta}_{0,x}$ and δ_x for $x=1,2,\dots,l$, the pseudo failure data of the components can be simulated by the Monte-Carlo method. Then, the pseudo failure time of the system can be calculated in terms of the system reliability model. The simulation procedure is repeated for N times, and the N pseudo failure times of the system are approximately fitted to the Weibull distribution. Further, the N pseudo failure times of the system is sorted in ascending order, which is denoted by $t_{ps,k}$, $k=1,2,\dots,N$, and the fitting precision is evaluated by the so-called correlation coefficient ρ [6]

$$\rho = \left| 1 - \frac{\sum_{k=1}^N (F(k) - \hat{F}(k))^2}{\sum_{k=1}^N (F(k) - \overline{F(k)})^2} \right|$$

where $F(k) = (k - 0.3)/(N + 0.4)$, $\hat{F}(k) = 1 - \exp\left(-\left(t_{ps,k}/\hat{\eta}_s\right)^{\hat{\delta}_s}\right)$,

$\overline{F(k)} = \frac{1}{N} \sum_{k=1}^N F(k)$, $\hat{\eta}_s$ and $\hat{\delta}_s$ are the scale and shape parameters of

the fitted Weibull distribution for the system. The closer ρ approximates 1, the more accurate the fitting precision is.

With the $\hat{\delta}_s$, the target with different lifetimes required by the producer and the consumer can be transferred to a new target at the same mission time t_{st} , given as

$$\begin{cases} R_{0,s}(t_{st}) = \exp\left(-\left(t_{st}/\eta_{0,s}\right)^{\hat{\delta}_s}\right) = \exp\left(\ln R_s \cdot \left(\frac{t_{st}}{t_{0,s}}\right)^{\hat{\delta}_s}\right) \\ R_{1,s}(t_{st}) = \exp\left(-\left(t_{st}/\eta_{1,s}\right)^{\hat{\delta}_s}\right) = \exp\left(\ln R_s \cdot \left(\frac{t_{st}}{t_{1,s}}\right)^{\hat{\delta}_s}\right) \end{cases} \quad (5)$$

According to the $R_{0,s}(t_{st})$ and $R_{1,s}(t_{st})$ with α_s and β_s , the system attribute acceptance sampling plan at t_{st} can be designed.

3.3. Equivalent binomial system data

3.3.1. Estimate the LLC of component reliability

After the ALRDT of the components, the ALLC of component reliability at t_{st} can be estimated using the censoring data and the useful degradation information during the test by the Bootstrap method [8, 19].

3.3.2. Calculate the equivalent binomial component data

Using two LLCs at different CLs, the equivalent binomial component data can be obtained by the curve fitting method. The theoretical basis of the method can be seen in [8], and the simplified method is given as follows. For the x th component, let (S_x, F_x) denote the equivalent binomial component data at t_{st} and $R_{L,x}(0.1)$ and $R_{L,x}(0.9)$ denote the LLCs of reliability at t_{st} when CL is 0.1 and 0.9, respectively; $x=1,2,\dots,l$. Then, (S_x, F_x) can be fully identified by [8]

$$\begin{cases} I_{R_{L,x}(0.1)}(S_x, F_x + 1) = 1 - 0.1 \\ I_{R_{L,x}(0.9)}(S_x, F_x + 1) = 1 - 0.9 \end{cases} \quad (6)$$

where $I_R(S_x, F_x + 1)$ is a Beta distribution function with parameters S_x and F_x , $N_x = S_x + F_x$, and we have

$$I_R(S_x, F_x + 1) = \sum_{i=0}^{F_x} C_{N_x}^{F_x} R^{N_x - F_x} (1 - R)^{F_x} \quad (7)$$

Note that S_x and F_x are generally decimal.

3.3.4. Calculate the equivalent binomial system data by the Bayesian method

The methods commonly used to synthesize the component reliability include the MML method, the Bayesian method, and Bootstrap method etc. In [8], it is verified that the estimate precision of the Bayesian method with the equivalent binomial component data is higher than other methods. The equivalent binomial system data

(S_s, F_s) can be obtained by the Bayesian method as follows

$$\begin{cases} N_s = \frac{\mu - v}{v - \mu^2}, S_s = N_s \mu, F_s = N(1 - \mu) \\ \mu = \prod_{x=1}^l \mu_x \\ v = \prod_{x=1}^l v_x \end{cases} \quad (8)$$

where N_s , S_s and F_s are the equivalent binomial system data, μ_x and v_x are first and second moments of reliability for the components, $x=1,2,\dots,l$, and they are calculated using the equivalent binomial component data by

$$\begin{cases} \mu_x = \frac{s_0 + S_x}{n_0 + N_x} \\ v_x = \frac{(s_0 + S_x)(s_0 + S_x + 1)}{(n_0 + N_x)(n_0 + N_x + 1)} \end{cases} \quad (9)$$

where $s_0 = 1/2$, $n_0 = 1$.

3.4. System reliability demonstration

3.4.1. System reliability demonstration through classical attribute acceptance sampling plan using the equivalent binomial system data

The steps of the decision procedure are given as follows.

Step 1: Let $n_s = [N_s]$, $[\cdot]$ is an integral function, the system classical attribute plan (n_s, c_s) is solved by

$$\begin{cases} n_s = [N_s] \\ \alpha'_s = 1 - \sum_{r=0}^{c_s} \Pr\{n_s, r | R_{0,s}(t_{st})\} \leq \alpha_s \\ \beta'_s = \sum_{r=0}^{c_s} \Pr\{n_s, r | R_{1,s}(t_{st})\} \leq \beta_s \end{cases} \quad (10)$$

where n_s is the sample size of the system and c_s is the acceptance number of failures at t_{st} , $N_s = S_s + F_s$, and $\Pr\{n_s, r | R\} = C_n^r (1 - R)^r R^{n-r}$.

1) When (n_s, c_s) can be solved, the reliability of the system is accepted if $c_s \geq F_s$ for all the solutions; the reliability of the system is rejected if $c_s < F_s$ and $(F_s - c_s) > (N_s - n_s)$ for all the solutions; otherwise, the decision cannot be made and the step 2 is considered.

2) When (n_s, c_s) cannot be obtained, the decision cannot be made and the step 2 is considered.

Step 2: Let $c_s < F_s$ and $n_s > N_s$, the system attribute sampling plan (n_s, c_s) is solved by

$$\begin{cases} c_s < F_s \\ n_s > N_s \\ \alpha'_s = 1 - \sum_{r=0}^{c_s} \Pr\{n_s, r | R_{0,s}(t_{st})\} \leq \alpha_s \\ \beta'_s = \sum_{r=0}^{c_s} \Pr\{n_s, r | R_{1,s}(t_{st})\} \leq \beta_s \end{cases} \quad (11)$$

The reliability of the system is rejected if the solution can be obtained; otherwise, the decision cannot be made, and the complementary system test will be considered, where the system Bayesian attribute sampling plan is designed.

3.4.2. System Bayesian reliability demonstration test plan

For the system Bayesian attribute acceptance sampling plan, the Beta distribution has been widely used as the prior distribution for binomial sampling as recommended in [17]. The prior distribution of system reliability can be expressed as follows [11].

$$\pi(R) = \frac{R^{p_a-1}(1-R)^{p_b-1}}{\beta(p_a, p_b)}, 0 \leq R \leq 1 \quad (12)$$

where p_a and p_b are the beta distribution parameters, and

$$\beta(p_a, p_b) = \frac{\Gamma(p_a)\Gamma(p_b)}{\Gamma(p_a + p_b)} \quad (13)$$

Then, with the equations (12) and (13), the system posterior distribution is

$$\pi(R|D) = \frac{R^{n_s-f_s+p_a-1}(1-R)^{p_b+f_s-1}}{\beta(n_s-f_s+p_a, p_b+f_s)} \quad (14)$$

where D denote the (n_s, f_s) , f_s is the number of system failures at t_{st} .

For binomial sampling,

$$\Pr\{\text{Accept} | R\} = \sum_{r=0}^{c_s} C_{n_s}^r (1-R)^r R^{n_s-r} \quad (15)$$

$$\Pr\{\text{Reject} | R\} = \sum_{r=c_s+1}^{n_s} C_{n_s}^r (1-R)^r R^{n_s-r} \quad (16)$$

By applying Bayesian theorem, the constraints of the risks can be expressed by

$$\begin{cases} \alpha'_s = \frac{\int_{R_{0,s}}^1 \Pr\{\text{Reject} | R\} \cdot \pi(R|D) dR}{\int_0^1 \pi(R|D) dR} \\ \beta'_s = \frac{\int_0^{R_{1,s}} \Pr\{\text{Accept} | R\} \cdot \pi(R|D) dR}{\int_0^1 \pi(R|D) dR} \end{cases} \quad (17)$$

where α'_s and β'_s are the actual values of risks.

With the equivalent binomial system data (S_s, F_s) at t_{st} , the prior parameters p_a and p_b can be obtained, and $p_a=S_s$ and $p_b=F_s$. Then, the test plan (n_s, c_s) can be derived by

$$\text{Min}[n_s]_{n_s, c_s} \quad (18)$$

subject to

$$\begin{cases} n_s \leq n_{\text{lim},s} \\ \alpha'_s = \frac{\int_{R_{0,x}}^1 \Pr\{\text{Reject} | R\} \cdot \pi(R|D) dR}{\int_0^1 \pi(R|D) dR} \leq \alpha_s \\ \beta'_s = \frac{\int_0^{R_{1,x}} \Pr\{\text{Accept} | R\} \cdot \pi(R|D) dR}{\int_0^1 \pi(R|D) dR} \leq \beta_s \end{cases} \quad (19)$$

where $n_{\text{lim},s}$ is the limit of n_s .

The n_s systems will be tested simultaneously until the time reaches t_{st} , the reliability of the system is accepted if $f_s \leq c_s$ and is rejected otherwise.

4. Illustrative example

Without loss of generality, assume that a series system comprises of three components, and the system reliability model is depicted in Fig. 2.

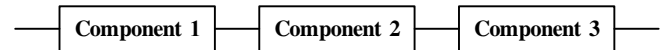


Fig. 2. System reliability model

The assumed reliability target of the system is shown in Table 1. According to the target, the procedure of system reliability demonstration is given as follows.

Table 1 The reliability targets of the system

Target	$t_{0,s}(R_s)$ (h)	$t_{1,s}(R_s)$ (h)	R_s	α_s	β_s
1	26280	17520	0.78	20%	20%

4.1. Time-censored ALRDT plans for the components

The lifetimes of the components are assumed to follow the Weibull distribution. And the Arrhenis model is employed when the temperature is the accelerating variable. The use temperatures and the accelerated temperatures for three components in ALRDT are shown in Table 2.

Table 2. The use temperatures and the accelerated temperatures for three components

x	Use temperature (K)	Accelerated temperature (K)
1	293	393
2	293	403
3	293	383

The assumed prior values of the accelerated model parameters and the shape parameters as well as the acceleration factors for three components are shown in Table 3.

Table 3. The prior values of model parameters

x	$\gamma_{0,x}$	$\gamma_{1,x}$	δ_x	α_x
1	25.5762	-0.0485	1.9	128
2	24.5620	-0.0431	1.3	114
3	28.1278	-0.0545	1.4	135

According to the reliability targets and the limits of the sample size and the test duration for three components shown in Table 4, the time-censored ALRDT plans are designed with the values of the design parameters α_x and δ_x for $x=1,2,3$ in Table 2, which are shown in Table 5.

Table 4. The reliability targets and the limits of the sample size and the test duration for three components

x	$t_{0,x}(R_x)$ (h)	$t_{1,x}(R_x)$ (h)	R_x	α_x	β_x	$n_{lim,x}$	$t_{lim,x}$ (h)
1	26280	17520	0.92	20%	20%	30	1000
2	26280	17520	0.93	20%	20%	30	1000
3	26280	17520	0.94	20%	20%	30	1000

Table 5. The time-censored ALRDT plans for three components

x	n_x	c_x	$t_{a0,x}$ (h)	α'_x	β'_x
1	30	5	264	16.79%	19.54%
2	30	10	736	19.36%	19.94%
3	30	9	576	18.28%	19.87%

4.2. System reliability target transformation

Assume that the reliability of three components satisfies the requirements of the corresponding targets respectively and the model parameters of three components shown in Table 3 are the estimate values. The pseudo failure times of the components are simulated using the Monte-Carlo method. Then, the pseudo failure time of the system can be obtained according to the system reliability model in Fig. 2. The simulation procedure is conducted for $N=100000$ times, and the N pseudo failure times of the system are fitted into the Weibull distribution and $\rho=0.9999$, which indicate that the Weibull distribution is proper to describe the statistical properties of the system life-time. And $\delta_s=1.61$.

Let $t_{st}=8760$ h, then $R_{0,s}(t_{st})$ and $R_{1,s}(t_{st})$ can be calculated by equation (5). The transferred target of the system is shown in Table 6.

Table 6. The transferred reliability target of the system

t_{st} (h)	$R_{0,s}(t_{st})$	$R_{1,s}(t_{st})$	α_s	β_s
8760	0.9585	0.9218	20%	20%

4.3. System reliability demonstration

4.3.1. Calculate the equivalent binomial system data

The assumed LLCs of three components when CL is 0.1 and 0.9 are shown in Table 7.

The equivalent binomial component data are calculated by equations (6) and (7) are shown in Table 8.

Table 7. The assumed LLCs of three components

x	CL=0.1	CL=0.9
1	0.9960	0.9729
2	0.9921	0.9561
3	0.9962	0.9731

Table 8. The equivalent binomial component data

x	S_x	F_x
1	146.5461	1.1101
2	102.7690	1.5278
3	148.9287	1.0713

Then, the equivalent binomial system data (S_s, F_s) are calculated by equations (8) and (9), where $(S_s, F_s) = (121.2495, 5.0488)$.

4.3.2. System reliability demonstration through attribute sampling plan

(1) According to the transferred target in Table 6, the system classical attribute sampling plan is designed and the decision is made with

(S_s, F_s) as follows.

Step1: Let $n_s = [N_s] = 126$, the solution cannot be solved by equation (10), the decision cannot be made. Then, the step 2 is considered.

Step2: Let $c_s \leq [F_s] = 5$ and $n_s > N_s$, the solution cannot be solved by equation (11), the decision cannot be made.

(2) Assume that $n_{lim,s} = 10$, the system Bayesian attribute sampling

plan is designed by equations (18) and (19) with (S_s, F_s) , which are shown in Table 9.

Table 9. The system Bayesian attribute sampling plan

n_s	c_s	α'_s	β'_s
5	3	17.02%	19.75%

Five systems will be arranged to undergo the test until the time reaches $t_{st}=8760$ h. After the complementary test, the reliability of the system will be accepted if the number of system failures is not greater than three and will be rejected otherwise.

4.4. System reliability demonstration for other targets

Another three reliability targets of the system are assumed and shown in Table 10. And suppose that the t_{st} and the (S_s, F_s) are unchanged, the transferred targets of the system are given in Table 11.

Table 10. Another three reliability targets of the system

Target	$t_{0,s}(R_s)$ (h)	$t_{1,s}(R_s)$ (h)	R_s	α_s	β_s
2	26280	17520	0.75	20%	20%
3	17520	8760	0.95	20%	20%
4	17520	8760	0.92	20%	20%

Table 11. The transferred reliability targets of the system

Target	$t_{0,s}(R_s)$ (h)	$R_{0,s}(t_{st})$	$R_{1,s}(t_{st})$	α_s	β_s
2	8760	0.9521	0.9101	20%	20%
3	8760	0.9833	0.95	20%	20%
4	8760	0.9731	0.92	20%	20%

According to the transferred targets, the corresponding system reliability demonstration test plans are designed and the decisions are made.

(1) System reliability demonstration for the target 2

Let $n_s = [N_s] = 126$, the system classical attribute sampling plan is solved and shown in Table 12. As $c_s > F_s$, the reliability of the system is accepted.

Table 12. The system classical attribute sampling plan when $n_s = 126$ for the target 2

n_s	c_s	α'_s	β'_s
126	8	15.11%	19.12%

(2) System reliability demonstration for the target 3

Let $n_s = [N_s] = 126$, the system classical attribute sampling plan is solved and shown in Table 13. As $c_s < F_s$ and $(F_s - c_s) > (N_s - n_s)$, the reliability of the system is rejected.

Table 13. The system classical attribute sampling plan when $n_s = 126$ for the target 3

n_s	c_s	α'_s	β'_s
126	3	15.98%	12.00%

(3) System reliability demonstration for the target 4

1) Let $n_s = [N_s] = 126$, the system classical attribute sampling plans are solved and shown in Table 14. As $c_s < F_s$ and $(F_s - c_s) < (N_s - n_s)$, the decision cannot be made. Then, the step 2 is considered.

2) Let $c_s = [F_s] = 5$ and $n_s > N_s$, the classical sampling plan can be solved, and one of the solutions is shown in Table 15. So the reliability of the system is rejected.

Table 14. The system classical attribute sampling plan when $n_s = 126$ for the target 4

Plan	n_s	c_s	α'_s	β'_s
1	126	5	12.61%	5.67%
2	126	6	5.50%	11.50%

Table 15. A system classical attribute sampling plan when $c_s = 5$ and $n_s > N_s$ for the target 4

n_s	c_s	α'_s	β'_s
127	5	12.95%	5.41%

5. Conclusion

(1) A system reliability demonstration test methodology with the equivalent binomial data from ALRDT of components based on the reliability target transformation is developed in this paper. The feasibility of the method is illustrated through a numerical example.

(2) The data from the ALRDT of components are used to estimate the LLCs of components and converted to the equivalent binomial component data by the curve fitting method. Then, they are synthesized to the equivalent binomial system data by the Bayesian method, which is utilized for system reliability demonstration. If the equivalent binomial system data is sufficient for decision-making, the system classical attribute sampling plan is employed and the system level test is not needed; otherwise, the system Bayesian attribute sampling plan will be designed and the complementary system test at the transformed mission time will be conducted. As the equivalent binomial system data are used to calculate the parameters of prior distribution, the sample size of the system level test is reduced. Additionally, the proposed method is also applicable to the complex systems with various types of component data, where the LLCs of components can be obtained. For the case that the lifetimes of the components follow different distributions, several types of distributions such as Weibull distribution and lognormal distribution can be used to fit the pseudo failure times of system and the one with maximum correlative coefficient ρ is selected to describe the statistic properties of the system. Then, the target of the system is transferred using the similar way shown in equation (5) according to the cdf expression of the selected distribution.

(3) In terms of the model parameter estimates for the components and the system reliability model, the system pseudo failure times can be simulated by the Monte-Carlo method and fitted to the Weibull distribution. Then, with the estimate of the shape parameter for system lifetime distribution, the system reliability target $t_{0,s}(R_s)$ and $t_{1,s}(R_s)$ can be transferred to the target $R_{0,s}(t_{st})$ and $R_{1,s}(t_{st})$ at the same specified mission time t_{st} . As the t_{st} is specified to meet the time constraint of the system level test and the ALRDT of components are employed, the reliability target with long lifetime can be demonstrated. Note that the t_{st} can not be too short; otherwise, $R_{0,s}(t_{st})$ and $R_{1,s}(t_{st})$ will become larger, and so does the sample size of the system level test.

Acknowledgement

The authors would like to thank the reviewers and the editor for their help in improving the paper. And this work was financially supported by the National Natural Science Foundation of China (No.51205402 and No.51105367).

References

- Chen WH, Chai X, Pan J, Hu JH, Lu XB. Accelerated demonstration test method based on Weibull distribution. Journal of Zhejiang University (Engineering Science) 2001, 35(1): 5–8.
- Jiang LP, Chen YH, Wu SH. A Bayesian plan of qualification test based on ENGS in binomial case. Systems Engineering, 2002; 20(6): 91–93.
- Jozani M J, Mirkamali S J. Improved attribute acceptance sampling plans based on maxima nomination sampling. Journal of Statistical

- Planning and Inference 2010; 140: 2448–2460.
4. Kim M, Yum BJ. Reliability acceptance sampling plans for the Weibull distribution under accelerated Type-I censoring. *Journal of Applied Statistics* 2008; 36(1):11–20.
5. Krasich M. Accelerated Reliability Testing Demonstration and Assurance Test Design. *Proceeding of IEEE Annual Reliability and Maintainability Symposium*, 2010.
6. Liu F, He Z, Cao ZQ, Yu GY. The discussion about the selection of the lifetime distributions for the mechanical reliability data. *Machinery Design and Manufacture* 1998; 6: 3–5.
7. Li HB, Cai H. Acquisition and application of the prior information of flight reliability on tactical missile test and evaluation. *System Engineering and Electronics* 1999; 21(3): 22–25.
8. Luo W, Zhang CH, Chen X, Tan YY. System reliability assessment as components undergo accelerated testing. *Proceeding of IEEE Annual Reliability and Maintainability Symposium*, 2011.
9. Markowski EP, Markowski, CA. Improved attribute acceptance sampling plans in the presence of misclassification error. *European Journal of Operational Research* 2002; 139: 501–510.
10. Mazumdar M. An optimum procedure for component testing in the demonstration of series system reliability. *IEEE Transactions on Reliability* 1977; R-26(5): 324–345.
11. Min ZM, Tao JY, Chen X, Zhang YA. A Bayes plan of reliability qualification test based on the mixed Beta distribution for success/failure product. *Acta Armamentarii* 2008; 29(2): 204–207.
12. Pendrill P L. Optimised measurement uncertainty and decision-making when sampling by variables or by attribute. *Measurement* 2006; 39: 829–840.
13. Rajgopal J, Mazumdar M. A system-based component test plan for a series system, with type-II censoring. *IEEE Transactions on Reliability* 1996; 45(3): 375–378.
14. Rajgopal J, Mazumdar M. A type-II censored log test time based component-testing procedure for a parallel system. *IEEE Transactions on Reliability* 1988; 37(4): 406–412.
15. Seo JH, Jung M, Kim CM. Design of accelerated life test sampling plans with a nonconstant shape parameter. *European Journal of Operational Research* 2009; 197:659–666.
16. Sheng Z, Fan DY. Bayes attribute acceptance-sampling plan. *IEEE Transactions on Reliability* 1987; 41(2): 307–309.
17. Ten L M, Xie M. Bayes reliability demonstration test plan for series-systems with binomial subsystem data. *Proceeding of IEEE Annual Reliability and Maintainability Symposium*, 1999.
18. Turner MD. A practical application of quantitative accelerated life testing in power systems engineering. *IEEE Transactions on Reliability* 2010; 59(1):91–101.
19. Xiao G, Li TT. *The Monte-Carlo methods in the system reliability Analysis*. China Science Press, 2003.
20. Yan JH, Mazumdar M. A Component-Testing Procedure For A Parallel System With Type II Censoring. *IEEE Transactions on Reliability* 1987; R-36(4): 425–428.

Wei LUO, Ph.D.

Chunhua ZHANG, Ph.D., D.Sc., Assoc. Prof.

Prof. Xun CHEN, Ph.D.

Yashun WANG, Ph.D.

Laboratory of Science and Technology on Integrated Logistics Support

College of Mechatronics and Automation

National University of Defense Technology

Yanwachi str., 47 Changsha, 410073, P.R.China

E-mails: luowei.nudt@gmail.com, wangyashun@nudt.edu.cn,

chzhang@nudt.edu.cn, chenxun@nudt.edu.cn

Jerzy MERKISZ
Piotr LIJEWSKI
Paweł FUĆ
Sylwester WEYMANN

EXHAUST EMISSION TESTS FROM NON-ROAD VEHICLES CONDUCTED WITH THE USE OF PEMS ANALYZERS

BADANIA EMISJI ZWIĄZKÓW TOKSYCZNYCH SPALIN Z POJAZDÓW O ZASTOSOWANIACH POZADROGOWYCH Z WYKORZYSTANIEM ANALIZATORÓW PEMS*

The paper discusses the issue of exhaust emissions from non-road vehicle engines. In the first part of the paper American regulations on the procedures of engine testing in operation were briefly characterized. The said regulations are a novel solution and were introduced as one of the first of this type worldwide. In the next part of the paper the authors presented the results of the exhaust emission tests from a farm tractor performed under actual operating conditions during fieldwork. For this purpose PEMS (Portable Emissions Measurement System) was used. The tests were carried out for different test procedures such as the NTE (Not-To-Exceed) procedure. The analysis of the test results was performed chiefly in the aspect of the NTE test applicable in the U.S. The analysis pertains chiefly to the engine operating conditions and exhaust emissions. European legislation currently does not require such tests and that is why the presented tests are related to the American procedures. The performed tests and their analysis led to a formulation of conclusions related to the engine operating conditions and its exhaust emissions.

Keywords: non-road vehicles, measurement of exhaust emissions under actual operating conditions.

Artykuł dotyczy problemu badań emisji związków toksycznych spalin z silników pojazdów o zastosowaniach pozadrogowych (non-road). W pierwszej części artykułu krótko scharakteryzowano przepisy amerykańskie nt. procedur badań silników w eksploatacji. Przepisy te są nowatorskim rozwiązaniem i zostały wprowadzone jako jedne z pierwszych tego typu rozwiązań na świecie. W dalszej części artykułu przedstawiono wyniki badań emisji związków toksycznych spalin silnika ciągnika rolniczego, wykonane w rzeczywistych warunkach eksploatacji, podczas wykonywania prac polowych. Do tego celu wykorzystano aparaturę PEMS (Portable Emissions Measurement System). Badania te wykonano dla różnych procedur badawczych, m.in. w teście NTE (Not-To-Exceed). Analizę wyników badań przeprowadzono głównie w aspekcie testu NTE, obowiązującego w Stanach Zjednoczonych. Analiza ta dotyczy przede wszystkim warunków pracy silników oraz emisji związków szkodliwych. Europejskie regulacje prawne w chwili obecnej nie nakładają obowiązku wykonywania takich badań, dlatego w zaprezentowane badania odnoszą się do procedur amerykańskich. Wykonane badania i ich analiza pozwoliły na sformułowanie wniosków dotyczących warunków pracy i emisji z silnika.

Słowa kluczowe: pojazdy o zastosowaniach pozadrogowych, pomiary emisji w rzeczywistych warunkach eksploatacji.

1. Introduction

For many years now works have been continued to reduce the negative impact of transport on the natural environment. A particular involvement of research and development centers is seen in works related to vehicle drivetrains and powertrains. In 2012 IARC (International Agency for Research on Cancer), a member of WHO (World Health Organization), in the report published in June 2012 qualified diesel exhaust gas to a group of carcinogenic factors [7]. Before that, diesel exhaust gas was classified as a group of 'probably' carcinogenic factors. Yet, in light of the latest research the diesel exhaust gas is classified as having the greatest carcinogenic risk [3, 14]. This is yet another factor that motivates to commit to research and development works aiming at a reduction of the negative impact of diesel engines on the environment. The works should focus on the technical solu-

tions reducing the exhaust emissions and a development of research methods and equipment. Only the combination of solutions in the above fields may bring measurable effects such as the improvement of the ecological indexes of combustion engines. Non-road vehicles are mostly fitted with diesel engines. Besides, contrary to on-road vehicles they are technologically obsolete and the admissible emission limits are much more liberal. Hence, the necessity of a technological improvement of these engines aiming at their reduced impact on the human health and natural environment.

One of the most significant aspects of exhaust emission testing is the adopted methodology. In recent years methods of exhaust emission testing under actual operating conditions have been developing rapidly. This type of testing is used increasingly as it provides invaluable information on the actual on-road exhaust emissions, information that is not obtainable under laboratory conditions [1, 5, 6, 10]. That is

(*) Tekst artykułu w polskiej wersji językowej dostępny w elektronicznym wydaniu kwartalnika na stronie www.ein.org.pl

why the results of such tests are so desirable. Since this is a relatively new trend, the testing methodology is not yet fully developed and commonly recognized. From the publications on this subject we know that many issues still remain unresolved. One of these issues is the selection of engine operating conditions during the tests. It is important that the conditions are representative of a given type of vehicle and that the results are comparable. Another issue is the problem of engine operating conditions under research tests. The problem of engine operating conditions under laboratory tests has been drawn attention to earlier [2, 4, 8, 9, 13, 11, 12, 15]. From the relevant published works conclusions are drawn that the engine operating conditions (engine load and speed) in laboratory tests, for both on-road and non-road vehicles, are not compliant with the conditions of actual operation. Despite numerous investigations and analyses of this problem it still remains unresolved.

Tests conducted under actual operating conditions indicate that the engine operation of vehicles of different categories (HDV – Heavy Duty Vehicles, LDV – Light Duty Vehicles, non-road) is characterized by specific operating parameters e.g. traction vehicle engines utilize a wide range of engine speeds while engines of some of the vehicles of non-road applications operate in a very limited range of engine speeds [1, 6, 11, 12, 15]. It is thus worth analyzing whether the testing methodology should be individually selected for a given engine application and whether current testing procedures take this fact into consideration.

2. Exhaust emission regulations for non-road vehicles

The procedures applicable in exhaust emission testing for non-road vehicles have been described and analyzed in earlier works [11, 12]. This paper focuses on the procedures related to the exhaust emission testing under actual operating conditions. One of the first regulations pertaining to this type of measurements was introduced by Environment Protection Agency based in USA [16]. According to these procedures NTE test and emission limits in this test were introduced as an additional tool for exhaust emission control (NTE is also a standard related to the described procedure). These tests are conducted under actual engine operating conditions. The NTE test was initially introduced for HDV engines and since 2011 it has been applicable for some of the non-road vehicles.

The NTE tests are not tied to any specific driving cycle of a vehicle or engine work points. There is no predefined mileage or test time. The tests cover a range of engine operation that falls within the boundaries of the controlled NTE zone, and the measurements include stationary and dynamic conditions (Fig. 1). The exhaust emissions are averaged from the engine work cycle lasting a minimum of 30 seconds (a 30 second window).

The NTE test sets a control zone limited by specific engine speed and load values:

- minimum engine speed is determined analogically to the speeds determined in the ESC test: $n_{\min} = n_{10} + 0,15(n_h - n_{10})$ (speed A in the ESC test is $n_A = n_{10} + 0,25(n_h - n_{10})$),
- engine load equal to or greater than 30% of the maximum engine torque,
- from NTE all engine speeds and loads are excluded for which the engine obtains an effective power lower than 30% of the maximum power,
- engine manufacturer may apply for exclusion from NTE of the speeds and loads for which the fuel consumption (BSFC – Break Specific Fuel Consumption) does not exceed 5% of the minimum unit fuel consumption if the manufacturer expects

the engine not to operate at these work points during regular operation. This does not apply to engines fitted with automatic transmission of a given number of speeds and vehicles fitted with manual transmission.

For EPA 2004 compliant engines the zones without particulate matter measurements were determined (depending on speed B in the ESC test). This does not apply to EPA 2007 compliant engines but in this case the manufactures may conditionally apply to EPA for exclusion of the PM measurement in these zones. Besides, the manufacturers may apply for a reduction of the NTE zone by a certain sub zone, if the operating time in this sub zone does not exceed 5% of the total operating time of the engine. These sub zones should have an elliptical or rectangular shape and its boundaries, at some point should be convergent with the boundary of the NTE zone.

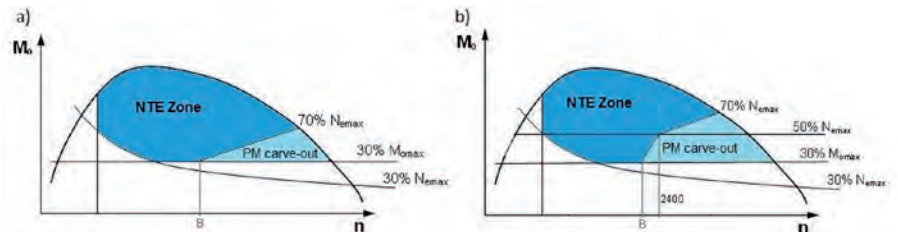


Fig. 1. Schematics of the NTE test for non-road engines, a) for engines of the maximum engine speed 2400 rpm, b) for engines of the maximum speed greater than 2400 rpm [16]

According to the requirements prescribed by the EPA all Tier - 4 compliant non-road vehicle engines must also comply with the NTE standard. For non-road vehicle engines of the power output greater than 130 kW the regulations have been applicable since 2011, for engines of the power output from 56–130 kW – since 2012 and for engines of the power output lower than 56 kW – since 2013. The unit exhaust emission limits in the NTE test have been set at 1.25 of the admissible unit emission of a single exhaust component from the Tier 4 standard. Only for engines that have the unit emission of nitric oxides lower than 2.5 g/kWh and the unit emission of particulate matter lower than 0.07 g/kWh this coefficient amounts to 1.5. The NTE regulations apply to the type approval tests and must be met for the whole engine life cycle [16].

The proposals of the future European regulations for HDV engines also provide for the exhaust emission tests in operation. A European equivalent of the NTE test is a proposal of a compliance test of the vehicle in operation with the requirements of the unit emissions, based on the determination of the emissions in the whole driving cycle as a function of engine operation expressed in kWh.

3. Methodology and object

In recent years interest in the on-road exhaust emission testing has grown significantly as this is the only way to obtain information on the actual exhaust emissions from a given vehicle. Such tests provide valuable and reliable test results that would otherwise be impossible to obtain under laboratory conditions on a chassis or engine dynamometer. The tests presented in the paper were carried out under actual conditions of operation of a farm tractor operating in the field using a cultivator (Fig. 2). The basic specifications of the tractor engine have been given in table 1.

The authors used Semtech DS by Sensors Inc. for the exhaust emission tests. This is a PEMS (Portable Emission Measurement System) analyzer that measures the concentration of the exhaust components (carbon dioxide, carbon monoxide, hydrocarbons and nitric oxides) and simultaneously measures the flow rate of the exhaust gas.

Table 1. The engine specifications of the tested farm tractor

Displacement / number of cylinders	6,4 dm ³ /6
Number of cylinders /valves	6/12
Maximum power output	122 kW / 1900 rpm
Maximum torque	698 Nm / 1350–1500 rpm
Aspiration	VGT turbocharger
Injection system	Common rail, max pressure: 160 MPa
Aftreatment system	Oxidation catalyst
Emission standard	Stage IIIB/Tier3



Fig. 2. The view of the tractor during the tests with the measurement equipment fitted

The measurement of the above emissions determines the vehicle on-road emission, unit emission and fuel consumption. The exhaust gas is introduced into the analyzer through a probe maintaining the temperature of 191°C. Then particulate matter is filtered out (diesel engines) and the exhaust is directed to the flame-ionizing detector (FID) where hydrocarbons concentration is measured. The exhaust gas is

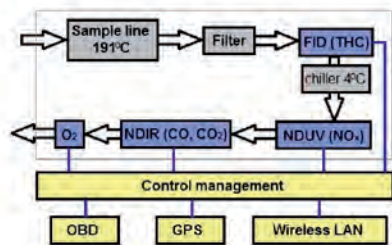


Fig. 3. Schematics of the Semtech DS analyzer

Table 2. Characteristics of SEMTECH DS – a portable exhaust emission analyzer

Parameter	Measurement method	Accuracy
Component concentration		
CO	NDIR – non-dispersive (infrared), range 0–10%	±3%
HC	FID – flame ionization, range 0–10 000 ppm	±2,5%
NO _x = NO + NO ₂	NDUV – non-dispersive (ultraviolet), range 0–3000 ppm	±3%
CO ₂	NDIR – non-dispersive (infrared), range 0–20%	±3%
O ₂	electrochemical, range 0–20%	±1%
Sampling frequency	1–4 Hz	±1%
Exhaust mass flow	Mass flow T _{max} to 700°C	±2,5% ±1% of the range
Warm-up time	15 min	
Response time	T ₉₀ < 1 s	
Supported diagnostic systems	SAE J1850/SAE J1979 (LDV) SAE J1708/SAE J1587 (HDV) CAN SAE J1939/J2284 (HDV)	

then chilled to the temperature of 4°C and the measurement of the concentration of nitric oxides (NDUV analyzer), carbon monoxide, carbon dioxide (NDIR analyzer) and oxygen follows in the listed order. The measurement of the oxygen concentration is realized with an electrochemical sensor. It is possible to add data sent directly from the vehicle diagnostic system to the central unit of the analyzer and use the GPS signal (Global Positioning System).

For the measurement of particulate matter SEMTECH-LAM (Laser Aerosol Monitor) was used. SEMTECH-LAM operates through laser light scattering and measures the concentration of fine particulate matter in the exhaust gas in real time. With two selectable ranges and variable dilution ratios, the analyzer is compatible with a variety of different engine types, vehicles and test conditions. It could be used as test stand equipment or for on-road testing. The dual sample port enables testing of the filter efficiency for engines fitted with a diesel particulate filter. The SEMTECH-LAM uses three mass flow controllers that are automatically adjusted to maintain the desired dilution ratio. The monitor contains a laser light scattering analyzer that measures fine particulates from 100 nm to 10 000 nm. The specifications of SEMTECH-LAM have been shown in table 3.

4. Test results and analysis

The conducted research enabled a determination of the exhaust emissions during the whole test cycle (the whole range of engine speeds and loads). The applied methodology enabled a determination of the exhaust emissions in the NTE test. The used methodology also allowed distinguishing of the NTE test complaint engine work points. Figure 4 shows the work points and the NTE test zone determined for the tested engine. During the tests the tractor was coupled to a cultivator. The aggregate operated in the field. During the tests the tractor operated at four different speeds, which resulted in changes in the engine loads caused by the increase in the resistance of the cultivator as the speed grew. This is seen in figure 4. The work points of the engine are accumulated around certain engine speeds. From the data obtained during the tests it results that only 61% of the total operating time of the test cycle the engine worked in the NTE test zone (Fig. 4). The duration of the whole test cycle was 4337 s., 2645 s. of which the tractor engine operated in the NTE test. That constitutes 61% of the total test time, which means that as much as almost 40% of the engine time of operation is not covered by the NTE test. The NTE test did not cover the engine operating areas with small loads (up to approximately 280 N·m) and low engine speeds (up to 1300 rpm) including idle. Idle is a frequently used engine operating area when performing light agricultural tasks.

Since the test cycles covered the engine operation outside of the NTE zone this was reflected in the exhaust emissions. Figure 5 shows the exhaust emission test results for the whole test cycle and for the NTE test. What is characteristic is that in the NTE test the exhaust emission of all toxic components is lower. The greatest differences are for hydrocarbons and nitric oxides. The emission of these components is lower in the NTE test by 25 and 23% respectively (Fig. 6). We also have a substantial difference in the emission of particulate matter. In the NTE test it is lower by 13% as compared to the emission from the whole test cycle. The smallest difference was observed for the emission of carbon monoxide, which was 9%. Based on the obtained

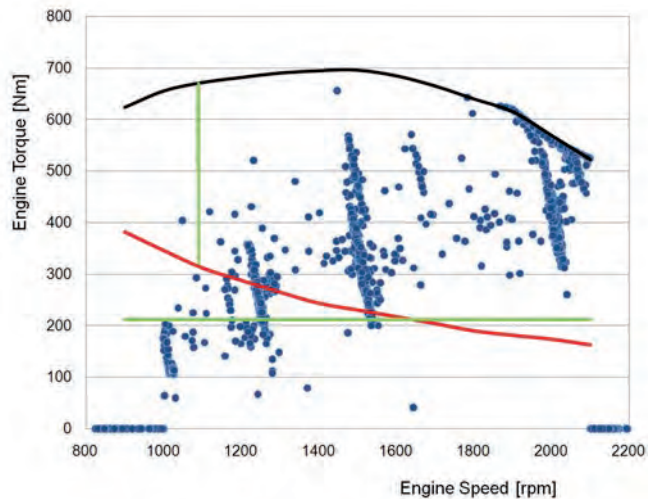


Fig. 4. Characteristics of the maximum engine torque of the tested engine. The work points and the NTE zone marked

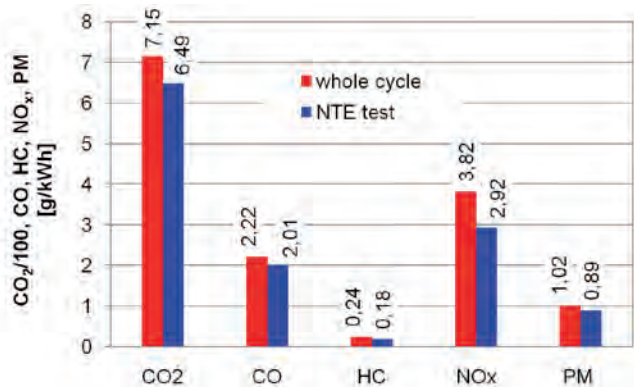


Fig. 5. Unit emission of the exhaust components from the tested engine under actual operating conditions

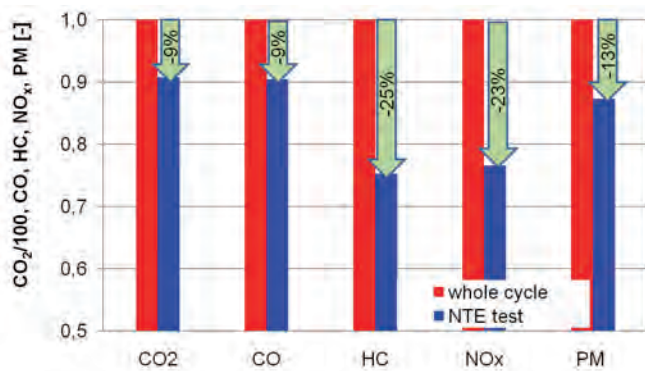


Fig. 6. Relative exhaust emissions from the engine of the tested tractor under actual operating conditions

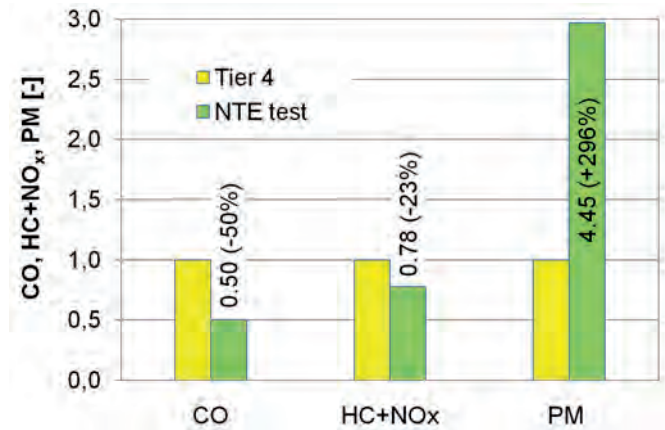


Fig. 7. Relative exhaust emissions from the engine of the tested tractor under actual operating conditions

results we can also conclude that the engine operating area in the NTE test was more advantageous in terms of fuel consumption than the whole test cycle because the unit emission of carbon dioxide in the NTE test was lower by 9%.

Figure 7 shows relative exhaust emissions from the engine of the tested tractor during operation under actual operating conditions as compared to the Tier 3 limits. The emission of carbon monoxide and the sum of the emissions of hydrocarbons and nitric oxides is lower than the Tier 3 limit while the emission of PM exceeds this limit significantly – it is almost three times higher.

5. Conclusions

Exhaust emission testing of non-road vehicles is a necessity. No emission control exists over most of these vehicles. The NTE test included in the American emission legislation is one of the first proposals of this type, yet we need to consider whether this proposal fully lives up to the requirements and conditions of non-road vehicle operation. The test results and their analysis presented in this paper prove that in the case of farm tractors the NTE test zone does not entirely reflect the actual tractor engine operation. In the case of the tests described in the paper almost 40% of the engine operating time fell outside of the NTE test zone. We should thus consider whether the procedure of this test should be modified. It seems it is purposeful to seek such testing solutions that will more accurately reflect engine actual operating conditions. The European proposal prescribes the determination of the exhaust emissions in operation based on the determination of work performed by the engine during the tests. We need to stress that the exhaust emission testing methodology under actual operating conditions is currently in its infancy and it will certainly be modified as the experience and additional information in this matter extends. Another problem are the emission limits for tests conducted under actual operating conditions. The regulations on the NTE test prescribe that these values are not to be greater than 1.25 of the limits included in the type approval standard (Tier 4). Based on the results presented in the paper and authors' experience we can state that meeting these requirements may be very difficult, especially for particulate matter. The test described in the paper is one of the first in its type and its results and conclusions motivate to continue works on this subject. The final determination of the requirements pertaining to the testing methodology for non-road vehicles under actual operating conditions requires a more extensive research on a greater number of objects performing a greater variety of works.

References

1. Abolhasani S, Frey HC, Kim K, Rasdorf W, Lewis P, Pang S. H. Real-World In-Use Activity, Fuel Use, and Emissions for Nonroad Construction Vehicles: A Case Study for Excavators. *Journal of the Air & Waste Management Association* 2010; 58: 1033–1046.

2. Andreae M, Salemm G, Kumar M, Sun Z. Emissions Certification Vehicle Cycles Based on Heavy Duty Engine Test Cycles. SAE Technical Paper 2012; 2012-01-0878.
3. Attfield M, D, Schleiff PL, Lubin JH. et al. The Diesel Exhaust in Miners Study: A Cohort Mortality Study With Emphasis on Lung Cancer. Journal of the National Cancer Institute 2012; 104(11): 869–883.
4. Bass E, Johnson J, Wildemann P. A Comparison of HEV Engine Operation and HD Engine Emissions Test Cycles. SAE Technical Paper 2000; 2000-01-3469.
5. Block M, Abolhasani S, Toscano F, Eric Persson E. PEMS Testing – Applications and Lessons Learned. 2012 PEMS Conference and Workshop, Riverside, California March 29th, 2012; (CD).
6. Giannelli RA. et. al. In-Use Emissions from Non-road Equipment for EPA Emissions Inventory Modeling (MOVES). SAE Technical Paper 2010; 2010-01-1952.
7. IARC: Diesel Engine Exhaust Carcinogenic. Press Release, 12 June, 2012; 213.
8. Jackson C, Sze C, Schenk C, Olson B, Laroo C. Comparison of Exhaust Emissions from Application of the Ramped Modal Cycle and Steady-State Nonroad Test. SAE Technical Paper 2005; 2005-01-1615.
9. Kulkarni NC, Gopalakrishna K. Co-relation Between Engine Test Bed Data and Vehicle Level Data to Generate Duty Cycle for Commercial Vehicles. SAE Technical Paper 2008; 2008-01-0696.
10. Lijewski P, Merkisz J, Fuc P, Pielecha J. Exhaust Emission Tests from Agricultural Machinery under Real Operating Conditions. SAE Technical Paper 2010; 2010-01-1949.
11. Merkisz J, Lijewski P. Time Density of Engine Operation in Non-road Vehicles in the Aspect of the Homologation Toxic Emission Test. SAE Paper 2010; 2010-01-1282.
12. Merkisz J, Lijewski P, Walasik S. The Analysis of Non-road Vehicle Engine Operating Conditions in Terms of Emission Regulations. Eksploatacja i Niezawodność – Maintenance and Reliability 2010; 1(45): 42–48.
13. Noren O, Pettersson O. Development of Relevant Work-Cycles and Emission Factors for Off-Road Machines. SAE Technical Paper 2011; 2001-01-3637.
14. Silverman DT, Samanic CM, Lubin JH et. al. The Diesel Exhaust in Miners Study: A Nested Case-Control Study of Lung Cancer and Diesel Exhaust. Journal of the National Cancer Institute 2012; 104(11): 855–868.
15. Ullman TL, Webb CC, Jackson CC, Doorlag MH. Nonroad Engine Activity Analysis and Transient Cycle Generation. SAE Technical Paper 1999; 1999-01-2800.
16. www.dieselnet.com

Prof. Jerzy MERKISZ, Ph.D., D.Sc. (Eng.)

Piotr LIJEWSKI, Ph.D. (Eng.)

Paweł FUĆ, Ph.D. (Eng.)

Institute of Combustion Engines and Transport

Poznań University of Technology

ul. Piotrowo 3, 60-965 Poznań, Poland

E-mail: piotr.lijewski@put.poznan.pl

Sylwester WEYMANN, M.Sc. (Eng.)

Industrial Institute of Agricultural Engineering

ul. Starołęcka 31, 60-963 Poznań, Poland

Bolesław KARWAT
Dariusz GŁOWIŃSKI
Emil STAŃCZYK

ANALYSIS OF THE INFLUENCE OF FACTORS ON THE PHOTOMETRY OF THE OPTICAL LIGHT SYSTEM OF CHMSL CAR LAMPS

ANALIZA CZYNNIKÓW WPŁYWAJĄCYCH NA FOTOMETRIĘ SYSTEMU OPTYCZNO-ŚWIETLNEGO LAMPY SAMOCHODOWEJ TYPU CHMSL*

The article presents an analysis of the construction of CHMSL (Centre High-Mounted Stop Lamp) car lamps and a study of the influence of individual components on the photometric parameters (light intensity). The authors have conducted a detailed study of the various design elements and the impact of their settings on each photometric parameter of the tested lamp. There is also a presentation of research results on the impact of plastic injection technologies used to manufacture the lamp, such as holding pressure, holding time and injection speed, on the photometric parameters of the CHMSL lamp's optical system.

Keywords: photometry, optical system, car lamp, plastics.

Artykuł zawiera analizę budowy lampy samochodowej typu CHMSL, (ang. Centre High-Mounted Stop Lamp) oraz badania wpływu poszczególnych jej elementów konstrukcyjnych na parametry fotometryczne (natężenie światła). Autorzy przeprowadzili szczegółowe badania w zakresie wpływu konstrukcji poszczególnych elementów i ich ustawienia względem siebie na parametry fotometryczne badanej lampy. Przedstawiono również wyniki badań w zakresie wpływu wykonania elementów lampy w technologii wtrysku tworzyw sztucznych takich jak: ciśnienie docisku, czas docisku i prędkość wtrysku na parametry fotometryczne całego systemu optyczno-światelnego lampy typu CHMSL.

Słowa kluczowe: fotometria, systemy optyczne, lampy samochodowe, tworzywa sztuczne.

1. Introduction

The automotive industry is associated with continuous development and with innovative solutions in design and technology being implemented in motor vehicles. The most spectacular solutions are those involving propulsion systems, where such changes cause motor vehicle power to surge while fuel consumption is reduced. However, the most rapid development and the greatest evolution are taking place in motor vehicle exterior lighting systems. At present, these are intricate and technologically advanced systems, the primary functions of which have expanded significantly. Only a few years ago the role of motor vehicle lighting systems was to improve the driver's visibility in adverse atmospheric conditions, signal his presence on the road and to inform others of his manoeuvres [8]. While fulfilling these fundamental requirements, the automotive industry has also come up with new lamp designs and some new ideas for lighting system solutions [17]. One of these solutions is extra lights for daytime driving, *Daytime Running Lights*, which, since 2011, in accordance with EU directive 2008/89/EC, have been required for all new motor vehicles, passenger cars, trucks, and buses.

A particularly rapidly developing trend in this sector is the application of *Light-Emitting Diodes* [4, 13] as a source of light on an ever-greater scale. LED diodes, due to their substantially lower consumption of electric energy, reduce fuel consumption and thus lower CO₂ emissions into the atmosphere [7, 13]. Due to smaller dimensions, lower heat emission and enhanced longevity, they increasingly tend to replace traditional halogen bulbs on the market [7, 12].

Among the new ideas and solutions, attention should be paid to the technological development of lighting not only with LED diodes,

but also using laser diodes [15] as a light source, which not long ago was a futuristic vision of lighting but right now is being implemented by a number of automotive companies in their models of the cars of the future. There is also work in progress on selective lighting, whose function of adapting to road conditions will allow drivers to selectively choose areas to be lit so as to limit negative impact on other road users [8, 9]. *Adaptive Front-Lighting System* constitutes a breakthrough in lighting technology [9]. It enables automatic adaptation to changing traffic conditions such as the speed of the vehicle, atmospheric conditions, curves in the road, etc. All these changes pose an ever-greater challenge to lamp designers and control-and-feed system designers, but most of all to the provisions of laws concerning safety and compliance of specific parameters with technical requirements.

The article contains an analysis of factors influencing the photometry of CHMSL lamps. In Poland such lamps are described as 'third brake lights' or else as 'central brake lights'. This lamp was introduced in 1986 in USA and Canada as part of the obligatory equipment for passenger cars. In Europe this type of lamp was not introduced until 1998. The function of the lamp is to provide an extra warning of a braking manoeuvre, especially in a situation when the main brake lights are not visible [17]. The implementation of CHMSL lamps has reduced by a few percentage points the number of road accidents characterised by rear-end collisions with a vehicle directly ahead in standard road traffic conditions and, in particular, in city traffic [16].

Within the study programme established to test the process of CHMSL lamp production, several tests and observations have been carried out. Their objective was to confirm the current knowledge on the process of design and manufacture of the tested lamp. The expected result was the identification of boundary parameters for the

(*) Tekst artykułu w polskiej wersji językowej dostępny w elektronicznym wydaniu kwartalnika na stronie www.ein.org.pl

manufacturing process which would enable assured improvements in the process's stability and maintenance of the required quality parameters for the end product.

2. Construction of the CHMSL car lamp

The tests were performed using a typical serially-produced CHMSL lamp, in which LED diodes were applied as a source of light and the exterior construction joined with ultrasonic welding. The tested lamp consisted of four major functional elements featured in figure 1, marked as follows: 1 – an external lens manufactured with the PMMA thermoplastic injection process, 2 – a Fresnel lens, also manufactured with the polycarbonate plastic (PC) injection process, 3 – a PCB (printed circuit board) with LED diodes, 4 – housing produced with the PC-ABS injection process, which, due to its properties, makes the lamp as a whole sturdier and resistant to breakage.

The performed study omitted structural elements of the CHMSL lamp with no influence on the photometric parameters (intensity of light), such as seals, rear wipers and mounting elements.

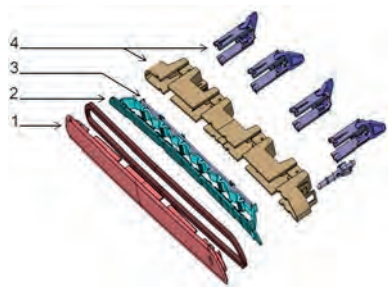


Fig.1. Construction of CHMSL lamp

The external lens is manufactured through the PMMA thermoplastic injection process using a screw injection moulding machine (by Demag) with a holding force of 200 Mg. The use of PMMA thermoplastic derives from its properties, i.e. high transparency at a 92% level; as well, it is an amorphous polymer, shiny, with a sparkling surface, characterised by good mechanical strength, resistance to chemicals, and very high resistance to atmospheric conditions.

In the sequence of thermoplastic injection into a mould socket, the holding process consists of three stages, for each of which the value of holding pressure is different. For amorphous polymers such as PMMA, the values in the individual stages should decrease in order to reduce the frozen-in residual stress.

The tested lamp used LED diodes, Lx E6SF series, made by Osram. These diodes are characterised by amber light, high effectiveness, and a 120° light emission angle. This diode has no convex external lens, so the emitted light does not undergo refraction when the boundary between two sources is crossed, as is the case with the traditional diodes, and it is reflected only from the concave reflector, which contains a connector emitting optical radiation.

The reduced angle of emission to 120°, as compared to 180° and greater in traditional diodes, reduces losses connected with light energy dispersion, and hence enhances the diode's efficiency. Apart from the above-mentioned properties for brake lights, one essential parameter is the lamp's reaction time, i.e. the inertia of the light source. For the sake of comparison, an LED diode reaches full luminous intensity within 30 μs, a traditional car bulb within 75 μs [3].

Thanks to its shape, the Fresnel lens applied in the tested lamp enables a substantial reduction in dimensions compared with a traditional lens with the same optical parameters. This is due to the structure of the lens, which consists of two dispersive collimator areas and a focusing collector. It is this very feature, i.e. small dimensions, and hence low production costs, that allow this lens to be widely used

for devices requiring small dimensions, high efficiency and low cost. Lenses of this type are characterised by a certain distortion on the edges; however, for industrial use this imperfection is not critical.

In the tested lamp, the optical element consists of several constituents: an inverted Fresnel lens, the lens itself, and cushion lenses situated on the external part. A lamp thus constructed is characterised by uniform dispersion of light, due to which the light emitted by point sources is close to a uniform beam of light. This lens is responsible for uniform propagation of light in a vertical plane within the required angular range, i.e. +10°/10° from the lamp's vertical axis.

The lamp housing and the external lens are joined through ultrasonic welding, i.e. a process inducing mechanical vibrations with frequencies of approximately 20 kHz in one of the two elements being connected. During this process the two elements being connected are situated so that the surfaces to be joined can touch one another.

3. Programme of study of the parameters influencing CHMSL lamp photometry

3.1. Formulation of the equation of state

One of the fundamental parameters defining lamp efficiency is intensity of emitted light. In the automotive industry this value is measured on a dozen or so points of a measuring grid, and is defined by standard no. E/ECE/324 of the Economic Commission for Europe [16].

In order to limit study costs, and on the basis of former observations concerning the CHMSL light lamp manufacturing process, an assumption has been made regarding only partial variations in the tested optical system. Likewise, assuming zero external interference, the tested optical system can be described by the equation of state (1)

$$B+C+D+[A(n)] = [E(n)], \quad (1)$$

using the following notation:

B, C, D – constant values (B – Fresnel lens, C – LED source of light, D – housing),

[E(n)] – output signal, light intensity (18-element matrix corresponding to light intensity at 18 points of measurement, $n = (1 \dots \infty) - \text{lamp}$),

[A(n)] – matrix of variables, A – external lens.

$$[A(n)] \begin{bmatrix} a(n) \\ b(n) \\ c(n) \\ d(n) \end{bmatrix}. \quad (2)$$

In the equation (1) [A(n)] denotes the matrix describing changes in the parameters of the external lens. It has been assumed that for every one of the n tested cases (lamps), an essential influence on the photometric parameters of the lamp appears precisely in that area. This variability ensures the high susceptibility of that element to changes in the parameters of the manufacturing process; the essential role played by the external lens in the lamp's optical system has necessitated certain detailed tests of precisely that element.

In order to define the main factors influencing changes in the constituent values of matrix [A(n)], the following tests have been performed:

- a(n) – impact of changes in holding time,
- b(n) – impact of changes in holding pressure,
- c(n) – impact of changes in injection speed,

d(n) – other factors not tested, but influencing the tested system, e.g. the lighting surface of the lens [11], the extent of dirt contamination [10], how precisely the external lens has been joined to the housing, etc.

The output variable $E(n)$ is the main parameter defining functionality and photometric efficiency, meaning the intensity of light as emitted by the tested lamp. Intensity of light was measured according to the SI system in Candelas (cd). In compliance with the standard E/ECE/324 for lamps in the S3 group, in which the tested lamp is classified, this parameter is measured at eighteen points of the measuring grid. These points are located on the grid with a scale of 5 angular degrees, in the $\pm 10^\circ$ range for the horizontal coordinate and in the $\pm 10^\circ/\pm 5^\circ$ range for the vertical coordinate. A recommended value is used to define the grid of intensity distribution through the definition of minimum and maximum values of intensity for each of the points, as a percentage value of nominal intensity at the central point of the grid. These points are set by an appropriate deviation from the central point (the point crossing through lamp axis H-0; V-0) by 5° or 10° in either the horizontal or vertical plane. The light intensity value at points H-0 and V-0 as per the valid standard for the tested lamp should fall within 25 to 110 cd. The standard E/ECE/324 in chapter 5 allows for reduction of that criterion to 95% [1].

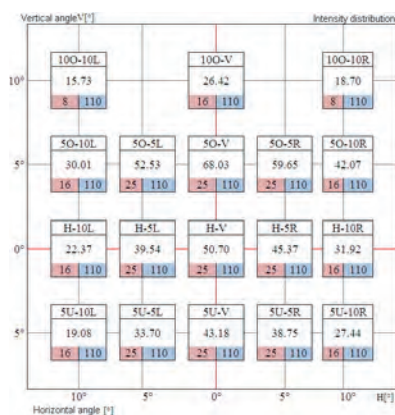


Fig. 2. Exemplary report from performed CHMSL lamp study

Figure 2 presents an exemplary measurement report, generated at the end of the study as a summary and a collection of measurement results. This report presents the grid of points. Individual measurement points are presented in figure 3, using the following notation: 1 – location of measurement point, 2 – measured value of light intensity in cd, 3 – minimum and maximum values of light intensity for that measurement point in cd.



Fig. 3. Description of measurement point

3.2. Description of measurement chain

The measurements of light intensity of the tested lamp were performed with the use of a device known as a goniophotometer. This device consists of a flex arm on which the lamp to be tested is mounted, a fixed sensor, a control-measurement apparatus, and an IT system provided with an application to carry out and edit measurement results. The arm on which the tested lamp is mounted enables changes in position so that during the measurement sequence the axis of the tested lamp is capable of assuming any of the eighteen different positions corresponding to the eighteen measurement points defined by the standard. When the CHMSL lamp is tested, the sensor is placed 25 metres away from the arm on which the lamp is installed. That dis-

tance is needed in order to preserve the inverse square law of distance, i.e. the measured intensity of light is directly proportional to the luminous intensity of the source, and inversely proportional to the square of the distance between the source being tested and the location of the measurement device, i.e. of sensor placement. To perform the study, a Goniophotometer GO-H1400, a dedicated device used for measuring light intensity, was applied.

The accuracy of the aforementioned device together with the measuring sensor SP 30 S0T-GO, which had already been used in the study, fulfils the requirements imposed on qualified devices as compliant with the "L" standard described in the standard DIN 5032, part 7 [6]. The discussed measuring device was built in the underground testing tunnel depicted in figure 4, which, thanks to its location and the additional covering of its walls with paint which absorbs reflected radiation, eliminates the influence of external distortion and guarantees suitable measurement conditions.



Fig. 4. Measurement tunnel for photometric study of various type of car lamps

3.3. Scope of the study

3.3.1. Study of the impact of lamp completeness

For the purpose of describing the functional impact of each of the lamp elements on the tested photometric parameters, tests were performed consisting of the measurement of the intensity of light emitted by parts of the complete optical system, i.e.:

- a system consisting of a light source in the form of PCBs installed in the housing with no optical elements,
- a system consisting of a light source and a Fresnel lens as well as a housing.

The last part of the study of the impact of lamp completeness on photometric parameters consisted of measurements of light intensity for an optical system consisting of a light source, Fresnel lens, external lens and housing, i.e. for the entire lamp.

3.3.2. Study of the impact of technological process of making external lens

In accordance with the equation of state (1), in which the elements of the matrix $A(n)$ are: $a(n)$, $b(n)$ and $c(n)$, a study was performed in order to define the impact of changes in the parameters of the injection process on the intensity of light emitted by the lamp being tested. In accordance with the primary assumptions, only the external lens manufacturing process was analysed. This does not mean, however, that the remaining lamp elements such as the Fresnel lens or the housing are not essential. Their functional significance in the entire optical system of the lamp is important even though a simplification has been assumed on the basis of the proven high stability and repeatability of the process for these elements. Such an assumption was made in chapter 1 while formulating the equation of state (1), where the thesis regarding the stability of these two components was described in terms of constant values B and C affecting the output value $E(n)$.

The study programme on the impact of the parameters of the injection process of the external lens on the intensity of light emitted by the CHMSL lamp covered changes in: holding time, holding pressure, and injection speed [2, 14, 18].

a) Impact of changes in holding time – a(n)

As part of the study, an analysis was made of the impact of change in the holding time parameter value on the quality of manufactured mouldings, and, in effect, on the intensity of light generated by the tested lamp. During the study, a change in parameter was forced by gradually reducing the given value of the set time by 1 s from nominal value, which was initially 7 s, while leaving the temperature of the injection mould for fixed and flexible parts as well as the constant speed of injection unchanged.

b) Impact of changes in holding pressure – b(n)

As part of the study on the impact of changes in holding profile, some gradual changes were introduced in each of the three stages, beginning with nominal values of 150 bar – stage 1, 130 bar – stage 2, 110 bar – stage 3; then pressure values were reduced by 2 bar in each of the stages, thus reaching values of 130–110–90 bar.

c) Impact of changes in injection speed – c(n)

During the course of the study there were proportional changes made in the injection speed at each of the 3 stages, similar to those made during injection pressure testing. The study commenced with the values 24–38–26 mm/s (test 1), followed by reductions of 2 mm/s, thus reaching values of 18–32–20 mm/s (test 4). The study was performed for 3 different additional conditions, with the mould temperature as the variable. While testing sample no. 1, when changes in speed were made, the standard temperature was maintained; while testing sample no. 2, the temperature was reduced by 5°C from nominal value; while testing sample no. 3, the temperature was reduced by 10°C.

4. Presentation of study results

4.1. Study of an optical system with a light source in the form of PCBs with LED diodes mounted in the CHMSL lamp housing

The tested light system may be described by the equation of state (3).

$$C+D = [E(n)]. \quad (3)$$

Figure 5 features the study results for the analysed system. It may be concluded that, for the majority of the 18 measurement points, the light intensity has such a low value that it does not fit within the measuring scale, whereas for the remaining points the incidental light intensity falls within the scale or even meets the requirements, as in the case with point 100-10R. The distribution is dispersed and not uniform, and the majority of the light emitted by each of the LED diodes constituting part of the light source is lost as a result of the dispersion of light rays in planes which are not tested and are functionally insignificant.

A system constructed in this way, despite combining power corresponding to the power emitted by a complete CHMSL lamp meeting the requirements of the standard E/ECE/324, does not fulfil that standard's requirements, as the majority of light energy is dispersed and lost. The functionality of a system thus constructed fails to fulfil the basic requirements.

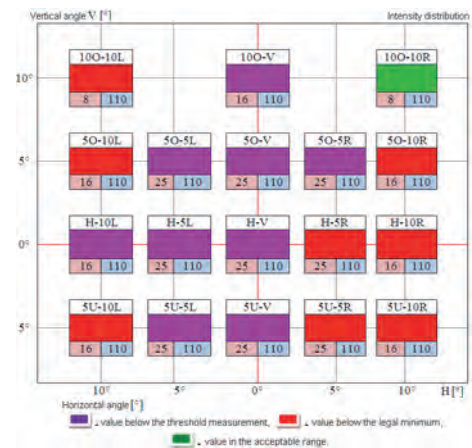


Fig. 5. Distribution of light intensity for the tested light system

4.2. Study of a lighting system with a light source in the form of PCBs with LED diodes mounted in the CHMSL lamp housing with a Fresnel lens

The tested light system may be described by the equation of state (4). In this case the tested light system has been additionally provided with a Fresnel lens.

$$B+C+D = [E(n)]. \quad (4)$$

Figure 6 features a diagram for eighteen tested points of the lamp. By analysing the diagram featuring the results of measurement of the system, one can observe significant improvement in the photometric parameters; however, for the majority of the eighteen points of measurement, the intensity of light is still below the lower boundary of the minimum value required by the standard E/ECE/324.

By analysing the diagram it can be seen that light intensity at points located on the main horizontal axis fulfils the requirements, as the measured value is within the required range; nonetheless one can still observe asymmetrical distribution, especially for extreme points for which the values are beyond the measurement boundaries. The non-linearity of the distribution is also caused by the low rigidity of a light system constructed in this way. In this form the incomplete lamp (no welding to join the housing and the external lens) indicates a high propensity to deformation and distortion.

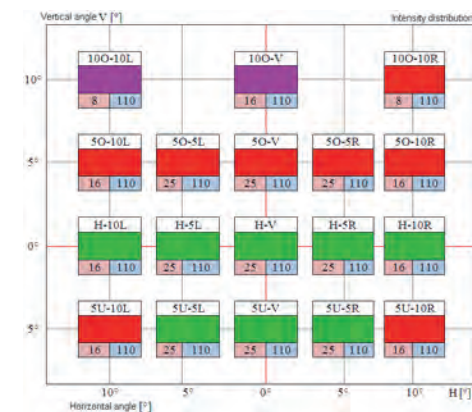


Fig. 6. Distribution of the intensity of light for the tested light system (notations as in fig. 6.)

4.3. Study of the light system with the source of light in the form of PCBs with LED diodes mounted in the CHMSL lamp housing, a Fresnel lens and an external lens

The tested light system may be described by the equation of state (5).

$$B+C+D+[A(n)] = [E(n)]. \quad (5)$$

In this case we have a complete lamp consisting of four elements, i.e. housing, source of light, Fresnel lens and external lens. A light system constructed in this way demonstrates the expected properties, i.e. the intensity of light falls within the required range for each of the measured points. This has been achieved by adding the ultimate element, i.e. the external lens, which, first of all, completes the entire construction, creating a uniform and closed solid (enhancing the rigidity of the system); secondly, it fulfils the role of an optical filter enabling the emission of waves ranging from 630 to approximately 780 nm, i.e. waves visible as red light [19]. The third function, being of key importance, is the optical function connected with 'cleaning up' the radiation emitted by the LED diodes and initially corrected by Fresnel lens, so that the distribution of radiation, in this case in the horizontal plane, is compliant with the requirements, i.e. so that it fits within the range of $+10^\circ/-5^\circ$. Such intensity of light has been achieved thanks to the specific shape of the external lens's internal surface, on which there are several asymmetrical prisms. It is important, for the calculation of the entire system, to accommodate the coefficient of light refraction at the time of crossing the boundary between two sources, PMMA thermoplastic and the air, which is 1.46 (compared with e.g. 1.6 for optical glass, 1.5 for water; and 1.0 for a vacuum) [5]. By studying the intensity of light emitted by the optical system constructed in this way, the impact of each of the constituting elements on the intensity of light at the defined points of measurement is observed. As can be seen, each of the elements fulfils an important role in the system; nonetheless, the function of the external lens is most complex and essential from the perspective of the functionality of the entire CHMSL lamp. The measurement results are presented in Figure 7.

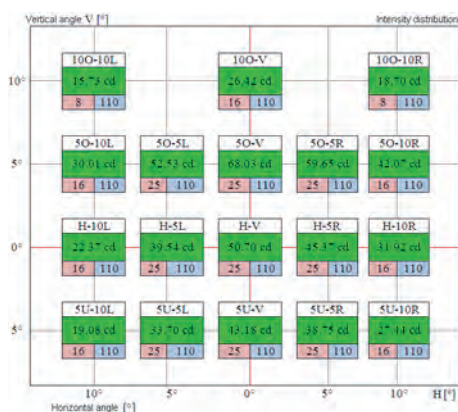


Fig. 7. Distribution of the intensity of light for the tested light system (notations as in fig. 6)

4.4. Impact of changes in the parameters of the injection process

4.4.1. Impact of changes in holding time – a(n)

The results point to relatively small changes in the intensity of light with respect to light intensity values obtained from the measurement of external lenses produced via the process, for which the holding time was 7 s. The study of changes in that value was completed with a holding time of 3 s. Any further reduction of that time caused

visible and unacceptable changes as well as geometrical deformations. The study results are featured in Figure 8.

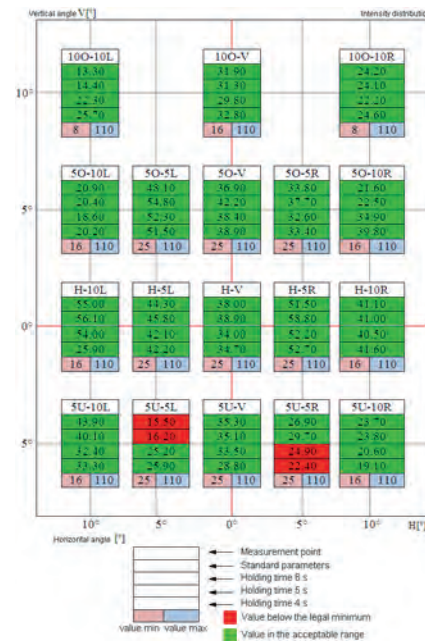


Fig. 8. Impact of changes in mould holding time on the intensity of light emitted by lamp

The analysis of the results indicates that a change in holding time value of 50% causes insignificant changes in light intensities at the measured points of approximately 2% of initial value. Thus it can be assumed that given conditions such as these, the impact of changes in that parameter on our output variable is insignificant. However, it should be remembered that an insufficient holding time may be a cause of deformation in the surface and could cause a deformation resulting from shrinkage of the thermoplastic material in the injection mould chamber.

4.4.2. Impact of changes in holding pressure – b(n)

The list of holding pressure values in the performed tests is presented in Table 1. A reduction in holding pressure to 130–110–90 bar was performed. Setting parameters below that limit causes unacceptable changes in the form of flawed mouldings and deformations resulting from plastic shrinkage. The performed study pointed to an inversely proportional relationship of changes in the intensity of light relative to changes in holding pressure in the central area of the grid of measurement points; reduction increases light intensity values. This rule holds as far as holding pressures of 142–122–102 bars.

The dependence observed in the first range, i.e. improvement of light parameters, results from, among other things, a reduction in the density of the sample. This change is the result of the reduced weight of the mouldings, which is a consequence of reduced holding pressure, i.e. of the supply, within the same time unit, of a smaller quantity of material. Further reduction in holding pressure would cause the appearance of deformations, as clearly indicated by measurements performed with the use of an optical projector. Poorer results on the edges are caused by greater deformations of optical elements, which appear in proportion to increasing distance from the centre of the lens. The results of the measurements are presented in figure 9.

One conclusion from these tests is the confirmation of the positive influence of a reduction in holding pressure value on the improvement of photometric parameters; however, this is observed only in the central part of the grid of measurement points, i.e. central part of the lens. One side effect is a deformation (flexion) of the element, as

Table 1. List of performed tests.

Test no.	Holding profile [bar]
Test 1	150–130–110
Test 2	148–128–108
Test 3	146–126–106
Test 4	144–124–104
Test 5	142–122–102
Test 6	140–120–100
Test 7	138–118–98
Test 8	136–116–96
Test 9	134–114–94
Test 10	132–112–92
Test 11	130–110–90

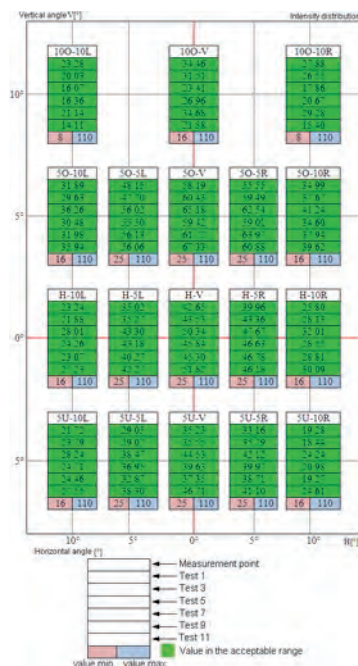


Fig. 9. Impact of changes in mould holding pressure on the intensity of the light emitted by the lamp

well as changes in the imaging of internal cushion lenses, which cause gradual deterioration of the optical parameters in the extreme ranges. These deformations are related to incomplete formation of the moulding due to insufficient pressure. This effect intensifies proportionately to distance from the centre of the moulding, which in this case is also the point of thermoplastic injection.

The tests indicate the feasibility of an improvement in the parameters of light intensity through a change in pressure value; however, such changes would probably be insignificant, a maximum of 5% over the present parameters of injection, and with a risk of deformations, which, within the initial range of parameter reduction, are not easily spotted; nonetheless, with a further reduction in holding parameters, they tend to increase and exert a negative influence on photometric parameters as well as on the geometry of the produced element.

4.4.3. Impact of changes in injection speed – c(n)

A list of injection speed values for various mould temperatures is presented in table 2.

The analysis of the results of tests presented in Figure 10 indicates a change in the photometric parameters of the tested lamp with respect to a change in plastic injection speed. In the first case, in which the injection mould maintained a nominal temperature, a reduction in injection speed caused an improvement in the photometric parameters. However, in a case where temperature was reduced by -5°C and -10°C , this dependence proceeded in the opposite direction, i.e. a reduction in the injection speed caused a reduction in light intensity value. Knowing that injection speed has an impact on the temperature of injected material resulting from flow through a gate channel, it can be concluded that in the first case the reduction in speed caused reduced friction, and thus a reduced impact of injection speed on temperature increase; in addition, reduced speed caused a prolongation of injection time, and hence an improvement in the formation and quality of mouldings. In the following two cases a reduction in speed, and thus a reduction in temperature growth resulting from the process of material injection, coincided with additional forced temperature reduction, which caused deterioration in the moulding parameters.

Table 2. List of performed tests

	Sample no. 1 Nominal temp. of mould	Sample no. 2 Temp. reduced by 5°C	Sample no. 3 Temp. reduced by 10°C
Test 1 [mm/s]	24 – 38 – 26	24 – 38 – 26	24 – 38 – 26
Test 2 [mm/s]	22 – 36 – 24	22 – 36 – 24	22 – 36 – 24
Test 3 [mm/s]	20 – 34 – 22	20 – 34 – 22	20 – 34 – 22
Test 4 [mm/s]	18 – 32 – 20	18 – 32 – 20	18 – 32 – 20

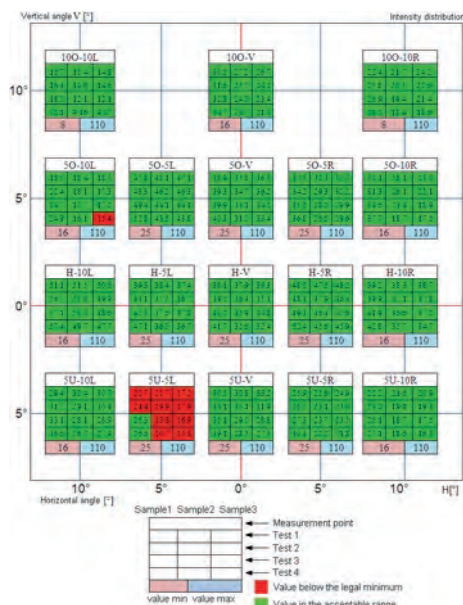


Fig. 10. Study of changes in the photometric parameters of the lamp at changing injection speeds

The performed tests showed that injection speed can be reduced at a given mould temperature; however, this extends cycle time, and hence increases costs. The conclusion regarding the impact of changes in mould temperature is also significant, as this should force better and more accurate monitoring of the systems responsible for the maintenance of temperatures at an appropriate level.

5. Summary

The article presents the results of the study of the impact of individual design elements and of the technological process of external lens manufacture on the photometric parameters of a third lamp, type CHMSL, that signals that a car is braking, applied in passenger cars, trucks and buses. The solutions currently in use in the automotive industry such as LED diodes as a source of light, or newly-developed laser diodes, pose utterly new challenges for designers and producers, and require greater accuracy, repeatability and stability from the manufacturing process.

The objective of the performed tests was to describe the variability of the manufacturing process and the impact of these changes on output value, i.e. the intensity of light emitted by the CHMSL lamp. The presented tests and observations are part of the optimisation of the manufacturing process which can be conducted using various methods, starting with theoretical analysis, to digital simulations or the performance of tests consisting of simulations of process variability in order to define acceptable tolerance ranges for process input

variables such as geometrical parameters of lamp elements, parameters of the injection process, etc.

The performed analyses indicated the proportional influence of input variables on output signal, which until now was merely an estimated value. The impact of changes in the parameters of injection process, apart from pointing to certain anomalies, particularly in connection with the temperature of the injection process, has caused a change in the system of injection moulding machine inspections, since the demonstrated instability of the process (frequently related in reality to technical condition), especially in the case of tested external lenses, has a critical effect on the parameters of the entire lighting system.

Based on this study, the fundamental parameters influencing the quality of the manufactured design elements of CHMSL lamps can be defined. Taken as a whole, the presented tests and experiments, which frequently consisted of forcing certain extreme conditions upon the technological process, have contributed to better familiarisation with the process and to its further optimisation. The results of the study will be successively implemented in the technological process of manufacturing CHMSL lamps and other lamps of similar construction.

Bibliography

1. Agreement concerning the adoption of uniform technical prescriptions for wheeled vehicles, equipment and parts which can be fitted and/or be used on wheeled vehicles and the conditions for reciprocal recognition of approvals granted on the basis of these prescriptions, 2010. <http://www.unece.org/fileadmin/DAM/trans/main/wp29/wp29regs/r7rev5e.pdf> [2012-11-25].
2. Bogucki M, Stączek P. Zastosowanie metody największego spadku w optymalizacji procesu wtryskiwania. *Eksploracja i Niezawodność – Maintenance and Reliability* 2003; 2:18–20.
3. Boguta A, Ostrowski S, Ozimek H. Energooszczędne półprzewodnikowe źródła światła stosowane w technice motoryzacyjnej. *Przegląd Elektrotechniczny*, ISSN 0033-2097, R. 86, 2007; 7: 224–226.
4. Eichhorn K. LEDs In Automotive Lighting. *Light-Emitting Diodes: Research, Manufacturing and Applications*, Germany 2006.
5. Freeman MH, Hull CC. *Optics*. Butterworth-Heinemann, an imprint of Elsevier, 2003.
6. GO-x Series Hardware Manual, 02/2009 LMT Lichtmesstechnik GmbH, Berlin.
7. Hofmann M, Byrne M. Comparison of LED Circuits. *Techzone Magazine*, Digi-Key, 2010; 44–49.
8. Kang B, Yong B, Park K. Performance evaluations of LED headlamps. *International Journal of Automotive Technology* 2010; 5:737–742.
9. Lukacs L, Dassanayake M, Magalhaes R. Benefits and challenges of controlling a LED AFS (adaptive front-lighting system) using fuzzy logic. *International Journal of Automotive Technology* 2011;4:579–588.
10. Łukasik M. Układ do oceny stopnia zabrudzenia powierzchni przepuszczających światło. *Prace Instytutu Elektrotechniki*, zeszyt 234, 2008: 181–195.
11. Močko W. Analiza wpływu wartości luminancji i pola powierzchni świetlnej klosza światła hamowania na widoczność sygnałów świetlnych. *Transport Samochodowy*, 2011; 1:87–97.
12. Neumann R, Kubena V. Future rear lighting trends – safety and styling aspects. *Progress in automobile lighting*, Held Laboratory of Lighting Technology, HERBERT UTZ VERLAG GMBH, 2001; 723–732.
13. Ortega AV, Silva IN. Neural network model for designing automotive devices using SMD LED. *International Journal of Automotive Technology* 2008; 2: 203210.
14. Saechling H. *Tworzywa sztuczne – poradnik*. WNT, Warszawa, 2000.
15. Sylvester J. Automotive Laser Diodes Soon to Light Up the Road <http://www.palomartechnologies.com/blog/bid/80740> [2012-11-25].
16. 'The Long-Term Effectiveness of Center High Mounted Stop Lamps in Passenger Cars and Light Trucks' NHTSA Technical Report, March 1998, U.S Department of Transportation.
17. Wordenweber B, Wallaschek J, Boyce P, Hoffman D. *Automotive Lighting and Human Vision*. Springer-Verlag Berlin Heidelberg, 2007.
18. Zawistowski H, Frenkler D. *Konstrukcja form wtryskowych do tworzyw termoplastycznych*. WNT, Warszawa, 1984.
19. Żagan W. *Podstawy techniki świetlnej*. Oficyna Wydawnicza Politechniki Warszawskiej, Warszawa, 2005.

Bolesław KARWAT, Ph.D., D.Sc. (Eng.), Assoc. Prof.
Dariusz GŁOWIŃSKI, M.Sc. (Eng.)
Emil STAŃCZYK, M.Sc. (Eng.)

Faculty of Mechanical Engineering and Robotics
 AGH University of Science and Technology
 Al. A. Mickiewicza 30, 30-059 Kraków, Poland
 E-mails: karwat@agh.edu.pl, dariusz.glowinski@interia.pl,
 stanczykemil@gmail.com

Gintautas BUREIKA
Giedrius BEKINTIS
Lionginas LIUDVINAVIČIUS
Gediminas VAIČIŪNAS

APPLYING ANALYTIC HIERARCHY PROCESS TO ASSESS TRAFFIC SAFETY RISK OF RAILWAY INFRASTRUCTURE

ZASTOSOWANIE PROCESU HIERARCHII ANALITYCZNEJ DO OCENY ZAGROŻENIA BEZPIECZEŃSTWA RUCHU W ODNIESIENIU DO INFRASTRUKTURY KOLEJOWEJ

The Analytic Hierarchy Process is described in recent research works as an emerging multicriteria decision-making approach to solving large, dynamic, and complex problems, which reflect real situations, such as strategic planning of management or resources, justification of introducing new technologies or determining the effectiveness of systems' operation. The paper presents an application of the Analytic Hierarchy Process to performance evaluation through a case study of Lithuanian railway traffic safety risk. The results of the performed study show that the application of the Analytic Hierarchy Process method can help railway traffic control managers effectively evaluate the railway infrastructure objects from the perspective of traffic safety risk and make long-term strategic plans for preventing the accidents on railway lines even under difficult economic and transportation conditions. A model for assessing railway infrastructure objects from the perspective of traffic safety risk, developed and realized by the authors for Lithuanian Railways two real lines, is presented. Finally, basic conclusions and recommendations are given.

Keywords: railway traffic risk, infrastructure objects, assessing of traffic risk, Analytic Hierarchy Process (AHP) method, coefficient of concordance.

Najnowsze prace badawcze opisują proces hierarchii analitycznej jako nowy wielokryterialny model podejmowania decyzji służący rozwiązywaniu dużych, dynamicznych i złożonych problemów, które odzwierciedlają rzeczywiste sytuacje, takie jak strategiczne planowanie zarządzania lub zasobów, uzasadnianie wprowadzenia nowych technologii lub określanie efektywności działania systemów. W pracy opisano zastosowanie procesu hierarchii analitycznej do oceny działania, przedstawiając studium przypadku dotyczące bezpieczeństwa ruchu kolejowego na Litwie. Wyniki przeprowadzonego badania wskazują, że stosowanie metody procesu hierarchii analitycznej może pomóc menedżerom ds. sterowania ruchem kolejowym skutecznie oceniać obiekty infrastruktury kolejowej z punktu widzenia zagrożenia bezpieczeństwa ruchu oraz konstruować długoterminowe plany strategiczne mające na celu zapobieganie wypadkom na liniach kolejowych, nawet w trudnych warunkach gospodarczych i transportowych. Przedstawiono model oceny obiektów infrastruktury kolejowej z punktu widzenia zagrożenia bezpieczeństwa ruchu drogowego, opracowany i zrealizowany przez autorów dla dwóch linii Kolei Litewskich. Na zakończenie, podano podstawowe wnioski i zalecenia.

Słowa kluczowe: zagrożenie bezpieczeństwa ruchu kolejowego, obiekty infrastruktury, ocena zagrożenia ruchu, metoda procesu hierarchii analitycznej (AHP), współczynnik konkordancji.

1. Introduction

Traffic safety is one of the main problems facing road and railway operators in many countries of the world. Traffic safety situation in Lithuania, despite the progress made in 2008, is still not good enough compared to the other European Union countries. The effective control and management of railway traffic, ensuring its safety, requires a comprehensive analysis of the state of the railway infrastructure objects and systemization of the obtained data. This would help to develop the effective urgent measures to considerably reduce railway traffic safety risks [1]. The component of railway infrastructure, causing many problems, associated with the collisions of trains with road vehicles and human injuries and mortalities, is level crossing. A comprehensive analysis of level crossings was performed for the period of several years (2003–2011) in Australia and the risk evaluation model ALCAM was suggested, and practically implemented by its governmental institutions. The experts from Great Britain also pay great attention to increasing traffic safety at railway level crossings with the help of the

developed traffic safety control model ALCRM [10]. The Safety Risk Model (SRM), which presents quantitative investigation of the potential accidents resulting from the operation and maintenance of the Great Britain rail network is widely applied too [12]. SRM comprises a total of 120 individual models, each representing a type of hazardous event. Other railway infrastructure components, causing problems to specialists dealing with the problems of railway traffic safety in the Baltic States, Poland and Finland, are railway stations, freight terminals and their sorting track yards, pipelines [4, 18, 20].

Railway traffic safety control is aimed at protecting people, their health and wealth, as well as improving traffic conditions, reducing harmful effect of rail transport on the environment and ensuring the realization of the general aims, associated with railway traffic safety and the relationship between railway systems of various countries. The control of railway traffic safety is regulated in Lithuania by the Lithuanian Law on Railway Traffic Safety. This law defines the rights and responsibilities of the state institutions, developing and implementing the policy of railway traffic safety, as well as the require-

ments to and the rights of the managers (carriers), and the investigation and registration of traffic accidents.

The aim of this paper is to present a traffic safety risk evaluation model developed by the authors with respect to various objects of the railway infrastructure, based on qualitative (expert) evaluation. In the considered risk management model, it is suggested to assess the damage made by railway traffic accidents, based on the criteria presented in the Lithuanian law on railway traffic safety.

The study of Japanese scientists [17] was conducted to evaluate the effect of potential risk factors – such as driving without a license, alcohol use, speed, seat belt, and helmet – use on fatality in motor vehicle traffic accidents. Human factors play an important role in the occurrence of railway traffic accidents too. They embrace the violation of traffic rules, ignorance of road signs and signals by train operators, their dizziness, tiredness, intoxication, etc. [6, 7, 15, 18]. However, traffic safety specialists emphasize that technical factors, including the provision of fencing, pedestrian and cattle crossings, lighting and signs, visibility, etc., can also increase traffic safety [2, 8, 21].

The application of multicriteria methods, especially, the AHP method, largely depends on calculation of the criteria weights, based on expert evaluation [13, 14]. The results obtained can be used for practical purposes if expert judgments are in good agreement [5]. The latter may be determined by the concordance coefficient obtained by ranking the available alternatives. The paper considers a possibility to apply the concordance coefficient in the cases, when expert evaluation is not based on ranking. The calculations reveal the dependence of the agreement of expert estimates on a particular method used. The highest degree of agreement has been obtained by using the direct ranking method. The effect of equally assessed criteria, i.e. the tied ranks, on the concordance coefficient and thereby on the level of expert judgments' agreement is usually insignificant and cannot change the results of rating.

For the reasons discussed above in the presented survey, the AHP method was chosen by the authors. It was applied to the analysis of transport sector, particularly, to the assessment of Lithuanian railway traffic risk. In the railway line environment, these groups of criteria (factors) were evaluated:

- 1) the intensity of railway and road traffic.
- 2) the degree of line traffic control (controllable, semi-automatic and fully automatic);
- 3) ambient conditions (rain, snow, darkness, fog, etc.);
- 4) other.

The infrastructure of Lithuanian Railways embraces the main lines of 2000 km of length, more than 500 level crossings (located at a distance of 4.2 km from each other), tens of railway stations, bridges, viaducts, several locomotive maintenance depots and one tunnel. In the present paper, all objects of the railway's infrastructure are clearly defined, the comprehensive data referring to them is presented and major criteria describing railway traffic safety are determined. The significance of these criteria is also determined, based on expert evaluation, and they are ranked according to this parameter. After evaluation of factors influence weight on the analysed railway line accident level, the urgent measures of increasing the traffic safety on infrastructure object can be ranked. The authors of the present paper offered the developed model for evaluating safety risk with respect to the objects of Lithuanian railway infrastructure. This model was applied on two Lithuanian Railways real lines situated on the main transport corridor (the IXB trans-European corridor) to investigate the level of traffic risk and recommend vital means to improve the situation on these lines. Suggested estimation process, based on worldwide scientifically grounded methods [3, 5, 7, 9, 11, 16], could be also used for assessing and managing traffic safety on the railways infrastructure objects of various country.

2. Railway infrastructure and identification of risk objects

The operator of Lithuanian railway infrastructure is the State Company "Lithuanian Railways" (the original name – AB "Lietuvos geležinkeliai"), which manages and regulates the traffic in the railway entire network. The railway sidings are private. Railway traffic is controlled by the State Inspection of Railways subordinate to the Ministry of Transport.

The investigation and assessment of traffic safety risks associated with railway infrastructure were performed in three stages:

1. The initial stage, which includes the collection (registration) of data on the objects of railway infrastructure and their systemizing, identification of threats, which may result in traffic accidents, expert evaluation of possible damage, the collection of data on the risks associated with the infrastructure objects and determination of the significance of risk factors.
2. Railway traffic risk analysis, when the risk level of an object or a set of objects, chosen based on particular criteria, taking into account the registered risk factors of the considered object or set of objects, is considered.
3. Traffic risk management, which embraces the selection of the required or recommended measures, aimed at reducing risks and associated with a particular object or a set of objects, selected based on particular factors.

At the initial stage of analysis, the data on the objects of Lithuanian Railway infrastructure presenting risk to traffic safety are collected. The risks presented by the following objects of railway infrastructure to railway traffic safety are considered and assessed by the evaluation model:

- 1) rolling stocks;
- 2) rails and automatic switches;
- 3) railway buildings;
- 4) level crossings;
- 5) signalling systems and automatic devices;
- 6) railway stations and terminals.

The main objective of railway traffic safety risk evaluation is a basic railway infrastructure component – the railway line. The railway network of the state consists of railway lines, which make the primary chain of the automatic and signalling system of traffic management.

Traffic safety on the railway line depends on the general factors as follows:

- 1) type of the railway line (single/double track);
- 2) availability of automatic train traffic control devices;
- 3) the conditions of track repair performance, with the traffic stopped or active;
- 4) operational (actual average) speed of the trains;
- 5) actual number of pairs of trains, running along the railway line per day;
- 6) the type of the traffic block-system (automatic or semi-automatic system);
- 7) type of the railway line (crossing – or not – any settlements);
- 8) the distance to the closest residential building;
- 9) type of the railway line (passing – or not – any stations);
- 10) fencing of the railway line;
- 11) the number of level crossings;
- 12) visibility of level crossings in both directions;
- 13) level crossing lighting (present or not present);
- 14) the number of automatic switches on the railway line;
- 15) the number of bridges;
- 16) the number of animal crossings;
- 17) the number of viaducts and overpasses;
- 18) the number of viaducts over water;
- 19) a description of the track largest grade (slope) of the railway line;
- 20) the smallest radius and length of a horizontal curve;

- 21) geometric errors of the gauge;
- 22) the highest superelevation of the rails.

The survey of experts' opinion (specialists in railway traffic safety and train maintenance) allowed the authors to determine the main risk factors for railway line traffic as follows:

- 1) single-track or double-track railway;
- 2) geometric errors in the railway track gauge;
- 3) the number of pairs of trains per day;
- 4) type and number of level crossings;
- 5) category of level crossing (intensity of road and train traffic);
- 6) availability of automatic control devices of train traffic;
- 7) the largest track grade and the track smallest horizontal curve.

3. Identification of traffic accident threats on railways

The analysis of the data on railway traffic safety risks allowed the authors to identify the main threats as follows:

- 1) the collision of trains;
- 2) train derailment;
- 3) the collision of rolling stock;
- 4) the derailment of rolling stock;
- 5) the collision of rolling stock and road vehicles at level crossings;
- 6) running of rolling stock vehicles over the people at level crossings;
- 7) the collision of rolling stock and some foreign bodies at level crossings;
- 8) the collision of rolling stock and people in the area of the railway and its equipment (buildings);
- 9) the collision of rolling stock and the objects of railway infrastructure;
- 10) the collision of rolling stock and other objects;
- 11) fire in the rolling stock;
- 12) signal passing at danger (SPAD)
- 13) breakage of the rolling stock wheels;
- 14) breakage of the rolling stock wheel-sets;
- 15) spontaneous uncoupling of automatic train carriage coupling;
- 16) rail breakage;
- 17) geometric gauge damage;
- 18) signalling error (erroneous train route design);
- 19) breakages in signalling, communication, contact systems and power equipment;
- 20) faults in other engineering equipment.

The threats to railway traffic are constantly revised during the operation of trains and infrastructure objects. Threats are identified by performing the following actions:

1. Investigating railway traffic accidents. It should be determined if the accident was caused by violation of a law regulating railway traffic safety.
2. The investigator of railway safety risks, having found the cause of the traffic accident, should check if this cause had already been registered as the risk factor in the traffic safety evaluation model.

To determine railway traffic safety risks, the potential threat harm (damage) should be determined (Rheinberger et al 2009, Shibata et al 1994). It is found, taking into account the factors given below:

1. Human safety.
2. Direct and indirect financial losses:
 - a) due to infrastructure damage;
 - b) due to damage to the rolling stock;
 - c) due to the harm to the environment;
 - d) due to train delay.

To perform the analysis of railway traffic safety risks, based on the suggested model and taking into account railway infrastructure objects, the following expert information is required:

1. Types of objects.
2. Threats typical of a particular object.
3. Factors, increasing the weight of threat criteria.
4. Relative values of factors, increasing the weight of threat criteria.
5. Factors, decreasing weight of threat criteria (control measures are offered).
6. The level of damage caused by the realized threat.

3.1. The determination of the railway infrastructure objects risk model

The application of the created model was demonstrated by considering two railway lines, representing Lithuanian Railways infrastructure. Their brief description is given below.

The first considered Lithuanian railway line is „Livintai – Gaiziūnai“:

- 1) railway type – a single-track railway;
- 2) railway track gauge – 1520 mm;
- 3) distance – 12 km;
- 4) automatic block system;
- 5) type of signalling – interlocking system;
- 6) communication system – analogue, digital;
- 7) railway traffic intensity – 63 pairs of trains per day;
- 8) allowable speed on the railway line for freight/ passenger trains – 90/120 km/h;
- 9) the number of level crossings – 1 unit;
- 10) the type of level crossings – 1 unregulated level crossing (the 3rd category level);
- 11) road traffic intensity at the level crossing – 12 vehicles/day;
- 12) the number of switches on the railway line (without railway station switches) – no switches;
- 13) the smallest radius of the road curve on the railway line – 833 m;
- 14) the largest track on the railway line – 7,9 ‰.

The second considered Lithuanian railway line “Kaišiadorys-Pravieniškės”:

- 1) railway type – a double-track railway;
- 2) railway track gauge – 1520 mm;
- 3) distance – 16 km;
- 4) automatic block system;
- 5) type of signalling – interlocking system;
- 6) communication system – analogue, digital;
- 7) railway traffic intensity – 43 pairs of trains per day;
- 8) allowable speed on the railway line for freight/ passenger trains:
- 9) even route – 80/120 km/h;
- 10) odd route – 90/120 km/h.
- 11) the number of level crossings – 1 unit;
- 12) the type of level crossings – 1 unregulated level crossing (the 3rd category level);
- 13) road traffic intensity at the level crossing – 1533 vehicles/day;
- 14) the number of switches on the railway line (without railway station switches) – no switches;
- 15) the smallest radius of the road curve on the railway line:
 - a) even route – 850 m;
 - b) odd route – 1373 m.
 - c) the largest track on the railway line:
 - d) even route – 5.8 ‰;
 - e) odd route – 5.5 ‰.

NOTE. The 3rd category is (51–100) trains and (251–700) vehicles per day according Lithuanian classification of level crossings.

3.2. Threats considered in the risk management model

Three threats common for the railway linewere chosen to reveal the operation of the risk estimation model:

- 1) Human injury (T1).
- 2) Derailment (T2).
- 3) The collision of rolling stock (T3).

For each of these 3 threats, the factors, increasing the weight of criteria, were identified below in the text.

The first threat T1. The factors, increasing the weight of the threat "Human injury" criteria:

- 1) T1F1 High allowable train speed (more than 100 km/h);
- 2) T1F2 Intense railway traffic (more than 50 pairs of trains per day on a double-track and more than 24 pairs of trains on a single-track railway);
- 3) T1F3 The railway in the state of track repair (with traffic stopped);
- 4) T1F4 The railway in the state of track repair (with traffic active);
- 5) T1F5 Regulated level crossing with low intensity road traffic (up to 500 vehicles per day);
- 6) T1F6 Unregulated level crossing with low intensity road traffic (up to 500 vehicles per day);
- 7) T1F7 Regulated level crossing with high intensity road traffic (more than 500 vehicles per day);
- 8) T1F8 Unregulated level crossing with high intensity road traffic (more than 500 vehicles per day).

The second threat T2. The factors, increasing realization weight of the threat "Derailment" criteria:

- 1) T2F1 High allowable maximum speed (more than 100 km/h);
- 2) T2F2 Intense railway traffic (more than 50 pairs of trains per day on a double-track and more than 24 pairs of trains on a single-track railway);
- 3) T2F3 The railway in the state of track repair (with traffic active);
- 4) T2F4 Passing a switch (switches);
- 5) T2F5 Railway curves of small radius (up to 700m);
- 6) T2F6 Railway track grade (a large grade of more than 8 ‰ and length of more than 2 km);
- 7) T2F7 Irregular straight railway track gauge (lower than 1517 mm or higher than 1525 mm);
- 8) T2F8 No automatic railway traffic regulating devices (on the passed railway line);
- 9) T2F9 The ambient temperature (minus 30°C and lower or plus 30°C and higher).

The third threat T3. The factors, increasing the realization weight of the threat „Collision of rolling stock“ criteria:

- 1) T3F1 The use of automatic block system on the railway line;
- 2) T3F2 The railway in the state of track repair with traffic stopped, when an even train is allowed to run on the odd track or vice versa;
- 3) T3F3 A single-track railway;
- 4) T3F4 The use of a parallel gauge (European and wide track gauges) on the railway line;
- 5) T3F5 High allowable maximum speed (more than 100 km/h);
- 6) T3F6 Intense railway traffic (more than 50 pairs of trains per day on a double-track and more than 24 pairs of trains on a single-track railway);
- 7) T3F7 Passing a switch (switches);
- 8) T3F8 No automatic railway traffic regulating devices (on the railway line).

4. Evaluating the factors, which increasing weight the threat criteria, by using the AHP method

Ranking is not the only method of comparing various objects. Experts may evaluate the objects (or the factors describing them) in the units of measurement of a particular scale, as well as in percent, or in any system of points. They may also determine the values of the criterion weights by the method of pairwise comparison. In this case, the sum of the criterion weights should be equal to one. If we wish to apply the concordance coefficient W for establishing the level of consistency of experts' judgements, any assessment of the objects should be transformed into ranking. This is not difficult to do because any method shows the significance of the objects as well.

For quantitative evaluation of the weights (significance) of the criteria describing the objects, the AHP (*Analytic Hierarchy Process*) pairwise comparison method was applied by Saaty [14] and later widely used by many other scientists [5, 19]. Experts compare all estimated factors (criteria) in pairs.

The pairwise comparison matrix is:

$$A = \begin{pmatrix} 1 & \frac{w_1}{w_2} & \dots & \frac{w_1}{w_m} \\ \frac{w_2}{w_1} & 1 & \dots & \frac{w_2}{w_m} \\ \dots & \dots & \dots & \dots \\ \frac{w_m}{w_1} & \frac{w_m}{w_2} & \dots & 1 \end{pmatrix}; \quad (1)$$

$$a_{ii}=1; a_{ij}=\frac{1}{a_{ji}} \text{ and } a_{ij} \neq 0.$$

where m – the number of compared factors (criteria).

T. Saaty devised a consistency test to distinguish the consistent comparisons (with acceptable deviations) from the inconsistent comparison (with unacceptable deviations). The consistency test involves the use of a "consistency ratio": $C.R. = (\lambda_{max} - n) / (n - 1) / R.I.$, where $R.I.$ is a random index whose value depends on RI is presented in the tables (Saaty 1980). If the value $C.R. \geq 0.1$, the decision maker has to redo the pairwise comparison matrix.

An example of determining the values of the weights of threat criteria, using the above-mentioned T. Saaty method and the filled in questionnaire of pairwise comparison of criteria obtained from the experts, is shown in Table 1, in Table 3 and in Table 5.

Applying the T. Saaty's AHP pairwise comparison method, the level of consistency of judgements is determined for each expert. In this case, the level of consistency of judgements of a group of experts based on the concordance coefficient was determined by calculating the T. Saaty weights of the criteria and ranking them according to the decrease of the weights. The method enables us to determine the level of judgements' consistency for an expert. The consistency of 20 experts' judgements was acceptable because the concordance coefficient was less than 0.1.

Evaluating the criteria (factors), increasing weight of threat criteria, the method of pairwise comparison was used. Performing risk analysis of traffic on Lithuanian Railways, a questionnaire survey of 12 experts of railway traffic control and management and 4 staff members (decision-makers) of the State Company "Lithuanian Railways" was made. Respondents had to compare the criteria determining the weight (sig-

Table 1. The comparison matrix of the factors, increasing the threat "Human injury" (threat T1)

Factors increasing threat realization	Values of comparable coefficients							
	T1F1	T1F2	T1F3	T1F4	T1F5	T1F6	T1F7	T1F8
T1F1. High allowable maximum speed (more than 100 km/h)	1	1/2	1/3	1/6	1/3	1/5	1/4	1/8
T1F2. Intense railway traffic (more than 50 pairs of trains per day on a double-track and more than 24 pairs of trains on a single-track railway)	2	1	1/2	1/5	1/2	1/4	1/3	1/6
T1F3. The railway in the state of track repair (with traffic stopped)	3	2	1	1/6	2	1/2	5	1/4
T1F4. The railway in the state of track repair (with traffic active)	6	5	6	1	4	2	4	1
T1F5. Regulated level crossing with low intensity road traffic of up to 500 vehicles per day	3	2	1/2	1/4	1	1/4	1/2	1/8
T1F6. Unregulated level crossing with low intensity road traffic of up to 500 vehicles per day	5	4	2	1/2	4	1	1/2	1/5
T1F7. Regulated level crossing with high intensity road traffic of more than 500 vehicles per day	4	3	1/5	1/4	2	2	1	1/3
T1F8. Unregulated level crossing with high intensity road traffic more than 500 vehicles per day	8	6	4	1	8	5	3	1

nificance) of the criteria at the particular hierarchical level neither with respect to a higher hierarchical level nor to non-structural criteria. Two questionnaires with inconsistent evaluation data were rejected. During the analysis, the factors, increasing the weight of each threat criteria, were compared with each other against the 9-point scale.

When the data elicited from experts were processed and the consistency of experts' judgements was validated by methods presented in the

papers of Sivilevičius et al (2010), the comparison matrices and values of the threat increasing factors were obtained in this research work.

4.1. Risk threat "Human injury"

The values of comparison matrix's factors, increasing the weight of the Threat "Human injury", are presented in Table 1.

Table 2. The weight values of the factors, increasing the threat "Human injury" (threat T1)

Threat increasing factors	Weight value
T1F1. High allowable maximum speed (more than 100 km/h)	0.021
T1F2. Intense railway traffic (more than 50 pairs of trains per day on a double-track and more than 24 pairs of trains on a single-track railway)	0.047
T1F3. The railway line in the state of track repair (with train traffic stopped)	0.077
T1F4. The railway line in the state of track repair (with train traffic active)	0.311
T1F5. Regulated level crossing with low intensity road traffic of up to 500 vehicles per day	0.033
T1F6. Unregulated level crossing with low intensity road traffic of up to 500 vehicles per day	0.101
T1F7. Regulated level crossing with high intensity road traffic of more than 500 vehicles per day	0.064
T1F8. Unregulated level crossing with high intensity road traffic of more than 500 vehicles per day	0.345

Table 3. The weight values of the factors, increasing the threat "Derailment" (threat T2)

Threat increasing factors	Weight value
T2F1. High allowable maximum speed (more than 100 km/h)	0.031
T2F2. Intense train traffic (more than 50 pairs of trains per day on a double-track and more than 24 pairs of trains on a single-track railway)	0.026
T2F3. The railway line in the state of track repair (with train traffic active)	0.220
T2F4. Passing a switch (switches)	0.120
T2F5. Railway track curves of small radius (up to 700m)	0.112
T2F6. Railway track grade (a large grade of more than 8 ‰ and length of more than 2 km)	0.029
T2F7. Irregular straight railway track gauge (lower than 1517 mm or higher than 1525 mm)	0.346
T2F8. No automatic railway traffic regulating devices (on the passed railway line)	0.068
T2F9. The ambient temperature (minus 30°C and lower or plus 30°C and higher)	0.047

Table 4. The weight values of the factors, increasing the threat "Collision of rolling stock" (threat T3)

Threat increasing factors	Weight value
T3F1. The use of automatic block system on the railway line	0.079
T3F2. The railway in the state of track repair (with train traffic stopped, when an even train is allowed to run on the odd track, or vice versa);	0.224
T3F3. A single-track railway	0.184
T3F4. The use of a parallel gauge (European and wide track gauges) on the railway line	0.239
T3F5. High allowable maximum speed (more than 100 km/h)	0.037
T3F6. Intense railway traffic (more than 50 pairs of trains per day on a double-track and more than 24 pairs of trains on a single-track railway)	0.076
T3F7. Passing a switch (switches)	0.113
T3F8. No automatic train traffic regulating devices (on the passed railway line)	0.048

Table 5. The assessment of the weight of the threat "Collision of rolling stock" criteria on the railway lines

Threat increasing factor	Weight of criteria	Infrastructure line (section)		
		"Livintai–Gaižiūnai"	"Kaišiadorys–Pravieniškės"	"Kaišiadorys–Pravieniškės" (railway under track repair)
T3F1. The use of automatic block system on the railway line	0.079	0.079	0,079	0.079
T3F2. The railway in the state of track repair (with traffic stopped, when an even train is allowed to run on the odd track or vice versa);	0.224	-	-	0.224
T3F3. A single-track railway	0.184	0.184	-	-
T3F4. The use of a parallel gauge (European and wide track gauges) on the railway line	0.239	-	-	-
T3F5. High allowable maximum speed (more than 100 km/h)	0.037	0.037	0.037	0.037
T3F6. Intense train traffic (more than 50 pairs of trains per day on a double-track and more than 24 pairs of trains on a single-track railway)	0.076	0.076	-	-
T3F7. Passing a switch (switches)	0.113	-	-	-
T3F8. No automatic railway traffic regulating devices (on the passed railway line)	0.048	0.048	-	-
The numerical value of threat weight of criteria	1.0	0.424	0.116	0.340
Threat realization weight of criteria	-	Medium	Low	Medium

Based on the data of the comparison matrix, presented in Table 1, and the validation of consistency of the compared coefficients, the weight values of the factors describing the threat "Human injury" are given in Table 2.

As was gained according AHP analyses, the threat factors T1F4 and T1F8 are the most determining factors of weight of threat T1 "Human injury" criteria.

4.2. Risk threat "Derailment"

The values of comparison matrix's factors, increasing the weight of the threat „Derailment“ criteria, were estimated. Based on the comparison matrix of the coefficients, given and the validation of the pre-

sented data, the values of the factors, increasing the weight the threat "Derailment" criteria, are obtained. They are presented in Table 3.

As is seen in Table 3, the threat factors T2F3 and T2F7 are the most determining factors of the weight of the threat T2 "Derailment" criteria.

4.3. Risk threat „Collision of rolling stock“

The values of comparison matrix's factors, increasing the weight of the threat "Collision of rolling stock" criteria, were estimated by realization of comparison matrix. Based on solved comparison matrix of the coefficients and the validation of the presented data, the values

Table 6. Assessment of the threat "Collision of rolling-stock" risk level

Name	Railway line		
	"Livintai–Gaižiūnai"	"Kaišiadorys–Pravieniškės"	"Kaišiadorys–Pravieniškės" (railway under track repair)
Threat	Medium	Low	Medium
Damage	High	High	High
Risk	High	Medium	High

Table 7. Comparison of traffic risk levels of two Lithuanian railway lines

Risk of threat „Human injury“	Railway line	
	„Livintai–Gaižiūnai“	„Kaišiadorys–Pravieniškės“
Risk of the threat „Human injury“	Low	Medium
Risk of the threat „Derailment“	Low	Low
Risk of the threat „Collision of rolling stock“	High	Medium
Total risk (determined based on the highest risk level)	High	Medium

of the factors, increasing the weight of the threat “Collision of rolling stock”, are obtained. They are presented in Table 4.

As is seen in Table 4, the threat factors T3F2 and T3F4 are the most determining factors of the weight of the threat T3 “Collision of rolling stock” criteria.

4.4. Risk assessment of the threat “Collision of rolling stock” in real lines of Lithuanian Railways

The results of the weight of the threat “Collision of rolling stock” criteria obtained for the considered infrastructure objects (railway lines) are presented in Table 5.

By calculating traffic risk level of the particular threats on the particular railway lines, the total risk of an object can be assessed. The comparative analysis of the risk level on the railway lines “Livintai–Gaižiūnai” and

“Kaišiadorys–Pravieniškės” (not during the track repair) is presented Table 7.

Finally, as is seen in Table 7, the risk of the threat “Derailment” has the low level on both analysed railway lines.

7. Discussion & conclusions

The authors developed the model of railway traffic risk management, focussing on the objects of railway infrastructure. This model may be used by railway managers for improving traffic safety strategy, establishing the priority of the required (urgent) measures and their correction.

The suggested railway traffic risk management model provides the information about the particular factors causing traffic risks and allows an identification of the areas or objects to be improved for vital

railway traffic safety. The suggested model enables for ranking basic railway infrastructure objects such as railway lines, according to their riskiness to traffic safety, and helps to determine the “weakest points” and to plan the organizational measures, required for eliminating the threats. First, all infrastructure objects, presenting considerable risk to railway traffic according to the results obtained by using the created model, were ranked. Then, the level of risk at all infrastructure objects was reduced to the “medium” and, finally, to “low” level.

The analysis of the threat “Human injury” has shown that the factor T1F8, associated with unregulated level crossing with high intensity road traffic up to 500 vehicles per day and found on the estimated railway line highly increases the weight of the considered threat realization criteria. The elimination of this factor would allow traffic accident threat to be reduced to the “low” level, thereby decreasing the risk of the threat “Human injury” to the “low”. The threat factors T2F3 and T2F7 are the most influential factors of the threat T2 “Derailment” criteria. The analysis of the threat “Collision of rolling stock” injury” has shown that the factors T3F2 and T3F4 are the most determining,

Respondents of 16 questionnaires had to compare the criteria determining the weight (significant) of the traffic safety criteria. The largest eigenvalue λ_{max} , C.I. (consistency index) and C.R. (consistency ratio) were calculated to ensure the sufficient reliability of presented traffic risk assessment. Limitations of applying this suggested model are to assess only the objects of entire railway infrastructure with identically the same signalling, automation and traffic management systems. The comprehensive (complex) traffic risk evaluation index of railway infrastructure object should be created for the future improvement the applicability of traffic risk management model.

References

1. Cacciabue PC. Human error risk management methodology for safety audit of a large railway organisation. *Applied Ergonomics* 2005; 36 (6): 709–718.
2. Chang H, Ju L. Effect of consecutive driving on accident risk: a comparison between passenger and freight train driving. *Accident Analysis and Prevention* 2008; 40 (6): 1844–1849.
3. Davey J, Wallace A, Stenson N, Freeman J. The experiences and perceptions of heavy vehicle drivers and train drivers of dangers at railway level crossings. *Accident Analysis and Prevention* 2008; 40 (3): 1217–1222.
4. Lama A, Smirnovs J, Naudžuns J. Road traffic safety in the Baltic States. *The Baltic Journal of Road and Bridge Engineering* 2006; 1 (1): 63–68. DOI: http://www.bjrbe.vgtu.lt/volumes/pdf/Volume1_Number1_08.pdf
5. Lin H. An application of fuzzy AHP for evaluating course website quality. *Computers Education* 2010; 54 (4): 877–888.
6. Lobb B. Trespassing on the tracks: a review of railway pedestrian safety research. *Journal of Safety Research* 2006; 37 (4): 359–365.
7. McCollister GM, Pflaum A. A model to predict the probability of highway rail crossing accident. In *Proc. of the Institution of Mechanical Engineering. Part F – Journal of Rail and Rapid Transit* 2007; 221 (3): 321–329.
8. Olejnik K. Critical analysis of the current traffic regulations concerning visibility from the position of a vehicle driver. *Quarterly Motor Transport* distributed by Motor Transport Institute, Warsaw, Poland 2003; 2: 69–80.
9. Podofilini L, Zio E, Vatn J. Risk-informed optimisation of railway tracks inspection and maintenance procedures. *Reliability Engineering & System Safety* 2006; 91 (1): 20–35.
10. Review of Network Rail’s All Level Crossing Risk Model (ALCRM). Project Leader: Dr Shane Turner. RSU/08/16 2008; 84.
11. Rheinberger CM, Bründl M, Rhyner J. Dealing with the white death: avalanche risk management for traffic routes. *Risk Analysis: An Official Publication Of The Society For Risk Analysis* 2009; 29 (1): 76–94.
12. RSSB. Learning from operational Experience. Annual Report 2011/2012. London 2012: 69.

13. Saaty TL. Decision-making with the AHP: Why is the principaleigenvector necessary? *European Journal of Operational Research* 2003; 145(1): 85–91.
14. Saaty TL. *The analytic hierarchy process*, McGraw-Hill, New York 1980.
15. Savage I. Does public education improve rail-highway crossing safety? *Accident Analysis and Prevention* 2006; 38(2): 310–316.
16. Shedden P, Scheepers R, Smith W, Ahmad A. Incorporating a knowledge perspective into security risk assessments. *VINE: The Journal of Information & Knowledge Management Systems* 2011; 41(2): 152–166.
17. Shibata A, Fukuda K. Risk factors of fatality in motor vehicle traffic accidents. *Accident Analysis & Prevention* 1994; 26(3): 391–397.
18. Silla A, Kallberg V-P. The development of railway safety in Finland. *Accident Analysis and Prevention* 2012; 45: 737–744.
19. Sivilevičius H, Maskeliūnaitė L. The criteria for identifying the quality of passengers' transportation by railway and their ranking using AHP method. *Transport* 2010; 25(4): 368–381.
20. Szybka J, Broniec Z, Pilch R. Forecasting the failure of a thermal pipeline on the basis of risk assessment and exploitation analysis. *Eksploatacja i Niezawodność – Maintenance and Reliability* 2011; 4: 5–10.
21. Tey LS, Ferreira L, Wallace A. Measuring driver responses at railway level crossings. *Accident Analysis and Prevention* 2011; 43: 2134–2141.

Gintautas BUREIKA, Ph.D., D.Sc., Assoc. Prof.

Lionginas LIUDVINAVIČIUS, Ph.D.

Gediminas VAIČIŪNAS, Ph.D., D.Sc., Assoc. Prof.

Railway Transport Department

Vilnius Gediminas Technical University

J. Basavičiaus str. 28, 03224 Vilnius, Lithuania

E-mails: gintautas.bureika@vgtu.lt, lionginas.liudvinavicius@vgtu.lt

gediminas.vaiciunas@vgtu.lt

Giedrius BEKINTIS, M.Sc.

UAB "Synergy Consulting", Ltd

Saltoniškių g.9, LT-08105, Vilnius, Lithuania

info@synergy.lt

Artūras KERŠYS
Dalius KALISINSKAS
Saugirdas PUKALSKAS
Andrius VILKAUSKAS
Robertas KERŠYS
Rolandas MAKARAS

INVESTIGATION OF THE INFLUENCE OF HYDROGEN USED IN INTERNAL COMBUSTION ENGINES ON EXHAUST EMISSION

BADANIE WPŁYWU WODORU STOSOWANEGO W SILNIKACH SPALINOWYCH NA EMISJĘ SPALIN

This article deals with the possibility to use hydrogen in gasoline and diesel engines. Hydrogen production in a vehicle and hydrogen generators mounted in a vehicle are overviewed. Under operation of the hydrogen generator electrical current changes with temperature, to stabilize current the current pulse generator is used. Modifications of an intake manifold were made in order to supply hydrogen to an engine. For this purpose a special universal plate to evenly mix the hydrogen with fuel mix was made designed. The experimental and rig tests were performed. The rig tests were carried out at constant 2200 rpm. It was found that smokiness, in both cases decreases with an additional deployment of hydrogen. Other indicators of the exhaust gas using the hydrogen in case of the rig tests are worse. A possible cause of negative influence is an excessive amount of hydrogen, which releases at 25 A current.

Keywords: hydrogen, fuel, exhaust gas, energetic.

Przedstawiony artykuł dotyczy możliwości wykorzystania wodoru w silnikach benzynowych i wysokoprężnych. Omówiono wytwarzanie wodoru w pojeździe oraz w generatorach wodoru zamontowanych w pojeździe. W trakcie funkcjonowania generatora wodoru prąd elektryczny zmienia się wraz z temperaturą; w celu stabilizacji prądu stosuje się generator impulsów prądowych. Aby dostarczyć wodór do silnika dokonano modyfikacji kolektora dolotowego. Do tego celu zaprojektowano specjalną uniwersalną płytę do równomiernego mieszania wodoru z mieszaną paliwową. Przeprowadzono próby eksperymentalne i próby na stanowisku badawczym. Próby na stanowisku badawczym prowadzono przy stałej prędkości obrotowej 2200 rpm. Stwierdzono, że zadymienie w obu przypadkach zmniejsza się wraz z dodatkowym wykorzystaniem wodoru. Inne wskaźniki spalin przy wykorzystaniu wodoru w przypadku badań na stanowisku badawczym wypadają mniej korzystnie. Możliwą przyczyną tego negatywnego oddziaływania jest nadmierna ilość wodoru, który uwalnia się w obecności prądu o wartości 25 A.

Słowa kluczowe: wodór, paliwo, spaliny, energetyczny.

1. Introduction

The high degree of the world's dependency on energy related with the expected future depletion of the worldwide petroleum reserves has led to big efforts in search for alternative energy sources such as nuclear, geothermal, biomass source etc. Alcohols, biomass based fuels, either single or blended with conventional petroleum based fuels are the most important alternative fuels for internal combustion engines [1].

Ecological environment and pollution is one of many problems solved in vehicles production that cause the rise of ecological requirements. Now we have standard Euro V [16]. The previous detailed investigations [7, 10] demonstrate that regulation of fuel supply system is not simple according to exhaust emission parameters like CO, HC, and O₂, and the air-fuel ratio is not homologous to these parameters. The outer characteristics, power and torque of internal combustion engines, are associated with ecological requirements by decreasing their limit values, because we cannot adjust performance of the fuel supply system to optimal characteristics when ecological requirements should be satisfied. Ecological requirements create special difficulties when solving the problem of alternative fuels using in internal com-

bustion engines. The analysis of environment pollution is very complicated, because many factors have an influence on exhaust emission contents [14].

The Problem of energy resources is the theme considered with growing attention every year on a world scale. Crisis shaking economy of the whole planet motivates to deal with the issue of energy resources much deeper. Vehicle manufacturers are more often talking about alternative energy resources and alternative cars: electro-mobiles, bio-fuel-driven engines, hydrogen internal combustion aggregates. The greatest vehicle manufacturers invest hundreds of millions into the investigation of a hydrogen engine. Specialists make predictions that hydrogen is almost an inexhaustible resource, without any pollution of environment; just we need to improve hydrogen extraction ways [9 – 11].

Efficiency of an internal combustion engine is improved by fuel enrichment with hydrogen. This is achieved by hydrogen injection into fuel mixture in the intake manifold [4, 8].

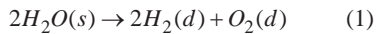
With hydrogen used as an additive for traditional fuels, characteristics of an internal combustion engine become higher, i.e. engine

power increases, fuel consumption and concentration of dangerous additives in exhaust decrease.

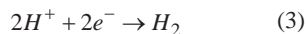
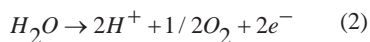
2. Hydrogen extraction and use in vehicles

During water electrolysis chemically-associated elements dissociate as electric current flows along them.

When water is subject to electrolysis



electric current flows through water, which dissociates into oxygen and hydrogen gas. Oxygen emits at anode and hydrogen emits at cathode on electrolysis element Fig. 1 [2].



To conduct these reactions under normal conditions required potential difference between anode and cathode is equal to 1,229 V. During the process all 100% of electric power is not converted into chemical energy of hydrogen. Energy loss appears so as ions transmitting electricity have heated water [4].

A hydrogen generator is used to produce hydrogen in a car Fig. 2. The Generator is filled with distilled water. Required amount of the water is refilled from a reservoir. Electrolysis reaction goes in a hydrogen generator. Electrodes obtain electrical charge from a battery in a car. To achieve more efficient hydrogen emission calcium hydroxide powder is added into the distilled water. Emitted hydrogen by pipe goes to the engine intake manifold. Then it mixed with air gets into cylinders of the engine. Fuel mixture enriched with hydrogen burns out faster and more evenly. The engine runs more silently and evenly, gas going out from the silencer is almost scentless and there is detectable a little dampness [7, 13].

Faraday's law is applied to evaluate efficiency of the hydrogen

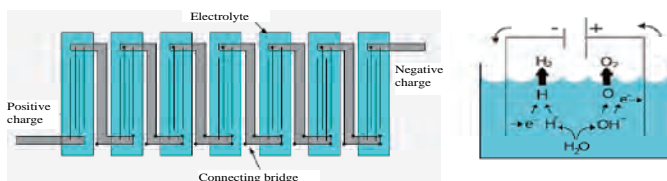


Fig. 1. Principal scheme of water electrolysis [3]

generator of the system and following to that law it is possible to calculate the volume of hydrogen emitted [4].

$$V_{H_2gen} = \frac{R \cdot I \cdot T \cdot t}{F \cdot p \cdot z} \quad (4)$$

where R – universal gas constant ($R=8,31J/mol\ K$); I – current strength; T – ambient temperature; t – time; F – Faraday's constant ($F=96485\ C/mol$); p – ambient pressure; z – amount of electrons, flowing along circuit to form one molecule: $z(H_2) = 2$, $z(O_2) = 4$.

Calculation of a hydrogen generator showed that with 25 A current hydrogen gas extractions is 1.88 l per minute. From one liter of water 1860 liters of hydrogen are extracted. Power of the hydrogen generator at the voltage of 13.8 V and the current of 25 A is equal to 345 W. Vehicle engine losses are 0.34 kW.

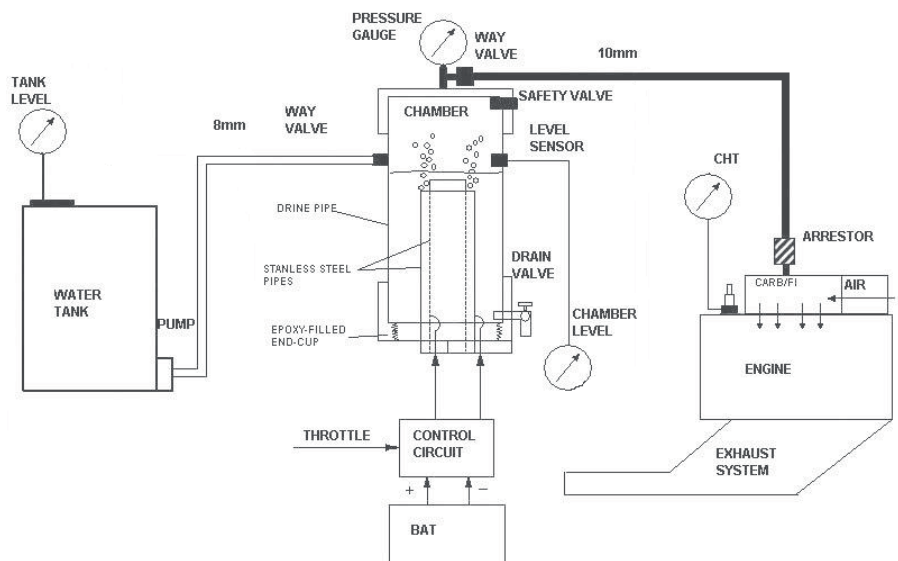


Fig. 2. Scheme of hydrogen generator

3. Influence of hydrogen used in ICE on fuel consumption and exhaust emission

In order to evaluate exhaust emission of an internal combustion engine an investigation has been performed. We chose for experiments popular three vehicles with gasoline internal combustion engines and three vehicles with diesel internal combustion engines in Lithuania. The working capacities of these engines are from 1500 to 2200 cm³ and the power from 60 to 89 kW (Table 1).

Table 1. Technical data of tested engines

Row. Nr.	Engine name	Fuel type	Year of manufacture	Power, kW	Working capacity, cm ³
1	Type 1	Gasoline	1986	89	2000
2	Type 2	Gasoline	1985	66	1800
3	Type 3	Gasoline	1987	63	1500
4	Type 4	Diesel	1995	70	2200
5	Type 5	Diesel	1997	60	1700
6	Type 6	Diesel	1998	81	1900

A hydrogen generator (model R130V12, H₂ - 130 l/h) is mounted in engine compartment. It has to meet safety requirements. If the engine does not run, the generator does not have to switch. A hydrogen generator is connected through relay.

Generator exciting voltage of winding is used to relay connection, so as voltage in it appears only when the engine is running, thus until an engine does not run, hydrogen generator does not work, as well, Fig.3.

In order to avoid overheating of hydrogen generator, thermo-relay is mounted within it, which disconnects exciting voltage of switching relay, until hydrogen generator gets cool.

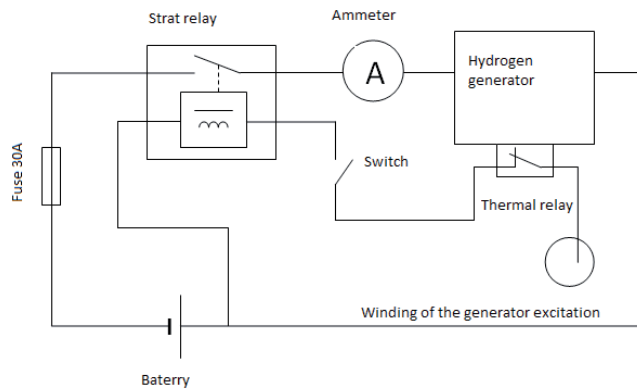


Fig.3. Electrical scheme of connection a hydrogen generator into circuit

For mixture of hydrogen the air intake system was modified. For this purpose the universal plate was constructed. This helped to mix hydrogen with the intake air (Fig.4).

It is noted that under operation of the hydrogen generator, it is practically impossible to maintain constant current, and the electrolyte starts to heat up. In case of cold electrolyte the current is too low, and under operation of the hydrogen generator, it grows too much. To solve the problem the current pulse generator was used (CPG). The installed universal plate is shown in Fig. 5.

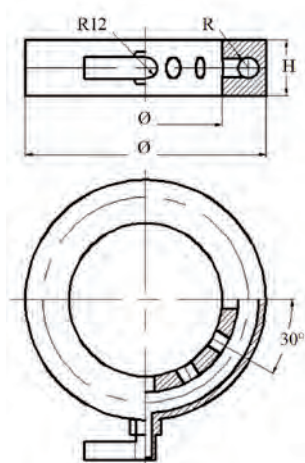


Fig.4. Universal plate

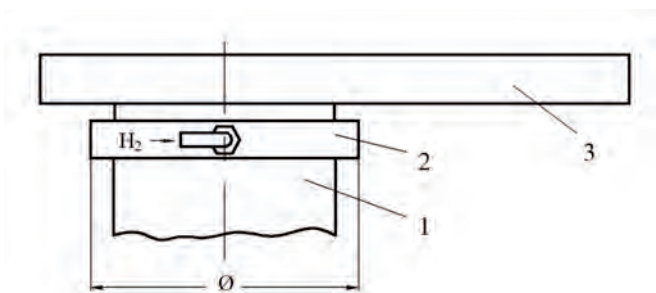


Fig.5. The installed universal plate: 1 – intake manifold; 2 – constructed plate; 3 – box of air filter

The principle of CPG operation are often cut offs of the circuit what is characterized by frequency (Hz), that is, how many times per second the circuit was cut off. This allows more efficient use of the car

power. It is also possible to get varying amount of exhaust gas with changing capacity, which depends on the current.

For measuring of exhaust gases, the engine diagnostic stands CORGHI GAS 810 + NO_x and BEA 460 which belongs to Transport Engineering Department of Kaunas University of Technology was chosen.

Fig. 6 shows the content of vehicle gasoline hydrocarbons (HC) at different engine modes. Fig. 6 shows that at low engine speeds the exhaust gas hydrocarbon content is more than at the higher speed. In addition, after the filing of hydrogen, the hydrocarbon content in the exhaust gases is reduced.

One of possible reasons is the oxidation of hydrocarbons. During explosion the flame spreads at high speed, so fuel burns better. The petrol engine working at low revolutions emits more hydrocarbons into environment than at higher revolutions. Reduction of hydrocarbon emission is observed when the fuel burns with hydrogen. By increasing the engine speed, the difference decreases and at maximum revolutions the hydrogen addition does not affect the exhaust gas composition.

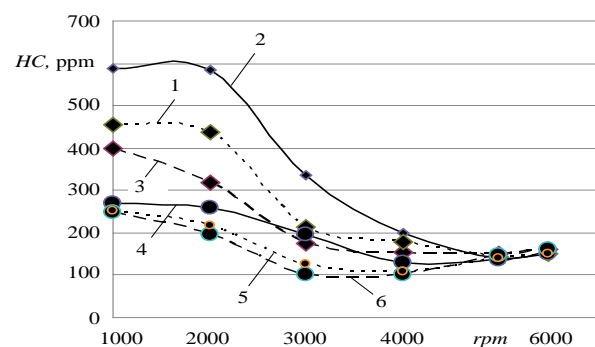


Fig. 6. Hydrocarbons of gasoline and gasoline with hydrogen: 1 – Type 3 gasoline; 2 – Type 1 gasoline; 3 – Type 2 gasoline; 4 – Type 1 (gasoline + H₂); 5 – Type 3 (gasoline + H₂); 6 – Type 2 (gasoline + H₂)

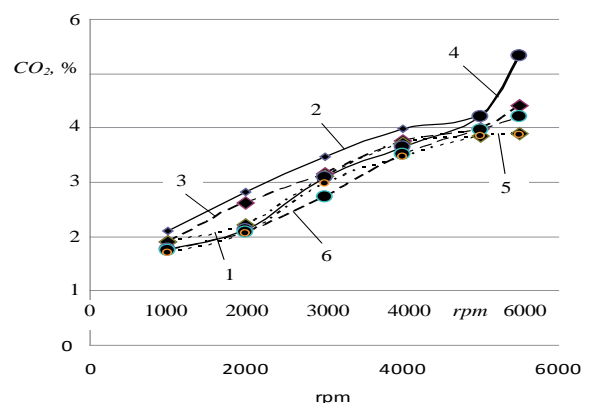


Fig. 7. Carbon dioxide of gasoline and gasoline with hydrogen: 1 – Type 3 gasoline; 2 – Type 1 gasoline; 3 – Type 2 gasoline; 4 – Type 1 (gasoline + H₂); 5 – Type 3 (gasoline + H₂); 6 – Type 2 (gasoline + H₂)

With increasing revolutions the valve opening time is shorter, and at the same time, the amount of air entering the cylinder is lower, which results in worse fuel combustion. Hydrogen feeding promotes better combustion of the mixture up to 3500 rpm. The best effect is the appearance at lower and medium engine speeds.

Fig. 7 shows emissions of carbon dioxide (CO₂) at different engine modes. Fig. 7 shows that the amount of CO₂ in the exhaust gas

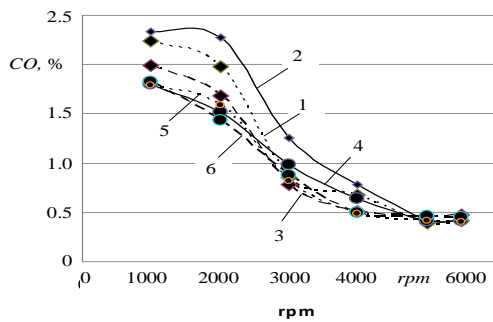


Fig. 8. Carbon monoxide of gasoline and gasoline with hydrogen: 1 – Type 3 gasoline; 2 – Type 1 gasoline; 3 – Type 2 gasoline; 4 – Type 1 (gasoline+ H_2); 5 – Type 3 (gasoline+ H_2); 6 – Type 2 (gasoline+ H_2)

increases as the engine speeds. CO_2 exhaust reduction is observed after the filing of additional hydrogen.

Fig. 8 shows emissions of carbon monoxide (CO) at different engine modes. In Fig. 8 it is shown that the maximum amount of CO in the exhaust gas is at lower engine speed.

CO is formed at high combustion temperatures and oxygen deficiency. Therefore, the fuel is oxidized not to the end. CO is reduced by about 14% when the fuel is burning along with the hydrogen. During engines operation at high revolutions hydrogen does not have any effect on the exhaust gas composition. Speeds decrease with increasing CO content. In case of further hydrogen the amount of CO in the exhaust gases further reduces.

Soot formation process in the local fuel oversaturated areas is during hydrocarbon pyrolysis, where according to the complex multi-level mechanism the fuel molecules break down and decompose. Smokiness of the diesel engines is more dependent on the chemical composition of the fuel, i.e. amount of aromatic hydrocarbons and the fuel ketene number, diffusion processes taking place in the chamber, complicated mechanism of the formation of soot particles and their combustion rate.

Fig. 9 shows the soot content of diesel vehicles with different engine speeds. The graph 9 shows that the soot content increases with engine speeds. The maximum amount of soot emissions is at the maximum engines speed. In case of addition of hydrogen, carbon black is reduced. The effect is due to the hydrogen, the fuel burns better, therefore, there is less emissions of soot.

Fig. 10 shows NO_x of the diesel vehicles, at different engine speeds. The graph 10 shows that the minimum amount of NO_x in the exhaust gases is at low engine speeds. With increasing engine speeds NO_x increases, but at the speeds higher than 3000 rpm NO_x stabilizes. Lower combustion temperature results in less NO_x .

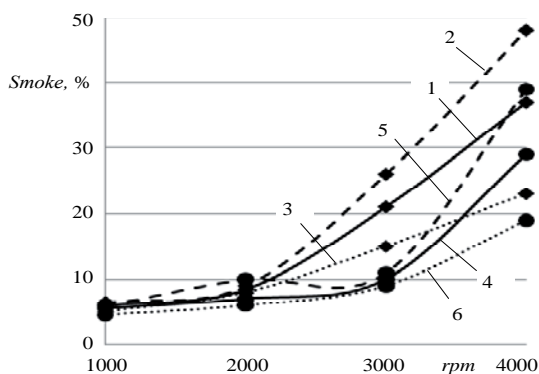


Fig. 9. The soot content of diesel vehicles at different engine speeds: 1 – Type 4 diesel; 2 – Type 5 diesel; 3 – Type 6 diesel; 4 – Type 4 (diesel+ H_2); 5 – Type 5 (diesel+ H_2); 6 – Type 6 (diesel+ H_2)

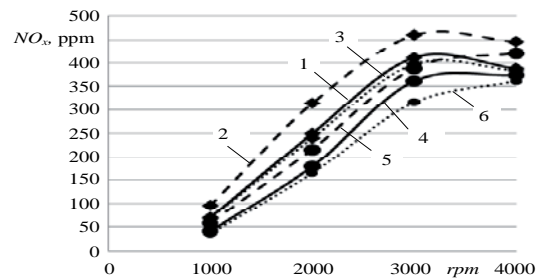


Fig. 10. NO_x of the diesel vehicles at different engine speeds: 1 – Type 4 diesel; 2 – Type 5 diesel; 3 – Type 6 diesel; 4 – Type 4 (diesel+ H_2); 5 – Type 5 (diesel+ H_2); 6 – Type 6 (diesel+ H_2)

When the intake valve opens, low pressure area, formed in the cylinder, is quickly filled with the air of atmospheric pressure. This compressed air binds to the fuel hydrocarbons (HC) and provides a basis for combustion, pushing the piston and creating the engine power.

During compression the piston begins to rise, the molecules of air and fuel due to their mutual friction heat up. Absorbing heat the molecules expand.

With the further going up of the piston, pressure in the cylinder continues to increase, so the friction between the molecules is also increasing, leading to the further increase in temperature, and further expanding of the molecules.

Absorbing heat, molecules of hydrocarbon break down into hydrogen and carbon, and oxygen molecules (O_2) decompose into two separate oxygen atoms. When the fuel is ignited one atom of the oxygen oxidizes (combines with them) two hydrogen atoms and creates water and two oxygen atoms with one carbon atom create carbon dioxide. With increasing oxidation, the newly formed water and carbon dioxide creates an additional pressure, which the engine turns into useful power that allows rotating crankshaft to drive a car. While the combustion chamber temperature remains below 2300 degrees Fahrenheit, nitrogen molecules remain inert, this means that they do not split into separate nitrogen atoms and do not bind to other gases. However, reaching 2300 degrees nitrogen molecules decompose and bind to oxygen to form NO_x compounds. Concentration of NO_x is less at lower engine's revolutions. With engine speed greater than 3000 rpm addition of hydrogen has much lower effect on NO_x formation.

One of the possible reasons is that the gas volume generated by hydrogen generator is too low when the engine is running at the speed higher than 3000 rpm.

To realize the analysis of impact of hydrogen gas on the diesel engine rig tests were carried out in the laboratory of Internal combustion engines of Automobile transport department of Vilnius Gediminas

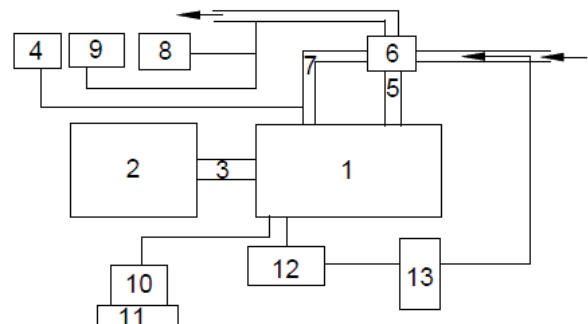


Fig. 11. Rig test structure: 1 – internal combustion diesel engine; 2 – dynamometer load KH 5543; 3 – power takeoff; 4 – HD 2304,0 Pressure Meter; 5 – exhaust manifold; 6 – turbo-compressor; 7 – intake manifold; 8 – smoke meter AVL DiCom 465; 9 – gas analyzer AVL DiCom 4000; 10 – fuel tank; 11 – scale for diesel consumption; 12 – battery; 13 – hydrogen generator.

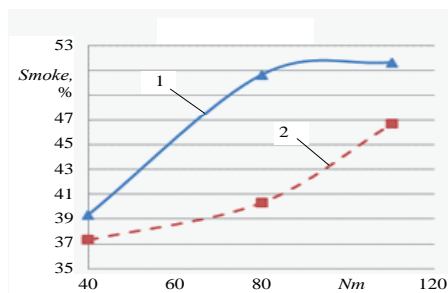


Fig. 12. The soot content of diesel vehicles at different engine speeds (2200 rpm): 1 – diesel; 2 – diesel+H₂

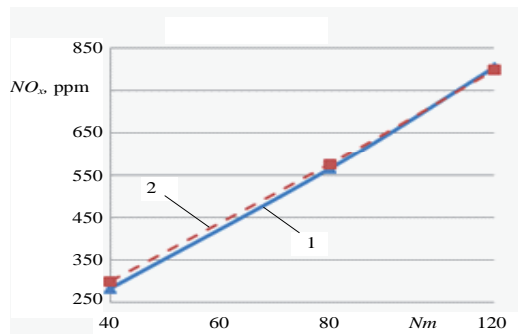


Fig. 13. NO_x of the diesel vehicles at different engine speeds (2200 rpm): 1 – diesel; 2 – diesel+H₂

Technical University (VG TU), using four-strokes diesel engine 1.9 TDI 66 kW, dynamometer load KI-5543, gas analyser AVL DiCom 4000, smoke meter AVL DiCom 465 and electronic scale SK-5000 to measure fuel consumption (Fig. 11).

Tests with both diesel and additional hydrogen were carried out three times. From the results obtained averages were derived and dependencies plotted.

Measurements were performed at the constant speed 2200 rpm, with variable load (40, 80 and 110 Nm). Fuel consumption with the additional hydrogen is slightly higher and at the load of 110 Nm both with diesel fuel and the additional deployment of hydrogen it does not change.

One of the reasons of the fuel consumption increase is possibly required the additional energy to go electrolysis in the hydrogen generator. The cause of the possible negative affect is an excessive amount of hydrogen, which is released at 25 A current. At higher currents the hydrogen generator is more heated, and the intensity of the heat causes an additional water steam. Therefore, it is appropriate to establish a suitable electric current, at which reduction in fuel consumption is to

be derived. With additional use of hydrogen the smokiness decreases from 5% to 20% throughout the entire load mode (Fig. 12).

NO_x amount increases with load. NO_x amount at low and medium loads, with additional use of hydrogen increases by 2–5%. At the load higher than 80 Nm, NO_x amount varies slightly. One of the possible causes is the increasing NO_x emissions due to the increased combustion temperatures Fig. 13. At the load higher than 80 Nm the hydrogen does not affect the amount of NO_x.

4. Conclusion

Having the results of investigation, the following was concluded:

1. The investigation established that the hydrogen addition to traditional fuels did not have significant impact on fuel consumption – at certain engine operating modes the fuel consumption with hydrogen additive increases.
2. CO is formed at high temperature, and oxygen deficiency. Therefore, the fuel is oxidized not completely. CO is reduced to 20% when the fuel combusts along with the hydrogen, CO reduction is due to the fact that there is no carbon in the supplied hydrogen-oxygen mixture. Hydrocarbon (C_xH_y) exposed in the atmosphere to the sunlight reacts with nitrogen oxides to form the main component of smog, ozone O₃. The introduction of hydrogen promotes better combustion of the mixture in the wider range of revolutions. Therefore, fewer hydrocarbons (42%) are discharged into the environment and probability less ozone is formed.
3. NO_x reacting with water forms nitric acid. At the sunlight NO_x reacts with other active components of atmosphere, commonly with hydrocarbons, and as the result of complex reactions photochemical oxidants (including ozone) are formed. These highly unstable combinations damage plants and irritate human respiratory and vision organs. It is important to reduce amount of NO_x in the exhaust gas. Mixing of the combustible mixture with the hydrogen reduces combustion temperature; therefore, environmental pollution is less (to 28%).
4. With applying the hydrogen CO₂ reduces by 1–5%. CO₂ amount in the atmosphere causes so called „greenhouse effect“, therefore it is very important to reduce its amount.
5. The results of rig tests performed vary from the road test ones. In case of road testing it is difficult to define the human factor, which is to be regarded as the main decisive factor causing the difference between the results obtained.
6. The results show that the hydrogen gas in an internal combustion engine in different engine operating ranges result in positive energy and environmental performance, therefore, it is appropriate to continue the research, finding the optimal adjustable engine parameters and amount of hydrogen gas provided.

References

1. Al-Hasan MI, Al-Momany M. The effect of iso-butanol-diesel blends on engine performance. *Transport* 2008; 23(4): 306–310.
2. Bortnikov L. Combustion of a Gasoline-Hydrogen-Air Mixture in a Reciprocating Internal Combustion Engine Cylinder and Determining the Optimum Gasoline-Hydrogen Ratio. *Combustion, Explosion, and Shock Waves* 2007; (43): 378–383.
3. Chernyak L, Boychenko S, Fedorovich L, Novikova V, Prentkovskienė R, Pukalskas S. Dependence of evaporation losses on petrol quality. *Transport* 2010; 25(4): 442–447.
4. Dulger Z, Ozelik K. Fuel Economy Improvement by on Board Electrolytic Hydrogen Production. *International Journal of Hydrogen Energy* 2000; 25: 895–897.
5. Fanhua M, Nashay N, Mingyue W, Long J, Renzhe C, Shuli Z. Hydrogen-enriched compressed natural gas as a fuel for engines. *Natural Gas* 2010; ISBN 978-953-307-112-1: 307–332.
6. Gandhi P. Effect of hydrogen enrichment on the combustion characteristics of a bio fuel diesel engine. *IOSRJEN* 2012; 2(1): 001–006.
7. Jarungthammachote S. Combined partial oxidation and carbon dioxide reforming process: A thermodynamic study. *Am. J. Applied Sci.* 2011; 8: 9–14.
8. Jarungthammachote S, Chuepeng S, Chaisermatwan P. Effect of hydrogen addition on diesel engine operation and NO_x emission: A thermodynamic study. *Am. J. Applied Sci.* 2012; 9: 1472–1478.

9. Jingding L. Formation and Restraint of Toxic Emissions in Hydrogen-Gasoline Mixture Fuelled Engines. *International Journal of Hydrogen Energy* 1998; (23): 971–975.
10. Labeckas G, Slavinskas S. The effect of ethanol, petrol and rapeseed oil blends on direct injection diesel engine performance and exhaust emissions. *Transport* 2010; 25(2): 116–128.
11. Lilik GK, Zhang H, Herreros JM, Haworth DC, Boehman AL. Hydrogen assisted diesel combustion. *International Journal of Hydrogen Energy* 2010; 35(9): 4382–4398.
12. Miyamoto T, Hasegawa H, Mikami M, Kojima N, Kabashima H. Effect of hydrogen addition to intake gas on combustion and exhaust emission characteristics of a diesel engine. *International Journal of Hydrogen Energy* 2011; 36: 13138–13149.
13. Santoso WB, Nur A, Ariyono S, Bakar RA. Combustion Characteristics of a Diesel-Hydrogen Dual Fuel Engine. *National Conference in Mechanical Engineering for Research and Post Graduate Studies* 2010; Malaysia, 23–32.
14. Saravanan N, Nagarajan G. Performance and emission studies on port injection of hydrogen with varied flow rates with Diesel as an ignition source. *Applied Energy* 2010; 87: 2218–2229.
15. Tang D, Ge J, Duan R, Zhang Y. Investigation on the combustion cyclic variability in a non-road diesel engine fuelled with diesel/bio-diesel blends. *International Conference on Electrical Information and Control Engineering* 2011; China, 2286–2289.
16. White Paper. Roadmap to single European transport area – towards a competitive and Transport Przemysłowy 2002; 3(9): 42–47.

Artūras KERŠYS, Ph.D., D.Sc., Assoc. Prof.

Dalius KALISINSKAS, Ph.D.

Department of Transport Engineering

Kaunas University of Technology

Kęstučio str., 27-220 Kaunas, Lithuania

E-mails: arturas.kersys@ktu.lt, dalius.kalisinskas@ktu.lt

Saugirdas PUKALSKAS, Ph.D., D.Sc., Assoc. Prof.

Department of Automobile Transport

Vilnius Gediminas Technical University

J. Basanavičiaus str., 28, Vilnius, Lithuania

E-mail: Saugirdas.pukalskas@vgtu.lt

Andrius VILKAUSKAS, Senior Researcher

Mechatronics Centre for Research, Studies and Information

Kaunas University of Technology

Kęstučio str., 27-206 Kaunas, Lithuania

E-mail: andrius.vilkauskas@ktu.lt

Robertas KERŠYS, Ph.D., D.Sc., Assoc. Prof.

Rolandas MAKARAS, Ph.D., D.Sc., Assoc. Prof.

Department of Transport Engineering

Kaunas University of Technology

Kęstučio str., 27-217 Kaunas, Lithuania

E-mails: robertas.kersys@ktu.lt, rolandas.makaras@ktu.lt

Wojciech CZUBA
Kazimierz FURMANIK

ANALYSIS OF A GRAIN MOTION IN THE TRANSFER AREA OF THE BELT CONVEYOR

ANALIZA RUCHU ZIARNA W PRZESTRZENI PRZESYPOWEJ PRZENOŚNIKA TAŚMOWEGO*

Transfer chutes are critical areas within conveyor transfer systems in terms of maintenance and high levels of energy consumption. Appropriate chute design allows material stream to be uniformly fed on the receiving conveyor with a desired stable tangential speed. This reduces the motion resistances and belt wear. Any construction work associated with a transfer chute should be preceded by a thorough analysis of the stream trajectory. The simplest case is to consider the motion of a single grain. The article presents an analysis of grain motion in a parallel chute and a methodology of calculating the impact angle and tangential speed of the grain at the point of contact with the receiving conveyor belt. Based on calculations made on developed model it was determined which of the basic input parameters have the most significant impact on the changes of observed output parameters.

Keywords: maintenance of belt conveyors, transfer stations, grain motion analysis.

Przenośnikowe węzły przesypowe są miejscami newralgicznymi z punktu widzenia eksploatacji jak również energochłonności systemów transportowych. Odpowiednie ukształtowanie konstrukcji przesypu, pozwala na podawanie strugi transportowanego urobku na przenośnik odbierający w sposób równomierny, stabilny i z pożądaną prędkością styczną. Dzięki temu zmniejszane są opory ruchu w przesypie, jak również zużycie taśmy. Prace konstrukcyjne związane z zabudową przesypu, powinny być poprzedzone gruntowną analizą trajektorii ruchu strugi. Najprostszym przypadkiem do rozpatrzenia jest ruch pojedynczego ziarna. W artykule przedstawiono analizę ruchu ziarna w przesypie równoległym oraz metodykę obliczeń kątów padania jak również prędkości stycznych ziarna w miejscu jego upadku na taśmę przenośnika odbierającego. Na podstawie obliczeń modelowych określono, które z podstawowych parametrów przesypu mają najistotniejszy wpływ na zmiany obserwowanych wielkości.

Słowa kluczowe: eksploatacja przenośników taśmowych, przesypy, analiza ruchu materiału.

1. Introduction

Conveyor transport systems are based mainly on conveyor belts, which are basic and universal means of transport of particulate materials. The structure of such systems can vary and usually consists of a few or several conveyors connected together with so called transfer chutes, where the transported material is directed from the feed conveyor onto the receiving one. These are usually critical places a source of dust and rapid energy transformations and require special attention from the designer, because a poorly designed chute may be the cause of costly failures and downtime. If a material stream is not fed tangentially from the feed conveyor to the receiving conveyor at a speed equal to the speed of the belt, there is a further increase of resistances and power consumption in the transfer point. In case of feeding a material stream with capacity Q [t/h] perpendicular to the receiving conveyor belt with the speed v [m/s], the resistance value is [1, 5, 10]:

$$W_z = \frac{Q \cdot v}{3,6} \quad [\text{N}] \quad (1)$$

and the loss of power due to energy transformations

$$N_z = W_z \cdot v = \frac{Q \cdot v^2}{3,6} \quad [\text{W}] \quad (2)$$

For example, for capacity $Q_{1-3} = 1000-3000-5000$ [t/h] and belt speed $v=1-6$ [m/s] results are shown at fig. 1.

From these data, it appears that the additional resistance and power dissipation for a single transfer chute can be significant, and it increases proportionally with a growing number of transfer chutes.

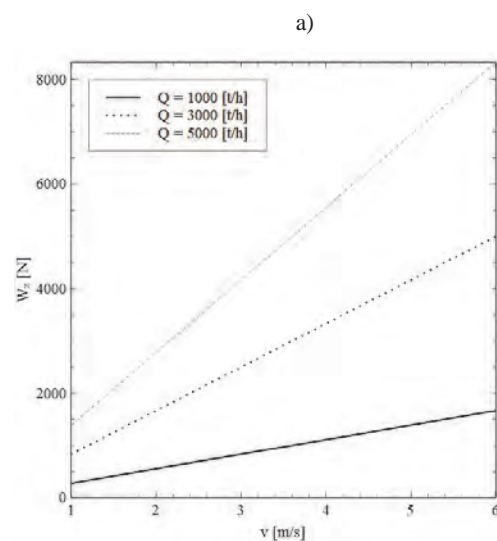
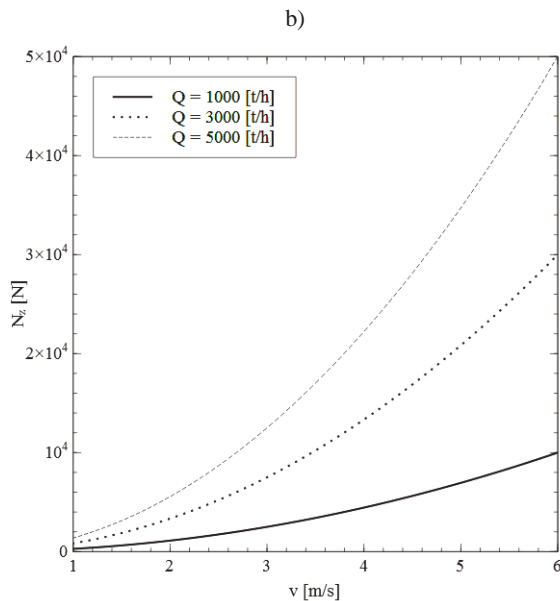


Fig. 1a. A graph of $W_z(v)$

(*) Tekst artykułu w polskiej wersji językowej dostępny w elektronicznym wydaniu kwartalnika na stronie www.ein.org.pl

Fig. 1b. Graph of: $N_z(v)$

In order to reduce the energy consumption of conveyor transport systems there is a need to look for better solutions of transfer chutes based on the analysis of construction and operation of previously used ones.

In this paper, the construction of typical transfer chutes is presented and analysis of the effect of geometrical and kinematic parameters of the chute on the grain motion and impact on the receiving conveyor belt was performed. These parameters have a significant influence on additional resistance, lost power and wear of the chute components as well as the belt life, so proper values are essential for the rational design of transfer points.

2. Construction of transfer chutes in conveyor transport systems

Conventional transfer chute design is relatively simple (figures 2–5). Fundamentally, standard steel sections and plates are used with additional removable linings made of other materials which acts as protection against wear. The correct combination and configuration of the above, as well as their geometric configuration and selection of construction materials determines the functionality of the solution. The transfer stations are also often equipped with various types of devices for measurement and control of the flow of material.

General scheme of a typical transfer station area is shown on Figure 2. It can be divided into the following four characteristic zones [9].

- Head chute** – space surrounding the front drum of a feed conveyor; at this point the separation of the material from the belt occurs and, depending on the design, free flight of a certain trajectory or capturing the material stream by chute components (such as impact plates).
- Free flight area** – an area in which the material falls freely, without contact with the elements of the chute; if the stream is dispersed, depending on how it was captured in zone A, a significant amount of air gets into it, which in turn leads to the formation and emission of dust.
- Loading chute** – the area where the material is getting in contact with the receiving conveyor belt; there may be elements of the lower intercept (chutes, slides), or is loaded directly to belt (within the hopper).
- Stream formation** – in this area loaded material stream is being formed to its final shape/cross section; it is very often equipped with de-deusting devices. The movement of material during

loading is usually turbulent and in this area should be stabilized.

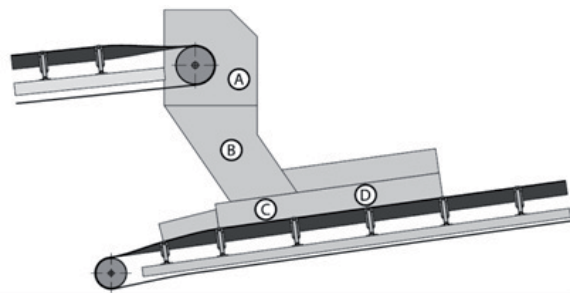


Fig. 2. General construction of typical transfer chute with indicated characteristic zones [9]

Depending on the requirements determined by the process and the properties of transported materials, structures of transfer chutes differs. The simplest classification can be division into transfer points, in which the direction of motion of the material stream changes (angle chutes), or remains the same (parallel chutes). Examples of such transfers are shown on figure 3. The whole transfer point contains many elements and devices, whose job is to direct the stream of transported material in such a way as to minimize the negative effects that occur during handling (additional resistance, increased belt wear, noise, etc.).

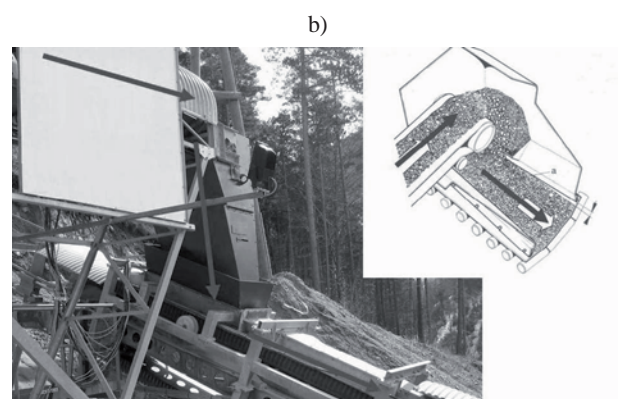
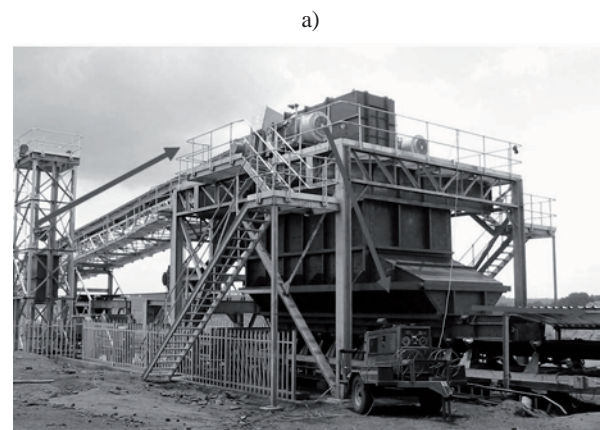


Fig. 3. View of a transfer chutes: a) parallel; b) angled [7]

Depending on the difference in height between the conveyors, and their arrangement, various kinds of components are used in aim to capture and redirect the stream. The three most commonly used solutions are: impact plate, chutes (straight or curved) and so called “rock box”, which are specially shaped pockets being filled by the material and after that stream reflects from successive layers of accumulated

heap. Typical chute structures are based on combinations of these elements. Terminology for structural elements is very diverse, there are many different authors who refer to the same components using different names.

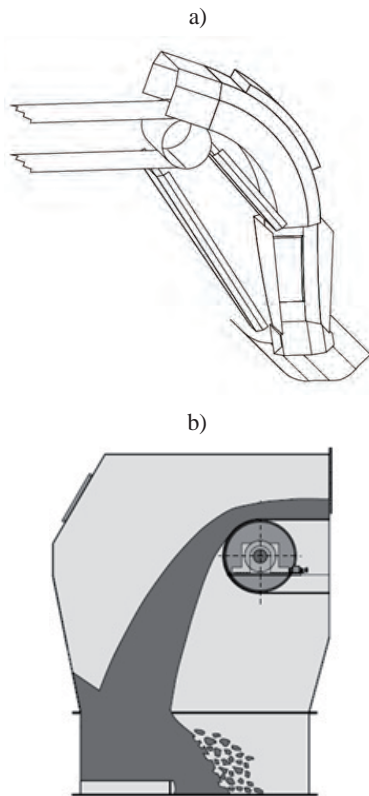


Fig. 4. Angled transfer point with straight and curved chutes (left) and a rock box construction (right)

The use of individual solutions is largely determined by physico-mechanical properties of the material: the size and hardness of solids, the degree of abrasiveness, the degree of moisture. Two commonly used solutions are transfer points of type impact plate to impact plate and impact plate to rock box [8]. In both cases, the stream of material is artificially and suddenly disturbed, which can lead to many problems in maintenance. These systems behave well in transport of free flowing dry materials. Selection criteria are based mainly on two aspects: blocking of the chute and wear of its components and receiving belt [4]. Recently the new type of construction, composed of curved chutes in capturing and loading zones, called Hood-and-Spoon is beginning to be widely used. It exhibits several advantages especially when material is sticky and cohesive. However, it is more costly than the traditional design and is not so well recognized in practice.

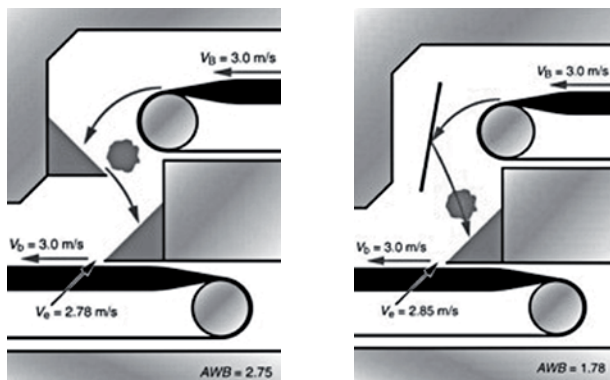


Fig. 5. Schemes of rock box to rock box transfer (left) and impact plate to rock box (right) [8]

Currently, more attention is paid to energy efficiency in the construction of transport machines and equipment is shown at figure 6. Motion of a single grain of diameter a was investigated. The aim was to determine the impact of changes in various parameters on the system response. In particular, the object of interest were the normal and tangential components of the velocity of grain in point of impact on the receiving conveyor belt.

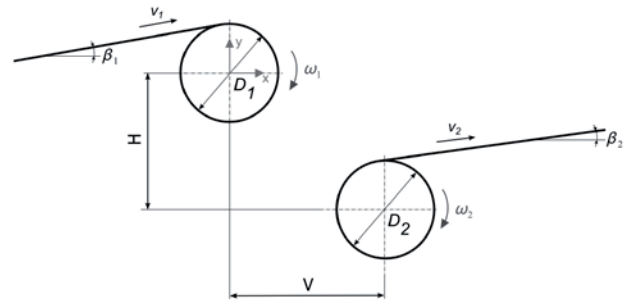


Fig. 6. Belt conveyors in parallel configuration

Input parameters:

- v_1, v_2 – belt speeds [m/s],
- β_1, β_2 – conveyors inclination [deg],
- ω_1, ω_2 – angular speeds of head drums [rad/s],
- H, V – horizontal and vertical distance from drums axis [m],
- D_1, D_2 – drums diameters [m],
- h_1, h_2 – belt thickness [m],
- a – grain diameter [m].

where: $v_i = \omega_i \cdot R_i$ and $R_i = \frac{D_i}{2}$ for $i=1,2$.

Several methods for trajectory calculation exist (Dunlop, Good-year, CEMA, MHEA, Booth, Korzeń). The differences are mainly due to the range of physical phenomena included, which are affecting the forces acting on the grain. These methods can be divided into three categories: analytical, graphical or combined. In each of the methods it is needed to determine the point of separation of the grain from the feed conveyor belt. The analysis conducted by the authors was based on the formulas derived in the standard CEMA (Conveyor Equipment Manufacturers [4]). The calculations take into account the effect of centrifugal force, but does not take into account the friction and adhesion forces between the belt and the grain. Three cases are considered depending on the angle of inclination of the feed conveyor:

1. $\beta_1 = 0$

1.1. If $\frac{v_s^2}{g \cdot r_1} \geq 1$, grain will separate at the point of contact between

the belt and head drum. Assuming that the origin is coincident with the axis of the drum, the coordinates of the point of separation for this case are $x_0 = 0$ and $y_0 = 0$.

1.2. If $\frac{v_s^2}{g \cdot r_1} < 1$, the grain before separation will traverse a certain

distance around the head drum until $\frac{v_s^2}{g \cdot r_1} = \cos \gamma$, where is

the angle between the vertical axis of the drum, and the point of separation of the grain. The coordinates of the point of separation for this case are $x_o = r_1 \cdot \sin \gamma$ and $y_o = r_1 \cdot \cos \gamma$ where-

in $\gamma = \arccos(\frac{v_s^2}{g \cdot r_1})$.

2. $\beta_1 > 0$

2.1. If $\frac{v_s^2}{g \cdot r_1} \geq 1$, grain will separate at the point of contact between

the belt and head drum. Taking into account the inclination of the conveyor, the coordinates of the point of separation for this case are $x_o = -r_1 \cdot \sin \beta_1$ and $y_o = r_1 \cdot \cos \beta_1$

2.2. If $\frac{v_s^2}{g \cdot r_1} < 1$ and , grain may separate at the point of contact

between the belt and head drum, however, it is likely that it will come in contact with the belt again. It is not clearly stated how to determine the point of separation. CEMA suggests that the grain after contact with the belt will travel some distance around the drum, and then the separation occurs (see p. 2.4).

2.3. If $\frac{v_s^2}{g \cdot r_1} = 1$, the grain will separate at point with coordinates

$$x_o = 0 \text{ and } y_o = r_1.$$

2.4. If $\frac{v_s^2}{g \cdot r_1} < \cos \beta_1$, the grain remains on the belt and will travel

some distance around the head drum, to the point in which the condition $\frac{v_s^2}{g \cdot r_1} < \cos \gamma$ is satisfied. The model assumes that

the separation occurs when the $\frac{v_s^2}{g \cdot r_1} \geq \cos \gamma$, thus separation point has coordinates $x_o = r_1 \cdot \cos \gamma$ and $y_o = r_1 \cdot \sin \beta_1$.

3. $\beta_1 < 0$

3.1. If $\frac{v_s^2}{g \cdot r_1} \geq \cos \beta_1$, the grain may separate at the initial point of

contact between the head drum and belt. This point will have coordinates $x_o = r_1 \cdot \sin \beta_1$ and $y_o = r_1 \cdot \cos \beta_1$.

3.2. If $\frac{v_s^2}{g \cdot r_1} < \cos \beta_1$, the speed v_s is too low for the separation at the

initial point of contact between the head drum and belt. The grain remains on the belt and will travel some distance around

the head drum, to the point in which the condition $\frac{v_s^2}{g \cdot r_1} \geq \cos \gamma$ is satisfied.

Speed v_s should be calculated taking into account the thickness of the belt h_1 [4]: $v_s = \omega_1 \cdot r_1$; where: $r_1 = R_1 + h_1 + a$.

After separation of the grain, free flight occurs. Air resistance were omitted in the analysis. CEMA method describes the trajectory equation in the coordinate system associated with the point of separation of the grain. From the point of view of positioning components responsible for capturing and directing material stream, it was decided to put the origin at the center of the head drum of feed conveyor. In such coordinate system the equations describing the movement of grain are as follows:

$$x(t) = x_0 + v_s \cdot \cos \theta \cdot t \quad (3)$$

$$y(t) = y_0 + v_s \cdot \sin \theta \cdot t - \frac{g \cdot t^2}{2} \quad (4)$$

where angle θ depending on the inclination angle and speed conditions of the conveyor is equal to β_1 or γ . By removing time from the above equations, trajectory of a grain in the xy plane is described:

$$y(x) = y_0 + (x - x_0) \cdot \tan \theta - \frac{g}{2} \cdot \left(\frac{x - x_0}{v_s \cdot \cos \theta} \right)^2 \quad (5)$$

Belt of the receiving conveyor was treated as perfectly rigid and inflexible. With these assumptions, it can be mathematically described as a line equation:

$$y_2(x) = \tan \beta_2 \cdot x + b \quad (6)$$

The value of the parameter b was calculated based on knowledge of the point of tangency of the belt and drum

$$x_e = V - r_2 \cdot \sin \beta_2 \quad (7)$$

$$y_e = r_2 \cdot \cos \beta_2 - H \quad (8)$$

where: $r_2 = R + h_2$

Based on equations (6), (7) i (8) was derived:

$$r_2 \cdot \cos \beta_2 - H = \tan \beta_2 \cdot (V - r_2 \cdot \sin \beta_2) + b \quad (9)$$

so:

$$b = r_2 \cdot \cos \beta_2 - H - \tan \beta_2 \cdot (V - r_2 \cdot \sin \beta_2) \quad (10)$$

Finally, the equation describing the belt is given by:

$$y_2(x) = \tan \beta_2 \cdot x + r_2 \cdot \cos \beta_2 - H - \tan \beta_2 \cdot (V - r_2 \cdot \sin \beta_2) \quad (11)$$

The coordinates of the impact point were calculated by comparing to each other right sides of equations (5) and (11)

$$y(x) = y_2(x) \text{ dla } x > 0 \quad (12)$$

$$y_0 + (x - x_0) \cdot \tan \theta - \frac{g}{2} \cdot \left(\frac{x - x_0}{v_s \cdot \cos \theta} \right)^2 = \tan \beta_2 \cdot x + b \quad (13)$$

arranging the equation (13):

$$\sigma \cdot x^2 + C_1 \cdot x + C_2 = 0 \quad (14)$$

where:

$$\sigma = \frac{g}{2 \cdot v_s^2 \cdot \cos^2 \theta} \quad (15)$$

$$C_1 = tg \beta_2 - 2 \cdot \sigma \cdot x_0 - tg \theta \quad (16)$$

$$C_2 = \sigma \cdot x_0^2 + x_0 \cdot tg \theta + b - y_0 \quad (17)$$

Solving the quadratic equation (12) and taking into account that searched coordinate $x > 0$, we obtain:

$$\Delta = C_1^2 - 4 \cdot \sigma \cdot C_2 \quad (18)$$

$$x_{c1} = \frac{-C_1 - \sqrt{\Delta}}{2 \cdot \sigma} \quad (19)$$

$$x_{c2} = \frac{-C_1 + \sqrt{\Delta}}{2 \cdot \sigma} \quad (20)$$

because $x_{c2} > 0$ it is substituted in the equation (5):

$$y_c = y_0 + (x - x_{c2}) \cdot tg \theta - \frac{g}{2} \cdot \left(\frac{x - x_{c2}}{v_s \cdot \cos \theta} \right)^2 \quad (21)$$

Thus, the point of impact of the grain at the belt of receiving conveyor has the coordinates x_{c2} , y_c . In order to determine the angle of impact of the grain, derivative of the equation of the trajectory with respect to x has to be calculated:

$$\frac{dy}{dx} = -2 \cdot \sigma \cdot (x - x_0) + tg \theta \quad (22)$$

Calculating value of the derivative at point $x = x_{c2}$ we get:

$$\left(\frac{dy}{dx} \right)_{x=x_{c2}} = -2 \cdot \sigma \cdot (x_{c2} - x_0) + tg \theta = tg \alpha \quad (23)$$

where: α - angle of impact in the global coordinate system hence:

$$\alpha = \arctg[-2 \cdot \sigma \cdot (x_{c2} - x_0) + tg \theta] \quad (24)$$

Total impact angle is a sum of α and β_2 (rys.7).

In the coordinate system associated with the center of the drum of a feed conveyor, velocity components of the grain at the point of contact with the belt of receiving conveyor are described by equations:

$$v_x = v_s \cdot \cos \theta \quad (25)$$

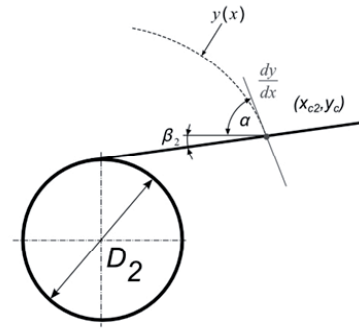


Fig. 7. Angle of impact of the grain on the belt of receiving conveyor

$$v_y = v_s \cdot \sin \theta - gt_c^2 \quad (26)$$

where:

$$t_c = \frac{x_{c2}}{v_s \cdot \cos \theta} \quad (27)$$

Magnitude of velocity vector is:

$$v = \sqrt{v_x^2 + v_y^2} \quad (28)$$

In the analysis, values of the velocity vector in the direction of the normal and tangential to the receiving conveyor belt were of interest. Given the inclination angle of the second conveyor, the angle of impact of the grain and its velocity components in global coordinate system at the moment of impact, values of velocity components normal and tangential to the receiving belt were calculated from:

$$v_n = v \cdot \sin(\alpha + \beta_2) \quad (29)$$

$$v_t = v \cdot \cos(\alpha + \beta_2) \quad (30)$$

4. Sensitivity analysis of the model

System was analyzed in terms of the influence of selected parameters on the value of the tangential velocity at the moment of impact of the grain on receiving conveyor belt. Following input parameters were chosen: inclination angles β_1 , β_2 , feed conveyor speed v_1 and horizontal distance H . Each of the factors was analyzed on two levels and results are shown on figures 8 and 9.

Table 1. The values of chosen transfer chute parameters

Parameter	min (-1)	max (+1)
v_1 [m/s]	1	3
β_1 [deg]	-15	15
β_2 [deg]	-15	15
H [m]	1	4

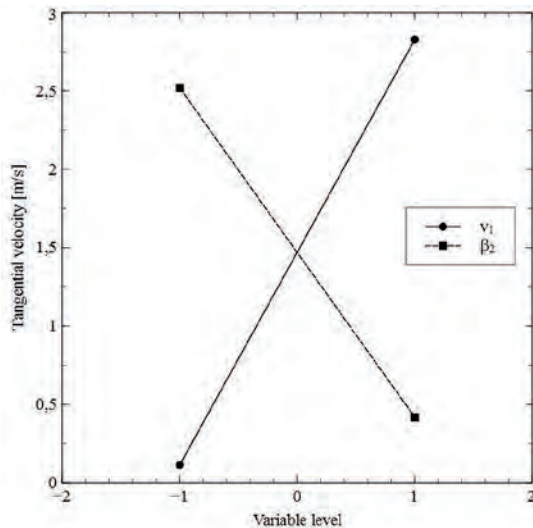


Fig. 8. Mean change in tangential velocity v_t depending on v_1 and β_2

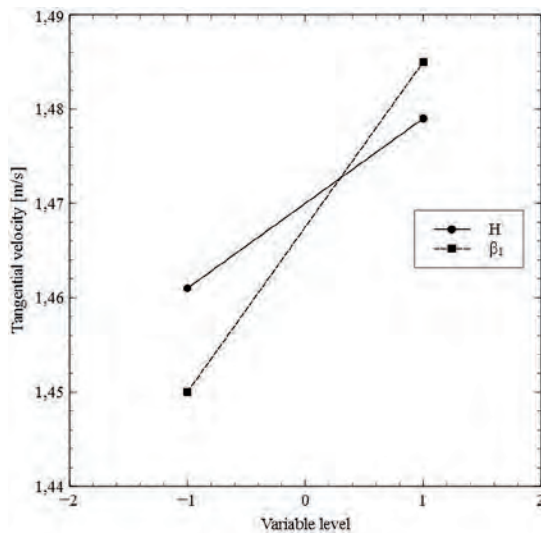


Fig. 9. Mean change in tangential velocity v_t depending on β_1 and H

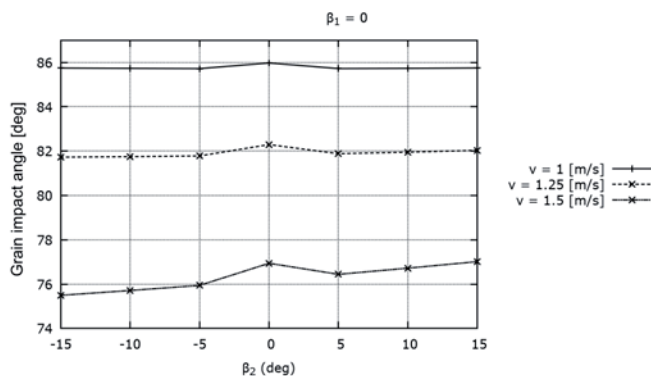


Fig. 10. Angle of impact of a grain depending on v_1 and β_2 for a constant value of $\beta_1 = 0^\circ$

The results showed that the predominant effects on the tangential velocity of grain at the point of its impact on the receiving conveyor belt are inclination of the second conveyor β_2 and the feed conveyor speed v_1 .

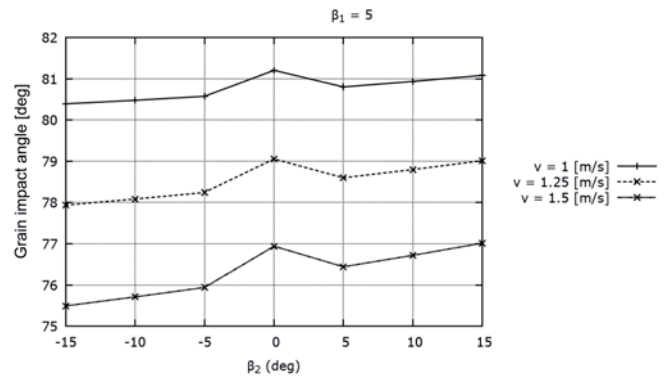


Fig. 11. Angle of impact of a grain depending on v_1 and β_2 for a constant value of $\beta_1 = 5^\circ$

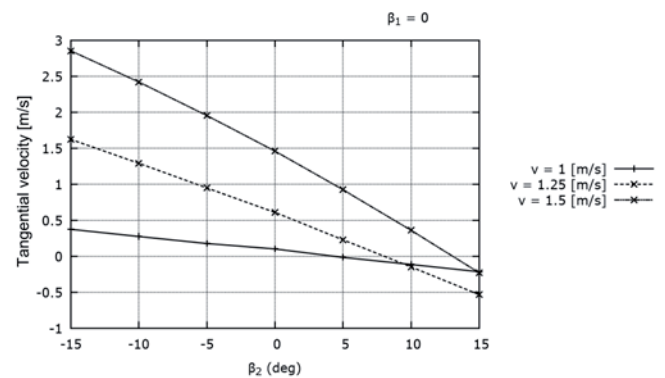


Fig. 12. Tangential velocity at the point of contact depending on v_1 and β_2 for a constant value of $\beta_1 = 0^\circ$

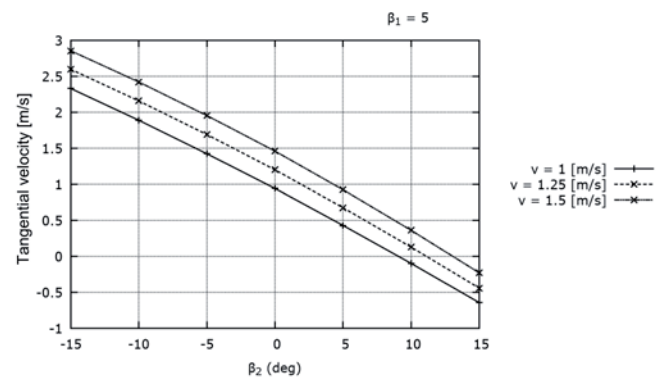


Fig. 13. Tangential velocity at the point of contact depending on v_1 and β_2 for a constant value of $\beta_1 = 5^\circ$

5. Examples of calculations

Based on the obtained in section 3 relationships, series of calculations were carried out. Speed and impact angle of the grain were determined for a selected range of parameter values β_1, β_2, v_1, H . Other model input parameters were constant. Sample results are shown in the figures 10–13.

Based on the results of calculations, conclusions on the desired configuration of conveyors to achieve favorable conditions for stream loading may be obtained.

6. Summary

In order to improve the efficiency of conveyor transport systems, components and conveyor assemblies are constantly being improved in terms of their adaptation to the growing transport requirements and a multi-action tasks are taken to reduce their energy intensity by reducing the resistance to motion. Transfer stations are one of the key areas of conveyor transport systems which adds considerable resistance and loss of power and a potential source of failure and increased wear of

belts. Optimization of chute construction is an actual and important problem to solve. Parameters obtained from the theoretical analysis of the grain motion can be useful in shaping the design elements for eliminating or reducing their defects. Knowledge of the trajectory of the material stream allows for the proper shaping and design of transfer station construction. These issues will be the subject of further research and construction design work carried out in this area.

References

1. Antoniuk J. Systemy transportu przenośnikami taśmowymi w górnictwie. Wydawnictwo Politechniki Śląskiej, Gliwice 2005.
2. Czuba W, Kulinowski P. Numeryczne obliczenia oporów załadunku urobku na taśmę przenośnik z wykorzystaniem metody elementów dyskretnych. *Transport Przemysłowy i Maszyny Robocze* 2011; 2 (12): 5–10.
3. Cyganiuk JA. Modelowanie przepływów strumieni materiałów ziarnistych na łukowych płytach odbojowych. *Transport Przemysłowy i Maszyny Robocze* 2011; 4 (14): 36–40.
4. Conveyor Equipment Manufacturers Association. *Belt Conveyors for Bulk Materials*. 5th ed. 2002.
5. Gładysiewicz L. *Przenośniki taśmowe. Teoria i obliczenia*. Oficyna Wydawnicza Politechniki Wrocławskiej 2003.
6. Huque ST. *Analytical and Numerical Investigations into Belt Conveyor Transfers*. Engineering. University of Wollongong 2004.
7. Kessler F, Prenner M. DEM – Simulation of Conveyor Transfer Chutes. *FME Transactions* 2009; 37 (4): 185–192.
8. Maton AE. *Transfer Station Design – Developments in the Iron Ore Industry*. Bulk Solid Handling 2007; 27 (2): 94–100.
9. Swinderman R, Todd PE, Marti AD, Goldbeck LJ, Marshall D, Strebel MG. *Foundations The Practical Resource for Cleaner, Safer, More Productive Dust & Material Control*. Engineering. 4th ed. Neponset, Illinois, U.S.A.: Martin Engineering Company.
10. Żur T, Hardygóra M. *Przenośniki taśmowe w górnictwie*. Wydawnictwo „Śląsk” Katowice 1979.

Wojciech CZUBA, M.Sc. (Eng.)

Kazimierz FURMANIK, Ph.D., D.Sc. (Eng.), Assoc. Prof.

Department of Mining, Dressing and Transport Machines

Faculty of Mechanical Engineering and Robotics

AGH University of Science and Technology in Cracow

Al. A. Mickiewicza 30, 30-059 Cracow, Poland

E-mails: wczuba@agh.edu.pl, fukaz@agh.edu.pl

Chao ZHANG
Shaoping WANG

SOLID LUBRICATED BEARINGS PERFORMANCE DEGRADATION ASSESSMENT: A FUZZY SELF-ORGANIZING MAP METHOD

OCENA OBNIŻENIA CHARAKTERYSTYK ŁOŻYSK ZE SMAREM STAŁYM: METODA ROZMYTYCH SAMOORGANIZUJĄCYCH SIĘ MAP

Solid lubricated bearings are common components in space mechanisms, and their reliability and performance degradation assessment are very crucial. In this study, a fuzzy self-organizing map method is used to perform performance degradation assessment. Feature vectors are constructed by indices of vibration as well as friction torque signal. Self-organizing map is then used to perform performance degradation assessment and the subjection of each feature vector to normal cluster on output layer is used as degradation indicator. Accelerated life test results show that this method can make effective performance degradation assessment and describe degradation degree in the whole life time.

Keywords: solid lubricated bearings, performance degradation, fuzzy self-organizing map.

Łożyska ze smarem stałym to powszechnie stosowane elementy urządzeń, a ich niezawodność i ocena degradacji charakterystyk są bardzo istotne. W przedstawionej pracy wykorzystano metodę rozmytych samoorganizujących się map do oceny obniżenia charakterystyk. Wektory cech skonstruowano za pomocą wskaźników wibracji, jak również sygnału momentu tarcia. Następnie dokonano oceny obniżenia charakterystyk z wykorzystaniem samoorganizującej się mapy, a za wskaźnik degradacji przyjęto przynależność każdego wektora cech do normalnej grupy w warstwie wyjściowej. Wyniki badań przyspieszonych pokazują, że przy użyciu omawianej metody można dokonywać skutecznej oceny obniżenia charakterystyk a także opisywać stopień degradacji w całym okresie eksploatacji.

Słowa kluczowe: łożyska ze smarem stałym, obniżenie charakterystyk, rozmyta mapa samoorganizująca się.

1. Introduction

Solid lubricated bearings are widely used in space mechanisms and other appliances, due to their characteristics of negligible vapor contamination, wide operating temperature and ignorable surface migration [17, 25]. Their failure might cause severe economic loss, or even catastrophic consequences. For this reason, reliability and performance degradation assessment of solid lubricated bearings have drawn more and more attention in this research field.

Many studies of failure mechanism and its influencing factors of solid lubricated bearings have been carried out. Early in 1980s, several researches by simulation methods were reported. These studies mainly focused on the tribological performance of solid lubricated bearings, including impact factors of wear rate [2, 6], influence of geometry and motion forms on dynamic performance [4, 5]. In 1990s and later, more experimental as well as simulation studies were carried out, aiming at investigating the process of particle generation [23], relationship between fault mechanism and outer stress and some other tribological behaviour [7, 17, 22, 29, 30]. These studies made further research on fault mechanism of solid lubricated bearings, as well as its relationship with environments and working conditions.

However, for the research of solid lubricated bearings, scholars merely concentrate on the fault mechanism analysis, while performance degradation assessment that can better meet the need to improve machine uptime and near-zero breakdown productivity has been scarcely studied [11]. Usually performance degradation assessment consists of two steps. Firstly, features which can reflect operating status should be extracted. And secondly, an assessment needs to be generated, describing degradation degree of the system. For solid lubricated bearings, several studies on their performance degradation

assessment have been performed. Using wear rate as a feature reflecting operating status, Meeks and Bohner studied prediction of bearing life by creating semi-empirical wear equations [15]. This assessment method is built based on data acquired when failure mode is known. However, in actual situation, this is not always the case, which makes this method not very practical. Later several experimental researches were carried out by NASA and ESA, assessing degradation degree of solid lubricated bearings by carefully dismantling and observing [1, 3, 9, 16]. Assessing methods in these studies may not be appropriate for performance degradation assessment of other solid lubricated bearings, because dismantling is not easy to perform. Moreover, these methods did not consider working condition and environment factors. A comprehensive and effective method which can realize real-time monitoring of operating status of solid lubricated bearings is emergently needed.

Signal processing has been extensively used for condition monitoring [14]. Based on feature vectors extracted from different kinds of signals by relevant signal processing methods, various researches on performance degradation assessment have been performed [8, 18–21, 32, 33]. These researches mainly focused on intelligent assessment methods, and self-organizing map (SOM) is one of them. Being a topology-preserving mapping from a high-dimensional input to a lower-dimensional output space, SOM is a prominent tool for data analysis and clustering [13]. Application of SOM in performance degradation assessment is mainly based on trajectory method, which observes the trajectory of the best matched unit (BMU) for the data of life tests [21]. This method can provide the time when a test object goes into a certain status, but for each input vector of SOM, only the BMU is considered, which makes it not accurate enough. Meanwhile, in this

method only the time of status transition can be observed, while degradation degree corresponding to each input vector is not illustrated.

In this study, a performance degradation assessment method for solid lubricated bearings based on fuzzy analysis of SOM output layer is proposed. Based on analysis of the consuming process of lubrication film in solid lubricated bearings, certain metrics of vibration and friction torque signal of solid lubricated bearings are selected to compose feature vectors. Then the fuzzy SOM which can quantitatively illustrate the degradation degree is used to describe the degradation process. Accelerated life test of solid lubricated bearings is conducted to evaluate the effectiveness of this approach under different working stresses.

This paper is organized as follows. In Section 2, consuming process of lubrication in solid lubricated bearings is analyzed, and feature vectors are composed based on processing of vibration and friction torque signal. Basis of SOM is then briefly presented and the proposed fuzzy SOM method is introduced. In Section 3, accelerated life test of four groups of solid lubricated bearings is conducted and performance degradation assessment is carried out based on the proposed fuzzy SOM method. Conclusions are in Section 4.

2. Technical background and methodology

2.1. Consuming of lubricant film and feature extraction

Different from bearings lubricated with oil or grease, solid lubricated bearings have their particular fault mechanisms. The structure of a solid lubricated bearing is shown in Figure 1.

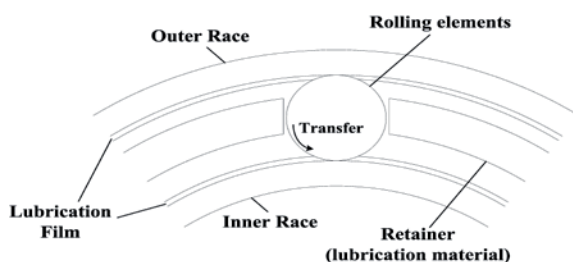


Fig. 1. Structure a solid lubricated bearing

When a solid lubricated bearing is working, no outer oil supply system is needed. As a result, solid lubricated bearings are also called self-lubricating bearings. In most cases, inner and outer races of solid lubricated bearings are coated with lubrication film, and retainer is made of lubricating material. Rolling elements are usually made of steel or ceramics, which are not lubrication material.

In solid lubricated bearings, lubrication film on inner and outer races as well as lubrication material of the retainer plays as lubricants. When a solid lubricated bearing is put into use, at first lubrication film on inner and outer races plays as lubricant and this part of lubricant gradually consumes. Meanwhile, lubrication material of retainer is transferred onto inner and outer races by the rotating and spinning of rolling elements and plays as complementary lubricant.

Due to different working condition, transfer rate of retainer lubricant can be different, and this will cause different effect on the performance degradation process of solid lubricated bearings. If the transfer rate is fluctuating within an appropriate range, a solid lubricated bearing might work for a relatively long time, and turns into failure after both two parts of lubrication film completely consumes. If this rate is small, the consumed lubricant of inner and outer races cannot be replenished in time, and a solid lubricated bearing might turn into failure in a faster speed. In these two cases, the bearing fails due to wear caused by lack of lubricant. This failure mode is called 'Failure Mode 1' in the rest of this paper.

However, if the transfer rate is big, transferred film will accumulate on inner and outer races, and in this case the bearing might not work smoothly. Excessive transferring of retainer lubrication material will make cage pockets become large and collision of balls on cage pockets will be stronger and aggravate the instability of retainer [26]. Both the accumulation and the instability will accelerate the degradation process and eventually cause the bearing to failure. This failure mode is called 'Failure Mode 2' in the rest of this paper.

As mentioned before, signal processing has been widely used in condition monitoring, as different kinds of signals contain large quantity of information of system operating status. For bearings, vibration signal has been most commonly used [24]. Compared with bearings lubricated with oil or grease, vibration signal of solid lubricated bearings should have its specific characteristics owing to the different failure mechanism. When a solid lubricated bearing is running, small particles and pits are gradually generated due to the wear of lubricants on inner and outer races as well as the transferred film. As the bearing is continuously running, each time a rolling element runs over a particle or a pit, an impulse is generated. As the number of particles and pits is increasing, more impulses are expected to occur. Therefore, impulses in vibration signal can be used as indication of performance degradation of solid lubricated bearings.

However, impulses caused by the rolling of rolling elements over particles and pits are weak, because the size of particles and pits is usually very small. Vibration signal measured by vibration sensor experiences a series of modulation process, and due to inherent deficiency of measuring system, much noise will be inevitably introduced into the acquired vibration signal [31]. Hence effective signal processing method is required to extract these impulses which are almost entirely buried in acquired signal from vibration sensor. Taking the similarity of the shape between an actual impulse and the well-known Morlet wavelet into account, the adaptive Morlet wavelet filter proposed in [12] is used here. RMS, Kurtosis and crest factor of each filtered signal are selected to construct feature vectors, following the method in [8].

Friction torque signal can also reflect the operating status of solid lubricated bearings [25]. If there is no liquid lubricant, bearing friction torque can be largely accounted for by Coulomb friction between opposing surfaces [27]. So far no quantitative relationship between indices of friction torque signal and performance degradation of solid lubricated bearings has been reported. Only in [15], C. R. Meeks qualitatively pointed out that transferred film could increase friction torque. In this study, RMS, crest factor and variation value of each friction torque signal, together with RMS, Kurtosis and crest factor of each filtered vibration signal are used to construct feature vectors.

With constructed feature vectors, an efficient performance degradation assessment method is needed. In the following sections, background of SOM is briefly introduced, and the proposed degradation assessment method is given in detail.

2.2. Theoretical background of SOM

The SOM is an artificial neural network developed by Kohonen in [10]. It is an unsupervised neural network which just has two layers and can organize itself according to the nature of the input training data. Basic structure of SOM is shown in Figure 2.

The number of nodes on the input layer equals the dimension of each input vector. On the output layer, neurons are connected with neighboring neurons and usually form a two dimensional regular lattice hexagonally. Each neuron on the output layer is represented by n -dimensional weight, and n also equals the dimension of each input vector. Before training, weight of each neuron of the output layer is stochastically determined. In the training process, this weight is continuously adjusted at a gradually decreasing rate, and neurons on the output layer gradually form into clusters.

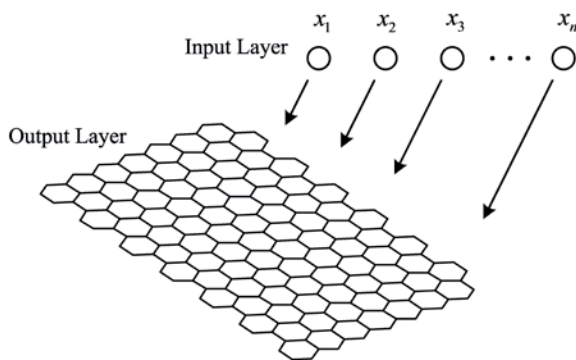


Fig. 2. Structure of SOM

After training, each neuron on the output layer has certain value of weight, and for each input vector, a distance of it and each neuron on the output layer can be calculated. The neuron with the minimum distance is called BMU. If data from normal, degradation and typical failure state are used to train the SOM, clusters representing different states of solid lubricated bearings would appear on the output layer. For a run-to-failure test of solid lubricated bearings, BMUs of extracted feature vectors at different time of the test should form into a trajectory, which can be used to describe the performance degradation process of solid lubricated bearings [21].

2.3. Fuzzy SOM

In the above trajectory method, for each input vector, the position of its BMU on the output layer is used to indicate the corresponding status. However, there exists two problems in this method. Firstly, in certain cases, the distance between the input vector and its BMU might be close to that between it and the neuron with the second smallest distance to it. Here this neuron is called the second BMU. If the BMU and the second BMU of an input vector do not belong to the same cluster, it might not be accurate enough to analyze the status of tested bearing just by observing the position of its BMU.

Secondly, dividing output layer into clusters by training result is a subjective process, and in certain cases, this subjectivity might lead to some problems. Figure 3(a) shows the output layer of a trained SOM and here the color of a neuron represents the distance between its neighboring neurons, as shown in the corresponding diagram on the right of the trained SOM in Figure 3(a). Thus neuron with color standing for bigger value can be treated as dividing line. A preliminary clustering result is shown in Figure 3(b), and it can be seen that it is not easy to determine whether the two neurons marked with a black square belong to cluster B or C here. In this case, the accuracy of trajectory method would be affected.

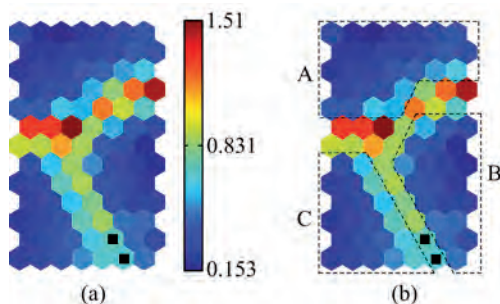


Fig. 3. A trained SOM and its clustering

To solve these two problems, a fuzzy analyzing method based on SOM is proposed in this study. Assuming that for certain type of solid lubricated bearing, there are typical data of normal state, degradation state and failure state. An SOM is trained based on typical data, and

there are clusters formed on output layer. Here l is used to represent the number of clusters on output layer and l can be determined using Davies-Boulding clustering index [28]. Normally, there will be one cluster corresponding to normal state. Specify normal state as the 1st state. For a run-to-failure test of the same type of bearing, a group of data is obtained, denoted as x_1, x_2, \dots, x_m , and m is the number of sampling points. Use n to represent the dimension of input vector.

For each input vector, the distance between it and each neuron in each cluster is calculated. Use $d_{j,k}^{(i)}$ to represent the distance between x_i , the i th input vector, and $w_{j,k}$, the j th neuron in the k th cluster. Here $i=1,2,\dots,m$, $k=1,2,\dots,l$, $j=1,2,\dots,s_k$, and s_k represents the number of neurons in the k th cluster. And $d_{j,k}^{(i)}$ can be expressed by

$$d_{j,k}^{(i)} = \|x_i - w_{j,k}\| \quad (1)$$

where $\|\cdot\|$ means Euclidean norm.

Use $D_{i,k}$ to represent the average distance between the i th input vector and each neuron in the k th cluster, as shown in

$$D_{i,k} = \frac{1}{s_k} \sum_{j=1}^{s_k} d_{j,k}^{(i)} \quad (2)$$

As the normal state has been specified as the 1st state, use (3) to define the subsection of the i th input vector to normal state.

$$S_i = \frac{\frac{1}{D_{i,1}}}{\sum_{k=1}^l \frac{1}{D_{i,k}}} \quad (3)$$

It can be seen from this derivation process that compared with conventional SOM method, the proposed fuzzy SOM method take the distance between an input vector and all neurons in all clusters into consideration. It uses the objection of an input vector to normal state as performance degradation indicator and is intuitionistic. For a run-to-failure test of solid lubricated bearings, following the curve of the subsection of each feature vector to normal state, the performance degradation assessment can be carried out. The method proposed in this paper is depicted in Figure 4.

3. Experimental results and analysis

3.1. Experiment rig

Accelerated life test was conducted to validate the effectiveness of the proposed method. Experiment rig is shown in Figure 5. Four groups of bearings were tested and Figure 5 only shows two of them. Each group had three pairs of bearings and was driven by a DC brushless motor. Vibration and friction torque signal for each group were obtained by corresponding sensors.

Before the test, each pair of bearings was preloaded axial loads. Vibration and friction torque signal were collected at the sample rate of 25.6 kHz and 50 Hz, respectively. Data collection was conducted every four hours, i.e. six times a day. Each collection lasted for 4 seconds. The test lasted for 47 days and at the end of the test, three of the four groups of bearings were in failure state. Note that this test was performed in nitrogen environment. Parameters and operat-

ing condition of tested bearings are shown in Table 1 and Table 2, respectively.

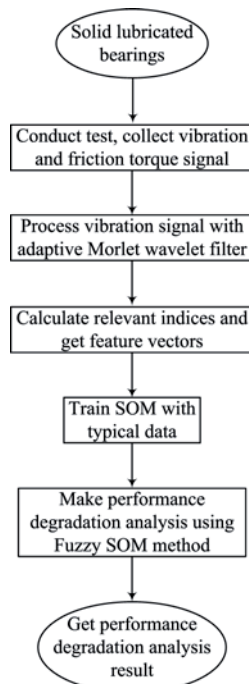


Fig. 4. The proposed performance degradation assessment method

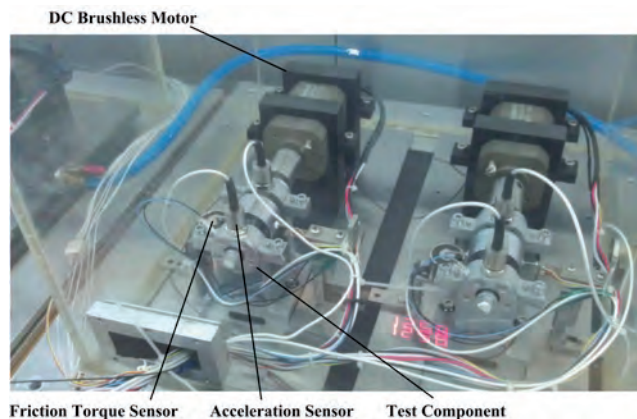


Fig. 5. Accelerated life test of solid lubricated bearings

Table 1. Parameters of tested bearings

Inner diameter (mm)	Outer diameter (mm)	Width (mm)	Ball number	Ball diameter (mm)
7	22	7	7	4.0

Table 2. Operation condition of tested bearings

Group Number	Rotation Velocity (rpm)	Axial Load (N)	Temperature (°C)
1	1500	20	20
2	1000	30	20
3	1500	30	20
4	1000	50	20

3.2. Results and analysis

Group 4 and Group 3 ended up at the 9th and the 31st day of the test, respectively. Group 2 ended up at the 45th day of the test. At the end of the test, Group 1 was still working. Dismantling results showed that there was large quantity of debris on inner and outer races of Group 4. For Group 3 and Group 2, a number of cracks and debris on inner and outer races as well as balls were observed. Group 1 was also dismantled after test and only small amount of debris and cracks were observed on inner and outer races. Combining with the observed results of the amplitude of vibration and friction torque signal, it can be concluded that Group 4 ended up in 'Failure Mode 2' and Group 3 and Group 2 ended up in 'Failure Mode 1'. For Group 1, certain degrees of performance degradation also took place.

Before the accelerated life test, a life test of the same type of solid lubricated bearings had been conducted. In this life test, the number of specimen is two, and both of them work under normal condition. Vibration and friction torque signal were also obtained. At the end of this test, one of the two specimen ended up in 'Failure Mode 1' and the other one ended up in 'Failure Mode 2'. Data acquired in this life test at typical status, i.e. normal, degradation and failure, are used to train an SOM and the trained SOM is then used to conduct the performance degradation assessment of solid lubricated bearings in the accelerated life test.

As mentioned above, for every time of signal acquisition, both in the previous life test and the accelerated life test, vibration signal is processed by adaptive Morlet wavelet filter. Then RMS, crest factor and kurtosis of the filtered vibration signal as well as RMS, crest factor and variation value of friction torque signal are calculated and used to construct feature vectors. These obtained vectors act as the input of SOM. Input dimension of SOM here is six. Number of neurons on the output layer and the ratio of side lengths are automatically determined by the SOM toolbox.

In final assessment of performance degradation of the four tested groups of bearings, trajectory method and the proposed fuzzy SOM method are adopted and results come out from these two methods are compared with each other. The SOM toolbox developed by Helsinki University of Technology is used. Firstly, SOM is trained by specified data, which consist of five groups, i.e. normal data, degradation and fault data of 'Failure Mode 1', and degradation and fault data of 'Failure Mode 2', respectively. These five groups are later labeled as 'N', 'D1', 'F1', 'D2' and 'F2' in SOM, respectively.

U-matrix of the trained SOM is shown in Figure 6(a). A preliminary clustering is made, judging by the color difference, and the result is also illustrated in Figure 6(a), and it can be seen that there are three clusters, marked with '1', '2' and '3', respectively. Figure 6(b) shows the Davies-Boulding clustering index curve. On this curve three gets minimum value, which shows that three is the optimal number of clusters. The labeled map is shown in Figure 6(c). It can be seen that cluster '1' corresponds to normal state, cluster '2' corresponds to degradation state and cluster '3' corresponds to failure state. Though in cluster '3', 'Failure Mode 1' and 'Failure Mode 2' can be further classified, here they are treated as the same cluster as we only consider the degradation degree, not specified failure mode.

Degradation trajectory of the four groups of tested bearings is shown in Figure 7. For Groups 1, 2 and 3, each point stands for the status in two days. For Group 4, each point represents the status in one day. It can be seen that Group 1 moves from normal state to degradation state at the 29th day. Group 2 moves from normal state to degradation state at the 25th day, then to failure state at the 43rd day. Group 3 moves from normal state to degradation state at the 13rd day, then to failure state at the 29th day. Group 4 moves from normal state to degradation state at the 3rd day, then to failure state at the 9th day. For Group 2, 3 and 4, time falling into failure state is broadly in line with judgments of test operators. However, degradation degree in degrada-

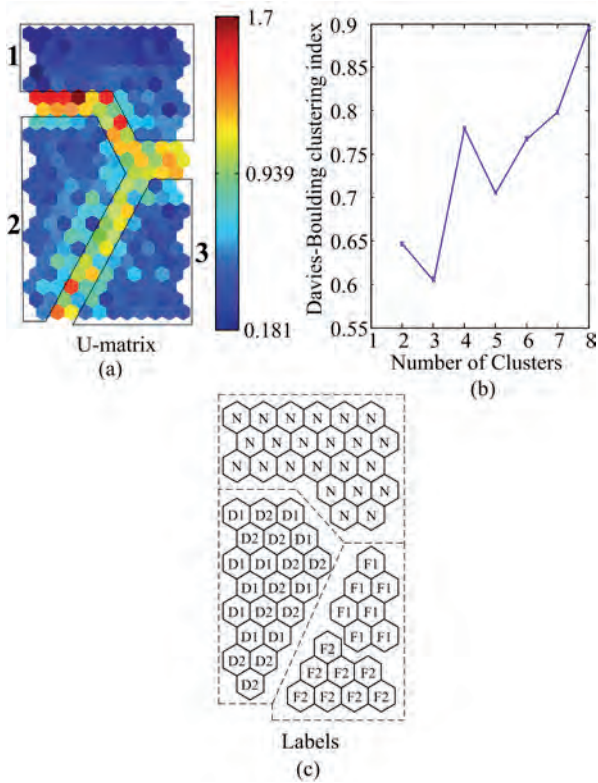


Fig. 6. Trained SOM with typical data (a) U-matrix and clustering, (b) Davies-Boulding clustering index curve, (c) Labeled map

tion state, corresponding to Cluster 2 in Figure 6(a) cannot be seen with trajectory method.

Then, with the method proposed in Section 2.3, performance degradation assessment of four tested groups is carried out, and the result is shown in Figure 8. 0.5 is selected as failure state threshold. Failure date of Group 2, 3 and 4 judged by trajectory method and fuzzy SOM method, as well as actual test result is compared in Table 3.

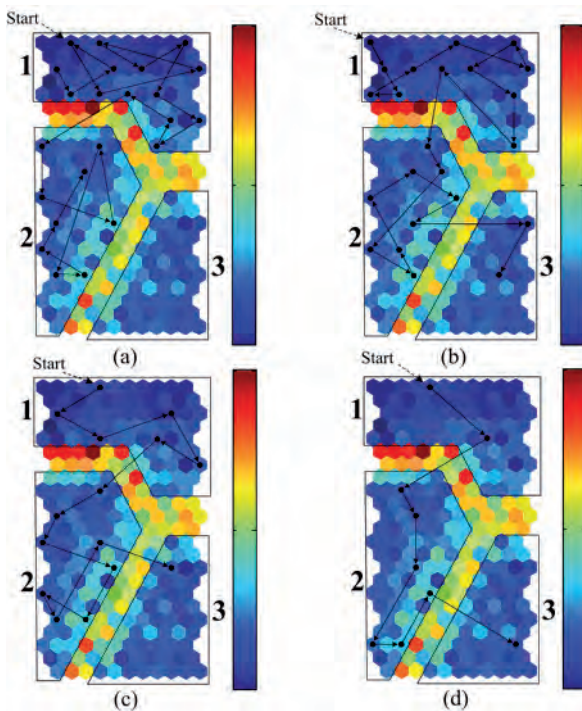


Fig. 7. Degradation trajectory of tested bearings (a) Group 1, (b) Group 2, (c) Group 3, (d) Group 4

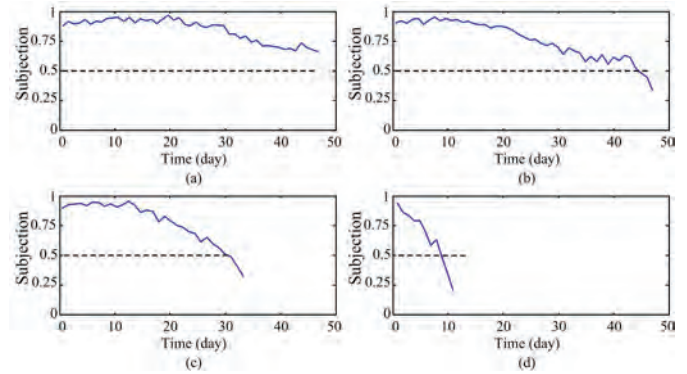


Fig. 8. Degradation curve of test bearings (a) Group 1, (b) Group 2, (c) Group 3, (d) Group 4

Table 3. Results comparison

Group Number	Actual Failure Date	Failure Date by Trajectory Method	Failure date by Fuzzy SOM Method
2	45	43	45
3	31	29	31
4	9	9	9

It can be seen that failure time of the four tested groups by fuzzy SOM method is in full accordance with test results. Moreover, before failure, degradation degree of the four groups of bearings can be clearly seen. In reality, this can give operators more time to conduct maintenance or replacement.

4. Conclusion

In this study, a new method for performance degradation assessment of solid lubricated bearings is proposed. After feature extraction based on vibration as well as friction torque signal, a fuzzy SOM is used to make performance degradation assessment. After training SOM with typical data, clusters are formed on output layer, and the subjection of an input vector to the cluster corresponding to normal state is used as performance degradation indicator. Accelerated life test results show that this method can give the time of transition to failure state as well as describe the degradation degree in the whole lifetime. Future studies should focus on the effect of training data selection on clustering forming of trained SOM and its accuracy of performance degradation assessment.

Acknowledgement: This research is supported by the civil aerospace project, the Natural Science Foundation (Grant no. 51175014) and Program 111 of China.

References

1. Bauer R, Fleischauer P. Torque characteristics of solid-lubricated precision bearings during oscillatory motion. Los Angeles: Space and Missile Systems Center Air Force Materiel Command; 1994.
2. Finkin EF. Theoretical-Analysis of Factors Controlling the Wear of Solid-Film-Lubricated Ball-Bearings. *Wear* 1984; 94 (2): 211–7.
3. Fusaro R, Jansen M. Preventing Spacecraft Failures Due to Tribological Problems. Orlando: NASA; 2001.
4. Gupta PK. Some Dynamic Effects in High-Speed Solid-Lubricated Ball-Bearings. *Asle Transactions* 1983; 26(3): 393–400.
5. Gupta PK, Dill JF, Bandow HE. Parametric Evaluation of a Solid-Lubricated Ball-Bearing. *Asle Transactions* 1985; 2 8 (1): 31–9.
6. Gupta PK, Forster NH. Modeling of Wear in a Solid-Lubricated Ball-Bearing. *Asle Transactions* 1987; 30 (1): 55–62.
7. Hiraoka N. Wear life mechanism of journal bearings with bonded MoS₂ film lubricants in air and vacuum. *Wear* 2001; 249 (10–11): 1014–20.
8. Huang RQ, Xi LF, Li XL, Liu CR, Qiu H, Lee J. Residual life predictions for ball bearings based on self-organizing map and back propagation neural network methods. *Mechanical Systems and Signal Processing* 2007; 21 (1): 193–207.
9. Jones W, Jansen M. Lubrication for Space Applications. Cleveland: NASA; 2005.
10. Kohonen T. Self-Organizing Maps. Springer; 1995.
11. Lee J. Measurement of machine performance degradation using a neural network model. *Computers in Industry* 1996; 30 (3): 193–209.
12. Lin J, Zuo MJ. Gearbox fault diagnosis using adaptive wavelet filter. *Mechanical Systems and Signal Processing* 2003; 17 (6): 1 259–69.
13. Mayer R, Rauber A. Visualising Clusters in Self-Organising Maps with Minimum Spanning Trees. *Artificial Neural Networks-Icann* 2010, Pt II 2010; 6353: 426–31.
14. Mcfadden PD, Smith JD. Vibration Monitoring of Rolling Element Bearings by the High-Frequency Resonance Technique – a Review. *Tribology International* 1984; 17(1): 3–10.
15. Meeks CR, Bohner J. Predicting Life of Solid-Lubricated Ball-Bearings. *Asle Transactions* 1986; 29(2): 203–13.
16. Murray F, Heshmat H, Fusaro R. Accelerated testing of space mechanisms. Cleveland: NASA; 1995.
17. Nishimura M, Suzuki M. Solid-lubricated ball bearings for use in a vacuum state – state-of-the-art. *Tribology International* 1999; 32 (11): 637–47.
18. Ocak H, Ertunc HM, Loparo KA. Online tracking of bearing wear using wavelet packet transform and hidden Markov models. *2006 IEEE 14th Signal Processing and Communications Applications, Vols 1 and 2* 2006: 137–40.
19. Ocak H, Loparo KA, Discenzo FM. Online tracking of bearing wear using wavelet packet decomposition and probabilistic modeling: A method for bearing prognostics. *Journal of Sound and Vibration* 2007; 302 (4–5): 951–61.
20. Pan Y, Chen J, Guo L. Robust bearing performance degradation assessment method based on improved wavelet packet-support vector data description. *Mechanical Systems and Signal Processing* 2009; 23 (3): 669–81.
21. Qiu H, Lee J, Lin J, Yu G. Robust performance degradation assessment methods for enhanced rolling element bearing prognostics. *Advanced Engineering Informatics* 2003; 17 (3–4): 127–40.
22. Rapoport L, Moshkovich A, Perflyev V, Lapsker I, Halperin G, Itovich Y, Etsion I. Friction and wear of MoS₂ films on laser textured steel surfaces. *Surface & Coatings Technology* 2008; 202 (14): 3332–40.
23. Saito T, Naka M, Ito H, Yamamoto T, Matsunaga S. Particle generation by solid-lubricated bearings and ball screws in vacuum environments. *Tribology Transactions* 1999; 42 (1): 162–7.
24. Tandon N, Choudhury A. A review of vibration and acoustic measurement methods for the detection of defects in rolling element bearings. *Tribology International* 1999; 32 (8): 469–80.
25. Todd MJ. Modeling of Ball-Bearings in Spacecraft. *Tribology International* 1990; 23 (2): 123–8.
26. Todd MJ. Solid Lubrication of Ball-Bearings for Spacecraft Mechanisms. *Tribology International* 1982; 15 (6): 331–7.
27. Todd MJ, Johnson KL. A Model for Coulomb Torque Hysteresis in Ball-Bearings. *International Journal of Mechanical Sciences* 1987; 29 (5): 339–54.
28. Wang L, Jiang MH, Lu YH, Noe F, Smith JC. Self-organizing map clustering analysis for molecular data. *Advances in Neural Networks – Issn* 2006, Pt 1 2006; 3971: 1250–5.
29. Xu GH, Lee JH, Hong L. Low-temperature tribological properties of solid lubricating coatings. *Contributions of Surface Engineering to Modern Manufacturing and Remanufacturing* 2002: 357–62.
30. Xu GZH, Lee JH, Liang H, Georing D. Tribological properties of solid-lubricating coatings on cylinder bore at low temperature. *Wear* 2004; 257 (1–2): 59–65.
31. Yiakopoulos CT, Antoniadis IA. Wavelet based demodulation of vibration signals generated by defects in rolling element bearings. *Shock and Vibration* 2002; 9 (6): 293–306.
32. Yu JB. Bearing performance degradation assessment using locality preserving projections. *Expert Systems with Applications* 2011; 38 (6): 7440–50.
33. Yu JB. Bearing performance degradation assessment using locality preserving projections and Gaussian mixture models. *Mechanical Systems and Signal Processing* 2011; 25 (7): 2573–88.

Chao ZHANG, Ph.D.

Prof. Shaoping WANG

School of Automation Science and Electrical Engineering
Beihang University

No. 37 Xueyuan Road, Haidian District, Beijing, China, 100191

E-mails: czhangstar@gmail.com, shaopingwang@vip.sina.com

Yan-Feng LI
Jinhua MI
Hong-Zhong HUANG
Shun-Peng ZHU
Ningcong XIAO

FAULT TREE ANALYSIS OF TRAIN REAR-END COLLISION ACCIDENT CONSIDERING COMMON CAUSE FAILURE

ANALIZA DRZEWA USZKODZEŃ DLA KOLIZJI TYLNEJ CZĘŚCI SKŁADU POCIĄGU Z UWZGLĘDNIENIEM USZKODZENIA SPOWODOWANEGO WSPÓLNĄ PRZYCZYNĄ

Along with the development of modern design technology and the increasing complication of modern engineering systems, component dependency has become a universal phenomenon during the failure analysis of systems. Ignoring the dependency among the failure behaviors of system components may lead to a huge error or even yield faulty results. In this paper, three types of models and two kinds of modeling methods are introduced for solving the common cause failure issues. The fault tree model of the train rear-end collision accident has been proposed based on the explicit modeling method. The probability of occurrence of the train rear-end collision accident is calculated using the square root model. The result shows that common cause failure has significant influences on the system reliability.

Keywords: common cause failure, train rear-end collision accident, fault tree analysis.

Wraz z rozwojem nowoczesnych technologii projektowania i rosnącej komplikacji nowoczesnych systemów inżynierskich, zależność między komponentami stała się zjawiskiem powszechnym w analizie uszkodzeń systemów. Ignorowanie zależności między zachowaniami uszkodzeniowymi komponentów systemu może doprowadzić do ogromnego błędu, a nawet dać całkowicie błędne wyniki. W niniejszej pracy, przedstawiono trzy typy modeli i dwa rodzaje metod modelowania służących do rozwiązywania typowych problemów związanych z uszkodzeniami spowodowanymi wspólną przyczyną. Zaproponowano model drzewa uszkodzeń dla kolizji tylnej części składu pociągu w oparciu o metodę modelowania bezpośredniego. Prawdopodobieństwo wystąpienia kolizji tylnej części składu pociągu obliczono przy użyciu modelu pierwiastka kwadratowego. Wynik pokazuje, że uszkodzenie spowodowane wspólną przyczyną ma znaczący wpływ na niezawodność systemu.

Słowa kluczowe: uszkodzenie spowodowane wspólną przyczyną, kolizja tylnej części składu pociągu, analiza drzewa uszkodzeń.

1. Introduction

Along with the increasing complexity and redundancy of modern engineering systems, the issue of independent failure of components is dwindling while the dependent failure is becoming more pronounced. In engineering, the dependency is a general characteristic of system failures. Implementing the quantitative analysis of fault tree under the assumption of independence between basic events as well as ignoring the relationships between them generally leads to a huge uncertainty or even lead to erroneous results.

Common cause failures (CCFs) have been an important issue in reliability analysis for several decades, especially when dealing with complex systems, as CCFs often dominate random hardware failures. Systems affected by CCFs are systems in which two or more events have the potential of occurring due to the same cause. Since the 1970s, different approaches have been used to describe the CCFs, such as a β -factor model [6], basic parameter (BP) model [19], the multiple Greek letter (MGL) model [7], α -factor model [13], and square-root model [8]. However, the issues on CCFs are still the focus of much research and there does not exist a general consensus as to which method is more suitable for dealing with CCFs. Several case studies in control system, complex computer system, and transmis-

sion system have been investigated using these models in [4, 9, 10, 21–23, 26]. For the analysis of rear-end crashes, Das et al. [5] applied the genetic programming modeling approach in safety research for crash count and severity classification, which provides independence for model development without restrictions on the distribution of data. Milho et al. [12] proposed and validated a multi-body dynamics based procedure for the design of energy absorbing structures and train collision scenarios. In this methodology, the moving components of a vehicle are described as sets of rigid bodies, with their relative motion constrained by kinematic joints. In recent years, the Federal Railroad Administration has been conducting research on passenger rail equipment crash worthiness to develop technical information [14, 18]. The passenger rail equipment crash worthiness research is focused on the development of structural crash worthiness and interior occupant protection tactics, whose results have been used in the development of railroad procurement specifications [16, 17] and industry standards [1, 2]. Tyrell et al. [15] conducted a full-scale train-to-train impact test of crash energy management to establish the degree of the enhanced performance of alternative design strategies for passenger rail crashworthiness. Though most efforts have been put forward on the safety of structural crashworthiness and/or passenger rail crashworthiness, they cannot accurately be used for safety and reliability assessment

of railway vehicle, further research on the fault tree analysis of train rear-end collision accident is expected.

Thus, the purpose of this paper is to incorporate common-cause failures into the fault tree analysis of train rear-end collision accident. It attempts to offer a basis for safety and reliability assessment of railway vehicle. This paper consists of 5 sections. In the rest sections, the existing models for CCF modeling are briefly introduced in Section 2. Two CCF modeling methods are presented in Section 3. Fault tree analysis of train rear-end collision accident considering CCF has been put forward in Section 4 and it is followed by a brief conclusion in Section 5.

2. Existing models for CCF modeling

2.1. Basic parameter model

Supposing a system is comprised of three components: A , B , and C . The total failure probability of component A includes the probability of independent failure of component A and the failure probability of dependent component B or C or both B and C while component A fails. Let A_i , B_i and C_i denote the independent failure events of components A , B and C , respectively. $P(A_i)$, $P(B_i)$ and $P(C_i)$ represent the failure probability of A_i , B_i and C_i . Thus, the total failure probability of A , B and C can be calculated respectively as follows.

$$P(A) = P(A_i) + P(AB) + P(AC) + P(ABC) \quad (1)$$

$$P(B) = P(B_i) + P(AB) + P(BC) + P(ABC) \quad (2)$$

$$P(C) = P(C_i) + P(AC) + P(BC) + P(ABC) \quad (3)$$

For the common cause component group composed of A , B and C , supposing that the components are statistically identical, the failure probability of any components can be expressed as:

$$Q_l = \sum_{k=1}^3 \binom{3-1}{k-1} Q_k \quad (4)$$

where Q_k denotes the simultaneous failure probability of any k components.

Similarly, for a system composed of m components, the total failure probability of the system can be obtained as:

$$Q_l = \sum_{k=1}^m \binom{m-1}{k-1} Q_k \quad (5)$$

where Q_l denotes the failure probability of the system which composed of m components, Q_k represents the simultaneous failure probability of any k components.

2.2. The β -factor model

The β -factor Model is one of the most commonly used CCF models, which was originally proposed by Fleming [6]. It assumes that a certain percentage of all failures are CCFs. The strength of common cause failure in this model is quantified by β factor. The β -factor

model is initially targeted for two-component parallel system. Two categories of failure are taken into account within the CCF model, that is, the independent failure of a certain component itself and the common cause failure. The total failure probability of a component is composed of two parts, the probability of independent failure denoted by Q_1 , and the common cause failure denoted by Q_2 . Then the common cause factor β is the fraction of the total failure probability attributable to dependent failures [3]:

$$\beta = \frac{Q_2}{Q} = \frac{Q_2}{Q_1 + Q_2} \quad (6)$$

The value β can also be obtained by the conditional probability that there is a CCF given that there is a failure, which is expressed as:

$$\beta = P(\text{CCF} | \text{Failure}) \quad (7)$$

This model is commonly used for its easy comprehension. The parameter value is based on engineering experience and the published statistics of CCF, and the range of β -factor is from 0 to 0.25 [3].

2.3. The Square-Root model

The square-root method is a simple bounding technique used to estimate the effect of CCFs on a system [8]. Consider a parallel system consisting of two components A and B . A_F , B_F , $A_F \cap B_F$ are the failure events of components A , B and the system, respectively. Then the unavailability of the system is defined as

$$P(A_F \cap B_F) \leq P(A_F), P(A_F \cap B_F) \leq P(B_F) \quad (8)$$

which also can be expressed as $P(A_F \cap B_F) \leq \min\{P(A_F), P(B_F)\}$.

If A and B are dependent, we can get

$$P(A_F \cap B_F) = P(A_F | B_F) P(B_F) \geq P(A_F) P(B_F) \quad (9)$$

Let $a = P(A_F)P(B_F)$ and $b = \min\{P(A_F), P(B_F)\}$, the square-root CCF model is then approximated using the geometric mean of a and b as follows

$$P(A_F \cap B_F) = \sqrt{ab} \quad (10)$$

Similarly, for a n -component parallel system, the upper and lower limit of the unavailability can be obtained by

$$a = \prod_{i=1}^n P(A_i), b = \min\{P(A_1), P(A_2), \dots, P(A_n)\} \quad (11)$$

In this paper, the square-root model is used to analyze the impact of CCF on the train rear-end collision accident.

3. Common cause failure modeling method

When dealing with the common cause failure, there are mainly two kinds of modeling methods for fault tree analysis with CCF, namely, implicit modeling and explicit modeling [25]. A fault tree is a well-arranged method of modeling the failure of a top event. The failure of a top event depends on other basic components. The dependencies between the components are modeled in a tree structure using AND- or OR-gates. The CCF part is not considered during the process of system reliability analysis only after it to get the probability of occurrence of the top event for the implicit method, while within it for the explicit method.

3.1. Implicit modeling for CCF

The implicit CCF model of a parallel system with 3 units (A , B and C) can be depicted as shown in Fig. 1. Using T represents the event “system failure”, and “ T_1 ” is the intermediate event that means “System failure without considering the impact of CCF”.

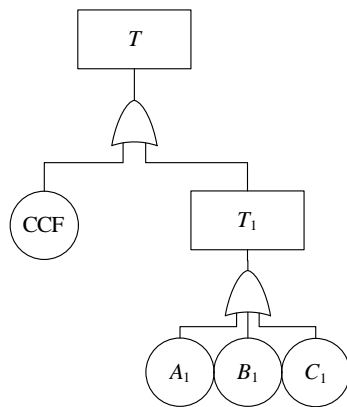


Fig. 1. Implicit model of CCF

Where the failure of each system unit is composed of its internal failure of a component (denoted as A_1 , B_1 and C_1) and CCF.

3.2. Explicit modeling of CCF

Suppose that the failure of each system unit is composed of its internal failure of a component (denoted as A_1 , B_1 and C_1) and the common cause failure (A_2 , B_2 and C_2). T is the event of “system failure”. The explicit model of a parallel system with 3 units (A , B and C) can be depicted as shown in Fig. 2.

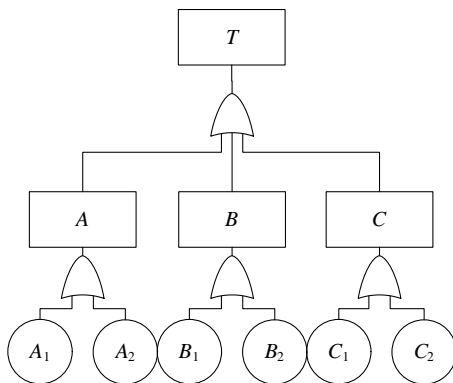


Fig. 2. Explicit modeling of CCF

From Fig.2, the system failure is directly caused by individual component failures, and the difference of explicit method and implicit

method is the former considering the CCF in component failure event and the latter in whole system.

4. Fault tree analysis of train rear-end collision accident considering CCF

4.1. Fault tree modeling of train rear-end collision accident

On condition that the single-track has only one railway, and assuming that the collision avoidance systems, such as a signal lamp control system, distance control system, train state communication and control system as well as the dispatching center danger warning systems, are put into use [11]. Fault tree analysis is one of the most important logic and probabilistic techniques used in system reliability assessment [24]. The faults can be events that are associated with component hardware failures, human errors, software errors, or any other pertinent events. A fault tree depicts the logical interrelationships of basic events that lead to the top event of the fault tree. The top event of the fault tree is the event for which the failure causes will be resolved and the failure probability determined. It defines the failure mode of the system that will be analyzed. A fault tree analysis (FTA) should be carried out through the following steps [20]: 1) identify the objective for the FTA; 2) define the top event, scope, resolution, ground rules of the fault tree; 3) construct and evaluate the fault tree; 4) interpret and present the results. The fault trees of train rear-end collision accident are shown in Fig. 3 – Fig. 5 and the codes and names of basic events are showed in Table 1.

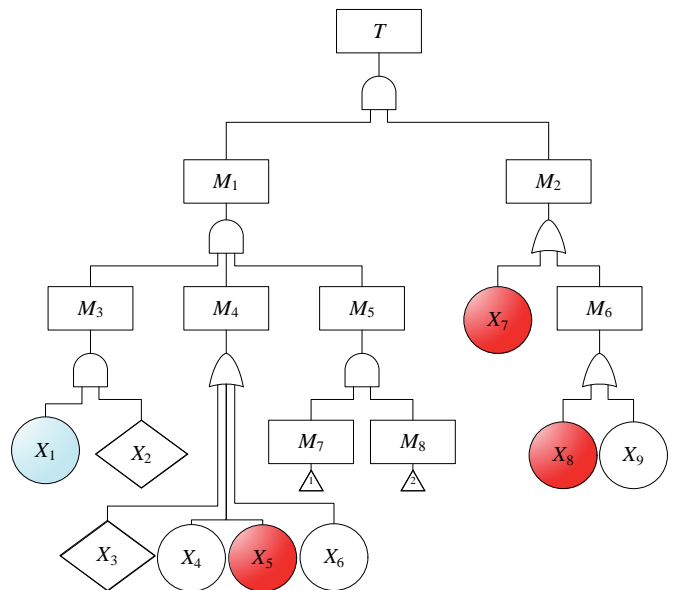


Fig. 3. The fault tree of train rear-end collision accident

4.2. Qualitative analysis

According to Fig. 3 – Fig. 5, the structure function of fault tree for the train rear-end collision accident can be obtained as follows:

$$\Phi(X) = X_1 \cdot X_2 \cdot (X_3 + X_4 + X_5 + X_6) \cdot (X_{10} + X_{11} + X_{12} + X_{13} + X_{14}) \cdot (X_{15} + X_{16} + X_{17} + X_{18} + X_{19}) \cdot (X_{20} + X_{21} + X_{22} + X_{23} + X_{24}) \cdot ((X_{28} + X_{29} + X_{30} + X_{31}) \cdot (X_{33} + X_{34} + X_{35}) + X_{32} + X_{25} + X_{26} + X_{27}) \cdot (X_7 + X_8 + X_9) \quad (12)$$

From Eq. (12), the train rear-end collision event has totally $1 \times 1 \times 4 \times 5 \times 5 \times 5 \times (4 \times 3 + 4) \times 3 = 24000$ failure modes, and there are 192

Table 1. The codes and names of basic events

Code	Event name	Code	Event name	Code	Event name
T	Train rear-end accident	X_1	Two trains are assigned on the same railway interval	X_{19}	Distance decision and control of back-train failure
M_1	Condition of rear-end existing	X_2	Only one rail on the same direction in this interval	X_{20}	Missing or error of Front-train state signal
M_2	Driver cannot avoid by braking	X_3	Dispatch order error	X_{21}	Human decision and control failure
M_3	Two trains on the same rail	X_4	Front-train stopped or crawling	X_{22}	Back-train did not receive the exact signal of front-train
M_4	Back-train faster than Front-Train	X_5	Driver break the order	X_{23}	Train state communicate and control error by environment
M_5	Collision avoidance system failure	X_6	Brake system abnormal	X_{24}	Back-train state decision and control failure
M_6	Driver brake fails	X_7	Driver unnoticed the danger	X_{25}	Too late to dispose the danger
M_7	Collision avoidance system failure	X_8	Too late to brake on visual distance	X_{26}	Improper disposition of danger
M_8	Manual intervention fails	X_9	Brake system failure	X_{27}	Dispatcher off-site
M_9	Signal lamp failure	X_{10}	Data acquisition of location error	X_{28}	Danger warning system has been closed
M_{10}	Distance control system failure	X_{11}	Error signal caused by human	X_{29}	Danger warning system did not get the accuracy data
M_{11}	Communicate and control system failure	X_{12}	Data acquisition logical error	X_{30}	The defect of danger distinguish software
M_{12}	Dispatcher is not aware of the danger	X_{13}	Error signal by environment	X_{31}	The irrational of the danger warning pattern
M_{13}	Dispatcher on-site but unwitnessed the danger	X_{14}	Signal output error	X_{32}	Abstracted of dispatcher
M_{14}	Danger warning measures failure	X_{15}	Mistake get target location	X_{33}	Information overload, task complicated
M_{15}	Human monitoring undetected the danger	X_{16}	Control order did not carry out exactly	X_{34}	Lack of experience
M_{16}	Danger warning system undetected the danger	X_{17}	Distance computing error	X_{35}	Unreasonable human-computer interface
M_{17}	Unnoticed the warn of the danger warning system	X_{18}	Distance control error by environment		

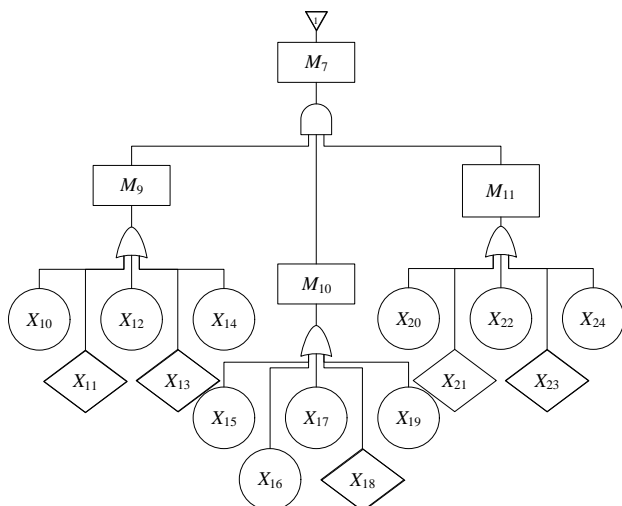


Fig. 4. Fault tree of the event “collision avoidance system failure”

failure modes even without subdividing the collision avoidance system. The level of detail FTA has direct influence on the quantity of these failure modes.

Due to the long event chain of the train rear-end collision accident, Eq. (12) shows that each failure mode occurs only when there

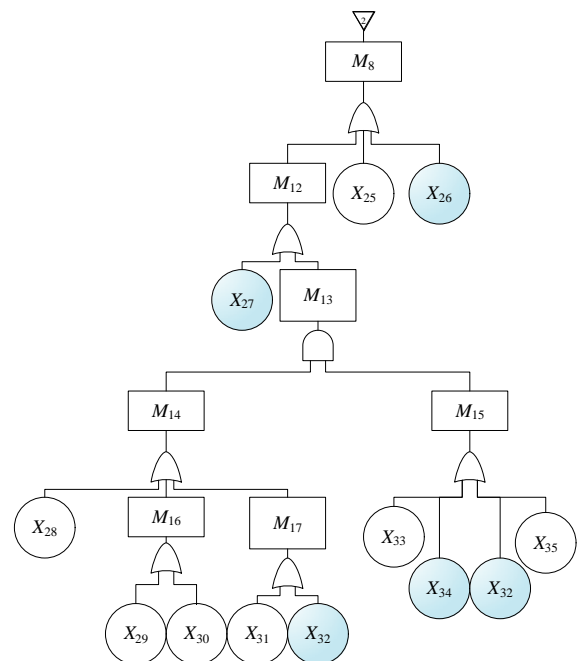


Fig. 5. The fault tree of “manual intervention fail”

are at least eight events occur at the same time. The probability of occurrence of a train rear-end collision event will be extremely low if all the basic events are independent, but as a result of the common cause failure, the probability of accident occurrence will be higher. In the following figures, the common cause failures caused by different reasons have been labeled by different colors.

4.3. Quantitative analysis

For the train rear-end collision accident, we assume that the failure probabilities of bottom events are known as listed in Table 2.

Table 2. The probability of bottom events

Code	Probabil-ity	Code	Probabil-ity	Code	Probabil-ity
X_{27}	0.020	X_{30}	0.002	X_{33}	0.001
X_{28}	0.001	X_{31}	0.005	X_{34}	0.020
X_{29}	0.001	X_{32}	0.020	X_{35}	0.001

The structure function of intermediate event “dispatcher is not aware of the danger” can be expressed as follows:

$$\Phi(X) = ((X_{28} + X_{29} + X_{30} + X_{31}) \cdot (X_{33} + X_{34} + X_{35}) + X_{32} + X_{27}) \quad (13)$$

Presume that the bottom events are independent, the probability of the event “dispatcher is not aware of the danger” can be calculated:

$$P(M_{12}) = 0.0398 \quad (14)$$

The occurrence of events “lack of experience” and “abstracted of dispatcher” are inter-actionable, thus, the common cause failures need to be considered. From Fig. 5 and engineering experience, the event “dispatcher off-site” is mutual exclusion with the event “dispatcher on-site but unwitnessed the danger”, and the events “danger warning system being closed”, “danger warning system undetected the danger” and “unnoticed the warn of the danger warning system” are mutual exclusion to each other. Therefore, the structure function of sub-tree M_{12} can be formulated as follows:

$$\begin{aligned} P(M_{12}) &= P((X_{28} + X_{29} + X_{30} + X_{31}) \cdot (X_{33} + X_{34} + X_{35}) + X_{32} + X_{27}) \\ &= P((X_{28} + X_{29} + X_{30} + X_{31}) \cdot (X_{33} + X_{34} + X_{35}) + X_{32}) + P(X_{27}) \end{aligned} \quad (15)$$

Let $X_a = X_{28} + X_{29} + X_{30} + X_{31}$ and $X_b = X_{33} + X_{35}$, this yields

$$\begin{aligned} P(X_a) &= P(X_{28} + X_{29} + X_{30} + X_{31}) \\ &= P(X_{28}) + P(X_{29} + X_{30}) + P(X_{31}) \\ &= 0.001 + (1 - (1 - 0.001)(1 - 0.002)) + 0.005 \approx 0.009 \end{aligned} \quad (16)$$

References

1. American Public Transportation Association, Member Services Department. Manual of Standards and Recommended Practices for Passenger Rail Equipment, 2004.
2. Association of American Railroads, Technical Services Division. Mechanical Section-Manual of Standards and Recommended Practices. Locomotive Crash worthiness Requirements, Standard S-580, 2005.

$$P(X_b) = P(X_{33} + X_{35}) = 1 - (1 - 0.001)(1 - 0.001) \approx 0.002 \quad (17)$$

Based on the analysis, Eq. (15) can be further simplified as:

$$\begin{aligned} P(M_{12}) &= P(X_a X_b + X_a X_{34} + X_{32}) + P(X_{27}) \\ &= P(X_a)P(X_b) + P(X_a)P(X_{34}) + P(X_{32}) - \\ &\quad P(X_a)P(X_b)P(X_{34}) - P(X_a)P(X_b)P(X_{32}) - \\ &\quad P(X_a)P(X_{34}X_{32}) + P(X_a)P(X_b)P(X_{34}X_{32}) + P(X_{27}) \end{aligned} \quad (18)$$

According to the square root model introduced in section 2.2, we can get the following expression.

$$\begin{aligned} P(X_{34}X_{32}) &= \sqrt{ab} = \sqrt{P(X_{34})P(X_{32})\min\{P(X_{34}), P(X_{32})\}} \\ &= \sqrt{0.020 \times 0.020 \times \min\{0.020, 0.020\}} = 0.0028 \end{aligned} \quad (19)$$

$$P(M_{12}) = 0.0402 \quad (20)$$

Compare with the probability without considering the CCF, the relative error for the probability of occurrence of top event considering CCF is:

$$\eta = \frac{0.0402 - 0.0398}{0.0402} \times 100\% = 1.01\% \quad (21)$$

From Eq. (21), it should be noted that the result without considering common cause failure lead to a huge deviation. It can be observed from the results that CCF has a remarkable effect on the reliability analysis of train rear-end collision accidents.

5. Conclusion

In this paper, common-cause failure modes have been incorporated into the fault tree analysis of train rear-end collision accident using the explicit fault tree modeling method and the square root mode. The probability of occurrence of the event “dispatcher is unaware of the danger” is $P(M_{12})=0.0402$. Under the assumptions that bottom events are independent, it is worth noting that the assessment without considering common cause failure shows a huge deviation. It demonstrated that CCF has a significant effect on the probability of occurrence of train rear-end collision accident, which offers a basis for safety and reliability assessment of railway vehicle.

Acknowledgments: This research was partially supported by the Open Project Program of Traction Power State Key Laboratory of Southwest Jiaotong University under the contract number TPL1101, the National Natural Science Foundation of China under the contract number 51075061, and the National Programs for High Technology Research and Development of China under the contract number 2007AA04Z403.

3. Börösök J, Schaefer S. Estimation and evaluation of common cause failures. Proceedings of the 2nd International Conference on Systems 2007 (ICON'07), Martinique, French, 2007: 41–46.
4. Cao SG, Chang YG, Wu G. Reliability analysis of launch control system with common cause failure. Journal of Sichuan Ordnance 2009; 30(11): 78–80.
5. Das A, Abdel-Aty MA. A combined frequency severity approach for the analysis of rear-end crashes on urban arterials. Safety Science 2011; 49(8-9): 1156–1163.
6. Fleming KN. A reliability model for common cause failures in redundant safety systems. Proceedings of the 6th Annual Pittsburgh Conference on Modeling and Simulation, University of Pittsburgh, 1975: 579–581.
7. Fleming KN, Mosleh A, Kelley AP. On the analysis of dependent failures in risk assessment and reliability evaluation. Nuclear Safety 1983; 24(5): 637–657.
8. Jin X, Hong YJ, Du H. Reliability analysis method of common cause failure system. Beijing: National Defense Industry Press, 2008.
9. Kančev D, Čepin M. Limitations of explicit modeling of common cause failures within fault trees. Proceedings of Annual Reliability and Maintainability Symposium (RAMS), Reno, NV, USA, 2012: 1–6.
10. Levitin G. Incorporating common-cause failures into nonrepairable multistate series-parallel system analysis. IEEE Transactions on Reliability 2001; 50(4): 380–388.
11. Li ZZ. Fault tree analysis of train crash accident and discussion on safety of complex systems. Industrial Engineering and Management 2011; 16(4): 1–8.
12. Milho JF, Ambrósio JAC, Pereira MFOS. Validated multibody model for train crash analysis. International Journal of Crashworthiness 2003; 8(4): 339–352.
13. Mosleh A, Siu NO. A multi-parameter event-based common-cause failure model. Proceedings of the 9th International Conference on Probabilistic Safety Assessment Management (PSA'87) 1987; Zurich, Switzerland, 1987; 1: 67–73.
14. Tyrell D. U.S. Rail equipment crashworthiness standards. “What can We Realistically Expect from Crashworthiness?” Rail Equipment Crashworthiness Symposium, Institute of Mechanical Engineers, London, England, 2001.
15. Tyrell D, Jacobsen K, Martinez E, Perlman AB. A train-to-train impact test of crash energy management passenger rail equipment: structural results. Proceedings of ASME International Mechanical Engineering Congress and Exposition (IMECE 2006), Chicago, Illinois, USA, 2006: 1–10.
16. Tyrell D, Martinez E, Jacobsen K, Parent D, Severson K, Priante M, Perlman AB. Overview of a crash energy management specification for passenger rail equipment. Proceedings of the 2006 IEEE/ASME Joint Rail Conference (JRC2006), Atlanta, GA, USA, 2006; 131–140.
17. Tyrell D, Severson KJ, Marquis BJ. Crashworthiness of Passenger Trains. U.S. Department of Transportation, DOT/FRA/ORD-97/10, 1998.
18. U.S. Department of Transportation, Federal Railroad Administration, 49 CFR Part 216 et al. Passenger Equipment Safety Standards, Final Rule. Federal Register, 1999.
19. Vaurio JK. Availability of redundant safety systems with common mode and undetected failures. Nuclear Engineering and Design 1980; 58(3): 415–424.
20. Vesley W, Dugan J, Fragola J, Minarick J, Railsback J. Fault tree handbook with aerospace applications. NASA, Washington, DC 20546, 2002.
21. Volkanovski A, Čepin M, Mavko B. Application of the fault tree analysis for assessment of power system reliability. Reliability Engineering & System Safety 2009; 94(6): 1116–1127.
22. Wang XM. A new system reliability model considering common cause failure. Shenyang: Northeastern University, 2005.
23. Xing L. Incorporating common-cause failures into the modular hierarchical systems analysis. IEEE Transactions on Reliability 2009; 58(1): 10–19.
24. Y.F. Li, H.Z. Huang, Y. Liu, N.C. Xiao, H.Q. Li. A new fault tree analysis method: fuzzy dynamic fault tree analysis. Eksploatacja i Niezawodność - Maintenance and Reliability 2012; 14(3): 208–214.
25. Zhou JY, Xie LY. Common cause failure mechanism and risk probability quantitative estimation of multi-state systems. Chinese Journal of Mechanical Engineering 2008; 44(10): 77–81.
26. Zhou ZB. Probabilistic safety assessment research and application based on Bayesian networks. Changsha: National University of Defense Technology, 2006.

Yan-Feng LI, Ph.D. candidate
Jinhua MI, Ph.D. candidate
Prof. Hong-Zhong HUANG, Ph.D.
Shun-Peng ZHU, Ph.D.
Ningcong XIAO, Ph.D.

School of Mechanical, Electronic, and Industrial Engineering
 University of Electronic Science and Technology of China
 No. 2006, Xiyuan Avenue, West Hi-Tech Zone
 Chengdu, Sichuan, P. R. China, 611731
 E-mail: hzhuang@uestc.edu.cn

Adam ROSINSKI
Tadeusz DABROWSKI

MODELLING RELIABILITY OF UNINTERRUPTIBLE POWER SUPPLY UNITS

MODELOWANIE NIEZAWODNOŚCI ZASILACZY BUFOROWYCH*

This paper discusses issues related to reliability of uninterruptible power supplies equipped with automatic protection mechanisms (short circuit protection – SCP, overload protection – OLP, overvoltage protection – OVP). Relationships for determining probability of system states: full operational capability, partial capability and failure were derived. The impact of time taken to restore the state of full operational capability on probability of different system states was also analysed.

Keywords: reliability, power supply, maintenance.

W artykule przedstawiono zagadnienia związane z niezawodnością zasilaczy buforowych wyposażonych w automatyczne zabezpieczenia (przeciwzwarciowe - SCP, przeciążeniowe - OLP, nad napięciowe - OVP). Wyznaczono zależności pozwalające określić prawdopodobieństwa przebywania systemu w stanach: pełnej zdatności, niepełnej zdatności i niezdatności. Dokonano również analizy wpływu czasu przywrócenia stanu pełnej zdatności na wartości prawdopodobieństw przebywania zasilacza w wyróżnionych stanach technicznych.

Słowa kluczowe: niezawodność, zasilacz, proces eksploatacji.

1. Introduction

Uninterruptible power supplies are exposed to various external factors, which over time can cause the system to switch from the state of full operational capability into the state of reached operational capability (failure). In order to increase probability of the state of full operational capability, the following protection devices are often used: short circuit protection, overload protection, overvoltage protection. In this paper reliability analysis of uninterruptible power supplies equipped with those devices was presented.

The reliability theory in respect of general considerations has had sound footing for many years [5, 9, 19]. Approaches towards reliability analysis presented in those publications allow for factoring in system structure: serial, parallel and serial-parallel. It is then possible to create transition graphs for above-mentioned states of capability. By employing an adequate mathematical apparatus (e.g. Chapman–Kolmogorov equation) a relationship is obtained for determining probability of system in given state [11, 12]. This type of methodology may be used for reliability analysis of uninterruptible power supply.

For references on operating principle and engineering of power supplies, the following publications are noteworthy [6, 18, 23]. Some of them discuss applications in specific areas of rail transport in particular [10].

Reliability analysis of power supply systems in presented in item [1]. Emergency power supplies (both static and dynamic type) received substantial attention. Using this solution increases the availability rate of the entire system.

Issues concerning reliability of power supply systems have been discussed for many years by different authors. The papers of most significance are items [3, 16, 17].

The paper [3] presents issues related to reliability of power supply systems. The relationship between reliability and investment outlays for its improvement was proven. Models of system reliability factoring in failure rate and repair rate were also presented. Probability distributions of reliability parameters were defined. Reliability graph was displayed which depicted the state of full and reached operational capability and a graph depicting down times of device.

Papers [16, 17] discuss issues related to reliability and quality of electric power systems. Examples of different power networks were given, reliability calculations were made. Values of certain reliability parameters were also given, which could be applied to other electric power supply system of that type.

Optimization problem of power supply system were described in paper [15]. Theoretics of optimisation were discussed. Consequently deriving optimisation procedures for analysed systems factoring in economic factors was possible. Some of the publications describe practical applications of such solutions [4].

Redundant sources of power were elaborated on in publications [8, 24, 25]. Their focus was very much on emergency power supplies such as: uninterruptible power supplies UPS, generating sets and environmentally friendly solutions i.e. solar panels and wind powered generators. Conducted analysis of above solutions proves unequivocally that they increase reliability parameters. Of course, required is control equipment switching between on-line electricity supplies and electricity grid management systems [20].

Item [8] describes reliability of power supply systems on the scale of United States of America. Profile of the organisations handling those issues was given: North American Electric Reliability Corporation (NERC). It was concluded, that using wind farms, solar panels and power generators increases reliability and power generating efficiency of the entire power system should terrorist attacks or natural disasters strike (e.g. hurricanes, tornadoes).

Despite studies completed on reliability of power supply systems, it seems necessary to carry out a functional analysis of power supplies and protection devices. That approach was presented under subsequent items of this paper.

2. Power supplies

Direct current and alternating current power supplies are widely used in many devices, including computer equipment. Power supply directly from the power network is the most convenient, both on-line and via a transformer. Substantial amount of devices, however, re-

(*) Tekst artykułu w polskiej wersji językowej dostępny w elektronicznym wydaniu kwartalnika na stronie www.ein.org.pl

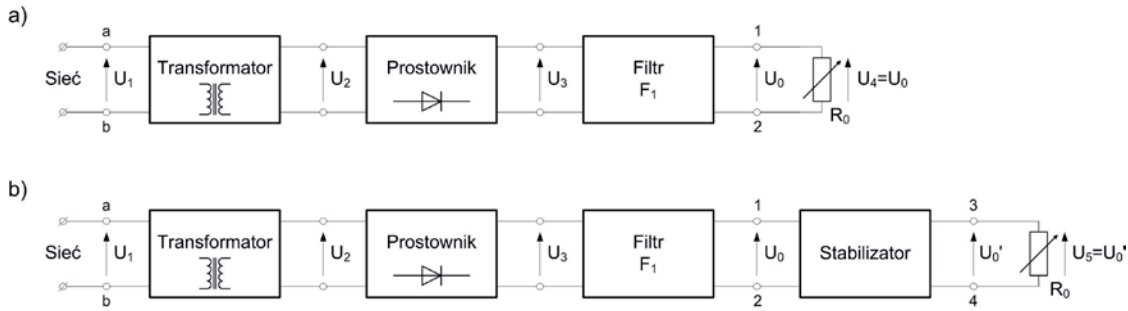


Fig. 1. Functional diagram of direct current power supply

quires direct current supply, hence direct current power supplies are used. They transform alternating current from the grid into stable direct current.

Figure 1. displays basic components of direct current power supplies. In general, they are equipped with the F_1 filter (fig. 1a) or - in more powerful versions - with additional voltage regulator (fig. 1b). The load marked as R_0 may have a variable value.

In order to protect the power supply from damage, the following protection devices are used:

- Short Circuit Protection – SCP,
- Over Load Protection – OLP,
- Over Voltage Protection – OVP.

Short circuit and overload protection devices protect the power supply's inputs and outputs from short-circuit over at the loaded side.

Overvoltage protection device protects units power by the power supply from overvoltage to maximum output voltage.

If power supply outputs were independent, neither short-circuit, overload nor overvoltage on any of the outputs should negatively affect functionality of other outputs.

Once the short-circuit, overload or the cause for overvoltage is removed, protection reset (either manually or automatically), the state of full operational capability should be restored on that output.

In general, power supplies interact with the broadly defined environment [14]. Therefore it is beyond doubt adequate reliability parameters have to be assured. Thus so important is the impact analysis of protection devices used in power supplies on selected reliability parameters [1, 7, 21, 22].

3. Reliability analysis of power supplies

The relationships occurring in power supply with protection devices (e.g. against short-circuit, overload and overvoltage) fitted to each of the two independent outputs have to be illustrated from the reliability perspective for purposes of the functional analysis. See figure 2 [13]. Those relationships do not cover all possible changes in system state of the power supply system (e.g. the transition from the state of full operational capability S_{PZ} to the state of reached operational capability S_N and reverse i.e. from S_N to S_{PZ} was ignored). Furthermore, failures on each output were assumed independent.

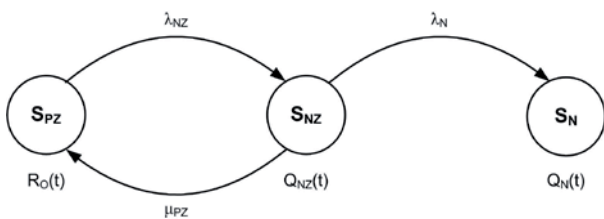


Fig. 2. Relationships occurring in uninterruptible power supply with protective devices

Denotations in figures:

$R_0(t)$ – the likelihood function of device in state of full operational capability,

$Q_{NZ}(t)$ – the likelihood function of device in state of partial operational capability,

$Q_N(t)$ – the likelihood function of device in state of reached operational capability,

λ_{NZ} – transition rate from the state of full operational capability into the state of partial operational capability,

μ_{PZ} – transition rate from the state of partial operational capability into the state of full operational capability,

λ_N – transition rate from the state of partial operational capability into the state of reached operational capability.

Failure of one output causes transition from the state of full operational capability S_{PZ} to the state of partial operational capability S_{NZ} . Removal of interference restores the state of full operational capability. Once the S_{NZ} state occurs (output failure), failure of the other, previously operational, output causes the power supply to switch into the state of reached operational capability S_N .

The relationship for determining probability of uninterruptible power supply unit in the state of full operational capability R_0 (1), partial capability Q_{NZ} (2) and reached capability Q_N (3) is obtained from mathematical analysis (Chapman–Kolmogorov equation).

$$R_0(t) = \left[\cos \left(\sqrt{2 \cdot \lambda_{NZ} \cdot (\mu_{PZ} + \lambda_N) - 4 \cdot \mu_{PZ} \cdot \lambda_{NZ} - \lambda_{NZ}^2 - (\mu_{PZ} + \lambda_N)^2} \cdot \frac{t}{2} \right) + \frac{\mu_{PZ} + \lambda_N - \lambda_{NZ}}{\sqrt{2 \cdot \lambda_{NZ} \cdot (\mu_{PZ} + \lambda_N) - 4 \cdot \mu_{PZ} \cdot \lambda_{NZ} - \lambda_{NZ}^2 - (\mu_{PZ} + \lambda_N)^2}} \cdot \sin \left(\sqrt{2 \cdot \lambda_{NZ} \cdot (\mu_{PZ} + \lambda_N) - 4 \cdot \mu_{PZ} \cdot \lambda_{NZ} - \lambda_{NZ}^2 - (\mu_{PZ} + \lambda_N)^2} \cdot \frac{t}{2} \right) \right] \cdot \exp \left[- \left(\frac{\lambda_{NZ} + \mu_{PZ} + \lambda_N}{2} \right) \cdot t \right] \quad (1)$$

$$Q_{NZ}(t) = \frac{2 \cdot \lambda_{NZ}}{\sqrt{2 \cdot \lambda_{NZ} \cdot \lambda_N - 2 \cdot \mu_{PZ} \cdot \lambda_{NZ} - \lambda_{NZ}^2 - (\mu_{PZ} + \lambda_N)^2}} \cdot \sin \left(\sqrt{2 \cdot \lambda_{NZ} \cdot \lambda_N - 2 \cdot \mu_{PZ} \cdot \lambda_{NZ} - \lambda_{NZ}^2 - (\mu_{PZ} + \lambda_N)^2} \cdot \frac{t}{2} \right) \cdot \exp \left[- \left(\frac{\lambda_{NZ} + \mu_{PZ} + \lambda_N}{2} \right) \cdot t \right] \quad (2)$$

$$Q_N(t) = 1 - \left[\cos \left(\sqrt{2 \cdot \lambda_{NZ} \cdot (\mu_{PZ} + \lambda_N) - 4 \cdot \mu_{PZ} \cdot \lambda_{NZ} - \lambda_{NZ}^2 - (\mu_{PZ} + \lambda_N)^2} \cdot \frac{t}{2} \right) + \frac{\mu_{PZ} + \lambda_N + \lambda_{NZ}}{\sqrt{2 \cdot \lambda_{NZ} \cdot (\mu_{PZ} + \lambda_N) - 4 \cdot \mu_{PZ} \cdot \lambda_{NZ} - \lambda_{NZ}^2 - (\mu_{PZ} + \lambda_N)^2}} \cdot \sin \left(\sqrt{2 \cdot \lambda_{NZ} \cdot (\mu_{PZ} + \lambda_N) - 4 \cdot \mu_{PZ} \cdot \lambda_{NZ} - \lambda_{NZ}^2 - (\mu_{PZ} + \lambda_N)^2} \cdot \frac{t}{2} \right) \right] \cdot \exp \left[- \left(\frac{\lambda_{NZ} + \mu_{PZ} + \lambda_N}{2} \right) \cdot t \right] \quad (3)$$

4. Modelling reliability of power supply units

Computer simulation and computer-aided analysis facilitate to relatively quickly determine the influence of change in reliability parameters of individual components on reliability of the entire system. Of course, the reliability structure of both the entire system and its components has to be known beforehand.

Computer aided-analysis enables to conduct impact analysis of the time taken to restore the state of full operational capability t_{PZ} on probability of the states of full operational capability R_O , partial capability Q_{NZ} and reached capability Q_N . That procedure is illustrated with below example.

Example

The following quantities were defined for the system:

- test duration - 1 year (values of this and the following parameters is given in [h]):

$$t = 8760 \text{ [h]}$$

- reliability of first power supply output track (including the receiver):

$$R_{NZ}(t) = 0,99$$

- reliability of second power supply output track (including the receiver):

$$R_N(t) = 0,999$$

Knowing the value of reliability $R_{NZ}(t)$, transition rate from the state of full operational capability into the state of partial operational capability may be estimated. Provided the up time is described by exponential distribution, the following relationship can be used:

$$R_{NZ}(t) = e^{-\lambda_{NZ}t} \text{ for } t \geq 0$$

thus

$$\lambda_{NZ} = -\frac{\ln R_{NZ}(t)}{t}$$

For $t = 8760 \text{ [h]}$ and $R_{NZ}(t) = 0,99$ we obtain:

$$\lambda_{NZ} = -\frac{\ln R_{NZ}(t)}{t} = -\frac{\ln 0,99}{8760} = 1,147298 \cdot 10^{-6} \left[\frac{1}{h} \right]$$

Knowing the value of reliability $R_N(t)$, transition rate from the state of partial operational capability into the state of full operational capability may be estimated. The following relationships are true for exponential distribution:

$$R_N(t) = e^{-\lambda_N t} \text{ for } t \geq 0$$

thus

$$\lambda_N = -\frac{\ln R_N(t)}{t}$$

For $t = 8760 \text{ [h]}$ and $R_N(t) = 0,999$ we obtain:

$$\lambda_N = -\frac{\ln R_N(t)}{t} = -\frac{\ln 0,999}{8760} = 1,142124 \cdot 10^{-7} \left[\frac{1}{h} \right]$$

transition rate from the state of partial operational capability to the state of full operational capability μ_{PZ} is – for exponential distribution – time inverse t_{PZ} :

$$\mu_{PZ} = \frac{1}{t_{PZ}}$$

The probability of analysed power supply in the above mentioned states of operational capability, assuming the time of restoring the state of full operational capability t_{PZ} falls within the interval

$t_{PZ} \in \langle 12; 168 \rangle \text{ [h]}$ (i.e. after recalculation into days

$t_{PZ} \in \langle 0,5 ; 7 \rangle \text{ [day]}$), is given by charts displayed in figures 3, 4

and 5. Values of time t_{PZ} were assumed based observation of actual systems.

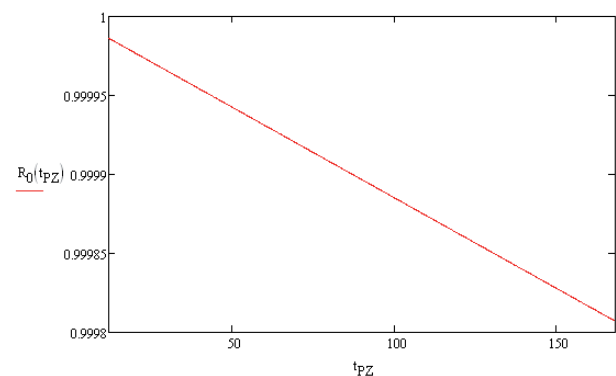


Fig. 3. The relationship between probability of power supply in the state of full operational capability R_0 as a function of time taken to restore full operational reliability t_{PZ}

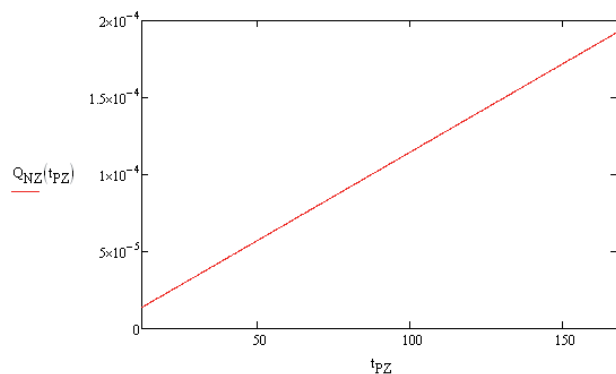


Fig. 4. The relationship between probability of power supply in the state of partial operational capability Q_{NZ} as a function of time taken to restore full operational reliability t_{PZ}

Figure 6 presents the relationship between probabilities of power supply being in the state of full operational capability R_O as a function of time taken to restore the state of full operational capability t_{PZ} on the assumption that t_{PZ} falls within the interval $t_{PZ} \in \langle 12; 8500 \rangle \text{ [h]}$

(i.e. after recalculation into days $t_{PZ} \in \langle 0,5 ; 354,17 \rangle \text{ [day]}$).

In charts presented in fig. 3, 4, 5, 6 and 7, denotations to the left of horizontal red lines mark the colour of analysed quantity line. Those are default denotations and colours used by computer-aided calculations software.

Analysis of relationships given in figures 3, 4, 5 and 6 concludes:

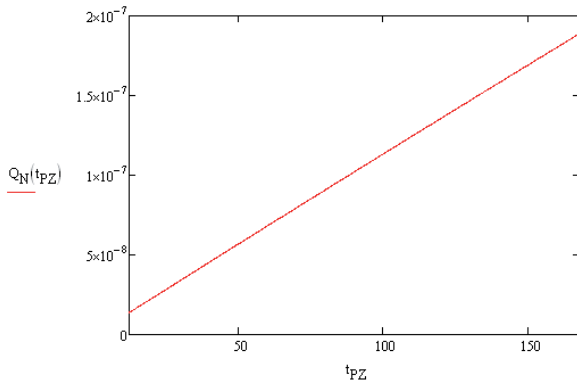


Fig. 5. The relationship between probability of power supply in the state of reached operational capability Q_N as a function of time taken to restore full operational reliability t_{PZ}

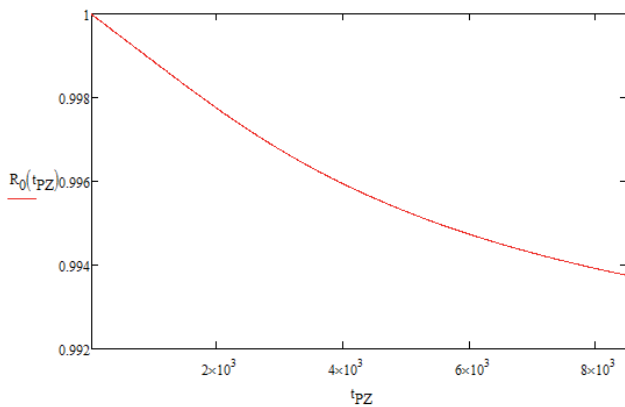


Fig. 6. The relationship between probability of power supply in the state of full operational capability R_0 as a function of time taken to restore full operational reliability $t_{PZ} \in \langle 0,5 ; 354,17 \rangle$ [day]

- the probability of power supply in the state of full operational capability R_0 as a function of time taken to restore full operational reliability t_{PZ} has maximum value for minimum value of t_{PZ} time,
- the probability of power supply in the state of partial operational capability Q_{NZ} as a function of time taken to restore full operational reliability t_{PZ} has maximum value for maximum value of t_{PZ} time,
- the probability of power supply in the state of reached operational capability Q_N as a function of time taken to restore full operational reliability t_{PZ} has maximum value for maximum value of t_{PZ} time,
- all three functions $R_0 = f(t_{PZ})$, $Q_{NZ} = f(t_{PZ})$, $Q_N = f(t_{PZ})$ are non-linear (according to relationships 1, 2 and 3; they resemble a straight line as per assumed t_{PZ}),
- the function $R_0 = f(t_{PZ})$ is a decreasing function,
- functions $Q_{NZ} = f(t_{PZ})$ and $Q_N = f(t_{PZ})$ are increasing functions.

Let us pose a question: how does the probability of either full or partial operational capability change relative to time taken to restore the state of full operational capability i.e. what is the shape of the

function $\overline{Q_N} = f(t_{PZ})$. Respective calculations produced results presented in table 1 and in fig. 7.

Table 1. Value of the function $\overline{Q_N} = f(t_{PZ})$

t_{PZ} [h]	$\overline{Q_N} = f(t_{PZ})$
12	0.99999986244571
24	0.999999972527389
36	0.999999958848280
48	0.999999945207325
60	0.999999931604508
72	0.999999918039844
84	0.999999904513311
96	0.999999891024905
108	0.999999877574628
120	0.999999864162479
132	0.999999850788460
144	0.999999837452543
156	0.999999824154743
168	0.999999810895060

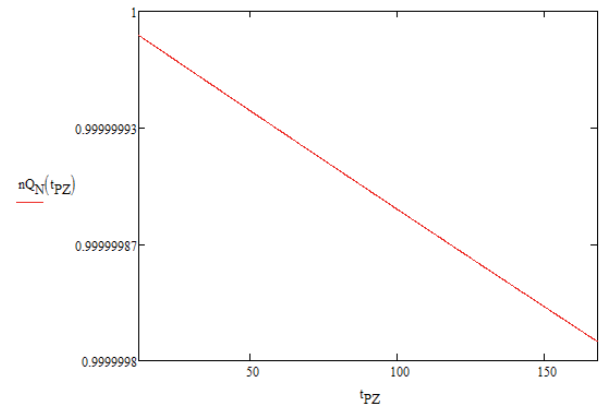


Fig. 7. The relationship between probability of power supply in the state of full or partial operational capability $\overline{Q_N}$ as a function of time taken to restore full operational reliability t_{PZ} (denotation in fig. nQ_N refers to the value of $\overline{Q_N}$).

What is clear, is that function $\overline{Q_N} = f(t_{PZ})$ has shape similar to function $R_0 = f(t_{PZ})$. However, for the same values of time taken to restore the state of full operational capability t_{PZ} , values of the function $\overline{Q_N}$ are greater than values of function R_0 .

Graphs presented in fig. 3, 4, 5 and 7 seem to be straight lines, therefore suggest there is a linear relationship between analysed values of probability as a function of time taken to restore the state of full operational capability t_{PZ} . The reason being that the value t_{PZ} was assumed $t_{PZ} \in \langle 12; 168 \rangle$ [h]. By analysing the fig. 6 chart and assum-

ing for purposes of the analysis solely the value $t_{PZ} \in \langle 12; 168 \rangle [h]$, we obtain „roughly” straight lines. Actually they are curves, defined by non-linear relationships (formulae (1), (2) and (3)).

5. Conclusions

Reliability analysis of power supplies was presented in this paper. It focused especially on the influence of time taken to restore the state of full operational capability on probability of the states of full operational capability R_0 , partial capability Q_{NZ} and reached capability Q_N .

Analysis of results obtained proves that all four functions $R_0 = f(t_{PZ})$,

$Q_{NZ} = f(t_{PZ})$, $Q_N = f(t_{PZ})$, $\overline{Q_N} = f(t_{PZ})$ are non-linear, func-

tions $R_0 = f(t_{PZ})$ and $\overline{Q_N} = f(t_{PZ})$ are decreasing functions,

whereas functions $Q_{NZ} = f(t_{PZ})$ and $Q_N = f(t_{PZ})$ are increasing

functions. Hence reliability of power supplies improves when the time taken to restore the state of full operational capability – i.e. repair – is shorter. Of course, costs involved are higher. Further studies should aim to determine the relationship between financial outlays – incurred to improve the repair time – and the probability of predefined technical conditions.

References

1. Baggin A. (editor) Handbook of power quality. John Wiley & Sons, 2008.
2. Bedkowski L, Dabrowski T. Basics of maintenance, vol. II Basic of operational reliability. Warsaw: Military Academy of Technology, 2006.
3. Billinton R, Allan RN. Reliability evaluation of power systems. New York: Plenum Press, 1996.
4. Borlase S. (editor). Smart Grids: Infrastructure, Technology, and Solutions. Taylor & Francis Group, 2012.
5. Epstein B, Weissman I. Mathematical models for systems reliability. CRC Press / Taylor & Francis Group, 2008.
6. Glover JD, Sarma MS, Overbye T. Power system analysis and design. Thomson, 2008.
7. Jaźwiński J, Ważyńska-Fiok K. Safety of systems. Warsaw: PWN, 1993.
8. Keyhani A, Marwali M. Smart power grids. Springer-Verlag, 2011.
9. Kołowrocki K, Soszyńska-Budny J. Reliability and safety of complex technical systems and processes. London: Springer, 2011.
10. Pilo E. (editor) Power supply, energy management and catenary problems. WIT Press 2010.
11. Rosiński A. Design of the electronic protection systems with utilization of the method of analysis of reliability structures. Proceedings of the Nineteenth International Conference On Systems Engineering ICSEng 2008, Las Vegas, USA 2008: 421–426.
12. Rosiński A. Reliability analysis of the electronic protection systems with mixed m-branches reliability structure. Proceedings of the International Conference European Safety and Reliability ESREL 2011, Troyes, France 2011: 2064–2071.
13. Rosinski A. Selected problems of uninterruptible power supply diagnostics. IX School – Conference "Computer Aided Metrology 2011", Waplewo 2011.
14. Siergiejczyk M. Operational effectiveness of transport telematic systems. Scientific papers of Warsaw University of Technology – Transport 2009; 67.
15. Soliman SA, Mantawy AH. Modern optimization techniques with applications in electric power systems. Springer Science+Business Media, 2012.
16. Sozanski J. Reliability of electric power supply. Warsaw: WNT, 1982.
17. Sozanski J. Reliability and operating quality of electric power system. Warsaw: WNT, 1990.
18. Sumper A, Baggin A. Electrical Energy Efficiency: Technologies and Applications. John Wiley & Sons Ltd, 2012.
19. Verma AK, Ajit S, Karanki DR. Reliability and safety engineering. London: Springer, 2010.
20. Wang L. (Ed.). Modeling and Control of Sustainable Power Systems. Springer-Verlag, 2012.
21. Ważyńska-Fiok K, Jaźwiński J. Reliability of technical systems. Warszawa: PWN, 1990.
22. Ważyńska-Fiok K. Basic of maintenance and reliability theory for transport systems. Warszawa: WPW, 1993.
23. Wiatr J, Boczkowski A, Orzechowski M. Overvoltage protection, selecting wires and their protection in low voltage wiring systems. Warsaw: MEDIUM Publishing House, 2010.
24. Wiatr J, Miegion M. UPS power supplies and accumulator batteries in emergency power systems. Warsaw: MEDIUM Publishing House, 2008.
25. Wiatr J. Generating sets in building emergency power systems. Warsaw: MEDIUM Publishing House, 2009.

Adam ROSINSKI, Ph.D. (Eng.)

Warsaw University of Technology

Faculty of Transport

Department of Telecommunications in Transport

ul. Koszykowa 75, 00-662 Warsaw, Poland

E-mail: adro@wt.pw.edu.pl

Tadeusz DABROWSKI, Ph.D. (Eng.)

Military University of Technology

Faculty of Electronics

ul. Generała S. Kaliskiego 2, 00-908 Warsaw, Poland

E-mail: tadeusz.dabrowski@wat.edu.pl

Krzysztof PARCZEWSKI
Henryk WNĘK

USING MOBILE SCALED VEHICLE TO INVESTIGATE THE TRUCK LATERAL STABILITY

WYKORZYSTANIE MOBILNEGO MODELU POJAZDU DO ANALIZY STATECZNOŚCI POPRZECZNEJ SAMOCHODU CIĘŻAROWEGO*

This paper presents the results of an attempt to transfer resistance to the side overturning of the vehicle to the mobile vehicle in the scale of ~ 1:5 on the real vehicle. Due to the substantial cost of testing and the danger of rollover real vehicle attempt was made to reproduce the behaviour of the vehicle, using the conditions of similarity. The paper presents methods of risk detection and control algorithms in stability systems equipped with a safety feature to prevent rollover. The analysis was based on the tests carried out at research training ground. Shows the results of tests on a real and a mobile smaller scale vehicles, and the values of obtained rollover risk indicators.

Keywords: stability of truck movement, testing of mobile scaled vehicles, vehicle stability, testing, rollover risk indicators

Praca przedstawia próbę przeniesienia wyników badań odporności na przewrócenie pojazdu na bok z mobilnego modelu pojazdu w skali ~1:5 na pojazd rzeczywisty. Z uwagi na znaczny koszt badań i niebezpieczeństwo przewrócenia pojazdu rzeczywistego starano się odwzorować zachowanie się pojazdu, wykorzystując warunki podobieństwa. W pracy przedstawiono sposoby detekcji zagrożenia oraz algorytmy sterowania układów stabilizacji toru jazdy wyposażonych w funkcję zabezpieczającą przed przewróceniem. Analizę przeprowadzono w oparciu o próby poligonowe. Przedstawiono wyniki badań pojazdu rzeczywistego i mobilnego modelu w mniejszej skali oraz uzyskane wartości wskaźników zagrożenia przewróceniem pojazdu.

Słowa kluczowe: stateczność ruchu samochodu ciężarowego, badania mobilnych modeli pojazdów, badania stateczności pojazdów, wskaźniki zagrożenia wywrotem.

1. Introduction

Rollover of the vehicle is about 2.5% of the total number of accidents, but they have about 20% of the total number of victims [5]. Such overturning of the vehicle occurs when the vehicle is rotated by ninety degrees or more relative to its longitudinal axis. Agency NHTSA (National Highway Traffic Safety Administration USA) [7] has evaluated a number of manoeuvres that may cause wheels lift on the road and rollover the vehicle. The results did not indicate in detail the manoeuvres that cause the loss of lateral stability of the vehicle. It should be noted that the study of large-scale test vehicle especially, are dangerous and costly. Attempts were made to determine the conditions of “limit” at which the vehicle is likely to rollover. To assess the vehicle stability both indicators are based on the mass and geometrical parameters of vehicles with varying degrees of simplicity and road tests are performed using standardized procedures vehicles developed by ISO and recommended by NHTSA, such as “J-turn”, “fishhook” or other similar testing procedures used at various proving grounds, testing of vehicles (presented in part 3).

The aim of the experimental research was not only to determine the significance of the mass and geometrical parameters on the propensity for overturning the vehicle, but also to determine limit values of indicators of the motion condition at which the vehicle may rollover.

In the following chapters is a description of the requirements and standardized tests carried out during the test vehicles. Then is a de-

scription of selected tests and their results. The last chapter contains the analysis, conclusions and summary of the main points of work.

2. Justification for the use of vehicles at a scale to test stability

Susceptibility testing of real vehicles to overturn on its side is expensive and dangerous. Real vehicle dynamics studies are carried out on research proving grounds - separate complexes roads, implementing road tests under controlled and repeatable conditions. In the world there are dozens of research training grounds used by carmakers to test vehicles in the summer and winter conditions.

The test track should allow for a wide variety of vehicle testing, standardized or developed by the tire manufacturers, carmakers or their teams. The most common test tracks components include torah to high-speed driving, paths to test vehicle dynamics (acceleration and braking), tracks the stability and steerability test (plate with a radius of ~ 100 m), tracks the motion stability tests, the surface of different factor of friction coefficient, with varying elevation angle, tracks with different surfaces and with wavy surface. The study requires the construction of off-road vehicle tracks a number of parts allowing for testing of the capability such as wading, overcoming obstacles, moving on soft and muddy ground. Due to the ever increasing range of vehicle tests carried out test tracks, due to the safety requirements, the requirements for the same track and testing costs increase.

(*) Tekst artykułu w polskiej wersji językowej dostępny w elektronicznym wydaniu kwartalnika na stronie www.ein.org.pl

Testing of vehicles on tracks research particularly defining characteristics movement stability, create rollover risk. The study of the stability of vehicles require special mounting arm, which supports the vehicle when wheels lift on from the road.



Fig. 1. The vehicle during the motion stability test

Therefore, searches are alternative methods to achieve similar results at lower cost. The use of the test vehicle on a scale of similar parameters, provides an alternative to the real vehicle test. If the scale is maintained similarity to the actual vehicle for example as the theory of Π -Buckingham, vehicle testing on a scale may replace costly and dangerous testing full-size vehicles. In addition, they provide the possibility of extending the scope of research and move closer to the conditions in which a loss of stability. The results of these tests can be used not only to evaluate the stability of a vehicle, but also for the analysis of: brake systems, suspension and vehicle protecting systems before rollover. Terms of similarity are shown by S. Brennan, S. Lapapong, S. Allyene, V. Gupta, E. Callejas, K. Romaniszyn [1, 2, 4, 5, 13] and by the authors [10, 11, 12]. Currently, there are 20 parameters compared to the size, mass and rigidity to the real and scaled vehicles.

Among the advantages of the use of vehicles on a scale motion stability experimental testing can distinguish [2, 6, 10, 12, 13, 15]:

- the cost of the scale vehicle tests is a much smaller than the full-size car, the same applies to supplies and spare parts,
- is much easier to make changes to the vehicle on a smaller scale,
- vehicle test on a smaller scale require less space (not required research track and can be done on a much smaller space),
- the possible overturning of the vehicle entails much lower repair costs and is much safer to use,
- the availability on the market of vehicles made in scale, radio-controlled or via cable, there is a wide range of models of different sizes and types that can serve as the basis for the construction of vehicles used in the tests.

3. Parameters of evaluation stability of the vehicle

The ability to maintain the desired trajectory is one of the most important aspects of automotive active safety. Every vehicle, along with his driver and their surrounding environment constitute a closed system of interaction that is unique. The task of assessing the behaviour of the vehicle stability is very difficult because of the large number of interacting components such as a driver – vehicle – trailer – shaping the way. Complete and accurate description of the behaviour of trucks with high located centre of mass must include the information received on the basis of the different types of research. Because this testing only set up a small piece of the entire field of vehicle behaviour, the results of this study can be considered to be relevant only in that area.

Experimental investigations allow an assessment of the stability and steerability of the vehicle in motion with constant and variable speed on the track straight and curvilinear, with or without taking into account the impact of the driver.

The most commonly used tests for testing the stability and steerability of vehicles includes:

- steady-state circular driving behaviour, in accordance with ISO 4138, ISO 14792 (trucks),
- double lane change manoeuvre, according to ISO 3888,
- single lane change manoeuvre, according to GOST P .2003, B32/03,
- step input manoeuvre with the linear angle escalation of the steering wheel, according to ISO 7401, ISO 14793 (trucks),
- sinusoidal input manoeuvre in the form of a one period (usually resulting in a single lane change manoeuvre), according to ISO 7401, ISO 14793 (trucks),
- continuous sinusoidal input manoeuvre, according to ISO 7401, ISO 14793 (trucks),
- pulse input manoeuvre, according to ISO 7401, ISO 14793 (trucks),
- random input manoeuvre, according to ISO 7401, ISO 14793 (trucks),
- manoeuvres developed by NHTSA: steady growth turning SIS (increasing steadily steer), “J-turn” and “fishhook”.

The tests carried out for the full loaded vehicle. Height of the mass centre and weight distribution of the load should be set so as to reflect an interesting application.

The test apparatus used in the study should allow to monitor the measured values and their transcripts. The basic parameters for measuring the stability of the vehicle include: vehicle longitudinal velocity V_L , lateral speed V_Q , vehicle sideslip angle β , lateral acceleration a_y , roll angle φ and vehicle body roll rate $\dot{\phi}$, yaw speed $\dot{\psi}$, steering wheel angle δ_H . Installation of test equipment on the vehicle should be in accordance with the recommendations of the manufacturer and, if possible, provide a direct measurement. In the case of indirect measurement, perform the appropriate correction.

Conducting tests on the real vehicles is associated with a high risk of rollover. For this reason simulation studies of mobile scaled vehicles under the conditions of similarity lead to increase security and reduce the cost of research.

4. Rollover risk detection

The susceptibility of the vehicle to overturning on the side is usually determined by parameters of a vehicle, the quasi-static conditions, with various degrees of simplifying the analysis. Threshold is determined by the parameters of the vehicle rollover. The ability to rollover is determined by level of lateral acceleration, on the vehicle driven along a circular path, (assuming that the vehicle does not operate outside forces). On this basis it has been developed resulting in the definition of the threshold value of the vehicle rollover in steady state conditions in the circle path: *SSRT* (static roll stability threshold) – defined as the maximum value of lateral acceleration at which there will be no rollover of the vehicle.

Based on this definition resulted in different indicators of stability, of which the simplest are the *SSF*, *TTR*, *RI_B*, *RT_{SYM}*, *DSI* and others. Criteria for assessing risk of rollover of the vehicle is provided in [11, 16].

However, during the real manoeuvres of the vehicle, a relatively rare set of motion conditions. Hence, there are some stretches of time in which the lateral acceleration threshold is reached, it does not mean that there will be a rollover. Since the acceleration of *SSRT* limited top range of stability of the vehicle, it is also limited at the bottom, to determine the extent to which it is possible to lose stability.

DRT (dynamic roll stability) – defined as the minimum peak lateral acceleration at which rollover occurs, while performing various manoeuvres of the vehicle (which can cause it to overturn). Figure 2 shows the dependence of the energy required for of the vehicle rollover as a function of lateral acceleration.

Point 0 in Figure 2 corresponds to driving on a straight road, the potential energy increases proportionally to the lateral acceleration until it reaches the point 1 – which corresponds to the lift on of one wheel on the road. Further increase in lateral acceleration causes the increase in potential energy to reach point 2 – equivalent to lift on of the other wheels (one side of the vehicle) on the road. At this point is reached the lateral acceleration (SSRT) necessary for vehicle rollover. Obtaining greater lateral acceleration results in a loss of stability of the vehicle. Similarly, the rollover occurs, even if the lateral acceleration is smaller, but the potential energy will increase to a point 3 (the point at which the vehicle rollover occurs, although there is no lateral acceleration).

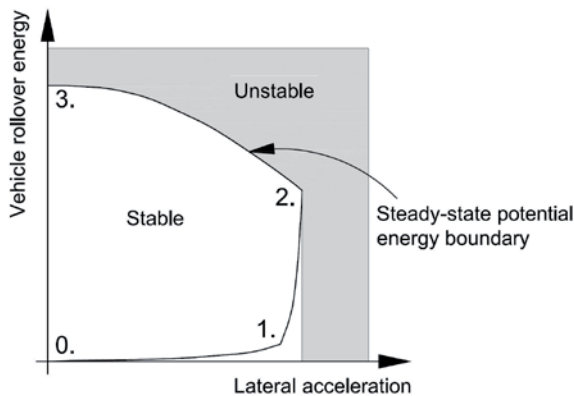


Fig. 2. The energy of the vehicle rollover as a function of the lateral acceleration [2]

It is assumed that the state of emergency occurs when it comes to interior wheels lift on of the of the vehicle from the road surface [2]. Detection of threat vehicle overturning is particularly important in the case of vehicle stability control systems is equipped with anti-roll function. These systems are usually activated only if necessary, adjust the track, the rest of the time do not affect on the vehicle performance. During rollover, the vehicle relatively quickly becomes unstable, which means that the rollover risk detection algorithm must be very sensitive, and stabilization of the system controller must be activated as soon as possible. As criteria values are used: the roll angle and roll rate (ϕ and $\dot{\phi}$), changing on one wheels axle loads (LTR – load transfer ratio), the critical energy rollover ($E_{critical}$) defined as the smallest energy required to lift on the wheel from the roadway and lateral acceleration limit value $a_{ycritical}$.

Below are shown a number of methods used to detect threat of the vehicle rollover, which can be used in the control algorithms in stability control systems. When choosing a method to take into account not only its effectiveness, but also the availability of the information needed to use in the drivers. These algorithms are based on parameters such as changing a single load wheel or wheels of one side of the vehicle, or the lateral acceleration acting on the center of mass and energy of the vehicle rollover. These methods can be divided into analyzing the causes and effects, resulting in a danger of the vehicle rollover. The method of using such a method causes a lateral acceleration and analyzing its derivative (dash). Analysis methods based on the effects of there are, methods based on the determination of the angle of the rolling, rollover energy, or analyzing the normal force acting on each wheel of the vehicle. It should be noted that to analysis can be used sensors of lateral acceleration in existing vehicle stability control systems. In the case of methods based on an analysis of wheel load deflection can use the parameters of the individual suspensions, which already requires the use of additional sensors. Methods based on estimating energy require an rollover vehicle parameters such as roll stiffness of the suspension, the suspension angular damping, the

weight of the vehicle and traffic parameters like: the roll angle and roll ratio and others.

4.1. Changing the wheel loads

Changing the wheel load is an important indicator used in the analysis of the vehicle rollover. Side changing the wheel loads determines the change of normal forces acting on the wheel, caused by the lateral acceleration of the center of mass and its lateral shift in Y direction, due to suspension deflection. Figure 3 shows the impact of the phenomenon of shifting the center of mass to the suspension deflection.

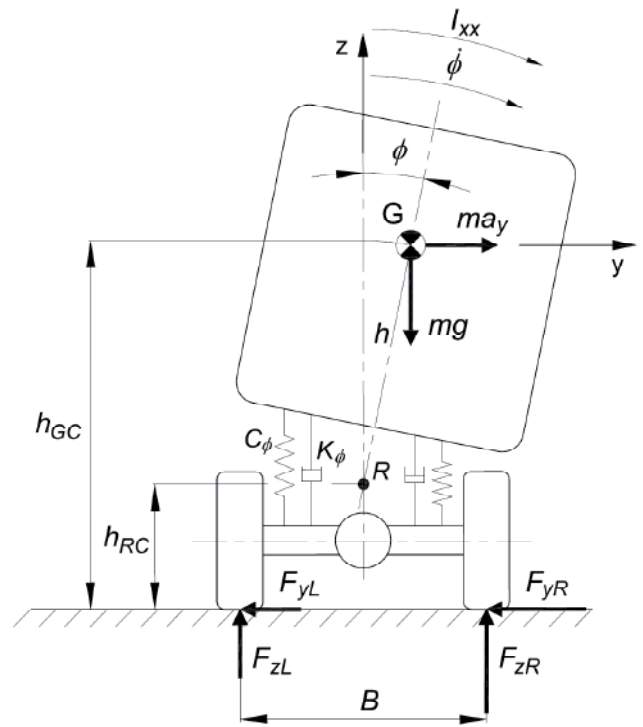


Fig. 3. Changing the wheel loads under the action of lateral force (shown in the transverse plan view)

Rate of change of wheel loads, (LTR) is defined as the ratio of the difference between the normal forces of the right and left side of the vehicle to their sum.

$$LTR = \frac{F_{zR} - F_{zL}}{F_{zR} + F_{zL}} \quad (4.1)$$

In the steady state, where $LTR = \pm 1$ wheels lose contact with the ground, which is read as a critical situation and can be used to control the anti-roll system of the vehicle. Under the unstable conditions the LTR limit should be lower.

4.2. Roll angle and roll rate

If the vehicle is equipped with sensors to measure the roll angle and roll rate (ϕ and $\dot{\phi}$), rollover threat detection can be performed with a simple analysis of these parameters. The simplest way to analyze this term limit roll angle $\phi_{critical}$ at which the driver, the fulfilment of the condition $|\phi| > \phi_{critical}$, starts to work.

As in the previous solution may be used to control the roll rate. In this case, the driver can be activated after fulfilling both conditions: $|\phi| > \phi_{critical}$ and $\dot{\phi} \cdot \text{sign}(\phi) > 0$.

4.3. Methods based on the energy

Overthrow threat detection and activation of the anti-roll driver can be implemented based on the energy of the vehicle rollover. "Emergency" is defined as when the inner wheel is lift on from the substrate. This energy consists of the potential energy accumulated in the suspension deflection and kinetic energy. Therefore, it is determined by the relationship:

$$E = \frac{1}{2} \cdot C_\phi \cdot \phi^2 - m \cdot g \cdot h \cdot (1 - \cos \phi) + \frac{1}{2} \cdot (I_{xx} + m \cdot h^2) \cdot \dot{\phi}^2 \quad (4.2)$$

The critical value of the rollover energy $E_{critical}$ can be defined as the minimum energy required to lift on the wheels of one side of the vehicle from the road. To rollover the vehicle, the total torque against roll axis, for the centre of mass motion, must be greater than the moment caused by the normal wheels force remain in contact with the road. Critical situation can be defined by the inequality moments acting on the vehicle:

$$\frac{1}{2} F_z \cdot B < F_y \cdot h_{GC} + C_\phi \cdot \phi + K_\phi \cdot \dot{\phi} \quad (4.3)$$

The critical value of the rollover energy $E_{critical}$ is determined by minimizing against roll angle ϕ and roll rate $\dot{\phi}$.

4.4. Methods based on the analysis of lateral acceleration

Vehicle roll stability analysis, based on the forces of inertia d'Alembert ($-m \cdot a_y$) acting on the centre of mass and the causing increase in the overturning moment. On vehicles equipped with stability control system lateral acceleration is measured and used it as a pointer indicating to the threat of the vehicle overturning, it becomes very attractive. Taking into account the impact of the suspension deflection complicates the analysis, so the number of solutions it has been ignored, resulting in low values of lateral acceleration limit. For a more detailed analysis allows to determine the value of the derivative of lateral acceleration (spurt). An additional complication is the fact that the measurement of acceleration has a significant noise and its elimination requires additional treatments.

4.5. System control algorithms prevent vehicle roll

Typically were used two control algorithms. One is based directly on the limit of the selected index: *LTR* wheel load changes, the rolling angle ϕ , lateral acceleration a_y or rollover energy E stored in general as $R_{critical}$ (labelled as \hat{R}). Dynamic switching control strategy (the second control algorithm) is based on a derivative of the ratio R . The idea is that the controller is operating in full if $R > \hat{R}$ and when it derivative rises $\dot{R} \cdot \text{sign}(R) > 0$ and its works only partially, when the derivative decreases $\dot{R} \cdot \text{sign}(R) \leq 0$.

The first algorithm was written in the form:

$$F_{xT} = \begin{cases} 0 & \text{dla } |R| \leq \hat{R} \\ -m \cdot a_{x\max} & \text{dla } |R| > \hat{R} \end{cases} \quad (4.4)$$

where $a_{x\max}$ – maximum attainable braking deceleration.

In the second case, the algorithm was described in the formula:

$$F_{xT} = \begin{cases} 0 & \text{dla } |R| \leq \hat{R} \\ -m \cdot a_{x\max} & \text{dla } |R| > \hat{R} \cup \dot{R} \cdot \text{sign}(R) > 0 \\ -\frac{|R| - \hat{R}}{R_{\max} - \hat{R}} \cdot m \cdot a_{x\max} & \text{dla } |R| > \hat{R} \cup \dot{R} \cdot \text{sign}(R) < 0 \end{cases} \quad (4.5)$$

These algorithms can also be used to adjust the vehicle wheel steering angle [9].

$$\delta_R = \begin{cases} 0 & \text{dla } |R| \leq \hat{R} \\ k_R \cdot \text{sign}(R) \cdot (|R| - \hat{R}) & \text{dla } |R| > \hat{R} \end{cases} \quad (4.6)$$

where k_R – correction factor of wheel steering angle.

4.6. The limit values of indicators

Correct operation of the drivers requires an estimate indication limits for their activation.

Changing a wheel load of the vehicle LTR

The first is a change of the wheel loads *LTR*. This indicator varies in the range from 0 to 1, the value 1 is obtained at the time of lift on the wheels from the road. In the most general form of this relationship is as follows [9]:

$$LTR_{critical} = \frac{F_{ZR} - F_{ZL}}{F_{ZR} + F_{ZL}} = \frac{2 \cdot m_s}{m \cdot B} \cdot \left[((h_{GC} - h_{RC}) + h_{GC} \cdot \cos \phi) \cdot \frac{a_y}{g} + h_{GC} \cdot \sin \phi \right] \quad (4.7)$$

In the next part shows the values of R obtained from the road tests of scaled and the normal size vehicle.

The roll angle

Another indicator is based on vehicle roll angle ϕ . It can be relatively easy to determine in the steady state conditions, with the formula:

$$\phi = \frac{mg \cdot (h_{GC} - h_{RC})}{K_\phi - mg \cdot (h_{GC} - h_{RC})} \cdot \frac{a_y}{g} \quad (4.8)$$

In a dynamic dependence on roll angle is much more complicated. It is therefore recommended that you use the real roll angle obtained from measurements. Typically, the limit value of the roll angle, there are 5÷7 degrees.

Energy rollover

Index based on the analysis of rollover energy is used to determine the normalized condition of the vehicle rollover. It has been proposed by Johansson and Gäfvert [3], and is defined by the relationship:

$$ROW_1 = 1 - \frac{E_{critical} - E}{E_{critical}} \quad (4.9)$$

The critical situation is achieved for $ROW_1 \geq 1$. The inclusion of the controller is done when it reaches the limit value of ROW_1 less than 1, this value can be determined experimentally. This implies that the controller should begin operation after exceeding the limit value of indicator $ROW_1 \leq ROW_{1\text{limit}}$. Attempt to estimate this parameter is shown below.

In the references, most of the materials can be found on the lateral acceleration limits. Figure 4 shows the recommendations proposed

by the NTRCI (National Transportation Research Center) [8]. Limit value of lateral acceleration for a truck with a high center of gravity, are dependent on the suspension and tires stiffness, and the car body treated as a rigid amount of 0.50 g, and for a car after taking into account the susceptibility of the suspension and tires – 0.35 g.

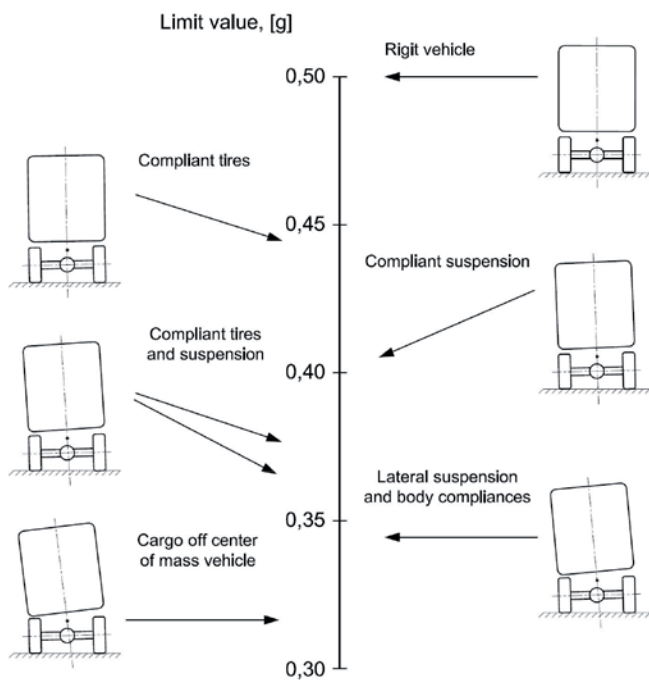


Fig. 4. Limit values threat of rollover in the steady conditions [14]

Due to the fact that the vehicle height of center of gravity, rigidity of the suspensions and their characteristics and the using of stabilizers, considerably influences on the lateral acceleration limit value. In the analysis of vehicles with other characteristics parameters must be made appropriate adjustments. In further analysis includes the impact of these factors on the limit rate values.

5. Investigation of the scaled and normal size vehicle

5.1. The scaled vehicle

For calibration the dynamics of real vehicle motion is used for radio-controlled model car on a scale ~1:5. The scaled vehicle is equipped with an internal combustion engine of a cylinder capacity 26 ccm, centrifugal clutch, gearbox, center and main gearbox, and rear-wheel drive. In order to maintain the conditions of similarity in

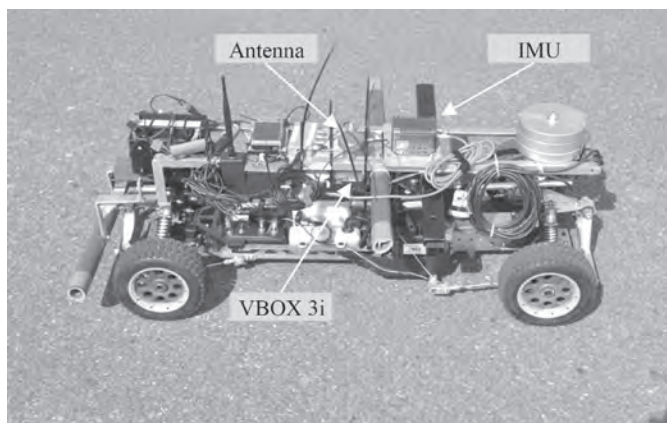


Fig. 5. Scaled vehicle with mounted the measuring apparatus

relation to the real vehicle's (special truck with a high located center of mass), a number of modifications that resulted among other changes: the wheelbase, center of mass, mass moments of inertia, suspension design front and rear axle and tire parameters. Scaled vehicle is equipped with appropriate measurement equipment allows the measurement and recording of relevant parameters of its motion. It was decided to use measuring equipment from Racelogic company – VBOX with the IMU module. Record the results of measurements were made on the Compact Flash memory card. Figure 5 shows the scaled vehicle with a installed measuring apparatus.

5.2. Field tests

For comparisons of selected two trials: driving in a circle with a fixed speed and manoeuvre extortion jump of the linear angle escalation of the steering wheel. Tests were carried out on the test track TATRA in Koprivnice (Czech Republic) in the case of a vehicle full scale [11, 12, 13] and at the airport in Kaniow near Czechowice-Dziedzice for scaled vehicle.

Figure 6 shows the path of the test drive in a circle and method of implementation the test of step input with linear angle escalation of the steering wheel.

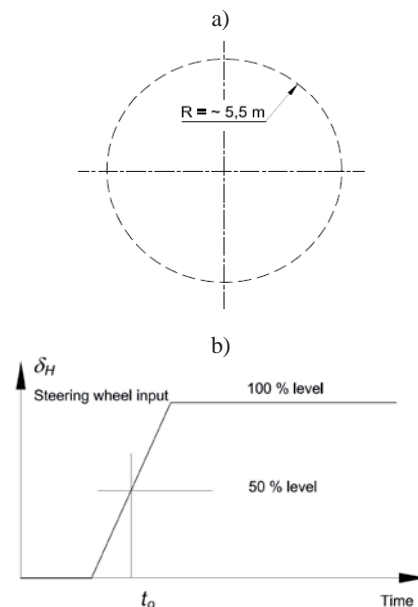


Fig. 6. Carried out tests: driving in a circle at a constant speed in a steady state conditions (a) and step input of the steering wheel (b)

5.3. Driving in a circle with a fixed speed

The trial was carried out at with velocity ~17 km/h and lateral acceleration ~4.5 m/s² (corresponding to real vehicle – speed ~40 km/h moving on the track with a radius of ~21.5 m). Figure 7 shows the course of the selected indicator and its derivative.

The graph shows that the dynamic component of the R ratio related to the derivative of the test under steady state conditions is rather small, and the components associated with the indicator has a value oscillating around the limit value (depending on equations (4.5) and (4.6)). In the case presented above may lead to activation of the vehicle stability control system.

5.4. Step input on the steering wheel

During the tests vehicle moved at a fixed speed on the straight, and then, in a designated area perform a rapid turn for a fixed steering wheel angle.

During the maneuver the derivative ratio \dot{R} is significantly increased in the first part of the maneuver and then decreases. Indicator R

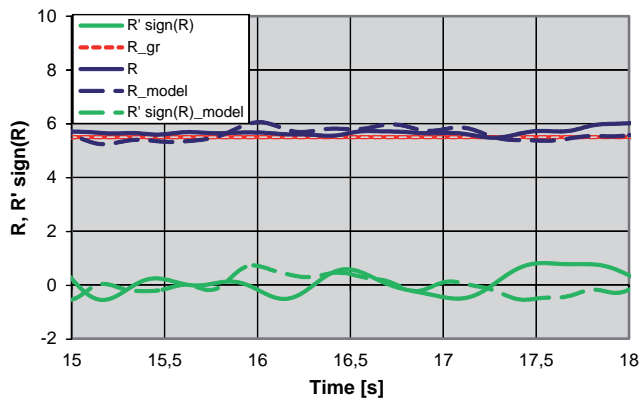


Fig. 7. The course of the selected indicator during the test circular driving at constant speed (the real vehicle marked with a continuous line, dashed line scaled vehicle)

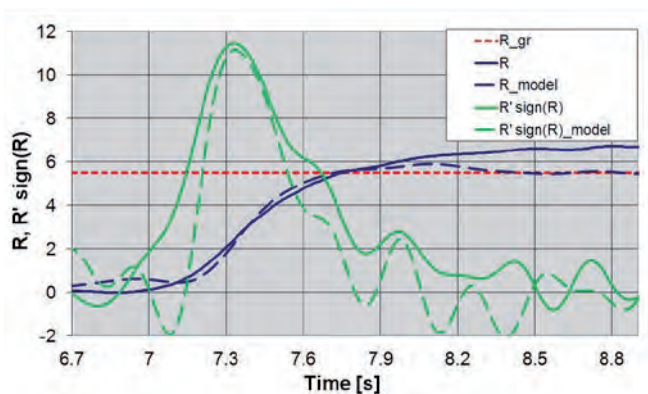


Fig. 8. The course selected indicator stepping while step input on the steering wheel (the real vehicle marked with a continuous line, dashed line scaled vehicle)

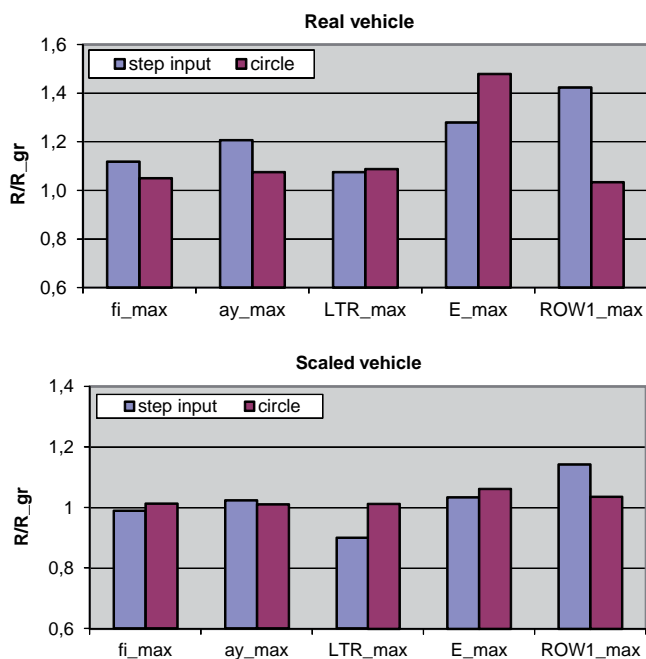


Fig. 9. Normalized values of threat indicators of vehicle rollover R/R^{gr}

ratio increases, but the increase is delayed in relation to the derivative of $\sim 0.6 \div 0.8$ sec. This time delay associated with the inertia of the vehicle, it is often referred to as a time to lift on the wheel (figure 8).

Analysis of different risk rollover indicators R has clarified differences between the various indicators and their derivatives for real and scaled vehicle. In Figures 9 and 10 shows the values of the indicators and their derivatives.

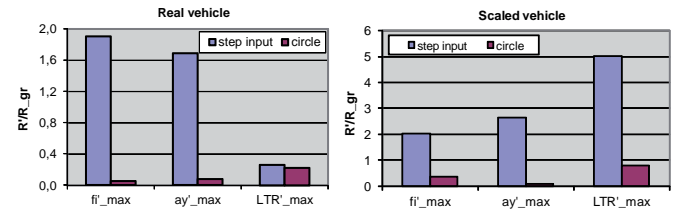


Fig. 10. Normalized values of vehicle rollover derivative risk indicators \dot{R} / R_{gr}

The comparison shows that both the real and the scaled vehicle have similar values of R for all parameters compared ϕ , a_y , LTR , E and ROW_1 . Differences obtained for the test fixed driving in a circle, are respectively, 11, 15, 16 and 19% and for the jumping extortion on the steering wheel the differences are smaller, and are approximately 4, 6, 7 and 28%. Slightly larger differences have derived indicators $\dot{\phi}$, \dot{a}_y , and especially large differences are observed at a ratio of wheel unloading one side of the vehicle $L\dot{T}R$.

6. Summary and Conclusions

Comparison of the results of simulations of the scaled vehicle with the results of real vehicle measurements show good agreement of the analyzed parameters. Generally, this allows to conclude that the mobile scaled vehicle can be used to determine the control parameters for vehicles equipped with stability control systems with function of anti-rollover. There is a good agreement for the parameters of the roll angle, lateral acceleration and wheel unloading one side of the vehicle. Larger differences indicate: rollover energy and ROW1 rate. Similar ratios derived values obtained for the roll angle and lateral acceleration. Large differences exist in the comparison rate derivative LTR.

Based on the presented simulation tests of scaled and real vehicle there are the following conclusions:

- good agreement was obtained for parameters characterizing the risk of the vehicle rollover, both tests: driving in a circle with a fixed speed and step input of the steering wheel confirmed this compliance
- scaled vehicle can be used to create software systems for vehicle stability control systems equipped with anti-roll function to determine the limits of indicators characterizing the risk of rollover,
- the further testing of the scaled vehicle and work to preserve similarities more compared parameters to the real vehicle, and should contribute to reducing differences in the investigated indicators.

Work was established during the project realization R & D NCBR no. PB 5478/B/T02/2011/40 „Evaluation of the stability of the real vehicle on the basis of the scaled vehicle.”

References

1. Brennan S, Alleyne A. The Illinois Roadway Simulator: A mechatronic testbed for vehicle dynamics and control. IEEE/ASME Transactions on Mechatronics 2000; 12, Vol. 5, No. 4: 349–359.
2. Dahleberg E. Commercial vehicle stability – focusing on rollover. Stockholm: Vehicle Dynamics, 2001.
3. Johansson B, Gäfvert M. Untripped SUV rollover detection and prevention. 43rd IEEE Conference on Decision and Control 2004; 14-17.
4. Lapapong S, Gupta V, Callejas E, Brennan S. Fidelity of using scaled vehicles for chassis dynamic studies. Vehicle System Dynamics 2009; 11 (47): 1401–1437.
5. Lapapong S. Vehicle rollover prediction for banked surfaces. Pennsylvania State University 2010.
6. Lozia Z. Ocena odporności pojazdu na przewrócenie na bok – wpływ stopnia skomplikowania modelu na wyniki obliczeń. Zeszyty Naukowe Instytutu Pojazdów Politechnika Warszawska 2010; 3(79).
7. NHTSA, Traffic Safety Facts 2003 – Final Report. U.S. Department of Transportation: National Highway Traffic and Safety Board 2004.
8. Pape D, Arant M, Nelson S, Franzese O, Knee H, LaClair T, Attanayake U, Hathaway R, Keil M, Ro K. Heavy truck rollover characterization (Phase B). NTRCI 2009.
9. Odenthal D, Bünte T, Ackermann J. Nonlinear steering and braking control for vehicle rollover avoidance. Proceedings of European Control Conference, Karlsruhe, Germany 1999.
10. Parczewski K, Wnęk H. Utilization of the car model to the analysis of the vehicle movement after the curvilinear truck. Eksploatacja i Niezawodność – Maintenance and Reliability 2010; 4 (48): 37–46.
11. Parczewski K, Wnęk H. Wykorzystanie kryteriów podobieństwa do analiz stateczności ruchu na podstawie mobilnego modelu samochodu ciężarowego. Logistyka 2012; 3.
12. Parczewski K, Wnęk H. Analiza wpływu parametrów masowych na stateczność ruchu samochodu ciężarowego w oparciu o badania mobilnego modelu pojazdu. Postępy Nauki i Techniki, SIMP 2012; 14: 208–223.
13. Romaniszyn KM. Mobilne modele samochodów do badań stateczności. Logistyka 2012; 3.
14. Winkler C. Rollover of Heavy Commercial Vehicles, University of Michigan Transportation Research Institute, Research Review Vol. 31 No. 4
15. Yih P. Radio controlled car model as a vehicle dynamics test bed. Mechanical Engineering Department. Stanford University 2000.
16. Yu H, Guvenc L, Ozguner U. Heavy-duty vehicle rollover detection and active roll control. Vehicle System Dynamics 2008; 6 (46): 451–470.

Key symbols

a_x	Longitudinal acceleration (along X axis)
a_y	lateral acceleration (along Y axis)
B	Wheel track
C_ϕ	Vehicle roll stiffness coefficient
$E_{critical}$	Vehicle rollover energy
F_{xT}	Braking force
F_y	Force acting respect to the Y axis
$F_{yL,R}$	Lateral force acting on left / right wheel
F_z	Force acting respect to the Z axis
$F_{zL,R}$	Normal force acting on left / right wheel
g	Gravitational acceleration
h	Distance between gravity centre and roll axis $h = h_{GC} - h_{RC}$
h_{GC}	Gravity centre height
h_{RC}	Roll centre height
I_{XX}	Vehicle mass moment of inertia respect to the X axis
K_ϕ	Vehicle roll damping coefficient
m	Mass of the vehicle
ms	Vehicle spring mass
δ_R	Wheel steering angle
δ_H	Steering wheel angle
ϕ	Vehicle roll angle
$\dot{\phi}$	Vehicle roll rate respect to the X axis

Krzysztof PARCZEWSKI, Ph.D. (Eng.)

Henryk WNEK, Ph.D. (Eng.)

University of Bielsko-Biala,

Department of Combustion Engines and Vehicles,

Willowa 2, PL – 43 309 Bielsko-Biala, Poland

E-mails: kparczewski@ath.bielsko.pl, hwnek@ath.bielsko.pl

Wojciech ZĘBALA
Bogdan SŁODKI
Grzegorz STRUZIKIEWICZ

PRODUCTIVITY AND RELIABILITY IMPROVEMENT IN TURNING INCONEL 718 ALLOY – CASE STUDY

POPRAWA PRODUKTYWNOŚCI I NIEZAWODNOŚCI TOCZENIA STOPU INCONEL 718 – STUDIUM PRZYPADKU*

The paper presents an investigation of Inconel 718 alloy finishing turning, using a procedure that allows the optimal cutting data to be found with a maximization of the metal removal rate as the optimization criterion. The optimization procedure does not allow the required values of the chosen surface roughness indicator, cutting force and cutting tool wedge temperature to be exceeded at the same time. The optimization procedure includes the preliminary cutting tests for establishing the range of cutting data (feed and depth of cut) for the correct chip breaking as well as research concerning micro-hardness measurements which enables the cold work zone to be determined and the minimal value of the feed to be defined. The functionality of the algorithm was verified by using the improvement in machining productivity and reliability of an aircraft engine element as an example.

Keywords: Inconel, turning, productivity, optimization, parameters, micro-hardness.

Artykuł opisuje badania obróbki wykończeniowej toczeniem stopu Inconel 718, mające na celu optymalizację parametrów skrawania z uwzględnieniem maksymalizacji objętościowej wydajności obróbki, jako kryterium optymalizacyjnego. Proponowana procedura uwzględnia wymagane w procesie ograniczenia dotyczące wartości parametru chropowatości obrabianej powierzchni, siły skrawania oraz maksymalnej temperatury w strefie skrawania. Procedura optymalizacyjna zawiera wstępne testy mające na celu ustalenie w lokalnych warunkach obróbki użytecznego zakresu parametrów skrawania (posuwu i głębokości skrawania) dla otrzymania korzystnej postaci wiórów. Wykonane pomiary mikrotwardości w strefie skrawania umożliwiły określenie wielkości strefy zgniotu warstwy wierzchniej, co z kolei pozwoliło na zdefiniowanie minimalnej wartości posuwu. Procedurę optymalizacyjną zweryfikowano na przykładzie obróbki wybranej powierzchni elementu silnika lotniczego. Osiągnięto znaczną poprawę produktywności i niezawodności procesu obróbki.

Słowa kluczowe: Inconel, toczenie, produktywność, optymalizacja, parametry, mikro-twardość.

Nomenclature

A_D	cutting layer cross section in mm ²
a_p	depth of cut in mm
D_c	work piece diameter in mm
f	feed rate in mm/rev
$F_c F_f F_p$	components of cutting force in N
i	number of passes
n	rotational speed in rev
Q_v	metal removal rate in cm ³ /min
Ra	surface roughness in μ m
t_1	cutting time for one pass in min
T_{cut}	temperature in °C
t_{cut}	total time of cutting in min
v_c	cutting speed in m/min
R^2	coefficient of determination

1. Introduction

Nickel-based alloys (HRSA) due to their good mechanical properties in high temperatures are commonly used in the aerospace industry, e.g. for parts in gas turbine engines. The most popular types of HRSA include Inconel 718, Inconel 625 and Waspaloy. About 45% of forgings and 15% of casts are made of Inconel 718 alloy [6, 29].

Although nickel-based alloys have good constructional properties they are difficult-to-cut materials. Inconel 718 can be characterized by

high hardness and high strength in elevated temperature which leads to high cutting resistance. This alloy has a tendency to work surface hardening. Its low thermal conductivity leads to high temperature developing in the cutting zone. These rise from around 900 °C at a low cutting speed of 30 m/min up to 1300 °C at 300 m/min [18].

Most nickel-based alloys' chemical composition includes 10–20% chromium, up to 8% aluminium and titanium combined, from 5 to 15% cobalt and small quantities of boron, zirconium, magnesium and carbon. The other additives include molybdenum, niobium and tungsten.

From the end of the seventies nickel alloys were the object of detailed research [4, 10, 12, 13, 15, 21–23, 26, 27, 34]. A lot of attention was paid to the quality of the surface and the integrity of the upper layer of elements made of nickel-based alloys [24, 31]. This is important for the durability, endurance fatigue, productivity and functionality of machined parts [2, 3, 5, 35, 36].

The machining process can take place only when the necessary force, properly situated in space and time, is applied to the work piece. The force acting on the cutting wedge must overcome the resistance of the work piece material, its elastic and plastic strains, and frictional resistance when a new surface is created [9, 28, 33].

An analysis of the bibliography, describing the phenomena taking place in the machining process, reveals the fact that when the cutting speed increases (with a constant value for the metal removal rate) the

(*) Tekst artykułu w polskiej wersji językowej dostępny w elektronicznym wydaniu kwartalnika na stronie www.ein.org.pl

cutting force decreases [14]. This enables thin-walled work pieces to be machined.

The influence of the cutting speed on the cutting force and the surface roughness is connected with the influence of the deformation speed of the cutting layer on the plasticity of the machined material and tool wear [11, 16]. The temperature in the cutting zone is closely related to the cutting speed and in general increases when the cutting speed increases. Heat changes the alloy microstructure and causes stress formation [25]. When a low cutting speed is applied, abrasive wear on the tool flank face is dominant [8]. A higher cutting speed causes adhesion wear and high cutting speed is also connected with diffusion wear [20].

There are many papers devoted to the optimization of Inconel 718 machining. The problems concerning the cutting optimization of Inconel 718 alloy, together with the optimization criterion of the surface roughness was presented in [1, 16–18, 35]. In [1] the optimization of the hybrid machining process with economical criterion was analysed. Another approach to machining data optimization was presented in [7], the main criterion being the maximization of tool life and the minimization of production cost.

A similar approach concerning the optimization of milling cutting data was presented by the authors in [19]. The optimization of cutting data by means of RSM (Response Surface Methodology) for ceramic tools was considered in [1]. A genetic algorithm coupled with an artificial neural network (ANN) as an intelligent optimization technique for machining parameters optimization of Inconel 718 was described in [30]. On the other hand, HSC turning optimization by means of Taguchi Grey Relational Analysis was described in [26].

Due to the physical properties of Inconel 718, as well as work piece surface hardening as a result of surface deformation and low thermal conductivity, there is a lack of specific results for machining process optimization with a productivity criterion. Thus, the authors tried to determine a procedure to find the optimal cutting data for Inconel 718 alloy finishing turning with a maximization of the metal removal rate (productivity) as the optimization criterion, that at the same time did not exceed the required values of the surface roughness indicators, cutting force and tool wedge temperature. The verification of the correctness of the algorithm's working is described in section 3.

2. Optimization procedure

The problem of a turning improvement with the optimization criterion of the maximum metal removal rate can be formulated in the following way, Eqs. (1–7):

$$a_p \min \leq a_p \leq a_p \max \quad (1)$$

$$f_{\min} \leq f \leq f_{\max} \quad (2)$$

$$v_c \min \leq v_c = f(n, D_c) \leq v_c \max \quad (3)$$

$$Q_v = f(v_c, f, a_p) \rightarrow Q_v \max \quad (4)$$

$$F \leq F_{\lim} \quad (5)$$

$$T_{cut} \leq T_{cut \lim} \quad (6)$$

$$Ra \leq Ra_{\lim} \quad (7)$$

Where: $Q_v \max$ – maximum metal removal rate; Ra_{\lim} – required value of surface roughness; F_{\lim} – acceptable value of cutting force components ($F_c \lim$, $F_f \lim$, $F_p \lim$), due to the strength of the grip part and the direct influence of the work piece surface layer properties; $T_{cut \lim}$ – acceptable temperature limit of the tool wedge.

Eqs. (1–3) determine the collection of the allowable values of the depth of cut, feed and cutting speed. The ranges for these values are based on the tool manufacturer's recommendations and specific investigations in the local machining conditions (e.g. correct chip breaking). The general productivity improvement procedure, based on experiments, is presented in Fig. 1. At the beginning of the proce-

cedure a range of cutting data and process optimization criterion must be defined. On the basis of the results, obtained from the successive steps of the optimization process, the correct cutting data can be selected. The scheme presented in Fig. 1 consists of the following steps:

- (1) Definition of optimization criterion (Q_v in this approach) and optimization limits (F , T_{cut} , Ra).
- (2) Preliminary cutting tests for establishing the cutting data range for correct chip breaking.
- (3) Establishment of the research method and measurement equipment. At this stage it is necessary to determine the final cutting data range for the tests.
- (4) Measurement tests (F , Ra , T_{cut}) for selected cutting data.
- (5) Research concerning micro-hardness measurements, which enables the reach of the cold work zone to be determined.
- (6) Determination and analysis of $F = f(Q_v)$, $T_{cut} = f(Q_v)$ and $Ra = f(Q_v)$ functions.
- (7) Analysis of the above functions leads to setting the optimal cutting data that fulfils the optimization criterion and limits.

3. Verification of the optimization procedure

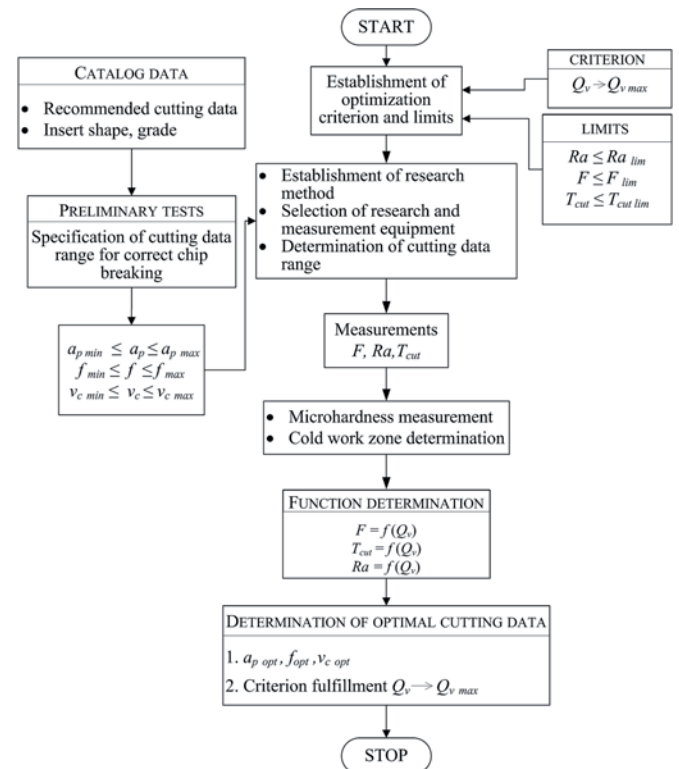


Fig. 1. Scheme of the productivity improvement procedure during turning ($Q_v \max$)

The optimization process of cutting data selection, according to the outline presented in Fig. 1, was performed for the selected surface (**) of the aircraft engine element (bush), manufactured using Inconel 718 alloy, Fig. 2a. The initial cutting data (Case1), selected from the tool manufacturer's recommendations (a_p , f and v_c) and the calculated values are shown in Table 1.

The surface roughness measured from the data was $Ra = 0.95 \mu m$ at $Q_v = 3,52 \text{ mm}^3/\text{min}$. These were initial cutting data with reference

Table 1. Initial cutting data and calculated values A_D , t_1 and t_{cut}

	a_p mm	f mm/rev	v_c m/min	A_D mm ²	t_1 min	t_{cut} min	i
Case1	1.1	0.080	40	0.088	0.374	2.25	6

to which the optimal parameters were investigated. Cutting experiments were performed on the research stand built on the base of the turning centre, with the cutting force measurement device. Fig. 2b is a photograph taken during the external surface machining of the element shown in Fig. 2a.

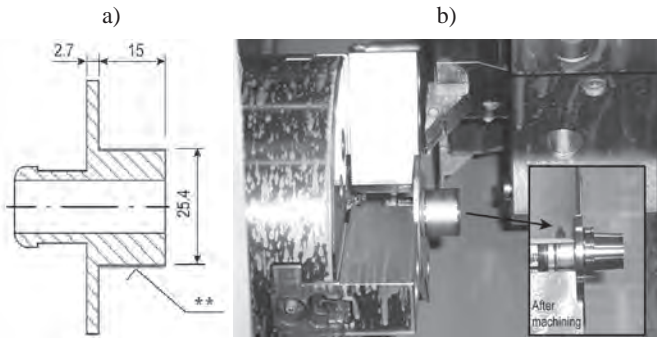


Fig. 2. Shape of semi-finished product (a) and photo of its machining (b)

Turning was carried out with a sintered carbide insert, VCMT 160404-SM with TiAlN coating, and $\alpha_n = 7^\circ$ clearance angle. The cutting insert was mounted in the tool-holder, SVJCR 2020K-16.

The optimization criterion – (maximization of Q_v) and constraints, Eq. (8) were determined as the first step of the procedure. F_f feed force and F_p radial force were not considered.

$$Ra \leq 1,15 \mu\text{m} \text{ and } F_c \leq 470 \text{ N and } T_{cut} \leq 650^\circ\text{C} \quad (8)$$

An analysis of SM type chipbreaker efficiency in an actual, local machining environment was performed and described in details [32, 37]. The results for $v_c = 50$ m/min are presented in Fig. 3a. The marks in this figure mean: “x” – unacceptable chip form, “0” – acceptable chip form, “+” – correct chip form. The main dimensions of the rake face shape are shown at the top. The conveyed tests revealed the fact that the most profitable chip forms came into being within the following range: cutting speed $v_c = 40$ -60 m/min, feed $f = 0.08$ -0.25 mm/rev and depth of cut $a_p > 1$ mm.

The values obtained for F_c cutting force and T_{cut} temperature, as a function of the feed and cutting speed, are presented in Fig. 3b and Fig. 4a, respectively. Examples of thermograms for the highest and the lowest temperature in the cutting zone, measured by means of an infrared camera, are shown in Fig. 4b and Fig. 4c, respectively.

When considering Fig. 3b it can be observed that for feed values greater than 0.1 mm/rev the cutting force increases more slowly as the feed increases. Generally, when the feed rises, the cross section of the cutting layer enlarges and the cutting resistance increases. With a feed value over 0.1 mm/rev only a slight increase in the cutting force occurs. This is due to the fact that a material decohesion process takes place below the cold work layer and the cutting resistance decreases. This is confirmed by the micro-hardness measurements of the work material in the cutting zone, described below. It suggests establishing a higher feed limit (over 0.1 mm/rev) than was initially proposed (0.08 mm/rev).

The influence of the cutting speed on the cutting wedge temperature is shown in Fig. 4. At a greater cutting speed, the temperature of the work material in the cutting zone is higher, which decreases the strength of the material being cut.

Observing the cutting wedge temperatures for different feed and cutting speed values it can be stated that as the feed increases up to about 0.18 mm/rev a decrease in temperature occurs. This probably is directly linked to the decrease in the thickness of the cold work layer in relation to the total thickness of the cutting layer. The cutting wedge temperature reaches a minimum value for each cutting speed in the

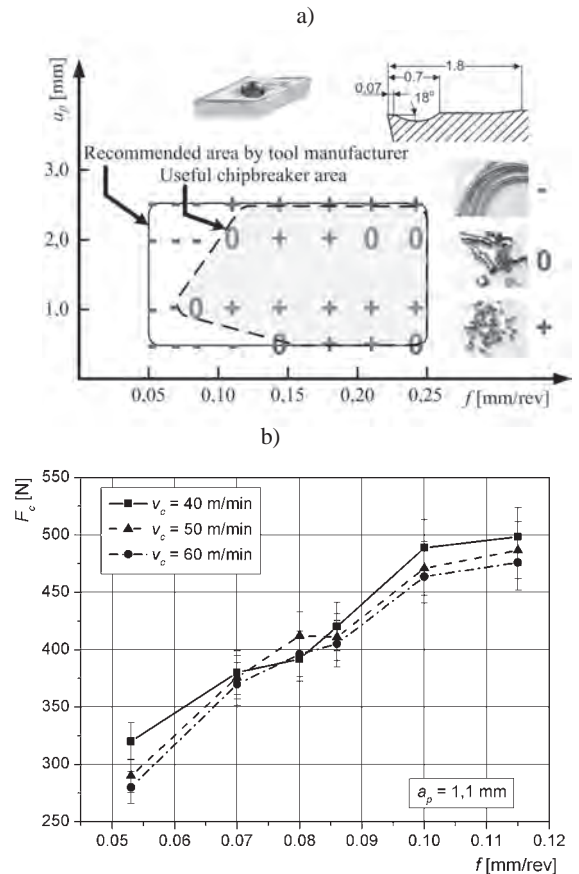


Fig. 3. Classification of chips forms with useful chipbreaker area type SM in local testing environment for $v_c = 50$ m/min, (a) and influence of feed on cutting force (b)

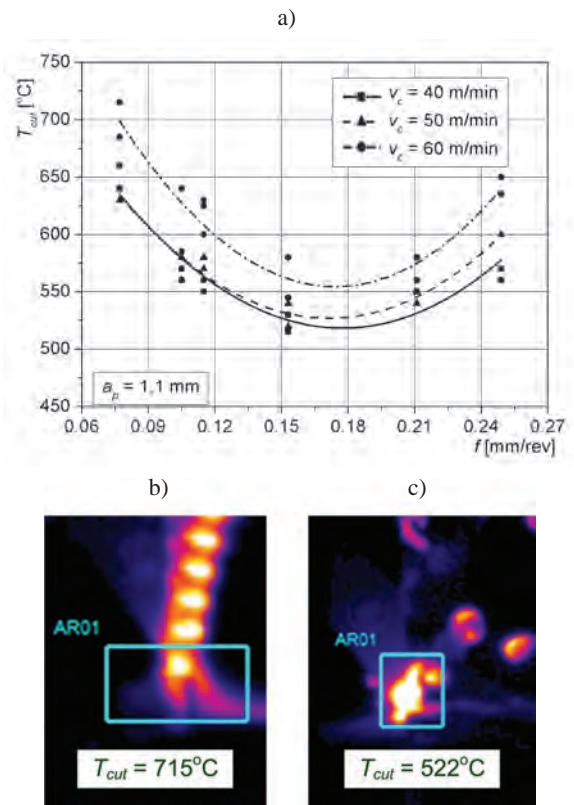


Fig. 4. Temperature of tool wedge: a) $T_{cut} = f(f, v_c)$, b) infra-red photo for $v_c = 60$ m/min and $f = 0.08$ mm/rev, c) infra-red photo for $v_c = 40$ m/min and $f = 0.15$ mm/rev

region of $f = 0.18$ mm/rev. With a greater feed value the cutting wedge temperature increases as the feed increases on account of the cutting layer cross section increase and simultaneously there is less and less influence from the cold work layer on the decohesion process.

To analyse chip morphology and the cold work zone of machined material, tests in which there was a sudden halt in the cutting process were performed. An example of a micro-section photograph, taken by a scanning microscope, is presented in Fig. 5a. The austenitic structure of the material, the size of the grain and the location of the infrequent titanium carbide particles can be observed (arrows in the picture).

Next, the micro-hardness $HV_{0.1}$ (Hannemann method) in the cutting zone, along the line situated inside the chip and the work piece (line AB in Fig. 5a), was measured. The diagram illustrating the influ-

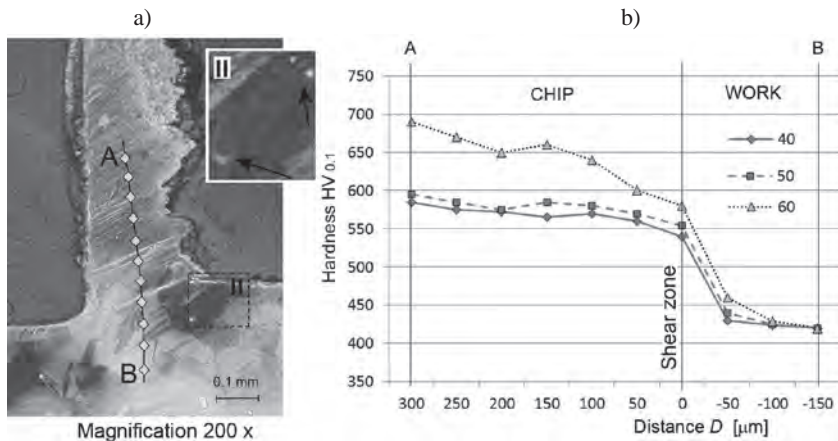


Fig. 5. Chip creation zone with titanium carbide particles indicated by arrows (a) and micro-hardness distribution along AB line for the feed $f = 0.1$ mm and cutting speed $v_c = 40; 50; 60$ m/min (b)

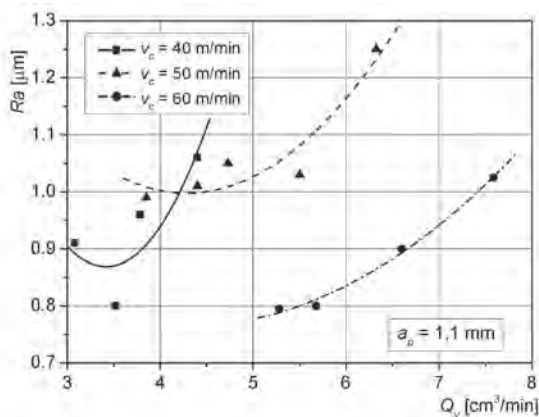


Fig. 6. Dependence of roughness parameter of machined surface Ra from metal removal rate for different cutting speeds

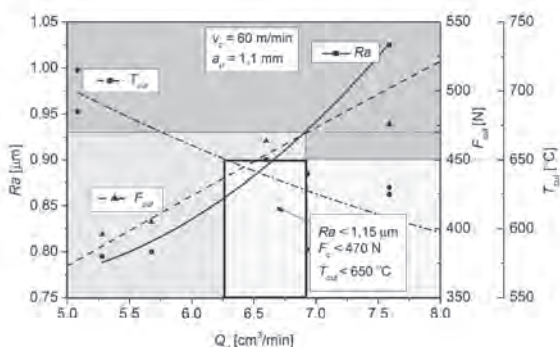


Fig. 7. Dependence of F_c , T_{cut} and Ra from metal removal rate for $v_c = 60$ m/min

ence of the cutting speed on the micro-hardness distribution for a feed $f = 0.1$ mm is presented in Fig. 5b.

Nickel based alloys harden during machining, which is caused by a significant plastic deformation in the area located straight in front of the cutting wedge. The size of this deformation changes as a function of the distance from the machined surface. It translates into a hardness increase from 420 $HV_{0.1}$ for the core material (near point B), to 540;554;580 $HV_{0.1}$ in the shear zone for $v_c = 40; 50; 60$ m/min, respectively, Fig. 5b. At a distance of approximately 0.1 mm from the machined surface, a significant decrease in hardness can be observed of 425–429 $HV_{0.1}$. This means that a feed of at least 0.1 mm or above should be recommended, so as to move the cutting edge below a hardened layer of the material. The results of the roughness measurements of the machined surface for different metal removal rates are presented in Fig. 6.

It can be observed, that at a slower cutting speed the roughness parameter Ra reaches acceptable values below 0.95 μm but the metal removal rate is low, below 4 cm^3/min . So, it seems to be reasonable to apply a cutting speed over 50 m/min.

Taking into consideration the investigations described above, appropriate ranges for the feed (0.1 mm $\leq f \leq 0.25$ mm) and cutting speed (50 m/min $\leq v_c \leq 60$ m/min) values were established. The depth of cut was set as in Case 1.

Using the measured data and the calculations, the diagram in Fig. 7 was created. The diagram enables the best values for the cutting data, which fulfil the imposed optimization limitations (8), to be selected.

The diagram in Fig. 7 with the Eqs. (9-11) permits the maximum metal removal rate for the cutting speed $v_c = 60$ m/min to be determined. This value was chosen from a range fulfilling the limit of T_{cut} temperature (diagram in Fig. 4a).

$$Ra = 1.20005 - 0.20395Q_v + 0.02386Q_v^2 \quad (R^2 = 0,98162) \quad (9)$$

$$T_{cut} = 1018.31177 - 80.68902Q_v + 3.50898Q_v^2 \quad (R^2 = 0,97467) \quad (10)$$

$$F_c = 96.5146 + 58.97511Q_v - 0.73246Q_v^2 \quad (R^2 = 0,97987) \quad (11)$$

The optimized cutting data were chosen for the maximum metal removal rate $Q_v = 6.92$ cm^3/min and these are presented in Table 2.

Table 2. Previously applied (Case1) and optimized cutting data for $v_c = 60$ m/min

	a_p mm	f mm/ rev	v_c m/ min	Ra μm	Q_v cm^3/min	T_{cut} $^{\circ}C$	F_c N
Initial cutting data (Case1)	1.1	0.080	40	0.95	3.52	580	392
Optimized cutting data	1.1	0.105	60	0.93	6.92	628	469

4. Conclusion

The results of the experimental tests allowed the best values for the cutting data in the conditions determined for the bush external surface machining, made of Inconel 718, to be established due to the maximization of the metal removal rate at the set limit values of F_c , T_{cut} and Ra . As a result of the optimization procedure an almost 97% productivity increase was achieved at, with a simultaneous small-scale

increase of surface roughness, up to the parameter value $Ra = 1,1 \mu\text{m}$ (admissible value $Ra_{\text{lim}} = 1,15 \mu\text{m}$) and an increase in the cutting force value by about 20% to the admissible limit. The machining process is more reliable taking into account the good chip formation and break-

ing for the optimized cutting data. The research proved the necessity for preliminary live machining tests in local operating features, which serve as a source of information for the optimization procedure.

References

1. Aruna M, Dhanalaksmi V. Design optimization of cutting parameters when turning Inconel 718 with cermet inserts. *World Academy of Science, Engineering and Technology* 2012; 61:952–956.
2. Arunachalam RM, Mannan MA, Spowage AC. Residual stress and surface roughness when facing age hardened Inconel 718 with CBN and ceramic cutting tools. *International Journal of Machine Tools and Manufacture* 2004; 44:879–887.
3. Arunachalam RM, Mannan MA, Spowage AC. Surface integrity when machining age hardened Inconel 718 with coated carbide cutting tools. *International Journal of Machine Tools and Manufacture* 2004; 44:1481–1491.
4. Arunachalam RM, Mannan MA. Machinability of nickel-based high temperature alloys. *Machining Science and Technology* 2000; 4:127–168.
5. Axinte DA, Gindy N, Fox K, Unanue I. Process monitoring to assist the workpiece surface quality in machining. *Machine Tools and Manufacture* 2004; 44:1091–1108.
6. Choudhoury IA, El-Baradic MA. Machinability of nickel-base super alloys: a general review. *Materials Processing Technology* 1998; 77:278–284.
7. Choudhoury SK, Appa Rao IVK. Optimization of cutting parameters for maximizing tool life. *International Journal of Machine Tools & Manufacture* 1999; 39:343–353.
8. D'Addona D, Segreto T, Simeone A, Teti R. ANN tool wear modelling in the machining of nickel superalloy industrial products. *CIRP Journal of Manufacturing Science and Technology* 2011; 4:33–37.
9. Devillez A, Schneider F, Dominiak S, Dudzinski D, Larrouquere D. Cutting forces and wear in dry machining of Inconel 718 with coated carbide tools. *Wear* 2007; 262:931–942.
10. Dudzinski D, Devilleza A, Moufkia A, Larrouquere D, Zerroukib V, Vigneau J. A review of developments towards dry and high speed machining of Inconel 718 alloy. *International Journal of Machine Tools and Manufacture* 2004; 44:439–456.
11. El-Hossainy TM, El-Zoghby AA, Badr MA, Maalawi KY, Nasr MF. Cutting Parameter Optimization when Machining Different Materials. *Materials and Manufacturing Processes* 2010; 25:1101–1114.
12. Ezugwu EO, Fadare DA, Bonneya J, Da Silvaa RB, Salesa WF. Modelling the correlation between cutting and process parameters in high-speed machining of Inconel 718 alloy using an artificial neural network. *International Journal of Machine Tools & Manufacture* 2005; 45:1375–1385.
13. Ezugwu EO. Key improvements in the machining of difficult-to-cut aerospace superalloys. *International Journal of Machine Tools and Manufacture* 2005; 45:1353–1367.
14. Fang N, Wu Q. A comparative study of the cutting forces in high speed machining of Ti–6Al–4V and Inconel 718 with a round cutting edge tool. *Journal of Materials Processing Technology* 2009; 209:4385–4389.
15. Gullu A, Karabulut S. Dynamic Chip Breaker Design for Inconel 718 Using Positive Angle Tool Holder. *Materials and Manufacturing Processes* 2008; 23:852–857.
16. Guo YB, Li W, Jawahir IS. Surface Integrity Characterization and Prediction in Machining of Hardened and Difficult-To-Machine Alloys: A State-Of-Art Research Review and Analysis. *Machining Science and Technology* 2009; 13:437–470.
17. Jonak J, Podgórski J, Zubrzycki J. Wybrane zagadnienia mechaniki procesu skrawania materiałów. *Eksploatacja i Niezawodność – Maintenance and Reliability* 2001; 5:27–31.
18. Kitagawa T, Kubo A, Maekawa K. Temperature and wear of cutting tools in high-speed machining of Inconel 718 and Ti-6Al-6V-2Sn. *Wear* 1997; 202:142–148.
19. Krain HR, Sharman ARC, Ridgway K. Optimization of tool life and productivity when end milling Inconel 718. *Materials Processing Technology* 2007; 189:153–161.
20. Liao YS, Shiue RH. Carbide tool wear mechanism in turning of Inconel 718 superalloy. *Wear*. 1996; 193:16–24.
21. Nalbant M, Altin A, Gokkaya H. The effect of cutting speed and cutting tool geometry on machinability properties of nickel-base Inconel 718 super alloys. *Materials&Design* 2007; 28:1334–1338.
22. Narutaki N, Yamane Y. Machining of difficult-to-cut materials. *International Journal of the Japan Society for Precision Engineering* 1993; 27:307–310.
23. Narutaki N, Yamane Y, Hayashib K, Kitagawac T, Uehara K. High-speed machining of Inconel 718 with ceramic tools. *CIRP Annals – Manufacturing Technology* 1993; 42:103–106.
24. Oktem H, Erzurumlu T, Kurtaran H. Application of response surface methodology in the optimization of cutting conditions for surface roughness. *Journal of Materials Processing Technology* 2005; 170:11–16.
25. Outeiro JC, Pina JC, M'Saoubi R, Pusavec F, Jawahir IS. Analysis of residual stresses induced by dry turning of difficult-to-machine materials. *CIRP Annals – Manufacturing Technology* 2008; 57:77–80.
26. Pawade RS, Joshi S. Mechanism of chip formation in high-speed turning of Inconel 718. *Machining Science and Technology* 2011; 15:132–152.
27. Pawade RS, Joshi S. Multi-objective optimization of surface roughness and cutting forces in high-speed turning of Inconel 718 using Taguchi grey relational analysis (TGRA). *The International Journal of Advanced Manufacturing Technology* 2011; 56:47–62.
28. Rusinek R. Drgania w procesie skrawania stopu tytanu. *Eksploatacja i Niezawodność – Maintenance and Reliability* 2010; 3:48–55.
29. Sandvik Coromant, Aerospace Engine – application guide 2004.
30. Senthilkumaar JS, Selvarani P, Arunachalam RM. Intelligent optimization and selection of machining parameters in finish turning and facing of Inconel 718. *The International Journal of Advanced Manufacturing Technology* 2012; 58:885–894.

31. Sharman ARC, Hughes JI, Ridgway K. An analysis of the residual stresses generated in Inconel 718TM when turning. *Journal of Materials Processing Technology* 2006; 173:359–367.
32. Słodki B, Zębala W. The analysis of selected chipbreakers efficiency in difficult-to-cut material turning in local operating features. *Naukowy Żurnal, National University in Chmielnicki, Ukraine* 2007; 1:179–189.
33. Taranenko G, Taranenko W, Świć A, Szabelski J. Modelowanie układów dynamicznych obróbki skrawaniem wałów o małej sztywności. *Eksplotacja i Niezawodność – Maintenance and Reliability* 2010; 4:4–15.
34. Thakur DG, Ramamoorthy B, Vijayaraghavan L. A Study on the Parameters in High-Speed Turning of Superalloy Inconel 718. *Materials and Manufacturing Processes* 2009; 24:497–503.
35. Wrigth PK, Chow JG. Deformation characteristic of nickel alloys during machining. *Journal of Engineering Materials and Technology* 1982; 104:85–93.
36. Yoo JT, Yoon JH, Lee HS, Youn SK. Material characterization of Inconel 718 from free bulging test at high temperature. *Journal of Mechanical Science and Technology* 2012; 26:2101–2105.
37. Zębala W, Słodki B. Some aspects of chipbreakers efficiency in difficult-to-cut materials turning. *Proc. of Int. Users' Conf. „Modelling Technology – Machining Solution”, Minneapolis, MN, USA* 2008; 14:1-14.

Wojciech ZĘBALA, Ph.D., D.Sc. (Eng.)

Bogdan SŁODKI, Ph.D. (Eng.)

Grzegorz STRUZIIEWICZ, Ph.D. (Eng.)

Production Engineering Institute, Mechanical Faculty

Cracow University of Technology

Al. Jana Pawła II 37, 31-864 Kraków, Poland

E-mail: zebala@mech.pk.edu.pl

Sylwia WERBIŃSKA-WOJCIECHOWSKA

TIME RESOURCE PROBLEM IN LOGISTICS SYSTEMS DEPENDABILITY MODELLING

PROBLEM REZERWOWANIA CZASOWEGO W MODELOWANIU NIEZAWODNOŚCI SYSTEMÓW LOGISTYCZNYCH*

Article presents an overview of some recent developments in the area of mathematical modelling of technical systems' maintenance decisions with the use of delay-time concept. Thus, the literature overview from 1984-2012 in the analysed research area is given. The problem of time relations occurred in logistic systems performance processes is investigated. Later, the example of DT model implementation in the area of logistic system of sixteen forklifts performance analysis is investigated.

Keywords: delay-time concept, dependability, logistic system.

W artykule przedstawiono zagadnienia związane z matematycznym modelowaniem utrzymania systemów technicznych w stanie zdolności z wykorzystaniem koncepcji opóźnień czasowych (DT). Przedstawiono przegląd literatury z badanego obszaru obejmujący okres 1984-2012. Następnie został omówiony problem relacji czasowych w systemach logistycznych. W ostatnim punkcie, został przedstawiony przykład zastosowania modelu DT do oceny niezawodności szesnastu wózków widłowych funkcjonujących w wybranym systemie.

Słowa Kluczowe: koncepcja opóźnień czasowych, niezawodność, system logistyczny.

1. Introduction

In any logistic system operating under an increasingly complex and diverse system environment, there is a need to take into account the possible unreliability of logistic system elements, which may lead to decrease of the system availability level. In the maintenance and reliability theory literature, there are many studies dealing with the problem of designing reliable and available logistic support systems for repairable items performance [61]. However, most of the developed models focus only on spare parts availability (see e.g. [12, 21]) or repair facilities availability (see e.g. [1, 7, 26, 47, 56, 57]), and the problem of possible interactions, which may occur between operational system and its logistic support system is usually not analysed. At the same time, dependability analyses being carried out with the use of known models are incomplete due to the lack of assessment of interactions between both the systems being in cooperation influence on the overall functional reliability.

The article focuses on the problem of logistic support system reliability modelling with the use of Delay Time Analysis (DTA). Consequently, a literature overview, as well as the issues of time relations occurred in logistics systems are presented. In the second part of the article, the focus is on analysis of the case company, which performs maintenance and service operations of forklifts. Moreover, there is used the basic model of system inspections with the use of DTA to evaluate the reliability of operating facilities.

2. Problem of time relations in technical systems performance modelling

In the case of complex systems, where the problem of relations between two consecutive subsystems modelling occurs and influence the overall system availability, many works indicate on operational processes time delays issues.

The problem of time delays occurrence characterises many physical and technical systems and is investigated e.g. in biology, mechan-

ics or economics [29]. In the 70s Twentieth century, time delay concept *Delay Operator* was used in modelling or forecasting processes performance [9]. Later, there were papers which are aimed at time delay concept implementation in other research areas, e.g. in logistics processes performance modelling, or technical systems maintenance modelling. Review of basic research issues related to the operational systems' time relations modelling is presented in [59].

In 1976. Christer (based on [18]) proposed the delay-time concept (DTC), which is used to this day in the theory of renewal processes in order to optimize the technical system downtime connected with not detected in time failures occurrence (time between inspections optimization problem). In the delay time concept, a fault which has developed in the system becoming visible at time u from new, if an inspection is carried out at that time. If the fault is not attended to, the faulty component fails after some further interval h which is called delay time of fault (Fig. 1).

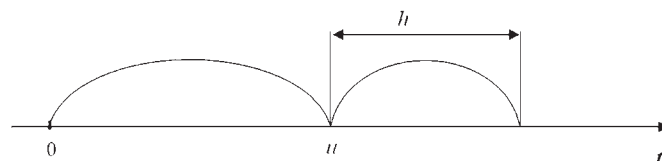


Fig. 1. Time delay conception [18]

There has been increasing effort to encourage the use of the delay-time concept in maintenance modelling of real-life systems. Many works have been carried out on the modelling of this concept to production plants (e.g. [2, 19, 36]). Moreover, well known models base on time-based preventive maintenance (e.g. [43, 53, 63]) or condition-based maintenance (e.g. [20, 40, 41, 55]). Other application areas regard to e.g. maintenance in civil engineering (e.g. [16]), or transport issues (e.g. [24, 37]).

The problem of imperfect inspections performance in technical systems is analysed e.g. in [3, 13, 15, 22, 34, 35, 44, 46, 52].

(*) Tekst artykułu w polskiej wersji językowej dostępny w elektronicznym wydaniu kwartalnika na stronie www.ein.org.pl

The main questions being investigated in such works are [15]:

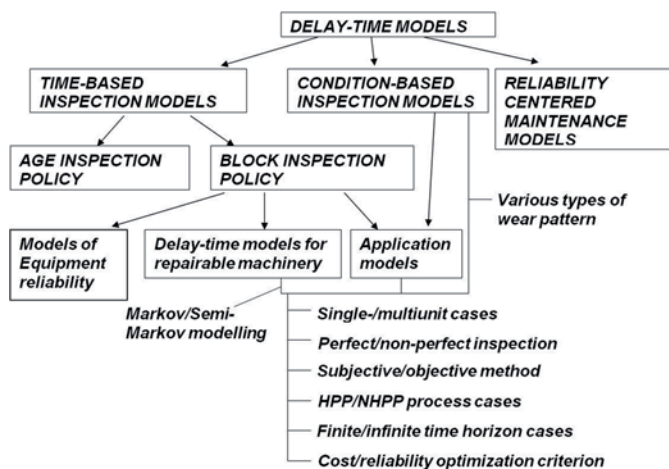
- How often vehicles should be maintained preventively or repaired/replaced?
- Is a reliability structure of a system safe?
- How often production plant should be maintained periodically?
- What is an economical and technical effectiveness of a performed maintenance?

Literature review of existing DT models can be found e.g. in [3, 4, 13, 14, 15, 17, 20, 35, 39, 44, 52] or in [31, 32, 33, 39], where the focus is on the possibilities of DT models implementation for multi-unit systems. In [30], there is presented the literature overview of single-unit systems with time delay maintenance processes modelling issues.

A literature review, in which delay-time models are investigated along with other PM models are given in [23, 27, 28, 38, 42, 48, 50].

One of the first publications which strictly investigated recent development in the delay-time modelling is given by Christer & Redmond [17]. Later, in [4] authors discuss the development of delay-time analysis as a means of modelling engineering aspects of maintenance problems. Christer in [15] reviews the recent cumulative knowledge and experience of delay time modelling from 80s and 90s Twentieth century. Author presents the basic delay-time model and discusses the main development directions including e.g. perfect/non-perfect inspection case, steady state and non-steady state conditions, or type of model's parameters estimation process.

Following these considerations, in the Fig. 2, there is presented the main classification of existing delay time models. In the presented scheme, there are defined three main groups of delay-time models according to the maintenance strategy used. First group is devoted to time-based inspection models. There, plenty of studies regard to block-replacement inspection policy, where inspection takes place



every T time units. The second group of models which deserve to be mentioned is condition- based maintenance models. There one can

Fig. 2. Classification scheme of delay-time models [39]

find models especially developed for production plant maintenance. The last group of models introduce the delay time concept in reliability centered maintenance. However, there is only few works regard to this maintenance area.

Moreover, when analysing the time relations modelling problems, there is also a necessity to investigate the issues of logistics delays occurrence during defence systems operational processes performance [45]. The main problem in this area is connected with definition how logistics processes performance delays affect unreliability (total downtime) of a military system (e.g. maintenance delay time

connected with spare parts delivery delays), and as a result, the main system dependability characteristics [60].

The presented defence approach may also be used in time analyses of production and technical systems performance, connected with [60]:

- delays occurred during operational processes performance (between consecutive operations),
- random lead times,
- spare parts availability.

The convenient example, which serves to illustrate the complexity of such problems is given in [60], where the system of systems with time resource model is developed. The model takes into account the possibility of logistic support system functional unreliability and allows for assessing the impact of logistic system failures on the overall system of systems dependability and economic characteristics.

2.1. Basic model of inspection based on the DTA implementation

One of the main inspection policy models, which are based on the DTA approach implementation, is given in [18]. The investigated simplest possible case of an inspection policy is characterized by the following assumptions:

- there is a constant time T between successive inspections which require d time units,
- inspection costs I units,
- inspections are perfect in that any defect present within the plant will be identified,
- inspections are independent of each other,
- faults are independent and arise within the technical system at a constant rate k for any inspection period,
- defects identified at an inspection will be repaired within the inspection period,
- breakdowns impose a small amount of downtime, d_b , compared to the inspection interval T and d ,
- the delay time of a fault is independent of the arrival time and has known pdf $f_h(h)$ and cdf $F_h(h)$.

For such assumptions there is possible to estimate the probability of a fault arising as a breakdown $P_b(T)$ [18]:

$$P_b(T) = \frac{1}{T} \int_0^T (T-h) f_h(h) dh \quad (1)$$

The expected downtime per unit time to be incurred operating an inspection policy of period T is given by $E_d(T)$, where [18]:

$$E_d(T) = \frac{kTd_bP_b(T) + d}{T + d} \quad (2)$$

Moreover, with average breakdown and inspection repair costs c_b and c_i respectively, the expected cost per unit time of maintaining the plant on an inspection system of period T is $C(T)$, where [18]:

$$C(T) = \frac{1}{(T+d)} \{ kT [c_bP_b(T) + c_i(1-P_b(T))] + 1 \} \quad (3)$$

Let's consider the second case, when the inspections are non-perfect. Thus, there is introduced a probability β that a specific defect will be identified at n th inspection, and a corresponding probability $(1-\beta)$ that it will not. For such an assumption the modified form of $P_b(T)$ is given by [18]:

$$P_b(T) = 1 - \left\{ \int_{y=0}^T \sum_{n=1}^{\infty} \frac{\beta}{T[(1-\beta)^{n-1}R(nT-y)]} dy \right\} \quad (4)$$

There exist many variations of the presented model, being investigated in known literature from reliability theory. Moreover, one can find few works in which the described model is used to real-life systems' reliability analysis performance. For example see [39].

3. Time relations in logistic systems performance

At the present time, in the era of competition, there is a problem of fully integration of the logistics systems in cooperation. Moreover, there is a necessity to eliminate any time delays which may influence the added value of a product [8]. Treating the supply chain disruptions as unexpected events occurrence, we can describe them as having uncertainty in supply chain operations. Uncertainty in the supply chain can be seen from different aspects, such as [51]:

- time (in the sense of duration of activity/process, starting/ending moment of activity realization, frequency of activity/demand occurrence),
- quantity (of supply, demand or physical transfer of goods),
- location/place (where activity starts/ends),
- quality (of service/products),
- cost (fluctuation, occurrence).

However, not every disruption occurrence leads to logistic system failure appearance. The critical factor which determines the logistic system failures is time. In a situation, when disruption (connected with e.g. improper delivery quality/quantity, improper location) occurs, there is a necessity to find out if we have enough time to correct the problem. When the spare time let us to remove the disruption – logistic system is not defined as failed. In other words, time redundant system has the ability to tolerate interruptions in their basic function for a specific period of time without having the negative impact on the system task performance.

Typically, the time redundant systems have a defined time resource that is larger than the time needed to perform the system total task [58]. *Time redundancy is to take additional time to complete the task (in relation to the time necessary for its execution), which can be used to restore the state of the system or improve its technical characteristics* [49, 58]. This means that the system with time resource tolerate faults with a short (usually specified) duration.

In the known literature, there is many works which investigate the problem of time redundancy (see e.g. [10, 11, 49, 58]). Moreover, taking into account the following issues [49, 58]:

- type of failure tolerance,
- type of time resource usage,
- type of time resource replenishment,

one can define the main types of time resource, which are described e.g. in [62].

The proper type of time resource choice depends on the type of modelled system, type of operational task, efficiency definition, and system's reliability structure. The main models classification of systems with time resource is given in [62].

4. Implementation of basic model of inspection based on DTA – case study

The basic DTA model implementation is analysed based on the information about operational and maintenance processes of forklifts, which are operated by considered case company [25]. The company specializes in servicing and carrying out a comprehensive overhaul of motor, diesel, gas, and electric lift trucks. It also prepares the necessary documentation for Office of Technical Inspection and supervises the maintenance processes of trucks subjected to technical inspection.

It also provides services for both, individual and businesses customers. These services encompass a full range of internal transport facilities providing and spare parts and tires supplying.

The necessary data, used in reliability analysis regard to eight years of trucks performance time period, since 2000 till 2008. The performance data include operational processes realization, repair and preventive maintenance times, types of replaced elements, and types of occurred failures. The shortest mileage of analysed forklifts is 2 800 working hours and the longest mileage is equal to 13 300 working hours.

4.1. Maintenance tasks being performed during analysed time period

In the first step of performed reliability and maintenance analysis, author gathered the data about maintenance tasks (replacing of elements, spare parts, repairs), being performed during analysed time period. The gathered information is classified into seven working groups: track frame and body, installation and electrical equipment, hydraulic circuit, lifting circuit, transmission, steering system, and brake system. In the table 1, there are presented the main maintenance tasks performed in lifting circuit during analysed time period.

The trucks inspection actions are performed according to the given operators manuals. During the inspection performance, there should be checked out if all circuits and transmission perform satisfactory, especially:

- security systems,
- forks and carriage,
- steering system,
- transmission,
- lighting system,
- signalling system,
- properness of performed maintenance actions,
- frame (in every 12 months).

Preventive maintenance actions are performed according to the trucks mileage indications. Moreover, inspections are performed after every 1000 working hours (e.g. mast, forks and axle maintenance), after every 2000 working hours (e.g. lifting system maintenance), or after every 3000 working hours (e.g. hydraulic system maintenance).

4.2. Main reliability characteristics of analysed system's elements

Electrical forklift is a repairable object, thus, it is repaired after its failure occurrence¹. Reliability analysis of forklifts has been per-

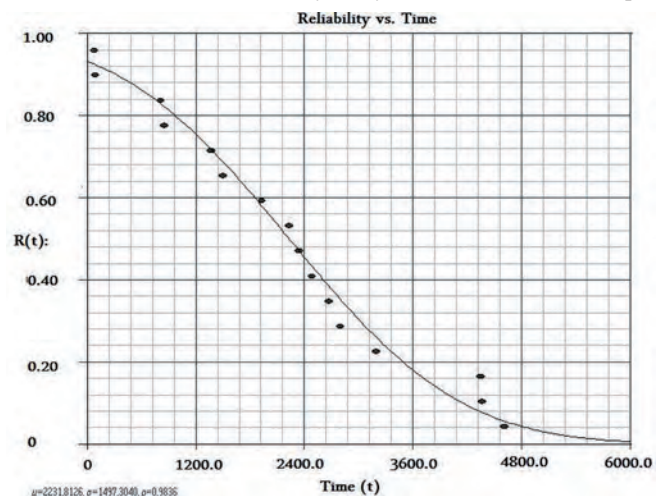
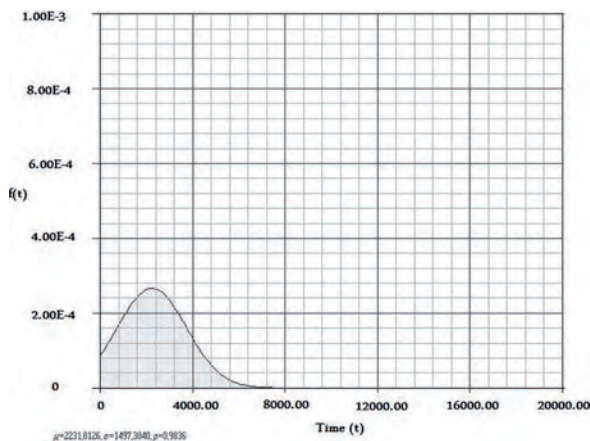


Fig. 3. The probability density function $R_1(t)$ of time to first failures for chosen trucks

¹ According to the definition given in dictionary of Operation by PNTTE, <http://www.eksplatacja.waw.pl/index.php.php?s=4000>

Table 1. Types and number of maintenance tasks being performed to provide lifting service [25]

Maintenance task	Maintenance actions' object	Number of performed maintenance actions	Maintenance task	Maintenance actions' object	Number of performed maintenance actions
replacement	mast rollers	22	repair	tilt cylinder	21
	mast support bearing	18		broken lifting chain	17
	lifting chain	18		mast rollers	14
	forks lock	14		lifting cylinder (sealing)	13
	lifting chain safety device	14		truck mast (welding, grinding)	10
	forks	12		lifting chain regulation	8
	mast roller	8		regulation of lifting and tilting functions	8
	tilt cylinder's pins	4		lifting chain's rollers cover	4
	tensioning screw	3			
	mast fixing screw	2			
	tilt cylinder	2			
	lifting cylinder	1			

Fig. 4. The probability function $f(t)$ of time between failures

formed based on the data from service manual where the information about trucks actual mileage, types and times of performed maintenance actions can be found. Thus, the obtained data of sixteen forklifts operational processes performance let author estimate the main reliability characteristics, e.g. probability distribution function of times to first failure of the chosen trucks. Moreover, there has been also the possibility to define the cumulative distribution function $F(t)$, or probability distribution function $f(t)$. The data analysis has been carried out with the use of Weibull ++ v. 6 software (distributed by ReliaSoft Co. USA), what gives the possibility to estimate e.g. probability functions of time to failure or repair time. The defined functions are a normal probability functions. The chosen reliability characteristics of analysed forklifts are given in Fig. 3–4.

4.3. Possibility of basic model of inspection implementation

The implementation of basic model of inspection based on DTA implementation and investigated in Section 2.1 needs estimation of the main model parameters:

- inspections time d is equal to 2 hours,
- downtime d_b connected with breakdowns removing equals 5.18 h (estimated as a mean repair time of all sixteen trucks in a given time period),
- total operational time of all trucks in a given time period is 131700 working hours,
- the constant rate k of fault occurrence is estimated at the level $k = 0.006363$ per hour (838 failures during analysed time period),
- MTBF equals 157 working hours, with standard deviation being equal to 381 working hours.

Taking into account the defined model parameters, the formula given in (2), when using formula (1), may be defined as:

$$E_d(T) = \frac{kT \left[\frac{1}{T} \int_0^T (T-h) f_h(h) dh \right] d_b + d}{T + d} \quad (5)$$

Substituting obtained values of model parameters into Equation (5) gives the following:

$$E_d(T) = \frac{(0.006363T) \left[\frac{1}{T} \int_0^T (T-h) f_h(h) dh \right] 5.18 + 2}{T + 2} \quad (6)$$

In the analysed model, there is also a necessity for delay time h distribution definition. This distribution function is independent on the system's elements failures occurrence and is defined by $f_h(h)$ and $F_h(h)$.

These distribution functions of delay time parameter h can be estimated using two methods, namely subjective and objective ones. In the known literature few models have been developed for these two approaches, for more information see e.g. [5, 6, 54]. The use of objective models requires a large amount of data in comparison with sur-

vey questionnaires which should reflect the operations of the analysed system over a considerable period of time.

When dealing with the analysed forklift system, there is no possibility to identify time moments u occurrence. Thus, there is no reliable information about the most appropriate distribution function for h parameter. As a result, there is a necessity to study different *pdf* functions of delay-time. In the article, author focuses on the exponential case, for which the distribution for the delay time is given by:

$$f_h(h) = ke^{-kh} \quad (7)$$

Substituting formula (7) into Equation (6) to obtain an expression for the downtime will give:

$$E_d(T) = \frac{(0,006363T) \left[\frac{1}{T} \int_0^T (T-h)ke^{-kh} dh \right] 5,18 + 2}{T + 2} \quad (8)$$

Taking into account the average failure rate k (in analysed case $k = 0.006363$) in the equation (8), there was possible to obtain results shown in Figure 5.

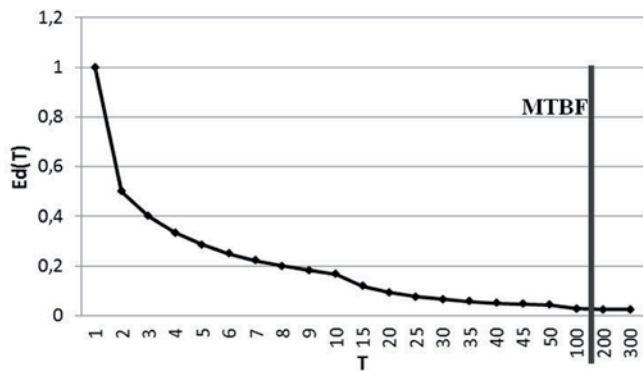


Fig. 5. Function $E_d(T)$ when using exponential distribution for delay time h

According to the Fig. 5, clearly can be seen that the function of the expected downtime stabilizes around the estimated value of MTBF. At the same time, the question arises which model parameters and how they affect the research results. Thus, there should be carried out the model sensitivity analysis. Moreover, it should be analysed the influence of various probability distribution functions of random variable h on the function $E_d(T)$. These issues will be also the subject of author's further research.

5. Summary

The use of inspection models based on DTA implementation and proper preventive maintenance system can be used to minimize the technical system downtime connected with undetected defects or damage occurrence. The article focuses on the application of one of the first inspection models based on DTA to analyse the system of forklifts performance. However, unfortunately the used model requires consideration of a number of simplifying assumptions that cannot always be met in practice. Firstly, the inspection actions are not always perfect, which means that not all occurred defects are identified during the inspection process performance. The second assumption, which is usually not fulfilled in practice regards to constant failure rate k .

Last and the most important problem is connected with the time delay h parameter estimation process. Usually, there is no relevant data that allow, with the use of mathematical functions, to estimate this random variable. This means, that there is no possibility to unambiguously determine the period T between system inspection actions performance. At the same time, it is expected that the combination of modeling based on DTA implementation and preventive maintenance tasks investigation may guarantee the expected number of undetected faults at the level of 5–10% (depending on the chosen probability distribution).

In order to determine whether the analysed inspection model which bases on DTA implementation is suitable for analysed system of sixteen forklifts dependability characteristics estimation, the input data should be complemented. The additional data gathering process should allow to define the time delay parameter and its probabilistic characteristics in more precise way.

References

1. Agrafiotis G. K., Tsoukalas M. Z. Reliability analysis and optimization applications of a two-unit standby redundant system with spare units. *Microelectronics Reliability* 1994; 34(9): 1469-1475.
2. Akbarov A., Christer A. H., Wang W. Problem identification in maintenance modelling: a case study. *International Journal of Production Research* 2008; 46(4): 1031-1046.
3. Alzubaidi, H. J. Maintenance modelling of a major hospital complex. PhD thesis. Salford: University of Salford, 1993.
4. Baker R. D., Christer A. H. Review of delay-time OR modelling of engineering aspects of maintenance. *European Journal of Operational Research* 1994; 73: 407-422.
5. Baker R. D., Wang W. Developing and testing the delay time model. *Journal of the Operational Research Society* 1993; 44: 361-374.
6. Baker R. D., Wang W. Estimating the delay time distribution of faults in repairable machinery for failure data. *IMA Journal of Mathematical Application in Business and Industry* 1992; 3: 259-282.
7. Barron Y., Frostig E., Levikson B. Analysis of R out of N systems with several repairmen, exponential life times & phase type repair times: An algorithmic approach. *European Journal of Operational Research* 2006; 169: 202-225.
8. Bogataj L., Bogataj M. The study of optimal additional investments in capabilities for reduction of delays in value chain. *International Journal of Production Economics* 2007; 108: 281-290.
9. Box G. E. P., Jenkins G. M. *Time Series Analysis Forecasting and Control*, California: Holden-Day, 1976.
10. Caban D., Maciejewski H. Time redundancy in a transportation logistics system. *Advances in safety and reliability. Proc. of the European Safety and Reliability Conference ESREL 2005, Tri City, Vol.1/ed. Kołowrocki K., Leigden: A. A. Balkema, 2005: 293-296.*
11. Caban D., Maciejewski H. Niezawodność systemów ze skumulowaną rezerwą czasową. *Materiały XXXI Zimowej Szkoły Niezawodności*, Radom: Instytut Technologii Eksploatacji, 2004: 74-80.
12. Catuneanu V. M., Moldovan C., Poptin, Fl., Gheorghin M. Optimum system availability and spare allocation. *Microelectronic Reliability* 1988; 28(3): 353-357.

13. Cho I. D., Parlar M. A survey of maintenance models for multi-unit systems. *European Journal of Operational Research* 1991; 51: 1-23.
14. Christer A. H. A Review of Delay Time Analysis for Modelling Plant Maintenance. in: *Stochastic Models in Reliability and Maintenance*, Osaki S. (ed.), Springer, 2002.
15. Christer A. H. Developments in delay time analysis for modelling plant maintenance. *Journal of the Operational Research Society* 1999; 50: 1120-1137.
16. Christer A. H. Modelling inspection policies for building maintenance. *Journal of the Operational Research Society* 1982; 33: 723-732.
17. Christer A. H., Redmond D. F. A recent mathematical development in maintenance theory. *IMA Journal of Mathematics Applied in Business and Industry* 1990; 2: 97-108.
18. Christer A. H., Waller W. M. Delay time models of industrial inspection maintenance problems. *Journal of the Operational Research Society* 1984; 35(3): 401-406.
19. Christer A. H., Wang W., Baker R. D. Sharp J.M. Modelling maintenance practice of production plant using the delay-time concept. *IMA Journal of Mathematics applied in Business and Industry* 1995; 6: 67-83.
20. Christer A. H., Wang W. A model of condition monitoring of a production plant. *International Journal of Production Research* 1992; 30(9): 2199-2211.
21. Coughlin R. J., Optimization for spares in a maintenance scenario. *Proceedings of Annual Reliability and Maintainability Symposium* 1984: 371-376.
22. Das, A. N., Sarmah, S. P. Preventive replacement models: an overview and their application in process industries. *European Journal of Industrial Engineering* 2010; 4(3): 280-307.
23. Dekker, R., Scarf, P. A. On the impact of optimisation models in maintenance decision making: the state of the art. *Reliability Engineering and System Safety* 1998; 60: 111-119.
24. Desa M. I., Christer A. H. Modelling in the absence of data: a case study of fleet maintenance in a developing country. *Journal of the Operational Research Society* 2001; 52: 247-260.
25. Dziurkowski P. Pomiar niezawodności elektrycznego wózka podnośnikowego X, Praca magisterska Wydziału Mechanicznego PWr. (niepublikowana), Wrocław, 2009.
26. Gross D., Pinkus C. E. Designing a support system for repairable items. *Computers & Operations Research* 1979; 6(2): 59-68.
27. Guo R., Ascher H., Love E. Towards practical and synthetical modelling of repairable systems. *Economic Quality Control* 2001; 16(2): 147-182.
28. Guo R., Ascher H., Love E. Generalized models of repairable systems a survey via stochastic processes formalism. *ORiON* 2000; 16(2): 87-128.
29. Hennes J.-C., Tarbouriech S. Stability conditions of constrained delay systems via positive invariance. *International Journal of Robust and Nonlinear Control* 1998; 8: 265-278.
30. Jodejko-Pietruczuk, A., Werbińska-Wojciechowska, S. Time between inspections optimization for technical object with time delay. *Journal of Polish Safety and Reliability Association Summer Safety and Reliability Seminars* 2013; 4(1): 35-41.
31. Jodejko-Pietruczuk, A., Werbińska-Wojciechowska, S. A delay-time model with imperfect inspections for multi-unit systems. *Journal of KONBiN* 2012; 3: 157-172.
32. Jodejko-Pietruczuk, A., Werbińska-Wojciechowska, S. Economical effectiveness of Delay Time approach using in Time-Based maintenance modelling, *Proc. of PSAM 11 & ESREL 2012 Conference*, 25-29 June 2012, Helsinki, Finland.
33. Jodejko-Pietruczuk, A., Werbińska-Wojciechowska, S. Analysis of Block-Inspection Policy parameters from economical and availability point of view. *Proc. of PSAM 11 & ESREL 2012 Conference*, 25-29 June 2012, Helsinki, Finland.
34. Kobbacy, K. A. H., Murthy D. N. P. *Complex System Maintenance Handbook*. Springer, 2008.
35. Lee, Ch. Applications of Delay Time Theory to Maintenance Practice of Complex Plant. PhD thesis. Salford: University of Salford, 1999.
36. LV, W., Wang, W. Modelling preventive maintenance based on the delay time concept in the context of a case study. *Eksplotacja i Niezawodność-Maintenance and Reliability* 2011; 3: 5-11.
37. Mabini M. C., Christer A. H. Controlling multi-indenture repairable inventories of multiple aircraft parts. *Journal of the Operational Research Society* 2002; 53: 1297-1307.
38. Mazzuchi T. A., van Noortwijk J. M., Kallen M. J. Maintenance optimization. Technical Report TR-2007-9, 2007.
39. Nowakowski T., Werbińska-Wojciechowska S. Developments of time dependencies modeling concepts. *Proc. of the European Safety and Reliability Conference, ESREL 2011*, Troyes, France, 18-22 September 2011, Leiden: CRC Press/Balkema, 2012: 832-838.
40. Okumura S. An Inspection Policy for Deteriorating Processes Using Delay-Time Concept. *International Transactions in Operational Research* 1997; 4(5-6): 365-375.
41. Okumura S., Jardine A. K. S., Yamashina, H. An inspection policy for a deteriorating single-unit system characterized by a delay-time model. *International Journal of Production Research* 1996; 34(9): 2441-2460.
42. Ozekici S. (ed.). *Reliability and Maintenance of Complex Systems*. NATO ASI Series, Series F: Computer and Systems Sciences, 154, Springer, 1996.
43. Pillay A., Wang J., Wall A. D. A maintenance study of fishing vessel equipment using delay-time analysis. *Journal of Quality in Maintenance Engineering* 2001; 7(2): 118-127.
44. Redmond, D. F. Delay Time Analysis in Maintenance. PhD thesis. Salford: University of Salford, 1997.
45. SadanandaUpadhya K., Srinivasan N. K. Availability of weapon systems with multiple failures and logistic delays. *International Journals of Quality and Reliability Management* 2003; 20(7): 836-846.
46. Sarkar A., Panja S. Ch., Sarkar B. Survey of maintenance policies for the Last 50 Years. *International Journal of Software Engineering and Applications* 2011; 2(3): 130-148.
47. Subramanian R., Natarajan R. An n-unit standby redundant system with r repair facilities and preventive maintenance. *Microelectronics Reliability* 1982; 22(3): 367-377.
48. Thomas L.C., Gaver D.P., Jacobs P.A. Inspection models and their application. *IMA Journal of Mathematics Applied in Business & Industry* 1991; 3: 283-303.

49. Ushakow I. Handbook of reliability engineering, New York: Wiley, 1994.
50. Valdez-Flores C., Feldman R. A survey of preventive maintenance models for stochastically deteriorating single-unit systems. *Naval Research Logistics* 1989; 36: 419-446.
51. Vljajic J. V., van der Vorst J. G. A. J., Hendrix E. M. T. Food supply chain network robustness – A literature review and research agenda. *Proc. of the International Conference on Management in Agrifood Chains and Networks*, 2008. Wageningen, the Netherlands, 2008.
52. Wang W. An overview of the recent advances in delay-time-based maintenance modeling. *Reliability Engineering and System Safety* 2012; 106: 165-178.
53. Wang W. Modeling planned maintenance with non-homogeneous defect arrivals and variable probability of defect identification. *Eksploracja i Niezawodnosc-Maintenance and Reliability* 2010; 2: 73-78.
54. Wang W. Subjective estimation of delay-time distribution in maintenance modelling. *European Journal of Operational Research* 1997; 99(3): 511-529.
55. Wang W., Christer A. H. Towards a general condition based maintenance model for a stochastic dynamic system. *Journal of the Operational Research Society* 2000; 51: 145-155.
56. Wang K-H., Hsieh Y. Reliability of a repairable system with spares and a removable repairman. *Microelectronics Reliability* 1995; 35(2): 197-208.
57. Wang K-H., Sivazlian B. D. Reliability of a system with warm standbys and repairmen. *Microelectronics Reliability* 1989; 29(5): 849-860.
58. Ważyńska-Fiok K., Jaźwiński J. *Niezawodność systemów technicznych*. Warszawa: PWN, 1990.
59. Werbińska-Wojciechowska S. Time dependencies in supply chain performance process. *Logistics and Transport* 2010; 1: 113-121.
60. Werbińska S. Model logistycznego wsparcia systemu eksploatacji środków transportu. *Rozprawa doktorska Wydziału Mechanicznego PWr.*, Wrocław: 2008.
61. Werbińska S. Model niezawodności systemu wsparcia logistycznego z zależnością czasową. *Logistyka* 2007; 3.
62. Werbińska S. Interactions between logistic and operational system – an availability model. In: *Risk, reliability and societal safety*. Eds Aven T., Vinnem J. E., Vol. 2, Leiden: Taylor and Francis, 2007: 2045-2052.
63. Zhao, J., Jia, X. An optimal policy of inspection for a component with delayed repair. *Eksploracja i Niezawodnosc-Maintenance and Reliability* 2009; 3: 20-23.

Sylwia WERBIŃSKA-WOJCIECHOWSKA, Ph.D. (Eng.)

Faculty of Mechanical Engineering

Institute of Machine Design and Operation

Wrocław University of Technology

Wybrzeże Wyspiańskiego 27, 50-370, Wrocław, Poland

e-mail: sylwia.werbinska@pwr.wroc.pl

František GREŠKOVIČ
Ľudmila DULEBOVÁ
Branislav DULEBA
Aneta KRZYŻAK

CRITERIA OF MAINTENANCE FOR ASSESSING THE SUITABILITY OF ALUMINUM ALLOYS FOR THE PRODUCTION OF INTERCHANGEABLE PARTS INJECTION MOLD

EKSPLOATACYJNE KRYTERIA OCENY PRZYDATNOŚCI STOPÓW ALUMINIUM DO PRODUKCJI WYMIENNYCH CZĘŚCI FORM WTRYSKOWYCH*

With increasing production of plastics crop up also the need to improve their processing abilities. New methods and materials in the construction of forms are examined. Low weight and easy machinability predestines aluminium alloys for use as a material for the production of injection moulds for manufacturing of small series production. The paper deals with the verification of the suitability for selected aluminium alloys for the production of mould inserts based on problem, which occurred at real injection mould used for small series production. Massive wear of material at contact of ejector pin made from 1.1203 and insert made of Al-alloy caused deformations at final moulding. At next experiments were four types of Al alloys used. At following materials hardness and wear of materials was evaluated. To simulate the adhesive wear of friction pairs 1.1203 - Al alloy with and without greasing was adhesive wear test machine AMSLER used with simulation of surface contact. Wear intensity was evaluated by the coefficient of friction.

Keywords: injection mould, aluminum alloy, friction pairs, adhesive wear, friction coefficient.

Z powodu zwiększenia produkcji różnorodnych elementów z tworzyw polimerowych zauważana jest konieczność poprawiania procesów przetwórczych, w tym konstrukcji maszyn i narzędzi do ich przetwórstwa. Dlatego badane są nowe metody i materiały w budowie form używanych w procesie wtryskiwania. Niska waga i dobra obrabialność stopów aluminium sprawiają, że materiały te są chętnie stosowane w produkcji form wtryskowych do produkcji małoseryjnej. Artykuł dotyczy weryfikacji przydatności wybranych stopów aluminium do produkcji wymiennych części form wtryskowych pod kątem zapewnienia jak najdłuższej prawidłowej eksploatacji narzędzi. Zagadnienie przedstawione w artykule dotyczy rzeczywistych problemów, które wystąpiły w formach wtryskowych stosowanych do produkcji krótkich serii. Występujące znaczne zużycie materiału na styku wypychacza wykonanego ze stali 1.1203 i części formy wykonanej ze stopów aluminium, oraz deformacje stopu aluminium wpływają na jakość przedmiotów produkowanych z tworzyw polimerowych. W kolejnych eksperymentach przetestowano cztery rodzaje stopów Al. Wyznaczono twardość materiałów i zużycie ściernie. Aby symulować współpracę węzłów tarcia 1.1203 – Al przeprowadzono testy z i bez użycia środka smarowego za pomocą urządzenia AMSLER.

Słowa kluczowe: wtryskiwanie, stopy aluminium, pary cierne, zużycie adhezyjne, współczynnik tarcia.

1. Introduction

The growing demand for tools for plastics processing intense the development of new types of plastics, as well as the rapid development of manufacturing, in particular, their application in various sectors of industrial activity. Of particular importance is that the production of elements of polymeric and the associated need for producing a growing number of tools for shape them is a significant factor in the various sectors of industrial activity.

The design of tools for forming the metal and plastics is one of the most challenging and difficult areas of engineering. Among most constructional and technologically sophisticated tools are included tools for deep drawing of sheets, tools for aluminium pressure forming and tools for plastic injection moulding – injection moulds [4, 7].

Moulds are complicated technical devices that must withstand high pressure, must provide high mouldings pressure while maintaining the precision cooperate of the various parts of the mould. Correctly constructed mould must ensure high repeatability of dimensional manufactured of elements, including mutually perpendicular planes forming, while allowing easy removal products or mouldings, from the

mould. Injection moulds work automatically. Design forms and methods of production are therefore a large field of knowledge and creation of new forms of injection involves significant financial costs.

Due to the high hydraulic pressure prevailing in the hydraulic system responsible for the correct operation of the mould, which translates into a much higher pressure in the mould cavity at injection mould, very important is quality of workmanship of the mould. Various maintenance conditions of the mould, under high load may cause deformation of the mould, when they are improperly designed [3, 5]. In order to ensure long-term and reliable maintenance of the mould, it is important to correct the submission of a few technical aspects such as mould design, selection of materials for its production intended for particular types of polymer materials and the optimization of processing conditions [2, 11, 15].

Moulds consist of functional and auxiliary parts. Each of these parts is manufactured with high precision, which is reflected in their cost. The material used in the manufacture of injection moulds must meet the required operating conditions, including temperature, pressure and abrasion resistance. The temperature of thermoplastic mate-

(*) Tekst artykułu w polskiej wersji językowej dostępny w elektronicznym wydaniu kwartalnika na stronie www.ein.org.pl

rial witch flowing into the mould die during the injection moulding process is very diverse. Depending on the type of material generally ranges between 120 and 300°C. The increased temperature and high pressure on the mold material, make it necessary to determine the abrasion resistance of the mold functional unit. This is particularly important in the processing of polymeric composites having a reinforcement material of high abrasive, e.g. quartz, graphite or other hard materials [12, 6, 10].

2. Non-ferrous materials used in the manufacturing of injection molds

For the production of moulds and its parts is the most commonly used tool steel, structural carbon steel and alloy steel. Nowadays are more and more non-ferrous materials used in the production of injection moulds [8]. The main reason for growing interest on the use of these materials is the pressure from the market to improve product quality and shorten production times [5, 12].

Non-ferrous metals, especially copper alloys and aluminium alloys are capable by its high conductivity to meet requirements for the production of these forms [13]. Non-ferrous materials also found their use in pre-production stages such as materials for moulds for small series production. These prototype forms become the subject of tests that will provide the necessary information for planning of their manufacturing and maintenance [6, 9, 12].

3. The problem and aim of the research

Figure 1 shows the portion of functional the injection mould, the insert forming the a casting cavity. Presented insert before the final surface treatment. The shaped insert is produced, as a part, to quickly modify casting cavity of injection mould. Replacement of only one part of the mold allows for a quick regulating the production of various elements in small series. You can easily verify the technology of production and change the parameters for injection molding. The choice of material for the production shown in Figure 1a shaped inserts based on the following assumptions: easy mechanical processing of the material and to determine future production batches of a small series of no more than 1,000. Based on these principles to produce inserts for injection mould selected material EN AW-1100.

Injection mold, with produced insert constructionally suited to the location of the die of plasticizing unit injection was mounted in the injection moulding tool arrangement at injection moulding machine Demag 25–80. For whole mould only one ejector pin was needed, located at the centre of the mould opposite to inlet. Ejector pin is responsible for the removal of the moulding from the mould cavity after the end of the injection cycle. Such prepared form has been tested consisting in the operation of the injection mould inserts by performing the injection moulding process.

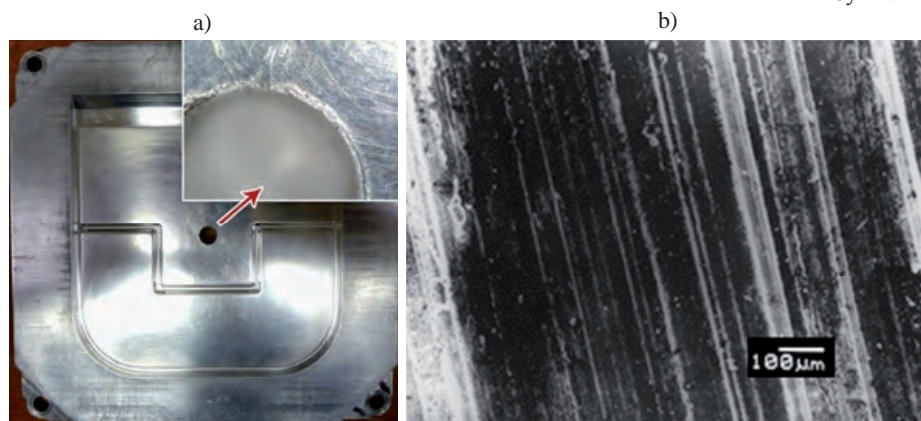


Fig. 1. Insert for injection molding with highlighted damaged surface

After production of the first batch of 100 cycles was considerable surface wear (inequalities and distortions) in place of contact of cavity and ejector from steel 1.1203. By analysis of the problem it was found that the material for the production of the cavity shape is insufficient for the resistance to the injection pressure, and by the contact with ejector material was breakaway. These micro-cracks consequently caused small deformations. These microcracks as a consequence, the continued operation of the mold, resulted in a small distortion of the material consisting of the formation of defects in the material due to wear and plastic deformation in some cases (Fig. 1b).

The aim of experiment was to the identify suitable material for the production of shaped inserts for injection moulds for small series production and comparison with previously used materials EN AW-1100. The suitable material would show better properties, including, inter alia, less wear direct influence on the stability of the mould insert parts.

Process of experiments: determination of the chemical composition of selected materials, comparison of material hardness and comparison of adhesive wear of friction pairs 1.1203 alloy with and without greasing.

Based on these findings, we will be able to identify material that will be quickly and easily machinable, but also suitable for the production of shaped cavities for experimental injection moulds for small series of plastic mouldings. The study will also estimate whether the material can be quickly and relatively easy to process on metal working machines.

4. Experimental part

4.1. The material and experimental methodology

The aim of experiments was to verify the suitability of selected aluminium alloys for the production of shaped inserts for injection forms. Operation in production does not exceed 1,000 pieces moulded of polymeric materials. Based on the experiments, the process of adhesive wear of form parts will be analyze, which effect is closest to wear in these devices and in operating conditions and their suitability for use in maintenance during production process.

Four types of aluminium alloys were used for experiments (chemical composition of this materials are in table 1):

- Alloy Al 324.0 – this type of alloy is used in the production of aluminium parts for automotive engines – marked A.
- Alloy Al 324.1 – composition is similar to alloy A. It differ by amount of alloying addition of Mn, which was reduced in the process of burn-casting up to 0.4%, and higher contents of Zn up to 12% – marked B.
- Alloy EN AB 43500 is alloy with good weld ability. Used for complex, medium-loaded casts like engine parts, compressor parts and so on – marked C.
- Alloy EN AW-1100 is the composition jest kompozycją with the highest content of aluminum over other materials. Aluminium content is 98.5%, which makes this material soft – marked D.

To determine the suitability of these materials, which satisfy the conditions of maintenance, for use in the manufacturing of parts for experimental moulds were done following experiments:

- Vickers hardness measurement,
- adhesive wear test without lubrication,
- adhesive wear test using lubrication.

Studies to determine adhesive wear of the material was carried out on samples of said friction material in the pairs of a disc-shaped counterbody. Friction roll has a 36 mm diameter and thickness of 10 mm (hardened steel

Table 1. Chemical composition of tested materials

Tested material	Contents of elements in materials in [%]											
	Al	Cu	Mg	Si	Fe	Mn	Ni	Zn	Pb	Sn	Ti	Cr
A – Al 324.0	89.2	0.740	0.295	7.76	0.444	0.668	0.010	1.260	0.038	0.011	0.018	0.010
B – Al 324.1	77.0	0.466	0.449	8.27	0.415	0.420	0.015	1.273	0.023	0.010	0.019	0.007
C – EN AB 43500	88.6	0.029	0.442	10.32	0.287	0.138	0.010	0.065	0.012	0.007	0.004	0.007
D – EN AW-1100	98.5	0.121	0.034	0.88	0.219	0.008	0.010	0.172	0.029	0.009	0.006	0.008

1.1203). The samples was made at the shape of flat splice plate, measuring 20x15x9 mm and made from tested Al alloys

Tribological properties of friction pairs tested were evaluated by measuring the shear friction coefficient, which was calculated from the friction torque [14]. The values of friction torque were recorded. Slip friction was evaluated according to time. The principle of the test is shown on Figure 2.

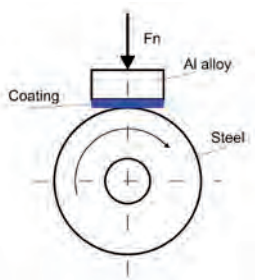


Fig. 2. Test principle of adhesive wear test

Based on the graphical representation, the friction torque was evaluated by the contact force and the disk radius and shear coefficient of friction at the base of the relationship [1]:

$$M_T = r F_T \quad (1)$$

$$\mu = F_T / F_N \quad (2)$$

where: M_T – friction torque [Nm], r – radius of the disk [m], F_T – friction force [N], F_N – contact force [N], μ – coefficient of friction shear.

Mounting of friction roll and mating was regulated to pressure in the contact area by compressing the spring by force of 50 kN. Steel roll made of steel was rotating at speed 200 min⁻¹. Deduction interval of friction torque was chosen according to the total time adequately to complete testing of samples depending on the timing of mating seizure of samples. For test of adhesive wear test machine AMSLER was used with surface contact, which allows testing of friction pairs

Friction tests were carried out with and without grease and as lubricant motor oil Madit M2T was used. Oil was applied in a thin layer with a brush on the surfaces of the sample. The whole surface of the sample was covered with a thin layer of oil.

4.2. Discussion of measured results

4.2.1. Evaluation of hardness of tested materials

Hardness of the tested samples was measured according to Vickers measuring method – HV 10 and the results are shown in Figure 3.

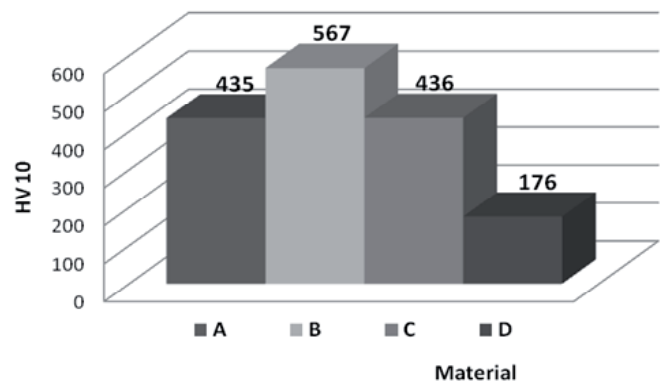


Fig. 3. Comparison of hardness of Al alloys

4.2.2. Evaluation of adhesive wear of friction pair metal – Al alloy

Friction pair: 1.1203 – Al 324.0 (sample A)

Crowding of material was observed during the test of adhesive wear without greasing - plastic displacement in the direction of the friction roll. Traces of the adhesive wear were also visible at the surface. They expressed themselves as transferred parts of material from the samples to surface of friction roll. Material transferred to the roll but also cause abrasive wear marks, showed as scratches. Sample A.1 seized after 17 seconds without greasing. Slip of sample with fixture occurred after seizure of sample.

During the test of adhesive wear with lubrication the duration to seizure several times extended. The results of friction torque, friction coefficient and the time intervals of data input are shown in Table 2. Figure 4 shows the progress of friction torque in dependence on time for samples with and without lubrication till seizing of samples. The sample and also friction roll have traces of abrasive wear, accrued as a result of interaction of ripped particles from the sample and adhering to roll. Duration of experiment until seizing was 58 minutes. Friction roll and the sample was exposed to high temperature generated by friction and it accelerated the process of ripping the particles from sample and its adhering to roll. These connections during the test caused abrasive wear of friction roll as well as its counterpart in the friction pair.

Friction pair: 1.1203 – Al 324.1 (sample B)

When measuring the friction torque without greasing the traces of abrasive wear were observed on sample caused by the rapture of the material from sample and sticking to the roll. In terms of tribology, we can say that this is a tearing mechanism. Interval till seizing of samples was 83 seconds. Slip of sample with fixture occurred after seizure of sample.

By measuring the friction torque using greasing the duration to seizure several times extended. On the sample surface are visible scratches incurred as a result of plastic displacement and scaly marks caused by delamination. Adhesive wear was also accompanied by abrasive wear. Abrasion was caused by material stuck to roll through

Table 2. The measured values of friction pair steel – material A with lubricant

Material	Values of friction torque M [N.m] and friction coefficient μ on time [sec]									
	1000 [sec]		4000 [sec]		4650 [sec]		4750 [sec]		5130 [sec]	
	M	μ	M	μ	M	μ	M	μ	M	μ
A.1	12	0.13	23	0.25	33	0.37	53	0.59	73	0.81
A.2	15	0.17	20	0.22	40	0.44	61	0.68	79	0.89
A.3	11	0.12	18	0.20	18	0.20	50	0.56	70	0.78

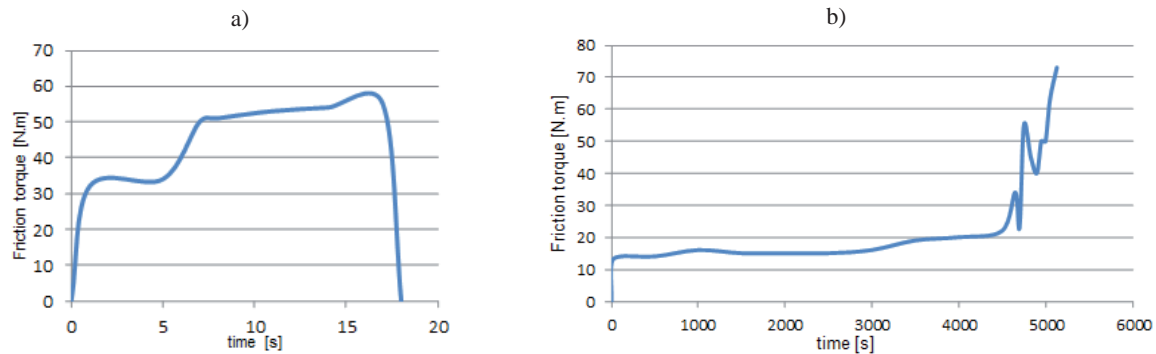


Fig. 4. Curve of friction torque vs. time- sample A.1 a) without lubrication , b) with lubrication

micro joints between roll and material samples. By creation of micro joints ripping of material from sample was observed.

The results of friction torque, friction coefficient and the time intervals of data input are shown in Table 3. Figure 5 shows the progress of friction torque in dependence on time for samples with and without lubrication till seizing of samples.

Friction pair: 1.1203 – EN AB 43500 (sample C)

Interval till seizing of samples without lubrication was 20 seconds. After seizing of sample adhesive wear occurred a consistent delamination of surface of sample. On friction roll particles transferred from sample were found.

During the test of adhesive wear with lubrication the duration to seizure several times extended. On sample was visible delamination and sideways displacement of material - plastic crowd-out effect. Material was not sticking to the friction roll. The test material was torn

off in the form of small swarf. Swarf immediately after breakaway falls off and further wasn't being stuck to friction roll.

The results of friction torque, friction coefficient and the time intervals of data input are shown in Table 4. Figure 6 shows the progress of friction torque in dependence on time for samples with and without lubrication till seizing of samples.

Friction pair: 1.1203 – EN AW-1100 (material D)

Interval till seizing of samples without lubrication was 6 seconds. Due to the low hardness of the material plastic displacement occurred almost immediately after starting the device and seizing of sample went through strong Van der Waals forces.

By measuring the friction torque using greasing the duration to seizure several times extended. Clearly visible delamination of surface with flaking particles of lamellar shape was observed on surface. The material was crowding out the sides and after loss of plastic abil-

Table 3. The measured values of friction pair steel – material B with lubricant

Material	Values of friction torque M [N.m] and friction coefficient μ on time [sec]									
	50 [sec]		100 [sec]		250 [sec]		350 [sec]		446 [sec]	
	M	μ	M	μ	M	μ	M	μ	M	μ
B.1	25	0.28	30	0.33	43	0.48	47	0.52	69	0.76
B.2	20	0.22	32	0.35	39	0.43	50	0.56	67	0.74
B.3	27	0.30	29	0.32	34	0.38	52	0.58	63	0.70

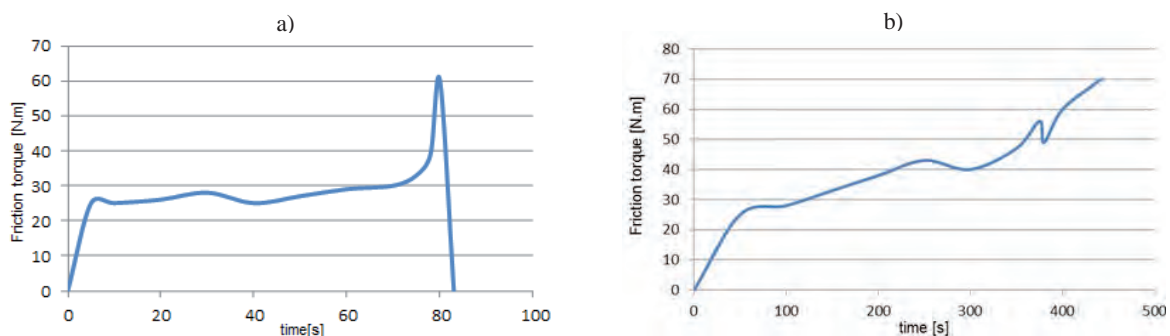


Fig. 5. Curve of friction torque vs. time – samples B.1 a) without lubrication , b) with lubrication

Table 4. The measured values of friction pair steel – material C with lubricant

Material	Values of friction torque M [N.m] and friction coefficient μ on time [sec]									
	500 [sec]		2000 [sec]		3500 [sec]		4250 [sec]		4790 [sec]	
	M	μ	M	μ	M	μ	M	μ	M	μ
C.1	18	0.20	17	0.19	23	0.26	28	0.31	72	0.80
C.2	15	0.17	20	0.2	32	0.36	38	0.42	65	0.72
C.3	12	0.13	15	0.17	26	0.29	25	0.28	60	0.67

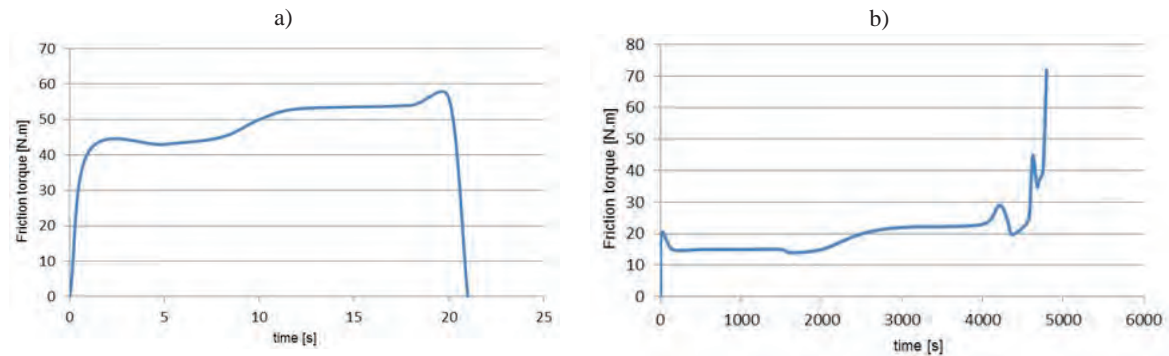


Fig. 6. Curve of friction torque vs. time- samples C.1 a) without lubrication, b) with lubrication

Table 5. The measured values of friction pair steel – material D with lubricant

Material	Values of friction torque M [N.m] and friction coefficient μ on time [sec]									
	30 [sec]		55 [sec]		80 [sec]		130 [sec]		180 [sec]	
	M	μ	M	μ	M	μ	M	μ	M	μ
D.1	27	0.30	30	0.33	32	0.35	35	0.39	64	0.71
D.2	25	0.28	32	0.35	35	0.39	38	0.42	67	0.74
D.3	20	0.22	29	0.32	29	0.32	37	0.41	62	0.69

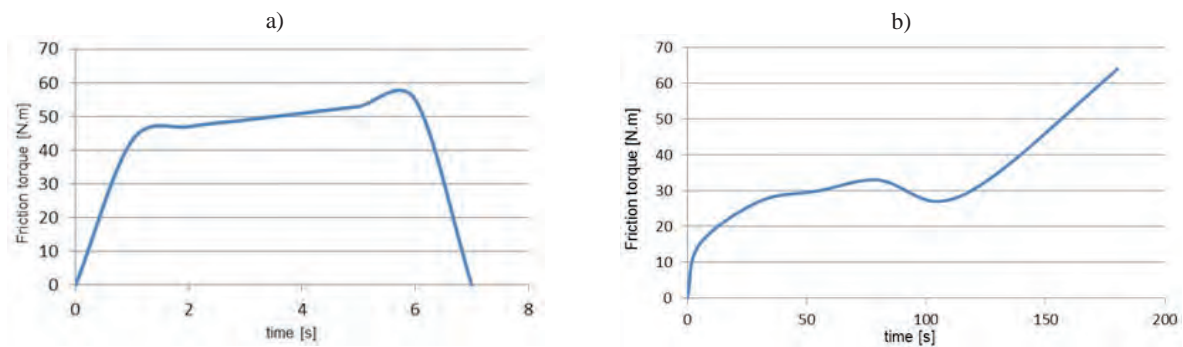
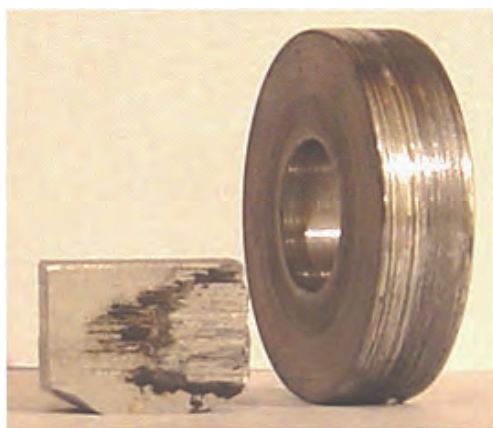
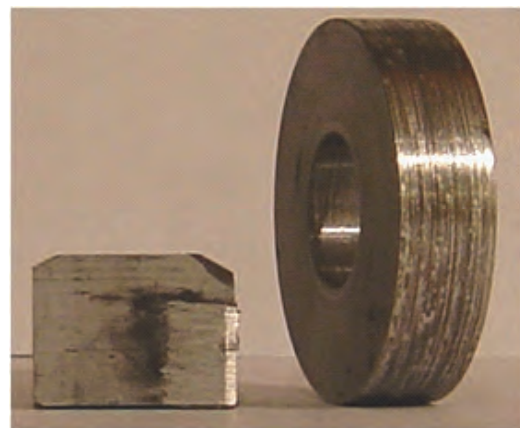


Fig. 7. Curve of friction torque vs. time – sample D.1 a) without lubrication, b) with lubrication



Material A



Material B

Fig. 8. Tested materials after wearing test

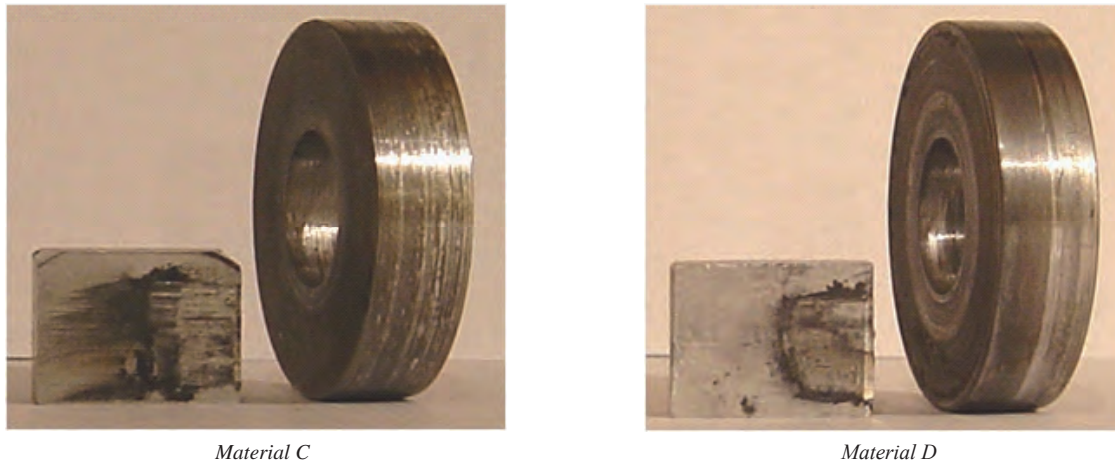


Fig. 8. Tested materials after wearing test

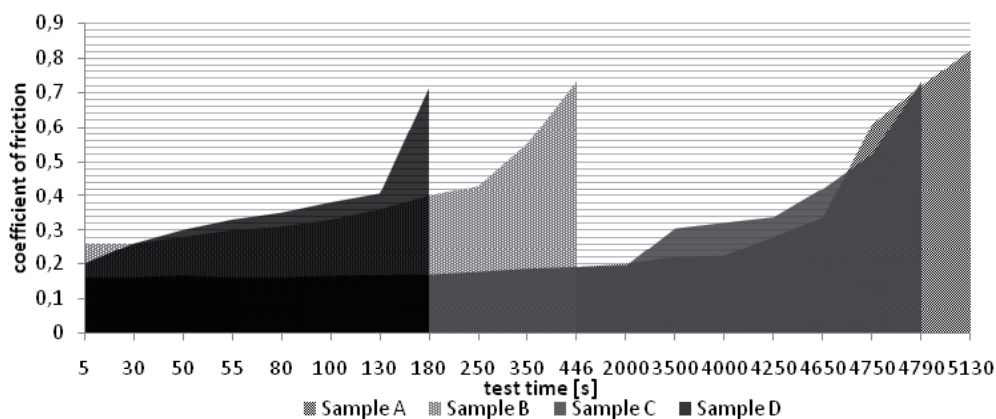


Fig. 9. The progress of the friction coefficient in dependence on the time

ity the disrupt of surface integrity began. There was no visible wear on the surface of roll.

The results of friction torque, friction coefficient and the time intervals of data input are shown in Table 5. Figure 7 shows the progress of friction torque in dependence on time for samples with and without lubrication till seizing of samples.

5. Conclusion

The experiments showed that at design of parts for injection moulds from on-ferrous materials (aluminium) are necessary to consider the properties of the alloy.

Based on the performed tests, we came to the following conclusions:

- Pure aluminium had not sufficient properties for a given application, as shown by tests on material EN AW-1100 (material D), which contained up to 98% aluminium. The time until the sample seized and the type of wear and tear, which occurred during the tests, indicate that the high-purity alloys are not suitable for the production of structural parts of the mould by mutual their movement relative to each other during the maintenance of the form.
- Al 324.1 alloy (material B) behaved at friction test better than material EN AW-1100, but the times to seizure and friction co-

efficient values show that even this alloy is not suitable for use in the manufacturing of moulds. Material contained large amounts of zinc, what caused great hardness of alloy in comparison with other studied alloys – up to 567 HV

- Alloys Al 324.0 and Al 324.0 (material A, C) after tests appeared to be most favorable for the production of parts for forms in terms of maintenance conditions. The optimal composition of the alloy guarantees sufficient operation time.
- The model test results showed that for the production of shaped parts of the mould is the most suitable tested alloy material B (stop Al 324.1). At the end of experiment, the material reached the highest coefficient of friction, the material seized after the longest time of maintenance. In practice, mould parts are not stressed to such an extreme way as samples at model test. Greasing is often permanently secured.

The aim of the experiment was to verify and confirm the practical choice of the most suitable non-ferrous materials from the supplied range of materials for the production of shaped parts of injection moulds. These materials can be used in the production of moulded parts of injection moulds for plastics and will ensure the most no-failure operation in small series production.

Acknowledgements: This paper is the result of the project PIRSES-GA-2010-269177 supported by The international project realized in range of Seventh Frame Programme of European Union (FP7), Marie Curie Actions, PEOPLE and the result of the project ITMS: 26220120060 supported by the Research & Development Operational Programme funded by the ERDF.

References

1. Blaškovič P, Balla J, Dzimko M. Tribológia. Bratislava: Alfa, 1990.
2. Galetz M, Seiferth S, Theile B, Glatzel U. Potential for adhesive wear in friction couples of UHMWPE running against oxidized zirconium, titanium nitride coatings, and cobaltchromium alloys, *Journal of Biomedical Materials Research Part B: Applied Biomaterials*, Volume 93B, Issue 2, 2010.
3. Garbacz T, Sikora JW. Selected aspects of coatings production in cellular co-extrusion process. The Polymer Processing Society. Banff, Canada 2010, R01–131.
4. Greškovič F, Dulebová L, Varga J. Technológie spracovania plastov. Vstrekovanie. Košice: SJF TU v Košiciach, 2010.
5. Greškovič F, Spišák E. Materiály foriem na spracovanie plastov. *Acta Metallurgica Slovaca* 2003; 9: 41–48.
6. Hidveghy J, Dusza J. Nekomovné konštrukčné materiály. Košice: TU v Košiciach, 1998.
7. Jachowicz T. Wybrane zagadnienia niezawodności obiektów technicznych. *Przetwórstwo tworzyw* 2009; 2 (128)/15: 34–45.
8. Kelly L, Mulvaney-Johnson R, Beechey P. The effect of copper alloy mold tooling on the performance of the injection molding process, *Polymer Engineering & Science*, 2011; 51 (9): 1837–1847.
9. Mandal D, Dutta BK, Panigrahy SC. Wear and friction behavior of stir cast aluminium-base short steel fiber reinforced composites. *Wear* 2004; 7–8 (257): 654–664.
10. McKellop H, Clarke I, Markolf K, Amstutz H. Friction and wear properties of polymer, metal, and ceramic prosthetic joint materials evaluated on a multichannel screening device, *Journal of Biomedical Materials Research* 2004; 15 (5): 619–653.
11. Michaeli W, Lindner F. Influence of Mould Materials on the Morphological and Mechanical Properties of Injection-Moulded Prototypes, *Macromolecular Materials and Engineering* 2001; 286 (4): 232–236.
12. Суберляк ОВ, Красінський ВВ, Шаповал ІМ. Прес-матеріали на основі комбінованого зв'язувального. Технологічні та експлуатаційні характеристики. *Хімічна промисловість України* 2009; 3: 52–54.
13. Štofko M, Štofková M. Neželezné kovy. Košice: Emilie, 2005.
14. Wojciechowski Ł, Nosal S. The application of free surface energy measurement to valuation of adhesive scuffing. *Eksploatacja i Niezawodność – Maintenance and Reliability* 2010; 1 (45): 83–90.
15. Xu J. Materials for Microcellular Injection Molding, *Microcellular Injection Molding*, 2010, Wiley, London, ISBN: 978-0-470-46612-4.

Prof. František GREŠKOVIČ, Ph.D., D.Sc. (Eng.)

Ľudmila DULEBOVÁ, Ph.D. (Eng.)

Branislav DULEBA, Eng.

Department of Technologies and Materials

Technical University of Košice

Mäsiarska 74, Košice, Slovakia

E-mails: frantisek.greskovic@tuke.sk,

ludmila.dulebova@tuke.sk, branislav.duleba@tuke.sk

Aneta KRZYŻAK, Ph.D. (Eng.)

Department of Polymer Processing

Lublin University of Technology

ul. Nadbystrzycka 36, 20-816 Lublin, Poland

E-mail: a.krzyzak@pollub.pl

Dong ZHOU
Xu JIA
Chuan LV
Yongxiang LI

MAINTAINABILITY ALLOCATION METHOD BASED ON TIME CHARACTERISTICS FOR COMPLEX EQUIPMENT

METODA ALOKACJI OBSŁUGIWALNOŚCI ZŁOŻONYCH URZĄDZEŃ OPARTA NA CHARAKTERYSTYKACH CZASOWYCH

Maintainability allocation is an important step in product quality design. Traditional allocation methods are limited such that the allocated mean time to repair for each unit design apartment cannot be totally controlled by the corresponding design apartment. This paper proposes a new time characteristics-based maintainability allocation method to solve the aforementioned problem. The relationship between design content and repair time is considered in this method, and repair time is divided into common and individual repair time. Common repair time, which is determined by the overall system design, is deducted from the total repair time. Individual repair time is allocated to the specific unit through proper traditional allocation method. A case study is performed, and results demonstrate that the new method is more suitable and effective than original methods in terms of maintainability allocation.

Keywords: maintainability, maintenance, allocation method, MTTR.

Alokacja obsługiwalności jest ważnym krokiem w projektowaniu jakości produktów. Tradycyjne metody alokacji są ograniczone w takim sensie, że alokowany średni czas do naprawy dla każdego działu projektowania jednostki produktu nie może być całkowicie kontrolowany przez odpowiedni dział projektowania. W niniejszej pracy zaproponowano rozwiązanie tego problemu wykorzystującą nową metodę alokacji obsługiwalności opartą na charakterystykach czasowych. W proponowanej metodzie bierze się pod uwagę związek między zawartością projektu a czasem naprawy, czas naprawy zaś dzieli się na wspólny i indywidualny. Wspólny czas naprawy, który zależy od ogólnej konstrukcji systemu, odejmuje się od całkowitego czasu naprawy. Indywidualny czas naprawy alokuje się do konkretnej jednostki za pomocą odpowiedniej tradycyjnej metody alokacji. W pracy przeprowadzono studium przypadku, którego wyniki pokazują, że nowa metoda jest bardziej odpowiednia i skuteczna jeśli chodzi o alokację obsługiwalności niż metody stosowane pierwotnie.

Słowa kluczowe: obsługiwalność, eksploatacja, metoda alokacji, średni czas do naprawy MTTR.

1. Introduction

Maintainability, defined as “the ability of an item under given conditions of use to be retained in or restored to a state in which it can perform a required function when maintenance is performed under given conditions and using stated procedures and resources,” is an important product characteristic [15]. Complex equipment with very complicated structures and a large number of entities can be promptly restored from a failure state through maintenance activities [19]. Mean time to repair (MTTR) is an important metric of system maintainability [11, 16].

Maintainability allocation is the process wherein the target or indicator of maintainability for a system is allocated to the target or indicator for subsystems or components; this process is an important task in the product design stage [3, 14]. The objectives of maintainability allocation are

- identify the target or indicator of maintainability for subsystems or components to guarantee the maintainability requirements of the system or product;
- clarify the maintainability target of the product to the supply side so that management becomes easy and reasonable.

Maintainability allocation is an essential and very cost-effective task in product design because all designs begin with clear targets or indicators; maintainability as an intrinsic characteristic of products

is determined in the design stage [9]. A rational allocation scheme allows equipment to be maintained with less time, at the lowest cost, with minimum impact on the environment, and with minimum expenditure of resources [4, 5].

A number of methods, such as equivalent allocation method, failure rate-based allocation method, trade-off of failure rate and design feature-based allocation method, and similar product maintainability data-based allocation method, are available for maintainability allocation [17]. Coulbaly proposed an approach for product maintainability prediction based on behavioral performance assessment [6]. Gero *et al.* presented a generic product model based on function, behavior, and structure concept to build a global and multi-view model through product data and other process information [13]. Barabadi *et al.* conducted a research on maintainability analysis and considered several environmental and operational conditions to compute repair time data and describe maintainability with a statistics-based indicator [1]. Song *et al.* proposed an allocation method based on the analytic hierarchy process to overcome the limitation of common methods when the design character is feckly; the researchers applied the method to an underwater vehicle [20]. Zhao *et al.* proposed a fuzzy maintainability allocation method and utilized interval analysis, fuzzy comprehensive evaluation, and the analytic hierarchy process to quantitatively analyze several considered influence factors in the process of maintainability allocation for numerical control machine tools [21]. Celestine *et*

al. proposed a new and computationally efficient heuristic algorithm for reliability and maintainability allocation in complex hierarchical systems [7]. Several researchers also utilized virtual reality systems and collaborative design environments to verify product functionalities and analyze maintainability after a product is designed [12, 22, 24]. However, when the aforementioned methods are employed in actual practice, design factors such as the maintenance access channel are not considered by the specific unit design department; the MTTR index allocated to each unit cannot be totally controlled by the corresponding design department, which is contrary to the purpose of allocation [8].

The purpose of this paper is to overcome the limitation of traditional allocation methods and improve the accuracy and effectiveness of the allocated MTTR index. A maintainability allocation model based on time characteristics is built to improve the applicability and operability of the allocation process in complex equipment and overcome the limitations of traditional methods.

This paper is organized as follows. Section 2 presents the commonly utilized maintainability allocation methods. The proposed maintainability allocation method based on time characteristics is described in Section 3. The results of the conducted case study, which show the efficiency and effectiveness of the proposed method, are discussed in Section 4. Section 5 provides the conclusions of this paper.

2. Commonly Utilized Maintainability Allocation Methods

Assuming that a system is composed of n units, the MTTR of the units and the MTTR of the system during the life cycle must fulfill the equation [2]

$$\bar{M}_{CT} = \frac{\sum_{i=1}^n \lambda_i \bar{M}_{CT_i}}{\sum_{i=1}^n \lambda_i} \quad (1)$$

where n is the total number of units, λ_i is the failure rate of unit i , and \bar{M}_{CT_i} is the MTTR of unit i . When, $i=1, 2, \dots, n$, \bar{M}_{CT} is the MTTR of the system.

The MTTR allocated to each unit must satisfy Equation (1). However, many solutions can satisfy the equation; thus, the appropriate solution must be determined based on the criteria of maintainability allocation.

2.1. Failure rate-based allocation method

The principle of this allocation method is that “the repair time allocated to the unit with high failure rate is short and vice versa.” The premise of this method is that the allocated or predicted values of the reliability metrics already exist. The MTTR distributed to each unit is calculated as

$$\bar{M}_{CT_i} = \frac{\bar{M}_{CT} \sum_{i=1}^n \lambda_i}{n \lambda_i} \quad (2)$$

where \bar{M}_{CT_i} is the MTTR distributed to unit i , \bar{M}_{CT} is the MTTR of the system, λ_i is the failure rate of unit i , and n is the total number of unit types.

Not all units in an upgraded system need to be redesigned because some of the units of the original system are adopted. Assuming that an upgraded system is composed of n subsystems among which L sub-

systems are employed from the original system, the maintainability allocation result of the new system follows the equation

$$\bar{M}_{CT_j} = \frac{\bar{M}_{CT} \sum_{i=1}^n \lambda_i - \sum_{i=1}^L \lambda_i \bar{M}_{CT_i}}{(n-L) \lambda_j}, \quad j=L+1, \dots, n \quad (3)$$

where \bar{M}_{CT_j} is the MTTR for newly designed subsystem j , \bar{M}_{CT} is the MTTR of the upgraded system, \bar{M}_{CT_i} is the MTTR of original subsystem i , and λ_i and λ_j are the failure rates of subsystems i and j , respectively.

The maintainability indicators $\{\bar{M}_{CT_i}\}$ allocated based on the failure rates are reasonable but may not be feasible. For example, one or a few indicators could be extremely small that they may be technically impossible to achieve. Indicators must be adjusted if they are technically difficult to realize or require high costs (including economic, time, and manpower cost). Based on the preliminary structure scheme, the various maintainability qualitative characteristics (e.g., complexity, accessibility, scalability, ease of replacement, testability) that influence repair time must be considered, and a trade-off must be made to determine the allocation results [10, 18, 23].

2.2. Trade-off of failure rate and design feature-based allocation method

Relevant factors such as complexity, accessibility, and testability are transformed into weight coefficients when the allocation method based on the trade-off of failure rate and the design features is utilized. The MTTR allocated to each unit is calculated as

$$\bar{M}_{CT_i} = \beta_i \bar{M}_{CT} \quad (4)$$

where \bar{M}_{CT_i} is the MTTR distributed to unit i , \bar{M}_{CT} is the MTTR of

the system, and $\beta_i = \frac{\bar{\lambda} k_i}{\lambda_i \bar{k}}$ is the weight coefficient of the repair time

for the unit. $\bar{\lambda} = \frac{\sum_{i=1}^n \lambda_i}{n}$ is the average failure rate of each unit,

$\bar{k} = \frac{\sum_{i=1}^n k_i}{n}$ is the average of each unit weight coefficient, and

$k_i = \sum_{j=1}^m k_{ij}$ is the weight coefficient of factor j in unit i .

For an upgraded system, the maintainability allocation result of the newly designed subsystem follows the equation

$$\bar{M}_{CT_j} = \frac{\bar{M}_{CT} \sum_{i=1}^n \lambda_i - \sum_{i=1}^L \lambda_i \bar{M}_{CT_i}}{\lambda_j \sum_{j=L+1}^n k_j} k_j, \quad j=L+1, \dots, n. \quad (5)$$

The designed maintainability characteristics should be clear when this method is utilized. The weight coefficients in this method are the indexes of the influence of factors on the maintainability indicators of each unit.

3. Time characteristics-based maintainability allocation model for complex equipment

3.1. Classification of repair time

Repair time is classified in this study given the fact that the different elements of repair time are controlled by different design departments in reality. Repair time is classified in two categories: common repair time and individual repair time.

1) Common repair time

The repair time determined by the overall system design or the upper design department, such as preparation time and approaching time determined by the overall layout, is defined as the common repair time in this level for product units in a certain level of the equipment. This type of time is determined by the overall design or upper level department and is not directly affected and controlled by product design in this level.

2) Individual repair time

The repair time determined by product design, such as assembly, changing, and adjustment time, is defined as the individual repair time in this level for product units in a certain level of the equipment. This type of time is determined by the department that designs the unit.

Considering that the formation mechanism of the different types of maintenance time is different, the types of maintenance time are influenced and controlled by different product design departments. The allocation method differs according to the categories of repair time as shown in Fig. 1.

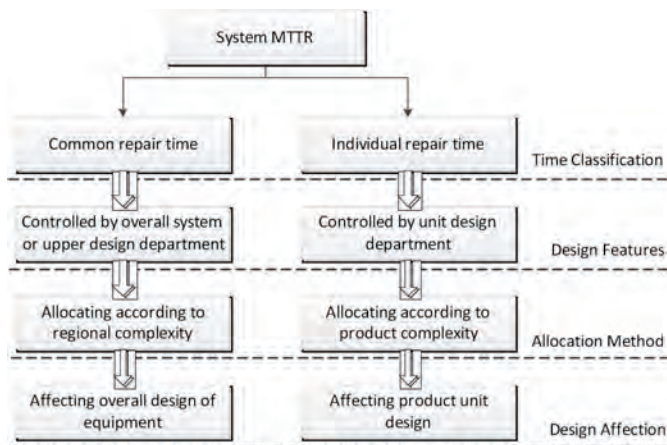


Fig. 1. Influence of the different types of time

3.2. Time of maintenance activities

Common repair time is related to the structure and layout of the system, maintenance access design, and product unit design features. The system theory, layout, function hierarchy, and main replaceable units should be mastered to identify common repair time. The identification of common repair time relies on information and data derived from equipment design, including the historical data of similar equipment, existing failure rate data of developing equipment, and data on the order of maintenance activities and factors influencing repair time.

Through the analysis of system maintenance activities, system repair time can be divided into the following: preparation, localization and diagnosis, approaching, correction, reassembly, adjustment, and checkout time.

Common repair time generally includes preparation, approaching, and reassembly time. However, accessing and reassembly time belong to individual repair time in some cases. The corresponding repair process when failure is isolated to a single replaceable unit (RU) is

shown in Fig. 2. The accessing channel to the fault belongs to the single RU, and accessing and reassembly time are the individual repair time of RU.



Fig. 2. Process of repairing a single RU

The single RU must be replaced to determine the fault when failure is isolated to an RU group of two or more RUs. The worst case is that the entire RU group is replaced; the accessing channel is shared by all RUs, and accessing and reassembly time are determined by the upper level design and belong to common repair time. The repair process in this case is shown in Fig. 3.

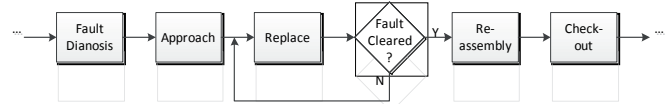


Fig. 3. Process of repairing an RU group

Common repair time can be determined through experience or composition of the time of basic maintenance activities. Individual repair time is calculated with a mathematical allocation model.

3.3. Theory of the method

The method of allocating repair time according to the different characteristics of the time of each maintenance activity is utilized based on the classification scheme of maintenance time. Common repair time is deducted from MTTR, and individual repair time is allocated further down to the level of subsystems and/or components through a suitable traditional allocation method. Each product design department obtains a maintenance time indicator that can be completely controlled. The use of this method can guarantee that the maintainability indicators of each product level are clear and the distribution process is reasonable, accurate, and feasible.

3.4. Allocation model

The repair time of an equipment system is classified, and the influencing factors are considered. Given that product information and the classification of repair time are different for the high-level and low-level product units, different allocation models are built for different product levels.

3.4.1. Allocation model for high-level products

For high-level products, we assume that the system consists of n subsystems (subsystem 1, subsystem 2, ..., subsystem n) and that the corresponding failure rates are $\lambda_1, \lambda_2, \dots, \lambda_n$. The repair time of the high-level products is analyzed. The framework of allocating repair time for high-level products is shown in Fig. 4.

According to the definition of common repair time and the above-mentioned classification method, common repair time includes preparation time T_p , approaching time T_A , and reassembly time T_R . Individual repair time is calculated by eliminating common repair time from the system MTTR.

1) Common repair time

The composition of preparation time is relatively simple; it is generally determined by a number of relatively fixed basic operational components, controlled by the overall sector of the equipment, and mainly influenced by the basic operations types. The method of confirming preparation time is similar products ratio method.

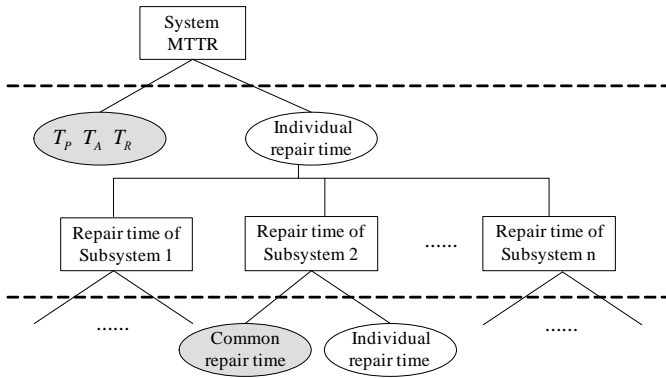


Fig. 4. Allocation model for high-level products

If the MTTR of the designing product is \bar{M}_{CT} and that of the similar product is \bar{M}'_{CT} and the preparation time for the similar products is , the preparation time for the designing product is

$$T_p = \frac{\bar{M}_{CT}}{\bar{M}'_{CT}} T'_p. \quad (6)$$

Approaching time refers to the time spent opening the flap, moving through the maintenance access channel, removing the obstacles in the channel, and external blocking of the replaceable unit by maintenance staff. The main factors that generally affect approaching time include access channel size, failure rate of the product units and components in the maintenance access channel area, flap type and opening time, fastener type, and others. Thus, common repair time is divided into three parts: time spent opening the flap of the access channel (T_{A1}), time spent moving and accessing the cabin that requires repair (T_{A2}), and time spent opening the fasteners and removing the obstacles near the replacement unit (T_{A3}). Approaching time T_A is

$$T_A = T_{A1} + T_{A2} + T_{A3}. \quad (7)$$

Approaching time is not equal to zero when the system shares the maintenance access channel; however, when each RU has its own maintenance access channel, approaching time belonging to common repair time is zero.

Reassembly involves the assembly of removed units in the channel and is regarded as the opposite of approaching process. Similar to approaching time, reassembly time is controlled by the overall sector or the upper level design department and is affected by the same factors that affect approaching time. Thus, T_R is

$$T_R = T_A \quad (8)$$

Common repair time T_{cmn} is calculated as

$$T_{cmn} = T_p + T_A + T_R \quad (9)$$

2) Individual repair time

After determining common repair time and eliminating common repair time from the system MTTR, individual repair time T_{idv} is obtained.

$$T_{idv} = \bar{M}_{CT} - T_{cmn} \quad (10)$$

Failure rate-based allocation method is utilized to allocate individual repair time to the lower level of the equipment.

$$\bar{M}_{CT_i} = \frac{\bar{\lambda}}{\lambda_i} T_{idv} \quad (11)$$

where \bar{M}_{CT_i} is the repair time allocated to subsystem i , λ_i is the failure rate of subsystem i , and $\bar{\lambda} = \frac{\sum_{i=1}^n \lambda_i}{n}$ is the average failure rate of all subsystems.

For the upgraded product, assuming that the system consists of n subsystems and that subsystems $1 \sim L (L < n)$ are existing products, the maintainability indicators of the newly designed subsystems are allocated as

$$\bar{M}_{CT_j} = \frac{T_{idv} \sum_{i=1}^n \lambda_i - \sum_{i=1}^L \lambda_i \bar{M}_{CT_i}}{(n-L) \lambda_j}, j = L+1, \dots, n \quad (12)$$

3.4.2. Allocation model for low-level products

The maintenance process for the low-level product unit mainly includes isolation, disassembly, and replacement, which are all determined by the design features of each unit. Thus, the time spent on the abovementioned activities belongs to individual repair time. The total individual repair time for all low-level units is

$$T_{RU_{idv}} = \bar{M}_{CT_i} - T_{RU_{cmn}} \quad (13)$$

where $T_{RU_{idv}}$ is the individual repair time allocated to the single RU, \bar{M}_{CT_i} is the time indicator allocated to subsystem i from system level using the high-level product allocation model, and $T_{RU_{cmn}}$ is the common repair time in this level.

The equipment replacement scheme should be considered in the late development stage to improve the precision of allocation. When failure is isolated to a single RU, the RU can be replaced individually to correct the fault. If failure is isolated to an RU group and the RUs in the group are irrelevant, the RU group can be regarded as a single RU. The group in which the RUs are replaced alternately is denoted as RU_{GE} . The group in which the RUs are all replaced is denoted as RU_{GA} . Maintainability allocation then involves the allocation of the system MTTR to $RU_1, \dots, RU_j, RU_{GE1}, \dots, RU_{GEk}, RU_{GA1}, \dots, RU_{GAs}$ according to the failure and design features of each RU or RU group. The framework of allocation of low-level repair time is shown in Fig. 5.

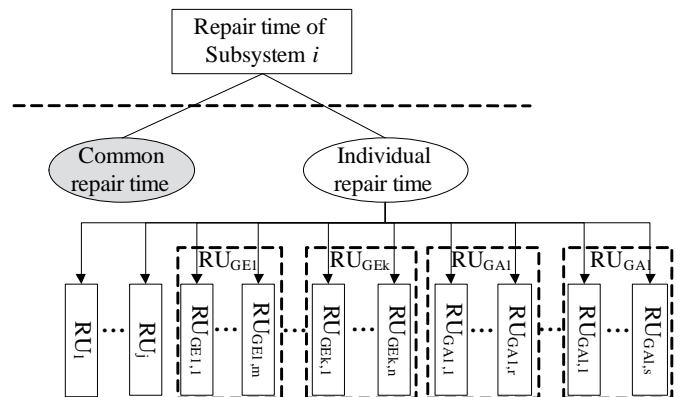


Fig. 5. Allocation model for low-level products

The average number of alternate replacements denoted as S_i needs to be calculated for the alternately replaced RU group RU_{GE1} . If the average of S_i is required to remedy the fault, the time spent replacing the RU group is S_i times the time for a single RU. In some cases, approaching and reassembly time also turn into S_i time. If the replaced RU group consists of r RUs, the corresponding time turns into r time.

The average number of replacements in the alternately replaced RU group consisting of m single RUs is

$$S_i = \left\lceil \frac{m+1}{2} \right\rceil \quad (14)$$

where $\lceil x \rceil$ is a maximum integer not larger than x .

Trade-off of failure rate and design feature-based allocation method is utilized in low-level product allocation. Six kinds of maintainability design features, namely, fault detection and isolation, maintenance channel, fasteners, internal assembly, replacement, and scalability, are considered. These features may be different for different products owing to specific circumstances.

Repair time differs because different maintenance schemes are employed. Repair time when the failure is isolated to an RU group differs from repair time when failure is isolated to a single RU. Isolating failure to an RU group causes all RUs to be replaced because of the failure of one RU. Thus, this scheme is more complex than the scheme that involves the isolation of failure to a single RU. Coefficient α_i is introduced to the model to correct the weight coefficient and to make the allocation reasonable and accurate.

If the failure is isolated to a single RU, the correct coefficient is

$$\alpha_i = 1.$$

If the failure is isolated to an RU group consisting of n RUs and the RUs are replaced alternately, the correct coefficient is

$$\alpha_i = S_i = \left\lceil \frac{m+1}{2} \right\rceil. \quad (15)$$

If the failure is isolated to an RU group consisting of r RUs and all the RUs are replaced, the correct coefficient is

$$\alpha_i = r.$$

The repair time allocated to each RU is calculated as

$$\bar{M}_{cti} = \frac{k'_i \sum_{i=1}^{j+k+l} \lambda_i}{\lambda_i \sum_{i=1}^{j+k+l} k'_i} T_{RUidv}, i=1, \dots, j, j+1, \dots, j+k, j+k+1, \dots, j+k+l \quad (16)$$

where $k'_i = \alpha_i k_i$ and $k_i = \sum_{j=1}^m k_{ij}$, m is the number of weight coefficients, k_{ij} is the weight coefficient of factor j in unit i .

For the upgraded product mentioned above, the maintainability indicators of the newly designed subsystems are allocated as

$$\bar{M}_{ctj} = \frac{T_{RUidv} \sum_{i=1}^n \lambda_i - \sum_{i=1}^L \lambda_i \bar{M}_{CTi}}{\lambda_j \sum_{j=L+1}^n k'_j} k'_j, j=L+1, \dots, n. \quad (17)$$

4. Case study

4.1. Analysis of system structure

The main functions of the Z-system of a certain aircraft are flight control, display management, and task data loading and recording. The system includes three subsystems: flight control, display management consisting of 10 LRUs, and mission computer subsystems (Fig. 7). The system MTTR target, which is 30 min, and the failure rate and design features of the three subsystems and 10 LRUs are provided. The goal is to determine the allocated maintainability index of each LRU in the display management subsystem.

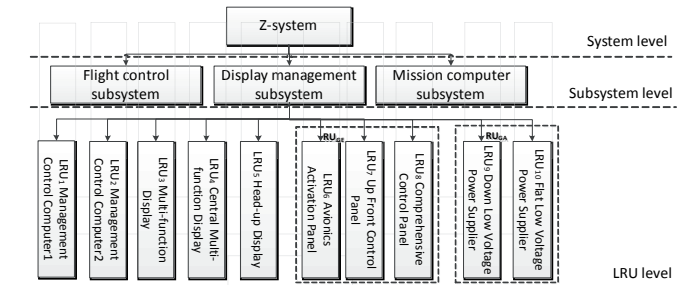


Fig. 6. Structure of the Z-system

Maintainability is fully considered in the design of the Zsystem. The design features include the following:

1. the installation position of each subsystem is concentrated in the equipment cabin, and the maintenance access channel is sufficient for observation and manual operation;
2. obstacles are removed when a maintenance personnel approaches each subsystem;
3. LRU is interchangeable, and no adjustment and calibration is required; thus, adjustment and checkout time are negligible;
4. In the diagnosis of failure, some failures can be isolated to a single LRU, some can be isolated to an alternately replaced LRU group, and others can be isolated to an entirely replaced LRU group.

The failure rate of each subsystem is shown in Table 1. Information on the LRUs is shown in Table 2.

Table 1. Failure rates of subsystems (/year)

Subsystem	Failure rate
Flight control	$\lambda_{FC}=0.0036$
Display management	$\lambda_{DM}=0.0049$
Mission computer	$\lambda_{MC}=0.0029$

4.2. Repair time allocation model

The system is divided into three levels, namely, system, subsystem, and LRU. The high-level product allocation model is utilized when the system level indicator is allocated to the subsystem level. The low-level product allocation model is utilized when the subsystem level indicator is allocated to the LRU level.

4.2.1. Allocation from system level to subsystem level

The high-level product allocation model is employed in this allocation process. Preparation, approaching, and reassembly time are determined by the overall system for the three subsystems. Preparation time T_p , approaching time T_A , and reassembly time T_R are therefore common repair time in the subsystem level. Based on experience, we obtain

$$T_P = 5 \text{ min}, T_A = 6 \text{ min}, T_R = 6 \text{ min}.$$

Thus, the common repair time of this level is

$$T_{cmn} = T_P + T_A + T_R = 17 \text{ min}.$$

The individual repair time that must be allocated to each subsystem is

$$T_{idv} = MTTR - T_{cmn} = 13 \text{ min}$$

According to failure rate-based allocation method and Equation (2), the MTTR of the display management subsystem is

$$\bar{M}_{CTDM} = \frac{\lambda_{FC} + \lambda_{DM} + \lambda_{MC}}{3 * \lambda_{DM}} = 10.0816 \text{ min}.$$

4.2.2. Allocation from subsystem level to LRU level

The main maintenance activities For RU₁, RU₂, ..., RU₅, RU_{GE1}, and RU_{GE2} are isolation, replacement, and reassembly. These activities are relevant to the diagnosis process and installation of each RU or RU group. The common repair time for the activities is zero. The use of trade-off of failure rate and design feature-based allocation method allows the determination of the time index for each RU or RU group.

For LRU₁, LRU₂, ..., LRU₅, the failure is isolated to a single RU; thus, $\alpha_i = 1$.

For LRU₆, LRU₇, LRU₈, the failure is isolated to an alternately replaced RU group RU_{GE1}; thus, $\alpha_i = 2$.

For LRU₉ and LRU₁₀, the failure is isolated to an alternately replaced RU group RU_{GE2}; thus, $\alpha_i = 2$.

According to Equation (16), the maintenance time allocated to each RU/RU group is

$$\begin{aligned} \bar{M}_{ct1} &= 7.0175 \text{ min} & \bar{M}_{ct2} &= 7.0175 \text{ min} \\ \bar{M}_{ct3} &= 7.2302 \text{ min} & \bar{M}_{ct4} &= 10.8454 \text{ min} \\ \bar{M}_{ct5} &= 3.5612 \text{ min} & \bar{M}_{ctGE1} &= 32.9101 \text{ min} \\ \bar{M}_{ctGE2} &= 11.0462 \text{ min} \end{aligned}$$

Table 2. Information on LRUs

RU/RU group	k_i of RU/RU group	α_i of RU/RU group	k'_i of RU/RU group	Failure rate of RU/RU group*	LRU name	LRU code	Obstacles in the channel to access LRU	Installation of LRU	Failure rate of LRU*	k_j of LRU**
RU ₁	8	1	8	0.00034	Management control computer 1	LRU ₁	No mechanical disassembly is required	Swing nut	0.00034	8
RU ₂	8	1	8	0.00034	Management control computer 2	LRU ₂	No mechanical disassembly is required	Swing nut	0.00034	8
RU ₃	8	1	8	0.00033	Multi-function display	LRU ₃	No mechanical disassembly is required	bolt	0.00033	8
RU ₄	12	1	12	0.00033	Central multi-function display	LRU ₄	No mechanical disassembly is required	bolt	0.00033	12
RU ₅	8	1	8	0.00067	Head-up display	LRU ₅	No mechanical disassembly is required	bolt	0.00067	8
RU _{GE1}	16	2	32	0.00029	Avionics activation panel	LRU ₆	Extensive disassembly is required	screws	5.044E-05	14
					Up front control pane	LRU ₇	Extensive disassembly is required	Insertion	4.322E-05	17
					Comprehensive control panel	LRU ₈	Extensive disassembly is required	screws	0.0002	17
RU _{GE2}	10	2	20	0.00054	Downlow-voltage power supplier	LRU ₉	Extensive disassembly is required	Insertion	0.00021	10
					Flat low-power supplier	LRU ₁₀	Extensive disassembly is required	Insertion	0.00033	10

*The unit of failure rate is year-1.

** of each LRU can be obtained with PRC military standard GJB/Z57.

Considering the structure characteristics of RU_{GE1}, the time spent removing the obstacles near the three line replaceable units belongs to the common repair time of the three RUs. The approaching and re-assembly time for both is 4 min, which is determined based on experience. The common repair time of three LRUs is

$$T_{RUcmn} = 8 \text{ min}$$

and

$$T_{RUidv} = \bar{M}_{ctGE1} - T_{RUcmn} = 24.9101 \text{ min}.$$

When T_{RUidv} is allocated to LRU₆, LRU₇ and LRU₈ through trade-off of failure rate and design feature-based allocation method, we obtain

$$\bar{M}_{ct6} = 42.3 \text{ min}$$

$$\bar{M}_{ct7} = 60 \text{ min}$$

$$\bar{M}_{ct8} = 13 \text{ min}$$

Similarly, we obtain the maintenance index of LRU₉ and LRU₁₀.

$$T_{RUcmn} = 4 \text{ min}$$

$$\bar{M}_{ct9} = 8.8916 \text{ min}$$

$$\bar{M}_{ct10} = 5.6583 \text{ min}$$

The results of the proposed allocation method and traditional allocation method are shown in Table 3 and Fig. 7.

The following conclusions are derived from the comparison of the results of the new allocation method and traditional trade-off of failure rate and design feature-based allocation method.

- Only a minimal amount of time is allocated to each LRU when the new method is utilized because common repair time is obtained from the indicator that will be allocated. Allocating a low MTTR to each LRU is appropriate because a low MTTR can influence the design process and improve the performance of equipment.

Table 3. Results of the proposed method (min)

Subsystem level T_{cmn}	RU/RU group	T_{RUcmn}	LRU code	Allocated time for LRU	Theoretical total time	Traditional method result	Actual maintenance time
17	RU ₁	0	LRU ₁	7.0175	24.0175	13.9005	27
	RU ₂	0	LRU ₂	7.0175	24.0175	13.9005	27
	RU ₃	0	LRU ₃	7.2302	24.2302	14.3218	29
	RU ₄	0	LRU ₄	10.8454	27.8454	21.4826	29
	RU ₅	0	LRU ₅	3.5612	20.5612	7.0540	21
	RU _{GE1}	8	LRU ₆	42.3	67.3	163.97	70
			LRU ₇	60	85	232.37	82
			LRU ₈	13	38	50.2157	36
	RU _{GE2}	4	LRU ₉	8.8916	29.8916	28.132	32
			LRU ₁₀	5.6583	26.6583	17.902	25

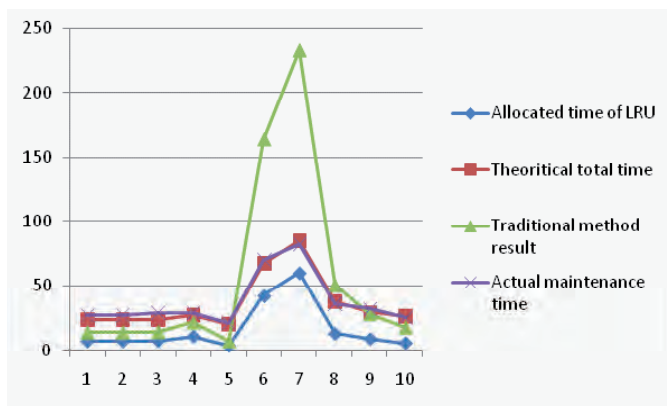


Fig. 7. Comparison of the results of the proposed and traditional method

- b) Theoretical total repair time is almost similar to actual repair time when the new method is employed, indicating that the new method is more accurate than traditional allocation methods.

5. Conclusions

Commonly utilized maintainability allocation methods are limited because design factors such as the maintenance access channel are not considered by the specific unit design department. The MTTR index allocated to each unit cannot be completely controlled by the corresponding design department, which is contrary to the purpose of allocation. A time characteristics-based maintainability allocation method is proposed in this study to address this problem. By considering the structure of the system and the determinants of repair time, repair time is classified into two categories: common repair time and individual repair time. High-level and low-level product unit allocation models are built based on the classification of repair time. The main difference between the new method and traditional methods is that common repair time is obtained and only individual repair time is allocated to low-level units. The case study shows that the new method is more accurate and much less complicated than the original methods, which is beneficial for equipment performance.

Acknowledgement: This research was partly financed by the State Key Laboratory of Virtual Reality Technology and System in Beihang University. The authors appreciate the support.

References

1. Abbas Barabadi, Javad Barabady, Tore Markeset. Maintainability analysis considering time-dependent and time-independent covariates. *Reliability Engineering and System Safety* 2011; 96: 210–217.
2. Birolini A. *Reliability engineering: theory and practice*. Springer Publishers 2007.
3. Dhillon BS. *Engineering Maintainability: How to design for reliability and ease maintenance*. Elsevier Science & Technology Books 1999; 73–74.
4. Blanchard BS, Verma D, Petersom EL. *Maintainability: a key to effective serviceability and maintenance management* New York. 1995.
5. Chen L, Cai JG. Using vector projection method to evaluate maintainability of mechanical system in design review. *Reliability Engineering and System Safety* 2003; 2(81): 147–154.
6. Coulibaly A, Houssin R, Mutel B. Maintainability and safety indicators at design stage for mechanical products. *Computers In Industry* 2008; 5(59): 438–449.
7. Celestine A. Ntuen, Eui H. Park. A heuristic program for reliability and maintainability allocation in complex hierarchical systems. *Computers & Industrial Engineering* 1993; 25: 345–348.
8. Zio E. *Reliability engineering: old problems and new challenges*. *Reliability Engineering and System Safety* 2009; 94(2): 125–141.
9. Gaoliang Peng, Yu, Haiquin, Xinhua Liu. A desktop virtual reality-based integrated system for complex product maintainability design and verification. *Assembly Automation* 2010; 30: 333–344.
10. Haiquan Yu, Gaoliang Peng, Wenjian Liu. A practical method for measuring product maintainability in a virtual environment. *Assembly Automation* 2011; 31(1): 53–61.
11. Jiang Kun, Cui Quanhui, Ju Xianli. BP-neural network-based MTTR calculation method. *Proceedings of 2010 Asia-Pacific International Symposium on Aerospace Technology* 2010; 1: 530–533.
12. Pomares J, Puente ST, Torres F. Virtual disassembly of products based on geometric models. *Computers In Industry* 2004; 55: 1–14.
13. Gero JS. Design prototypes: a knowledge representation schema for design. *Artificial Intelligence Magazine* 1990; 11(4): 26–36.
14. Lu Zhong, Sun Youchao. Research on maintainability evaluation model based on fuzzy theory. *Chinese Journal of Aeronautics* 2007; 20: 402–407.
15. MIL-STD-721C. Definitions of terms for reliability and maintainability. US Department of Defense 1981.

16. MIL-HDBK-470A. designing and developing maintainable products and systems. US Department of Defense. 1997.
17. PRC military standard GJB/Z 57. Maintainability Prediction And Allocation Handbook. Beijing. 1994
18. Pedro Moreu De Leon, Vicente Gonzalez-PridaDiza, Luis Barbera Martinez. A practical method for the maintainability assessment in industrial devices using indicators and specific attributes. Reliability Engineering and System Safety. 2012; 100: 84–92.
19. Qiang Miao, Liu Liu, Yuan Feng, Michael Pecht. Complex system maintainability verification with limited samples. Microelectronics Reliability. 2011; 51: 294–299.
20. Qingwei Liang, Baowei Song, Minquan Zhao. Study on the methods of maintainability allocation of under water vehicle. WRI World Congress On Computer Science And Information Engineering. 2009; 256–261.
21. Qingbo Hao, Zhaojun Yang, Fei Chen. A fuzzy maintainability allocation method for NC machine tools based on interval analysis. 2011 9th International Conference On Reliability, Maintainability And Safety (ICRMS). 2011; 889–896.
22. Qinghui Wang, Jingrong Li. Interactive visualization of complex dynamic virtual environments for industrial assemblies. Computers In Industry. 2006; 57: 366–377.
23. Xuan F. Zha, H. Du. Knowledge-intensive collaborative design modeling and support. Computers In Industry. 2006; 57: 39–56.
24. Zhong Lu, Youchao Sun. maintainability virtual evaluation method based on fuzzy multiple attribute decision making theory for civil aircraft system. 8th International Conference On Reliability, Maintainability And Safety (ICRMS). 2009; 684–689.

Assistant Prof. Dong ZHOU

Xu JIA

Prof. Chuan LV

Yongxiang LI

School of Reliability and Systems Engineering

BeihangUniversity

37#Xueyuan Road, Beijing, China

E-mails: zhoudong@buaa.edu.cn, jiaxudm@dse.buaa.edu.cn,

lc@buaa.edu.cn, liyongxiang0912@126.com

Tong YIFEI
Tang ZHAOHUI
Ye WEI
Yang ZHEN

RESEARCH ON ENERGY-SAVING OPTIMIZATION DESIGN OF BRIDGE CRANE

BADANIA DOTYCZĄCE OPTYMALIZACJI ENERGOOSZCZĘDNOŚCI KONSTRUKCJI SUWNICY POMOSTOWEJ

Bridge crane is one of the most widely used cranes in our country, which is indispensable equipment for material conveying in the modern production. The security of bridge crane is always focused on when being used. The important indicators of crane performances include strength, stiffness, and crane weight, which mainly depend on the structure design of the bridge crane. So it is of importance to research on energy-saving optimization design by means of finite element analysis, ADMAS and Matlab. In this paper, the framework of energy-saving optimization is proposed. Secondly, taking 50 t – 31.5 m bridge crane as research object, its structure is described and the FE model of the bridge cranes is developed for the finite element analysis. Thirdly, shape optimal mathematical model of the crane is proposed for shape optimization as well as size optimal mathematical model for size optimization and topology optimal mathematical model for topology optimization. Besides, further comprehensive energy-saving optimizations are carried out as well as cross-section optimization. Finally, system-level energy-saving optimization design of bridge crane is further carried out with energy-saving transmission design results feedback to energy-saving optimization design of metal structure. The optimization results show that structural optimization design can reduce total mass of crane greatly by using the finite element analysis and optimization technology premised on the design requirements of cranes such as stiffness, strength and so on, thus energy-saving design can be achieved.

Keywords: Energy-saving design, Lightweight design, Shape optimization, Size optimization, Topology optimization, Bridge crane, HyperWorks.

Suwnica pomostowa jest jednym z najczęściej używanych typów suwnic w Chinach i stanowi niezbędne wyposażenie do transportu materiałów w nowoczesnej produkcji. Kluczową kwestią dotyczącą obsługi suwnicy pomostowej jest zawsze bezpieczeństwo. Ważnymi wskaźnikami wydajności suwnicy są m.in. wytrzymałość, sztywność oraz ciężar suwnicy, które zależą głównie od konstrukcji suwnicy. Konieczne są zatem badania nad optymalizacją energooszczędności konstrukcji za pomocą analizy elementów skończonych, ADMAS oraz Matlab. W niniejszej pracy zaproponowano koncepcję optymalizacji energooszczędności. Po drugie, opisano budowę suwnicy pomostowej (50 t – 31.5 m) oraz opracowano model MES suwnicy do analizy metodą elementów skończonych. Po trzecie, przyjmując minimalną pojemność jako funkcję celu, wysokość i szerokość suwnicy jako zmienne projektowe, a naprężenie, energię odkształcenia, modalnych jako ograniczenia, ustalono optymalny model matematyczny kształtu żurawia dla celów optymalizacyjnego projektowania kształtu. Po czwarte, przyjmując minimalny udział objętościowy jako funkcję celu, a grubości płyt jako zmienne projektowe, ustalono optymalny model matematyczny rozmiarów do celów optymalizacyjnego projektowania rozmiarów. Po piąte, przyjmując minimalny udział objętościowy jako funkcję celu, a gęstości materiału każdego z elementów jako zmienne projektowe, ustalono optymalny model matematyczny topologii do celów optymalizacyjnego projektowania topologii. Wreszcie, wykonano multidyscyplinarny energooszczędny projekt optymalizacyjny systemu suwnicy pomostowej, a wyniki energooszczędnego projektowania układu napędu zostały wykorzystane jako informacja zwrotna przy energooszczędnym projektowaniu optymalizacyjnym konstrukcji metalowej. Wyniki optymalizacji pokazują, że optymalizacyjne projektowanie konstrukcji z wykorzystaniem analizy MES oraz technologii optymalizacji opartej na wymogach projektowych dla suwnic, takich jak sztywność, wytrzymałość itd., może znacznie obniżyć całkowitą masę dźwigu, a co za tym idzie zwiększyć jego energooszczędność.

Słowa kluczowe: Energooszczędna konstrukcja, lekka konstrukcja, multidyscyplinarna optymalizacja, suwnica pomostowa, HyperWorks.

1. Introduction

Empirical design is often used for the structure design of bridge crane, which determines the design parameters of bridge crane and furthermore improve the performance. The traditional design method can't work out accurate performance data resulting in the safe coefficient of crane over the design requirements greatly, which leads to the waste of materials and energy consumption, etc [9].

At present, simplified structure to reduce the weight and lightweight design based heuristic algorithm are usually adopted to achieve energy saving, most of which focus on single structural design improvement. With the rapid development of finite element analysis (FEA) technique [8, 10], the traditional design method is gradually replaced by finite element analysis and design. There is quite a lot of finite element analysis software, such as: ANSYS, ABAQUS, and HyperWorks, etc [5, 11]. However, purely from structural design to reduce the weight of the crane has been very limited, and blindly to

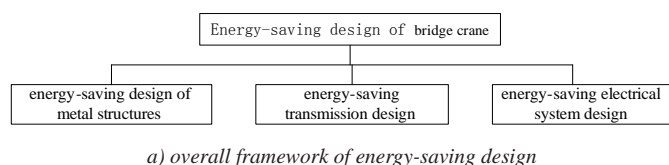
reduce the weight would be a security risk. On the other hand, crane is a complex system composed of many subsystems, among which there exist weak or strong coupling relationship. Thus, Crane energy-saving design is a multi-disciplinary coupling engineering problem involving structural design, mechanical transmission and electrical control, which is not a simple superposition and permutations of various disciplines design. Therefore it is of urgent need from multidisciplinary point of view of structure, mechanical transmission and electrical control to study the system-level energy-saving design of crane.

The present work was carried out in order to obtain simulation data of the bridge crane. In the next section, the framework of energy-saving optimization design is proposed. In Section 3, FE model of double girder crane is developed using commercial program HyperWorks and the loading and the results of finite element analysis are given and discussed. Shape, size and topology optimization are further carried out as well as comprehensive optimization and the results of structural optimization are analyzed. In Section 4, overall energy-saving optimization design of bridge crane is further carried out with energy-saving transmission design results feedback to energy-saving optimization design of metal structure. Finally, research conclusions are summarized.

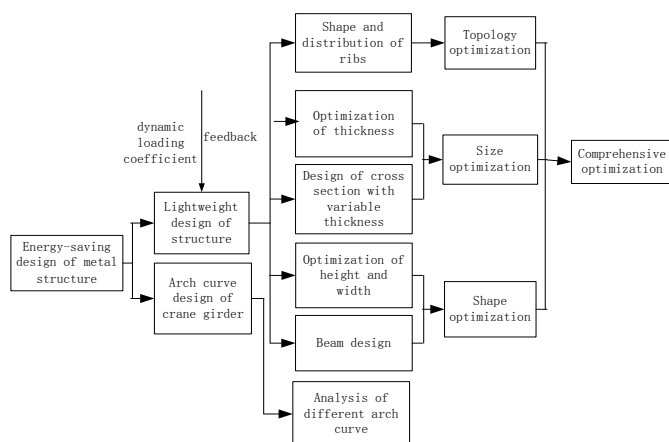
2. Energy-saving optimization design framework

The presented research on crane energy-saving design technology includes three parts respectively: energy-saving design of metal structures, energy-saving transmission design and energy-saving electrical system design. Energy-saving design of metal structure involves structural lightweight design and arch curve design of beam, energy-saving transmission system design involves dynamic loading, transmission efficiency and components lightweight and energy-saving electric system design involves power loss.

In addition, optimal design of lifting findings dynamic loading and components lightweight are feedback to structure lightweight design for further design optimization. Also, arch curve can reduce climbing energy consumption, thereby reducing motor power losses. The arch curve optimization results need feedback for electrical energy-saving. The optimization design can be illustrated as shown in Fig. 1.

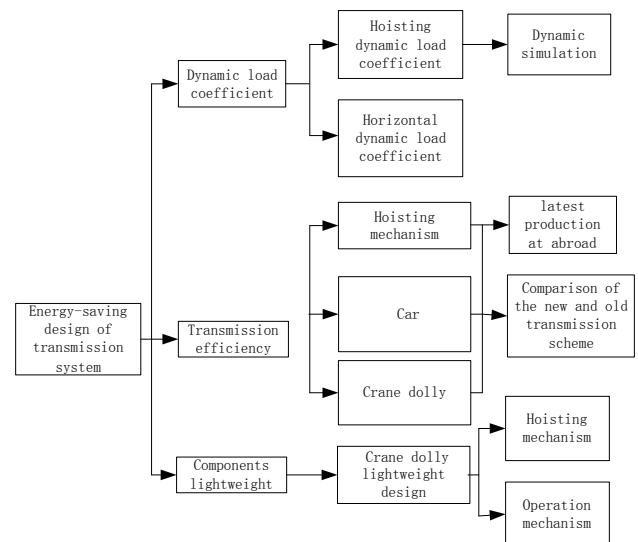


a) overall framework of energy-saving design

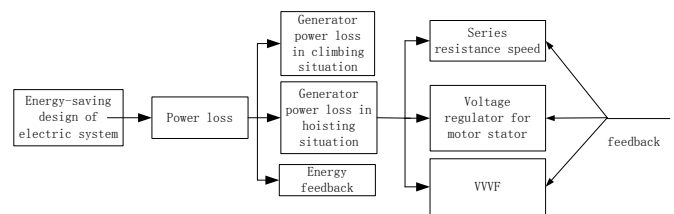


b) energy-saving design of metal structure

Fig. 1a-b. Energy-saving optimization design framework



c) energy-saving design of transmission design



d) energy-saving design of electrical system design

Fig. 1c-d. Energy-saving optimization design framework

3. Energy-saving optimization design of metal structure of bridge crane

3.1. Development of FE model of double girder crane

Take a bridge crane used in a practical project as the research object, which is a 50t-31.5m double girder crane whose material parameter and usage are as follows:

- material: ordinary carbon steel Q345;
- Length of the crane (): 31.5m;
- maximum lifting height: 12m;
- hoisting speed: 7.8 m/min;
- moving speed of the car: 38.5 m/min;
- moving speed of the cart: 87.3 m/min.

And according to the GBT 3811-2008 "Crane design standard", the working-level of car is M5, and the working-level of cart is M6 [1].

3.2. Geometric modeling of double girder crane

According to the engineering drawing, geometric model of the bridge crane is established by PRO/E, whose structure components include the up and down plates of end girders, the side plates of end

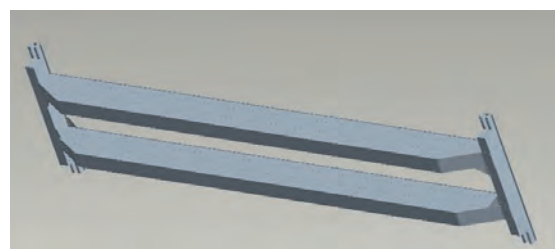


Fig. 2. Geometric model of double girder crane

girders, up and down plates of main girders, the side plates of main girders, multiple belly boards, feet frame and various connection boards. The simplified geometric model is shown as Fig. 2.

3.3. Model Processing

Import the geometric model of bridge crane into HyperMesh, and clear it. Owing to that each plate is thin, partition the plates with shell elements for finite element simulation analysis. The shell elements should be created on the middle surface of the geometry. A group of middle surfaces should be constructed by using "Midsurface" panel. The imported model contains some connectivity error or some other defects, so the operations as follows should be carried out after importing file model:

- 1) Delete the unsheared surfaces.
- 2) Fill the gaps (repair the missed surfaces).
- 3) Set the tolerance values of geometric cleaning.
- 4) Combine the red free edges with "Equivalence".
- 5) Delete the repeated surfaces.

3.4. Mesh partitioning of double girder crane

Welds connections between each board are taken place of the rigid connections and mesh elements are created on extraction midsurface [2]. The calculation capacity and calculation efficiency must be considered when mesh partitioning. Finer the elements meshed are, more accordant the partitioned model is with the actual condition, while computing time and memory usage will be increased largely. After taking all the above factors into account synthetically, set the element size as 50mm×50mm for finite element analysis. The Spot-welds are used to simulate the connections between the end and main girders [7].

Due to that the bridge crane structure is symmetrical, take half of the model as research object in order to reduce the computing time and memory usage. The FE model of bridge cranes is shown in Fig. 3.

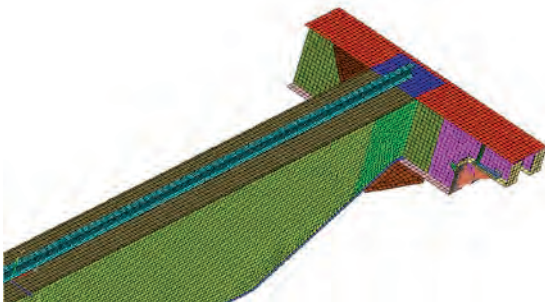


Fig. 3. Finite element model

3.5. Loading and static analysis

Both end girders and main girders are processed as simply supported beams [12, 13, 14]. Loading is illustrated as in Fig.4.

Constraint loadings of the crane are described as follows:

The movement in x, y, z directions and the rotation in z direction of position 1 are restrained;

The movement in y, z direction and the rotation in z direction of position 4 are restrained;

The movement in z direction and the rotation in x, y direction of position 2, 3 are restrained because of the symmetry.

The loadings on both of the main girders are as follows:

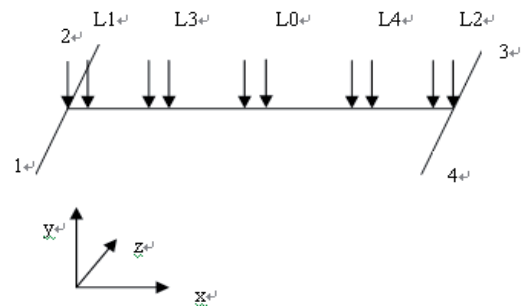


Fig. 4. Loadings illustration

- Rated hoisting loading : = 50 t
- The car mass is 15.765 t
- Self-vibration load factor = 1.1
- Lifting dynamic load factor = 1.14
- Horizontal inertial force of Crane as volume force: acceleration is 0.32m/s².
- Cart gravity as volume force

L0, L1, L2, L3, L4 denote the loadings on different positions of one main girder respectively called five work conditions, and the magnitude of the loadings (L0, L1, L2, L3, L4) is 322.2485 KN. Five work conditions are calculated in finite analysis as Table 1.

Table 1. Five work conditions description

Work conditions	Cart gravity (m/s ²)	Cart mass (t)	Self-vibration factor	Horizontal inertial force of crane (m/s ²)	Rotated loading (t)	Lifting move load factor	Load position
1	9.8	15.765	1.1	0.32	50	1.14	Middle of the beam
2	9.8	15.765	1.1	0.32	50	1.14	Left end of the beam
3	9.8	15.765	1.1	0.32	50	1.14	Right end of the beam
4	9.8	15.765	1.1	0.32	50	1.14	Left 1/4 of the beam
5	9.8	15.765	1.1	0.32	50	1.14	Right 1/4 of the beam

According to requirements of the crane design in GBT 3811-2008 "Crane Design" combined with actual usage, requirements for the stiffness of the crane girder are as follows:

$$f \leq \frac{1}{800} s$$

Where, f is the deflection displacement, S is the span of the crane [4].

And requirements for the stress of the crane girder are as follows:

- Material: Q345;
- Yield stress ;
- Allowable stress defined by engineering design.

After Loading on different locations of the main girder, the results of finite element analysis are shown in Fig. 5 and Fig. 6.

Analyzing and comparing different conditions of loads to obtain the conclusions that when loading on the middle of the main girder, the maximum displacement of 40.3 mm appears on the middle of the main girder, and the maximum stress of 91.6 MPa occurs on the middle of the main girders. According to the results of FEA, the total mass of the initial model is 18.9 t.

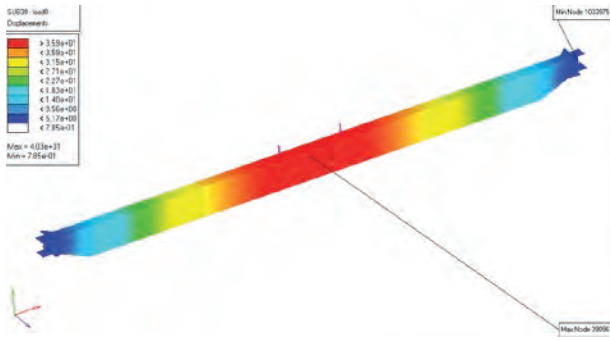


Fig. 5. Displacement cloud

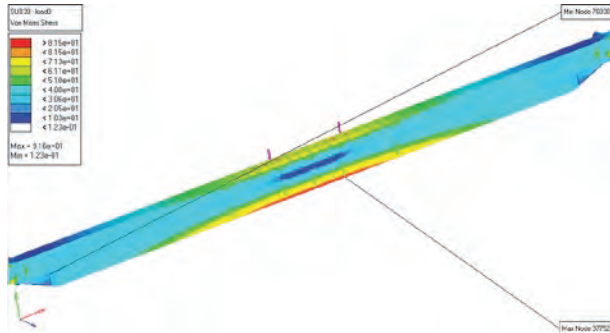


Fig. 6. Stress cloud

3.6. Structural optimization of double girder crane

3.6.1. Shape optimization

The shape optimal mathematical model is proposed as follows which takes the minimum volume as objective function, the height and width of the crane as design variables, and the scopes of stress, strain energy, modal as constraints:

$$\text{Min} \quad V'(X) = V'(\text{Height}', \text{Width}')$$

$$\text{Design variables:} \quad \begin{aligned} -5 \leq \text{Height}' \leq 20 \\ -5 \leq \text{Width}' \leq 20 \end{aligned}$$

$$C_j = \frac{1}{2} u_j^T f_j \leq 1.1 \times 10^7 J \quad j = 1, \dots, 5$$

$$\text{S.T.} \quad \begin{aligned} Ku &= f \\ \sigma &\leq 150 \text{ MPa} \\ F &\geq 3 \end{aligned}$$

Where, $V'(X)$ denotes the volume fraction; C_j denotes the total strain energy of the crane under the j^{th} load; K denotes the stiffness matrix of the system; f denotes the load; u denotes the node displacement vector under the load f ; σ denotes the stress; F denotes the natural frequency. Objective function $V'(X)$, constraint function C_j and σ can be obtained from structural response of the finite element analysis.

Use optistruct solver to optimize the girder by selecting morph optimization tool, the optimization results of the main girder are shown as follows:

$$\text{Volume} = 2.2\text{E}+09 \text{ mm}^3, \text{ Mass} = 17.36 \text{ t}$$

$$\text{Height}' = 1.03, \text{ Width}' = 1.74$$

After shape optimization:

$$\text{Height} = 1724 \text{ mm} - 1.03 \times 50 \text{ mm} = 1672.5 \text{ mm}$$

$$\text{Width} = 600 \text{ mm} - 1.74 \times 50 \text{ mm} = 513 \text{ mm}$$

$$\text{Height/Width} = 1672.5/513 = 3.26$$

By analyzing the results of finite element analysis, the structure performance (including strength, stiffness and modal) after topology optimization meet the requirements of crane design specifications greatly, which are shown in Fig.7 and Fig. 8.

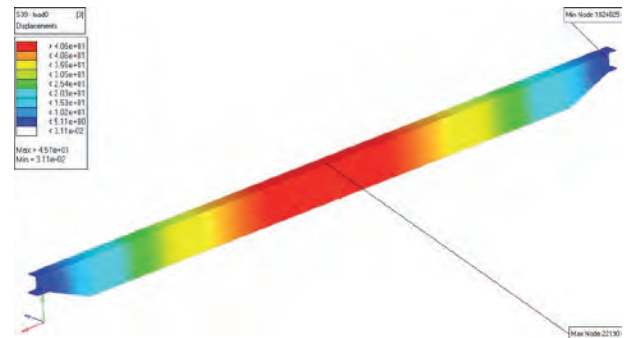


Fig. 7. Displacement cloud-Shape optimization

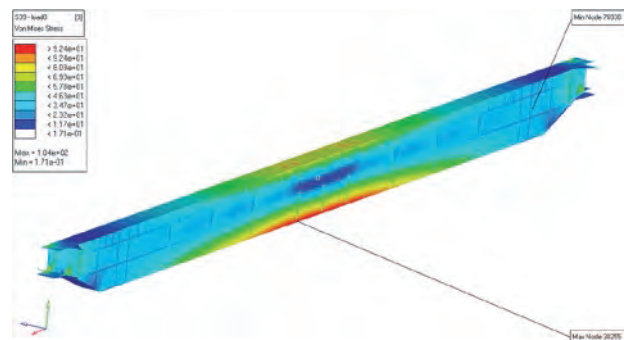


Fig. 8. Stress cloud-Shape optimization

Analyzing and comparing different conditions of loads to obtain the conclusions that when loading on the middle of the main girder, the maximum displacement of 45.7 mm appears on the middle of the main girder, and the maximum stress of 98.6 MPa occurs on the middle of the main girders. The total mass of the model after shape optimization is 17.4t, which has reduced by 7.9%.

Compare the maximum displacement and maximum stress before and after topology optimization, the result is given as in Table 2.

Table 2. Comparison of the stress and displacement

Load step	Before		Afer	
	Stress (MPa)	Displacement (mm)	Stress (MPa)	Displacement (mm)
L0	91.6	40.3	104	45.7
L1/L2	80.2		87.2	
L3/L4	74.5		74.4	

The above analysis results show that structure performance of the various plates, some materials of which have been reasonably removed, meets the design requirements as well. Meanwhile, the total mass of structure is 17.4 t, which has reduced by 1.5 t.

3.6.2. Size optimization

Furth optimizing of the structure after shape optimization was carried out in our research. Taking the minimum volume as the objective function, the thicknesses of the plates as the design variables, the scopes of the stress, strain energy and modal as constraints, the size optimal mathematical model is proposed as follows:

$$\text{Min} \quad V(X) = V(x_1, x_2, \dots, x_{18})$$

$$C_j = \frac{1}{2} u_j^T f_j \leq 1.1 \times 10^7 J \quad j = 1, \dots, 5$$

$$\begin{aligned} \text{S.T.} \quad & Ku = f \\ & \sigma \leq 150 \text{ MPa} \\ & F \geq 3 \end{aligned}$$

Where denote the thicknesses of plates, denotes the total volume of the crane, the rest of variable parameters denotes as the above. Use the Optistruct solver to optimize girders by size optimization tool. The optimization results of the thicknesses of the plates are shown in the Table 3.

Table 3. Comparison the thicknesses before and after optimization

Main optimal size	Before (mm)	After (mm)
Upper plates	24	20.9
Upper plates 1	18	10.3
Upper plates 2	24	21.1
Small Ribbed plates	8	10
Big Ribbed plates	8	5.1
Junction plate	40	27.7

By analyzing the results of size optimization, the structure performance (including strength, stiffness and modal) after topology optimization meet the requirements of crane design specifications greatly. The results of finite element analysis after size optimization are shown in Fig. 9 and Fig. 10.

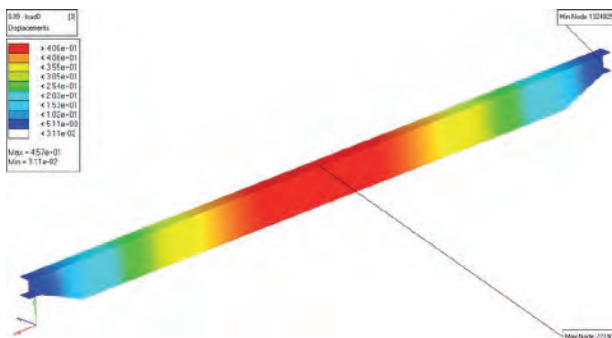


Fig. 9. Displacement cloud- Size optimization

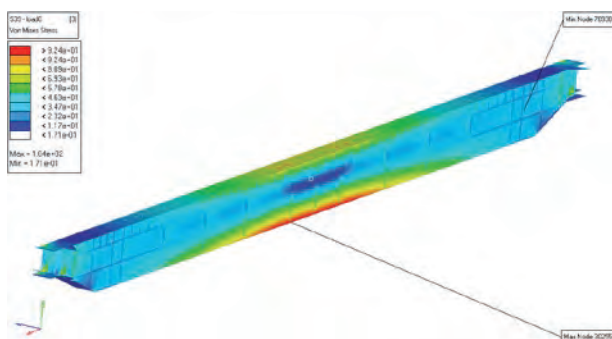


Fig. 10. Stress cloud- Size optimization

The maximum displacement of 46.4 mm appears on the middle of the main girder, and the maximum stress of 135 MPa occurs on the end of the main girders. The total mass of the model after size optimization is 17.6 t, which has reduced by 6.9%.

The comparison of initial model and final model is shown in the Table 4.

Table 4. Comparing the stress and displacement

Load step	Initial model		Final model	
	Stress (MPa)	Displacement (mm)	Stress (MPa)	Displacement (mm)
L0	91.6	40.3	135	46.4
L1/L2	80.2		132	
L3/L4	74.5		126	

From the above analysis results, it can be found easily that the structure performance after shape and size optimization meets the requirements of crane design specifications greatly. Moreover, after size optimization, the total mass of the main girder changes into 17.6 t which has been reduced by 1.3 t.

3.6.3. Topology optimization

Furth optimizing of the structure after shape and size optimization was carried out. The topology optimal mathematical model is proposed as follows which takes the minimum volume fraction as objective function, the material density of each element as design variables, and the scopes of stress, strain energy, modal as constraints:

$$\text{Min} \quad X = x_1, x_2, \dots, x_n$$

$$C_j = \frac{1}{2} u_j^T f_j \leq 1.1 \times 10^7 J \quad j = 1, \dots, 5$$

$$\begin{aligned} \text{S.T.} \quad & Ku = f \\ & \sigma \leq 150 \text{ MPa} \\ & F \geq 3 \end{aligned}$$

Where, $X = x_1, x_2, \dots, x_n$ denotes the material density of each element; and the rest of variable parameters denotes as the above. Use Optistruct solver to optimize the girder by selecting Topology Optimization tool, the optimization results of the main girder are shown in Fig. 11.



Fig. 11. Density graph-Topology optimization

By analyzing the results of topology optimization, the structure performance (including strength, stiffness and modal) after topology optimization meet the requirements of crane design specifications greatly. The results of finite element analysis after topology optimization are shown in Fig. 12 and Fig. 13.

Analyzing and comparing different conditions of loads to obtain the conclusions that when loading on the middle of the main girder, the maximum displacement of 39.8 mm appears on the middle of the main girder, and the maximum stress of 116 MPa occurs on the end of the main girders. The total mass of the model after topology optimization is 17.0 t, which has reduced by 10.05%.

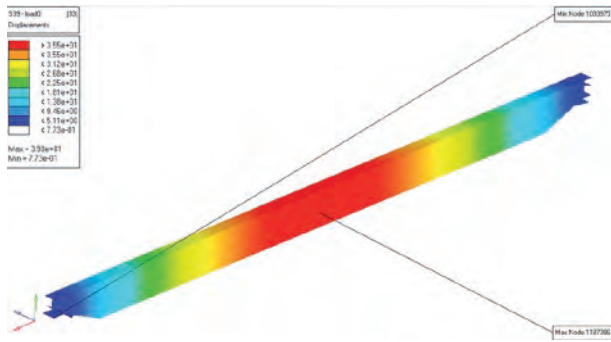


Fig. 12. Displacement cloud – Topology optimization

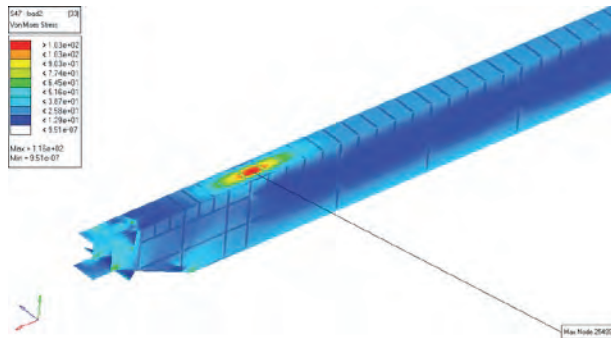


Fig. 13. Stress cloud – Topology optimization

Compare the maximum displacement and maximum stress before and after topology optimization, the result is given as in Table 5.

Table 5. Comparison of the stress and displacement

Load step	Before		Afer	
	Stress (MPa)	Displacement (mm)	Stress (MPa)	Displacement (mm)
L0	91.6	40.3	88.9	39.8
L1/L2	80.2		109	
L3/L4	74.5		116	

The above analysis results show that structure performance of the various plates, some materials of which have been reasonably removed, meets the design requirements as well. Meanwhile, the total mass of structure is 17.0 t, which has reduced by 1.9 t.

3.7. Comprehensive “shape+size” optimization

The comprehensive optimization means to carry out size optimization for the crane model obtained after shape optimization. That is to remodelling according to shape optimization result and make size optimization. The optimization variables, constraint function and objective function are the same as mathematical optimization model of size optimization. The optimization results are shown as follows:

Volume = 2.04E+09 mm³ Mass = 16.1 t

Table 6. Comparison the thicknesses before and after optimization

Main optimal size	Before (mm)	After (mm)
Upper plates	24	21.5
Upper plates 1	18	8.7
Upper plates 2	6	6
Small Ribbed plates	6	6
Big Ribbed plates	8	5.2
Junction plate	8	3

The optimization results of the thicknesses of the plates are shown in the Table 6.

By analyzing the results of size optimization, the structure performance (including strength, stiffness and modal) after topology optimization meet the requirements of crane design specifications greatly. The results of finite element analysis after size optimization are shown in Fig. 14 and Fig. 15.

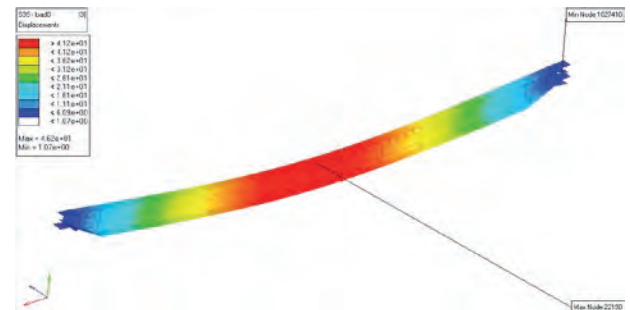


Fig. 14. Displacement cloud – “shape+size” optimization

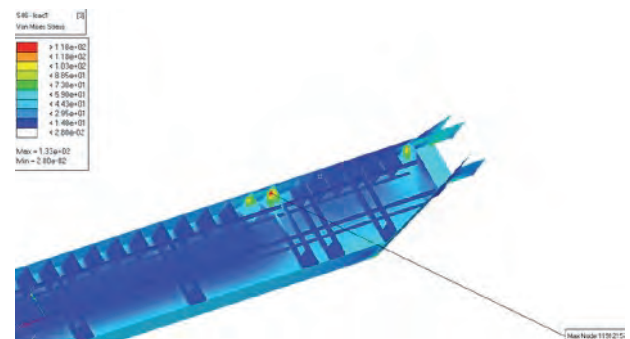


Fig. 15. Stress cloud – “shape+size” optimization

The comparison of initial model and final model is shown in the Table 7.

Table 7. Comparing the stress and displacement

Load step	Initial model		Final model	
	Stress (MPa)	Displacement (mm)	Stress (MPa)	Displacement (mm)
L0	91.6	40.3	125	46.2
L1/L2	80.2		128	
L3/L4	74.5		133	

From the above analysis results, it can be found easily that the structure performance after shape and size optimization meets the requirements of crane design specifications greatly. Moreover, after size optimization, the total mass of the main girder changes into 16.1 t which has been reduced by 14.8%.

3.8. Comprehensive “shape+size+topology” optimization

The comprehensive optimization means to carry out topology optimization for the crane model obtained after “shape+size” optimization. That is to remodelling according to “shape+size” optimization result and make topology optimization. The optimization variables, constraint function and objective function are the same as mathematical optimization model of topology optimization. The optimization results are shown as follows:

Mass=15.8t.

The optimization results of the main girder are shown in Fig.16.

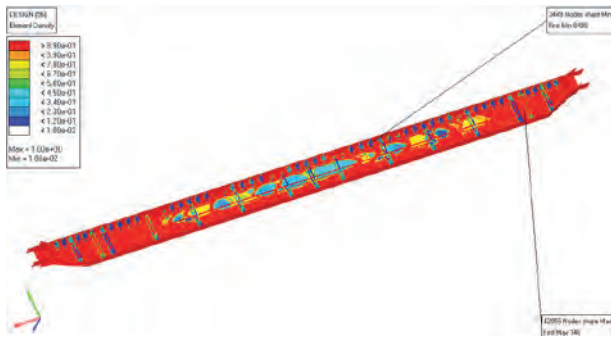


Fig. 16. Density graph – “shape+size+topology” optimization

By analyzing the results of topology optimization, the structure performance (including strength, stiffness and modal) after optimization meet the requirements of crane design specifications greatly. The results of finite element analysis after topology optimization are shown in Fig. 17 and Fig. 18:



Fig. 17. Displacement cloud – “shape+size+topology” optimization

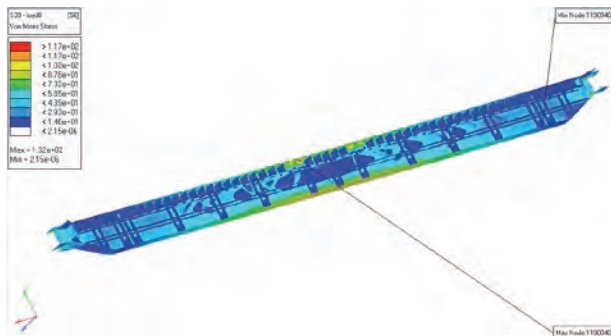


Fig. 18. Stress cloud – “shape+size+topology” optimization

Compare the maximum displacement and maximum stress before and after topology optimization, the result is given as in Table 8.

Table 8. Comparison of the stress and displacement

Load step	Before		After	
	Stress (MPa)	Displacement (mm)	Stress (MPa)	Displacement (mm)
L0	91.6	40.3	132	46
L1/L2	80.2		132	
L3/L4	74.5		128	

The above analysis results show that structure performance of the various plates, some materials of which have been reasonably removed, meets the design requirements as well. Meanwhile, the total mass of structure is 15.5 t, which has reduced by 18%.

3.9. Cross-section optimization

The optimization means to carry out size optimization for plate thickness of each plate of main girder, so as to realize Cross-section optimization design of main girder.

Table 9. Design variables and their range

No	Design variable	Initial value (mm)	Lower range value (mm)	Higher range value (mm)
1	Up1 (up plates)	24	1	50
2	Up2 (up plates)	24	1	50
3	Up3 (up plates)	24	1	50
4	Down1 (under plates 2)	24	1	50
5	Down2 (under plates 2)	24	1	50
6	Down3 (under plates 2)	24	1	50
7	Down18 (under plates 1)	18	1	30
8	Ribbed plates1	8	1	10
9	Ribbed plates2	8	1	10
10	Ribbed slab	8	1	10
11	Left1 (sternum)	6	4	15
12	Left2 (sternum)	6		15
13	Left3 (sternum)	6	4	15
14	Right1 (sternum)	6	4	15
15	Right2 (sternum)	6	4	15
16	Right3 (sternum)	6	4	15

Use the Optistruct solver to optimize girders by size optimization tool, the optimization results of the main girder are shown as follows:

Volume= 1.97E+09 mm³, Mass = 15.5t

The optimization variable values are shown in the Table 10.

Table 10. Comparison the thicknesses before and after optimization

No	Design variable	Before (mm)	After (mm)
1	Up1 (up plates)	24	1
2	Up2 (up plates)	24	1
3	Up3 (up plates)	24	1
4	Down1 (under plates 2)	24	1
5	Down2 (under plates 2)	24	1
6	Down3 (under plates 2)	24	1
7	Down18 (under plates 1)	18	1
8	Ribbed plates1	8	1
9	Ribbed plates2	8	1
10	Ribbed slab	8	1
11	Left1 (sternum)	6	4
12	Left2 (sternum)	6	
13	Left3 (sternum)	6	4
14	Right1 (sternum)	6	4
15	Right2 (sternum)	6	4
16	Right3 (sternum)	6	4

By analyzing the results of finite element analysis, the structure performance (including strength, stiffness and modal) after topology

optimization meet the requirements of crane design specifications greatly, which are shown in Fig. 19 and Fig. 20.

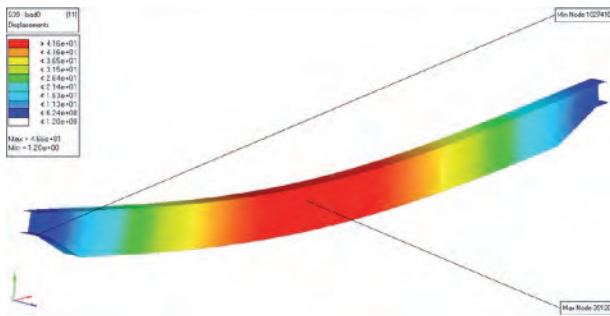


Fig. 19. Displacement cloud – Cross-section optimization

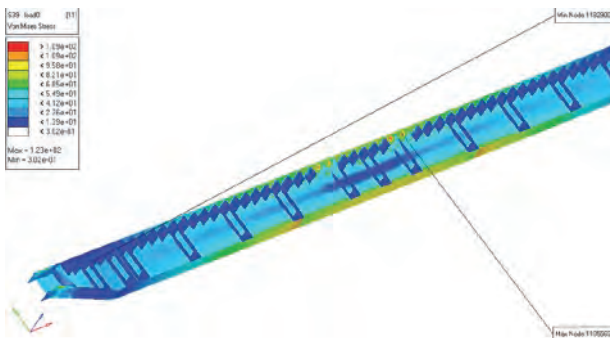


Fig. 20. Stress cloud – Cross-section optimization

Analyzing and comparing different conditions of loads to obtain the conclusions that when loading on the middle of the main girder, the maximum displacement of 46.6 mm appears on the middle of the main girder, and the maximum stress of 123 MPa occurs on the middle of the main girders. The total mass of the model after shape optimization is 15.5 t, which has reduced by 18%.

Compare the maximum displacement and maximum stress before and after topology optimization, the result is given as in Table 11.

Table 11. Comparison of the stress and displacement

Load step	Before		After	
	Stress (MPa)	Displacement (mm)	Stress (MPa)	Displacement (mm)
L0	91.6	40.3	123	46.6
L1/L2	80.2		108	
L3/L4	74.5		110	

The above analysis results show that structure performance of the various plates, some materials of which have been reasonably removed, meets the design requirements as well. Meanwhile, the total mass of structure is 15.5 t, which has reduced by 3.4 t.

3.10. Overall stability analysis of main girder

According to the requirements of “the crane design manual” for box section structure, “when aspect ratio (height/width) denoted by $h/b \leq 3$ or $3 < h/b \leq 6$ & $\frac{l}{b} \leq 95 \frac{235}{\sigma_s}$, the lateral buckling stability of the flexural components don't need verify.”

In our research, the results are as follows:

Before optimization: $h=1724$ mm, $b=600$ mm, $h/b=2.87$, so $h/b \leq 3$,

After optimization: $h=1742$ mm, $b=540$ mm, $h/b=3.19$, and $l=31500$ mm, $l/b=58.3$, $\sigma_s=253$ MPa. So $3 < h/b \leq 6$ & $\frac{l}{b} \leq 95 \frac{235}{\sigma_s}$.

Therefore, lateral buckling stability conforms to the design requirements.

4. System-level energy-saving optimization design of bridge crane

Energy-saving transmission design is researched by our research group in dynamic simulation and speed regulation of hoisting mechanism as well as optimization and innovation of transmission mechanism scheme reported in literature [13, 14]. Thus, self-vibration load factor in Section 3.4 is reduced from 1.14 to 1.11 under VVVF and the car mass in Section 3.4 is reduced from 15.765 t to 14.4 t. System-level multidisciplinary energy-saving optimization design of bridge crane can be further carried out with energy-saving transmission design results feedback to energy-saving optimization design of metal structure. By repeating the above modelling and analysis in Section 3, the system-level multidisciplinary energy-saving optimization results are shown in Table 12.

Table 12. System-level energy-saving optimization results

Optimization method	Mass after optimization (t)	Percentage decrease
	18.9	
Shape optimization	17.1	9.52%
Size optimization	17.3	8.46%
Topology optimization	16.9	10.58%
“Shape+size” optimization	15.6	17.46%
“Shape+size+topology” optimization	15.5	17.99%
Cross-section optimization	14.9	21.16%

5. Conclusions

The framework of energy-saving optimization design of bridge crane is proposed. And the structure optimization design of bridge crane by using finite element analysis technology is discussed in this paper in detail. This research seeks to get more reasonable, lightweight and energy-saving structure on the basis of insuring the performances of crane, and to provide the design reference for bridge crane. The main results of this research can be concluded as follows:

1. The results of finite element analysis show that the concentrated stress occurs on the middle of main girders under full load.
2. For the cranes which meet the design requirements, shape optimization is researched. The total mass of the structure after shape optimization changes into 17.4 t / 17.1 t (optimization design of metal structure/system-level energy-saving optimization) and it is reduced by 1.5 t / 1.8 t compared with the initial model.
3. Size optimization is researched after shape optimization. The total mass of the structure after size optimization changes into 17.6 t / 17.3 t and it is reduced by 1.3 t / 1.6 t.
4. Topology optimization based on density methodology is used after shape and size optimization. The total mass of the structure after topology optimization changes into 17.0 t / 16.9 t and it is reduced by 1.9 t / 2.0 t compared with the initial model.
5. The total mass of the structure after “shape+size” optimization changes into 16.1 t / 15.6 t and it is reduced by 2.8 t / 3.3 t compared with the initial model.

6. The total mass of the structure after "shape+size+topology" optimization changes into 15.5 t/15.5 t and it is reduced by 3.4 t/3.4 t compared with the initial model.
7. The total mass of the structure after cross-section optimization changes into 15.5 t/14.9 t and it is reduced by 3.4 t/4.0 t compared with the initial model.

Finite element structure optimization technique not only can assure stiffness, strength and other performances requirements of the crane, but also can greatly reduce the use of materials by lightweight design.

Acknowledgements: *This work was financially supported by National Foundation of General Administration of Quality Supervision and Inspection (2012QK178), Program of Science Foundation of General Administration of Quality Supervision and Inspection of Jiangsu Province (KJ103708) and "excellence plans-zijin star" Foundation of Nanjing University of Science. The supports are gratefully acknowledged.*

References

1. Dongchen Qin, Yingjia Wang, Xiaofang Zhu, Jiangyi Chen, Zhuli Liu. Optimized design of the main beam of crane based on MSC1Patran/Nastran. *Machinery for Lifting and transportation* 2007;7:24–26.
2. Deng Hongguang, Bai Tianxiang, Sheng Yanzhong, You Sikun. The optimum design of single girder bridge-crane based on FEM. *Steel construction* 2009;2:46–48.
3. Fan Yuanxun, Bu Tingchun, Li Shuishui. Co-simulating on lifting dynamic load of bridge crane based on ADAMS and MATLAB. *Heavy Machinery* 2011; (5): 30–32.
4. GBT3811-2008 "Crane design standard".
5. Kwasniewski L, Hongyi Li, Wekezer J et al. Finite element analysis of vehicle-bridge interaction. *Finite Element in Analysis and Design* 2006; 42: 950–959.
6. Li Shuishui, Fan Yuanxun, Bu Tingchun. Introduction for new hoisting mechanism of a crane. *Machinery Design & Manufacture* 2012; (5): 275–276.
7. Luo Hui, Yi Haipeng, Luo Huixin. The malfunction about the bridge crane girder based on FEM. *Construction Machinery* 2007; 2: 67–69.
8. Styles M, Comston P, Kalyanasundaram S. Finite element modeling of core thickness effects in aluminum foam/composite sandwich structures under flexural loading. *Composite Structures* 2008; 86: 227–232.
9. Ning Zhaoyang, Ruo Yongxin, Ren Chengao, et al. ANSYS application in design of the main beam of crane. *Machinery for Lifting and transportation* 2008; 5: 31–33.
10. Shukla PP, Lawrence J. Mathematical modelling of the fibre laser surface processing of a zirconia engineering ceramic by means of three-dimensional finite-element analysis. *Proceedings of the Institution of Mechanical Engineers, Part C (Journal of Mechanical Engineering Science)* 2011; 225(C4): 949–64.
11. Markowski T, Mucha J, Witkowski W. FEM analysis of clinching joint machine's C-frame rigidity. *Eksplotacja i Niezawodność – Maintenance and Reliability* 2013; 15(1): 51–57.
12. Wang Fumian. Discussion about the static stiffness design of the bridge crane and the related problems. *Machinery for Lifting and transportation* 2009; 12: 42–44.
13. Yang Menglin, Qin Dongchen, Liu Zhuli, Wang Ying-jia. Research on structure optimization design of bridge crane box beam. *Design and research* 2008; 4: 23–24.
14. Zhixin Zhang. The Application of ANSYS into Optimizing Design of Main Beam in Joist Portal Crane. *Machinery technology and management on construction* 2009; 8: 91–93.

Prof. Tong YIFEI

Researcher Tang ZHAOHUI M.E. candidate

Researcher Ye WEI M.E. candidate

Researcher Yang ZHEN M.E.

Nanjing University of Science and Technology, School of Mechanical Engineering 402, 210094 Nanjing, People's Republic of China

E-mails: tyf51129@yahoo.com.cn, 453651434@qq.com,

837288965@qq.com gaochunyangzhen@163.com

Anna ŻYCZYŃSKA

THE PRIMARY ENERGY FACTOR FOR THE URBAN HEATING SYSTEM WITH THE HEAT SOURCE WORKING IN ASSOCIATION

WSPÓŁCZYNNIK NAKŁADU NIEODNAWIALNEJ ENERGII PIERWOTNEJ DLA MIEJSKIEGO SYSTEMU CIEPŁOWNICZEGO ZE ŹRÓDŁEM CIEPŁA PRACUJĄCYM W SKOJARZENIU*

The paper explores the methodology for determining primary energy factor based on EU directives and domestic regulations. The estimation of the above mentioned coefficient for a selected urban heating system was performed on the basis of real measurements obtained during the operation of a system and conveyed by the producers as well as heating distributor. The analysis was conducted for the several variants and extended over four years, that is from 2008 to 2011. The results achieved in the operating conditions were compared to the values obligatory to apply in calculations.

Keywords: primary energy, primary energy factor, final energy, cogeneration, heating system, heat source.

W artykule przedstawiono metodykę określania współczynnika nakładu nieodnawialnej energii pierwotnej w oparciu o dyrektywy UE oraz przepisy krajowe. Na podstawie rzeczywistych pomiarów uzyskanych podczas eksploatacji układu i przekazanych przez producentów i dystrybutora ciepła, przeprowadzono obliczenia w/w współczynnika dla wybranego miejskiego systemu ciepłowniczego. Analizę wykonano dla kilku wariantów i objęto nią okres czterech lat tj. od 2008 r. do 2011 r. Wyniki otrzymane w warunkach eksploatacyjnych zostały porównane z wartościami obowiązującymi do stosowania w obliczeniach.

Słowa kluczowe: energia pierwotna, współczynnik nakładu nieodnawialnej energii pierwotnej, energia końcowa, kogeneracja, system ciepłowniczy, źródło ciepła.

1. Preface

The energy policy of many countries aims at reducing the energy consumption, and thereby, the CO₂ emission into the atmosphere. The generation of energy in cogeneration systems and the proper heating distribution to the final consumer play a vital part in such a case. Cogeneration is a technological process in which heat and electric energy are simultaneously generated, as opposed to the separate generation of electric energy in a typical condensation power plant and heat in a classic heating station. For this reason, currently, for centralised heating systems, primary energy factor is defined in order to generate and deliver the energy carrier or energy to the building (w_i). The share of electric energy to heat buildings is reduced due to its high values w_i [1, 2, 3, 5, 6, 9, 10, 12, 13, 15, 17, 18]. The coefficient w_i is used to determine the annual computational index of the demand for nonrenewable primary energy to heat, ventilate, cool and prepare warm water (marked as EP). According to the domestic regulations, EP is one of the decisive parameters in meeting the requirements in terms of energy economy and maintaining its consumption at the rationally low for a building. The coefficient w_i determines the final result of calculations of energy characteristics of a building which is featured in the energy certificate. EP is expressed in kWh during the year per unit of room area of adjustable temperature [kWh/m²year]. Its small values indicate low demand of a building for primary energy. The EP value is defined on the basis of the demand of a building for usable and final energy. The quantity of usable energy is calculated at computational parameters as well as the so called standard edge conditions of external and internal environment. However, if final energy is calculated, the total efficiency of installation systems in which the building is equipped is taken into account. According to the EU and domestic directives, the computation of final energy into nonrenew-

able primary energy is performed by the expenditure coefficient of nonrenewable primary energy. In view of the above mentioned fact, the value of such a coefficient for heating system (w_H) has a decisive impact on EP index of a building, similarly to the expenditure coefficients of nonrenewable primary energy resulting from the use of energy carriers, such as coal, heating oil, natural gas, renewable energy or electric energy.

In accordance with the domestic regulations, the value of coefficient w_i should be assumed from [14] or calculated on the basis of information on a heating system. In this paper, the method of calculations and the obtained values of coefficient w_i as w_H (only for heating) for selected urban heating system are presented. The analysis was conducted for several variants on the basis of the real outcomes of measurements over the years 2008-2011 which were obtained in operating conditions from the producers and a heating distributor. The achieved final results were compared to the values contained in the current domestic regulations.

2. The Description of Urban Heating System (UHS)

Heat required by heating demands for the selected urban heating system is produced by the two sources (designated 'big' as A and 'small' as B) which produce electric energy as well as heat in cogeneration, and in the case of the rise in the demand of heat, additionally, in the conventional way. The urban heating system is the main recipient of heat obtained from the above mentioned sources. It is only the small amount of heat that is sold directly by producers beyond this system. The diagrams of energy production in A source are presented in a fig.1, whereas in B source in a fig. 2. The distribution of heat is through low-parameter as well as high-parameter heat distribution network, individual network, and group network to four categories of

(*) Tekst artykułu w polskiej wersji językowej dostępny w elektronicznym wydaniu kwartalnika na stronie www.ein.org.pl

Table 1. The data typical of source A [4, 19]

Type of fuel	Parameter	2011 r.	2010 r.	2009 r.	2008 r.
Coal	Quantity [Mg]	21 181	47 391	20 904	20 845
	Calorific value [kJ/kg]	21 531	21 077	21 273	21 330
	Energy in fuel [GJ]	456 048	998 860	444 691	444 624
Natural gas	Quantity [tys. m ³]	272 166	248 451	227 427	230 216
	Calorific value [kJ/m ³]	36 132	36 116	36 099	36 217
	Energy in fuel [GJ]	9 833 902	8 973 056	8 209 887	8 337 733
Fuel oil (only for individual needs of a source)	Quantity [Mg]	152	219	17	32
	Calorific value [kJ/kg]	40 190	40 190	40 190	40 190
	Energy in fuel [GJ]	6 109	8 802	683	1 286
Total amount of energy in fuel [GJ]		10 296 059	9 980 718	8 655 261	8 783 643
Share of energy from fuel	Coal [%]	4,43	10,01	5,14	5,06
	Natural gas [%]	95,51%	89,90	94,85	94,92
	Fuel oil [%]	0,06	0,09	0,01	0,01
Electric energy production					
Sale of energy [GJ]		4 435 866	4 051 645	3 728 981	3 816 270
Individual needs [GJ]		44 557	56 210	23 382	37 246
Total amount of energy [GJ]		4 480 423	4 107 856	3 752 363	3 853 516
Share of sale [%]		99,0	98,6	99,4	99,0
Share of individual needs [%]		1,0	1,4	0,6	1,0

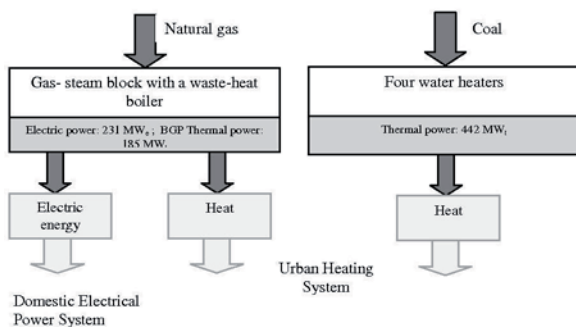


Fig. 1. The diagram of energy generation in source A.

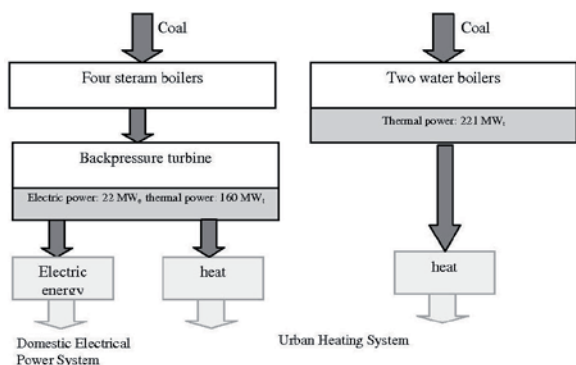


Fig. 2. The diagram of energy generation in source B.

recipients. The area of supply is divided into three spheres, such as supply only through A source, or only through B source, and through the third sphere, common for the both sources. In 2011 the participation of source A in the total sale of heat to the heat system was 68,1%, whereas source B 31,9% [4, 11, 19]. The data typical of source A is presented in table 1, data concerning source B is shown in table 2, whereas data referring to heat consumption from both sources over the years 2008–2011 is in table 3.

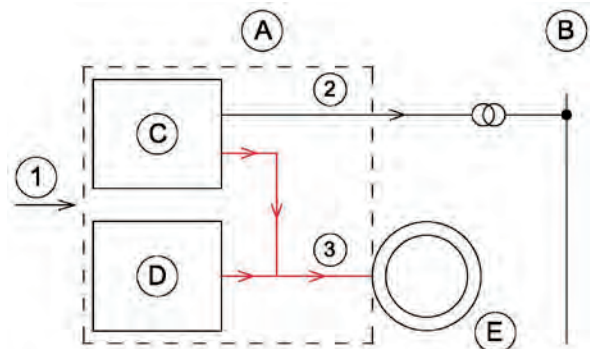


Fig. 3. A diagram illustrating the method of balancing energy in the existing system: A – heat and electric energy source; B – electro-energetic network; C – the production of electric energy and heat in association; D – the production of heat; E – heating consumers; 1 – energy supplied in fuel; 2 – electric energy (sold and the individual needs of source); 3 – heat supplied to the consumer [7]

Table 2. The data typical of source B [4, 19]

Type of fuel	Parameter	2011 r.	2010 r.	2009 r.	2008 r.
Coal	Amount [Mg]	115 030	124 914	121 185	124 543
	Calorific value [kJ/kg]	20 351	20 796	21 364	20 935
	Energy in fuel [GJ]	2 340 967	2 597 718	2 588 991	2 607 300
Natural gas (only for individual needs of a source)	Amount [tys. m ³]	20,6	16,9	17,8	34,3
	Calorific value [kJ/m ³]	36 742	36 585	36 423	36 093
	Energy in fuel [GJ]	756	617	647	1 237
Total amount of energy in fuel [GJ]		2 341 723	2 598 335	2 589 638	2 608 538
The participation of energy from fuel	Coal [%]	99,97	99,98	99,97	99,95
	Natural gas [%]	0,03	0,02	0,03	0,05
The production of electric energy					
Sale of energy [GJ]		250 234	269 447	257 824	264 885
Individual needs [GJ]		49 962	52 098	51 556	58 237
The amount of energy in total[GJ]		300 196	321 545	309 380	323 122
Share of sale [%]		83,4	83,8	83,3	82,0
Individual needs share [%]		16,6	16,2	16,7	18,0

Table 3. Heat collection from sources A and B [4, 19]

Recipient	2011 r.	2010 r.	2009 r.	2008 r.
Urban Heating System (UHS) [GJ]	3 980 836	4 402 986	4 064 271	4 038 320
Source A[GJ] *)	172	196	191	189
Source B [GJ] *)	55 936	84 113	74 858	67 160
The amount of heat in total [GJ]	4 036 944	4 487 295	4 139 320	4 105 669
The participation of UHS [%]	98,610	98,121	98,187	98,360
The participation of source A [%] *)	0,004	0,004	0,005	0,005
The participation of source B [%] *)	1,386	1,874	1,808	1,636
*)recipients of heat outside UHS				

3. The Methodology for Determining Coefficient w_H

On the basis of [7, 8] as well as domestic assumptions in line with [14], presented in table 4, information obtained from the producers and distributor of heat, the dependence (1) is used in order to determine w_H for the urban heating system, assuming the production of electric and heat energy in association, according to the diagram shown in fig.3.

$$w_H = \frac{\sum_i Q_{P,i} \cdot w_i - \sum_j E_{EC,j} \cdot w_{el}}{\sum_k Q_{OD,k}} \quad (1)$$

where:

w_H – the expenditure coefficient of nonrenewable primary energy for the selected Urban heating system,

w_i – primary energy factor for i-th fuel assumed in accordance with the domestic principles presented in [14],

w_{el} – expenditure coefficient of nonrenewable primary energy for electric energy,

$Q_{P,i}$ – energy supplied in i-th fuel,

$E_{EC,j}$ – electric energy produced in j-tym energy source, used in a source and added to the domestic electro-energetic system,

$Q_{OD,k}$ – heat supplied by urban heating system to the k-th recipient.

4. The Results of Calculations

Calculations w_H were conducted by three methods and denoted as variants W1, W2 and W3 working on the following assumptions for every computational method:

W1 – according to the principles contained in the domestic regulations [14] when $w_{el} = 3,0$

W2 – it is assumed that source A is a condensed power station and is characterised by eigenvalue w_{el} A source, whereas for source B it is assumed $w_{el} = 3,0$ (on account of the lack of full information), average index w_{el}^* is determined as weighted mean in relation to electric energy produced in particular sources.

W3A – according to the principles contained in UE directives, that is assuming $w_{el} = 2,5$ [7],

W3B – according to the principles contained in UE directives, that is assuming $w_{el} = 2,8$ [8]

The values of primary energy, defined according to the current domestic regulations, and heat (with the assumptions as for variant W1) are presented in Fig. 4; whereas the relations between primary energy contained in natural gas and the final electric energy for heating source A, whose characteristics determines the value w_H , are shown in Fig. 5. The values of expenditure coefficient of electric energy on the assumptions as for variant W2 are presented in Fig. 6. The results of computations w_H for particular variants are provided in Table 5.

Table 4. Primary energy factor in line with [14]

No	Final energy carrier	Expenditure coefficient w_i
1	Fuel / Energy source	Heating oil
2		Natural gas
3		Liquid gas
4		Hard coal
5		Brown coal
6		Biomass
7		Thermal solar energy collector
8	Heat from cogeneration ¹⁾	Hard coal,,Natural gas ³⁾
9		Renewable energy (biogas, biomass)
10	Local heating systems	Heat from coal heating station
11		Heat from gas/oil heating station
12		Heat from biomass Heating station
13	Electric energy	Mixed production ²⁾
14		PV systems ⁴⁾

¹⁾ associated production of electric energy and heat,
²⁾ concerns supplying from systemic electro-energetic network,
³⁾ in case of lack of information on calorific parameters of network heat from heat and power station (cogeneration), it is assumed that $w_H = 1,2$,
⁴⁾ photovoltaic cells (the production of electric energy from solar energy)
comment: thermal solar collector – $w_H = 0,0$

Table 5. Expenditure coefficients of the consumption of nonrenewable primary energy (w_H) for particular variants [4, 19]

The coefficient of the consumption of non-renewable primary energy	2011	2010	2009	2008
variant W1	-0,1091*	0,1223	0,0445	0,0004
variant W2	0,5457	0,6716	0,5793	0,5823
variant W3A	0,4830	0,6158	0,5351	0,5090
variant W3B	0,1278	0,3197	0,2407	0,2038

*) in line with [2], in the case of negative values w_H , a value amounting to 0 must be assumed

Table 6. The share of production of electric energy to total energy generated in a source [4, 19]

	2011	2010	2009	2008
The production of heat in a source A - Q_{coA} [GJ]	3 103 499	3 369 995	2 964 692	2 932 408
The production of heat in a source B - Q_{coB} [GJ]	1 455 690	1 671 277	1 700 692	1 679 791
The production of electric energy in a source A - Q_{elA} [GJ]	4 480 423	4 107 856	3 752 363	3 853 516
The production of electric energy in a source B - Q_{elB} [GJ]	300 196	321 545	309 380	323 122
Index ϕ_{elA}	0,591	0,549	0,559	0,568
Index ϕ_{elB}	0,166	0,155	0,148	0,156

The amount of primary energy and the sale of heat on the assumptions as for variant W1

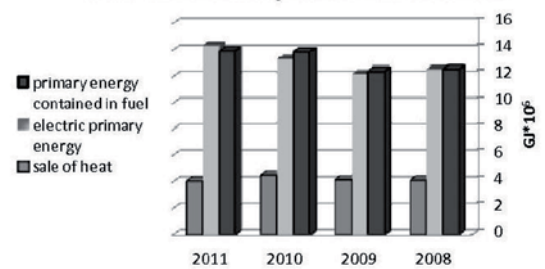


Fig. 4. The amount of primary energy contained in fuel, electric primary energy and the sale of heat on the assumptions as for variant W1

The amount of primary energy assuming variant W2

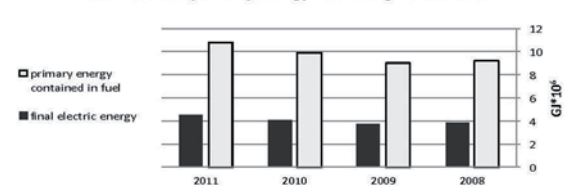
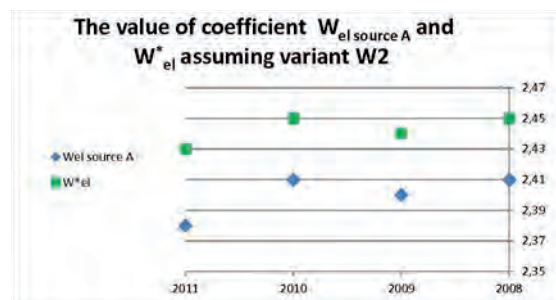


Fig. 5. The amount of primary energy contained in fuel and final electric energy assuming variant W2

In order to provide a full characteristic of heating system for both heat sources, the share of the production of electric energy, in relation to total energy generated in a given heat source according to dependence (2), is assumed. (computational results are shown in table 6).

$$f_{el} = \frac{Q_{el}}{Q_{el} + Q_{co}} \quad (2)$$

Fig. 6. The value of coefficient $W_{el \text{ source A}}$ and W_{el}^* assuming variant W2

5. Summary

Values w_H for particular computational variants, provided in tables 5, differ substantially due to the fact that value w_{el} is assumed to computations according to the dependence (1). After the analysis on the data obtained on the basis of the measurements of operating system and the achieved results, the best solution while calculating w_H for a heating system is to assume the expenditure coefficient of nonrenewable primary energy for the energy generation, typical of a given system ($w_{el \text{ source}}$ or w_{el}^*). Such a coefficient is dependent upon the structure of heat and electric

energy generation in a source as well as upon the conditions prevailing in a system during its operation. Thus it is justified to determine the actual value of coefficient for the electric energy, in contrast to assuming the value $w_{el} = 3$ (according to domestic regulations) in no respect of specificity of heating source operation. Thus in such a case, w_H assumes a negative value. As calculations show, the analysed urban heating system supplied by associated sources, value w_{el}^* altered insignificantly from 2,43 to 2,45 during the four-year research. Making use of the real value of coefficient w_{el}^* , one obtains a coefficient w_H for the system in 2011 at the level of 0,5457, which means that it is considerably lower than values in tables for the conventional energy carriers as well as value $w_H = 0,8$ contained in [14] for heat from cogeneration at natural gas and coal combustion.

According to the widely accessible information, it appears that in different cities in the country in heating systems, supplied by the

power and heat stations producing energy from cogeneration, primary energy factor is within $0,47 \div 0,80$. Therefore, assuming $w_{el} = 3$ which is recommended in the domestic regulations, is unjustified.

The value w_{el} should be lowered after collecting data from the sources producing energy in cogeneration in the whole country. Assuming the values $w_{el} = 2,8$ or $w_{el} = 2,5$, at the same structure of energy production, w_H is always positive and close to the values obtained in the sample computations in UE directives.

In 2011, heat energy, supplied by the analysed heating system, was at about 85% from the energy produced in cogeneration, which consequently, allowed for obtaining a very low w_H coefficient. For this reason, in accordance with ecological requirements as well as demands on nonrenewable primary energy, such a heating system is rated as the most appropriate source of building supply, located in the area of heat energy supply.

Bibliography

1. Balaras C, Droutsas K, Dascalaki E, Kontoyiannidis S. Heating energy consumption and resulting environmental impact of European apartment buildings. *Energy and Buildings* 2005; 37: 429–442.
2. Climent F, Pardo A. Decoupling factors on the energy–output linkage: The Spanish case. *Energy Policy* 2007; 35: 522–528.
3. Cursino dos Santos AH, Werneck Fagá MT, Moutinho dos Santos E. The risks of an energy efficiency policy for buildings based solely on the consumption evaluation of final energy. *Electrical Power and Energy Systems* 2013; 44: 70–77.
4. Data concerning the types, parameters and amounts of fuel consumption, as well as the generation and sale of electric and heat energy obtained by a producer and heating distributor over the years 2008–2011.
5. Georges L, Massart C, Van Moeseke G, De Herde A. Environmental and economic performance of heating systems for energy-efficient dwellings: Case of passive and low-energy single-family houses. *Energy Policy* 2013; 40: 452–464.
6. Hassine I, Eicker U. Impact of load structure variation and solar thermal energy integration on an existing district heating network. *Applied Thermal Engineering* 2013; 50: 1437–1446.
7. Heating systems in buildings – Method for calculation of system energy requirements and system efficiencies – Part 2.2.5. Space heating generation systems, the performance and quality of district heating and large volume system CEN/TC 228 WI 00228 027, 2004–12.
8. Heating systems in buildings – Method for calculation of system energy requirements and system efficiencies – Part 4-5 Space heating generation systems, the performance and quality of district heating and large volume system CEN/TC 228 WI 027, 2006-08, prEN 15316-4-5: 2006 (E).
9. Howarda B, Parshall L, Thompson J, Hammer S, Dickinson J, Modi V. Spatial distribution of urban building energy consumption by end use. *Energy and Buildings* 2012; 45: 141–151.
10. Johansson P, Nylander A, Johnsson F. Primary energy use for heating in the Swedish building sector—Current trends and proposed target. *Energy Policy* 2007; 35: 1386–1404.
11. Cogeneration as a main part in the environment protection- the realisation of improvement policy of energetic efficiency by the producers and distributors of energy in Lublin District, on the basis of Lublin. Lublin Energy Company, Polish Energy Group Górnictwo and Conventional Energy S.A. branch in Lublin Wrotków, Megatem EC – Lublin LLC. conference: ECOFORUM Lublin: 09. 2011.
12. Landweher M, Jochem E. From primary to final energy consumption-Analysing structural and efficiency changes on the energy supply side. *Energy Policy* 1997; Vol.25: 697–702.
13. Loncar D, I. Ridjan I. Medium term development prospects of cogeneration district heating systems in transition country - Croatian case. *Energy* 2012; 48: 32–39.
14. The resolution of Ministry of Infrastructure from 6.11.2008 in the case of the methodology for the computations of energy characteristics of a building and flat or the part of a building as the separate technical-usable whole as well as the way of preparing a certificate of energy characteristics. (Dz.U. nr 201/2008 r., poz. 1240).
15. Shimoda Y, Nagota T, Isayama N, Mizuno M. Verification of energy efficiency of district heating and cooling system by simulation considering design and operation parameters. *Building and Environment* 2003; 43: 569–577.
16. The expenditure coefficient w_H of nonrenewable primary energy for heat distributed by Energy Company in Siedlce LLC Siedlce: 0.1. 2010.
17. Verda V, Colella F. Primary energy savings through thermal storage in district heating networks. *Energy* 2011; 36: 4278–4286.
18. Zhi-Ping S. Total energy system analysis of heating. *Energy* 2000; 25: 807–822.
19. Życzynska A, Surmacz P, Dyś G. The estimation of the index of primary energy expenditure for Lublin heating system as well as the amount of heat in urban heating system generated in cogeneration. Fundacja Rozwoju Politechniki Lubelskiej; Lublin: 03. 2012.

Anna ŻYCZYŃSKA, Ph.D. (Eng.)

Department of Historic Object Conservation

Faculty of Building and Architectures

Lublin University of Technology

Nadbystrzycka 40 street, 20-816 Lublin, Poland

E-mail: a.zyczynska@pollub.pl

INFORMATION FOR AUTHORS

Terms and Conditions of Publication:

- The quarterly „Maintenance and Reliability” publishes original papers written in Polish with an English translation.
- Translation into English is done by the Authors after they have received information from the Editorial Office about the outcome of the review process and have introduced the necessary modifications in accordance with the suggestions of the referees!
- Acceptance of papers for publication is based on two independent reviews commissioned by the Editor.

Fees:

- Pursuant to a resolution of the Board of PNTTE, as of 2009 the publication fee for one text is 600 zloty + VAT.
- Coloured graphical elements in the submitted text require agreement from the Editor and are charged extra.

Technical requirements:

- After receiving positive reviews and after acceptance of the paper for publication, the text must be submitted in a Microsoft Word document format.
- Drawings and photos should be additionally submitted in the form of graphical files in the *.tif, *.jpg or *.cdr (v. X3) formats.
- A manuscript should include (in accordance with the enclosed correct manuscript format: *.pdf, *.doc):
- names of authors, title, abstract, and key words that should complement the title and abstract (in Polish and in English)
- the text in Polish and in English with a clear division into sections (please, do not divide words in the text);
- tables, drawings, graphs, and photos included in the text should have descriptive two-language captions,
- if this can be avoided, no formulae and symbols should be inserted into text paragraphs by means of a formula editor
- references (written in accordance with the required reference format)
- author data – first names and surnames along with scientific titles, affiliation, address, phone number, fax, and e-mail address
- The Editor reserves the right to abridge and adjust the manuscripts.
- All submissions should be accompanied by a submission form.

Editor contact info: (Submissions should be sent to the Editor's address)

Editorial Office of „Eksplotacja i Niezawodność - Maintenance and Reliability”
Nadbystrzycka 36, 20-618 Lublin, Poland
e-mail: office@ein.org.pl

INFORMATION FOR SUBSCRIBERS

Fees

Yearly subscription fee (four issues) is 100 zloty and includes delivery costs.

Subscribers receive any additional special issues published during their year of subscription free of charge.

Orders

Subscription orders along with authorization to issue a VAT invoice without receiver's signature should be sent to the Editor's address.

Note

In accordance with the requirements of citation databases, proper citation of publications appearing in our Quarterly should include the full name of the journal in Polish and English without Polish diacritical marks, i.e.,

Eksplotacja i Niezawodność – Maintenance and Reliability.

No text or photograph published in „Maintenance and Reliability” can be reproduced without the Editor's written consent.